LYSOSOMAL STORAGE DISEASE PHENOTYPES IN INDUCED PLURIPOTENT STEM CELL MODELS OF HUNTINGTON'S DISEASE

A thesis submitted to Cardiff University for the degree of

Doctor of Philosophy

Brendan Patrick Kelly

School of Biosciences

2022

SUMMARY

Huntington's disease (HD) is a heritable, autosomal dominant, neurodegenerative disease associated with the loss of medium spiny neurons (MSNs), cognitive and motor defects, and ultimately death. Though it is a monogenic disease and is caused by an expanded CAG trinucleotide repeat in the huntingtin gene (*HTT*), the precise pathomechanism underlying HD is unknown. However, lysosomal expansion, lipid dyshomeostasis, defects in autophagy, and mitochondrial function, have all been reported in HD. These phenotypes are commonly observed in lysosomal storage disorders (LSDs) and in particular, similarities with Niemann Pick Type C disease (NP-C), suggest a link between the two diseases. Thus, the repurposing of n-butyl-deoxy-nojirimycin (miglustat), a competitive inhibitor of glycosphingolipid synthesis, which is currently used for treatment of NP-C, Gaucher, and Pompe diseases, has been suggested for treatment of HD.

This thesis aimed to assess lysosomal storage in HD, by using neural progenitors and neurons differentiated from HD patient-derived iPSCs, to compare HD cells to isogenic-corrected versions. We identified phenotypic differences in HD lines relative to the isogenic control cells, related to endolysosomal structure, lipid dyshomeostasis, autophagy, and mitochondrial structure and function. Miglustat treatment was associated with moderate improvement related to mitochondrial length, lipid storage, and autophagosome accumulation.

Finally, we report the generation of two HTT knockout lines, one of which was generated from the aforementioned HD patient-derived iPSCs. The HTT knockouts facilitated investigation into wildtype huntingtin function and conferred the ability to make three-way comparisons with which gain or loss of HTT function in HD could be approached. Importantly, the HTT knockouts allowed for interrogation into the relationship between HTT and Niemann-Pick type C1 (NPC1), the protein that is defective in NP-C disease. The results here failed to evidence a wildtype role for HTT related to NPC1, or to the lysosomal or late endosomal compartments. However, dysregulation in autophagy and gene expression related to development were identified in HTT knockouts, which could help to

resolve wildtype HTT function. Together, this data has expanded the basic cell biology of HD and supplied new tools with which huntingtin function might be examined.

ACKNOWLEDGEMENTS

I would sincerely like to thank my supervisors Nick Allen an Emyr Lloyd-Evans. I am extremely grateful for having had the opportunity to work with and learn from each of you. I would also like to thank Richard Moon and Idorsia for funding this project. Also, thank you to Amy Sprowles and Sean Craig, and all of the other amazing science teachers that have inspired and helped me, along the way.

I would like to thank my lab mates as well. Bridget, Rafa, Hannah, Sophie, Charlie, Kim, Kirkham, and Shipley, thank you for being like a great big extended nutty family.

Thanks to my actual nutty family, to my Mom and Rog, my Dad and Anne, Ryan, Meghan. It's been a long-few-years - thanks for sharing this journey with me. Also, to my grandmas, Katie, and LuAnn.

Finally, and mostly, I would like to thank my amazing wife, Guanzi. Thank you for being by my side for all of this, and for your love, kindness, smile, and endless patience. Also, for taking such good care of Bear, during this crazy write-up period.

ABBREVIATIONS

24S-OHC	24S-Hydroxycholesterol
ABCA1	ATP-binding cassette transporter 1
ApoE	apolipoprotein E
ASMase	acid sphingomyelinase
ATG	autophagy related genes
ATP	adenosine triphosphate
BCA	bicinchoninic acid
BDNF	brain derived neurotrophic factor
BSA	bovine serum albumin
Ca^{2+}	calcium ion
Cas9	CRISPR associated protein 9
CAV1	caveolin 1
CDase	acid ceramidase
CerS	ceramide synthase
CERT	ceramide transfer protein
CLEAR	co-ordinated lysosomal expression and regulation
CNS	central nervous system
CRISPR	clustered regularly interspaced short palindromic repeats
CTxB	cholera toxin subunit B
DMEM	Dulbecco's modified Eagle's medium
DMSO	dimethylsulfoxide
DNA	deoxyribonucleic acid
ECM	extracellular matrix
ER	endoplasmic reticulum
ESC	embryonic stem cell
FAT	fast axonal trafficking
FBS	fetal bovine serum
FITC	fluorescein isothiocyanate
GABA	gamma aminobutyric acid
GalCer	galactosylceramide
GBA	glucocerebrosidase (glucosyl ceramidase)
GCase	glucocerebrosidase
GCS	glucosylceramide synthase
GluCer	glucosylceramide
GSL	glycoshpingolipid
HAP	huntintin associated protein
HD	Huntington's disease
HEAT	Huntington, Elongation Factor 3, PR65/A, TOR
HIP	huntintin interacting protein
HIPPI	HIP1 protein interactor
HMG	3-hydroxy-3-methylglutaryl
HMGCR	3-hydroxy-3-methylglutaryl coenzyme A reductase

HMGCS	3-hydroxy-3-methylglutaryl (HMG)-CoA synthase
HTT	huntingtin
IB	inclusion body
ICC	immunocytochemistry
IL	interleukin
iN	induced neurons
iPSC	induced pluripotent stem cells
JNK	cJUN N-terminal kinase
KO	knockout
LacCer	lactosylceramid
LAL	lysosomal acid lipase
LAMP	lysosome-associated membrane glycoprotein
LBPA	lysobisphosphatidic acid
LC3	Microtubule-associated protein light chain 3
LDL	low-density lipoprotein
LE	late endosome
LIMP	lysosomal integral membrane protein
LMPS	lysosomal membrane proteins
LPMC	lysosome-peroxisome membrane contact
LRP1	low density lipoprotein receptor related protein 1
LSD	lysosomal storage disorder
LXR	liver X receptor
M6P	mannose 6 phosphate
MCS	membrane contact sites
mHTT	mutant huntintin
mRNA	messenger RNA
MSN	medium spiny neuron
mTOR	mammalian target of rapamycin
mTORC1	mammalian target of rapamycin complex 1
MVB	multivesicular bodies
NPC	neural progenitor cell
NP-C	Niemann-Pick type C disease
NPC1	Niemann-Pick type C1 protein
NPC2	Niemann-Pick type C2 protein
NRSE	neuron restrictive silencer element
NSC	neural stem cell
PBS	phoshate buffered saline
PEI	polyethylenimine
PFA	paraformaldehyde
PGC1α	peroxisome proliferator-activated receptor-γ coactivator 1α
PM	plasma membrane
PolyQ	polyglutamine
RAB	Ras-associated binding protein
REST	repressor element 1 silencing transcription factor

RNA	ribonucleic acid
RNA Seq	RNA sequencing
ROS	reactive oxygen species
Sap B	saposin B
Sap C	saposin C
Sap D	saposin D
SCAP	sterol regulatory element-binding protein cleavage-activating protein
SK	sphingosine kinase
SM	sphingomyelinase
SREBP	sterol response element binding protein
TEM	transmission electron microscopy
TFEB	transcription factor EB
TLC	thin layer chromatography
TNF-α	tumor necrosis factor alpha
TPR	translocated promoter region
UDP	uridine diphosphate
ULK1	Unc-51 like autophagy activating kinase
UTR	untranslated region
wtHTT	wildtype huntingtin
β-gal	beta galactosidase

CONTENTS

FIGURES

1 INTRODUCTION

1.1 The Lysosome

1.1.1 Overview

The lysosome was first described by Christian De Duve in 1955, who when conducting cell fractionation studies into mechanisms underlying insulin function, observed increased acid phosphatase activity after sample perturbation, leading to the visualization of the vacuoles that contained the enzyme. The term lysosome is a portmanteau of the Greek words, 'lúsis (loosen) + soma' (body) due to its initial characterization as an organelle with an acidic interior and digestive function. In this sense lysosomes were inaccurately designated as the "cellular stomach," and this misnomer is now understood as a gross oversimplification, as later research has uncovered the lysosome in a complex, dynamic, transitional, and multifunctional role and one that is central to regulating cell function (Settembre et al. 2011b).

Lysosomes are cytoplasmic organelles, accounting for roughly 5% of the intracellular volume, and usually range between 0.1 and 1.2 µm in diameter. They contain a glycosylated inner membrane that protects from over 60 acid hydrolases and other degradative enzymes contained inside of the lumen (Figure 1.1)(Ballabio and Bonifacino 2020). Here, the enzymes function optimally as pH is maintained between 4.5 and 5.5 by the proton transport action of vacuolar ATPases (V-ATPases) balanced by a counterflux of other ion species such as Cl^-, Na^+, and K^+. The soluble enzymes work in concert with more than 120 lysosomal membrane proteins (LMPS), towards lysosomal functioning and processing of biological polymers e.g., proteins, nucleic acids, carbohydrates, and entire organelles arriving from upstream points in the endocytic and autophagic pathways (Finkbeiner 2020). Accordingly, mutations to proteins that contribute to proper lysosomal function give rise to a class of hereditary syndromes known as lysosomal storage disorders (LSDs), which are characterized by metabolic dysfunction, neurodegeneration, and impaired growth (Perera and Zoncu 2016). As such, there is mounting evidence, from our lab as well as others, for lysosomal and other vesicle trafficking defects in HD (Table 1.3). Of particular interest to our lab is the striking phenotypic resemblance between HD

and Niemann Pick Type C disease (NP-C) (Table 1.3). Therefore, a survey of lysosomal structure, processes, and associations is merited.

1.1.2 The evolutionary origins of the lysosome

Eukaryogenesis is thought to have occurred with the endosymbiotic incorporation of a protobacterial mitochondrial ancestor into an archael host. However, the evolutionary origin of the eukaryotic endomembrane system, a defining characteristic separating eukaryotes from prokaryotes, which includes organelles such as the endoplasmic reticulum, nucleus, Golgi, lysosomes, peroxisomes, and autophagosomes remains unresolved (Gould et al. 2016). Several models for the origin of the endomembrane system have been suggested. One such model proposes a *de novo* origin, and that the endomembrane system arose in an archaeal ancestor to all eukaryotic organisms, which permitted the phagocytosis of the mitochodrial precursor cell. Other models propose a syntrophic development by which the protobacterial endosymbiont was incorporated into the host through a non-phagocytic mechanism, and that the ATP provided by the protomitochondria, permitted the formation of a complex endomembrane system (Martin et al. 2015c). Along this line of reasoning, the most recent and simple theory proposes that the endomembrane system developed in the asgardarcheon host, from the outer membrane vesicles secreted by its protomitochondrial endosymbiont (Jékely 2007; Gould 2018). The further the diversity of intracellular compartments and organelles has been proposed to have occurred via the 'organelle paralogy hypothesis' which posits that because the machinery involved in vesicle trafficking involves several highly-conserved protein families, each acting on a specific organelle or transport pathway, and because organelle and pathway identity rely on combinatorial protein-to-protein interactions, iterative variations (due copy number variants or genetic mutations) in these interactions could have contributed to organelle complexity and subcellular localization (Dacks and Field 2018). In any case there is much yet to be clarified regarding this topic.

1.1.3 Lysosomal composition

The lumen of the lysosome is bound by a single, 7-10 nm wide, phospholipid bilayer that on its interior contains a glycoprotein layer (glycocalyx) to protect against lysosomal

autolysis. The lysosomal membrane is comprised mostly (> 80%) of lysosome-associated membrane proteins (LAMP) 1 and LAMP2 and lysosome integral membrane protein 2 (LIMP2) along with other proteins that are highly glycosylated at their lumenal domains. The lysosomal membrane not only acts as a barrier to isolate the acidic and hydrolytic lumenal contents from the rest of the cell, but is critical for filling essential roles in a diverse range of cellular processes including lipid metabolism, signaling, phagocytosis, autophagy, membrane repair, import and efflux, viral infection, and cell death (Schwake et al. 2013). To carry out these functions, the membrane is enriched with more than 50 types of LMPs, which are shuttled via dileucine and tyrosine targeting motifs, and bound to adaptor proteins in, the Golgi, before transport to the lysosome (Saftig and Klumperman 2009; Luzio et al. 2014). Though the function of many LMPs remains elusive, many are critical to proper cell function and defects often result in lysosomal storage disorders. One LMP, Niemann-Pick type C1 (NPC1), which is mutated in NP-C, is a central focus of this study (Carstea et al. 1997).

The lysosomal lumen is largely populated by soluble hydrolytic proteins with an acidic pH optima, which degrade macromolecules (e.g., proteins, carbohydrates, nucleic acids) into their constituent components. Before sequestration to the lysosomal lumen, proenzyme forms of the soluble hydrolases are synthesized in the rough endoplasmic reticulum (ER), trafficked to the *cis*-Golgi where the majority are tagged with a mannose-6-phosphate (M6P), before binding to M6P-receptors in the *trans*-Golgi network. The hydrolases are then delivered to endosomes where M6P-receptors are cleaved and recycled, before final transport to the lysosome (Luzio et al. 2007). Other soluble proteins are transported in a M6P-independent manner, binding through alternative receptors e.g., LIMP-2, or sortilin (Braulke and Bonifacino 2009). In addition to the hydrolytic enzymes, lysosomal activator proteins (LAPs) are present which frequently aid lipid catabolism by solubilizing and presenting lipid substrates to their matching enzyme. Transport proteins are also present, e.g., Niemann-Pick type C2 protein (NPC2), which act as solute carriers to export the products of lysosomal degradation. As with LMPs, hydrolases and activator proteins are critical to normal cell function with defects often resulting in LSDs.

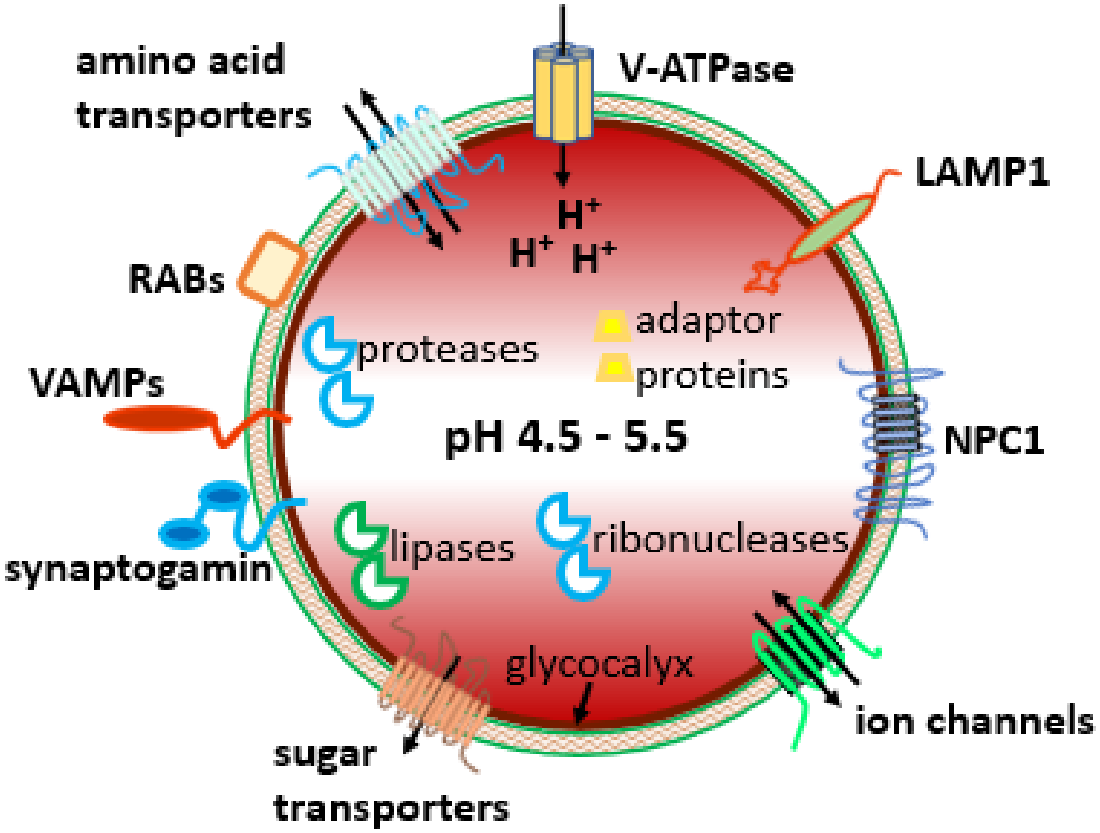

Figure 1.1. Basic lysosomal structure and composition.

1.1.4 Lysosomal function

Appropriate lysosome form is critical to proper lysosomal function, which in turn is fundamental to a complexity of cellular processes that are indispensable to cell survival and overall health. Lysosomal processing is essential for removal of toxins, the elimination of impaired organelles, the termination of signal transduction, and the maintenance of metabolic homeostasis (Wang et al. 2007). It is well established that lysosomes degrade and recycle macromolecular input arriving from the endocytosis, autophagic, secretory, and phagocytic pathways, while outputting the derivative monomers. It is this control of endocytosis from, and exocytosis to, the plasma membrane that enables the interactions between the cell and its environment to be

precisely regulated (Doherty and McMahon 2009). Appropriately, the concept of the lysosome as merely a recycling compartment has shifted towards inclusion of the lysosome as a key signaling regulator in a sophisticated network of cellular adaptation, which integrates several cellular parameters e.g., nutrient concentration, energy levels, and stressors, to regulate cellular and organismal metabolism (Perera and Zoncu 2016; Ballabio and Bonifacino 2020). As such, the lysosome plays roles in major cellular pathways, including endocytosis, autophagy, Ca^{2+} signaling and homeostasis, while also interacting with other organelles, e.g., mitochondria, the ER, and the Golgi complex

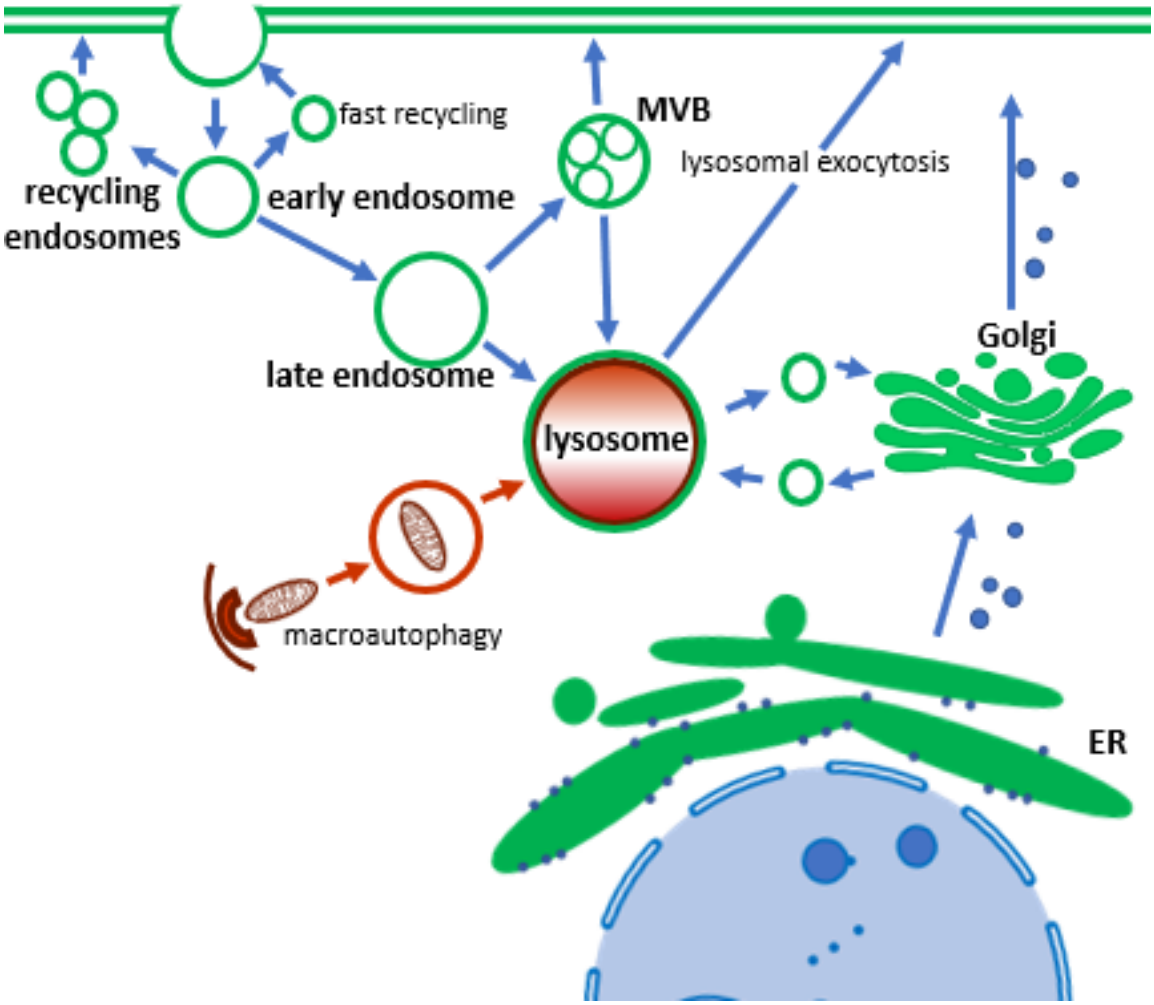

Figure 1.2 Basic outline of the endolysosomal system.

(Ballabio and Bonifacino 2020). At the transcriptional level, the coordination of these programs are carried out by the coordinated lysosomal expression and regulation (CLEAR) gene regulatory networks which are modulated by a control circuit involving lysosomal calcium signaling, and transcription factor EB (TFEB) (Medina et al. 2015). Because of the central role of the lysosome in these interconnected cellular processes, it is unsurprising that lysosomal dysfunction would activate the pathogenic cascades observed in LSDs.

1.1.4.1 The role of the lysosome in endocytosis

There are at least five endocytic mechanisms which dictate the lipid and protein composition of the plasma membrane and regulate a cell's interface and communication with its external environment, of these the clathrin-mediated pathway is the most widely documented (Van Meel and Klumperman 2008). Spatiotemporally, endocytosis begins on the outer leaflet of the plasma membrane, with the *de novo* production of internal membranes from the PM. Here, fission of the plasma membrane leads to the formation of vesicles which envelop PM lipids, integral proteins, and extracellular fluid for internalization (Doherty and McMahon 2009). Once internalized, the vesicles carrying the cargo undergo a series of maturation steps, first developing into the early endosome (Klumperman and Raposo 2014). From here, the cargo is either returned to the cell surface for recycling, by recycling endosomes, or alternatively to the late endosome. Late endosomes that have matured, are also called multivesicular bodies (MVBs) and it is these that fuse with lysosomes to form endolysosomes, which are the likely domain for break down and recycling to occur (Luzio et al. 2014; Xu and Ren 2015).

1.1.4.2 The role of the lysosome in exocytosis

Exocytosis, which can be described as the fusion of internal membranes, with the plasma membrane, can be considered the morphological counterbalance to endocytosis (Doherty and McMahon 2009). Through this process, the cell expels specific chemicals to the extracellular space and delivers lipids and proteins to the PM (Doherty and McMahon 2009). Exocytosis intersects the endocytic and autophagic systems at several points; in particular, lysosomal exocytosis, is important in cellular clearance, membrane repair,

ECM remodeling, intercellular signaling, and is essential to CNS function with pathogenic consequences, if defective (Buratta et al. 2020).

Lysosomal exocytosis can be triggered by PM damage, which results in rapid Ca^{2+} influx , in PM resealing, reduced membrane tension, sphingomyelin release, and LAMP1 localization to the PM (Reddy et al. 2001; Andrews et al. 2014). In the CNS, lysosomal exocytosis, induced by neuronal activity can trigger the secretion of lysosomal enzymes towards degradation of the local extracellular matrix, leading to long-term synaptic structural changes, while conversely, cerrebellin-1 (CBLN1) released from axonal lysosomes can generate the formation of new synapses (Ibata and Yuzaki 2021). Lysosomal exocytosis was shown to be involved in ATP release, and in response to different stimuli, may contribute to astrocytic intercellular signaling by promoting the extracellular release of the ATP needed for Ca^{2+} wave propagation in neurons (Zhang et al. 2007). However, this mechanism might also contribute to neurodegenerative pathways, as Ca^{2+}-mediated lysosomal exocytosis, brought about by oxidative stress in astrocytes, was shown to be responsible for lysosomal release of ATP into the extracellular space, and because ATP at too high of concentrations is toxic to neurons, lysosomal exocytosis might contribute and extend the oxidative-stress induced cellular damage, to the tissue level (Li et al. 2019).

1.1.4.3 The role of the lysosome in autophagy

Autophagy is a set of three processes, microautophagy, chaperone mediated autophagy (CMA) and macroautophagy, whereby intracytoplasmic macromolecules and organelles are targeted to the lysosome for degradation or reuse (Malik et al. 2019). Microautophagy, is a generally non-selective process by which the lysosome reorganizes its membrane, towards engulfing cytosolic material via pinocytosis, while in CMA, cytoplasmic proteins are selectively translocated into the lysosomal lumen for degradation. Macroautophagy, is the path by which transient, double-membraned organelles, autophagosomes, sequester and shuttle cytoplasmic contents e.g., organelles and most long-lived proteins, to the lysosome. The autophagosome then fuses with the

lysosome (or the amphisome) to form the autolysosome, where substrates are degraded into their constituent molecules, and recycled into metabolic processes.

Lysosomal function is central to autophagy, and the balance between autophagic and lysosomal networks are tightly intertwined through a TFEB-mediated autoregulatory loop, which by acting as a master regulator of both lysosomal and autophagy genes, TFEB coordinates biogenesis and lysosomal-autophagosome fusion (amongst other processes) (Settembre et al. 2011a; Settembre et al. 2013). This loop is modulated by lysosomal Ca^{2+} signaling, and release triggers calcineurin activation, which dephosphorylates TFEB, to induce biogenesis and autophagy. (Settembre et al. 2011a; Medina et al. 2015).

Especially in neurons, high levels of basal macroautophagy are critical for homeostasis, because unlike non-neuronal cells, post-mitotic and non-proliferative neurons, are unable to dilute accumulated cellular waste through division. Thus, proper, and efficient lysosome function is critical to autolysosomal function, with dysfunction frequently observed in neurodegenerative diseases including Huntington's disease. Moreover, reduced autophagosomal clearance is observed in most LSDs, including NP-C (Ballabio and Gieselmann 2009; Son et al. 2012). In this regard, however, HD is distinct in that autophagy is not only dysfunctional, but wildtype huntingtin also is thought to perform several functions in regulating the dynamics of autophagy (Martin et al. 2015b).

1.2 Lipid metabolism

Lipid molecules contribute to roughly 60% of nervous tissue where they are fundamental to cellular integrity and the propagation of electrical and chemical signals (Tamiji and Crawford 2010). The three main families of lipids: glycerolipids, sphingolipids, and sterols are composed of hundreds of lipid species of varied structure and function. Proper lipid synthesis and catabolism are necessary for cell health and disruption in these pathways can give rise to LSDs. Several studies have evidenced lipid dyshomeostasis in HD, though it remains undetermined as to whether this indicates a primary pathogenic event, or whether it is secondary (Desplats et al. 2007b; Valenza and Cattaneo 2011; Handley et al. 2016; Di Pardo et al. 2017b). Moreover, recent studies in the Lloyd-Evans lab highlighted disruption, in particular, to ganglioside GM1, cholesterol, and sphingomyelin (Haslett

2015; Clark 2017). The lysosome is the primary site of lipid catabolism; therefore, a summary of lipid transport and metabolism is merited, especially as impairments here result in the lipid accumulation observed in LSDs.

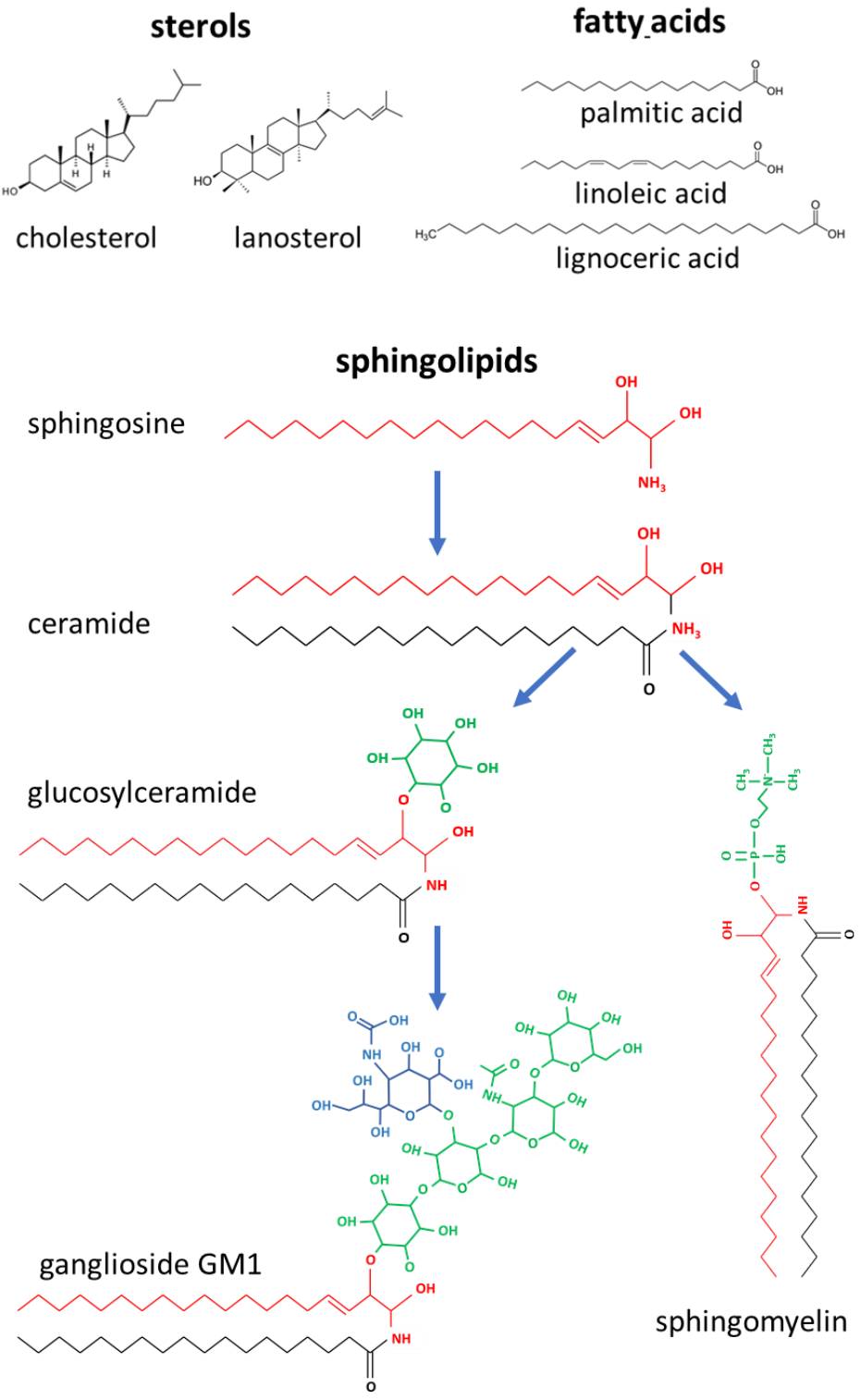

Figure 1.3. Examples of basic structures in the main lipid families.

1.2.1 Sphingolipids

Sphingolipids constitute nearly 20% of the lipids of the CNS and largely reside on the outer leaflet of the plasma membrane; they function in a structural capacity in neurons, while also contributing towards regulating cellular communication, neuronal differentiation, and maturation (Bouscary et al.). Diseases involving dysregulation of sphingolipid metabolism form a subcategory of LSDs, the sphingolipidoses, which includes GM1 gangliosidosis, Sandhoff disease, Gaucher's disease, and Niemann-Pick type C; sphingolipid dysregulation has been linked to neurodegenerative processes in other diseases as well e.g., PD and ALS, though the mechanisms underlying the patterns of storage and how this storage results in neurodegeneration remains unclear (Lloyd-Evans et al. 2008).

Sphingolipids, defined by their underlying structure, are usually constituted by a long-chain 18 carbon amino-alcohol backbone (Figure 1.3), the modification of which produces the vast sphingolipid diversity (Gault et al. 2010). Sphingolipids, can be separated into either sphingomyelins or glycosphingolipids, the former consisting of a ceramide attached to a phosphocholine or phosphoethanolamine headgroup, while the latter are composed of sphingosine linked to a glycan moiety (Garg and Smith 2017). More complex sphingolipids are formed as these lipid anchors can then be decorated with a variety of charged, neutral, phosphorylated and/or glycosylated moieties, which contribute to both polar and nonpolar regions, thus, conferring amphipathic properties, which explains their propensity to aggregate into membranous structures (Gault et al. 2010). Furthermore, the wide diversity in sphingolipid chemical structures enables them to perform distinctive roles within cellular metabolism (Merrill Jr and Sandhoff 2002). However, despite the large sphingolipid diversity, their generation and degradation are governed by common synthetic pathways, centered around ceramide production, and can be thought of as an array of interconnected networks that diverge from a common entry point to be broken down by a single breakdown pathway (Gault et al. 2010).

1.2.2 Sphingolipid metabolism

De novo synthesis

Cells acquire sphingolipids intrinsically via de novo biosynthesis and extrinsically through uptake and recycling, acquisition is centered around the production of ceramide (Figure 1.4). De novo ceramide synthesis occurs via the sphingolipid biosynthetic pathway, and is initiated on the cytosolic surface of the ER, as the localized enzyme, serine palmitoyl transferase (SPT) condenses palmitoyl-CoA and L-serine to yield 3-keto-dihydrosphinganine (3KS) (Braun and Snell 1968; Stoffel et al. 1968). Subsequent reduction of 3KS by 3-ketosphinganine reductase (KDSR) yields dihydrosphinganine. Next, fatty acyl-CoA is coupled to the dihydrosphinganine by ceramide synthase (CerS), resulting in the formation of dihydroceramides that vary in the length of the amide-bound fatty acid. Lastly, double bond formation between carbons C-4 and C-5 is mediated by dihydroceramide desaturase (DEGS) resulting in nascent ceramides which are then shuttled, via the ceramide transfer protein (CERT), to the Golgi, where they act as substrates in the synthesis of more complex sphingolipids such as sphingomyelin or glycosphingolipids e.g., gangliosides (Wigger et al. 2019).

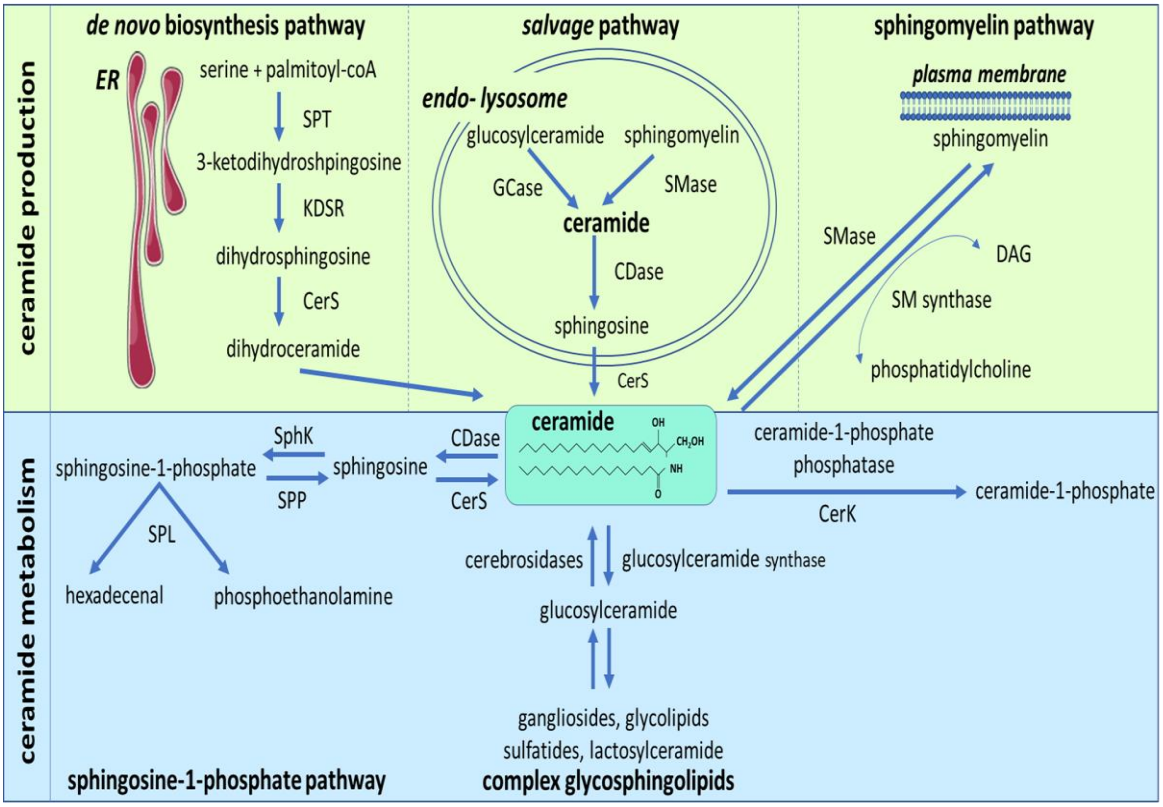

Figure 1.4. Summary of metabolic pathways of sphingolipid production. Modified from Falluel-Morel et al. (2008) and Tan-Chen et al. (2020)

1.2.2.1 Sphingolipid Recycling

1.2.2.1.1 The salvage pathway

Sphingolipid recycling can be divided and categorized by the subcellular location in which the processes occur, as either lysosomal or nonlysosomal. The salvage pathway refers to a process of sphingosine recycling and constitutive degradation of long chain sphingoid bases. The salvage pathway has been shown to play an important role in ceramide metabolism and function, by modulating ceramide biosynthesis and ceramide-dependent cell signaling. This process occurs mainly in the lysosome, and competes with de novo synthesis to provide input for sphingolipid production, supplying free sphingosine (de novo mainly produces dihydro sphingosine) for production of between 50 and 90% of cellular glycosphingolipids, depending on cell type (Gillard et al. 1998; Kitatani et al. 2008; Schulze and Sandhoff 2011). In the lysosome, glycosphingolipid breakdown occurs as sugar residues are cleaved, resulting in the formation of glucosylceramide (GluCer), galactosylceramide (GalCer), which are then hydrolyzed by β-glucocerebrosidases (GCase) or β-galactosidases (β-gal) to form ceramide. Additional lysosomal ceramide formation occurs via the hydrolysis of sphingomyelin, mediated by acid sphingomyelinase (ASMase). Ceramide input from these lysosomal pathways can then be deacylated by acid ceramidases (CDase) to form sphingosine. The sphingosine can then be exported from the lysosome to the cytoplasm, where it can subsequently be reacylated by ceramide synthase (CerS) to from ceramide. It is important to note that defects in the function of these hydrolytic enzymes and dysregulation along the ceramide-sphingosine axis has been observed and is a likely contributor to several neurodegenerative and LSDs, and aberrant sphingosine efflux has been implicated as a causal factor of NP-C (Lloyd-Evans et al. 2008; Young et al. 2012).

1.2.2.1.2 The sphingomyelinase pathway

Nonlysosomal recycling via the sphingomyelinase pathway can occur on the plasma membrane (or in association with lipoproteins), in a bidirectional reaction. Here, ceramide is generated by the breakdown of sphingomyelin, which is degraded by ASMase to yield ceramide, in-turn ceramide can be deacylated by acid-neutral ceramidases to produce free sphingosine. In the other direction, sphingomyelin synthase converts ceramide to sphingomyelin by the addition of a phosphocholine molecule, the product of

phosphatidylcholine breakdown into diacylglycerol (Jenkins et al. 2009; Merscher and Fornoni 2014). Sphingomyelinase and its associated enzymes and activator proteins, are critical to lysosomal sphingomyelin turnover, as defects are responsible for sphingolipid accumulation, and contribute to dysfunction in a major fraction of LSDs, including all of the sphingolipidoses as well as NP-C. (Young et al. 2012).

1.2.2.2 Sphingolipid degradation

Proper sphingolipid degradation is indispensable for regulating lipid homeostasis and healthy cell functioning. Because lipids are not excreted as readily as more hydrophilic molecules, and failure to do so results in lipid accumulation, there is a substantial evolutionary risk leveraged against the benefits of lipid production, in that organisms must be capable of catabolizing each lipid that is synthesized (Gault et al. 2010; Young et al. 2012; Garg and Smith 2017). Therefore, it is understandable, that for each enzyme that produces a particular sphingolipid, there is a corresponding and diametrically opposite enzyme capable of breaking down the generated product. The concept of LSDs is fundamentally based on lipid accumulation due to specific defects in catabolic enzymes, and mutations in sphingolipid catabolizing enzymes are causative factors in a substantial number of these diseases (Gault et al. 2010). Parallel with the production of hundreds of individual sphingolipid variants from an input of a few sphingolipid precursors, there is a single common terminal degradation pathway, as all sphingolipids are broken down in a step-wise manner into their constituent components from ceramide to, sphingosine, sphingosine-1-phosphate, and finally to hexadecenal and phosphoethanolamine (Gault et al. 2010).

The initial step in the degradation process is carried out through the deacylation of ceramide into sphingosine by ceramidase enzymes, which are classified according to their respective pH optima. Acid ceramidase is responsible for the ceramide breakdown in the lysosome, and defects in this enzyme lead to Farber disease. In the second step, sphingosine is converted to sphingosine-1-phosphate by members of the DAG kinase family, sphingosine kinases 1 or 2 (SK1 or SK2). Though similar, SK1 and SK2 vary slightly in their subcellular localization and substrate specificity. Generally, however, SK1 and SK2 are cytosolic (though indirectly membrane-associated) and phosphorylate sphingosine at the C-1 hydroxy, in and ATP-dependent manner, to produce sphingosine-1-phosphate

(S1P). In the final step of sphingolipid catabolism, phosphorylated sphingoid bases, are converted to hexadecenal and phosphoethanolamine, by sphingosine-1-phosphate lyase on the cytosolic face of the ER.

1.2.2.3 Gangliosides

Gangliosides represent one of many classes of glycolipids and therefore contain a carbohydrate linked to a hydrophobic lipid moiety through a covalent, glycosidic bond. More specifically, gangliosides (and globosides) are glycosphingolipids and therefore their lipid moiety exists as a sphingoid base or ceramide. In particular, gangliosides are defined by the presence of one or more sialic acids (N-acetylneuraminic acid or N-glycolylneuraminic acid) attached to the carbohydrate moiety. Gangliosides are especially important in CNS tissue where they constitute 10-12% of the lipid content, largely localized to the PM where they are anchored by their ceramide group, while their glycan moiety is exposed on the cell surface. Gangliosides function in cell recognition, adhesion, signal transduction, and in regulating calcium homeostasis (Robert K et al. 2011; Breiden and Sandhoff 2018; Sandhoff and Sandhoff 2018b). Dysfunctions in ganglioside metabolism are common in disease, and are classified as, gangliosidoses. Moreover, defects in ganglioside metabolism are seen in HD and NP-C (Maglione et al. 2010).

1.2.2.4 Ganglioside Synthesis

As with other sphingolipids, ganglioside synthesis begins in the ER, with the production of ceramide (Figure 1.5). Ceramide is then transferred to the cytosolic face of the Golgi complex by ceramide ER transfer protein (CERT) or via vesicular transport. Notably, glucosylceramide synthase then mediates the first step for the majority of downstream glycosphingolipid synthesis by linking a UDP-glucose (uridine diphosphate glucose) molecule to the C1 hydroxyl position on the sphingosine base, to yield GluCer. Following this, the glucosylceramides are transferred to the luminal leaflet of the Golgi where a galactose moiety is added by lactosylceramide synthase, resulting in lactosylceramide (LacCer), which forms the basis for the majority of gangliosides, with the exception of ganglioside GM4. LacCer, acts as a substrate to facilitate GSL anabolism into various GSL series. In neurons, the basic ganglioside GM3 is generated by the addition of a sialic acid to the galactosyl moiety of LacCer by GM3 synthase. Additional sialylation reactions, yield GD3, and then GT3 which are the molecular foundations for the a, b, and c series of

gangliosides, respectively. Following the a-series progression to the ganglioside GM1, the next step involves the conversion of GM3 to GM2 by GM2 synthase, and then from GM2 to GM1 through GM1 synthase (Gault et al. 2010; Robert K et al. 2011; Sandhoff and Sandhoff 2018b). Notably, however, diseases associated with defective ganglioside synthesis are extremely rare, while malfunctions along catabolic pathways lead to several well-known diseases (Figure 1.6).

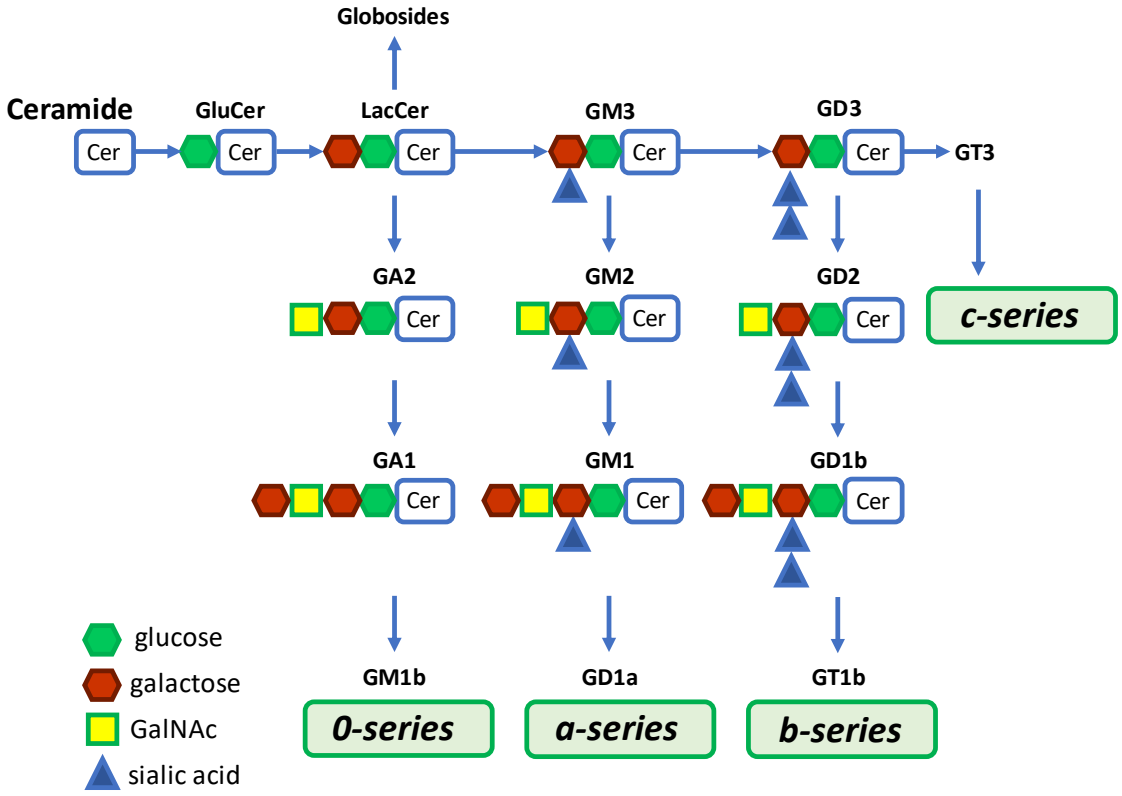

Figure 1.5. Outline of ganglioside synthesis.

1.2.2.5 Ganglioside Catabolism

Ganglioside degradation begins as gangliosides are endocytosed and trafficked to late endosomes and lysosomes where, lipid-binding cofactors, specifically sphingolipid activator proteins (SAPs), work in concert with soluble glycosidases, lipases, and phospholipases towards catabolism; notably, this process is thought to occur in intralysosomal vesicles (ILVs). For example, in complex gangliosides, stepwise removal of

terminal sialic acid molecules by neuraminidases, results in GM1. Next, GM1 degradation proceeds as GM1-β-galactosidase, in cooperation with GM2 activator protein or saposin B, mediates the removal of the terminal galactose to generate GM2. Following this, β-hexosaminidase A and GM2 activator protein, act to release the terminal N-acetylgalactosamine residue to form GM3, which can be broken down to LacCer by an α-sialidase and Sap B. LacCer is degraded to GluCer by The Sap B or Sap C-assisted action of β-galactosidase, while the glucosyl residue is cleaved by Sap C-assisted β-glucosidase. Finally, acid ceramidase and Sap D coordinate to split ceramide into its constituents sphingoid base and free fatty acids (Sandhoff and Sandhoff 2018a). Since sphingolipids are mainly recycled, with limited de novo synthesis, it is unsurprising that several LSDs are associated with malfunctions in these hydrolytic steps (Figure 1.6).

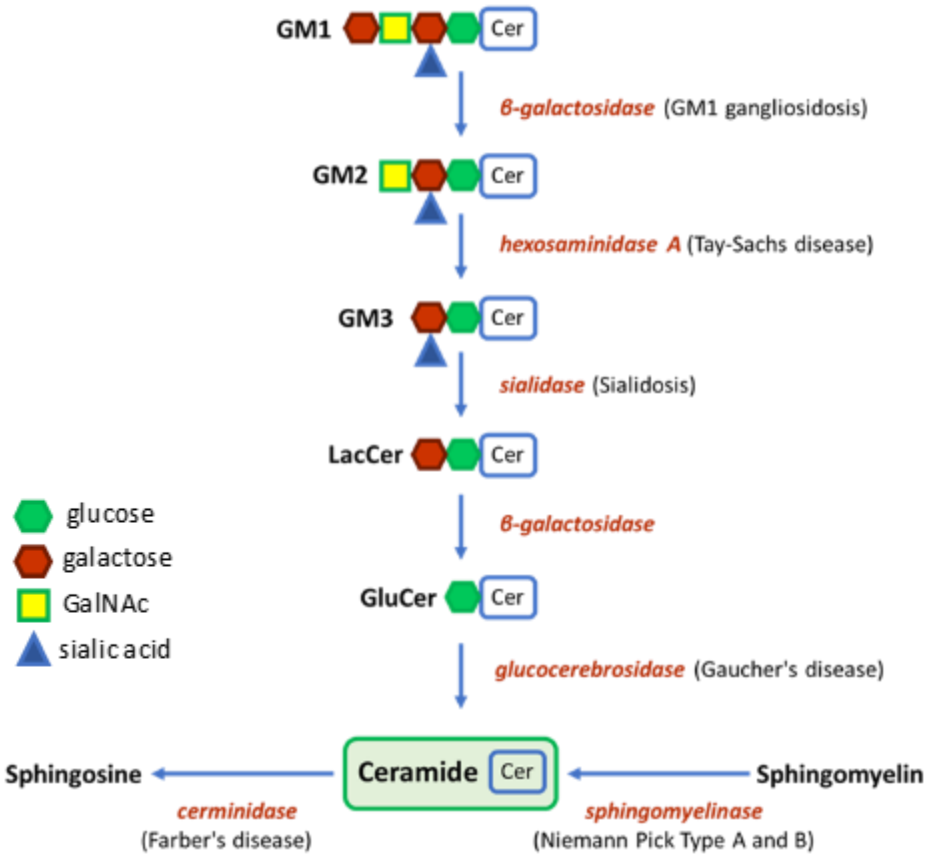

Figure 1.6. Sphingolipid catabolic pathways, associated enzymes, and diseases.

1.2.2.6 Cholesterol

Cholesterol is the most abundant and well studied lipid in mammalian cells, however, understanding of the cholesterol-associated pathways and metabolic processes are incomplete. Cholesterol is a main component of cell membranes and is a precursor to numerous biological molecules. Though the CNS only accounts for roughly 2% of the body, it contains roughly 25% of the cholesterol, and of that, cholesterol is mainly (70% - 80%) incorporated into myelin, thus underscoring its importance, especially in the CNS (Dietschy and Turley 2004; Ikonen and Zhou 2021). Cholesterol metabolism in the brain differs from that occurring in peripheral tissues, as the blood brain barrier prevents cholesterol uptake from circulation (with the exception of 27-hydroxycholesterol or via the scavenger receptor class B type I), thus nearly all CNS cholesterol synthesis and recycling are regulated locally and independently of the rest of the body (Jeske and Dietschy 1980; Björkhem and Meaney 2004). The rate of cholesterol synthesis in neurons and glial cells is greatest during embryogenesis and childhood. However, in adults, neuron populations become reliant on cholesterol-containing lipoproteins secreted by glial cells, as they gradually lose their capacity for *de novo* synthesis (Vitali et al. 2014). There is substantial evidence to demonstrate the importance of cholesterol's role in multiple biological processes and overall cell functioning, while defective cholesterol homeostasis has been observed in numerous diseases. As such, dysregulation in cholesterol levels and turnover are frequently observed in neurodegenerative and lysosomal storage diseases, again including NP-C and HD (Björkhem and Meaney 2004; Sitaula and Burris 2016; Parenti et al. 2021).

1.2.2.6.1 De novo synthesis

De novo biosynthesis of cholesterol can be upregulated by brain derived neurotrophic factor (BDNF) and begins with the starting input of acetyl-coenzyme A (acetyl-CoA), produced in, and transported from, mitochondria. The initial step in the pathway occurs in the cytosol, as 3-hydroxy-3-methylglutaryl (HMG)-CoA synthase (HMGCS) condenses one molecule of acetyl-coenzyme A and one molecule of acetoacetyl-CoA to yield one molecule of HMG-CoA, with subsequent steps occurring in the ER (Figure 1.7). Next, in the rate-limiting step, HMG-CoA is reduced to mevalonic acid by HMG-CoA reductase (HMGCR), which then undergoes a series of steps and is further phosphorylated to

isopentyl pyrophosphate, which is then converted to geranyl pyrophosphate. Geranyl pyrophosphate is then combined with another isopentyl pyrophosphate to make farnesyl pyrophosphate. Two molecules of farnesyl pyrophosphate are then condensed via squalene synthase to form squalene, which is then cyclized to yield lanosterol. From here processes leading from lanosterol to cholesterol can diverge into the Bloch or Kandutsch-Russel pathways, with the latter (or a modified version thereof) being the most prevalent in CNS tissue, where the absolute rate of *de novo* CNS cholesterol synthesis is relatively low (Mitsche et al. 2015; Sitaula and Burris 2016).

1.2.2.6.2 Cholesterol uptake in neurons

Cholesterol is essential to, and involved in, several CNS functions including, structural maintenance, regulation of lipid and membrane fluidity, transport, permeability of ions and metabolites, action potential propagation, as well as neuron growth and development (González-Guevara et al. 2020). Accordingly, cholesterol distribution and metabolism are subjects of great interest. While the synthesis of cholesterol is critical during neurodevelopment, adult neurons primarily rely on uptake of extracellular cholesterol released from glial cells (mainly astrocytes) which are thought to produce roughly 95% of cholesterol in the brain (Dietschy 2009). For example, from astrocytes, after synthesis, cholesterol can be shuttled from the ER to endosomes, or into the extracellular space mediated by ATP-binding cassette transporters (ABCA1). Cholesterol is then chaperoned by apolipoprotein E (ApoE) in low-density lipoprotein (LDL) complexes, to the neuronal LRP1 (Low-Density Lipoprotein Receptor-Related Protein 1) receptors where they are internalized through receptor-mediated endocytosis and transported to early endocytic sorting compartments. The receptors are returned to the plasma membrane, and cholesterol esters are hydrolyzed by acid lipase in late endosomes or lysosomes. The resulting unesterified cholesterol, can then exit the endolysosomal system and be transported to other cellular compartments through a variety of pathways. The mechanics of cholesterol egress and transport are largely undefined and contested, though evidence points to both vesicular and nonvesicular means (Hölttä-Vuori and Ikonen 2006). Models suggest egress is mediated by lysosomal membrane proteins including for example, LIMP2, LAMP1, and LAMP2, NPC1 and NPC2. Models for trafficking to other compartments, include mediation through STARD3 (MLN64) and

ORP1, or RAB proteins to mitochondria or the Golgi, respectively (Hölttä-Vuori et al. 2002; Charman et al. 2010). Moreover, It has been suggested that due to the low concentration of cholesterol in the lysosomal limiting membrane, that directional cholesterol transport involving sterol transfer proteins, to another organelle through membrane contact sites, is likely (Kolter and Sandhoff 2005b; Luo et al. 2017). Growing evidence is supportive of this suggestion, and a recent study implicated lysosome-peroxisome membrane contact as a key path for LDL-cholesterol trafficking (Chu et al. 2015; Petrov et al. 2016; Ikonen and Zhou 2021). Particularly challenging, especially in relation to cholesterol's potential role in LSDs, is that cholesterol is rarely transported alone, and instead is primarily coupled with other lipids, phosphoinositides, phosphatidylserine, and sphingolipids, for example (Ikonen and Zhou 2021).

1.2.2.6.3 Cholesterol regulation

By a well understood pathway, regulation of cholesterol homeostasis can occur by dynamics involving the dissociation of insulin-induced protein 1 and 2, sterol-regulatory element-binding protein, and SREBP cleavage-activating proteins (INSIG 1, INSIG 2, SREBP, and SCAP, respectively), which complex in close association with the ER membrane when cholesterol levels are high, but dissociate when levels are reduced. Dissociation allows SREBP and SCAP to migrate to the Golgi complex, where SCAP cleaves and releases SREBP in its active transcription factor form, where it translocates to the nucleus and activates cholesterol-related genes involved in synthesis and trafficking (Ikonen and Zhou 2021). It is then of significance, that mutant HTT has been shown to alter SREBP-2 translocation and maturation, cholesterol homeostasis, and the expression levels of genes involved in cholesterol biosynthetic pathways (Vitali et al. 2014; Ikonen and Zhou 2021).

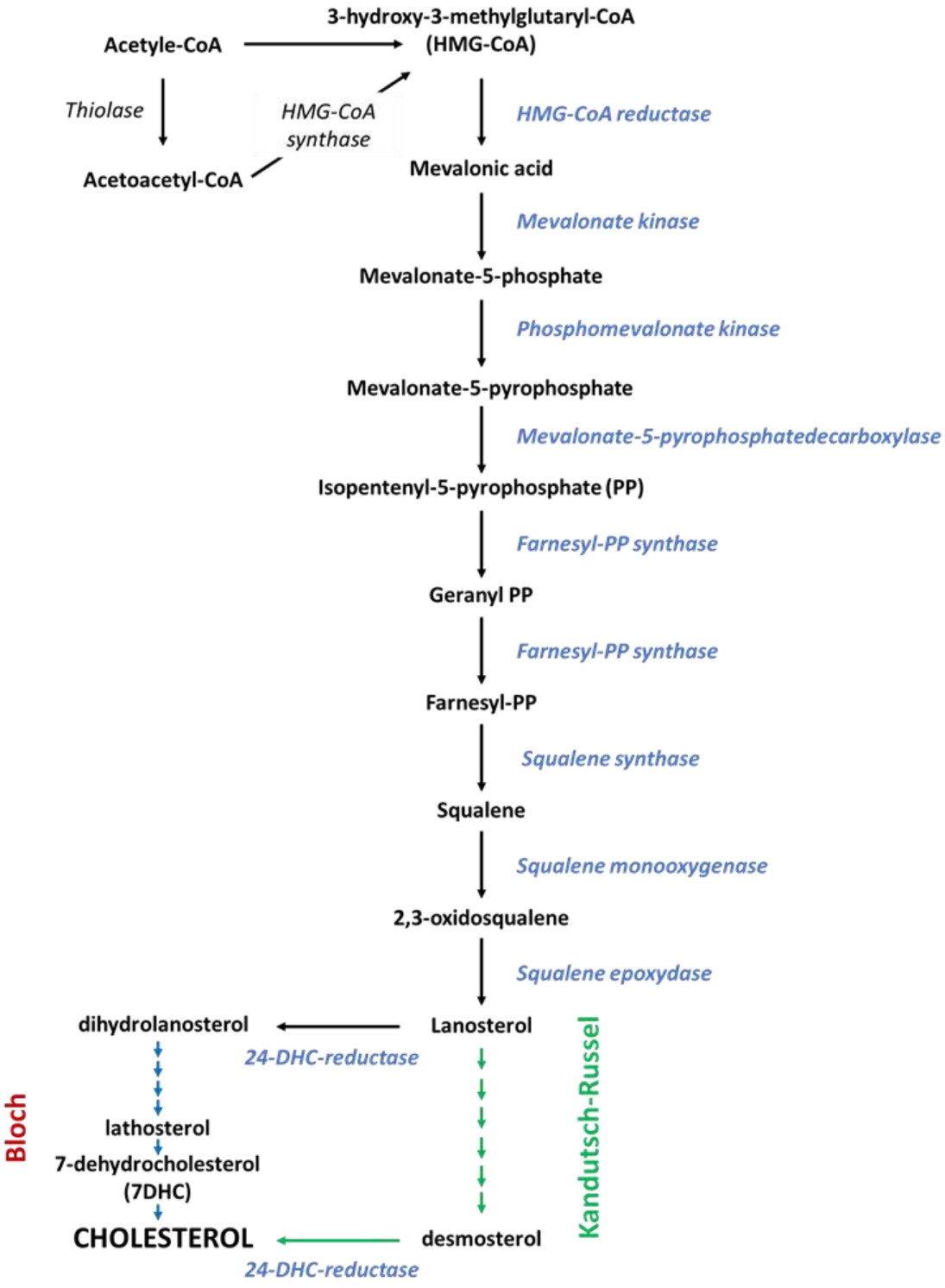

Figure 1.7. Outline of *De novo* cholesterol synthesis.

1.3 Lysosomal storage diseases

1.3.1 Overview

The proper functioning of the lysosome is critical to cell health and lysosomal dysfunction is responsible for a class of metabolic disorders referred to as lysosomal storage diseases (LSDs). Currently, over 70 LSDs affecting up to 1 in 5000 births, have been identified; these are frequently caused by monogenic mutations coding for lysosomal proteins (lysosomal hydrolases, membrane proteins, lipid and ion transporters, enzyme modifiers or activators) and less frequently from nonlysosomal proteins (Platt et al. 2018). These mutations translate to an altered protein structure with aberrant function that result in lysosomal accumulation of unmetabolized or partially digested macromolecules; this accumulation is referred to as primary storage (Figure 1.8). Primary storage materials such as sphingolipids, glycosaminoglycans, glycogen, or glycoproteins comprise the majority of the storage material and accordingly form the basis on which most LSDs are labeled. (Walkley et al. 2018). As a consequence of primary storage, secondary storage, which arises from non-enzymatic lysosomal proteins, frequently develops as additional macromolecules accumulate (Platt et al. 2018; Martina et al. 2020). Lysosomal storage and dysfunction can activate complex pathogenic cascades that present clinically in a multitude of ways, and while CNS pathology occurs in the majority, symptoms are commonly observed in other organ systems as well (Vitner et al. 2010; Cox and Cachon-Gonzalez 2012; Platt et al. 2018). Variations in the susceptibility of specific neuronal populations to LSDs are thought to arise from variations in lipid ingestion, synthesis, and sequestration profiles associated with each subtype (Platt et al. 1994).

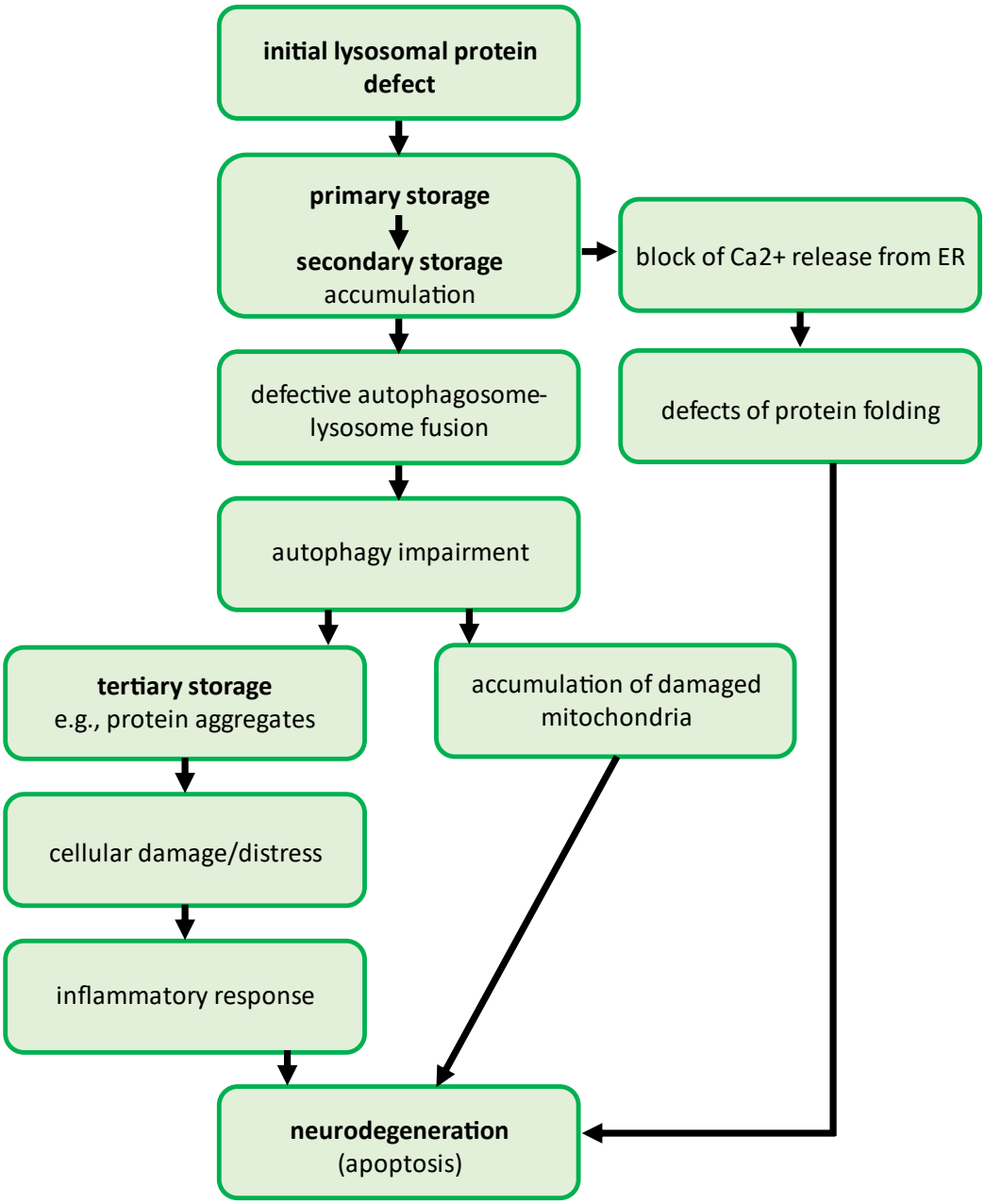

Figure 1.8. Progression from initial lysosomal defect to neurodegeneration in LSDs (Breiden and Sandhoff 2020)

1.3.2 Primary storage

In the case of individual lysosomal hydrolase mutations, which underlie 50 out of the 70 LSDs, primary storage material can usually be identified simply as the target substrate that accrues due to insufficient catabolic activity (Walkley et al. 2018). However, mechanisms underlying storage are more nuanced and complex than would be expected from a simple one enzyme-one substrate relationship, not only because enzymes are often promiscuous to more than one substrate, but it has become clear that alternative

pathomechanisms also are contributory, though these remain poorly understood (Walkley et al. 2018). Examples of contributory pathomechanisms, and associated LSDs, include upstream post-translational modifications (multiple sulfatase deficiency), faulty trafficking of lysosomal enzymes (mucolipidoses 2 and 3), defective solute carriers (cystinosis), impaired non-enzymatic activator proteins (saposin activator protein deficiencies), oxidative stress, multienzyme assembly defects (galactosialidosis) and lysosomal membrane protein malfunction in NPC and Danon disease (Parenti et al. 2021). Moreover, soluble transmembrane lysosomal proteins with unclear functionality are hypothesized to be involved in an array of processes including but not limited to, vesicle fusion, pH regulation, substrate salvage, and lipid trafficking, which in turn are thought to trigger not only substrate accumulation, but also Ca^{2+} dyshomeostasis. (Martina et al. 2020).

1.3.3 Secondary storage

While the origin of primary storage can often be identified, mechanisms underlying secondary storage, are inadequately understood (Walkley and Vanier 2009). Secondary storage usually occurs as accumulation of lipids including cholesterol, phospholipids, and glycosphingolipids. This accumulation is considered to play a significant role in pathogenesis, as evidenced by the increased concentration of storage species in brain regions most impaired (Parenti et al. 2021). However, secondary storage can obscure cause and effect relationships, making it difficult to pinpoint the principal cause of a disease. For example, and relevant here, decades after discovering the mutated proteins responsible for NP-C, it remains unclear which metabolite is primarily accumulating, as cholesterol, GSLs, sphingomyelin, and sphingosine have all been suggested (Lloyd-Evans and Platt 2010). As such, NP-C is similar to HD in that not only are there overlapping lipid-related phenotypes common to both diseases, but that the principle causal mechanism underlying each disease remains unknown (Valenza et al. 2005b; Lloyd-Evans et al. 2008; Lloyd-Evans and Platt 2010; Di Pardo et al. 2017a).

1.3.4 Additional LSD-associated phenotypes

Lysosomal dysfunction and associated storage can precipitate a complex pathological cascade of downstream events that can affect a multitude of functions and ultimately affect cell survival (Martina et al. 2020). For example, cholesterol accumulation has been

linked to defective vesicle trafficking and the impairment of lysosomal fusion to endosomes or autophagosomes, by the aberrant distribution of soluble N-ethylmaleimide-sensitive factor attachment protein receptors (SNAREs) in cholesterol-enriched lysosomal membranes, and locking them in assembled complexes. Loss of SNARE function can lead to inhibited presynaptic SNARE-complex formation, reduced synaptic vesicle recycling, and neurodegeneration (Fraldi et al. 2010; Sambri et al. 2017). The LSD-associated defects in autophagy are nearly universal and can contribute to further downstream effects. For example, impaired lysosome-to-autophagosome fusion can inhibit autolysosome formation, thus disrupting macroautophagy, resulting in irregular mitochondria and accumulation of tertiary storage material e.g., toxic protein aggregates (Cox and Cachon-Gonzalez 2012; Martina et al. 2020). Other examples include, accumulation of toxic metabolites, Ca^{2+} dyshomeostasis, signaling abnormalities, ER stress, oxidative stress, defects in protein folding, inflammatory and innate immune responses, and apoptosis (Cox and Cachon-Gonzalez 2012; Platt et al. 2018; Breiden and Sandhoff 2020). Such phenotypes are not limited to LSDs, however, and can occur in neurodegenerative disorders like Alzheimer's, Parkinson's and Huntington's disease, where protein aggregation and mitochondrial dysfunction are also present (Breiden and Sandhoff 2020).

1.3.5 New technologies and therapies

The knowledge relating to LSD etiology, while expanding rapidly, is largely incomplete. Nevertheless, several successful therapies have been developed and new approaches are being pioneered. Current treatments are largely centered around enzyme replacement, while substrate reduction and chaperone therapies have also been developed. Most recently several gene therapy and genome editing approaches, and adjuvant therapies to target downstream pathways are in progress (Platt et al. 2018; Breiden and Sandhoff 2020). Recent advances in technology have aided in the characterization of lysosomal biology and LSDs, with the development of new diagnostics and novel therapeutic targets. Combining high-throughput phenotyping, such as high-content imaging, with genomic approaches, and metabolic approaches in association with gene editing is becoming widespread, and holds promise for elucidating lysosomal biology and for identifying new treatments (Parenti et al. 2021).

1.4 Niemann Pick Disease

1.4.1 Overview

Niemann-Pick type C is an autosomal recessive, LSD, and exhibits an estimated incidence between 1:89000 and 1:120,000. NP-C is characterized by endolysosomal lipid storage with a diverse symptom profile across visceral, neurological, and psychiatric domains, which can emerge at any time between perinatal period and adulthood. NP-C has traditionally been categorized as a cellular cholesterol trafficking defect and correspondingly, the principal laboratory diagnostic involves filipin staining of patient fibroblasts, with positive results demonstrating the accumulation of unesterified cholesterol in the perinuclear region, however, in the brain, ganglioside storage is the prominent feature. Nonetheless, NP-C cells display a complex lipid storage profile and impairment of LE and lysosome fusion that could be attributed to a variety of causes (Platt et al. 2014). The precise pathomechanisms underlying NP-C are unresolved and though it is known to be caused by mutations to the *NPC1* or *NPC2* genes, precisely how the mutated NPC1 and NPC2 proteins initially alter lysosome function is debated (Lachmann et al. 2004). Though there is no cure, several potential therapies for Niemann Pick type C have been developed and are undergoing testing, including miglustat, HPβCD (cyclodextrin), and HSP70 (Vanier 2010; Patterson et al. 2020a; Patterson et al. 2020b).

1.4.2 NP-C: Clinical manifestations

NP-C symptoms are very heterogeneous and can emerge throughout life into the fifties, with disease progression trajectories tracking differently based on the age of onset for nervous system involvement. In neonatal patients NP-C proceeds rapidly to fatality from systemic hepatic or respiratory failure, while early infantile onset and late infantile onset usually result in death between ages 3-5 or 7-12, respectively. Patients with juvenile onset usually survive until adolescence or later, and often can live until the age of 30. The systemic components may be absent or reduced in nearly 50% of the adult patients. However, when present, they precede the chronic and neurological disease components, with death occurring at an average of 38 years of age. Systemic abnormalities include cholestatic jaundice (in the neonatal period) or hepatosplenomegaly during infancy or childhood. The neurologic symptoms include cerebellar ataxia, dysarthria, and

progressive dementia, marked by neurodegeneration, especially of cerebellar Purkinje and striatal neurons. The majority of patients exhibit vertical supranuclear gaze palsy; cataplexy, seizures, and dystonia are also quite typical, and psychiatric disruption is common in late-onset patients. In the terminal stages, patients develop pyramidal signs and spasticity, and pronounced dysphagia, followed by death typically within 7 to 12 years (Vanier 2010; Patterson et al. 2020b).

1.4.3 NPC1 and NPC2 proteins

The NPC2 protein is a small (132 amino acid), soluble, mannose-6-phosphate-targeted, and secretable, lysosomal glycoprotein that functions as a cholesterol transporter in the lysosome (Okamura et al. 1999; Vanier and Millat 2004; Babalola et al. 2007). Initially identified as a major secreted protein in the epididymis, secretion was later found to occur from the liver and astrocytes, though its function in this regard are unclear (Naureckiene et al. 2000; Friedland et al. 2003; Mutka et al. 2004). NPC2 has been shown to bind cholesterol and related compounds, but not other lipid species; crystal structure suggests that sterol binding occurs in a hydrophobic pocket formed between two β-sheets. Liposomal model systems show that the NPC2 cholesterol transfer rate is modulated by pH, temperature, ionic-strength, and by lipid composition of liposomal model membranes; lysosomal anionic phospholipids, phosphatidyl inositol, and ceramide increased cholesterol transfer by NPC2, while sphingomyelin reduced rates (Babalola et al. 2007; Xu et al. 2007; Luo et al. 2017).

NPC1, located in the limiting membrane of the late endosome and lysosome, is a 140 kDa protein, comprised of 1,278 amino acids, with 13 trans-membrane domains, 3 hydrophobic intralumenal loops, and a small cytoplasmic C-terminal tail which contains a lysosomal targeting motif (Ioannou 2005). NPC1 shares extensive homology with the transmembrane domains of PATCHED-1 (*PTCH1*), with the cholesterol biosynthesis regulating SREBP cleavage-activating protein (SCAP), and NPC1 contains sterol sensing domains in trans-membranes 3-7 (Chin et al. 1984; Hua et al. 1996; Johnson et al. 1996; Carstea et al. 1997; Davies et al. 2000). Moreover, NPC1 exhibits shared topological similarities, namely, two large hydrophilic loops, with the resistance-nodulation-cell division (RND) permease superfamily, whose members largely function in proton driven transmembrane substrate export. Recently, crystallography and cryo-EM studies have

been published showing NPC1 structure, its N-terminal domain complexed with cholesterol (and 25-hydroxycholesterol), and elucidated the presence of pH-dependent conformational changes that could connect NPC1's sterol sensing domain to its N-terminal domain (Kwon et al. 2009; Gong et al. 2016; Qian et al. 2020). Moreover, a motif on the C-terminal tail that interfaces with clathrin adaptor AP-1, is thought to be critical for LE and lysosomal targeting and function. It is intriguing that almost 1/3 of the mutations found in patients, however, are due to mutations in the cysteine-rich third lumenal domain, whose function is unknown; appropriately, though NPC1 structure is becoming clearer, the relationship between structural defects and pathogenesis remains obscure (Vanier 2015).

1.4.4 NP-C pathogenesis

The cause of NP-C is unknown. A distinctive feature of NP-C is that mutations in either *NPC1* or *NPC2* genes produce identical cellular pathologies, though the genes translate into quite different proteins, which suggests that they act on the same pathway. Moreover, NP-C is distinctive regarding its inclusion as an LSD, because unlike the majority of lysosomal storage diseases, neither protein is a hydrolytic enzyme. The functional relationship between NPC1 and NPC2 is not completely understood, because while NPC2 is known to be a cholesterol transporter, the function of NPC1 is contested, and though NPC1 possesses a sterol sensing domain, evidence of NPC1-mediated cholesterol transfer has only been inferred through mutational and computational models (Okamura et al. 1999; Sleat et al. 2004; Vanier 2015; Wheeler et al. 2019). Contrasting models posit different explanations based on the initial storage metabolite in these complex lipid accumulation cascades (Lloyd-Evans and Platt 2010; Platt et al. 2014). The prevailing model suggests that aberrant cholesterol efflux is the principal cause of NP-C, while alternative models postulate that dysregulated sphingosine or sphingolipid dyshomeostasis are the primary drivers of NP-C disease (Lloyd-Evans et al. 2008; Platt et al. 2014).

The cellular profile of NP-C is marked by storage of varied classes of lipid species including cholesterol, sphingomyelin, glycosphingolipids, and sphingosine. By mass, cholesterol and sphingomyelin storage are the most pronounced in peripheral tissues, while, in the brain, glycosphingolipids are the most abundant, and though intracellular distribution of

sphingomyelin and cholesterol are perturbed, there is no evidence for increased abundance of either species in CNS tissue. Unique to NP-C, however, sphingosine storage has been observed in all tissues, and displays a larger fold increase (12x in the periphery and 4x in the brain) than other NP-C storage lipids; this was also shown to correspond to reductions in lysosomal calcium stores. Reduced lysosomal calcium can ultimately result in the reduced upregulation of the CLEAR network which regulates lysosomal function and autophagy (Lloyd-Evans et al. 2008; Wheeler and Sillence 2020). A distinguishing feature of NP-C is the impediment in the endolysosomal pathway at the late endosome. It is thought that this blockage, due to impaired LE-to-lysosome fusion and vesicular transport, might result in late endosomal accumulation of lipids in the LE. Moreover, gene expression, sphingosine-1-phosphate signaling, disrupted autophagy, and mitochondrial function have all been reported. In response, several models have been proposed to explain the functions of NPC1 and NPC2, to identify the primary cause of storage and the primary metabolite responsible for cellular phenotypes observed in NP-C (Lloyd-Evans and Platt 2010).

1.4.4.1 Trafficking

In NP-C, late endosomal motility is impaired, tubulovesicular transport from the late endosome is blocked, and Annexin 2-associated late endosomal trafficking is altered (Ko et al. 2001; Zhang et al. 2001; Lebrand et al. 2002; Mayran et al. 2003; Ganley and Pfeffer 2006; Schweitzer et al. 2009). Ganglioside trafficking visualized by CTxB exhibited abnormal retrograde trafficking to the Golgi (Pagano 2003). Endosomal recycling is reduced in NP-C, and Rab4-positive early endosomal recycling is inhibited, while the internalized transferrin receptor, a classic marker of the endosomal recycling pathway, is mislocalized (Pagano 2003; Wastney et al. 2003; Choudhury et al. 2004; Pipalia et al. 2007; Schweitzer et al. 2009). Recently, the subcellular localization patterns of clinically relevant NPC1 mutants were grouped into three classes, and these classes corresponded with disease severity. The first set of NPC1 mutants corresponded to those observed in milder and adult-onset forms of NP-C and were similar in distribution to the wildtype NPC1, while more severe clinical phenotypes and earlier onset corresponded to the second and third classes of mutants. The second class of NPC1 mutants were partially trafficked to lysosomes, though primarily localized to the ER, while the third group of

mutants were entirely localized to the ER, thus supporting a role for trafficking in NP-C pathogenesis (Shammas et al. 2019).

1.4.4.2 Lipid dyshomeostasis

1.4.4.2.1 Cholesterol

In NP-C disease, impaired cholesterol egress from the lysosome is a prominent cellular feature in the liver and spleen, however this is not the case in the brain. While biochemical analyses of postmortem samples showed no differences in cholesterol levels, histochemical measurements of filipin in the NP-C mouse brain revealed cholesterol localization to LAMP1 positive organelles, which themselves were increased in count and intensity (Vanier 1999; Zervas et al. 2001a). In cultured murine sympathetic NPC null cells, global cholesterol was found to be unchanged, however cholesterol was reduced in the distal axons, and increased in the cell bodies and proximal axons (Karten et al. 2002). Taken together, these results suggest that though total intracellular cholesterol content might remain unchanged, cholesterol distribution is abnormal in NP-C.

The model whereby cholesterol storage is primary to the pathogenic cascade observed in NP-C is suggested to arise due to cholesterol sequestration to the lysosome during endocytosis and hence, due to NPC1 inactivation, unesterified cholesterol can not then be exported to the ER, resulting in cholesterol dyshomeostasis and exacerbating disease progression (Pentchev et al. 1985; Liscum and Faust 1987; Liscum et al. 1989). Counterarguments to this model, highlight the inconclusive nature of the proposed role for NPC1 as a direct cholesterol transporter and propose that NPC1 might function in another capacity, perhaps regulated by cholesterol, for transport of other cargo. Moreover, alternative routes for cholesterol export from the lysosome, evidence of lysosomal cholesterol egress in NPC1 knockouts, and failure of cholesterol reduction to rescue CNS deficits, also detract from the strength of this model and bolster the validity of alternative explanations (Erickson et al. 2000; te Vruchte et al. 2004; Narita et al. 2005; Babalola et al. 2007; Lloyd-Evans et al. 2008; Walter et al. 2009; Lloyd-Evans and Platt 2010).

1.4.4.2.2 Sphingomyelin

Niemann-Pick A and B were determined to be caused primarily by deficient acid-sphingomyelinase activity, however, in NP-C whether defective ASMase is the principal driver of the disease remains unclear. In NP-C, similar to types A and B, liver and spleen cells exhibit storage of several GSLs, cholesterol, LBPA, and sphingomyelin. In the brain, sphingomyelin and cholesterol levels are not elevated, though both are mislocalized and exhibit identical subcellular distribution, which is perhaps unsurprising as they exhibit strong affinity (Schroeder et al. 1994; Simons and Ikonen 1997; Reagan et al. 2000; Patterson 2001; Tamura et al. 2006). However, because sphingomyelin storage is relatively moderate and the ratio of cholesterol to sphingomyelin is greater than in types A and B, it was postulated that sphingomyelin accumulation occurs secondarily to that of cholesterol (Vanier 2015). There is however, evidence to support a chronology in which sphingomyelin accumulation precedes cholesterol storage, as ASMase transfection reduced cholesterol accumulation in NPC1 null cells, and sphingomyelin was shown to inhibit cholesterol transfer by NPC2, while conversely ceramide, a product of ASMase facilitated it (Devlin et al. 2010; Gallala et al. 2011).

1.4.4.2.3 Sphingosine

Sphingosine is increased approximately 4-fold in the CNS and 12-fold in the periphery, and due to its protonated form at low pH, lysosomal export is likely transporter-dependent. There is substantial evidence to indicate that in NP-C, abnormal accumulation in the lysosome might arise due to NPC1 dysfunction and that NPC1 is at least in part, a sphingosine transporter (Rodriguez-Lafrasse et al. 1994; te Vruchte et al. 2004; Lloyd-Evans et al. 2008). To support this, exogenous addition of amphiphilic amines, including U18666A and sphingosine, reproduces the NP-C phenotype in wildtype cells (Roff et al. 1991; Lloyd-Evans et al. 2008). Moreover, the chronology of pathogenic events observed in response to NPC1 inactivation indicated that sphingosine levels increased within minutes, leading to reductions in lysosomal calcium loading (thus disrupting NAADP-signaling and LE/lysosomal fusion), to be followed hours later by increases in sphingolipids and cholesterol; thereby, presenting NPC1 as a sphingosine transporter, which was later supported by molecular modeling (Lloyd-Evans et al. 2008; Wheeler et al. 2019). Building on this model, in conjunction with data showing Miglustat-mediated NP-C

rescue via GBA2 inhibition, support the possibility that dysfunctional NPC1 efflux leads to reduced cytoplasmic sphingosine, and thus decreased GBA2 inhibition. This results in increased hydrolysis of GluCer and reduced cytosolic GluCer, a vATPase activator. Dysregulated vATPase activation, then leads to defective lysosomal acidification and trafficking (Höglinger et al. 2015; Chakraborty et al. 2017; Höglinger et al. 2017; Wheeler et al. 2019; Wheeler and Sillence 2020). By contrast, measurements of radiolabeled and fluorescent sphingosine showing that NPC1 null cells have an expanded capacity to store sphingosine, with unrestricted efflux from the LE/lysosome, evidenced against a crucial role for NPC1 as a sphingosine exporter (Blom et al. 2012). However, it was argued that these measurements were likely taken outside of the normal and rapid metabolic processing window for sphingosine, and later efforts demonstrated an increase in lysosomal sphingosine retention within a more physiologically relevant time scale (30 minutes). Moreover, even if NPC1 does transport other molecules, this does not exclude the possibility that NPC1 might act as a multisubstrate efflux pump and function in sphingosine export (Blom et al. 2012; Höglinger et al. 2015).

1.4.4.2.4 Glycosphingolipids

In the NPC brain, when compared to other lipids, glycosphingolipids exhibit the greatest increases (Zervas et al. 2001b; te Vruchte et al. 2004). Gangliosides GM2 and GM3, in particular, though normally present in small amounts, respectively exhibited 3-5x and 10-15x increases in NP-C patient autopsy samples, and storage of glucosylceramide, lactosylceramide, and asialo-GM2 were also observed (Vanier 1999). In mice unable to synthesize GM1 and GM2 the NP-C phenotype was still present, however, neurons displayed cholesterol reductions, supporting the premise that cholesterol storage is dependent on ganglioside storage, and that NPC1 function is more closely connected to GSL homeostasis, than cholesterol (Gondré-Lewis et al. 2003). Correspondingly, heterozygous deletion of GM3 synthase results in reduced cholesterol, sphingomyelin and amelioration of symptoms (Lee et al. 2014). Indeed, inhibition of glucosylceramide at the first step of GSL biosynthesis, by Miglustat, was shown to benefit NP-C patients and was approved for use in Europe in 2009 (Zervas et al. 2001b; Patterson et al. 2007; Pineda et al. 2009).

1.4.4.3 Autophagy

Several studies have shown misregulated autophagy in NP-C, though reports are inconsistent. Slowed autophagy has been observed corresponding to autophagosomes that are unable to fuse with lysosomes (Ko et al. 2005; Pacheco et al. 2007; Sarkar et al. 2013). In contrast, ESC-derived neurons and fibroblast models displayed increased autophagic activity. Explanations for reduced levels of autophagy cite possible overlapping processes involving the endocytic block at the LE, including those pertaining to defects in fusion, pH, calcium, and cholesterol (Koga et al. 2010; Aldrich et al. 2015; Wijdeven et al. 2016; Zhang et al. 2016). On the contrary, increased autophagosome proliferation is thought to be possibly a compensatory mechanism to counter the decreased autolysosomal clearance attributed to reductions in lysosomal protease activity caused by lipid accumulation (Pacheco et al. 2007; Elrick et al. 2012; Sarkar et al. 2013; Wheeler and Sillence 2020). Moreover, impaired mitophagy was observed in NP-C neuronal models (Kennedy et al. 2014).

1.4.4.4 Mitochondrial function

Impaired mitochondrial function and energy metabolism also occur in NP-C, as increased reactive oxygen species (ROS), increased lactate secretion, and reduced oxygen consumption, respiration, ATP synthase activity and ATP transport across mitochondrial membranes (Yu et al. 2005; Koh et al. 2006; Klein et al. 2011; Visentin et al. 2013; Kennedy et al. 2014; Torres et al. 2017; Wang et al. 2018). Recently, a new inducible, integrated, and isogenic or i^3 neuronal platform, was used to demonstrate that both basal and maximal oxygen consumption rates were reduced in NPC1 null cells (Prabhu et al. 2021). Metabolic defects are largely attributed to excessive mitochondrial cholesterol observed in NP-C (Torres et al. 2017; Solsona-Vilarrasa et al. 2019). Efforts to clarify this mechanism, showed that while NPC1-deficient cells display increased levels of mitochondrial cholesterol, cholesterol transport to the inner mitochondrial membrane is not affected; reducing MLN64 (STARD3) led to reduced cholesterol transport and mitochondrial cholesterol levels, which supports the model in which NPC2 transports cholesterol independently of NPC1 (Charman et al. 2010; Lloyd-Evans and Platt 2010; Kennedy et al. 2012). Moreover, recent gene expression data linked repressed mitochondrial biogenesis to functional defects independent of cholesterol accumulation,

to suggest that cholesterol accumulation itself is not the cause of dysfunction and instead is linked to impaired sphingosine-1-phosphate (S1P) signaling through S1P receptor 1 (S1PR1) mistargeting and subsequent upregulation of mitochondrial biogenesis repressor circuits. (Yambire et al. 2019; Wheeler and Sillence 2020).

1.5 Therapeutic intervention and Miglustat

There is no cure for NP-C, however 9 clinical trials for therapeutic intervention are underway. As of Jan 20, 2022 the efficacy of cyclodextrins (hydroxypropyl-β-cyclodextrin, adrabetadex, VTS-270) is being tested in 6 trials (phase 1, 2, and 3), Arimoclomol, is being evaluated in a phase 2/3 trial, N-Acetyl-L-Leucine is in phase 1/2, while miglustat is undergoing phase 4 clinical trials in China (data from clinicaltrials.gov). Treatment strategies have been targeted to various elements of the disease cascade. Cyclodextrins, cyclic oligosaccharides, previously used to solubilize drugs for delivery, were shown to mobilize and reduce cellular cholesterol stores in NP-C mouse and cat models (Camargo et al. 2001; Davidson et al. 2009; Liu et al. 2009; Vite et al. 2015). Hydroxypropyl-β-cyclodextrin (HPβCD), has shown promising results, with patients exhibiting slowed disease progression along with reductions in neuronal damage biomarkers, however, the precise mechanism of action is unclear and due to its low permeability across the blood brain barrier (0.1 - 1.0%) it has to be administered intrathecally (Ory et al. 2017). Arimoclomol has shown promise in phase 2-3 clinical trials with a 74% reduction in disease progression (Mengel et al. 2021). Arimoclomol stimulates the expression of heatshock protein 70 (HSP70), which is thought to correct mutant NPC1 protein misfolding. N-acetyl-L-leucine, a modified version of leucine used to treat vertigo, led to significant reduction in disease and clinical improvement in a small phase 2 study, though 93.8% of patients were on the standard care agent, miglustat (Bremova-Ertl et al. 2021). N-acetyl-L-Leucine reduces lysosomal volume and is thought to alter glucose and antioxidant metabolism (Kaya et al. 2021). Currently, however, the only therapy approved for NP-C, is miglustat.

Miglustat is an imminosugar administered as part of a substrate reduction therapy, acting by competitive inhibition of glucosylceramide synthase, towards reducing GluCer at the first step in GSL biosynthesis, which consequently, reduces overall lysosomal lipid

accumulation. Miglustat was initially developed as a potential HIV treatment, and though it was not used in this capacity, it was later applied as a substrate reduction strategy and was first proposed as a treatment for glycosphingolipids, proving to be beneficial in treating not only NP-C, but Gaucher disease types 1 and 3 (Matos et al. 1999; Platt et al. 2001; Lachmann et al. 2004; Patterson et al. 2007). Miglustat has been approved to treat NP-C patients in the EU, Japan, and Canada; though the FDA has not approved miglustat for use in the USA, it is often prescribed (Sun 2018).

The mechanism of action was later revisited, however, as miglustat treated NP-C mice, though showing improvement, still exhibited increased neural GluCer and unaltered ganglioside GM2 and GM3 levels; it was later determined that miglustat acted more to inhibit GBA2, a cytoplasmic glucosylceramidase, than glucosylceramide synthase (Nietupski et al. 2012; Ridley et al. 2013). Moreover, a specific inhibitor of GBA2 has shown effectiveness in mouse NPC1-deficient mice, and conversely, GM2 and GM3-synthase deletion conferred no benefit, which suggests that GSL accumulation is not the primary dysfunction in NP-C (Liu et al. 2000; Lee et al. 2014; Marques et al. 2015). Regardless of the particular molecular mechanism, miglustat has demonstrated effectiveness in treating more than one disease, and due to the previous work describing similar disease phenotypes in NP-C and HD, it is reasonable to test the effects of miglustat in HD models.

1.6 Huntington's Disease

1.6.1 Background

Huntington's disease was first clinically described in 1872 and designated "hereditary chorea" by George Huntington. HD is a heritable and terminal illness and over the course of the disease, patients experience progressive declining psychiatric, motor, and cognitive health. These declines result from neurodegeneration, mainly of medium spiny neurons (MSNs) in the striatum, though neurodegeneration also occurs in the cortex. HD is autosomal dominant, and arises from an expanded CAG repeat in the huntingtin gene *(HTT)*, which encodes the protein (HTT), with a correspondingly elongated polyglutamine (polyQ) tract. (Reiner et al. 1988; Albin et al. 1992; MacDonald et al. 1993; Sapp et al. 2001). However, despite massive efforts, resulting in several promising explanations and potential treatments for HD, the precise pathological mechanisms underlying the causal link from mutation to neuronal death remains unknown.

1.6.2 Epidemiology

HD occurs equally in both males and females with onset usually occurring between the ages of 35 and 44 (Harper 1992; Duyao et al. 1993). Based on a metadata analysis of 13 studies, global prevalence was determined to equal roughly 2.71 per 100,000 people (Pringsheim et al. 2012). The highest rates of prevalence occur in western countries (North America, Australia, and Europe) with estimates ranging between 9.71 and 13.7 per 100,000 people (Fisher and Hayden 2014; Baig et al. 2016; Rawlins et al. 2016; Kay et al. 2018). A study conducted in South Africa identified a reduced frequency in the black population compared with those of mixed ancestry, or whites, at 0.25, 2.10, and 5.10 per 100,000 individuals, respectively (Baine et al. 2016). Studies across Japan, Korea, Taiwan, and Hong Kong reported dramatically reduced rates with prevalence estimates between 0.1 and 0.72 per 100, 000 people (Chang et al. 1994; Adachi and Nakashima 1999; Chen and Lai 2010; Kim et al. 2015; Kay et al. 2018).

1.6.3 HD: Clinical manifestations

1.6.3.1 Selective neurodegeneration

Examination of HD patient live-imaging and post-mortem samples, showed substantial cell death and selective neurodegeneration, with significant cell loss and atrophy, mainly, but not exclusive to the striatum and the cortex, with correlation data attributing CAG length to 66-78% of the striatal loss (Vonsattel et al. 1985; Penney Jr et al. 1997; Vonsattel and DiFiglia 1998; Culjkovic et al. 1999; Zuccato et al. 2010; Hadzi et al. 2012; Podvin et al. 2019)

The majority of cell loss occurs in the striatum, which acts as the information input hub of the basal ganglia by integrating excitatory, sensorimotor, motivational, and cognitive behavioral output from the cortex, to project to the globus pallidus and substantia nigra (Groves 1983; Alexander 1994; Graybiel 1998; Heinsen et al. 1999; Bolam et al. 2000; Miller et al. 2008). More specifically, in the caudate and putamen, medium spiny neurons which constitute > 90% of the regional population, and function as the sole output of the striatum, are most affected (Gutekunst et al. 1995b; Vonsattel and DiFiglia 1998; Rubinstein 2003; Gusella and MacDonald 2006).

Other affected regions include the midbrain, pons, thalamus, substantia nigra, cortical layers III, V, and VI, the CA1 region of the hippocampus, the parietal lobe, cerebellar Purkinje cells, lateral tuberal nuclei in the hypothalamus, and the centromedial-parafascicular complex in the thalamus (Jeste et al. 1984; Vonsattel et al. 1985; Kremer et al. 1991; Kremer 1992; Spargo et al. 1993; Macdonald et al. 1997; Heinsen et al. 1999; Macdonald and Halliday 2002; Podvin et al. 2019).

1.6.3.2 Cognitive manifestations

HD patients display cognitive deficits, prior to, and independent of motor impairments, with increasing severity as the disease progresses (Stout et al. 2011). In the prodromal phase, detectable impairments in executive functioning, memory, processing speed, spatial perception, are measurable approximately 15 years before onset (Duff et al. 2010; Stout et al. 2011).

In later stages, though symptomology varies widely in HD, patients frequently experience deterioration in speech, acquisition of new motor skills, and executive functioning i.e., flexible and dynamic planning, organization, focus, and integration of information, resulting in a decline in the ability for flexible and reflective decision making (Craufurd and Snowden 2002; Walker 2007). Finally, death ensues after roughly 15-20 years of cognitive decline.

1.6.3.3 Psychiatric symptoms

Psychiatric and behavioral symptoms also typically manifest as anxiety, depression, irritability, psychosis, and often as suicidal ideation (up to 20% of HD cases) (Hubers et al. 2012; Wiprich and Bonan 2021). Following pneumonia and other infections, suicide is the third most frequent cause of death (6.6%) occurring much more frequently (up to 10x greater) than is encountered in the non-HD population (Di Maio et al. 1993; Craufurd and Snowden 2002; van Duijn et al. 2021).

1.6.3.4 Motor impairments

Clinical assessment of motor dysfunction is subdivided into early and late stages, with chorea occurring in the early stages, though this symptom is often lacking in juvenile patients. In the late stages, chorea associated with HD decreases, while the voluntary movements are impaired, causing bradykinesia, akinesia, dystonia, and motor incoordination. (Walker 2007; Wiprich and Bonan 2021). Dysarthria and dysphagia are also common features of HD as muscles necessary for speech interfere with respiratory, laryngeal, velopharyngeal and articulatory muscle activities, with some patients losing the ability to talk (Roos 2010).

1.6.3.5 Genetic cause of HD

The gene responsible for HD was first localized to chromosome 4 by identification of a genetic marker (G8) specific to HD patients (Gusella et al. 1983). Next, precise localization of the huntingtin gene (*HTT*) alternatively known as interesting transcript 15 (*IT15*) on the terminal portion of the short arm of chromosome 4 (4p16.3) was identified (Bućan et al. 1990). Shortly thereafter, the expansion of a CAG trinucleotide tract in the first exon, was identified, with age of onset determined by, and inversely proportional to, the length of the repeat (Figure 1.9), and where a CAG trinucleotide repeat greater than 36 results in HD

(Table 1) (Gusella et al. 1983; Andrew et al. 1993; MacDonald et al. 1993; Myers 2004). While HD is usually inherited, de novo emergence (sporadic HD) is estimated to occur in about 10% of the HD population and most frequently due to expansion in the paternal germline. (Warby et al. 2009)

CAG trinucleotide number	Classification	Effect	Reference
< 27	normal results	no risk of HD	(Ross and Tabrizi 2011)
27 - 35	intermediate	offspring potentially at risk	(Killoran et al. 2013)
36 - 39	reduced penetrance	later age of onset, offspring at risk	(Rubinsztein et al. 1996)
≥ 40	full penetrance	will develop HD in normal life span, offspring at risk	(Buren et al. 2016)
≥ 50	juvenile	early onset	(Cowan and Raymond 2006; Bates et al. 2015)

Table 1.1 CAG trinucleotide-repeat length and Huntington disease prognosis.

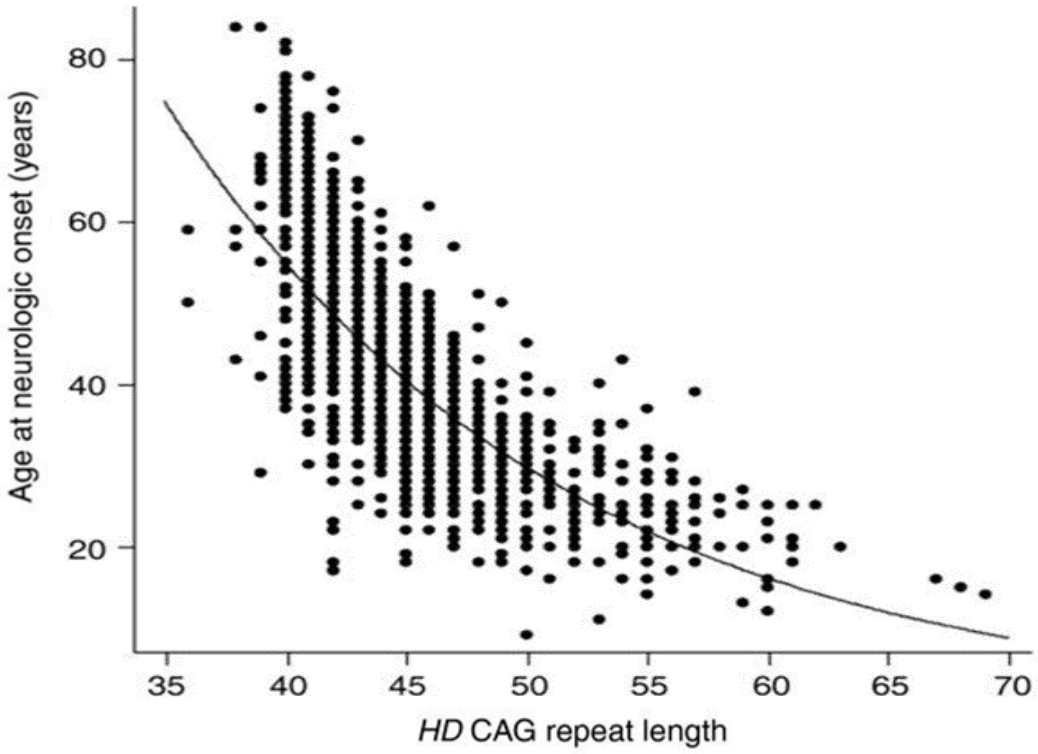

Figure 1.9: CAG trinucleotide repeat length is associated with age of onset. (Gusella and MacDonald 2009)

In humans, *HTT* is located on the p-arm of chromosome 4 from position 3,041,422 to 3,243,960, across a length of 202,539 bp, and contains 67 exons (MacDonald et al. 1993; Kent et al. 2002). The huntingtin gene encodes a 348 kDa protein comprised of 3,144 amino acids, and the CAG repeat translates into a corresponding polyQ tract. The expanded CAG repeat seen in HD patients is thought to be responsible for neurodegeneration and death of medium spiny neurons of the striatum, cortical-striato projection neurons, and altered glial dynamics (Reiner et al. 1988; Albin et al. 1992; Sapp et al. 2001). However, the precise mechanisms underlying HD remain unclear and there are no effective preventative or curative treatments (Coppen and Roos 2017)

Efforts towards understanding the causes of HD have largely been directed at identifying and characterizing the role of both the wildtype and mutant huntingtin protein, their interaction targets, and examination of associated downstream biochemical phenotypes, while more recently others have considered pathological attributes originating prior to and independent of translation, at the epigenetic, genomic and transcriptional levels (Gusella and MacDonald 2000; Ng et al. 2013; Sathasivam et al. 2013b; Lee et al. 2015; Lee et al. 2019).

1.6.4 Huntingtin protein

1.6.4.1 Wildtype huntingtin

Mammalian HTT is highly conserved, and critical for development in mice, while vestiges of HTT (some with a single Q) are observed at the protostome-deuterostome divide, with urchins displaying a 17 amino acid NHQQ tract (Saudou and Humbert 2016). The N-terminus contains 17 amino acids which form an amphipathic alpha-helix for anchoring into the ER (Atwal et al. 2007). Secondary structure of HTT shows that at a polyQ length of 17, this is a flexible multi-conformational region that can form an alpha-helix, random coil, or extended loop, followed by a proline rich domain (specific to Mammalia), which is comparatively rigid and exhibits a straight or kinked conformation and may act to stabilize the polyQ region. While the remaining regions of the protein remain less characterized, several HEAT domains (important for protein-to-protein interactions have been identified (Atwal et al. 2007; Palidwor et al. 2009). The predicted structure suggests that HTT functions as a scaffold protein (Caviston and Holzbaur 2009).

HTT is present spatially and temporally throughout most tissues and is critical to development as absence in knockout mice is embryonically lethal between days (E)8.5 and (E)10 (Duyao et al. 1995; Nasir et al. 1995a; Zeitlin et al. 1995). The normal and mutant forms of huntingtin have been shown to be expressed at similar levels in the CNS and are also present in peripheral tissues. Within the brain, huntingtin was found predominantly in neurons and was present in cell bodies, dendrites, and also in the nerve terminals, and transiently transfected HTT was shown to localize with the Golgi and clathrin coated vesicles (Trottier et al. 1995; Strehlow et al. 2007). However, disentangling the role of HTT in the

neuropathogenesis of HD has been problematic, in part, because it is pleiotropic and multifunctional, with over 350 confirmed interaction partners, many of which associate differentially with the wildtype and mHTT, notably huntingtin interacting proteins (HIPs) and huntingtin associated proteins (HAPs); these cover a broad range of functions involving synaptic transmission, cytoskeletal organization, signal transduction, and transcription (Kaltenbach et al. 2007; Culver et al. 2012). Correspondingly, interactome mapping and Gene Ontology enrichment analysis show a breadth of huntingtin-related processes including transcription, translation initiation, nucleic acid binding, DNA maintenance, intracellular transport, calcium signaling, proteostasis, mitochondrial function, cytoskeletal organization, clathrin-mediated endocytosis, GABA receptor signaling, and autophagy, amongst many others (Culver et al. 2012; Shirasaki et al. 2012; Labbadia and Morimoto 2013).

Process	Properties	References
vesicle trafficking	- HTT: contains HEAT domains - HTT interacts with components of molecular motor (directly or indirectly) e.g., HAP1, p150^{glued}. - HTT transports: lysosomes, endosomes, autophagosomes - HTT transports vesicles positive for BDNF, GABA-receptors - HTT RNAi: disrupted axonal transport - HTT knockdown: disrupted iron transport - HTT gene expression and proteomics: intracellular transport	(Takano and Gusella 2002; Gunawardena et al. 2003; Gauthier et al. 2004; Caviston et al. 2007; Lumsden et al. 2007; Strehlow et al. 2007; Colin et al. 2008; Caviston and Holzbaur 2009; Caviston et al. 2011; Culver et al. 2012; Shirasaki et al. 2012; Liot et al. 2013; Zala et al. 2013; Wong and Holzbaur 2014)
autophagy	- HTT homology with yeast autophagy proteins - polyQ deletion promotes autophagy in mice - LC3 interacting repeats in HTT - HTT binding to p62 promotes cargo loading - Interaction with ULK1 and mTOR, to initiate autophagy	(DiFiglia et al. 1995; Sharp et al. 1995; Ochaba et al. 2014; Rui et al. 2015a)
mitochondrial function	- HTT knockout mESCs: abolished ATP production, increased glycolysis, increased ketogenesis - HTT knockout mESCs: loss of structural integrity	(Ismailoglu et al. 2014)
development	- HTT Knockout: lethal to mouse embryos, defects in gastrulation - HTT Knockdown mice: abnormal cortex and striatum formation, neuron loss in basal ganglia early death	(Duyao et al. 1995; Nasir et al. 1995a; White et al. 1997; Lumsden et al. 2007)
anti-apoptosis	- HTT neuroprotective against apoptotic genes, serum withdrawal, mitochondrial toxins - HTT overexpression neuroprotective against ischemic injury and NMDA-mediated excitotoxicity - HTT knockout zebrafish: reduced BDNF and increased apoptosis	(Zeitlin et al. 1995; Rigamonti et al. 2000; Zhang et al. 2003b; Leavitt et al. 2006)
cognition	- HTT heterozygous mice: cognitive deficiencies	(Nasir et al. 1995a)
mitosis	- HTT RNAi: decreased mitotic spindle length and misorientation during mitosis	(Godin et al. 2010)
transcriptional regulation	- HTT interacts with transcription factors: CREBP, NeuroD, p53 - HTT interacts with nuclear receptors: LXR, peroxisome proliferator-activated receptor-γ - HTT binds REST/NRSE to derepress BDNF transcription	(Steffan et al. 2000; Zuccato et al. 2001; Marcora et al. 2003; Zuccato et al. 2003a; Zuccato et al. 2003b; Cha 2007; Futter et al. 2009)

Table 1.2. List of properties associated with wildtype huntingtin.

1.6.4.2 Huntington Isoforms

To complicate matters, HTT is present in two different isoforms (10,366 bp and of 13,711 bp), the latter of which is enriched in the brain, and includes an additional 3' UTR, while alternative splicing also occurs (Lin et al. 1993; Hughes et al. 2014). Importantly, aberrant splicing of mHTT mRNA, results in a shortened form, containing HTT-exon 1 and the 5' region of intron 1, which translates to a truncated protein (Sathasivam et al. 2013a). Post-translational proteolysis occurs at several sites, and associated proteases were found to be upregulated in the HD patient brain, and are thought to contribute to the accretion of toxic N-terminal fragments (Benn et al. 2005; Graham et al. 2006; Atwal et al. 2007).

1.6.4.3 Mutant Huntingtin

1.6.4.4 Expanded CAG Repeat

At the transcriptional level, a toxic role for mutant transcripts has also been suggested as CAG repeats, in HD (and other trinucleotide repeat disorders) can form hairpin structures and are more frequently retained to the nucleus, suggesting that *HTT* mRNA may form double-stranded RNA conformations *in vivo* which aberrantly interact with ds-RNA binding proteins, leading to abnormal RNA metabolism (De Mezer et al. 2011). More recent research evidences that the CAG repeat not the polyQ region drives the timing of HD onset, with additional mechanisms involving DNA-repair, somatic expansion of the CAG repeat in post-mitotic neurons (particularly in the striatum and cortex), and genetic modifier influences also likely contributing (Gonitel et al. 2008; Swami et al. 2009; De Mezer et al. 2011; Lee et al. 2015; Lee et al. 2019).

1.6.4.5 Toxic N-Terminal Fragment

Proteolytic cleavage of mHTT, which yields a toxic N-terminal fragment has been shown to be integral to the progression of HD, as these form aggregates, occurring as nuclear inclusions in dystrophic neurites. Whether aggregates are toxic is disputed, though aggregate reduction has been linked to a milder disease phenotype (Sanchez et al. 2003; Sathasivam et al. 2013a; Jimenez-Sanchez et al. 2017). Mis-splicing events occur in a length-dependent manner, with the frequency directly proportional to increased CAG length; as the CAG

trinucleotide repeat increases, so does the concentration and aggregation of toxic fragments. The truncated N-terminal version is shuttled to the nucleus more readily, however the polyQ interacts with the nuclear pore protein translocated promoter region (TPR), to decrease export and increase aggregation and nuclear accumulation, resulting in sequestration to the hallmark inclusion bodies (IBs) observed in HD Neurons (Cornett et al. 2005; Neueder et al. 2017). Similar aggregates and proteotoxicity is seen in other polyQ disorders, as well as in Alzheimer's and Parkinson's disease (Arrasate and Finkbeiner 2005). The link between aggregates and IBs with disease progression remains unclear, however, as it has been shown that though nuclear localization of mHTT is required for apoptosis, neurodegeneration is not necessarily caused by aggregate formation, as seen in the dentate nucleus of HD patients, and that IBs may function in a neuroprotective capacity (Becher et al. 1998; Saudou et al. 1998).

1.7 Cellular pathology in HD

1.7.1 Gain of function

HD pathogenesis is largely thought to occur due to a novel gain of mHTT function. While HTT-null mice experience embryonic death and mice expressing less than 50% of HTT experience developmental defects, mHTT homozygous humans and mice do survive, and an individual expressing only one functional HTT protein was observed to be normal, thus complete loss of wildtype function was eliminated as an all encompassing explanation for pathogenesis (Ambrose et al. 1994; Duyao et al. 1995; Nasir et al. 1995a; Zeitlin et al. 1995; White et al. 1997; Auerbach et al. 2001). Moreover, in transgenic mice models mHTT expression alone is sufficient to induce HD-like phenotypes (Zhang et al. 2003b). Another line of reasoning to suggest the gain of function, is supported by the lack of role for haploinsufficiency in other polyglutamine diseases, which do however exhibit strong correlations between age of onset and increased polyglutamine length, as well as emergent structural properties e.g., aggregates and nuclear inclusions (Walker 2007). The structure of polyglutamine strands themselves provide strong evidence for a gain of function as once past a minimum threshold of 37 in HD, they begin to form dimers, trimers, oligomers, and finally aggregates, which

overwhelm the cell's ability to degrade them; these aggregates then recruit and interfere with normal proteins including those that interact with wtHTT, suggesting the possibility of a dominant-negative effect (Dröge and Wanker 2002; Busch et al. 2003; Rubinstein 2003; Gauthier et al. 2004; Rangone et al. 2004; Mills et al. 2005; Zuccato et al. 2005; Walker 2007). Direct evidence for mHTT and caveolin-1 (Cav1) interaction, suggest a gain of function role towards promoting post-Golgi trafficking defects and lipid dysfunction (Trushina et al. 2014). Furthermore, vesicle trafficking defects in anterograde and retrograde BDNF transport, were rescued by allele-specific mHTT silencing in patient hESC-derived neurons (Drouet et al. 2014). Finally, gene expression comparisons across an allelic panel of knock-in mice with varied CAG lengths versus an HTT null mouse, suggest a simple gain of function over a dominant-negative or mixed gain/loss model as well, as expression correlating to increased CAG-length failed to overlap with the knockout-related gene set; however energy and lipid metabolism pathways, from the differing gene sets did converge, and interestingly, on cholesterol biosynthesis (Jacobsen et al. 2011).

1.7.2 Loss of function

There is evidence that HD pathogenesis is, in part, the result of loss of wildtype HTT function, as wtHTT is fundamental to development, neuroprotection and anti-apoptosis mechanisms, and mitotic spindle dynamics (Table 1.2). Wildtype huntingtin functions in a developmental and anti-apoptotic capacity, as HTT-null mouse embryos exhibit developmental defects and death, and though HD is not a result of nullizygous mutations, mice heterozygous for functional wtHTT, displayed increased motor activity, cognitive deficiencies, and loss of neurons in the subthalamic nucleus of the basal ganglia, thus supporting a pathogenic link to HTT haploinsufficiency (Duyao et al. 1995; Nasir et al. 1995a; Zeitlin et al. 1995; O'Kusky et al. 1999; Dragatsis et al. 2000). Wildtype HTT has been shown to inhibit transcriptional repression of BDNF through cytoplasmic sequestration of repressor element-1 transcription factor/neuron restrictive silencer element (REST/NRSE), and increased nuclear REST/NRSE is present in HD, which implicates reduced trophic support from loss of wtHTT-mediated transcriptional regulation in HD pathogenesis (Zuccato et al. 2001; Zuccato et al. 2003a). Direct evidence for apoptotic and neuroprotective properties of huntingtin was established

in vitro as wtHTT overexpression in ST14A conditionally immortalized rat striatal cells, reduced cell death in the presence of transient expression of pro-apoptotic genes Caspase-9, and BCL2 homologues Bik and Bak (mHTT overexpression resulted in increased susceptibility), serum withdrawal, and exposure to mitochondrial toxins, suggesting wildtype HTT action on components of the common death effector pathway and on mitochondria-related apoptosis (Rigamonti et al. 2000). Increased polyQ length reduces HTT binding to HIP1, allowing free HIP1 to bind with HIP1 protein interactor (HIPPI) and form pro-apoptotic HIPPI-Hip1 heterodimers, which can complex with procaspase-8 to trigger the cell death pathway and activate proteolytic enzymes like caspase-3 (Gervais et al. 2002). Moreover, wtHTT overexpression protects against ischemic injury, and in a dose-dependent manner is neuroprotective against NMDA-mediated excitotoxicity, to suggest a model whereby in HD, excitotoxic stress induces caspase-3-mediated cleavage of mHTT, increasing toxic N-terminal fragments and aggregation, leading to depletion of wtHTT in neurons, with a corresponding inability to counteract pro-apoptotic stimuli (Zhang et al. 2003b; Leavitt et al. 2006). RNAi-mediated silencing of HTT resulted in decreased mitotic spindle length and misorientation during mitosis through mislocalization of the dynactin subunit $p150^{glued}$, dynein, and NuMA, leading to disrupted axonal transport and apoptosis (Godin et al. 2010). Thus, several essential cell processes are dependent on the normal function of wtHTT, and in our lab accumulating evidence supports a possible role for wtHTT in NPC1 function, possibly related to NPC1 trafficking, whereby the loss of wtHTT results in NPC1 dysfunction or mislocalization and a similar disease profile.

1.7.3 Endolysosomal structural defects

Structural irregularities in the lysosome have been observed in models of HD. In mouse striatal cells, exogenous cytoplasmic HTT was shown to induce endolysosomal and autophagic activity and localization to enlarged lysosome-like structures, which corresponds to observations of increased huntingtin-positive, endolysosome-like vacuoles in patient brains (Sapp et al. 1997; Kegel et al. 2000). Lysotracker is used to measure relative acidic compartment volume as a universal biomarker for LSDs (Te Vruchte et al. 2014) and increased Lysotracker area evidenced expansion in HD patient-derived iPSC and iPSC-derived

neuronal models (Camnasio et al. 2012). More specific to HD, patient iPSC-derived GABAergic medium spiny-like neurons also exhibited increased lysosome/autophagosome content (Nekrasov et al. 2016). R6/2 mouse iPSC models recapitulate some but not all HD phenotypes, nonetheless, increased lysosome counts were observed and related to increased mRNA levels of lysosome-related genes in these models (Castiglioni et al. 2012). Lysosomal positioning, which coordinates cellular metabolic processes through mTORC1 activation and anabolism on the periphery, versus starvation, catabolism, and autophagy in the perinuclear region, is also altered in HD models, as LAMP1 and LAMP2 staining indicated the presence of a significantly altered and perinuclear distribution in immortalized embryonic striatal STHdh and mouse knock-in Q111 models, respectively (Koga and Cuervo 2011; Korolchuk et al. 2011; Erie et al. 2015). In addition to earlier works, altered morphology and mislocalization of endolysosomal vacuoles in HD models have also been observed in the Lloyd-Evans lab (Haslett 2015; Clark 2017).

1.7.4 Trafficking defects

HD is associated with a number of trafficking defects and has been shown to localize with the Golgi and clathrin-coated vesicles, suggesting a role in trafficking (Strehlow et al. 2007). HTT contains multiple HEAT domains and is involved with the regulation of axonal transport and vesicle trafficking through HAP1 interaction, to mediate dynein, kinesins, and dynactin (Caviston and Holzbaur 2009; Guo et al. 2018), and facilitates transport of autophagosomes, endosomes, lysosomes, and mitochondria. HTT deficiency impairs transport efficacy (Trushina et al. 2004; Caviston et al. 2011; Liot et al. 2013; Wong and Holzbaur 2014), while HAP1 deficiency results in striatal neurodegeneration in mice, dependent on Rhes-mediated sumoylation of mHTT (Liu et al. 2020). Increased HAP40, which is observed in HD STHdhQ111 mouse striatal cells, facilitates recruitment of HTT by RAB5 to early endosomes, and regulates early endosome motility, with HD models exhibiting altered endosome and endocytic activity (Pal et al. 2006). In HD, reduced lysosomal mobility was observed in STHdhQ111 mouse striatal cells in contrast to STHdhQ7 controls, which in addition to the perinuclear localization, suggests that mHTT might decrease anterograde or promote retrograde lysosomal transport (Erie et al. 2015). Inhibition of fast axonal trafficking (FAT)

has also been linked to HD pathogenesis, through activation of cJun N-terminal kinase (JNK)-mediated phosphorylation of kinesin-1 in mouse and squid models, which decreases kinesin-1 to microtubule binding affinity (Szebenyi et al. 2003; Morfini et al. 2009). In *drosophila* and *C. elegans* axons, mHTT aggregate formation impeded synaptic vesicle and mitochondrial transport (Li et al. 1999; Li et al. 2001; Parker et al. 2001; Gunawardena et al. 2003; Chang et al. 2006; Sinadinos et al. 2009). Consistent with its predicted role as a scaffold protein, huntingtin was shown to regulate selective autophagy through binding to p62 and ULK1 (Rui et al. 2015a). Huntington also facilitates endocytosis, vesicle recycling and endosomal trafficking through interactions with HIP1 and HIPR, which in turn, participate in clathrin-mediated endocytosis, membrane invagination, and the assembly of the clathrin coating (Engqvist-Goldstein et al. 2001; Waelter et al. 2001; Legendre-Guillemin et al. 2002) which along with caveolin-dependent endocytosis are disrupted by mHTT (Trushina et al. 2006a; Li and Conforti 2013; Yu et al. 2014). Moreover, HTT regulates anterograde and retrograde mitochondrial movement (Trushina et al. 2004). In neuronal models, regulated secretory trafficking of Val-BDNF from the Golgi is also impaired, by mHTT expression (del Toro et al. 2006). In HD patient fibroblasts, and HD mouse models, mHTT was found to inhibit Rab11, resulting in reduced recycling vesicle biogenesis and altered transport of the glutamate transporter EAAC1, which is associated with oxidative stress and neurodegeneration. Given the variety of interdependent processes associated with trafficking it is unsurprising that dysfunction in HD results in such an array of defects.

1.7.5 Impaired autophagy in HD

Defective basal autophagy is sufficient to produce neuronal death (Hara et al. 2006; Komatsu et al. 2006). Autophagic dysfunction as a result of mHTT is well known in research and is often used in primary screens to detect proteins involved in lysosome-mediated macroautophagy, by elimination of mHTT aggregates (Croce and Yamamoto 2019). PolyQ deletion enhanced autophagic activity in *drosophila* and mice, with the latter also exhibiting increased lifespans (Zheng et al. 2010). Ultrastructurally, cells expressing mHTT display an increase in number and size of autophagosomes compared to wildtype counterparts and the accumulated substrate was observed to exhibit a 'fingerprint' conformation (Kegel et al.

2000; Nagata et al. 2004; Sarkar and Rubinsztein 2008; Del Toro et al. 2009). In HD mouse and human models, increased number of autophagosomes were observed, however, it was noted that many were empty, likely resulting from inefficient mitochondrial loading during selective autophagy (Kegel et al. 2000; Petersén et al. 2001; Martinez-Vicente et al. 2010). An increase in autophagosome and lysosome-like structures was also confirmed using postmortem samples (Sunwoo et al. 2010; Tepper et al. 2018). Autophagic activity was upregulated in several models including HD patient and patient iPSC-derived neurons, and isogenic HEK293 models (Camnasio et al. 2012; Nixon and Yang 2012; Nekrasov et al. 2016; Morozova et al. 2018). These results suggest that despite an increase in the number of autophagic vacuoles, impaired degradation was responsible for the accumulation of undigested cargo, thus contributing to neurotoxicity.

At the transcriptional level, the process of autophagy begins with the expression of several genes, primarily, Autophagy Related Genes (ATGs), some of which (ATG23, ATG11, VAC8), exhibit structural similarity to mammalian HTT. ATG genes orchestrate formation of the autophagosome and have been linked to a number of diseases, including metabolic and neurodegenerative, with conditional ATG-knockout mice displaying progressive motor deficits and accumulation of protein aggregates in neurons (Fraiberg and Elazar 2020). Moreover, HTT coimmunoprecipitates with ATG11-interacting proteins in mammals, pointing to a conserved role for HTT as an autophagy-related scaffold protein, and linking loss of HTT function to protein clearance impairment (Ochaba et al. 2014). Follow up studies in *drosophila* and mouse fibroblasts demonstrated that loss of HTT leads to decreased response to starvation, thus support the role for HTT as a scaffold for selective autophagy. As a scaffold, HTT is thought to promote cargo recognition and autophagy initiation by mediating the binding of p62 to the autophagy-initiating kinase ULK1, while simultaneously releasing ULK1 from mTORC1 to induce autophagosome formation with associated LC3 proteins; the expanded polyQ disrupts this process (Ochaba et al. 2014; Gelman et al. 2015; Rui et al. 2015b; Croce and Yamamoto 2019; Franco-Iborra et al. 2021). A recent study, presented a model of endolysosomal pathway dysregulation in HD, wherein as opposed to autophagosome fusion with RAB7 positive late endosomes (MVBs) leading mostly to

exocytosis, these organelles become overloaded with mHTT, and become either dysfunctional or targeted to the lysosome for further processing, thereby comparatively reducing MVB and amphisome-based exocytosis, and resulting instead in the accumulation of MVBs, amphisomes, and autolysosomes, similar to what is observed in HD brain sections (Zhou et al. 2021). In sum, autophagy disruption has been shown to occur at several points in HD and in response to mHTT, moreover these defects overlap largely with lysosomal function, though it remains unclear how these proposed interactions and mechanisms specifically correspond to HD pathogenesis. Therapy targeted towards upregulation of autophagy has been proposed using rapamycin in combination with lithium and other compounds, or phenoxazine, as these were shown to be protective in HD models (Ravikumar et al. 2004; Rubinsztein 2006; Tsvetkov et al. 2010; Sarkar et al. 2013). More recently, however, due to negative side-effects associated with rapamycin, alternatives such as SAFit2 are being suggested (Bailus et al. 2021).

1.7.6 Mitochondrial dysfunction

Mitochondrial defects are pervasive in LSDs, and are particularly relevant to neurons which depend largely on oxidative phosphorylation for ATP and fine-tuned calcium signaling, and are highly implicated in HD pathogenesis (Costa and Scorrano 2012; Plotegher and Duchen 2017). In HD, defects in mitochondrial structure are commonly observed (Kegel et al. 2000; Wong and Holzbaur 2014; Franco-Iborra et al. 2021). Wildtype huntingtin is indispensable to proper mitochondrial function in mESCs, as HTT knockouts displayed bioenergetic shifts including, abolished ATP production, markedly increased glycolysis, a shift towards ketogenesis, and loss of structural integrity (Ismailoglu et al. 2014). Amongst other defects, reduced mitochondrial membrane potential, lipid and calcium dyshomeostasis, disturbed mitochondrial protein import, increased fission, and enzymatic dysregulation occur in response to mHTT (Panov et al. 2002; Lim et al. 2008; Damiano et al. 2010; Reddy and Shirendeb 2012; Yano et al. 2014). Mutant huntingtin represses transcription of peroxisome proliferator-activated receptor-γ coactivator 1α (PGC1α), a gene responsible for mitochondrial biosynthesis, which is reduced in HD patients; loss of PGC1 results in HD-like phenotypes and striatal neurodegeneration in mice (Wu et al. 1999; Cui et al. 2006).

Defective fusion and fission dynamics, coupled with impaired mitophagy, results in the accumulation of damaged mitochondria, impaired cellular metabolism, oxidative stress, inhibited response to energy demands, increased ROS, and reduced bioenergetic capacity observed in neurons; this is particularly damaging to neurons, due to their elevated energy requirements and postmitotic state (Kegel et al. 2000; Seong et al. 2005; Mason et al. 2013; Wong and Holzbaur 2014; Xu et al. 2017; Gardiner et al. 2018; Ooi et al. 2019a; Franco-Iborra et al. 2021). CAG repeat length was shown to be correlated to altered mitochondrial respiration and oxidative stress in isogenic hESC-derived neural cells, while in HD patient fibroblasts, bioenergetic malfunctions, reduced ATP concentration, maximal respiration, spare capacity, and complex II dependent respiration, were observed to correlate to age of onset (Gardiner et al. 2018; Ooi et al. 2019a). Our lab has also evidenced bioenergetic defects due to CAG length, as patient-derived HD NPCs, exhibited decreased basal and maximal respiration, and reduced ATP production (Donaldson 2019b).

1.7.7 Cholesterol and GSL dyshomeostasis

1.7.7.1 Cholesterol

While cholesterol storage figures prominently in NP-C disease and in several LSDs, accounts of cholesterol accumulation in HD are varied on account of model variation, sample preparation, and detection method, however, there are clear defects in gene expression and metabolism that result in cholesterol dyshomeostasis. In HDhQ111 mouse striatal knock-in cells cholesterol accumulation, measured with filipin or by enzyme activity, displayed increased plasma membrane localization, increased intracellular deposits, and an overall increase in cholesterol concentration, while age-dependent accumulation in YAC72 mouse striatal neurons was reported using filipin and thin layer chromatography (Trushina et al. 2006b; del Toro et al. 2010a). Increased cholesterol was observed in R6/2 mouse striatal cells, as measured by isotope-dilution mass spectrometry (Boussicault et al. 2016). Increased cholesterol was also detected by Amplex Red colorimetric enzyme assays in primary rat neurons overexpressing mHTT, 109Q knock-in mice, and in HD patient postmortem caudate and putamen samples (del Toro et al. 2010a; Luthi-Carter et al. 2010), however, it was

argued that the sample extraction methods used were inappropriate and the opposite results were obtained when this was corrected (Marullo et al. 2012). Reductions in cholesterol were also reported in YAC128 HD mouse striatum, R6/2 mice and in human HD fibroblasts in delipidated medium (in normal medium there was no difference), and YAC72 mice (GS-MS), and $Hdh^{(Q140/140)}$ primary mouse neurons (Valenza et al. 2005a; Valenza et al. 2007a; Valenza et al. 2010; Marullo et al. 2012; Ritch et al. 2012). However, GS-MS was applied to HD patient tissue, and increased cholesterol was recorded in the putamen while cholesterol esters were increased in both the caudate and putamen (Kreilaus et al. 2016; Phillips et al. 2020). More recently, hyperspectral fluorescent microscopy and spectral phaser analysis was used to identify a shift in HD cell membranes from a highly packed to a loosely packed, and liquid ordered to liquid disordered phase, in PC12 and HEK293 cells expressing exon 1 of mHTT, thus supporting previous findings of reduced membrane cholesterol (Sameni et al. 2018). Interestingly, cholesterol was significantly increased in ES-derived HTT knockout neural stem cells compared to wildtypes and HTT (140Q/7Q) cells (which did not differ) as measured enzymatically by Amplex Red, pointing to a response due to loss of function (Ritch et al. 2012).

Previous observations in our lab largely confirmed previous reports of cholesterol accumulation and mistrafficking across a wide array of HD models, though results were somewhat inconsistent. Increased filipin staining, perinuclear and punctate distribution was observed across several cell lines including human iPSC-derived neural stem cells (Q60 AND Q109), ST14A cells (Q120), HD patient (Q180) iPSC-derived NSCs, with subsequent rescue by cyclodextrin or miglustat (Haslett 2015). Further work, using patient HD fibroblasts, (Q60 and Q180), STHdh (Q111) and ST14A HD cells evidenced punctate, perinuclear filipin staining, resembling phenotypes observed in cells treated with U18666A, a small-molecular inhibitor of NPC1, used to phenocopy NP-C disease (Clark 2017). However, conflicting results were obtained as enzyme assays on STHdh cells exhibited increased cholesterol, while cholesterol levels, though nonsignificant, were reduced in ST14A HD cells despite previous indications of increased cholesterol levels in this cell line, as measured with thin layer chromatography (Haslett 2015; Clark 2017). The importance of cell models and culture conditions was

highlighted in HD patient iPSC-derived NPCs as neither Q60 nor Q109 cells displayed cholesterol mislocalization, TLC revealed no differences in cholesterol, and contrary to previous findings in our lab, miglustat-mediated rescue was not definitively reproduced in these experiments, unless culture medium was supplemented with 10% FBS (Clark 2017). Interestingly, and pertinent to aforementioned results observed in ES-derived HTT knockout NSCs, work by Rafael Badell-Grau demonstrated cholesterol storage in response to anti-HTT siRNA knockdown in SHSY5Y cells.

While measurements of cholesterol content produced inconsistent results, evidence of cholesterol dyshomeostasis has been clearly identified, though how this contributes to the pathophysiology of HD is less certain. A direct link has been suggested, as mHTT was shown to directly interact with caveolin-1, leading to trafficking defects, cholesterol dyshomeostasis and ER/Golgi storage, neuronal inclusions, and motor decline in mice (Trushina et al. 2006a; Trushina et al. 2014) Several malfunctional processes have been suggested, as pathogenesis has been connected to transcriptional dysregulation of sterol regulatory element-binding proteins (SREBPs), liver X receptors (LXR), and PGC1α, and to reduced expression of genes involved in cholesterol biosynthesis, including HMGCR, CYP51, 7-dehydrocholesterol 7-reductase and DHCR24 (Valenza et al. 2005b; Valenza et al. 2007b; Samara et al. 2014). Expression of metabolic markers of synthesis such as zymosterol and lathosterol, and turnover were also decreased proportionally to CAG length, and while cholesterol levels in HD mouse astrocytes were similar to their wildtype counterparts, expression levels of genes critical to astrocyte-to-neuron cellular cholesterol efflux including ABCA1 and ApoE were reduced, possibly in response to reduced biosynthesis (Valenza et al. 2007a; Valenza et al. 2010). The brain-specific rate-limiting enzyme, CYP46A1, was observed to be decreased in the HD patient putamen, R6/2 mice, and in striatal HD cell lines, while knockdown of CYP46A1 resulted in reduced 24S-OHC levels, spontaneous striatal neurodegeneration, and motor impairments using *in vivo* mouse models (Boussicault et al. 2016; Kreilaus et al. 2016), which agree with previous observations of reduced 24-hydroxycholesterol in HD patient plasma samples, and reduced elimination of brain cholesterol (Leoni et al. 2008). Other avenues of research implicate cholesterol dyshomeostasis towards eliciting impaired

microglial lipid uptake and ApoE binding, and an altered inflammatory profile as increased cytokines, TNFα, IL-6 and IL-8 were observed in premanifest and postmortem HD (Bjorkqvist et al. 2008; González-Guevara et al. 2020). In summary, defects in cholesterol homeostasis are strongly implicated in HD and this dysregulation might contribute to HD pathogenesis and progression.

1.7.7.2 Gangliosides

There is increasing evidence to support a role for aberrant ganglioside dynamics, in neurodegenerative diseases including PD, AD, and HD, while this is already well supported in several LSDs including NP-C, and the gangliosidoses, the specific mechanisms underlying the contribution of ganglioside abnormalities to HD pathology has yet to be clearly determined (Di Pardo and Maglione 2018). Much focus has been on ganglioside GM1 in HD, as external application of GM1 to mice, rats, and gerbils, attenuates neuronal damage and promotes neuronal survival in response to a variety of insults e.g., excitatory amino acid exposure or ischemia; it is suggested to play a neuroprotective and/or a neurotrophic role, and to mediate excitotoxicity and oxidative damage (Mahadik et al. 1988; Lombardi et al. 1989; Skaper et al. 1991; Lombardi and Moroni 1992; Mahadik et al. 1993; Ferrari and Greene 1996; Bachis et al. 2002; Fighera et al. 2006; Schneider 2014).

Reduced ganglioside and GM1 levels were observed across several HD models. R6/1 mouse corticostriatal lysates displayed a 38% reduction in GM1, which paralleled an overall reduction in ganglioside concentrations seen in HD patient post-mortem caudate samples (Desplats et al. 2007a). In R6/1 mice, significant reductions were observed in all major gangliosides with the exception of GD3, though ganglioside reductions were not observed in the post-mortem HD patient cerebellum, these were generally increased along with a significant increase in GM1 (Denny et al. 2010). GM1 deficits were later confirmed in HD STHdh$^{111/111}$ cells, YAC128 mice (striatum, cortex, and neurons), rat striatal ST14A cells overexpressing an N-terminal mHTT fragment, in HD patient fibroblasts, and in derived primary mouse neurons (Maglione et al. 2010; Di Pardo et al. 2012). Altered GM1 storage was observed by other groups to suggest altered GM1 trafficking and mislocalization in HD.

In HDhQ11 mouse striatal cells GM1 displayed increased colocalization with caveolin and NMDA receptors (NR1 and NR2B), and an increased concentration at the plasma membrane, suggesting increased content in lipid rafts and a mHTT contribution to NMDA-mediated excitotoxicity that could be rescued with simvastatin or cyclodextrin (del Toro et al. 2010a). Similarly, GM1 storage, increased punctate distribution, and an obstruction in lysosome-to-Golgi trafficking, were also observed during previous experiments in our lab using ST14A (Q120), STHdh, SH-SY5Y, and HD patient fibroblasts; trafficking defects were marginally rescued by hydroxy-propyl-β-cyclodextrin and greater improvements were observed with miglustat treatment (Haslett 2015; Clark 2017). A more recent comparison of brain sphingolipid profiles in 13 clinically advanced HD patients (Vonsattel 4) against age and sex matched controls, identified region-specific fatty acyl chain-length shifts in the HD caudate, from reduced very long (C22-C26), to increased long chain (C13-C21) ceramides, sphingomyelins, and lactosylceramides; this accompanied reduced expression of ceramide synthase 1 (responsible for long chain fatty acid synthesis), and was positively correlated to a longer CAG repeat, earlier time of death, and resembled shifts observed in other neurodegenerative diseases (Phillips et al. 2021).

The ganglioside reductions as reported in the aforementioned models, correspond to reduced expression of genes involved in ganglioside synthesis pathways. Expression of glucosyltransferases and sialyltransferases were reduced in R6/1 mice, while expression of *St3galt5* (the gene that codes for the GM3 synthase enzyme), responsible for synthesis of the ganglio-series of gangliosides was reduced in HD patient caudate samples (Desplats et al. 2007a). *St3gal5*, *B4galnt1* (GM2/GD2 synthase), *St8sia1* (GD3 synthase), and *St8sia3* (GT3 synthase), and notably, *Ucgc* (glucosylceramide synthase) which catalyzes the first glycosylation step in ganglioside biosynthesis, were all significantly downregulated in YAC128 mice striatal and cortical lysates (Maglione et al. 2010). Cerebellar *Ucgc* (glucosylceramide synthase) and *B4galnt1* (GM2/GD2 synthase) reductions were later confirmed in R6/1 mice, while examinations of postmortem HD patient cerebellar RNA evidenced corresponding reductions in *GALGT1* (GM2/GD2 synthase), *SIAT8A* (GD3 synthase), and *SIAT9* (GM3 synthase) (Denny et al. 2010). In sum, these data suggest that reduced gene expression for

key biosynthetic enzymes, especially at critical and early steps in the pathway, lead to downstream deficits in ganglioside levels, and increased susceptibility to neurodegenerative factors.

The link between aberrant ganglioside metabolism in HD and neurodegeneration was strengthened as the decreased levels of GM1 biosynthesis in HD models were shown to correspond to heightened susceptibility to apoptosis (Maglione et al. 2010). GM1 infusion into YAC128 mice reduced mHTT toxicity, increased cell survival, improved motor function, and increased DARPP32 expression in the striatum (Maglione et al. 2010; Di Pardo et al. 2012). The protective effects were linked to GM1-induced AKT-mediated mHTT phosphorylation at various serine residues, including serine 13 and 16 of the highly conserved N17 N-terminal domain that influences, intracellular localization, aggregation, cell membrane association (especially to mitochondria, and also the ER an Golgi), and calcium homeostasis; phosphorylation of these residues was shown to prevent toxic mHTT cleavage and neuronal cell death *in vitro* (Atwal et al. 2007; Rockabrand et al. 2007; Di Pardo et al. 2012). The apoptotic effects of GM1 insufficiency were recapitulated through pharmacologically reducing cellular GM1 content by small molecule (PPMP) inhibition of glucosylceramide synthase in wild-type mouse striatal STHdh$^{7/7}$ cells, which was rescued by GM1 treatment (Maglione et al. 2010). Collectively, these studies point to ganglioside dysfunction as a source of neurodegeneration in HD and present a possible target for therapeutic intervention.

1.8 Convergent themes in HD and NP-C

Huntington's disease studies have pointed to huntingtin involvement in endolysosomal and related systems. Several cellular phenotypes are suggestive of a primary defect related to lysosomal storage and LSD-related metabolic phenotypes. While the genetic causes and clinical presentations are distinct, recent work in our lab has identified cellular phenotypes common to HD and NP-C including lipid storage, trafficking defects, and calcium signaling, as well as interactions between NPC1 and both wildtype and mutant huntingtin proteins, which

suggests the possible presence of a shared pathway or mechanism. As the primary defect in both diseases is still debated, the exact nature of this putative process remains unclear,

there is, however, considerable evidence to indicate that HD might not only be a neurodegenerative disease but that at least in part, there might be a primary link between mHTT and protein dysfunction in the lysosome, leading to analogous substrate accumulation and downstream pathologies, resulting ultimately in neuronal death. In order to more clearly

understand HD it may be helpful to narrow the framework of, and investigate HD, not only as a neurodegenerative disorder, but as a LSD, and more specifically, to understand HD pathologies that converge with those previously described in NP-C might provide new insight into the etiology of both diseases and routes for shared therapeutic approaches.

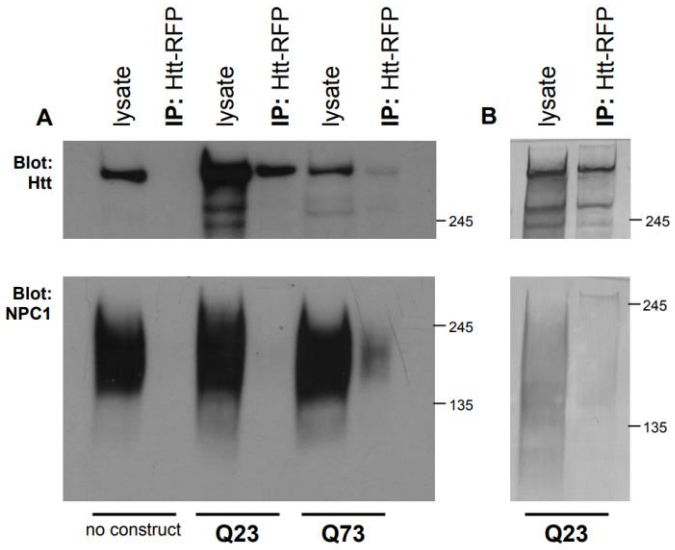

Figure 1.10. Co-immunoprecipitation of NPC1 with huntingtin. PC12 cells expressing either RFP-tagged Q23 huntingtin, RFP-tagged Q73 huntingtin, or no construct, probed for huntingtin and NPC1 indicating association between the two proteins (Clark 2017).

1.8.1 HTT and mHTT co-immunoprecipitates with NPC1

Co-immunoprecipitation experiments were previously performed in our lab in which PC12 cells expressing RFP-tagged wildtype (Q23) or mutant (Q73) huntingtin isolates were separated and probed for NPC1 (Figure 1.10). Results evidenced an interaction between both mutant and wildtype huntingtin proteins with NPC1, which establishes the possibility of a direct link as huntingtin may bind with NPC1, or an indirect link where the two proteins might complex. The interaction between wtHTT and NPC1 points to a role for huntingtin towards NPC1 in normal functioning, the loss of which might result in an NP-C phenotype. Conversely, the interaction between mHTT and NPC1 offers the possibility for a toxic gain of function. Both loss of normal function and gain of function could explain NP-C phenotypes in HD. For example, previously observed NPC1 in HD mislocalization, could be attributed to trafficking defects due to deficiencies of wildtype protein, or potentially that mHTT aggregates act as a molecular net, trapping NPC1 (Clark 2017).

1.8.2 Common LSD Phenotypes in NPC and HD

LSDs typically display common structural pathologies, including, lysosomal expansion, aberrant lysosomal accumulation, mislocalization, and altered morphology (Karten et al. 2002; Platt et al. 2012; Te Vruchte et al. 2014; Roney et al. 2021). Similar to those observed in NP-C, lysosomal storage disease phenotypes have been observed in HD (Table 1.3) and wildtype HTT and mHTT have been shown to directly interact with and may reside in lysosomal structures (Kegel et al. 2000; Kang et al. 2007; Martin et al. 2015a). Examples of lysosomal storage, expansion and altered lysosomal morphology have been documented in several models, with increased volume corresponding to polyQ length (Kegel et al. 2000; Valenza et al. 2007a; Valenza et al. 2010; Koga et al. 2011; Camnasio et al. 2012; Castiglioni et al. 2012; Martin et al. 2015a; Martin et al. 2015b). In addition to earlier works, mislocalization of endolysosomal vacuoles has also been observed in the Lloyd-Evans lab (Koga et al. 2011; Haslett 2015; Clark 2017).

Lysosomal storage diseases also regularly exhibit several functional disruptions that suggest a shared pathology between NP-C and HD. In NP-C, lipid storage (Vanier 1983; Pentchev et

al. 1985; Liscum and Faust 1987; Liscum et al. 1989; Butler et al. 1993; Harzer et al. 2003; Lachmann et al. 2004), calcium dyshomeostasis (Lloyd-Evans et al. 2008), autophagic dysfunction and increased autophagosome counts (Ko et al. 2005; Pacheco et al. 2007; Ballabio and Gieselmann 2009; Ordonez et al. 2012; Sarkar et al. 2013), and impaired mitochondrial metabolism, have all been observed (Yu et al. 2005; Koh et al. 2006; Klein et al. 2011; Visentin et al. 2013; Kennedy et al. 2014; Torres et al. 2017; Wang et al. 2018). Correspondingly, in HD, lipid dyshomeostasis has been reported (Desplats et al. 2007b; Valenza and Cattaneo 2011; Haslett 2015; Handley et al. 2016; Clark 2017; Di Pardo et al. 2017b). Reduced ER calcium and disrupted mitochondrial Ca^{2+} have been observed in HD models (Panov et al. 2002; Bezprozvanny and Hayden 2004; De Mario et al. 2016). Mitochondrial dysfunction in HD has been comprehensively documented (Damiano et al. 2010), and autophagy has also been shown to be impaired in HD (Croce and Yamamoto 2019).

	LSD phenotype	NP-C	HD	References
Endolysosomal structure	lysosomal volume, number are increased, and distribution is altered	increased volume increased numbers perinuclear distribution	increased volume increased number perinuclear distribution mHTT accumulation	(Kegel et al. 2000; Kang et al. 2007; Valenza et al. 2007a; Karten et al. 2009; Valenza et al. 2010; Koga and Cuervo 2011; Korolchuk et al. 2011; Te Vruchte et al. 2014; Erie et al. 2015; Martin et al. 2015a; Lee et al. 2020; Roney et al. 2021)
Lipid metabolism	storage and mislocalization	cholesterol sphingolipids	cholesterol sphingolipids	(Vanier 1983; Pentchev et al. 1985; Schroeder et al. 1994; Simons and Ikonen 1997; Vanier 1999; Liscum 2000; Reagan et al. 2000; Patterson 2001; Zervas et al. 2001a; Karten et al. 2002; Valenza et al. 2005b; Tamura et al. 2006; Trushina et al. 2006a; Valenza et al. 2007a; Lloyd-Evans et al. 2008; del Toro et al. 2010a; Devlin et al. 2010; Lloyd-Evans and Platt 2010; Luthi-Carter et al. 2010; Valenza et al. 2010; Gallala et al. 2011; Marullo et al. 2012; Ritch et al. 2012; Vanier 2015; Boussicault et al. 2016; Kreilaus et al. 2016; Phillips et al. 2020)
Trafficking	defective lysosomal trafficking in the endolysosomal or autophagy pathways	impaired LE motility blocked transport from LE trafficking to Golgi	impaired vesicle trafficking altered endosome motility reduced lysosome mobility BDNF from Golgi	(Ko et al. 2001; Zhang et al. 2001; Lebrand et al. 2002; Mayran et al. 2003; Pagano 2003; Wastney et al. 2003; Choudhury et al. 2004; Trushina et al. 2004; del Toro et al. 2006; Ganley and Pfeffer 2006; Pal et al. 2006; Pipalia et al. 2007; Schweitzer et al. 2009; Caviston et al. 2011; Liot et al. 2013; Wong and Holzbaur 2014; Erie et al. 2015; Shammas et al. 2019)
Calcium dyshomeostasis	Ca^{2+} levels altered in organelles e.g., lysosome, ER, mitochondria.	lysosome dyshomeostasis	increased cytoplasmic stores increased ER release	(Bezprozvanny and Hayden 2004; Lloyd-Evans et al. 2008; Lloyd-Evans and Platt 2011; Giacomello et al. 2013)

Impaired autophagy	defects in autophagy-related structures and processes	impaired fusion to lysosome increased proliferation impaired mitophagy	increased size and count inefficient mitochondrial loading impaired mitophagy	(Kegel et al. 2000; Nagata et al. 2004; Ko et al. 2005; Pacheco et al. 2007; Sarkar and Rubinsztein 2008; Del Toro et al. 2009; Elrick et al. 2012; Sarkar et al. 2013; Kennedy et al. 2014; Martin et al. 2015a; Wheeler and Sillence 2020)
ER stress	ER response to accumulated or misfolded proteins	activated ERAD altered ER-phagy	inhibited UPS and ERAD altered secretory pathway	(Shenkman et al. 2015; Schultz et al. 2018; Zheng et al. 2018; Shacham et al. 2019; Yañez et al. 2020)
Mitochondrial stress	altered function and energy metabolism	decreased length impaired function reduced ATP synthase increased ROS	decreased length impaired function reduced ATP production increased ROS	(Yu et al. 2005; Koh et al. 2006; Klein et al. 2011; Kennedy et al. 2012; Ordonez et al. 2012; Visentin et al. 2013; Torres et al. 2017; Wang et al. 2018; Prabhu et al. 2021)

Table 1.3 List of published LSD phenotypes common to both NP-C and HD.

1.9 Models

Due to impracticalities involved with primary cells, most cell-based HD studies have relied on immortalized cell lines, mitotic patient-derived cells, or mouse models which are suboptimal for many reasons. Immortalized cells are *de facto* abnormal, and cells often exhibit altered metabolic profiles which can obscure selective HD phenotypes (Ritch et al. 2012). Mitotic cells differ from non-dividing cells in several fundamental ways; the subcellular localization of HTT is different between mitotic cells and post-mitotic cells and fundamental metabolic processes such as autophagy take on a more critical role in non-dividing cells (Malik et al. 2019). Moreover, non-neuronal cells, by definition, do not undergo neurodegeneration, and thus do not permit modelling of the neurodegenerative aspect of HD. Animal models are also inadequate, as for example, most mouse models fail to completely exhibit neurodegenerative changes associated with human HD, as only a few mouse models display slight neuronal loss in the striatum (Denny et al. 2010). Hence, a more analogous model system to study HD neurodegeneration, and develop new treatments would be advantageous.

With the combined application of induced pluripotent stem cells (iPSCs), CRISPR/Cas9, and neuronal differentiation protocols with increasing precision regarding subtype-specificity, it has become possible to compare disease phenotypes across modified genetic backgrounds in a relevant cellular context e.g., MSNs from HD patient-derived iPSCs (Takahashi et al., 2007; Chambers et al., 2009; Carri et al., 2013; Kemp et al., 2016). Patient fibroblast or blood samples are easy to obtain, and reprogramming methods have improved the ease and efficiency at which these samples can be reprogrammed to a pluripotent state. Once iPSCs have been generated, subsequent gene editing using CRISPR/Cas9 can be performed on a portion of the population to generate isogenic cell lines, allowing for side-by-side comparisons within a backdrop wherein all other factors are relatively identical. CRISPR/Cas9, allows for verifiable targeting, and with minimal chance for off-target insertion, the edited gene's expression can remain under the control of the endogenous promoter and therefore more accurately reflect actual cellular protein concentration and associated

phenotypes. Finally, the ability to then direct the differentiation of the iPSCs towards the tissue that is primarily affected in the disease is critical, as cell types vary with regards to their susceptibility to disease. Such a model for HD was developed in our lab as iPSCs originally derived from a juvenile female patient were edited in order to correct the huntingtin gene by reducing the roughly 109 CAG repeats to 22 (Juopperi et al. 2012; Donaldson 2019b). Several groups have used iPSC-based platforms to investigate HD metabolic dysfunction (Tables 1.4 and 1.5).

Cell type	CAG length	HD phenotype	References
iPSCs	71/109	Increased expression of oxidative stress factor (SOD1)	(Szlachcic et al. 2015)
	71/109	Altered expression of embryonic development genes Decreased expression of DNA damage response genes	(Świtońska et al. 2019)
iPSCs, NPCs	72	Altered mitochondrial morphology Reduced number and area of mitochondria Reduced OPA1 co-localization with mitochondria Significantly decreased basal respiration rate Increased dependence on glycolysis Increased basal intracellular calcium levels Reduced PGC1α and TFAM (iPSCs) mRNA expression Increased basal superoxide levels Increased expression: GSH GCLc (iPSCs), SOD2, NRF2 (NPCs)	(Lopes et al. 2020)
	43/42, 43/39, 45	Increased lysosomal activity	(Camnasio et al. 2012)
	42, 44 (iPSCs) 46, 69, 70, 99 (NPCs)	Increased gene expression: ubiquitin-related genes (iPSCs) Reduced expression: FOXO4 (iPSCs) Stable CAG length (NPCs)	(Mollica et al. 2018)
NPCs	60, 109, 180	Altered gene expression: cell signaling, cell cycling, assembly, embryonic and cell development, axon guidance. Decreased expression of actin protein	(Hd iPsc 2012)
	72	Reduced BDNF expression Increased gene expression: RE1, SNAP25, BDNF, SYP	(Charbord et al. 2013)
	72	Increased gene expression: FOXP2, NETRIN Decreased gene expression: DARPP32, CTIP2, FOXP1, ISL1, TBR1, PAX6 Altered gene expression: Netrin receptor genes	(Ring et al. 2015)
	60	Increased AKT/mTOR signaling effector proteins	(Martín-Flores et al. 2016)
	50, 60, 66, 109	Increased susceptibility to H_20_2 mediated oxidative stress	(Consortium 2020)
	46,69,70,99	Increased FOXO1 and FOXO4 levels Increased proteosome activity	(Liu et al. 2017)

Table 1.4 Examples of HD models using iPSCs, and NPCs derived from iPS cells. Modified from Csobonyeiova *et al.* (2020) and Monk and Connor (2021) .

CAG length	HD phenotype in neurons differentiated from iPSCs	Reference
60,109,180	Altered gene expression: cell growth, proliferation, cell function, cell-to-cell signaling, embryonic development Calcium dyshomeostasis in response to glutamate CAG repeat instability Increased cell death upon BDNF depletion	(Hd iPsc 2012)
72	Enhanced caspase activity due to growth factor deprivation	(Zhang et al. 2010)
72	Decreased expression: cytoskeletal and oxidative stress response proteins Increased expression: antioxidant response, double-strand DNA damage response, ATM, p53, H2AX	(Chae et al. 2012)
72	Increased macroautophagy	(Camnasio et al. 2012)
100	Decreased ATP and mitochondrial membrane potential Increased mitochondrial ROS production, cell death (lactate dehydrogenase) mitochondrial fragmentation. Rescue of several defects with DPR1 or p53	(Guo et al. 2013)
109,180	Decreased expression: DNA damage response, G-protein signaling, oxidative stress repair genes A2A adenosine receptor agonists rescue HD phenotypes	(Chiu et al. 2015)
40,42,47	Increased lysosome and autophagosome counts Increased lysosomal activity SOC-mediated calcium dysfunction Phenotype rescue by NF-kB inhibition	(Nekrasov et al. 2016)
60,109	Reduced expression: calcium signaling pathway genes (GRIN2B, AMPA receptor, CREB, CACNA1C, CAMK)	(Consortium 2017)
180	Mitochondrial dysfunction - rescued by isogenic correction	(Xu et al. 2017)
46,69,70,99	Oxidated stress induced increased cell death Reduced FOXO4 and increased AKT Reduced proteosome activity	(Liu et al. 2017)
40,42,47	Decreased mitochondrial density in neurites Nuclear calcium homeostasis disruption did not alter HD pathology	(Nekrasov and Kiselev 2018)
40,42,47	Upregulation of store-operated calcium entry	(Vigont et al. 2018)

50, 60, 66, 109	Deficit in maximal mitochondrial respiration Decreased expression of glycolysis genes Decreased glycolysis and OXPHOS proteins	(Consortium 2020)
47,69	Increased presence of cytoplasmic vacuoles Aggregates of autophagosomes and autolysosomes	(Malankhanova et al. 2020)
66,71,109	PIAS1 knockdown increased genomic integrity and DNA damage repair	(Morozko et al. 2021)
40,42,47,76	Disrupted calcium signaling independent of CAG length	(Vigont et al. 2018)

Table 1.5 Examples of neuronal models derived from iPSCs. Modified from Csobonyeiova *et al.* (2020) and Monk and Connor (2021) .

1.10 Project Aims

Our objective is to build upon previous findings, to identify, investigate, and clarify LSD phenotypes in HD, by assessing common structural and functional phenotypes, and shared genetic pathways.

Primary objectives:

In chapter 3, we will describe the generation and validation of CRISPR-mediated knockout of huntingtin in two iPSC lines. In addition, we will characterize neural progenitor cells, and neurons that were differentiated from HD109, isogenic-corrected wtHTT, and knockout iPSCs (HD109, $HD22^{ISO\text{-}109}$, and HTT-KO $^{ISO\text{-}109}$).

In chapter 4, we will investigate structural characteristics suggestive of lysosomal dysfunction in HD. To do this we will use HD isogenic NPC and neuronal lines for a three-way comparison of disease, control, and knockout. We will use HTT knockout cells to investigate LSD-related gain or loss of function phenotypes in HD, and to test the specific hypothesis that HTT is directly involved with transport of NPC1 to the lysosomal membrane. In addition, we will investigate structural changes associated with miglustat treatment in neuronal models.

In chapter 5, we will use the aforementioned cellular models for functional characterization of phenotypes associated with LSDs. We will again use knockout lines to examine possible gain of mHTT or loss of wtHTT function, and will treat neurons with miglustat to identify potential rescue effects.

In chapter 6, we use RNA sequencing for comparisons of differential expression and pathway analysis and to compare HD109, $HD22^{ISO\text{-}109}$, HTT-KO $^{ISO\text{-}109}$ neurons. These analyses will also be used to compare HD109, $HD22^{ISO\text{-}109}$ both with and without miglustat treatment.

2 MATERIALS AND METHODS

Cell Culture Reagent	Supplier	Catalogue Number
mTeSR1	Stem Cell Technologies	85875
Stemcell Banker	AMS Biotechnology Ltd	11890
TrypLE Express Enzyme	Thermo Fisher	12604021
ReLeSR	Stem Cell Technologies	05873
Accutase	Innovative Cell Technologies	AT104-500
Matrigel - Growth Factor Reduced	Corning	354230
Advanced DMEM/F-12	Life Technologies	12634028
Knockout DMEM/F-12	Life Technologies	12660012
BrainPhys Neuronal Medium	Stem Cell Technologies	05790
Neurobasal	Life Technologies	21103049
DPBS	Life Technologies	4107523
Chemically Defined Lipid Concentrate	Gibco	11905031
Polyethyleneimine MW ~ 750K	Sigma	181978
Borate Buffer	Thermo Fisher	28341
Laminin	Santa Cruz Biotechnology	92079046
Glutamax	Thermo Fisher	35050038
Penicillin-Streptomycin	Life Technologies Limited	4183303
Anti-Anti	Gibco	15240062
PluriSIn-1	Stem Cell Technologies	72824
MACS NeuroBrew-21	Miltenyi Biotec Ltd	1011907511
MACS NeuroBrew-21 w/o Vitamin A	Miltenyi Biotec Ltd	1011907511
ROCK inhibitor Y-27632	Hello Bio	300001634
SB431542	Stratech Ltd	51414
LDN193189 dihydrochloride	Bio-Techne Ltd	6053/10
StemMACS IWR-1-endo	Miltenyi Biotec Ltd	130-110-491
Human/Murine/Rat Activin A	Peprotech EC Ltd	120-14
CHIR 99021 Trihydrochloride	Hello Bio	HB1262
PD0332991 isethionate	Bio-Techne Ltd	4786/10
DAPT	Bio-Techne Ltd	2634/10
Forskolin	Bio-Techne Ltd	1099
BDNF Human	Hello Bio	300001798
GABA	Bio-Techne Ltd	0344
Ascorbic Acid	Sigma	A4544
Calcium Chloride	Sigma	499609
Polyethyleneimine	Sigma	181978-100G
Borate Buffer 20x	Thermofisher	28341

Table 2.1. List of cell culture reagents.

2.1 Cell Lines

The Kolf2 cells used in this study were previously generated from patient fibroblasts via Sendai viral vectors, through the Sanger Institute's HipSci initiative (Table 2.2). HD109 iPSCs were generated by the HD iPSC Consortium, from patient fibroblasts, through retroviral transduction. Isogenic-corrected versions of the HD109 cells, HD22$^{ISO-109}$ cells were provided as a kind gift from, Prof. Nick Allen and Dr. Jasmine Donaldson (Table 2.2). HAP1 cells (Horizon Discovery), are near-haplozygous chronic myeloid leukemia cells and are derived KBM-7 cells (Table 2.2).

Cell Lines	Donor	PolyQ length	References
HD109	female age 9	109/19	(Hd iPsc 2012)
HD22$^{ISO-109}$	female age 9	22/21	(Donaldson 2019b)
Kolf2-C1	male age 55-59	22/22	(Streeter et al. 2017)
HAP1 WT	male age 39	n/a	(Andersson et al. 1987)
HAP1 KO	male age 39	Q0/0 (2bp deletion exon 3)	(Essletzbichler et al. 2014) Horizon Discovery Group (Cat # C631)

Table 2.2. List of cell lines used.

2.1.1 Cell culture

iPS Cells were thawed at 37°C, suspended in Advanced DMEM/F12 (Thermofisher), centrifuged at 200 g for 5 minutes, media was replaced, and cells were plated on growth factor-reduced Matrigel-coated (Corning) tissue-culture plates into mTesR1 (Stem Cell Technologies) supplemented with 10 µM Y27632 (Abcam) and incubated at 37°C with 5% CO_2. After 48 hours, Y27632 was removed, and medium was replaced with fresh mTeSR1 which was replaced every other day. For routine passaging, cells were detached with ReLeSR™ (Stem Cell Technologies), gently dissociated, and replated as small clumps. Single-cell passaging was carried out by dissociation with Tryple Select Enzyme (Life Technologies) and subsequent plating into medium with 10 µM Y27632. Prior to freezing mTeSR1 was supplemented with Penicillin-Streptomycin (Life Technologies) or anti-anti (Gibco) in order to minimize risk of contamination. Cells were frozen at between 1 to 3 million cells per 0.5 ml Stem-Cell banker (Amsbio) and stored in at - 80°C (short-term) or in liquid nitrogen (long-term).

HAP1 cells (Horizon Discovery) were cultured in Iscove's Modified Dulbecco's Medium (Gibco) containing 10% fetal bovine serum (FBS), containing Penicillin-Streptomycin (Life Technologies), or anti-anti (Gibco). At roughly 70% confluency, cells were trypsanized (0.05%) and passaged. Cells were frozen in 90% FBS with 10% DMSO and stored in at - 80°C or in liquid nitrogen (long-term).

Neuronal differentiation medium	Components
SLI	Advanced DMEM/F12 with 1% Penicillin/Streptomycin, and 1% Glutamax, 1% Neurobrew-21 without retinoic acid, 10 µM SB431542, 1 µM LDN 193189, 1.5 µM IWR1.
LIA	Advanced DMEM/F12 with 1% Penicillin/Streptomycin, and 1% Glutamax, 1% Neurobrew-21 without retinoic acid, 10 µM SB431542, 1 µM LDN 193189, 1.5 µM IWR1, and 25 ng/ml Activin-A.
SJA	Advanced DMEM/F12 with 1% Penicillin/Streptomycin or Anti-Anti, and 1% Glutamax, 2% Neurobrew-21 with retinoic acid, 2 µM PD0332991 isethionate, 10 µM DAPT, 10 ng/ml BDNF, 0.5 µM LM22A4, 10 µM Forskolin, 3 µM CHIR 99021 trihydrochloride, 0.3 mM GABA, 1.8 mM CaCl2, and 0.2 mM Ascorbic Acid.
SJB	48% Advanced DMEM/F12 and 48% Neurobasal-A with 1% Penicillin/Streptomycin or Anti-Anti, 1% Glutamax, 2% Neurobrew-21 with retinoic acid, 2 µM PD0332991 isethionate, 10 ng/ml BDNF, 0.5 µM LM22A4, 3 µM CHIR 99021 trihydrochloride, 1.8 mM CaCl2, and 0.2 mM Ascorbic Acid.
BrainPhys Maturation Medium	BrainPhys, 2% Neurobrew-21 with Retinoic Acid, 10 ng/ml BDNF, and 0.5 µM LM22A4.

Table 2.3. Media composition for directed neuronal differentiation.

2.1.2 Neural progenitor differentiation

iPSCs were plated as single cells at 4.0 x 10^5 cells per well of a 12-well dish. After 24 hours, cells were rinsed three times with DPBS with Ca^{2+} and Mg^{2+} (Life Technologies) and then cultured, with daily 2 ml medium changes, for eight days, in SLI medium. On day 8 cells were dissociated to single cells with Accutase and replated 1:2 on a Matrigel-coated plates, for eight more days with daily, 2 ml changes of LIA medium (Figure 2.1). Chemically defined lipid concentrate was added to LIA at 1:1000 if progenitors were to be assayed.

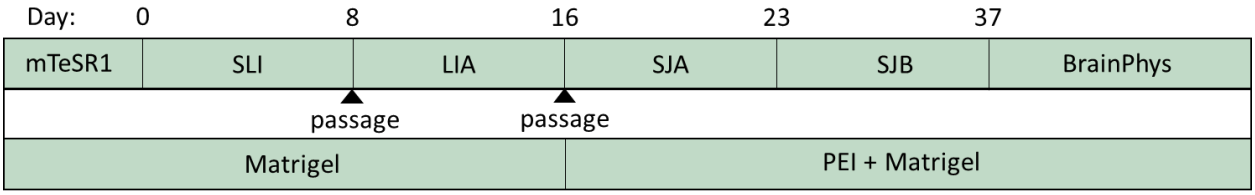

Figure 2.1. Outline of neuronal differentiation from iPSCs.

2.1.3 Medium spiny neuronal differentiation

Day 16 NPCs were dissociated to single cells with Accutase and split at a 1:3 ratio onto wells or coverslips coated with either Matrigel, or a combination of PEI (0.1% polyethyleneimine in 1x borate buffer) and Matrigel. Briefly, culture surfaces were coated with PEI, incubated overnight at room temperature. The following day, PEI was completely aspirated, washed 4 times with DPBS (without Ca^{2+} and Mg^{2+}) and dried for 1 hour at room temperature before coating with Matrigel. Cells were cultured in SJA from days 16 to 23 and SJB supplemented with 1:1000 lipid concentrate from days 23 to 37, with half media changes on alternate days. Finally, cells were cultured in Brain Phys maturation medium until assayed, with half of the medium exchanged every third day (Figure 2.1).

2.2 Generation of Knockout Lines

2.2.1 Guide-RNA formation

Two CRISPR RNAs (crRNA) and a trans-activating crRNA (tracrRNA) were prepared in IDT duplex buffer (100 mM potassium acetate with 30 mM Hepes buffer), to make two separate 45 µM crRNA: 45 µM tracrRNA complexes. In one tube, tracrRNA Alt-R CRISPR-Cas9 tracrRNA - ATTO™ 550 (Integrated DNA technologies) was mixed with the crRNA containing the guide RNA sequence 5’-GAAGGACTTGAGGGACTCGA to target exon1 E12.1. In the second tube, fluorescently labeled, Alt-R CRISPR-Cas9 tracrRNA - ATTO™ 550 (Integrated DNA technologies, Coralville, USA) was mixed with the crRNA containing the guide RNA sequence at 5'-TCAGCCACAGCCGGGCCGGG to target and bind exon1 P76.3. Both tubes were then heated at 95°C and slowly cooled to room temperature to anneal the guide RNA (gRNA) complexes.

2.2.2 Ribonucleoprotein-complex preparation

2.5 µl of 6.2 µg/µl (61 pmoles) Cas9 (163.7 kDa) in 10 mM Tris-HCL (pH 7.4), 300 mM NaCl, 0.1 mM EDTA, and 1 mM DTT was separately mixed with 2.5 µl (112.5 pmoles) of each gRNA complex. Each solution was then incubated at room temperature for 10 - 20 minutes, and finally combined 1:1 immediately prior to electroporation.

Guide RNA	Nuclease	Position	PAM	Sequence
upstream HTT KO	SpCas9	exon1 E12.1	AGG	5'-GAAGGACTTGAGGGACTCGA-3'
downstream HTT KO	SpCas9	exon1 P76.3	TGG	5'-TCAGCCACAGCCGGGCCGGG-3'

Table 2.4. Guide RNA sequences.

2.2.3 Nucleofection

Prior to electroporation, HD109 and KOLF2 iPSCs were cultured to 80% confluency on Laminin-coated (2.5 µg/ml) wells. Medium was replaced containing 10 µM Y27632 (Abcam, Cambridge, UK) for roughly 1 hour before they were then dissociated into single cells with Accutase (Stem Cell Technologies), collected at 1 x 10^6 cells per nucleofection reaction in TeSR-E8 (Stem Cell Technologies) with Y27632 (10 µM), and centrifuged for 5 minutes at 200 g, in 15 ml centrifuge tubes. Pellets were then resuspended in 100 µl complete P3 buffer (82 µl P3 and 18 µl of P3-supplement) supplied in the P3 Primary Cell 4D-Nucleofector X Kit (Lonza) with the addition of 10 µl of Cas9/gRNA solution for an overall 1 x 10^6 cells, 20 µg Cas9, 20 µg gRNA per reaction. For each cell line (HD109 and Kolf2), 100 µl of cell solution was transferred to a cuvette and electroporated on an Amaxa 4D-Nucleofector (Lonza), using the primary cell line P3 CA137 program. Immediately, following electroporation, the cuvette was gently flooded with 1 ml of TeSR-E8 with 10 µM Y27632 and transferred to one well of a 6-well plate containing 2 ml TeSR-E8 with 10 µM Y27632. Cells were cultured for 24 hours before harvesting again for FACS sorting.

2.2.4 FACS sorting

Both targeted cell lines as well as a non-targeted controls were harvested for FACS. Sorting was performed by Mark Bishop, using a FACS Aria Fusion (BD Biosciences). After sorting, cells were cultured on 10 cm dishes until colonies could be individually picked.

2.2.5 Colony screening and sequencing

Once 96 colonies from each line were picked and split, genomic DNA was collected from each colony for subsequent PCR screening to identify knockout candidates. DNA was collected using QuickExtract DNA Extraction Solution (Epicentre) according to the manufacturer's protocol. Immediately, after extraction (to prevent DNA degradation),

samples were amplified using LA Taq DNA Polymerase (TaKaRa), in 10 µl reactions, according to Table 2.5.

PCR component	volume (µl)
LA Taq® DNA Polymerase	0.1
GC1 Buffer	5
DNTPs	1.6
Forward Primer (10 pMol/µl)	0.5
Reverse Primer (10 pMol/µl)	0.5
H_20	1.3
Template DNA (~ 100 ng)	1
Total Volume	10

Table 2.5. Components of PCR cocktail used for amplifying over the CRISPR-targeted region.

Samples were then cycled according to the following program (Table 2.6):

Temperature (°C)	Time	Cycles
94	5 min	1
94	30 sec	35
65	30 sec	
72	90 sec	
72	10 min	1
4	∞	1

Table 2.6. Thermocycler settings used for amplifying over the CRISPR-targeted region.

Samples were then run on a 2% agarose gel and visualized using a Gel Doc EZ Imager (Bio-Rad). PCR product from clones that were identified to have a disruption to both HTT alleles, was cleaned using a QIAquick PCR purification kit (Qiagen) and then sent for sequencing to Eurofins UK, for verification. Primers used for sequencing included:

Primer	Sequence
Sequencing Forward	5'- ATTCATTGCCCCGGTGC
Sequencing Reverse #1	5'- CTGGGTCACTCTGTCTCTG
Sequencing Reverse #2	5'- GGCTGAGGAAGCTGAGGAG

Table 2.7. List of sequencing primers for HTT knockout validation.

2.2.6 Western blotting

Cells were rinsed in in DPBS, harvested in 50 µl ice-cold radio-immunoprecipitation assay buffer (RIPA), per well of a 6-well plate and concentration and collected into microcentrifuge tubes. Samples were subjected to 1 freeze-thaw cycle, then pipetted and vortexed several times before centrifugation at 14,000g for 15 minutes to pellet cell debris. Supernatant was stored at -20°C, while protein concentrations of the subsamples were quantified by bicinchoninic acid assay (BCA).

For BCA subsamples were then taken and diluted 1:5, and 1:20 (in triplicate) and compared with a standard curve generated with concentrations of BSA ranging from 0 - 75 µg/ml, by incubation for 30 min at 37°C with a 0.02% $CuSO_4$ in bicinchoninic acid solution, on a flat-bottom 96-well plate (Greiner). Absorbance 570 nm was measured using a Tecan Infinite F50 microplate reader (Tecan) and associated Magellan for F50 software (Tecan).

For each sample, 50 µg of protein was heated for 15 minutes at 95°C in NuPage LDS sample loading buffer (Invitrogen), to denature, linearize, and add negative charge to the proteins. Samples and 5 µl protein standard (NEB), were loaded into a NuPage 3-8% Tris-Acetate protein gel (Invitrogen) and separated in NuPage Tris-Acetate SDS Running Buffer (Invitrogen) at 150 V. Samples were then transferred to a methanol-activated PVDF membrane in a 4°C room for 15 hours at 35 milliamps in NuPage transfer buffer (Invitrogen) containing 20% methanol and 1x NuPage antioxidant.

Membranes were washed 3 times for 5 minutes in Tris-buffered saline containing 0.1% Tween-20 (TBST), before blocking in a 5% powered milk TBST solution for 2 hours. Next membranes were incubated overnight at 4°C in polyQ-independent anti-HTT primary antibodies (Table 2.8) in a 1% powered milk and TBST solution. Rinsing, blocking, and incubation were repeated the following day, for anti-vinculin loading controls (Table 2.8).

Primary antibody	Host	Dilution	Supplier	Catalogue number
HTT	mouse	1:200	Merck Millipore	MAB2166
Vinculin	rabbit	1:1000	St. John's Laboratory	STJ97117

Table 2.8. Antibodies used for HTT knockout validation through immunoblotting.

Membranes were then washed three times for 10 minutes each in TBST and blocked for 1 hour in a 5% milk-TBST solution, before probing with secondary antibody infra-red dye conjugates (Table 2.9) in 5% milk and TBST, for 1 hour at room temperature, in the dark. Membranes were washed three times for 10 minutes at room temperature before visualizing on a LI-COR Odyssey CLx (LI-COR Biosciences) imaging system.

Name	Reactivity	Host	Dilution	Supplier	Catalogue number
IRDye® 800CW Goat anti-Mouse IgG	mouse	goat	1:15,000	LI-COR	ab216772
IRDye® 680RD Goat anti-Rabbit IgG	rabbit	goat	1:15,000	LI-COR	ab216777

Table 2.9. Secondary antibodies used for HTT knockout validation through immunoblotting.

2.2.7 CRISPR off-target detection

To identify insertions or deletions from potential off-target CRISPR cleavage, we used Deskgen software (www.deskgen.com). Both guide RNAs, were set to a threshold of 55 out of 100, to compute and identify similar DNA sequences and protospacer adjacent motifs, which could be targeted above this threshold. Candidate sequences in coding regions and their corresponding genes were identified using the ENSEMBL (www.ensembl.org) genome browser. The biological and molecular function of candidate genes were compared in (www.geneontology.org) to assess whether each might interact the endolysosomal system and alter potential endolysosomal dynamics.

STARD8 PCR and sequencing

Sequences surrounding potential off-target sites were amplified by PCR, using the sequences (Table 2.10) and thermocycler settings below (Table 2.11).

Primer	Sequence
Forward	5'- GGATCAAGAGCAAACGCAGC
Reverse	5'- CAGGCAAGGGTAGTCAGAGA

Table 2.10. Primers used for PCR amplification of potential off-target CRISPR cleavage in STARD8.

Temperature (°C)	Time	Cycles
94	5 min	1
94	30 sec	45
62	40 sec	
72	90 sec	
4	∞	1

Table 2.11. Thermocycler settings used for PCR amplification of potential off-target CRISPR cleavage in STARD8

Bands from PCR reactions were harvested and cleaned up using a QIAquick Gel Extraction kit (Qiagen). DNA was then sent to Eurofins for sequencing using the primers below (Table 2.12).

Primer	Sequence
Sequencing Forward #1	5'- CTTATACCCCCAACTCTTCCC
Sequencing Forward #2	5'- TATACCCCCAACTCTTCCCC
Sequencing Forward #5	5'- ACCTGAGTGACAACATGGCA

Table 2.12. Sequencing primers used for sanger sequencing over STARD8 locus

2.3 Cell imaging

The AX10 inverted microscope (Zeiss) was used with a Colibri LED light (Zeiss), and samples were imaged with a monochrome Axiocam MRm CCD digital camera (Zeiss) and Axiovision 4.7.1 software (Zeiss).

The Opera Phenix (PerkinElmer) high-content screening system with four solid state lasers at 375 nm, 488 nm, 561 nm, 640 nm, was used with a 40x water immersion lens with a numerical aperture (NA) of 1.1 and 63x water immersion with a NA of 1.15. Samples were imaged with up to four parallel confocal detection channels through a true point confocal, microlens-enhanced wide-view Nipkow spinning disk, 16-bit sCMOS 4.7 Megapixel camera, and Harmony high content imaging software (PerkinElmer). The analysis features of the Harmony software were not used in this study.

Images were also obtained using a Leica SP8 laser scanning confocal microscope with 405 nm, 488 nm, 560 nm, 640 nm solid state lasers, a prism-based spectral confocal system, with galvanometer and resonant scanners, two standard photomultiplier tubes, and one hybrid

photon detector (Leica). Leica Application Suite X (Leica) and Volocity 6.3.1 software (PerkinElmer) were used in analyses.

2.3.1 Paraformaldehyde fixation

Cells were washed three times with DPBS, then incubated in 4% paraformaldehyde solution (PFA) for 10 minutes at room temperature. Cells were then rinsed three more times with DPBS, and either immediately processed for antibody staining, or stored in DPBS at 4°C until further processing. PFA was used unless otherwise stated for fixation as methanol can degrade lipids.

2.3.2 Blocking buffer

Blocking buffer was prepared to prevent non-specific antibody binding and to permeabilize cell membranes. Blocking buffer consists of a 1% bovine serum albumin (BSA) and 0.1 - 0.3% Triton-X (or 0.01% saponin) in DPBS solution and was stored at -20°C and thawed prior to use.

2.3.3 Nuclear counterstaining

Cell nuclei were stained with Hoechst-33342 (Thermofisher) or propidium iodide at 2 µg/ml rinsed again three times and stored in DPBS at 4°C until further processing.

2.3.4 Antibody staining

Fixed cells were incubated in permeabilization buffer (unless otherwise noted) and then overnight at 4°C in blocking buffer, supplemented with the relevant primary antibodies (Table 2.13). Cells were then rinsed three times in DPBS and incubated at room temperature for 30 minutes, without light, in secondary antibody and blocking buffer (Table 2.14). Cells were then rinsed again three times with DBPS prior to nuclear staining and left immersed in DPBS until observation.

1° Antibody	Species	Supplier (Catalogue number)	Dilution	Permeabilization buffer	Blocking buffer
Huntingtin (D7F7) XP®	rabbit monoclonal	Cell Signaling #5656	1:100	0.3% Triton X in PBS, 30 min, RT	10% NGS + 0.3% Triton X in PBS
Nestin	mouse monoclonal	Merck MAB5326	1:500	0.1% Triton X in PBS, 30 min, RT	10% FBS + 0.1% Triton X in PBS

SOX2	rabbit polyclonal	Merck ab5603	1:500	0.1% Triton X in PBS, 30 min, RT	10% FBS + 0.1% Triton X in PBS
OCT4	rabbit polyclonal	Abcam, ab19857	1:100	0.1% Triton X in PBS, 30 min, RT	10% FBS + 0.1% Triton X in PBS
TRA-1-60	mouse monoclonal	Abcam ab16288	1:500	0.1% Triton X in PBS, 30 min, RT	10% FBS + 0.1% Triton X in PBS
TRA-1-81	mouse monoclonal	Abcam ab16289	1:500	0.1% Triton X in PBS, 30 min, RT	10% FBS + 0.1% Triton X in PBS
NANOG	mouse monoclonal	BD Pharmingen 560791	1:200	0.1% Triton X in PBS, 30 min, RT	10% FBS + 0.1% Triton X in PBS
SSEA4	mouse monoclonal	DSHB, MC-813-70	1:50	0.1% Triton X in PBS, 30 min, RT	10% FBS + 0.1% Triton X in PBS
GM130	mouse polyclonal	Abcam, ab169276	1:200	0.1% Triton X in PBS, 30 min, RT	10% FBS + 0.1% Triton X in PBS
LAMP1	rat monoclonal	DSHB, 1D48	1:200	0.1% Triton X in PBS, 30 min, RT	10% FBS + 0.1% Triton X in PBS
NPC1	rabbit	Novus NB400-148	1:200	0.1% Triton X in PBS, 30 min, RT	10% FBS + 0.1% Triton X in PBS
NPC2	rabbit	Sigma HPA000835	1:200	0.1% Triton X in PBS, 30 min, RT	10% FBS + 0.1% Triton X in PBS
CTIP2	rat monoclonal	Abcam, ab18465	1:500	0.3% Triton X in PBS, 60 min, RT	3% NGS + 0.3% Triton X in PBS
DARPP32	rabbit monoclonal	Abcam ab40801	1:500	0.1% Triton X in PBS, 30 min, RT	10% FBS + 0.1% Triton X in PBS
NeuN	chicken	Aves labs, NUN	1:500	0.1% Triton X in PBS, 30 min, RT	10% FBS + 0.1% Triton X in PBS
MAP2	mouse monoclonal	Sigma m1406	1:200	0.1% Triton X in PBS, 30 min, RT	10% FBS + 0.1% Triton X in PBS
NESTIN	mouse monoclonal	Millipore MAB5326	1:200	0.1% Triton X in PBS, 30 min, RT	10% FBS + 0.1% Triton X in PBS
z-PLBPA	mouse	Echelon, z-PLBPA	1:100	Not used	10% FBS + 0.05% saponin in PBS

Table 2.13. List of primary antibodies used for immunocytochemical analyses.

2° Antibody	Supplier	Catalogue Number	Dilution
Alexa-Fluor anti-rabbit 488	Invitrogen	A11008	1:500
Alexa-Fluor anti-chicken 488	Invitrogen	A11309	1:500
DyLight horse anti-rabbit 488	Vector Labs	DI-1088	1:500
Alexa-Fluor anti-mouse 555	Invitrogen	A28180	1:500
Alexa-Fluor anti-rat 555	Invitrogen	A21434	1:500
Alexa-Fluor anti-rat 594	Invitrogen	A11007	1:500
Alexa-Fluor 647 anti-mouse	Invitrogen	A21235	1:500
Alexa-Fluor 647 anti-rat	Invitrogen	A32733	1:500

Table 2.14. List of secondary antibodies used for immunocytochemical analyses.

2.3.5 Filipin

Filipin complex contains eight isomeric components, of which filipin III is the main constituent (Table 2.15). Filipin is a polyene macrolide which binds to unesterified cholesterol and exhibits excitation and emission at 380 nm and 450 nm, respectively (Arthur et al. 2011; Vanier and Latour 2015). To visualize cellular cholesterol, cells were fixed and incubated in a 125 µg/ml filipin solution in DMEM with 10% FCS for 30 min at room temperature. Cells were then rinsed three times with DPBS, and counterstained with propidium iodide before visualization.

Stain	Dilution	Supplier	Catalogue number
Filipin complex from *Streptomyces filipinensis*	125 µg/ml	Sigma-Aldrich	F9765
Cholera Toxin B subunit	1 µg/ml	Sigma-Aldrich	C1655
CYTO-ID® Autophagy detection kit	2 µl/ml	Enzo life sciences	ENZ-51031-K200

Table 2.15. List of reagents used for cellular staining.

2.3.6 FITC-CTxB

Localization measurements of cellular ganglioside GM1, were performed using cholera toxin subunit B (CTxB, Table 2.15) conjugated to fluorescein isothiocyanate (FITC). CTxB exclusively binds ganglioside GM1 and FITC displays excitation and emission spectra at 490 nm and 525 nm, respectively. To stain, cells were rinsed three times with PBS, then incubated overnight at 4°C in a 1 µg/ml solution of (FITC-CTxB) in HBSS solution. The following day cells were rinsed again three times with DPBS and visualized.

2.3.7 CYTO-ID

To measure autophagosome area, cells were labelled using Cyto-ID Autophagy Detection Kit (Table 2.15) which relies on a cationic amphiphilic tracer dye to selectively stain autophagic compartments including pre-autophagosomes, autophagosomes, and autophagolysosomes, while excluding lysosomes. Cells were cultured in either standard differentiation medium, or in starvation conditions, 60 µM chloroquine in DPBS (with $Ca^{2+}$and Mg^{2+}) for the final 4 hours, to induce autophagy. Cells were labelled according to the manufacturer's protocol. Briefly, cells were washed two times with a 2% fetal bovine serum (FBS) in phenol red-free RPMI 1640. Cells were then incubated at 37°C in assay buffer supplemented with 5% FBS and

2 µl/ml Cyto-ID green dye and 1 µl/mg Hoechst 33342, for 30 minutes in light-free conditions, rinsed with DPBS and fixed in 4% PFA before imaging.

2.3.8 Mitotracker CMT-ROS

To observe mitochondrial morphology, Mitotracker Orange CMTM-ROS, a fluorescent dye that passively diffuses across the plasma membrane and accumulates in the mitochondria of live cells, via a thiol-reactive chloromethyl moiety, was used. NPCs were grown in 1:1000 SLI and LIA medium with the addition of lipid concentrate at 1:1000, both with and without 50 µM miglustat for the final seven days before live staining and imaging with mitotracker CMT-ROS, at day 18. To stain, a 200nM working solution of Mitotracker was prepared. Cells were washed with DPBS, before adding 200ul Mitotracker solution into wells. Cells were incubated for 15 minutes at 37°C before the Mitotracker solution was removed. Cells were washed twice with DPBS and left in a final volume of 200 µl per well, before immediate image acquisition on the Opera-Phenix.

2.3.9 Microscopy analysis

2.3.9.1 Particle area measurements

Total particle area measurements were carried out in ImageJ as described by Cook *et al.* (2020a). Z-stacks were compressed to a single plane by maximum intensity projection, in which voxels exhibiting the maximum intensity in each plane are represented, to offset any potential differences in vesicle positioning in the z-plane. Images were imported and changed to 8-bit monochrome, then areas of interest were thresholded and selected such that only fluorescent regions indicating NPC1, NPC2, LAMP1, or LPBPA, excluding the nucleus, were calculated. Particles under 0.0005 inches were removed to disclude debris and noise. The total fluorescent area was then divided by the number of measured cells to quantify area per cell. LBPA measurements in NPCs were carried out by Rhys Meredith.

2.3.9.2 Perinuclear area measurements

Calculations of NPC1 area in perinuclear regions were carried out using a modified version of the method outlined by Erie *et al*. (2015). Briefly, nuclei were outlined by free hand in ImageJ as determined by Hoechst staining. The nuclear outline was then expanded outward by 2 µm

using the "Enlarge" function to define the out boundary of the perinuclear region. The particle area between the outer perinuclear region and the nucleus was then measured and the particle area located in the perinuclear region as a percent of combined nuclear and perinuclear area was calculated by the following equation 100*(perinuclear fluorescent area) (perinuclear area + nuclear area). The nuclear area was included in the denominator to offset variations in perinuclear area that arise by applying the "Enlarge" function to a nonuniform population of nuclei.

2.3.9.3 Colocalization analysis

Cells were costained with LAMP1 and NPC1, imaged with the Leica-SP8 laser confocal microscope using a 63x oil-immersion lens with a NA of 1.4 and a refraction index of 1.51. Images were imported into Volocity 6.3.1 software (Perkin Elmer) and for each cell, hand-drawn regions of interest were selected which included all areas of cytoplasm, excluding that which overlapped with the Hoechst-stained nucleus, as calculating overlap in this region can impart bias. Thresholding was carried out using the method, described in Costes *et al.* (2004). Manders colocalization coefficients for both channels were then calculated to determine the proportion of overlap by each probe as they relate to one another (M1 and M2) as delineated by Manders *et al.* (1993).

2.3.9.4 Phenotype comparisons

Comparisons of ganglioside GM1 and cholesterol across NPCs were carried out by sorting cells into categories based on vesicle storage phenotypes. Filipin was used to visualize cholesterol and cells that displayed two or more puncta, or a large single cluster of puncta (mainly in the perinuclear region), were counted against cells lacking this phenotype, for each cell line. Cells stained with CTxB, used to visualized GM1, were classed into three categories including cells exhibiting two or more large punctate, cells with a primarily plasma membrane distribution, and cells with a diffuse distribution of GM1. U18666A was used as a positive control in both cases, as it is known to elicit an NP-C phenotype.

2.3.9.5 Mitotracker CMT-ROS

Images were acquired using the Opera Phenix, using a 40x water-immersion lens across a Z-stack consisting of 3 planes separated by 2 µm. Mitochondrial morphology was determined using Harmony software (Perkin Elmer) according to the following analysis parameters:

Analysis Sequence "4TH PHENOLOGIC MITOCHONDRIA"

Input Image	Input
	Flatfield Correction : Advanced Brightfield Correction **Stack Processing :** Maximum Projection **Min. Global Binning :** Dynamic

Find Nuclei	Input	Method	Output
	Channel : HOECHST 33342 **ROI :** None	**Method :** M Diameter : 22 µm Splitting Sensitivity : 0.48 Common Threshold : 0	Output Population : ALL NUCLEI

Calculate Morphology Properties	Input	Method	Output
	Population : ALL NUCLEI **Region :** Nucleus	**Method :** STAR Channel : HOECHST 33342 Symmetry Threshold Compactness Axial Radial Profile Profile Width : 1.184 µm **Sliding Parabola** Curvature : 10 **Texture SER** Scale : 1 px Normalization by : Kernel	Property Prefix : Nucleus

Select Population	Input	Method	Output
	Population : ALL NUCLEI	**Method :** Linear Classifier Number of Classes : 4 Nucleus Symmetry 02 Nucleus Symmetry 03 Nucleus Symmetry 04 Nucleus Symmetry 05 Nucleus Symmetry 12 Nucleus Symmetry 13 Nucleus Symmetry 14 Nucleus Symmetry 15 Nucleus Threshold Compactness 30% Nucleus Threshold Compactness 40% Nucleus Threshold Compactness 50% Nucleus Threshold Compactness 60% Nucleus Axial Small Length Nucleus Axial Length Ratio Nucleus Radial Mean Nucleus Radial Relative Deviation Nucleus Profile 1/2 Nucleus Profile 2/2	Output Population A : Class A Output Population B : Class B Output Population C : Class C Output Population D : Class D

Find Surrounding Region	Input	Method	Output
	Channel : MitoTracker Orange **Population :** Class A **Region :** Nucleus	**Method :** C Common Threshold : 0.46 Individual Threshold : 0	Output Region : CYTOPLASM

Filter Image	Input	Method	Output
	Channel : MitoTracker Orange	**Method :** Texture SER Filter : SER Bright Scale : 0.75 px Normalization by : Unnormalized	Output Image : SER Bright

Find Image Region	Input	Method	Output
	Channel : SER Bright **ROI :** Class A **ROI Region :** CYTOPLASM	**Method :** Absolute Threshold Lowest Intensity : ≥ 500 Highest Intensity : ≤ INF Split into Objects Area : > 0.5 px² Fill Holes	Output Population : MITOCHONDRIA Output Region : MITOCHONDRIAL REGION

Calculate Morphology Properties (2)	Input	Method	Output
	Population : MITOCHONDRIA **Region :** MITOCHONDRIAL REGION	**Method :** Standard Area Roundness Width Length Ratio Width to Length	Property Prefix : MITOCHONDRIAL REGION

Calculate Intensity Properties	Input	Method	Output
	Channel : SER Bright **Population :** MITOCHONDRIA **Region :** MITOCHONDRIAL REGION	**Method :** Standard Mean	Property Prefix : Intensity MITOCHONDRIAL REGION SER Bright

Calculate Texture Properties	Input	Method	Output
	Channel : SER Bright **Population :** MITOCHONDRIA **Region :** MITOCHONDRIAL REGION	**Method :** SER Features Scale : 0 px Normalization by : Kernel SER Spot SER Hole SER Edge SER Ridge SER Valley SER Saddle SER Bright SER Dark	Property Prefix : MITOCHONDRIAL REGION SER Bright

Define Results	Results
	Method : List of Outputs **Population : MITOCHONDRIA** Number of Objects MITOCHONDRIAL REGION Area [µm²] : Mean MITOCHONDRIAL REGION Roundness : Mean MITOCHONDRIAL REGION Width [µm] : Mean MITOCHONDRIAL REGION Length [µm] : Mean MITOCHONDRIAL REGION Ratio Width to Length : Mean Intensity MITOCHONDRIAL REGION SER Bright Mean : Mean MITOCHONDRIAL REGION SER Bright SER Spot 0 px : Mean MITOCHONDRIAL REGION SER Bright SER Hole 0 px : Mean MITOCHONDRIAL REGION SER Bright SER Edge 0 px : Mean MITOCHONDRIAL REGION SER Bright SER Ridge 0 px : Mean MITOCHONDRIAL REGION SER Bright SER Valley 0 px : Mean MITOCHONDRIAL REGION SER Bright SER Saddle 0 px : Mean MITOCHONDRIAL REGION SER Bright SER Bright 0 px : Mean MITOCHONDRIAL REGION SER Bright SER Dark 0 px : Mean **Object Results** Population : ALL NUCLEI : None Population : Class B : None Population : Class C : None Population : Class D : None Population : Class A : None Population : MITOCHONDRIA : ALL

Acapella version: 5.0.1.124082. Timestamp: 2022-06-27 18:20:39 +0100.

2.4 Electron Microscopy

Day 16 neural progenitors were thawed and plated at 8 x 10^5 cells per glass coverslip, coated with either PDL or PEI. After coating, coverslips were then covered with an additional 80 µl droplet of low-growth factor Matrigel at 1:50 in knockout DMEM (Gibco). Matrigel was replaced with a 100 µl of cells in SJA medium with Rock inhibitor (10 µM). Three batches of cells were cultured for two different durations according to the MSN protocol, by Kim Jones and me. Two of the differentiations extended to day 32, and the other until day 47. Test wells were treated with 50 µM miglustat, for the final seven days. Positive controls were treated with 2 µM U18666A for 24 hours prior to fixation. To fix, cells were then rinsed three times in DPBS before overnight incubation at 4°C in a 2.5% Glutaraldehyde (Agar Scientific) in 0.1 M Cacodylate Buffer (pH 7.2). Samples were then rinsed three more times in 0.1 M Cacodylate Buffer and transported to the TEM facility (Bristol, UK)

Cells were then postfixed in 1% osmium tetroxide in a 0.1% cacodylate buffer for 30 minutes at room temperature. Next cells were washed three times, each for 10 minutes, in 0.1 cacodylate buffer. Samples were then serially dehydrated, through rinsing in sequentially increasing concentrations of ethanol: 70 %, 80 %, 90 %, 96 %, 100 %, 100 %, 100 %, for 10 mins each. Coverslips were then removed from the culture plate and embedded in one drop of resin for 1 hour at room temperature, before a second drop was added on top, and left for three days, to polymerize.

Coverslips were removed by alternating immersion in liquid nitrogen and boiling water five times; cells were left in liquid nitrogen until bubbling ceased, and in boiling water for two minutes each. Resin pellets were then stained with a drop of a 3.0 % uranyl acetate solution in water filtered through a 0.2 µm filter, for 10 minutes in darkness. Next, cells were given two, five-minute washes in distilled water, before Lead citrate, or Reynolds' staining (Reynolds, 1963).

To stain samples, 282 mM lead nitrate solution was mixed with a 189 mM sodium citrate solution in a 1:1 ratio. Next a 1 M sodium hydroxide was at added to make a final 15.96% NaOH solution.

2.4.1 Ultrastructural analysis

To compare differences in vesicle populations across cell lines, organelles greater than 0.3 µm in diameter were counted and categorized based on morphology into fingerprint bodies, curvilinear bodies, ganglioside storage bodies and empty vesicles. Averaged vesicle counts per cell for each well were compared by one-way ANOVA and Tukey's multiple comparisons or Kruskal-Wallis and Dunn's multiple comparisons, as appropriate.

2.5 Seahorse

Mitochondrial function was assessed using the Agilent Seahorse XF Mito Stress test, by direct measurement of the oxygen consumption rate. Day 16 NPCs were plated at 2.5 x 10^5 cells in 200 µl SJA containing 10 µM Y27632 per well of a 96-well plate with half-medium changes every other day for 8 days, until Day 24. Samples were positioned such that no wells were on the edge of the 96 well plate and each sample contained between 6 and 9 technical replicates (one well per technical replicate). Half of the samples were treated during the final 7 days with 50 µM miglustat.

On the day before the Seahorse assay was to be conducted, the 96 well Seahorse XFe sensor cartridge (Agilent), which contains the two fluorophores, one that measures the oxygen consumption rate (OCR) corresponding to respiration, and one that detects proton excretion corresponding to the extracellular acidification rate (ECAR) and glycolysis, was hydrated by adding 200 µl of Seahorse XF Calibrant (Agilent) solution to each well of the utility plate in which it was incubated overnight in a non-CO_2 incubator at 37°C. The Seahorse XFe Analyzer and Wave software (Agilent) were powered on, in order to allow the internal temperature to stabilize overnight.

On the day the assay was to be performed, 50 ml of Seahorse assay medium was prepared by supplementing Seahorse XF basal medium (Agilent) to a final concentration containing 2.0 mM Glutamax (Thermo Fisher) 1.0 mM sodium pyruvate (Thermo Fisher), and 10 mM

glucose (Merck). The complete medium was then warmed to 37°C in a non-CO_2 incubator. During this time wells were photographed for later use in cell count-based normalization.

Cells were then washed three times with and left in 180 µl of seahorse medium, before being placed in a non-CO_2 incubator at 37°C for one hour. Oligomycin, Carbonyl cyanide-4 (trifluoromethoxy) phenylhydrazone (FCCP), and rotenone/antimycin (Agilent) were prepared in complete Seahorse medium to be injected to a final concentration of 1.0 µM oligomycin, 1.0 FCCP 1.0 µM, and 0.5 µM rotenone/antimycin. Once the Seahorse machine was calibrated and after cell incubation was complete, the Seahorse Mito Stress test was performed.

Post assay normalization was also conducted using Calcein AM and propidium iodide. Medium in the wells was replaced with 100 µl of PBS. Then 100 µl of a 4 µl/ml Calcein AM, and 4 µl/ml propidium iodide was added to each well. Cells were incubated at 37°C for 30 minutes and gently washed three times, before fluorescence Calcein AM (485 nm/535 nm) propidium iodide (530 nm/620 nm) was measured at nine points per well on a SpectraMAX Gemini EM fluorescence plate reader (Molecular Devices). Nine data points per well were then averaged and normalization for each well was computed based on these averages.

2.6 Lysosomal enzyme assays

2.6.1 Sample preparation

Cells were rinsed twice DPBS then detached using Tryple Select Enzyme. Cells were then resuspended and centrifuged/washed three times in 5 ml DPBS at 200 g for 5 minutes. Finally, DPBS was removed, and pellets were stored at -80°C until protein concentration could be estimated through bicinchoninic acid assay (BCA).

2.6.2 Bicinchoninic acid assay

Immediately prior to performing the BCA, cell pellets were resuspended in MilliQ water, and subcellular fractionation was performed by 3 additional freeze-thaw cycles before being passed through a 26-gauge needle 20 times. Next, homogenate was centrifuged at 13,000g at 4°C for 30 minutes. The liquid fraction was transferred to a new vial from which

subsamples were then taken and diluted 1:5, 1:10, 1:20 (in triplicate) and compared with a standard curve generated with concentrations of BSA ranging from 0 - 75 µg/ml, by incubation for 30 min at 37°C with a 0.02% $CuSO_4$ in bicinchoninic acid solution, on a flat-bottom 96-well plate (Greiner). Absorbance 570 nm was measured using a Tecan Infinite F50 microplate reader (Tecan) and associated Magellan for F50 software (Tecan). Each sample was then diluted to 1 µg/µl and divided into 40 µg (40 µl) aliquots, corresponding to one enzyme assay per vial, and stored at -80°C to minimize enzyme degradation due to unnecessary freezing and thawing.

2.6.3 Fluorometric analysis of enzyme activity

Enzyme assays were carried out by Callum Higgins and individual enzyme assay conditions are summarized in (Table 2.16). Briefly, 10 µl of reaction buffer was added to each well of a flat-bottom 96-well microplate. Next, 2 µg (2 µl) of sample was added to each well (at least three repeats per sample). To compensate for background fluorescence, control samples were heat-inactivated at 95°C for 15 minutes. Standards for each substrate were also added to generate a standard curve with concentrations ranging from 0 - 200 µM. The assay was initiated, by the addition of 8 µl artificial fluorogenic substrate (diluted in reaction buffer). Plates were then incubated at 37°C for the indicated time period (Table 2.16). Enzyme reactions were stopped by the addition of 180 µl of the designated stop buffer (Table 2.16). Fluorescence of the unbound fluorophores present in each sample was measured with a SpectraMAX Gemini EM fluorescence plate reader (Molecular Devices), with the exception of p-nitroanilide, in which an Tecan Infinite F50 microplate reader and Magellan for F50 software were used with an absorption of 405 nm.

Enzyme measured	Reagent	Reagent function	37°C	References
β-glucosidase (GCase)	4-Methylumbelliferone (4MU) (Sigma) 4-methylumbeliferyl-β-D-glucopyranoside (2 mM) (Sigma) CBE (500 µM) Sodium acetate, pH5.6 + 0.1% triton + 0.2% NaTc (Sigma) Glycine/NaOH, pH 10.6	Standard Substrate Inhibitor Reaction Buffer Stop Buffer	1 hr	(Butterworth and Broadhead 1977; Sawkar et al. 2002)
β-Galactosidase (β-gal)	4MU 4MU-β-galactosidase (2 mM) 1-deoxygalactonojirimycin (1 mM) Sodium acetate, pH4.5 + 0.1% 5mM NaCL + 0.2% NaTc Glycine/NaOH, pH 10.6	Standard Substrate Inhibitor Reaction Buffer Stop Buffer	1 hr	(Nowakowski et al. 1988; Nowroozi et al. 2001)
Acid Sphingomyelinase (aSMase)	HMU (Moscerdam) HMU-Phosphorylcholine (0.5 mM) (Moscerdam) Zolendronic acid (1 mM) Sodium acetate, pH4.5 + 0.2% NaTc + 0.02% NaAz Na2CO3, pH10.9 + 2.5% triton	Standard Substrate Inhibitor Reaction Buffer Stop Buffer	1 hr	(Van Diggelen et al. 2005)
α-galactosidase A (αGal A)	4MU 4MU-α-D-galactopyranoside (2 mM) (Sigma) N-butyldeoxygalactonojirimycin (1 mM) Phosphate citrate, pH4.5 Glycine/NaOH, pH10.6	Standard Substrate Inhibitor Reaction Buffer Stop Buffer	1 hr	(Mayes et al. 1981; Olivova et al. 2009; Caudron et al. 2015)
Total Hexosaminidase (Total HEX)	4MU 4MU-N-acetyl-β-D-glucosamine (2 mM) (Sigma) Phosphate Citrate, pH4.6 + 0.01% triton Na2CO3, pH10.9	Standard Substrate Reaction Buffer Stop Buffer	1 hr	(Bayleran et al. 1987)
Hexosaminidase A (HEXA)	4MU 4MU-N-acetyl-β-D-glucosamine-6-sulphate (2 mM) (Calbiochem) Phosphate Citrate, pH4.6 + 0.01% triton Na2CO3, pH10.9	Standard Substrate Reaction Buffer Stop Buffer	1 hr	(Bayleran et al. 1987)
Hexosaminidase B (HEXB)	4MU 4MU-N-acetyl-β-D-glucosamine-6-sulphate (2 mM) (Calbiochem) Phosphate Citrate, pH4.6 + 0.01% triton Na2CO3, pH10.9	Standard Substrate Reaction Buffer Stop Buffer	2 hr at 50°C to deactivate HEXA	(Suzuki 1987)

β-glucuronidase (GUSB)	4MU 4MU-β-D-glucuronide (2 mM) Suramin (100 µM) (Sigma) Sodium acetate, pH4 + 0.1% triton Na2CO3, pH10.9	Standard Substrate Reaction Buffer Stop Buffer	1hr	(Kosugi et al. 1990; Bramwell et al. 2014)
α-L-iduronidase (IDU)	4MU 4MU-α-L-iduronate (1 mM) (Carbosynth) Sodium formiate, pH3.2 Na2CO3, pH10.9	Standard Substrate Reaction Buffer Stop Buffer	1hr	(Hopwood et al. 1979; Kingma et al. 2013)
α-N-acetylglucosaminidase (NAGLU)	4MU 4MU-α-N-acetylglucosaminide (1 mM) (Sigma) Sodium acetate, pH4.5 Glycine/NaOH, pH10.6	Standard Substrate Reaction Buffer Stop Buffer	4 hr	(Mauri et al. 2013)
Acid α-glucosidase (α-Glu)	4MU 4MU-α-glucopyranoside (4 mM) (Sigma) Phosphate citrate, pH4 + 0.1% acarbose Glycine/NaOH, pH10.6	Standard Substrate Reaction Buffer Stop Buffer	4 hr	(Broadhead and Butterworth 1978; Jack et al. 2006)
α-fucosidase (α-Fuc)	4MU 4MU-α-L-lucopyranomide (1 mM) (Sigma) Deoxyfuconojirimycin hydrochloride (20 nM) (Santa Cruz, Dallas, USA) Phosphate Citrate, pH5 Na2CO3, pH10.9	Standard Substrate Inhibitor Reaction Buffer Stop Buffer	1 hr	(Winchester et al. 1990)
α-mannosidase (α-Man)	4MU 4MU-α-D-mannopyranoside (2 mM) (Sigma) Swarinosine (80 nM) (Carbosynth) Sodium acetate, pH4.5 + 0.1% triton Glycine/NaOH pH10.6	Standard Substrate Inhibitor Reaction Buffer Stop Buffer	1 hr	(Prence and Natowicz 1992; Gotoda et al. 1998)
Sialadase (NEU)	4MU 4MU-N-acetyl neuraminic acid (0.2 mM) (Toronto) Sodium acetate, pH4.5 Glycine/NaOH pH10.6	Standard Substrate Reaction Buffer Stop Buffer	4 hr	(Winter et al. 1980; Yamada et al. 1983; Hayre et al. 2012)
Aspartylglucosaminidase (AGA)	AMC (Carbosynth) L-aspartic acid-β-7-amido-4-methyl coumarin (1 mM) (Carbosynth) L-asperagine (1 mM) Phoshate citrate, pH6.5 Phosphate citrate, pH4.5	Standard Substrate Inhibitor Reaction Buffer Stop Buffer	17 hr	(Vozyi et al. 1993)

Cathepsin B (CTSB)	AMC Z-Arg-Arg-7-amido-4-methylcoumarin (50 µM) (Marck) Z-Phe-Ala-diazomethylurtone (10 µM) Sodium acetate, pH5.5 + 0.8mM EDTA + 8mM DTT	Standard Substrate Inhibitor Reaction Buffer	30 min	(Barrett and Kirschke 1981; Headlam et al. 2006; Creasy et al. 2007; Viswanathan et al. 2012)
Cathepsin D/E (CTSD/E)	MCA 7-methoxycoumarin-4-acetyl-Gly-Lys-Pro-Ile-Leu-Phe-Phe-Arg-Leu-Lys-dintrophrnyl-D-Arg-amide (50 µM) (Eruto Life Sciences, NY) Phosphate citrate, pH4.5 + 2 mM EDTA + 50 mM NaCl	Standard Substrate Reaction Buffer	1 hr	(Ismael et al. 2016)
Cathepsin L (CTSL)	AMC Z-Phe-Arg-7-amido-4-methylcoumarin (50 µM) (Bachem) Z-Phe-Ala-diazomethylketone (10 µM) Phosphate citrate, pH5.5 + 0.005% BRU + 2.5 mM EDTA + 8 mM DTT	Standard Substrate Inhibitor Reaction Buffer	30 min	(Barrett and Kirschke 1981; Headlam et al. 2006; Creasy et al. 2007; Viswanathan et al. 2012)
Palmitoyl-protein thioesterase 1 (PPT1)	4MU 4MU-6-thiopalmitoyl β-D-glucoside (0.5 mM) (Carbosynth) ABC44 (200nM) (Sigma) Phosphate citrate, pH4 + 15mM DTT + 0.375% triton + 0.1U β-glucosidase Na2CO3, pH10.9 + 0.025% triton	Standard Substrate Inhibitor Reaction Buffer Stop Buffer	4 hr	(Van Diggelen et al. 1999)
Tripeptidyl-peptidase 1 (TPPT1)	AMC Ala-Ala-Phe-7-amido-4-methylcoumarin (0.5 mM) (Bachem) Sodium acetate, pH4.5 + 0.05% triton + 10% EDTA Phosphate citrate, pH4.5	Standard Substrate Reaction Buffer Stop Buffer	1 hr	(Beckenkamp et al. 2015)
Dipeptidyl peptidase enzymes (DPP)	p-nitoanilide (Sigma) Gly-pro-p-nitroanilide (2.5 mM) (Santa Cruz) Tris HCl, pH7.4 Sodium acetate, pH4.4	Standard Substrate Reaction Buffer Stop Buffer	2 hr	(Beckenkamp et al. 2015)
Acid Lipase (LAL)	4MU 4MU-oleate (0.1 mg/ml) (Carbosynth) Orlistat (1 µM) Sodium acetate, pH4 + 1% triton Na2CO3, pH10.9	Standard Substrate Inhibitor Reaction Buffer Stop Buffer	1 hr	(Moheimani et al. 2012)
Acid Phosphatase (APs)	4MU 4MU-Phosphate (150 µM) (Sigma) Acetate buffer, pH5 + 0.2% triton Glycine/NaOH, pH10.6	Standard Substrate Reaction Buffer Stop Buffer	1 hr	(Leake et al. 1982)

Table 2.16. List of enzyme assay conditions.

2.7 RNA-Seq

2.7.1 Cell culture modifications

Cells were cultured by Kim Jones and myself according to the standard MSN differentiation protocol, with slight modifications upon transfer to SJA medium. Cells were cultured in SJA medium for 7 days, with the addition of 0.5 mM valproic acid and with LM22A4 removed. DAPT was only included in the medium for the first three days. At week two, cells were fed with equal parts SJB and BrainPhys (Stem Cell Technologies), with the addition of 0.5 mM valproic acid. For the third and final week, cells were cultured in SJB without CHIR 99021 trihydrochloride. Experimental wells were treated with 50 µM miglustat throughout the entire duration of the final 7 days.

2.7.2 Sample preparation

Total RNA was collected using RNeasy RNA isolation and purification kit according to the manufacturer's instructions, including the additional step of adding DNAse1. Samples with an A260/280 nanodrop reading> 1.9 (75 in total or 3 per subclone) were selected and stored at -80C° until delivery to Novogene for further processing as outlined below (Figure 2.2)

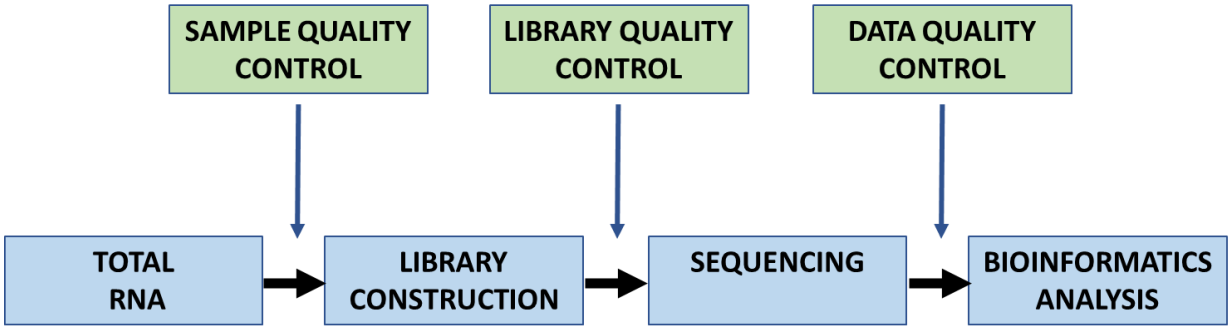

Figure 2.2. Outline of Novogene RNA sequencing workflow. Adapted from Novogene RNA-Seq Quantification Analysis Report.

2.7.3 Sample quality control

The best of three samples per subclone (5 per condition) were selected for library construction (Table 2.17). Preliminary QC was carried out by agarose gel electrophoresis. Sample quantitation was carried out on a nanodrop. Sample integrity was measured on an Agilent 2100 bioanalyzer. Purity was assessed by nanodrop.

CELL LINE	Subclone	Sample Name	Nucleic Acid ID	Concentration(ng/ ul)	Volume(ul)	Total amount(ug)	RIN
HD109	1	H109_3	EKRN210012917-1A	18	18	0.324	9.3
	2	H109_2h	EKRN210012922-1A	39	17	0.663	9.6
	3	H109n1	EKRN210012925-1A	53	18	0.954	9.7
	4	H109_2f	EKRN210012927-1A	15	16	0.24	9.1
	5	H109_3h	EKRN210012930-1A	27	15	0.405	9.7
HD22 ISO-109	1	I5h9_1	EKRN210012932-1A	12	17	0.204	8.8
	2	I5h9_3	EKRN210012937-1A	52	16	0.832	9.7
	3	I3h2_1	EKRN210012938-1A	27	15	0.405	9
	4	I3h2_2	EKRN210012942-1A	27	16	0.432	9.5
	5	I3h2_3	EKRN210012946-1A	35	16	0.56	8.5
HTTKO ISO-109	1	HKO_1	EKRN210012949-1A	9	15	0.135	9.6
	2	HKO_2	EKRN210012952-1A	7	12	0.084	8.9
	3	HKO_3	EKRN210012955-1A	9	15	0.135	9.1
	4	HKO_4	EKRN210012957-1A	13	14	0.182	9.7
	5	HKO_5	EKRN210012961-1A	7	16	0.112	8.7
HD109 + Miglustat	1	MH109_3	EKRN210012964-1A	16	18	0.288	9.1
	2	MH109_2h	EKRN210012965-1A	32	18	0.576	9.8
	3	MH109n1	EKRN210012968-1A	8	21	0.168	8.6
	4	MH109_2f	EKRN210012971-1A	14	20	0.28	9.2
	5	MH109_3h	EKRN210012974-1A	28	18	0.504	9.7
HD22 ISO-109 + Miglustat	1	MI5h9_w3	EKRN210012979-1A	14	18	0.252	9
	2	MI5h9_1	EKRN210012982-1A	12	22	0.264	8.6
	3	MI3h2_1	EKRN210012984-1A	13	21	0.273	9.3
	4	MI3h2_4	EKRN210012987-1A	9	23	0.207	8.9
	5	MI3H2_5	EKRN210012990-1A	6	23	0.138	8.5

Table 2.17. Quality of RNA samples used in RNA-Seq.

2.7.4 Library construction

Poly-T oligo-attached magnetic beads were used to isolate mRNA from total RNA. Following fragmentation, the first cDNA strand was synthesized using random hexamer primers, and second strand cDNA synthesis was achieved using either dUTP for a directional library or dTTP for non-directional. The cDNA library was quantified with QUBIT and real-time PCR and size distribution was assessed with the bioanalyzer (Novogene Manual).

2.7.5 Clustering and sequencing

Index-coded samples were clustered according to the manufacturer's instructions. Subsequently, library preparations were sequenced using an Illumina platform for and paired-end reads were generated (Novogene Manual). HD109 and isogenic controls were sequenced to an average read depth of 100 million reads per sample and all others were sequenced to an average read depth of 30 million reads per sample on the Illumina NovaSeq 6000. Sequenced reads were aligned to the Homo Sapiens, version (GRCh38/hg38) reference genome.

Raw data (raw reads) of FASTQ format were firstly processed through fastp. In this step, clean data (clean reads) were obtained by removing reads containing adapter and poly-N sequences and reads with low quality. At the same time, the quality scores, Q20 and Q30, were calculated and data with a quality score greater than Q30 were selected for the analysis, meaning that more than 80% of the

raw data has an error rate less than 1/1000, or correct to 99.9% (Figure 2.3A). GC distribution was also determined to be equally distributed (Figure 2.3B). Suboptimal reads were then eliminated before proceeding to the analysis (Figure 2.3C).

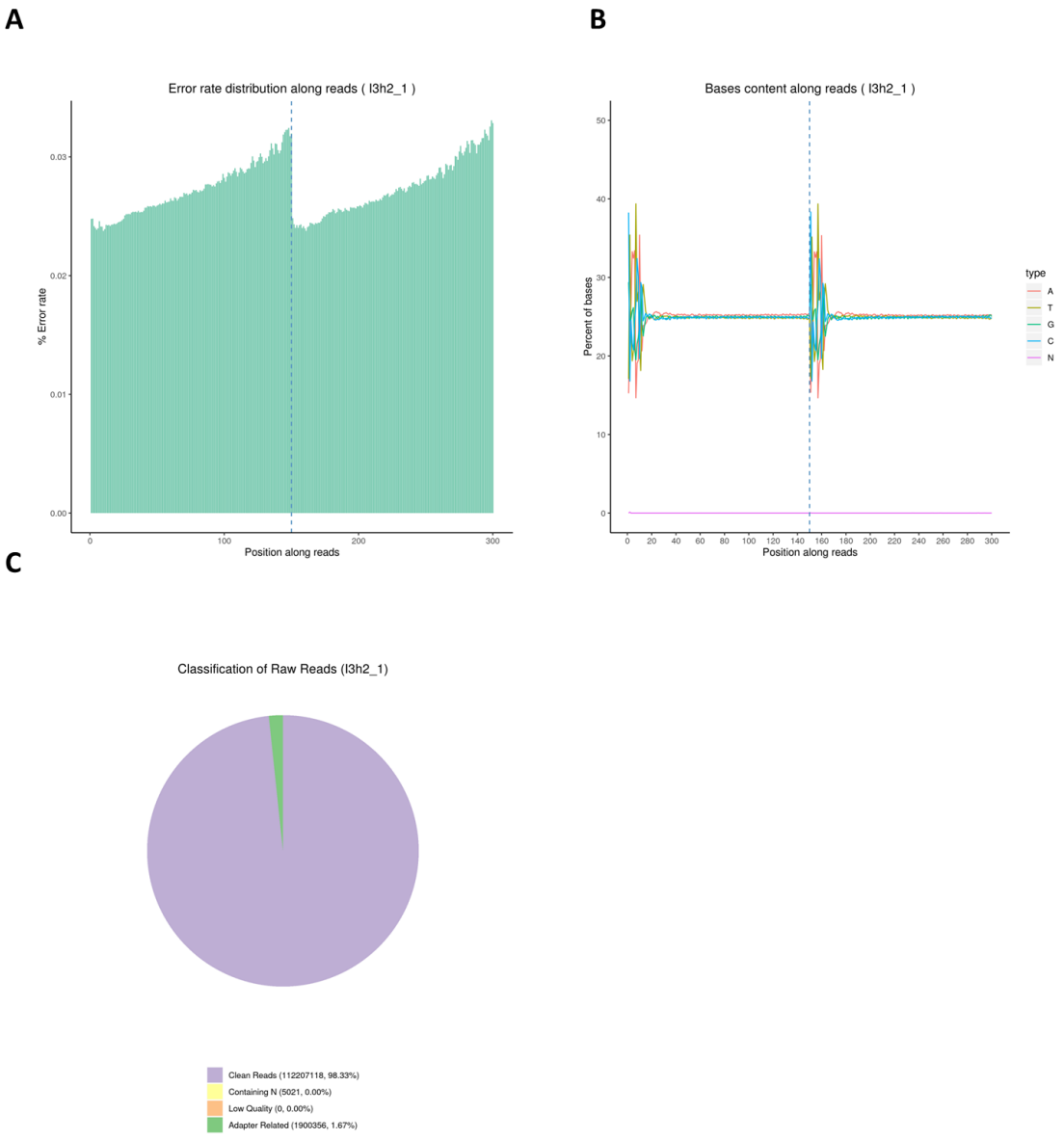

Figure 2.3. RNA Seq quality control. A) Representative graph of error rate distribution of reads. B) Nucleotide content along reads. C) Classification of reads with clean reads used in analysis.

Mapping

Reads were mapped to (GRCh38/hg38 version 93). Mapped reads are summarized (Figure 2.4A). Pie chart shows distribution. The circle plot shows the proportion of mapped reads along different chromosomes.

A

Sample name	Total reads	Total mapped reads	Uniquely mapped reads	Multiple mapped reads	Total mapping rate	Uniquely mapping rate	Multiple mapping rate
H109_2f	217120392	206582125	201259008	5323117	95.15%	92.69%	2.45%
H109_2h	224993974	214983007	209475725	5507282	95.55%	93.10%	2.45%
H109_3	215340938	205357537	200048264	5309273	95.36%	92.90%	2.47%
H109_3h	218766568	208440900	202814208	5626692	95.28%	92.71%	2.57%
H109n1	238472038	227080771	220532266	6548505	95.22%	92.48%	2.75%
HKO_1	73517494	70936443	69204201	1732242	96.49%	94.13%	2.36%
HKO_2	79278710	75729357	73960022	1769335	95.52%	93.29%	2.23%
HKO_3	95782206	91627399	89447186	2180213	95.66%	93.39%	2.28%
HKO_4	95710934	91515301	89264019	2251282	95.62%	93.26%	2.35%
HKO_5	79298534	75596443	73821684	1774759	95.33%	93.09%	2.24%
I3h2_1	224414236	212934907	207272129	5662778	94.88%	92.36%	2.52%
I3h2_2	213320660	203032631	197822326	5210305	95.18%	92.73%	2.44%
I3h2_5	252419304	240707491	234098481	6609010	95.36%	92.74%	2.62%
I5h9_1	232243284	221313442	215096358	6217084	95.29%	92.62%	2.68%
I5h9_w3	215690046	206075236	200594038	5481198	95.54%	93.00%	2.54%
MH109_2f	81582214	75303631	73420108	1883523	92.30%	90.00%	2.31%
MH109_2h	74455678	70914583	69163133	1751450	95.24%	92.89%	2.35%
MH109_3h	99799754	95187783	92817830	2369953	95.38%	93.00%	2.37%
MH109_3	84519346	80614997	78579591	2035406	95.38%	92.97%	2.41%
MH109n1	68215054	65087935	63428614	1659321	95.42%	92.98%	2.43%
MI3h2_1	77292930	73738691	71920274	1818417	95.40%	93.05%	2.35%
MI3h2_2	69122838	65914680	64319857	1594823	95.36%	93.05%	2.31%
MI3h2_5	76220884	72803837	71019533	1784304	95.52%	93.18%	2.34%
MI5h9_1	70054698	66657506	65034518	1622988	95.15%	92.83%	2.32%
MI5h9_w3	72248164	68874378	67125861	1748517	95.33%	92.91%	2.42%

B

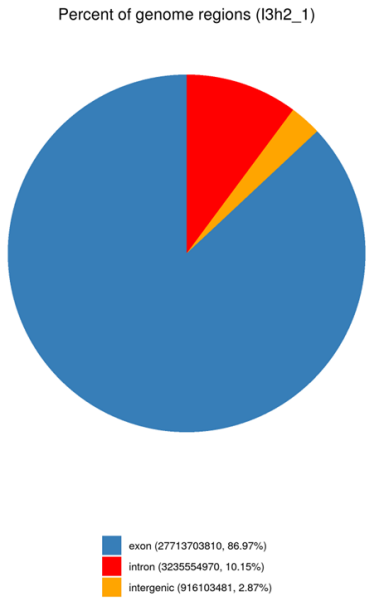

Figure 2.4. Information regarding mapped reads. A) Table indicating mapped read information. B) Example pie chart to indicate the genomic regions to which the reads were mapped.

2.8 Statistical Analyses

Unless otherwise noted, all data was analyzed with GraphPad Prism Version 8.0 (GraphPad Software, San Diego, USA). For two-way comparisons, unpaired t-tests were performed. For multiple comparisons made across cell lines subjected to a single differentiation, one-way ANOVAs, with Tukey's multiple comparisons tests were used. Two-way ANOVAs with Tukey's multiple comparisons tests were used when multiple differentiations were carried out, with the differentiated pool of cells and cell lines as the independent variables.

3 GENERATION AND CHARACTERIZATION OF HD AND HTT KNOCKOUT CELL LINES

3.1 Summary

To enable comparison of phenotypes between HD and control cell lines, without confounding genetic background effects, previous work in our lab used CRISPR gene editing to reduce the expanded CAG repeat present in the HD109 iPSC line to a wildtype CAG repeat length of 22 ($HD22^{ISO-109}$) (Donaldson 2019a). These lines were used for cell phenotyping throughout this thesis. To extend this framework, to determine whether mHTT-associated phenotypes reflected gain or loss of HTT function we also generated two biallelic HTT knockout lines, one isogenic with the HD109 and $HD22^{ISO-109}$ lines and one from an unrelated reference iPSC line, KOLF2. Throughout this thesis comparisons were primarily made between isogenic cell lines derived from the HD109 background, including controls ($HD22^{ISO-109}$), diseased (HD109) cells, and HTT knockouts ($HTT\text{-}KO^{ISO-109}$). Supplemental comparisons to evaluate the effects of HTT deletion, were also made between the KOLF2 and $KOLF2^{HTT-KO}$ as well as between HAP1 and $HAP1^{HTT-KO}$ cells, to assess the consistency across three biologically distinct cell lines. It should be noted, however, that whilst both the HD109 and KOLF2 are iPSC lines the HAP1 cells are an unrelated and haplozygous model.

Knockout models were developed using a dual gRNA-directed CRISPR-Cas9 mediated deletion within exon 1 of the huntingtin gene and validated through sequencing, immunofluorescent microscopy, and western blotting. Potential off-target Cas9 endonuclease effects were investigated and both HD and KOLF2 knockout lines were found to be intact. Edited iPSCs were differentiated according to a modified version of the MSN differentiation protocol developed by Smith-Geater *et al*. (2020) Telezhkin *et al.* (2016), and Arber *et al.* (2015) into either NPCs or neurons for use in the lysosomal storage phenotype comparisons to occur in subsequent chapters of this thesis. Therefore, characterization of cell lines at both stages was necessary to ensure that comparisons of these phenotypes and miglustat-related rescue effects would occur within a similar cellular backdrop, as well as to detect any obvious differences in differentiation potential.

3.2 Introduction

Isogenic models have been used extensively in disease research. Specific to HD, several isogenic iPSC and ESC lines have been developed, with the correction of pathogenic CAG-repeats to a non-pathogenic length, that evidenced rescue of disease-associated phenotypes; including altered mitochondrial bioenergetics, gene expression, DNA damage, neural rosette formation, neurogenesis, neuronal proliferation rates, and viability (An et al. 2012; Xu et al. 2017; Ruzo et al. 2018; Donaldson 2019a; Ooi et al. 2019b). Additionally, HTT knockout animal models have shown HTT function to be associated with, altered autophagy, lysosomal lumenal composition and degradation, structural and functional mitochondrial defects, and embryonic lethality (Ismailoglu et al. 2014; Ochaba et al. 2014; Ruzo et al. 2018). At the beginning of this project no model existed that combined HD patient-derived isogenic, disease, and knockout iPS cells, though a comparable hESC model had previously been developed which allowed for the identification of shared phenotypes specific to mutant HTT and HTT knockouts, including dysregulation in neural plate mitotic spindle orientation, multinucleated neurons and NPCs, impaired neural rosette spatial self-organization, and chromosomal instability (Ruzo et al. 2018). Thus, the absence of three-way phenotypic comparisons across isogenic mutant, wildtype, and knockout iPSCs, NPCs, and neurons, highlights the need for such an investigation, and one which could be used to interrogate phenotypes associated with the endolysosomal system.

Whilst medium spiny neurons are selectively vulnerable to degeneration in HD, recent studies have also highlighted neurodevelopmental phenotypes, that may be particularly associated with juvenile (high CAG repeat length) forms of the disease. In particular, phenotypes associated with proliferating and postmitotic cells (NPCs vs neurons) may differ. While it has been shown that the age profiles of differentiated neurons in culture remain representative of early development, neurons are fundamentally different from NPCs in that neurons are post-mitotic and as such are unable to dilute misfolded proteins and damaged organelles by division (Son et al. 2012; Stein et al. 2014; Paşca et al. 2015). As such, it is probable that lysosomal storage phenotypes might manifest more

prominently in neurons than in NPCs. Therefore, to compare phenotypes within a stage that more closely approximates those that are selectively vulnerable in HD and to establish that comparisons would be made across similar cellular populations in subsequent experiments, each line was characterized after terminal neuronal differentiation as well as at neural progenitor stages and in the undifferentiated iPSCs. To achieve this, it was first necessary to characterize the differentiation of each cell line at these stages.

Finally, because one objective of this thesis was to compare potential rescue of lysosome-storage phenotypes seen in HD by treatment with the LSD-approved drug miglustat, and because it has been well documented that treatment with inhibitors of glycosphingolipid biosynthesis can induce structural abnormalities in cultured rat neurons (Schwarz et al. 1995; Schwarz and Futerman 1997,1998; Bodennec et al. 2002; Kacher and Futerman 2006), it was necessary to assess whether miglustat treatment would elicit a conspicuous effect on the composition of the cellular populations which, if present, might confound the results of further experiments.

3.3 Aims

The primary aims of work in this chapter were:

1. To generate and validate HTT knockouts in HD109 and KOLF2 cell lines

2. To assess the pluripotency of knockout iPSCs, and to characterize the differentiation of each cell line along the neuronal pathway to derive NPCs and neurons.

3. To evaluate the effects of miglustat on neuronal culture.

3.4 Results

3.4.1 CRISPR-Cas9 mediated knockout of HTT in HD109 and KOLF2 cell lines

Deskgen software (www.deskgen.com) was used to design two distinct guide RNAs for targeting regions upstream and downstream of the CAG repeats, in *HTT* exon 1. Deskgen relies on experimental data input and cognitive machine learning algorithms, to optimize guide RNA selection based on increasing the intended effect of high targeting efficiency, while reducing unintended effects by selecting for low-probability of off-target events in both coding and non-coding regions of the genome (Hough et al. 2016). CRISPR-Cas9

endonuclease targeting to these sites was predicted to introduce two double-stranded cuts which, when repaired through non-homologous end joining, would result in a 200 bp excision and an out-of-frame reading sequence leading to a premature stop codon, which would then be subjected to nonsense-mediated decay (Figure 3.1).

iPSCs were electroporated with CRISPR-Cas9 ribonucleoprotein (RNP) complexes. The RNP complex incorporates a target-specific CRISPR RNA (crRNA), an Alt-R Cas9 endonuclease, and a transactivating crRNA (tracrRNA) that possesses an ATTO-550 fluorescent dye attached to the 5' end. The main advantage of this method is that the Cas9 activity is transient and acts to minimise potential off-target endonuclease activity (for example as seen using plasmid of viral delivery methods), in addition incorporation of the fluorescent marker into successfully transfected cells allows for subsequent isolation and enrichment by FACs sorting, thus reducing the time and material costs involved with colony screening. As such, the upper 10% of cells with the highest fluorescent signal intensity were selected for plating, totaling ~8,000 KOLF2 and ~12,000 HD109 positively labeled cells. From each of these, 96 colonies were picked and screened for successful gene editing.

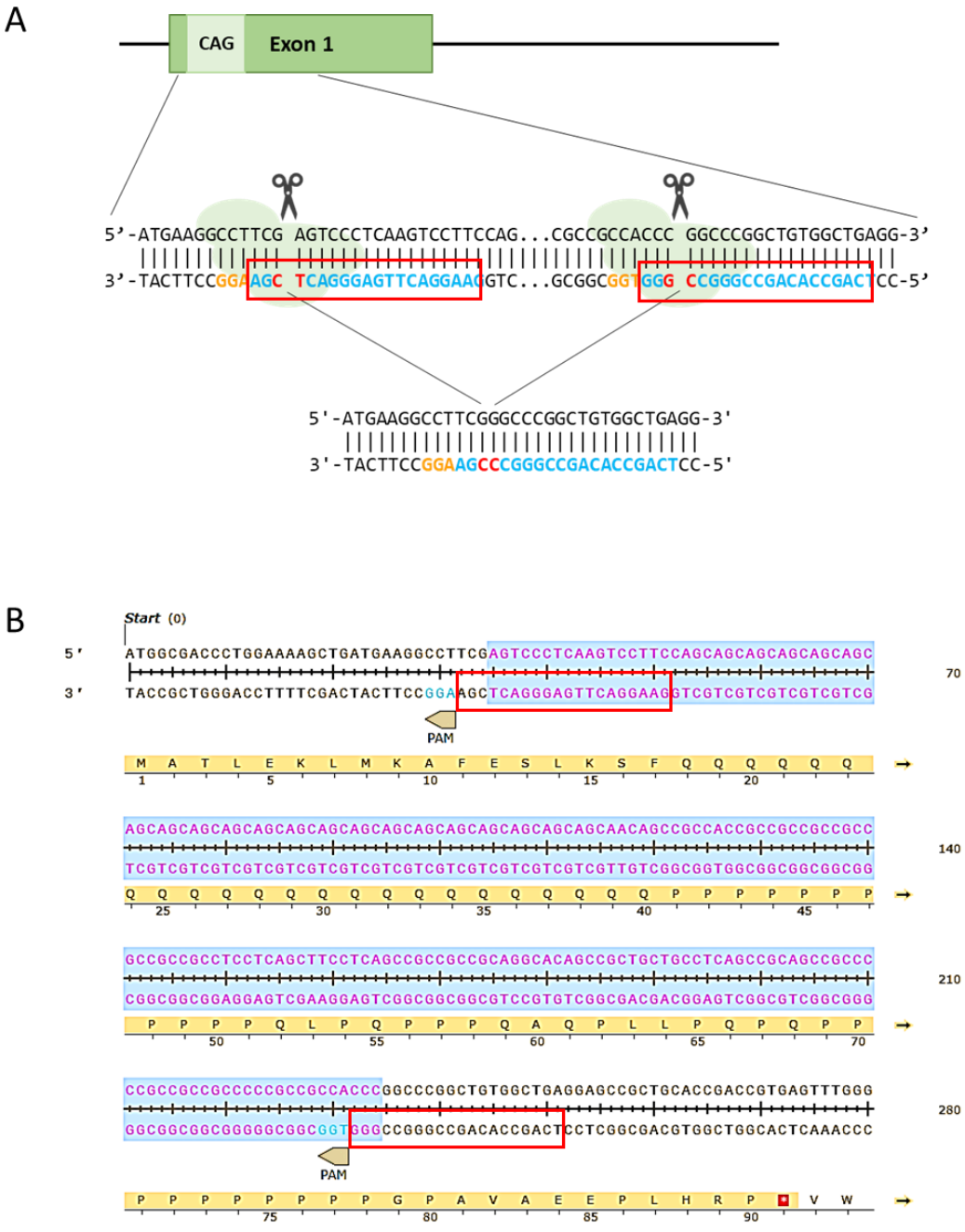

Figure 3.1. Schematic depicting the strategy for CRISPR-mediated knockout of HTT. A) Two guide RNAs (in red boxes) and PAMs (orange font, respectively) promote double strand cleavage between red nucleotides. Once cleaved, recombination via non-homologous end joining produces the product on the bottom, which leads to a premature stop codon and/or nonsense-mediated decay. B) HTT exon 1 nucleotide and amino acid sequences. Guide RNAs (in red boxes) and the highlighted region is targeted for deletion.

3.4.2 PCR screening of targeted clones

For each colony, genomic DNA was extracted and the region surrounding the predicted CRISPR cleavage sites in *HTT* exon 1 was amplified by PCR (Figure 3.2A) and visualized by agarose gel electrophoresis (Figure 3.2B). Candidate HTT knockout alleles were identified by the presence of a 284 bp band, while the untargeted HD109 gave bands of 480 bp and 751 bp corresponding to the wildtype and HD CAG-expanded alleles, respectively. Untargeted KOLF2 cells displayed a single band at 484 bp (Figure 3.2B). Heterozygous

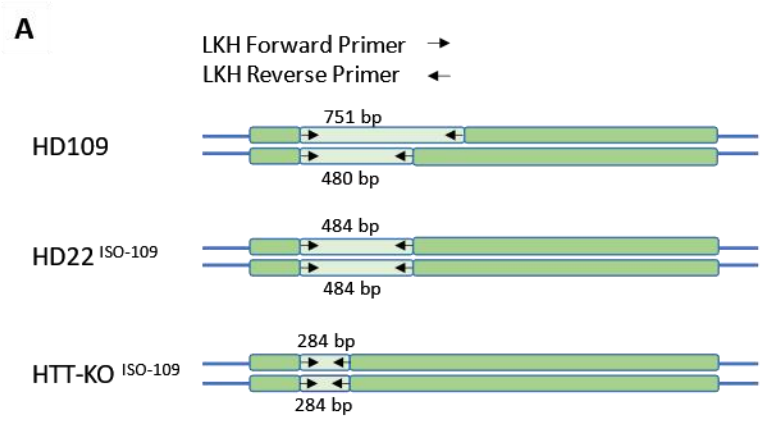

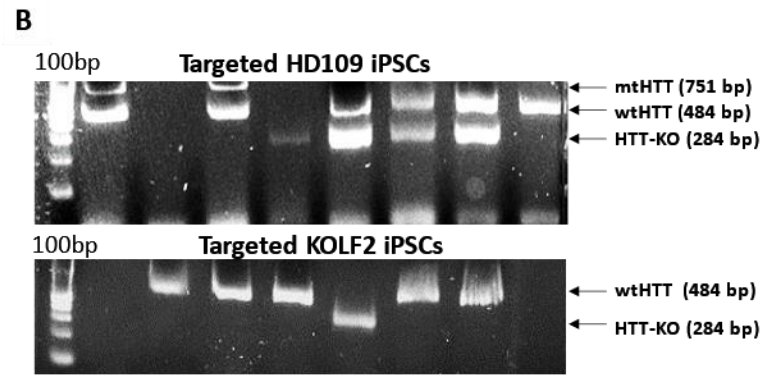

C

Cell Line	Homozygous candidate	Heterozygous wt/-	Heterozygous mt/-
HD109	6 (6.25%)	11 (11.45%)	8 (9.38%)
KOLF2	2 (2.08%)	6 (6.25%)	0

Figure 3.2. PCR screen for HTT knockout. A) Schematic of PCR screen to identify subclones with potential HTT knockout. B) PCR screen to identify colonies containing 200 bp deletions indicative of potential knockouts. C) Percent of screened clones displaying PCR products indicative of homozygous or heterozygous HTT deletion.

knockouts, leaving only one mutant or wildtype *HTT* were also identified, screened, and confirmed, though not further discussed here. The targeting efficiency of the HD109 cells was higher than that observed in the KOLF2 cell lines (Figure 3.2C), though the reasons for this were not explored. The screen identified 6 candidate homozygous and 11 candidate heterozygous knockout HD109 clones and identified 2 candidate homozygous and 6 candidate heterozygous knockout KOLF2 clones (Figure 3.2C).

3.4.3 HTT Knockout Validation

3.4.3.1 Sanger sequencing

To verify Cas9 cleavage and out-of-frame NHEJ at each *HTT* allele in the HD109 and KOLF2 cell lines, PCR products were cloned and sequenced (Figure 3.3). One double knockout from six HD109 candidates, and one double knockout from two KOLF2 candidates, were confirmed to be edited to give frameshift mutations in both alleles. The HD109 double knockout clone contained no detectable indels and resulted in the predicted sequence and premature stop codon (Figure 3.3). The KOLF2 double knockout clone contained single nucleotide insertions at both alleles, but still introducing a reading frameshift and premature stop codon (Figure 3.3). Thus, both HD109 and KOLF2 clones were predicted to undergo nonsense-mediated decay and abolished HTT production.

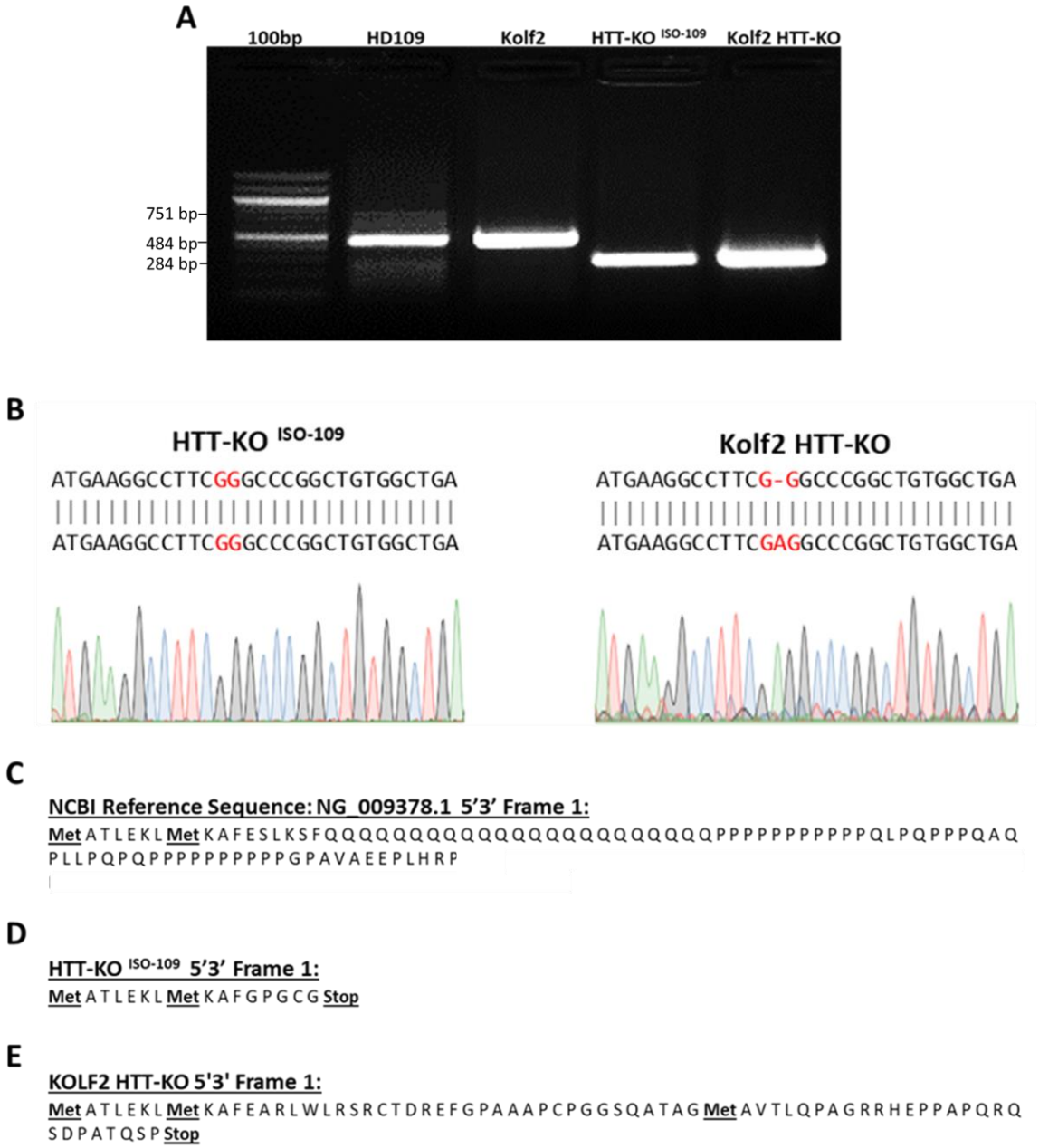

Figure 3.3. Knockout validation by Sanger sequencing. A) Candidate, homozygous HTT knockout subclones were PCR purified and processed for sequencing. B) Sequencing results for HD109 and Kolf2 HTT knockouts. Reference genome (top), resulting sequence (middle), call outs (bottom). C) Translated reference sequence shown to the end of exon 1. D) HD109 HTT knockout exhibiting no indels and an early stop codon, and E) KOLF2 HTT knockout amino acid sequence with a single nucleotide insertion and premature stop codon.

3.4.3.2 Immunocytochemistry

Next, to show presence or absence of HTT protein expression in the HD109, HD22 $^{ISO-109}$, HTT-KO $^{ISO-109}$, KOLF2 and KOLF2 $^{HTT-/-}$ iPSCs were stained with anti-huntingtin specific antibody D7F7 (Figures 3.4 - 3.6A). Cells displayed clear differences as the cytoplasmic and often punctate distribution of the HTT antibody can be seen in nontargeted iPSCs, while it is absent in their knockout counterparts. Thus, this data supports the claim that HTT has successfully been removed. To confirm the D7F7 specificity we also stained HAP1 and previously validated HTT knockout HAP1 $^{HTT-/-}$ cells (Figure 3.6B)

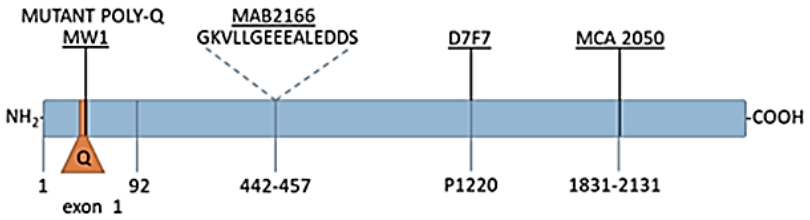

Figure 3.4. Diagram of huntingtin antibody-binding epitopes.

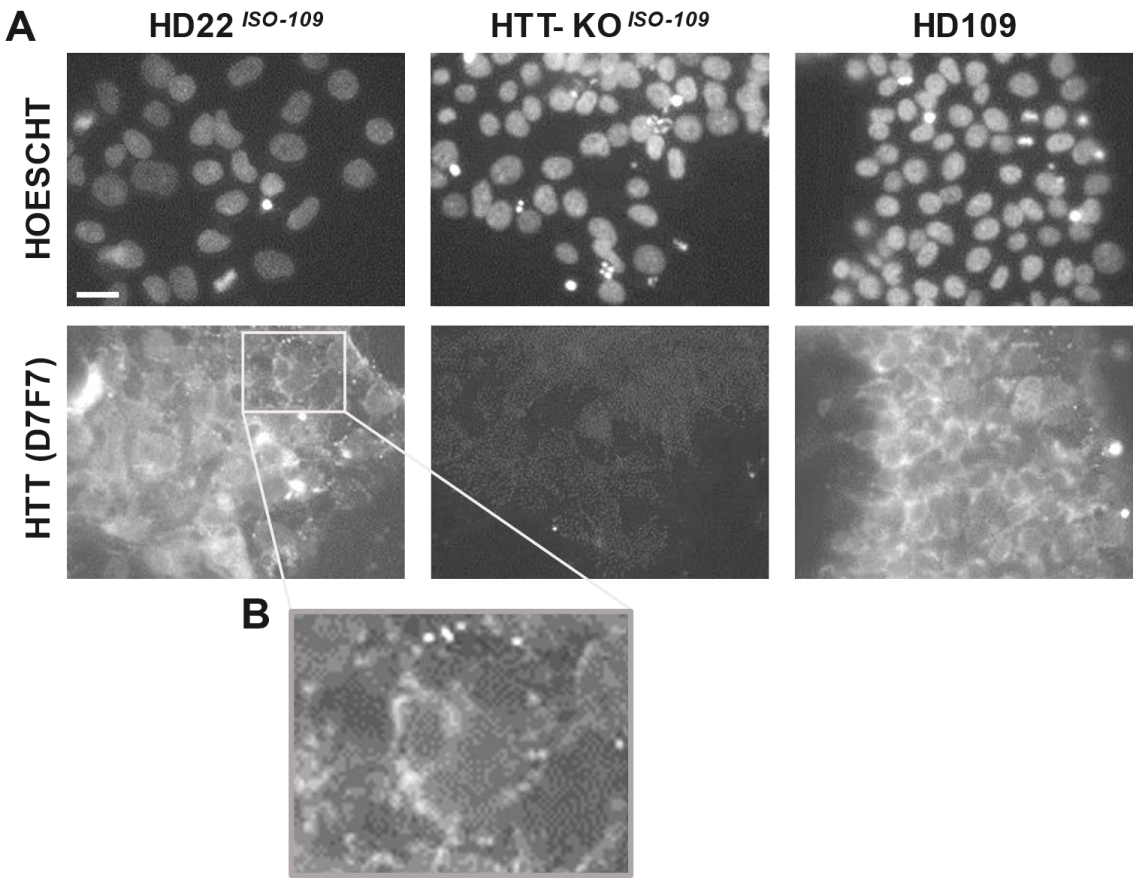

Figure 3.5. Knockout validation by antibody staining of HD109 cells. iPSCs were stained with anti-huntingtin (D7F7) rabbit monoclonal antibody and Hoescht. A) Both HD109 and isogenic HD22$^{ISO-109}$ iPS cell lines show positive staining, while the knockout shows none. B) Huntingtin protein displaying a punctate distribution. Brightfield images at 40x on the AX10 inverted microscope. Scale bar = 10 µm

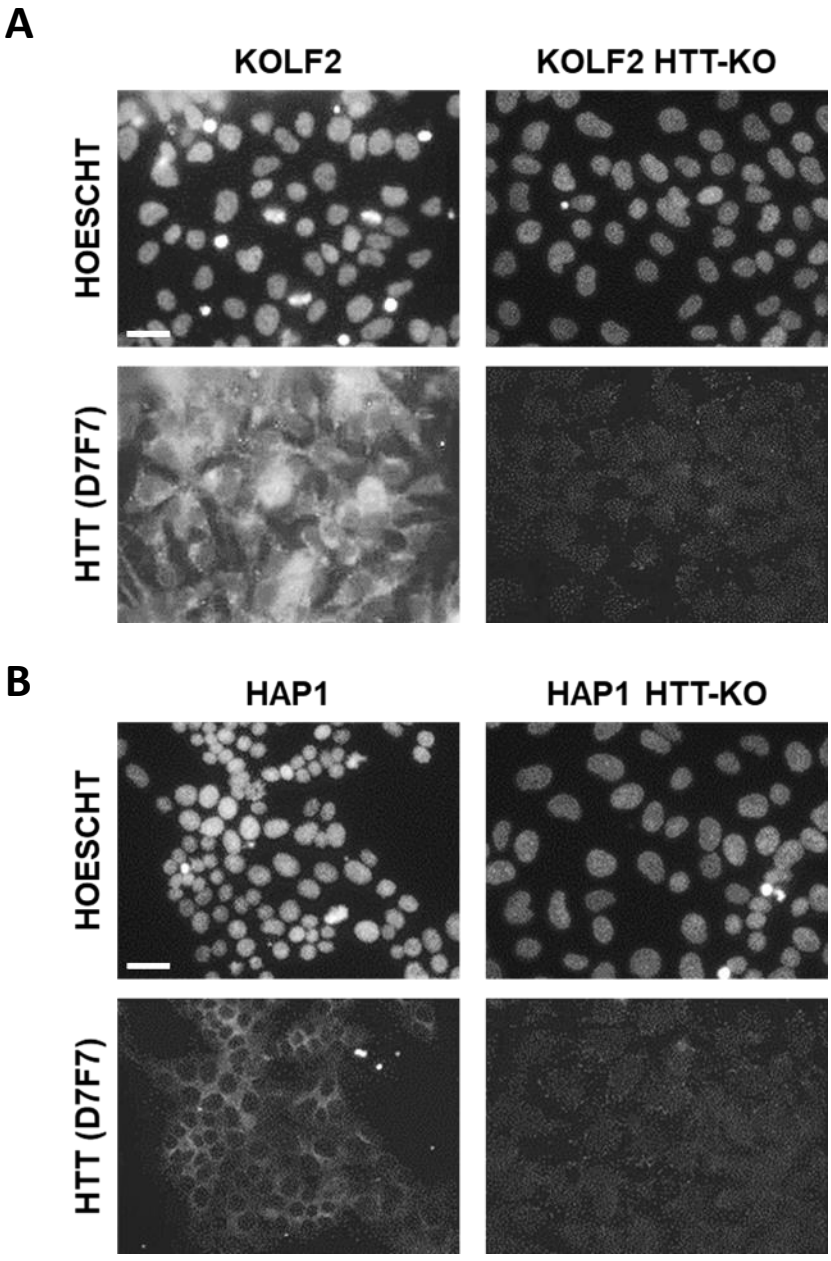

Figure 3.6. Knockout validation by antibody staining of KOLF2 and HAP1 cells. A) KOLF2 and B) HAP1 cells were stained with anti-huntingtin (D7F7) rabbit monoclonal antibody and Hoescht. Brightfield images at 40x on the AX10 inverted microscope. Scale bar = 10 µm.

3.4.3.3 Western blotting

Additionally, western blotting for all cell lines was carried out using the MW1 (Figure 3.8B), MCA2050 (Figure 3.8C) and MAB 2166 antibodies (Figure 3.8A). Presence of HTT in non-targeted cell lines, and absence in knockout cells was confirmed in the presence of the vinculin loading control. Thus, in conjunction with the sequencing and ICC data, the immunoblots provided sufficient evidence to show that HTT was not being produced in the knockout cells and could be utilized in future experiments.

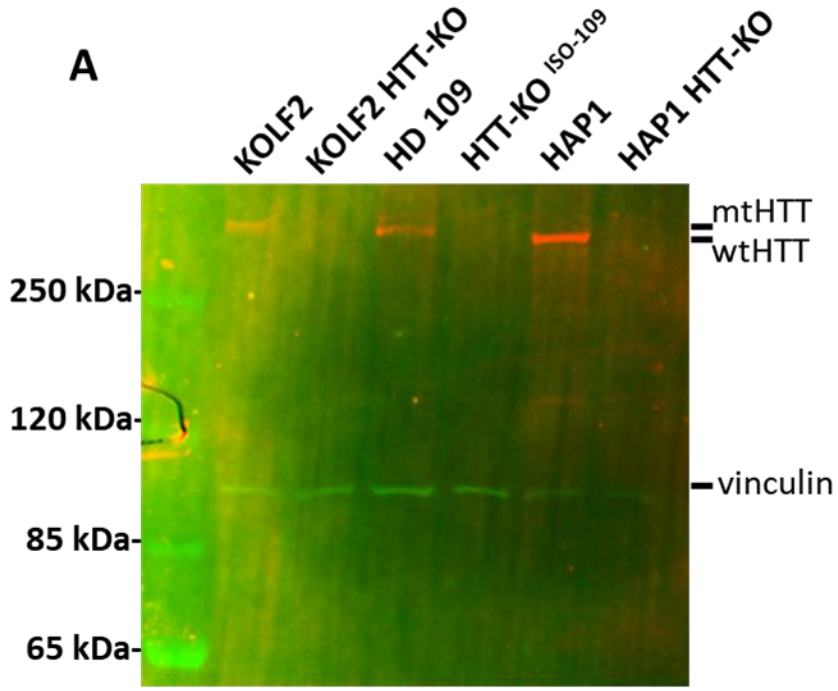

Figure 3.7. Western blotting to validate the knockout of huntingtin. A) Cell lysates were stained with poly-Q independent 2166 antibody. Cytoskeletal protein, vinculin, was used as a loading control.

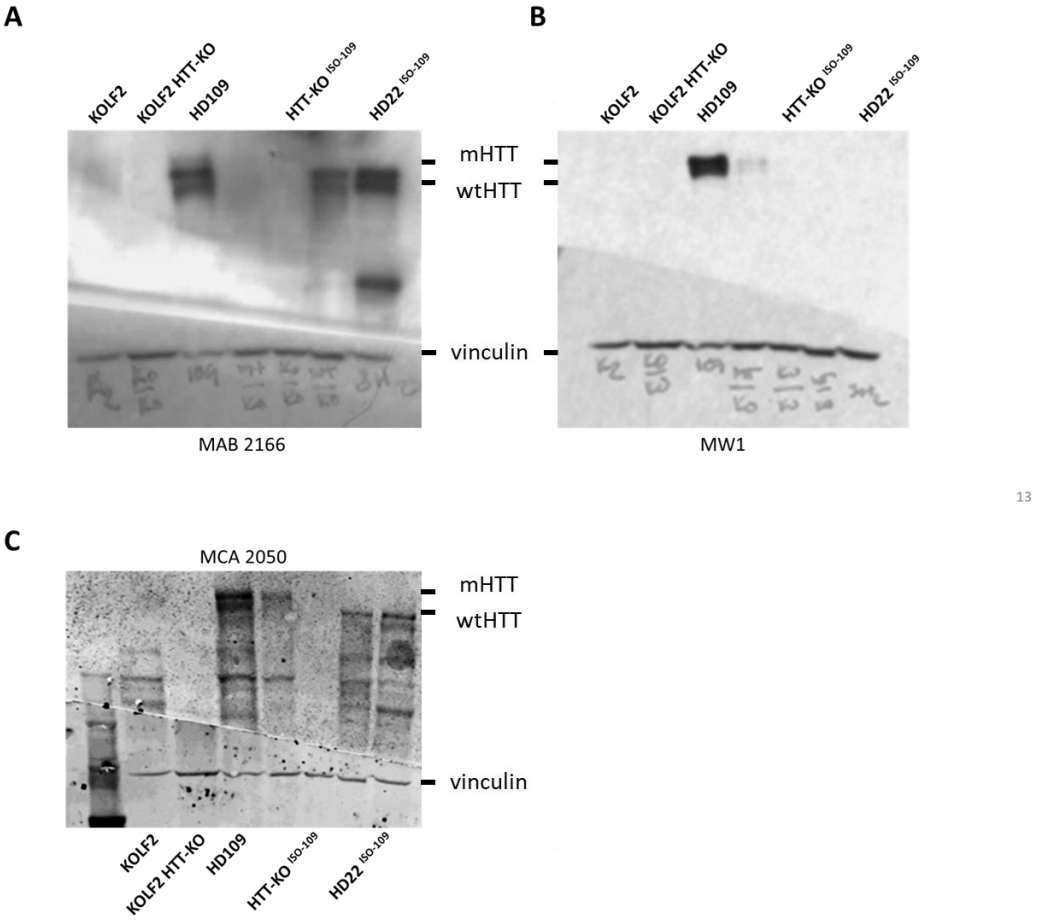

Figure 3.8. Additional western blots used to validate knockouts. A) MAB2166 antibody targets both mutant and wildtype HTT. B) MW1 antibody, exclusively targets the mutant allele. C) MCA2050 which binds to both mutant and wildtype HTT.

3.4.3.4 Evaluating potential CRISPR/Cas9 off-target effects

Next, to a practical extent, it was necessary to verify that genome modification through the application of CRISPR-Cas9, did not result in non-specific cleavage and alteration of genes that might impact the function of the endolysosomal system and influence subsequent phenotypic assays. Our approach was first to exclude all genomic regions that exhibited low sequence similarity in our evaluations, as evidence indicates minimal impact on the whole-genome mutational load in human iPSCs due to CRISPR gene editing (Suzuki et al. 2014). However, despite the optimized targeting fidelity of the Alt-R CRISPR-Cas9 tracrRNA - ATTO™

550 ribonuclear protein-based system and while potential for off-target insertions or deletions are unlikely, they are still possible especially in regions of high sequence similarity, and thus these regions were the targeted for inspection (Fu et al. 2014; Vakulskas et al. 2018).

To identify similar sequences, deskgen software which processes queries through an off-target scoring system based on work done by Hsu *et al.* (2013) was employed. The queries for both guide RNA sequences used here, returned a total of six coding genes that contained regions with high sequence similarity to the guide RNAs, as well as weighted PAM nucleotide composition and proximity to the homologous region, to suggest that these regions might be prone to off-target effects (Figure 3.8A).

For each of the six candidate genes, the Gene Ontology annotation modules within the Uniprot database (https://www.uniprot.org/) were reviewed in order to ascertain whether any might impact the endolysosomal system and give rise to potential lysosomal storage phenotypes, if altered. Of the six candidate genes, the potential disruption of the StAR-related lipid transfer protein 8 gene (*STARD8*), was of concern because of its involvement with lipid binding (Figure 3.8B). Genomic integrity at the STARD8 locus was therefore confirmed by PCR and sequencing of a 667 bp region inclusive of the potential off-target site, in exons 10 and 11 of the *STARD8* gene (Figures 3.8C and 3.8D). The resultant chromatograms showed no evidence of insertions or deletions in the region. Therefore, because there were no obvious alterations due to Cas9 off-target cleavage, it was determined that quality control in this regard, was sufficiently completed and that further model validation steps could be undertaken.

A

Sequence	PAM	Similarity	Mismatch	Gene Name	Locus
GGTGGACTTGAGGGACTCGG	TGG	1	2,3,20	ARHGAP4	chrX@ 153913483-153913506
GAAGGACTGCAGGTACTCGA	AGG	0	9,10,14	FGR	chr1@ 27612970-27612993
TGATCCACAGCCGGGCCGAG	CAG	1	2,4,19	SIPA1L2	chr1@ 232439250-232439273
TCAGCCACAGCCAGGCCGTG	GAG	1	13,19	PDZD7	chr10@ 101021836-101021859
TCAGCCAGGGCTGGGCCGGG	AGG	1	8,9,12	STARD8	chrX@ 68722478-68722501
TCAGCCACGGCCAGGCAGGG	GGG	0	9,13,7	SPOCD1	chr1@ 31800557-31800580
TCAGCCACAGGCAGGCCAGG	TGG	0	11,13,18	BUB1-PAK6	chr15@ 40266342-40266365
TCAGCCACAGCCTGGCCCTG	TGG	0	13,18,19	ABCC10	chr6@ 43432317-43432340

B

Gene	GO Molecular Function	GO Biological Processes
ARHGAP4	https://www.ebi.ac.uk/QuickGO/annotations?geneProductId=P98171	https://www.ebi.ac.uk/QuickGO/annotations?geneProductId=P98171
FGR	https://www.ebi.ac.uk/QuickGO/annotations?geneProductId=P09769	https://www.ebi.ac.uk/QuickGO/annotations?geneProductId=P09769
SIPA1L2	https://www.ebi.ac.uk/QuickGO/annotations?geneProductId=Q9P2F8	https://www.ebi.ac.uk/QuickGO/annotations?geneProductId=Q9P2F8
PDZD7	https://www.ebi.ac.uk/QuickGO/annotations?geneProductId=Q9H5P4	https://www.ebi.ac.uk/QuickGO/annotations?geneProductId=Q9H5P4
STARD8	https://www.ebi.ac.uk/QuickGO/annotations?geneProductId=Q92502	https://www.ebi.ac.uk/QuickGO/annotations?geneProductId=Q92502
SPOCD1	N/A	https://www.ebi.ac.uk/QuickGO/annotations?geneProductId=Q6ZMY3
BUB1-PAK6	N/A	https://www.ebi.ac.uk/QuickGO/annotations?geneProductId=H3BTB9
ABCC10	https://www.ebi.ac.uk/QuickGO/annotations?geneProductId=Q5T3U5	https://www.ebi.ac.uk/QuickGO/annotations?geneProductId=Q5T3U5

C

Gene Product	Symbol	Qualifier	GO Term
UniProtKB:Q92502	STARD8	involved_in	GO:0050790 regulation of catalytic activity
UniProtKB:Q92502	STARD8	involved_in	GO:0050790 regulation of catalytic activity
UniProtKB:Q92502	STARD8	involved_in	GO:0035023 regulation of Rho protein signal transduction
UniProtKB:Q92502	STARD8	enables	GO:0005096 GTPase activator activity
UniProtKB:Q92502	STARD8	involved_in	GO:0030036 actin cytoskeleton organization
UniProtKB:Q92502	STARD8	involved_in	GO:0007165 signal transduction
UniProtKB:Q92502	STARD8	enables	GO:0008289 lipid binding

D

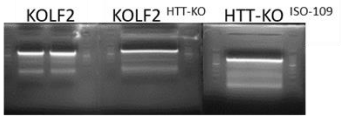

E

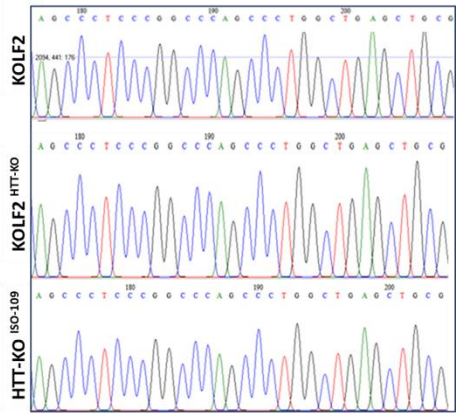

Figure 3.9. Quality control check for off-target CRISPR activity. A) Query into potential CRISPR off-target binding sites from DESKGEN (www.deskgen.com), results in six coding genes with low probability for unintentional targeting. B) Gene ontology URLs for genes susceptible for off-target Cas9 cleavage. C) GO annotations for STARD8 (https://www.ebi.ac.uk/QuickGO/annotations?geneProductId=Q92502). D) PCR to amplify *STARD8* locus for sequencing to detect indels. E) Sequencing results showing no insertions or deletions in either HTT-KO $^{ISO-109}$ or KOLF2 $^{HTT-KO}$ cell lines.

3.4.4 Cell type characterization

An extensive characterization of the pluripotency and potential for neuronal differentiation in HD109 and HD22 $^{ISO-109}$ cells, was carried out previously by Jasmine Donaldson (2019a). To add to this, the pluripotency and neurogenic potential in the HTT-KO $^{ISO-109}$ and KOLF2 $^{HTT-KO}$ as well as in the HD109, HD22 $^{ISO-109}$, and KOLF2 cells, was assessed to confirm that the models, used henceforth, provided a similar cellular background which could be used to investigate lysosomal storage phenotypes. Finally, the effects of miglustat on differentiation of HD109 and HD22 $^{ISO-109}$ cells was tested, to determine whether the drug itself might fundamentally alter the cellular composition of the cultures.

3.4.4.1 Pluripotency markers

Pluripotency was assessed by antibody staining against core pluripotency markers, OCT4 and NANOG, and cell surface antigens SSEA4, TRA 1-60, and TRA 1-80, all of which are routinely used to identify iPSCs. All iPS cell lines tested positive for each of these antibodies (Figure 3.10).

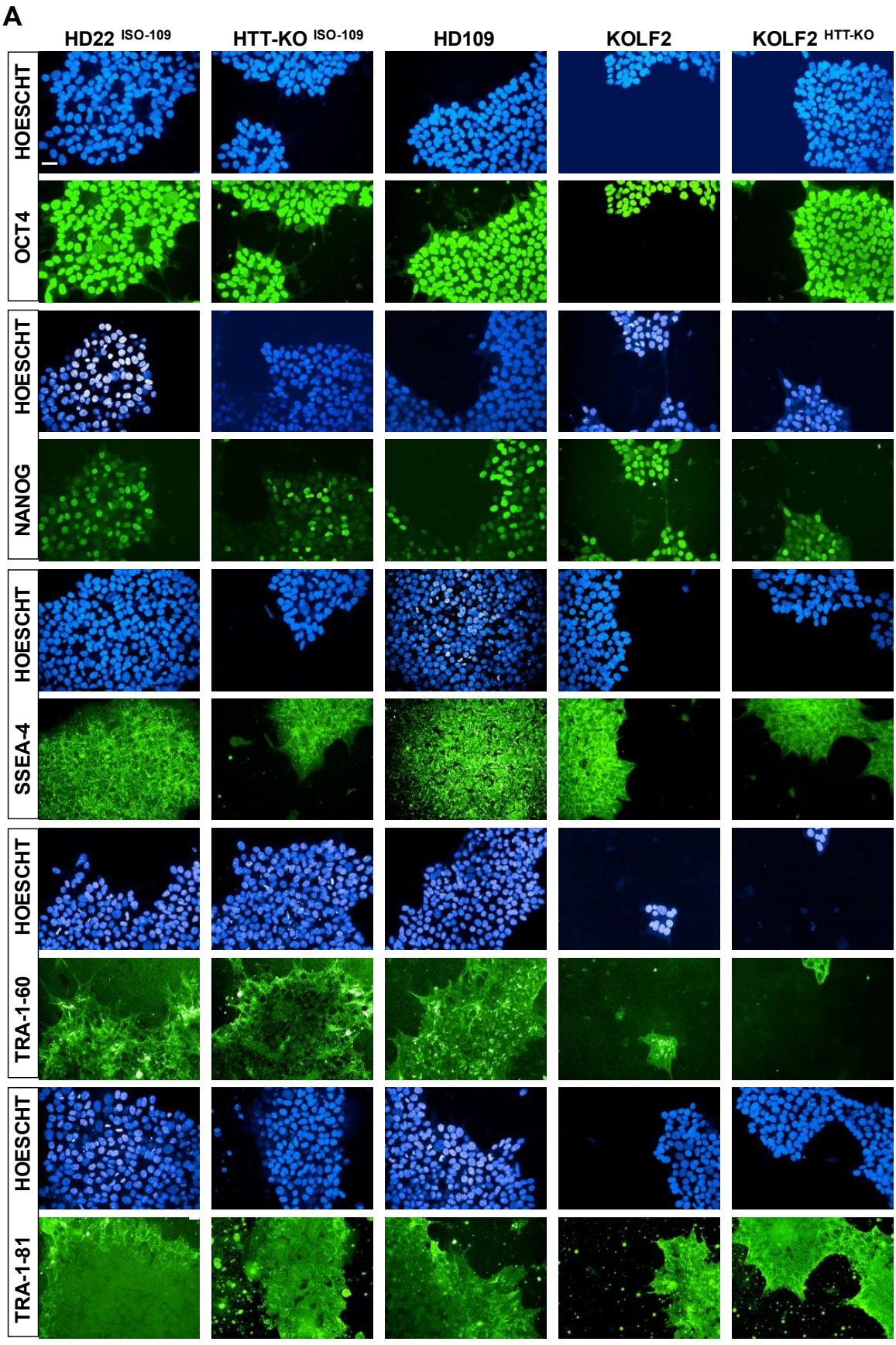

Figure 3.10. Immunofluorescence microscopy images of iPSC colonies stained with pluripotency markers OCT4, NANOG, SSEA4, TRA-1-60, and TRA-1-81. A) Images taken on the Opera Phenix using a 40x water-immersion. Scale bar = 10 µm.

3.4.4.2 Characterization through neuronal differentiation

The potential for HTT knockout cells to differentiate into neural progenitor cells and neurons was assessed. It was reasoned that the progression through neuronal differentiation was important to monitor, not only because these models would be applied towards phenotype screens later in this thesis, but also because it was possible that mechanisms that underlying embryonic death and neurodevelopmental defects associated with HTT null animal models *in vivo* might elicit a related effect during the differentiation process (Duyao et al. 1995; Nasir et al. 1995a; Zeitlin et al. 1995; Lo Sardo et al. 2012; Ruzo et al. 2018). To determine whether this was the case, we observed and compared the percentages of cells expressing of NPC markers in HTT knockouts with wildtype cells after 16 days of directed differentiation from iPSCs to NPCs as well as in terminally differentiated neurons.

3.4.4.3 Neural progenitor markers

iPSC neural differentiation was carried out by applying an optimized version of the classic dual-SMAD inhibition protocol with additional WNT pathway inhibition to direct forebrain neural progenitor commitment (Chambers et al. 2009; Telezhkin et al. 2016; Smith-Geater et al. 2020). Cells were cultured for eight days in SLI medium containing SB431542 a small molecule inhibitor of TGFβ-activin receptor ALK4/5/7 phosphorylation, as well as LDN 193189, a BMP pathway inhibitor of ALK1, ALK2/3/6 receptors, and IWR1 a tankyrase and WNT pathway inhibitor. From day 8 through day 16, cells were cultured in LIA medium in which SB431542 was removed and replaced with Activin-A, a SMAD2 activator and promoter of lateral ganglionic eminence fate specification, while LDN 193189, and IWR1 were retained.

On day 16, the percentage of cells that expressed nestin, an intermediate filament protein specific to neuroepithelial stem cells, as well as SOX2 a core pluripotency factor critical for neural differentiation, which is upregulated in and is a marker for, proliferating neural progenitors were calculated (Lendahl et al. 1990; Graham et al. 2003; Zhang and Cui 2014). The HD and KOLF2 lines exhibited high percentages of nestin and SOX2 positive cells, for which neither HD nor HTT knockouts differed significantly from controls (Figures 3.11 and

3.12). We also compared the expression of CTIP2, a transcription factor and critical regulator of MSN differentiation, striatal achitecture, and patch development, that is upregulated in response to Activin (Arlotta et al. 2008; Arber et al. 2015). CTIP2 was expressed similarly in HD22 $^{ISO-109}$, HD109, and HTT-KO $^{ISO-109}$, as well as in KOLF2 and KOLF2 $^{HTT-KO}$ cells (Figures 3.13 and 3.14). Statistical comparisons indicated that the percent of NPCs expressing CTIP2 in KOLF2 wildtype and knockouts were not different across three independent differentiations. However, only one differentiation was carried out for the HD patient-derived lines, and though there were no obvious differences across the three wells sampled, no statistical analyses were performed.

In summary, no differences in the cell populations were observed, and it was concluded that for the purpose of subsequent lysosomal phenotyping experiments in NPCs, that these results provided enough evidence to move forward under the assumption that comparisons would be made using similar NPC populations across our cell lines.

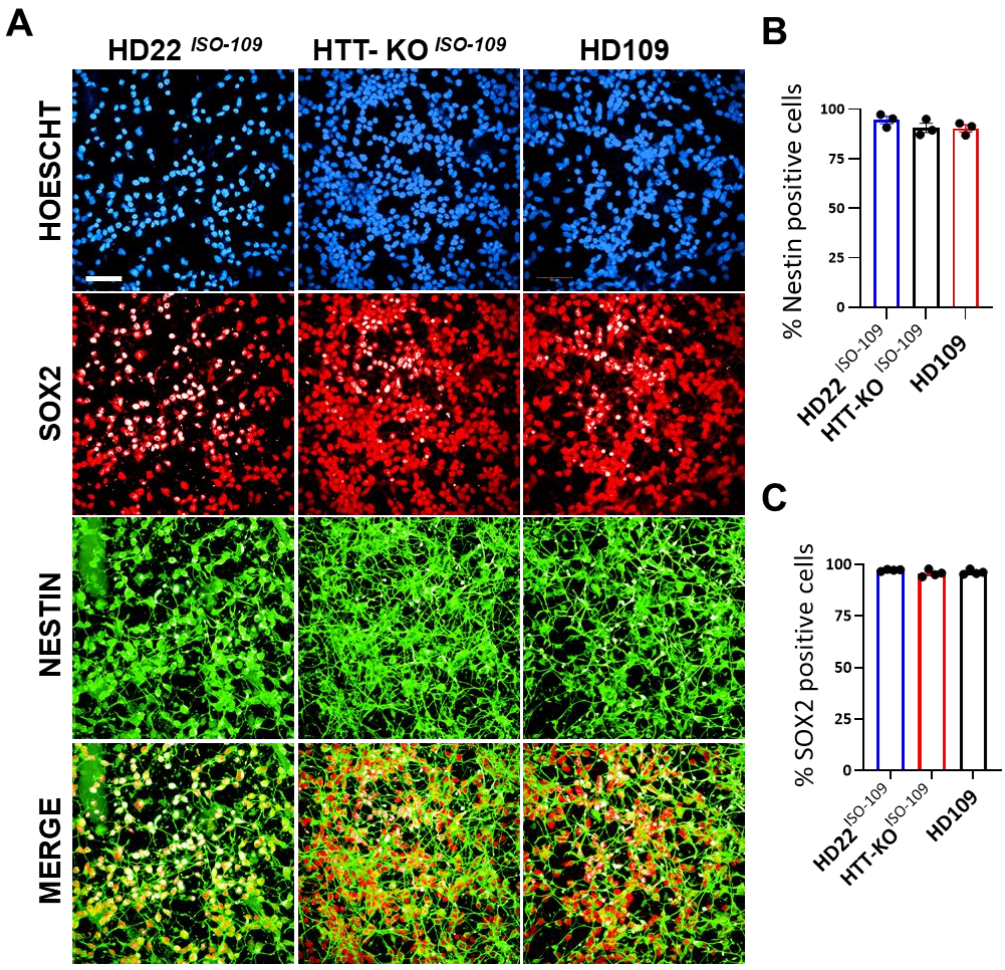

Figure 3.11. Day 16 NPCs, HD patient-derived cells lines express neural progenitor markers. A) Knockout cells differentiate into nestin and SOX2 positive NPCs. Images taken at 40x on the Opera Phenix. B) 94.42% of HD22 $^{ISO-109}$, 90.29% of HTT-KO $^{ISO-109}$, and 90.52% of HD109 cells expressed nestin and were not significantly different (One-way ANOVA; Tukey's multiple comparisons test; N = 3 differentiations, n = 3 technical replicates). C) 97.25% of HD22 $^{ISO-109}$, 95.65% HTT-KO $^{ISO-109}$, and 96.21% of HD109 cells expressed SOX2 and did not significantly differ (One-way ANOVA; Tukey's multiple comparisons test; N = 4 differentiations, n = 3 technical replicates). Data are presented as mean ± SEM for each cell line with the means for individual differentiations indicated by black circles. Scale bar = 50 µm.

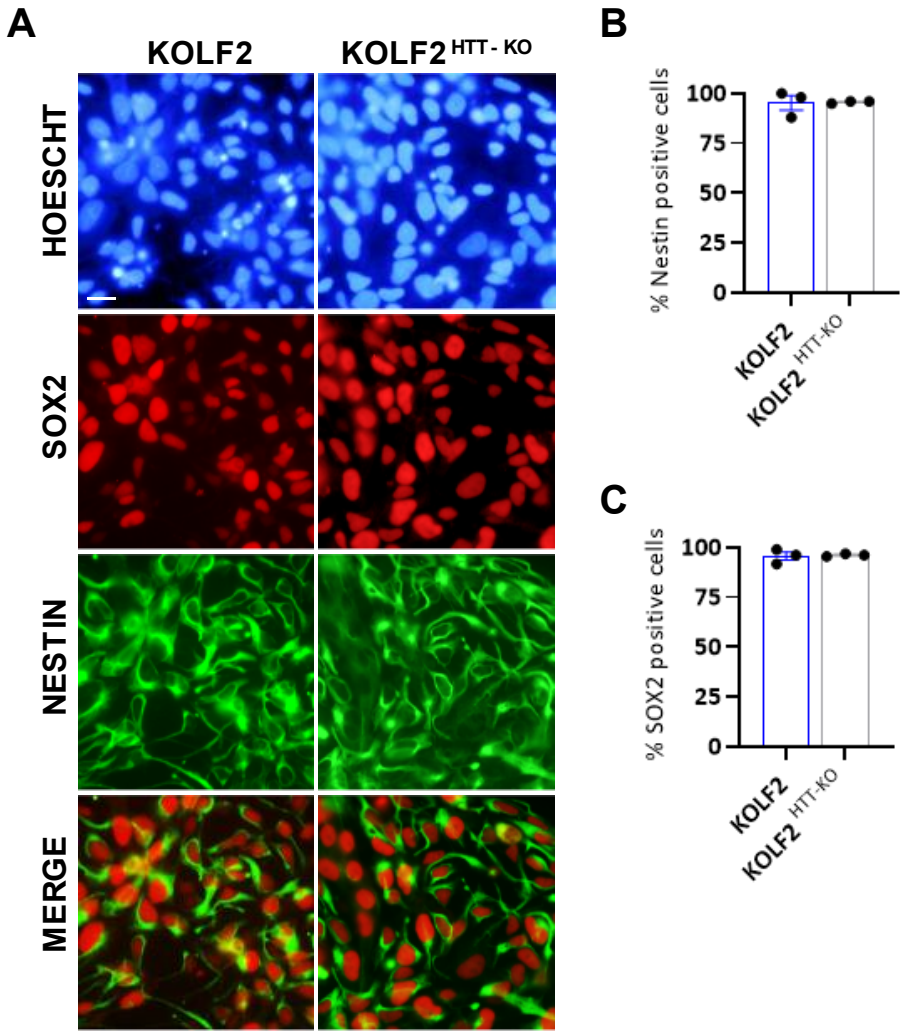

Figure 3.12. Day 16 NPCs, KOLF2 and KOLF2 knockout express NPC markers. A) Knockout cells differentiate into nestin and SOX2 positive NPCs. Images taken at 63x on the Opera Phenix. B) An average of 95.33% of KOLF2 and 95.75% KOLF2 $^{HTT\text{-}KO}$ cells expressed nestin and were not significantly different (Mann-Whitney; p = 0.6; N = 3 differentiations, n = 3 technical replicates). C) An average of 95.66% of KOLF2 and 96.19% of KOLF2 $^{HTT\text{-}KO}$ cells expressed SOX2 and were not significantly different (Unpaired t-test; p = 0.8206; N = 3 differentiations, n = 3 technical replicates). Data are presented as mean ± SEM for each cell line with the means for individual differentiations indicated by black circles. Scale bar = 10 µm.

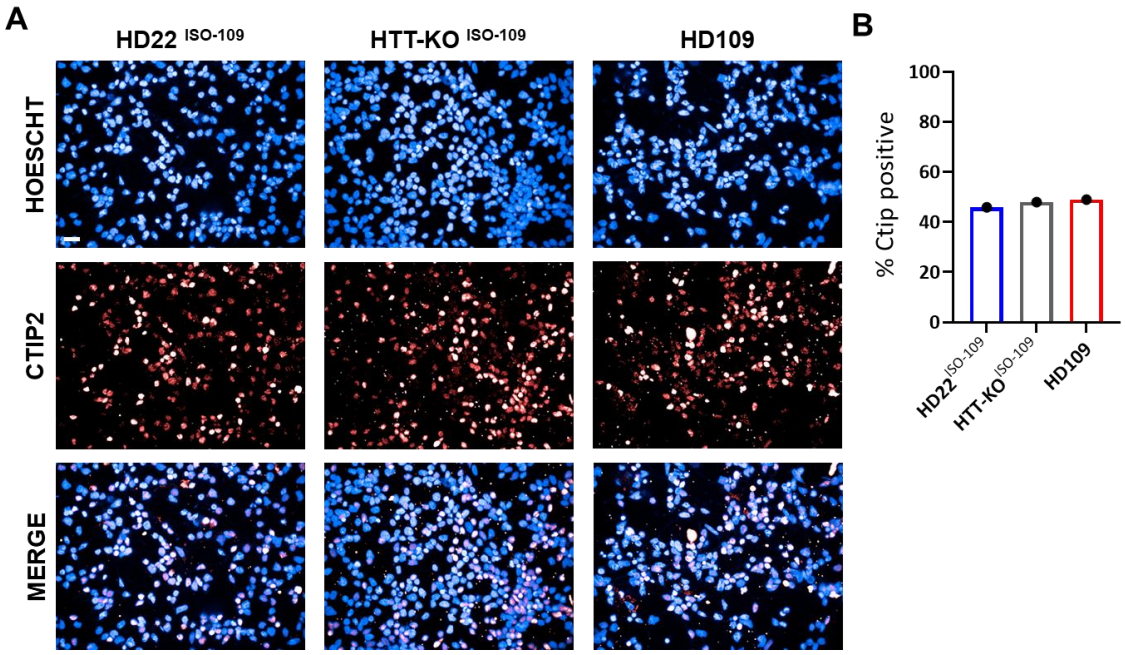

Figure 3.13. Day 16 HD and knockout NPCs express CTIP2. A) Panel with CTIP2 and Hoescht staining taken on the Opera Phenix at 40x. B) CTIP2 expression averaged 45.90% in HD22 $^{ISO-109}$, 47.94% in HTT-KO $^{ISO-109}$, and 48.98 in HD109 (N = 1 differentiation, n = 3 technical replicates). Data presented as mean of the three wells that were sampled. Scale bar = 10 µm.

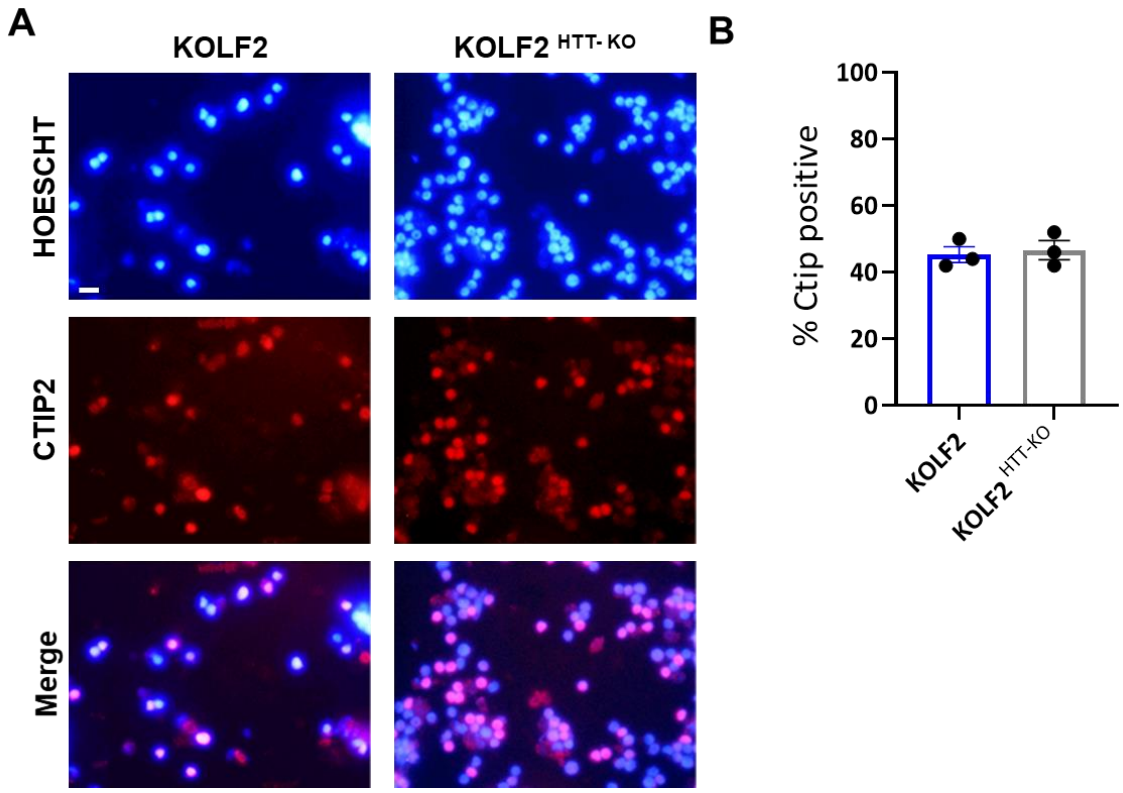

Figure 3.14. Day 16 knockout NPCs express CTIP2. A) Cells stained with CTIP2 and Hoescht imaged on the Zeiss AX10 inverted microscope at 40x oil-immersion. B) CTIP2 expression averaged 46.67% in KOLF2 and 45.33% KOLF2 $^{HTT\text{-}KO}$ and were not significantly different (unpaired t-test; p = 0.7415; N = 3 differentiations, n = 3 technical replicates). Data presented as mean +/- SEM. Scale bar = 10 µm.

3.4.4.4 Neuronal markers

Neuronal differentiation of each cell line was next evaluated by immunostaining with the pan-neuronal marker MAP2. Terminal differentiation was promoted using the protocol of (Telezhkin et al. 2016) and cultures compare with and without the addition of 50 µM miglustat for the final 8 days of differentiation. Nearly every cell in both untreated and miglustat-treated cultures were positively stained for MAP2 (Figure 3.15). Though no statistical analyses were performed, this data is consistent with previous work which evidenced no difference, due to mutant HTT or HTT knockout, in the abundance of MAP2 positive cells differentiated from iPSCs or hESCs into neurons (Ruzo et al. 2018; Donaldson 2019a). Moreover, MAP2 positive neuronal abundance was not altered by miglustat treatment. Thus, we concluded that for later experiments these cells were fundamentally neuronal, though subtype specificity could not be concluded from this experiment.

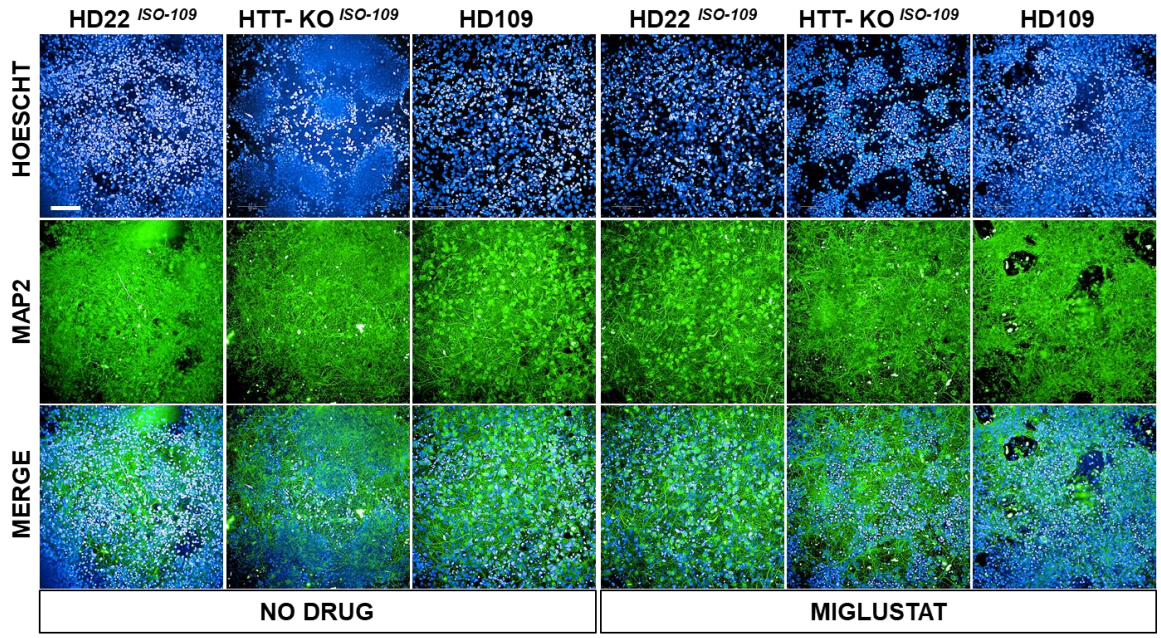

Figure 3.15. Immunofluorescent images of day 54 neurons cells expressing MAP2. A) Day 54 neurons treated with 50 µM miglustat for 8 days (right) and untreated cells (left). Cells were imaged on the Opera Phenix at 20x magnification; scale bar = 100 µm.

To ascertain the capacity for neuronal differentiation towards an MSN-like fate, we stained cultures for co-localization of the striatal markers CTIP2 and DARPP32 (Figure 3.16A). Importantly, neurons coexpressing CTIP2 and DARPP32 were seen in all cultures regardless of the status of huntingtin, or miglustat, thus further validating these models. The percentage of cells that expressed CTIP2 above a shared threshold, did not differ between HD or isogenic cells in response to miglustat treatment (Figure 3.16B). These results are consistent with previously recorded measurements of HD109 and HD22 $^{ISO-109}$ which showed an increase in relative gene expression of DARPP32 and CTIP2 using the same protocol (Donaldson 2019a).

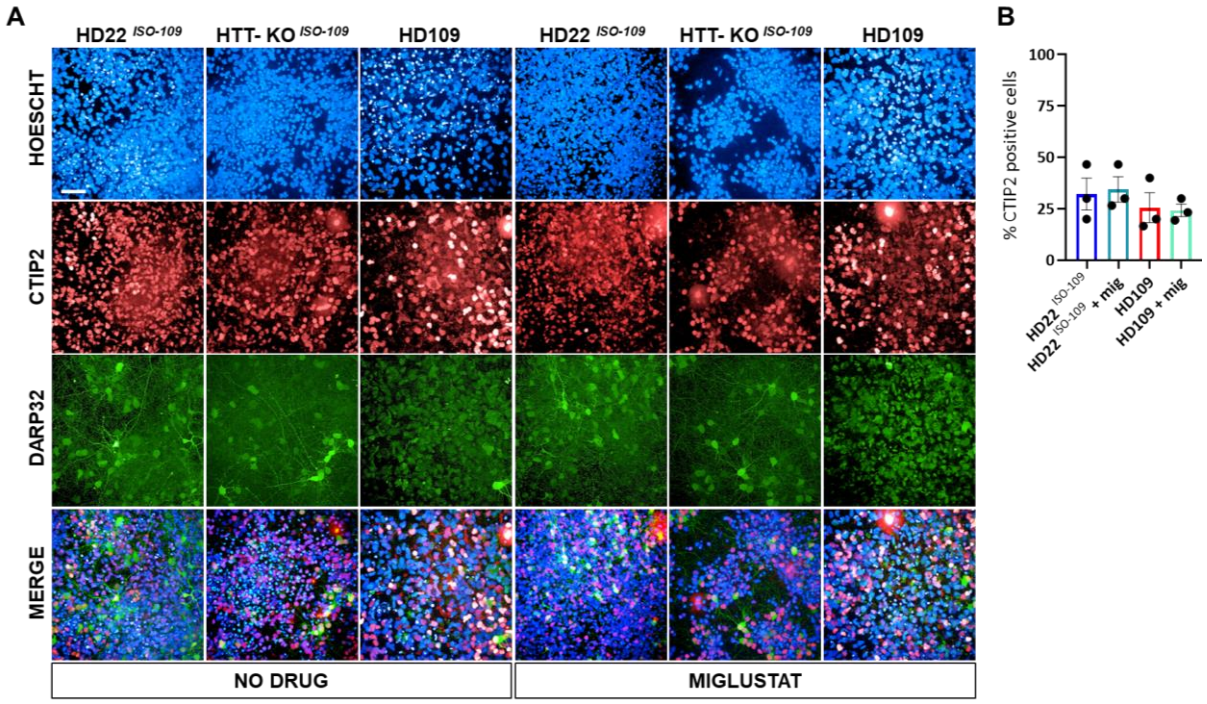

Figure 3.16. Immunofluorescence images of day 54 neurons cells stained with CTIP2 and DARPP32. A) Day 54 neurons treated with 50 µM miglustat for 8 days (right) and untreated cells (left). Cells were imaged on the Opera Phenix at 40x magnification; scale bar = 50 µm. B) Without miglustat cells expressing averaged 42.86% in HD22$^{ISO-109}$ and 38.17% in HD109; with 8 days of 50 µM miglustat, CTIP2 expression averaged 43.95% in HD22 $^{ISO-109}$ and 36.41% in HD109 and were not significantly different (one-way ANOVA with Tukey's post hoc multiple comparisons test; N = 3 differentiations, n = 3 technical replicates). Data presented as mean +/- SEM.

3.4.5 Discussion

In this chapter, to complement a previously generated isogenic mHTT-corrected HD iPSCs established by Donaldson (2019a), is a description of HTT knockout iPSCs to be used to assess and compare HD-related loss-of-function phenotypes within an isogenic background. There is a description of the generation and validation of two huntingtin knockout cell lines, one derived from an HD patient and the other from an established and well characterized KOLF2 cell line. A computational approach to identify genes that were susceptible to CRISPR-Cas9 off-target cleavage, revealed *STARD8* as a possible candidate, and further investigation confirmed the integrity of the locus in question, in both knockout lines. All cell lines displayed appropriate cell identity markers at the iPSC, NPC, and neuronal stages and discrepancies in the composition of the cell populations were not observed. Thus, though this was not a comprehensive evaluation, for the purpose of this thesis, our findings indicate that the cell lines are able to comparably differentiate into the neuronal subtypes used for phenotypic comparisons in subsequent chapters.

In the last decade genome editing techniques have been greatly improved with the development and subsequent optimization of the CRISPR-Cas9 system, which has exceeded other nuclease-based gene editing systems, such as zinc-finger nucleases (ZFNs) and transcription activator-like effector nucleases (TALENs), in terms of simplicity of design, versatility, and application (Chira et al. 2017). Applying this editing technique to iPSCs has proven beneficial to the field of disease modelling in that it has permitted researchers to discern abnormal phenotypes resulting from a specific causative mutation without the confounding effects that might arise due to comparisons made using cells with different genetic backgrounds (Ben Jehuda et al. 2018). However, while primary patient-derived disease-affected cells are considered the 'gold standard' for disease modelling, these materials are often difficult to obtain, and are variable in terms of scalability (Elitt et al. 2018). Thus, the self-renewal property of iPSCs provides a means to overcome this hurdle, while the pluripotent potential of iPSCs permits differentiation towards the disease-affected cell type, further enhancing the ability to understand and model disease.

The editing efficiency of the HD109 cells were comparable to reports using the same reagents and FACS enrichment technique in HEK-293 and Jurkat cells, though the KOLF2 cell line fell below (Schubert et al. 2017). An explanation for the variability and shortcoming with regards to editing efficiency in the KOLF2 line was not pursued but might be explained by differences in technical or biological conditions. It is likely that in our reported efficiency is an underestimate, because there were likely several more successfully targeted clones that went undetected, as our primary PCR screen was oriented towards identification of large 200 bp deletions, though Cas9 cleavage is often followed by small insertions or deletions, which could have similarly disrupted translation. Due to time constraints, further screening was not pursued, though the original stock obtained from the FACS enrichment step was retained and stored for future studies.

The classic method for understanding the function of a protein is to observe the effects on the model system when that protein is removed. The model system reported here, not only allows for three-way comparisons of HD related phenotypes and thus the ability to interpret observations in terms of HTT loss, but critically, it differs from *in vivo* models in that while HTT null mice die during embryogenesis, HTT knockout stem cells remain viable through terminal neuronal differentiation (Ismailoglu et al. 2014; Ruzo et al. 2018). Thus, this model allows for closer inspection of HTT protein function that parallels an early neurodevelopmental time window, which has not been possible *in vivo*.

From the initial screen, two KOLF2 and six HD109 candidates for homozygous deletion of HTT were identified. However, after the Sanger sequencing step, most of the candidates were eliminated, as chromatograms evidenced in-frame repair of either one or both alleles, which would result in a deletion surrounding and including the CAG trinucleotide repeat region, but would leave the majority of the remaining HTT protein to be translated. These lines, along with several confirmed heterozygous mutant and wildtype HTT knockouts, identified from the initial pool, provide a potentially interesting set of resources for future experiments into CAG-specific deletion, or heterozygous HTT-related phenotypes, but that was not an emphasis in this study, and therefore was not pursued.

While at the genetic level it was clear that HTT should not be expressed in our knockouts, leaky expression at the protein level, caused by translation re-initiation or skipping of the edited exon, is not an uncommon phenomenon and has been shown to occur in roughly one-third of quantified haplozygous HAP1 cells, which were also used in this thesis (Smits et al. 2019). Moreover, stop codon readthrough has been shown to occur in the presence of aminoglycosidic antibiotics including streptomycin, which was used routinely in cell culture to safeguard against bacterial infections during the lengthy neuronal differentiation time span; a summary of this phenomenon can be found in Malik *et al.,* (2010). Therefore, the two candidate knockout clones were assessed at the protein level, by ICC and western blotting (in medium supplemented with pen/strep), to confirm that HTT was not being translated. Numerous attempts at confirmation by immunofluorescence microscopy using the MAB2166, MCA2050, or MW1 antibodies were undertaken with poor results. However, successful staining was accomplished using the D7F7 antibody which revealed the clear presence of HTT in the wildtype iPSCs and HAP1 cells, and a contrasting absence in all of the knockout lines. This was further supported with western blotting as bands can be seen in wildtype and HD cell lines, with no bands present in the knockout samples. Taken together, the results from the ICC and western blotting, which probed epitopes spanning the majority of the length of the HTT protein, provided sufficient evidence to therefore conclude that residual protein expression was not occurring.

It is notable however, that at the 5' region of *HTT*, Cas9 targeting was guided to a region 34 nucleotides downstream of the *HTT* start codon, compared with 47 in Ruzo et al. (2018) and 55 in Dabrowska et al. (2020). This could result in the translation of 16 amino acids in the HD knockout and more in the KOLF2, before a stop codon would be encountered, of which the first 11 match those found the wildtype HTT protein. Therefore, it is possible that the N-terminal 11 amino acids which could contribute to the pathogenic processes in HD (Zuccato et al. 2010; Saudou and Humbert 2016), could be translated, and that this fragment would have remained undetected, as none of the antibodies used here, probed epitopes in this region and while there are antibodies specific to the first 1-17 amino acids in the HTT protein, there are none to bind to the first 11 amino acids. To be certain that this fragment is

not retained or translated, it might be useful to test for the presence of RNA fragments by qPCR or perhaps by the addition of a protein tag immediately flanking this region. However, it was reasoned that in these models, it is likely that degradation of these transcripts would likely occur through nonsense-mediated mRNA decay prior to translation, so additional steps to confirm the absence of these fragments were not undertaken.

Off-target cleavage is of concern when using CRISPR-Cas9, as this can result in the insertion or deletion of nucleotides into coding regions with unpredictable downstream effects. Because scanning the entire genome in search for these potential errors would have been prohibitively expensive, the scope of quality control was reduced through the application of software to predict genetic loci that were susceptible to cleavage. From these, genes likely to be influential in lysosomal metabolism were focused on. Using this approach, the pool of candidates was narrowed to a single gene, *STARD8,* which was determined to be unaffected. Therefore, it was concluded, that to a reasonable extent, our isogenic and knockout cell models were genetically equivalent and not subjected to obvious editing errors.

In summary, our cellular models exhibited, in similar proportions, cell identity markers consistent with those conventionally described at the iPSC, NPC, and neuronal timepoints, with no significant differences observed related to the presence of mutant HTT or the absence of HTT. These results assured us that comparisons of lysosomal phenotypes within the context of relatively similar developmental backgrounds could be made. The absence of evidence for differences between HD and isogenic wildtype cell lines is in agreement with earlier work conducted in our lab, which detailed similar antibody staining supported by qPCR-based gene expression data, at similar timepoints, using the same differentiation protocol (Donaldson 2019a). While reductions in developmental speed and increased cell death were shown to be associated with neurons derived from HD patient iPSCs, as reported by the HD iPSC Consortium (2017), and could alter the composition of the cellular population, this was not assessed here. Our findings are in agreement with previous comparisons using HTT-null iPSC and hESC models, in which comparable expression of pluripotency, neuroepithelial protein, and postmitotic neuronal markers were observed in knockouts, wildtypes, and HD cell cultures (Ruzo et al. 2018; Dabrowska et al. 2020). It can

be broadly concluded that cells used throughout this thesis are NPCs and neurons, and more specifically one in which a fraction of neurons exhibit properties of striatal MSN properties, which experience the greatest neurodegeneration in HD (Vonsattel et al. 2008). This model system therefore provides a suitable cellular background with which to compare lysosomal phenotypes.

Finally, because treatment with glycosphingolipid biosynthesis inhibitors has been shown to markedly alter the outgrowth of dendrites, axons, and delay synaptogenesis in primary rat neurons, the effects of miglustat treatment on the late stages of neuronal differentiation was assessed (Schwarz et al. 1995; Schwarz and Futerman 1997,1998; Bodennec et al. 2002; Kacher and Futerman 2006). The data indicated that miglustat was not affecting the differentiation potential and that the HD, isogenic, and HTT null cell populations were similar. While comparisons of dendrite outgrowth, axonal length, and synaptogenesis would have been useful, these were not performed, though images from this experiment are saved and could be examined.

4 INVESTIGATION OF STRUCTURAL DEFECTS IN HUNTINGTON'S DISEASE

4.1 Introduction

4.1.1 Endolysosomal proteins and distribution in NP-C and HD

4.1.1.1 Endolysosomal proteins in NP-C and HD

Several phenotypes common to lysosomal storage diseases have been reported in HD, indicating that defects related to the endolysosomal system are present in HD (summarized in Chapter 1.7 and 1.8). In particular, the presence of shared phenotypes with Niemann-Pick disease, to the exclusion of phenotypic overlap with other LSDs, suggests that there might be common mechanisms underlying cell pathology in both HD and NPC. This possibility was supported by previous work in our lab which showed NPC1 co-immunoprecipitation with both wildtype and mutant HTT (Figure 1.10) (Clark 2017), thus suggesting that a shared mechanism might be related to a direct interaction between huntingtin and NPC1, and specifically leading to the hypothesis that trafficking defects associated with mHTT, might be inhibiting NPC1 localization to the LE/lysosome. If correct, then in HD, we might observe similar structural defects as those occurring due to NPC1 dysfunction in NP-C disease. Thus, in this chapter abnormal structural characteristics observed in NP-C are examined in HD models, and because these phenotypes might differ in dividing cells when compared to post-mitotic neurons, the structural phenotypes were first examined in neural progenitor cells and then in neurons.

In LSDs, the hallmark phenotype of substrate accumulation is also associated with a structural enlargement and altered distribution of lysosomes, lysosome-related vesicles, and lysosomal proteins. These phenotypes can be assayed by image analysis of LAMP1 or Lysotracker staining. For example LAMP1 expression is increased in NP-C patient-derived NSCs (Sung et al. 2017) and in models of HD Lysotracker staining has shown, increased lysosomal intensity, numbers, and volume in mouse and human NPCs (Camnasio et al. 2012; Castiglioni et al. 2012). In contrast, in mHTT knock-in mice, while Lysotracker-labeled vesicles were larger, their numbers were reduced (Del Toro et al. 2009). Experiments from our lab further demonstrated an altered endolysosomal compartment in HD, and moreover, provided evidence for the possibility of a shared, drug-targetable mechanism common to NP-C and HD, as robust increases in lysosomal area, as

determined by Lysotracker staining, were reported in iPSC-derived NSCs and in HD ST14A rat striatal NPCs, the latter of which was reversable with HPβCD, a promising candidate drug to treat NP-C (Haslett 2015). However, further experiments, using HD STHdh mouse striatal cells, produced inconsistent evidence of lysosomal expansion in HD cells, showing reduced Lysotracker staining, Lysosensor was similar to the controls, and LAMP1 remained unchanged or possibly only slightly increased, though perinuclearly distributed (Clark 2017). Additionally, and related to the HTT knockout lines used in this thesis, it was shown that LAMP1 protein levels and LAMP2 puncta were slightly increased in HTT-knockout MEFs (Rui et al. 2015a), which hints at the possibility of a loss-of-function in HD and potential structural overlap with NP-C. Thus, to clarify the inconsistent reports of lysosomal expansion in HD and to interrogate the role of HTT by its removal, lysosomal expansion was investigated in our NPC models.

Lysosomal expansion has also been reported in neuronal models of HD and this phenotype is similar to that seen in NP-C. In NPC1-mutant mouse brain sections, cholesterol and gangliosides were shown to localize to LAMP1-positive vesicles, which occurred in greater numbers and with higher signal intensity than in the wildtypes (Zervas et al. 2001a). In neuronal models of NP-C, endolysosomal expansion is prevalent and increased LAMP1 signal intensity, size, and punctate, perinuclear distribution have been reported in NPC1 knockout isogenic induced neuronal (iN) models (Prabhu et al. 2021). In HD, increased lysosomal area has been observed in iPSC-derived neurons as determined by Lysotracker staining (Camnasio et al. 2012; Nekrasov et al. 2016). More recently, LAMP1 protein levels and density were shown to be increased with mHTT overexpression in mouse brains (Brattås et al. 2021), and immunocytochemical analysis of HD patient iNs showed increased number and size of LAMP1-positive vesicles sequestered largely to neurites, though total LAMP1 protein levels were not found to be altered (Pircs et al. 2021). In our lab, Lysotracker was used to evidence lysosomal expansion in iPSC-derived neurons (Q60) and LAMP2 immunofluorescence was used across an allelic mHTT series (Q21, Q33, Q60, and Q109) of iPSC-derived neurons to show lysosomal expansion commensurate with increased polyQ length (Haslett 2015). However, LAMP1 in our isogenic neuronal models has yet to be examined.

In addition to changes in common lysosomal markers, the levels and distributions of NPC1 and NPC2 proteins, were also reported to be altered in HD models, which could suggest a mechanistic link, between NP-C and HD. ST14A cells exhibited strikingly increased levels and a perinuclear distribution of NPC1, and similarly in STHdh cells, NPC1 staining was brighter and more punctate, however, reduced levels of NPC1 were observed in Q180 NSCs, and thus whether NPC1 is altered with mHTT remains unresolved (Haslett 2015; Clark 2017). A sharp increase and a more punctate distribution of NPC2 was also observed in ST14A cells, suggestive of a potential compensatory mechanism for an HTT-associated absence of NPC1 from large regions of the cells; this was further supported by immunoblotting which indicated a three-fold increase in NPC2 in STHdh cells (Haslett 2015; Clark 2017). These proteins, however, have not been assessed in human models of HD, and because inconsistencies regarding NPC1 were found, along with the pronounced NPC2 phenotype reported in mouse lines, investigation using our models is merited.

4.1.1.2 Late-endosomal proteins in NP-C and HD

Elevated levels of lysobisphosphatidic acid (LBPA) are a prominent cellular phenotype of Niemann Pick disease. LBPA, also known as bis(monoacylglycero)phosphate (BMP) is an anionic phospholipid which while comprising less than 1% of the total lipid mass in cells, constitutes nearly 15% of the lipid composition in the late endosome, where it is exclusively localized and thought to regulate cholesterol levels (Kobayashi et al. 1998; Kobayashi et al. 2001; Kobayashi et al. 2002; Chevallier et al. 2008), and functions in membrane fluidity and charge (Schulze and Sandhoff 2011), to effectuate intermembrane cholesterol transfer (Liu 2012). LBPA was observed to accumulate in NP-C patient brain samples (Rouser et al. 1968), and LBPA levels from NPC1-null and NPC1-mutant mouse liver, patient liver and spleen autopsy sections, and patient fibroblasts were shown to be elevated in NP-C (Vanier 1983; Vanier et al. 1996; Sleat et al. 2004; Chevallier et al. 2008; Davidson et al. 2009), and inducible using U18666A (Chevallier et al. 2008).

In previous work, image analysis of LBPA staining in HD models showed cellular LBPA accumulation and storage profiles comparable to those seen in NP-C models. Elevated levels and perinuclear localization of LBPA was observed in patient iPSC-derived NSCs

(Q180) and ST14A (Q120) rat cells, suggestive of late endosomal lipid storage, and thin-layer chromatography indicated a significant cellular LBPA increase in ST14A (Q120) and PC12 (Q145) cells (Haslett 2015). Further studies in our lab corroborated these results as HD patient fibroblasts (Q60) and (Q180) exhibited increased LBPA, as did STHdh and ST14A HD models (Clark 2017). Interestingly, in HD, this increase was less severe than what was observed in U18666A-treated Niemann Pick-like control cells, suggesting that this phenotype is less pronounced in HD than in NP-C (Clark 2017). In contrast, HD patient iPSC-derived NPCs (Q60 and Q109) showed no increase in LBPA (Clark 2017), and examinations of wildtype iPSC-derived neurons (Q33) produced variable results (Haslett 2015). Thus, it is unknown whether LBPA accumulation is a consistent feature of HD, and consequently, this was further examined here.

4.1.1.3 Endolysosomal NPC1 distribution in NP-C and HD

In addition to vesicle expansion, a perinuclear endolysosomal distribution, is a distinctive feature of NP-C (Vanier 2010), that has also been reported in HD. Particularly, the perinuclear distribution of NPC1 (as well as LAMP1), a pattern that is characteristic of proteins retained to the ER, has been observed in juvenile patient NP-C fibroblasts, CHO cells, heterokaryon, and U18666A-treated models of Niemann Pick type C (Frolov et al. 2001; Ko et al. 2001; Blom et al. 2003; Ohgane et al. 2013). Though the mechanisms underlying this are unclear, one line of reasoning suggests that loss of NPC1 function and subsequent cholesterol accumulation, produces a conformational change in oxysterol-binding protein-related protein 1 (ORP1L), which promotes complexing with RAB7, and the subsequent attachment of endolysosomes to dynein for transport to the cell interior, and because cholesterol egress is halted, NPC1-positive vesicles are unable to detach from dynein, and remain immobilized in the perinuclear region (Wheeler et al. 2019). Similar phenotypes were reported by our lab and others, as a perinuclear endolysosomal distribution has been observed in (Q111) STHdh cells (Erie et al. 2015; Clark 2017) and dense perinuclear NPC1 localization has been reported in (Q120) ST14A rat NPCs and (Q180) NSCs (Haslett 2015).

Collectively, these studies suggest that we would expect to see an increased NPC1 density surrounding the nucleus in mHTT cells, which could indicate trafficking dysfunction and altered metabolic dynamics in HD. Moreover, if defective NPC1

transport to the lysosome occurs with mHTT or HTT knockout, we might expect to see altered vesicle distribution as late endocytic movements are dependent on intact NPC1 (Zhang et al. 2001) and movements of organelles containing mutated NPC1 were shown to be impaired (Ko et al. 2001). Therefore, because NPC1 positioning was previously observed to be altered in both HD and NP-C models, we wanted to ascertain whether these results were reproducible in our HD NPCs which would support the suggested link between mHTT, NPC1, and the NP-C phenotypes previously described in HD models. Moreover, we wanted to determine if NPC1 positioning was affected by HTT knockout, which could suggest a relationship between HTT and NPC1 transport, evidencing for a loss of HTT function in HD.

4.1.2 NPC1 colocalization to the lysosome

Co-immunoprecipitation experiments were previously performed in our lab in which PC12 cells expressing RFP-tagged wildtype (Q23) or mutant (Q73) huntingtin isolates were separated and probed for NPC1 (Figure 1.10). Results evidenced an interaction between both mutant and wildtype huntingtin proteins with NPC1, which established the possibility of a direct link, as HTT may bind with NPC1, or an indirect link wherein the two proteins might associate as part of a larger protein complex. The interaction between wtHTT and NPC1 points to a role for huntingtin towards NPC1 in normal functioning, the loss of which might result in an NP-C phenotype. Conversely, the interaction between mHTT and NPC1 offers the possibility for a toxic gain of function. However, both loss of normal function and gain of function could explain NP-C phenotypes in HD. For example, previously observed NPC1 mislocalization in HD models, could be attributed to trafficking defects due to deficits in wildtype protein, or potentially, that mHTT aggregates act as a molecular net, trapping NPC1 in an abnormal distribution (Clark 2017).

Relatedly, previous work in our lab using HD ST*Hdh* HTT (Q111) knock-in mouse striatal cells, showed reductions in NPC1 localization to LBPA-positive late endosomal and lysosomal compartments, while LBPA colocalized less with LAMP1 (Clark 2017), it however, remains unclear as to whether NPC1 abnormally colocalizes with LAMP1, and investigating this could clarify the relationship between NPC1 and these vesicle populations. Immunoblots comparing these same cell lines indicated that NPC2 levels were increased in HD (Clark 2017), and increased levels, and altered distribution of NPC2

were also reported in ST14A cells (Haslett 2015). Thus, it was decided to compare the colocalization of NPC1 with LAMP1, and with NPC2 which mainly resides in the lumen of cathepsin D-positive lysosomes as these have previously been shown to colocalize in wildtype cells (Blom et al. 2003; Zhang et al. 2003a; Liscum and Sturley 2004; Poirier et al. 2013).

The rationale for conducting this experiment is that the function of a protein can be often articulated by its association with specific intracellular compartments, other proteins, or molecules through comparisons of the distribution of fluorescently labelled markers and while some molecules are too small to determine accurate colocalization, due to physical limitations in the microscope resolution, the association of a protein to intracellular compartments such as endosomes, mitochondria, microtubules, etc., have been deemed appropriate (Dunn et al., 2011). Therefore, a reduction in NPC1 transport to the late endosome or lysosome due to mutant HTT or HTT knockout might reproduce the loss of NPC1 function observed in NP-C and could explain overlapping phenotypes. That being said, however, a lack of differences in colocalization might be the result of a backup transport mechanism, or simply that HTT is not involved in NPC1 transport. In any case, this information was important for clarification into one of the main hypotheses of this thesis, which if true, could result in decreased NPC1 colocalization with LAMP1 or NPC2.

4.1.3 Autophagic dysfunction in HD

The importance of efficient waste recycling and clearance is critical in neurons, due to their extensive and often bipolar morphology, excitable nature and corresponding energy requirements, as well as their post-mitotic state and inability to dilute accumulated cargo through division (Malik et al. 2019). Disruption to the coordinated processes of macroautophagy, chaperone-mediated autophagy (CMA), and microautophagy have been implicated as contributing to neurodegeneration (Nixon and Yang 2012), and because autophagic function is reliant on the ability of lysosomes to break down and recycle autophagy substrates, it is not surprising that altered autophagic flux and accumulation of autophagic substrates is observed in a number of neurodegenerative diseases, lysosomal storage diseases including NP-C, and HD (summarized in Chapter 1.5.4.5 and 1.8.7) (Ravikumar et al. 2004; Ko et al. 2005; Yim and Mizushima 2020; Parenti et al. 2021).

In NP-C, evidence from affected patient liver, and fibroblasts suggest increased autophagic induction and flux, while in mouse models and CHO cells, a block in autophagic degradative activity was noted, hence, imbalances in these two processes have been proposed to result in cell stress and cell death (Pacheco et al. 2007; Pacheco and Lieberman 2008; Sarkar et al. 2013). Increased counts of autophagic vacuoles, increased LC3 levels, and cell death was reported in NPC1-deficient mouse Purkinje neurons, (Ko et al. 2005), and while in ES-derived NPC1 mutant neurons, spontaneous activation of autophagy also occurred, a block in autophagic progression and reduced mitochondrial clearance was observed (Ordonez et al. 2012). Interestingly, combination therapy involving miglustat, cyclodextrin, and allopregnanolone, has been shown to alter autophagosome substrate composition, in Purkinje neurons from NP-C mouse brain sections (Hovakimyan et al. 2013).

In HD, there is ample evidence that autophagy is increased with mHTT and increased autophagosome-like structures were reported in human post-mortem brain samples and mouse models (Davies et al. 1997; Sapp et al. 1997; Kegel et al. 2000; Ravikumar et al. 2004; Camnasio et al. 2012). In HD iPSC-derived neuronal models increased autophagosome counts were observed (Nekrasov et al. 2016), and accumulation in the autophagic compartment was seen in HD patient-derived iPSCs, induced neurons, and isogenic iPSC-derived neurons (Camnasio et al. 2012; Malankhanova et al. 2020; Pircs et al. 2021).

The upregulation of macroautophagy and chaperone-mediated autophagy are thought to result from increased demand for mHTT clearance in HD (Ravikumar et al. 2002; Qin et al. 2003; Qi et al. 2012). Additionally, expansion of the autophagic compartment, was recently attributed to disrupted transport caused by polyQ-mediated disruptions in the HTT/HAP1 motor complex, and corresponding reductions in autophagosome-lysosome fusion events (Wong and Holzbaur 2014). More recently, in mouse brain sections, the presence of mHTT in autophagosomes was associated with altered autophagosome/MVB dynamics, from the exocytosis of intraluminal vesicles and towards increased lysosomal fusion, perhaps in order to mediate the effects of chronic mHTT aggregation, and thus resulting in accumulation of autophagic vesicles (Zhou et al. 2021). In any case, though the mechanisms underlying autophagosome accumulation have yet to be fully

understood, this is a prominent phenotype, and one that might be useful to assay in our model system for validation purposes.

Relevant to the investigations into autophagy in our HTT knockout models, mice exhibiting heterozygous polyQ deletion displayed increases in autophagy, increased clearance of mHTT neuropil aggregates, and homozygous polyQ knockouts showed increased longevity (Zheng et al. 2010), which in conjunction with results showing HTT colocalization with autophagosomes and structural similarity to mTOR, suggests the possibility of a normal role for HTT in autophagy, that is lost in HD (Atwal et al. 2007; Zheng et al. 2010). Pronounced increases in autophagy markers, lipofuscin and ubiquitin, were observed in conditional HTT knockout and HD mice, which provided further evidence to support a necessary role for HTT in autophagy (Ochaba et al. 2014). Moreover, loss of HTT function was shown to reduce starvation-induced, macroautophagy, in *Drosophila*, resulting in a model of HTT function as an evolutionarily conserved scaffold (with homology to a yeast protein, ATG11), and in association with p62 and ULK1, is required for nutrient-independent, selective-autophagy (aggrephagy, lipophagy, and mitophagy), though dispensable for starvation-induced, non-selective, autophagy (Ochaba et al. 2014; Rui et al. 2015a). Recently, silencing wtHTT and mHTT in HD-patient iN models, showed increased levels of LC3II, with no changes in p62, and reductions in LAMP1, to suggest that while silencing mHTT might produce a reduction of HD phenotypes related to LAMP1 accumulation, the silencing of wtHTT produced another type of autophagic disruption with further increases in LC3B relative to those already observed in HD, which likely arises due to loss of wildtype HTT function (Pircs et al. 2021).

In light of this body of evidence, we hypothesized that relative to the isogenic lines, at basal levels the area of autophagic vesicles would be increased in the mHTT and HTT knockouts. In response to starvation, it was expected that in HD cells, that autophagosomes would increase and accumulate even further, while in the knockouts it was expected that there would be a limited response and no increase in autophagosome area. Moreover, we wanted to determine whether miglustat treatment might reduce accumulation in HD neurons, as this has been shown in combination therapy with cyclodextrin and allopregnanolone to reduce autophagosome accumulation in NP-C

(Hovakimyan et al. 2013), though no rescue effects were observed due to miglustat-treatment alone (Soga et al. 2015).

4.1.4 Mitochondrial dysfunction in HD

Neurons are reliant on functional and bioenergetically competent mitochondria, with appropriate mitochondrial fission and fusion cycles, especially to maintain synaptic plasticity as neuronal mitochondria are characterized by high oxygen consumption rates, to meet high energy requirements (especially near the synapse), to support processes such as neurotransmitter release, neurite outgrowth and, synapse formation (Haun et al. 2013; Yin et al. 2016; Mamelak 2017; Pantiya et al. 2020). Correspondingly, while several neurodegenerative diseases have been linked to disrupted mitochondrial function, defects related to mitochondrial structure and the dynamics of fusion and fission events have also been implicated (Bossy-Wetzel et al. 2003; Chan 2007). Moreover, mitochondrial dysfunction and the accumulation of damaged mitochondria frequently occur in LSDs (Lieberman et al. 2012; Parenti et al. 2021).

Mitochondrial fragmentation is a pronounced phenotype observed in hESC-derived NPC1 knockdown neurons and while NPC1 fibroblasts display low levels of mitochondrial fragmentation, the magnitude of fragmentation that occurs in neurons indicates that in NPC1, mitochondrial defects, coupled with a block in mitophagic clearance, promotes selective neuronal effects in NP-C (Ordonez et al. 2012). Using HD lymphoblasts and striatal precursors from HD knock-in Q111 mice, Costa et al. (2010) demonstrated that in the presence of mHTT, mitochondria undergo cristae remodelling and increased fission. These results were reproduced in Q111 striatal neurons (Manczak and Reddy 2015), in mouse neurons (Song et al. 2011; Shirendeb et al. 2012), and in rat cortical neurons transfected with mHTT (Song et al. 2011; Haun et al. 2013). Mechanisms proposed to be underlying increased fragmentation and neurodegeneration center around the imbalances in GTPase proteins essential for mitochondrial division (Drp1 and Fis1) and fusion (Mfn1, Mfn2 and Opa1) (Manczak and Reddy 2015). Increased fragmentation results in increased cytochrome C release, and heightened susceptibility to apoptosis (Costa et al. 2010). Similar to NP-C, defects in autophagosome transport have been observed in both HTT-depleted neurons and neurons expressing mHTT, and both were shown to be associated with inefficient degradation of mitochondria, and thus it was

suggested that disrupted HTT and HAP1-regulated autophagosome transport in neurons results in defective mitochondrial clearance and cell death (Wong and Holzbaur 2014). Considering these lines of evidence, we hypothesized that we would see increased mitochondrial fragmentation in our HD109 lines relative to the isogenic controls, and moreover, that due to the overlapping phenotypes and possible underlying mechanisms shared between NP-C and HD, that treatment with miglustat might rescue the disease phenotype.

4.1.5 Ultrastructure of neuronal models of HD

Transmission electron microscopy developed by Max Knoll and Ernst Ruska in 1931, (Knoll and Ruska 1932) has been used in the identification and characterization of intracellular ultrastructure and substrate compositions in lysosomes, autophagosomes, and peroxisomes for decades (Novikoff et al. 1956; Ashford and Porter 1962; De Duve and Baudhuin 1966). TEM continues to be used as one of the most precise methods for augmenting, complementing, or replacing biochemical data and for quantifying properties associated with intracellular vesicles (Eskelinen 2008). Accordingly, TEM was applied towards identifying and comparing storage phenotypes in our neuronal models of HD and their responses to miglustat treatment, and to investigate phenotypes that might emerge due to the knockout of huntingtin and potential commonalities with NP-C.

Electron microscopy has been used not only to identify novel LSD storage phenotypes, but also as a diagnostic tool to trace storage phenotypes back to the accumulated storage material and then the underlying disease; in fact, it is the only way to diagnose various forms of NCL (Alroy and Ucci 2006). This is possible because intravesicular storage morphologies are dependent on the molecular properties associated with the nondegraded substrate, which can provide information regarding the causative endolysosomal protein defect, (Table 4.1) (Galvin et al. 2008; Vitner et al. 2010; Martina et al. 2020). Redundancy in the storage morphologies, which are common, may limit the scope of inference which can be applied, and morphology alone may not provide conclusive evidence for the origin of, or for the mechanism underlying a particular LSD (e.g., CLNs and gangliosidoses in table 4.1). Nonetheless, EM could provide clues into pathogenesis and permit comparisons, to determine effects of mHTT, HTT knockout, and miglustat treatment. Another important element to consider when using EM to evaluate

LSD phenotypes, is the degree to which the pathology manifests, in a tissue specific context as there are numerous accounts of phenotype heterogeneity, and presence or absence determined by tissue-type (Alroy and Ucci 2006; Galvin et al. 2008). So, though our models were not without limitations, they still provided a unique opportunity to survey and compare storage in a disease-analogous cell context, which might also provide information regarding possible mechanisms of pathogenesis.

Shortly after the identification of the huntingtin gene, EM was largely applied towards the immunocytochemical analysis of HTT distribution, and several groups reported features of huntingtin suggestive of a link with the endolysosomal system. In human cortical neurons, HTT is concentrated in the somatodendritic cytoplasm, associated with vesicle membranes and dendritic microtubules, corresponds to isolation in synaptosome related cell fractions, and exhibits immunoreactivity that overlaps synaptic vesicle proteins (DiFiglia et al. 1995). In rat cortical neurons, HTT was observed to be discretely patterned on Golgi and Golgi-related vesicles, microtubules and associated vesicles, and because HTT was distributed throughout the cytoplasm, as opposed to the axon terminal patterning generally associated with vesicle associated proteins, a role for HTT in vesicle trafficking was suggested (DiFiglia et al. 1995). Similarly, in human striatal samples HTT was localized to the cytoplasm, especially in association with microtubules and to synaptic vesicles, which corroborated HTT's role in trafficking as well as in cytoskeletal anchoring (Gutekunst et al. 1995a). Moreover, in the striatum, cortex, and the globus pallidus, HTT was found in punctate, cytoplasmic, and predominantly perinuclear, MVB-like granules, that resembled a cathepsin D staining distribution to the endolysosomal pathway, thereby distinguishing a potential sequestration vesicle, to further strengthen the argument for endolysosomal involvement (DiFiglia et al. 1997). In R6/2 mice, neuropil aggregates in the axon terminals were partially colocalized with synaptic vesicles that accumulated with symptom onset, expanding the breadth of HTT function to include possible roles in synaptic transmission and neuronal communication (Li et al. 1999). While EM and biochemical analyses have provided evidence in support of huntingtin's association with the endomembrane system, the nature of the association remains unclear, though more recent efforts have connected the mutant form of huntingtin to disturbances in this system.

In macrophages, axons, pericytes, Schwann cells, smooth muscle cells, fibroblasts, vascular endothelium, and melanocytes, obtained from NP-C patients biopsies, the presence of loosely arranged, dark, osmiophilic-dense, lamellated structures, amongst a clear matrix were reported inside lysosomes, with macrophages and then axons being the most affected (Boustany et al. 1990). In human NP-C patient fibroblasts, cholesterol crystals and lamellae were reported (Pentchev et al. 1994). Fractional cellular area calculations, indicated increases in lamellar inclusions at the site of cholesterol accumulation, in NPC1 deficient rat retinal ganglionic neurons, with additional increases in primary lysosomes, endosomes, multilamellar inclusions, and residular bodies (Demais et al. 2016). Lamellar inclusions contained surface-labelled GM1 and cell-intrinsic cholesterol, and because they exhibited CD63 and LAMP1, the origins were determined to be late endosomal and lysosomal (Demais et al. 2016). In a model similar to the ones developed for this thesis, characteristic multilamellar structures were also reported in NPC1-knockout hiPSC-derived i^3Neurons (Prabhu et al. 2021).

TEM on HD patient lymphoblasts, showed increased size and counts of Cathepsin B and D positive autophagosomes, indicating a lysosomal origin, corresponded to increases in CAG repeat-length (Nagata et al. 2004). Recently, with improved imaging techniques, direct links between HD and altered endolysosomal regulation have been identified. Cryo-electron tomography was used to show that, in mice and human, amyloid-like fibrillar inclusions formed by mHTT exon 1, interact with, cause deformation in, and reduce membrane dynamics in lysosomal, mitochondrial, and ER membranes, while remaining absent from autophagic structures, thereby emphasizing a relationship between mHTT inclusions and intracellular membrane form and function. (Arrasate and Finkbeiner 2005; Slow et al. 2005; Bäuerlein et al. 2017). Most recently, in Q175 mice, mHTT was shown to recruit to LAMP1-positive, endolysosomal organelles, which in presymptomatic mice resembled MVBs that, concurrent with cellular reductions in MVB-related exocytosis markers, developed into autolysosomes as the disease progressed, indicating a shift in endolysosomal homeostasis from exocytosis towards lysosomal fusion and degradation (Demais et al. 2016; Zhou et al. 2021). These findings support a direct influence by mHTT towards altered endolysosomal dynamics, and because perturbations on this system in LSD-based neurodegenerative diseases are often

accompanied and identifiable by visible ultrastructural storage phenotypes, we considered it important to directly examine these in our cellular models.

Disease	Storage morphology	Defective protein	Main storage material
GM1 gangliosides	Intraluminal thick lamellar, whorl/zebra like structures membranous cytoplasmic bodies concentric ring-like	β-Galactosidase	GM1 ganglioside
GM2 gangliosidosis (Sandhoff)		β-Hexosaminidase A and B	GM2 ganglioside and related glycolipids
GM2 gangliosidosis (Tay-Sachs)		β-Hexosaminidase A	GM2 ganglioside and related glycolipids
Gaucher	Twisted tubular structures	β-Glucosidase or saposin C activator	GlcCer
Fabry	Dark clumps, membrane associated thick whorl/zebra like structures	α-Galactosidase A	Globotriaosylceramide and blood group B substances
Niemann-Pick Type A	Light multiple small lamellar bodies	Sphingomyelinase	Sphingomyelin
Niemann-Pick Type C	Single lamellar structure	NPC1 and 2	Sphingosine
Metachromatic leukodystrophy	Lamellar pattern/alternation of dark and light band	Arylsulfatase A or saposin B activator	Sulfated glycolipids and GM1 ganglioside
Globoid cell leukodystrophy (Krabbe)	Tubules with electron dense deposits	Galactocerebroside β-galactosidase	Galactosylceramide
Farber	Curvilinear tubular bodies/zebra-like bodies	Ceramidase	Ceramide
CLN1 (INCL, LINCL, JNCL, and ANCL)	Fingerprint/ curvilinear profile like structures	PPT1, palmitoyl protein thioesterase	Saposins A and D
CLN2 (LINCL and JNCL)		TPP1, tripeptidyl peptidase 1, lysosomal enzyme	Subunit c of ATP synthase
CLN3 (JNCL,Batten)		CLN3, lysosomal Transmembrane protein	Subunit c of ATP synthase
CLN6 (LINCL)		CLN6, transmembrane protein of ER	Subunit c of ATP synthase
CLN8		CLN8, transmembrane	Subunit c of ATP synthase
CLN8 (LINCL, Northern epilepsy)		CLN8, transmembrane protein of ER	Subunit c of ATP synthase
CLN10 (LINCL)		Cathepsin D	Saposins A and D
MPS	Fine floccular material	Assorted enzymes	GACs
Fucosidosis	Sparse fibrillar structure	α-fucosidase	Oligosaccharides

Table 4.1. Storage materials and defective proteins associated with selected lysosomal storage diseases. Adapted from Alshehri 2019, Vitner, 2010, and Alroy and Ucci, 2006. (Alshehri, 2019; Alroy and Ucci, 2006; Vitner, 2010; Gravel 1995; Lawson, 2016; Zappatini-Tommasi 1992; Ferreira; 2017; Gregoire, 1966; Vogler, 1987)

4.2 Aims

- To examine and identify common structural and ultrastructural phenotypes found in LSDs and specifically NP-C, in our HD models.
- To examine the effects HTT knockout in the context of the autophagosome-endolysosomal system.
- To test the hypothesis that HTT is involved in NPC1 transport to the lysosome.
- To screen for possible rescue effects associated with miglustat treatment.

4.3 Results

4.3.1 Neural progenitor models of HD and HTT knockout

In this section, using the models described in Chapter 3, HD patient-derived neural progenitors were compared with isogenic-corrected versions. Moreover, to examine potential loss of function associated with HD (summarized in Chapter 1.7.2), HTT knockouts were added, allowing for three-way phenotype comparisons across $HD22^{ISO-109}$, HD109, and $HTTKO^{ISO-109}$ cell lines. To corroborate results obtained from the patient-derived knockouts, two additional HTT knockout $KOLF2^{HTT-KO}$ iPSCs lines were also examined. In addition, loss of HTT function was examined in human haploid HAP1 cell lines, providing a non-neuronal model system for comparison.

4.3.1.1 Areas of LAMP1, NPC1, and NPC2 are unaltered with HTT status in day 16 NPCs and HAP1 cells

In order to assess expansion of the lysosomal compartment in NPCs, day 16 neural progenitor cells cultures were stained with antibodies for LAMP1, NPC1, and NPC2 and measured according to the methods described in Cook et al. (2020a). In each case, the area was not found to significantly differ across comparisons of isogenic, HD109s, and HTT-knockouts (Figure 4.1). Thus, these results suggest a lack of effect resulting from the presence of mHTT, which is inconsistent with previous findings. However, it should be noted that in HD109s all three probes on average exhibited higher areas, and potentially, because these phenotypes were not pronounced, a small effect size coupled with low replication in

our models, could have resulted in insufficient power with which to detect a difference, and a corresponding increase in the likelihood of committing a type 2 error.

To check whether this were the case, using LAMP1 area, and a two-way comparison of HD109 and isogenic controls, the effect size was computed to equal 1.17, and power was calculated using G*Power 3.1.9.7 software (Faul et al. 2007), β was determined to equal only 0.32, which is markedly below the commonly applied threshold of 0.8, meaning that there was only a 32% chance of detecting a true negative result (in which the null hypothesis would accurately be rejected), which contrasts the conventional threshold of 80%. Moreover, the fact that these results were obtained by carrying out only a single differentiation and due to the variability, that arises due to extended lengths of time in culture, along with the innate clonal and cell line variability, it would have been advisable to repeat this experiment at least two more times, in order to draw a more robust conclusion.

LAMP1, NPC1, and NPC2 area in knockout cells was also unaltered and as such, failed to support the hypothesis for a loss of function mechanism in HD (Figure 4.1). Additionally, the areas of the three proteins in HTT knockouts and wildtypes were compared using KOLF2 and the HAP1 cell lines (Figure 4.2), which reiterated the lack of differences observed in HD patient HTT knockout cells.

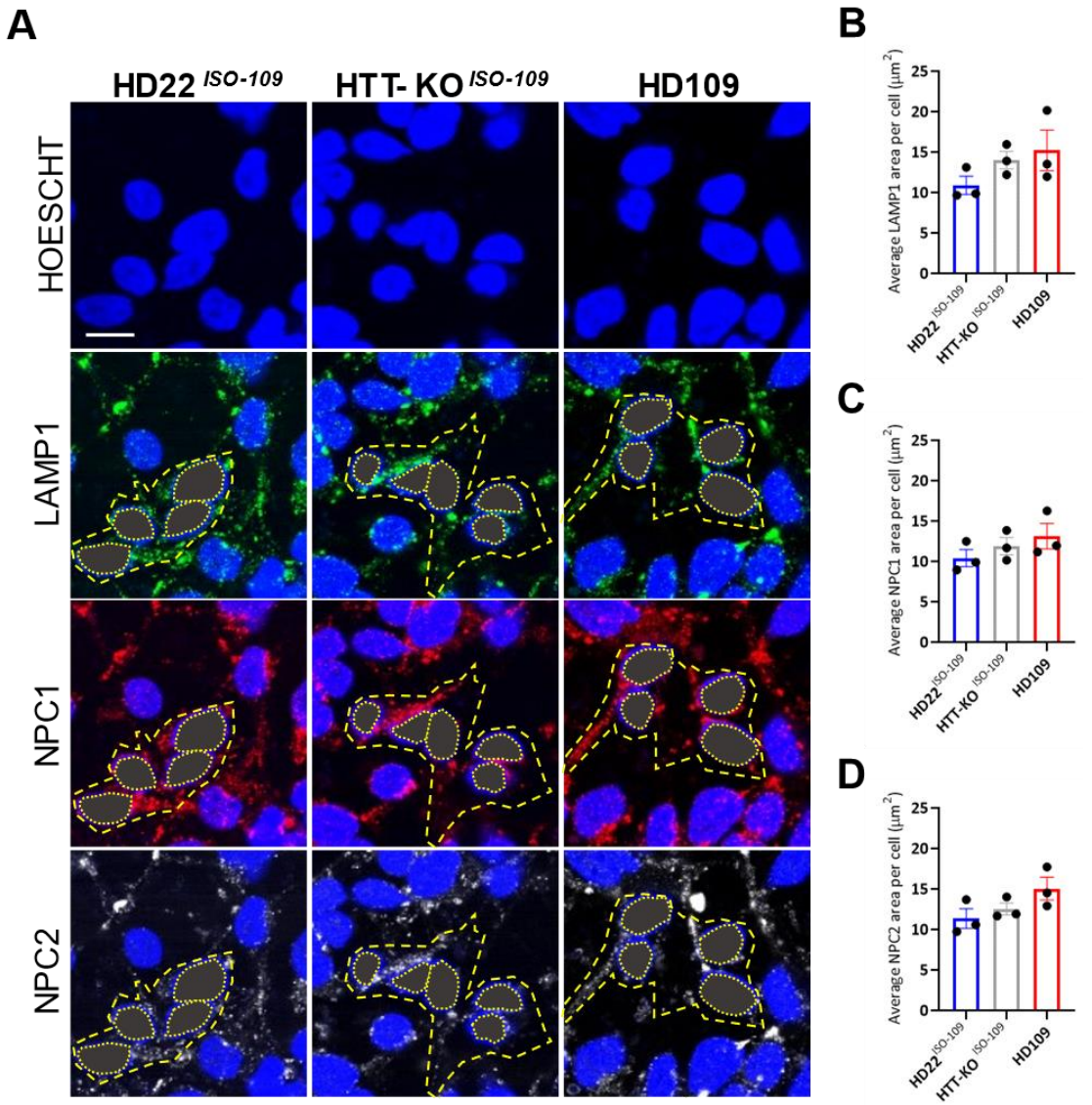

Figure 4.1. No differences detected in area comparisons of lysosomal markers in HD patient-derived neural progenitors. A) Day 16 NPCs stained with antibodies against LAMP1, NPC1, and NPC2 exhibit the presence of lysosomal proteins which were used to calculate lysosomal area. Average cytoplasmic area of B) LAMP1, C) NPC1, and D) NPC2 were measured using ImageJ software. One-way ANOVA with Holm-Šídák's multiple comparisons test; n = 3 technical replicates (wells), 22-38 cells measured per well. Total cells measured per genotype: $HD22^{ISO-109}$ = 102, $HTTKO^{ISO-109}$ = 84, and HD109 = 82. Bars represent mean cellular area ± SEM for each cell line and black circles represent the mean cellular area per well. Scale bar = 10 µm.

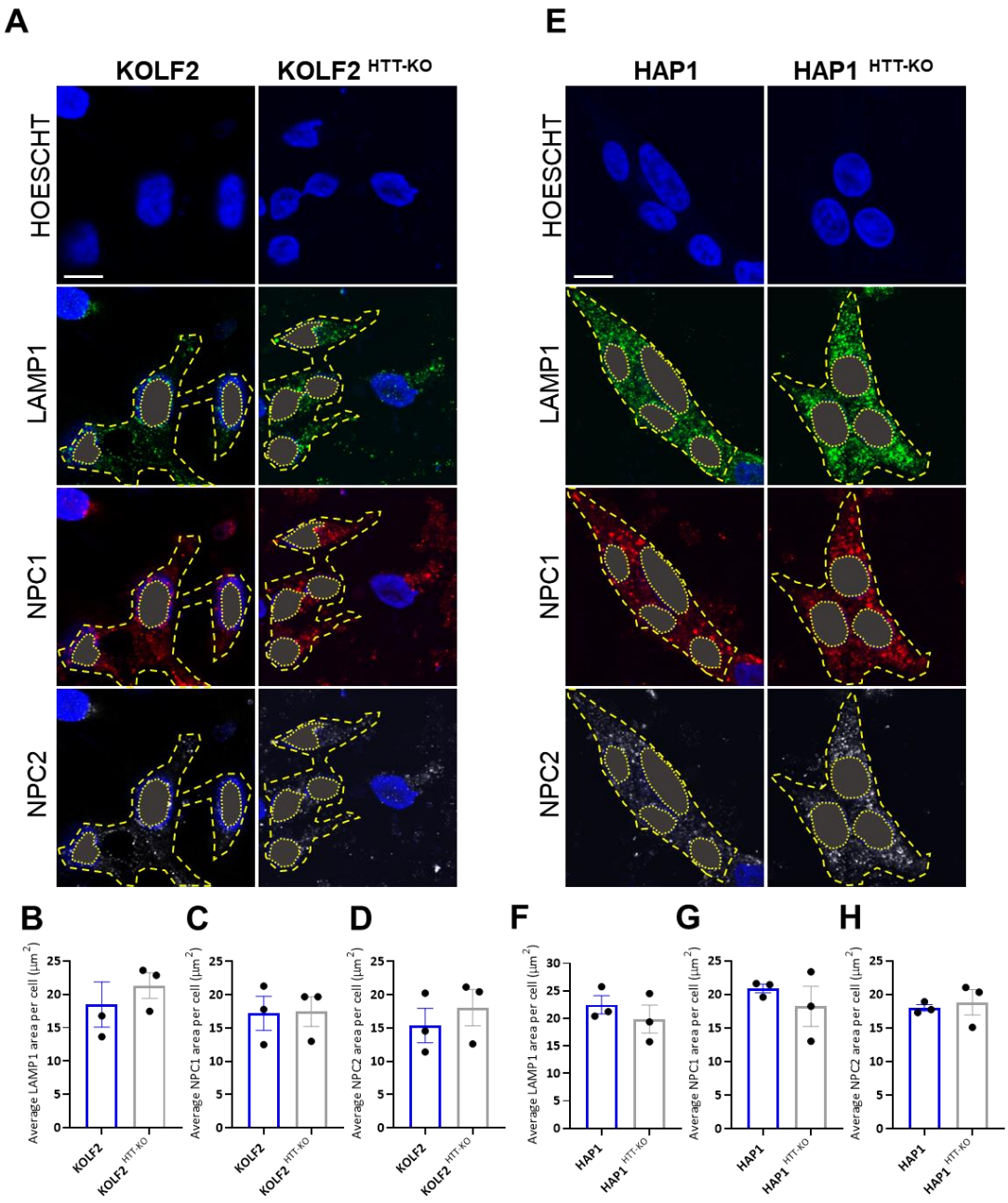

Figure 4.2. No differences detected in area comparisons of lysosomal markers in KOLF2 NPCs and HAP1 cells. A) Day 16 neural progenitors and E) HAP1 cells stained with antibodies against LAMP1, NPC1, and NPC2 exhibit the presence of lysosomal proteins which were used to calculate lysosomal area. In KOLF2 cells, average cytoplasmic area of B) LAMP1, C) NPC1, and D) NPC2 as well as in HAP1 cells F) LAMP1, G) NPC1, and H) NPC2 were measured using ImageJ software. Unpaired T-test; n = 3 technical replicates (wells), 20-35 cells measured per well. Total cells measured per genotype: KOLF2 = 88, KOLF2 HTT-KO = 80, HAP1 = 94, and HAP1 HTT-KO = 91. Bars represent mean cellular area ± SEM for each cell line and black circles represent the mean cellular area per well. Scale bar = 10 µm.

4.3.1.2 LBPA area is unaltered with HTT status in HD patient-derived NPCs

To determine whether LBPA levels are increased in HD, model cells were stained with anti-LBPA antibodies and imaged in 4 planes (0-4 µm at 1 µm increments) along the Z-axis, in order to survey a broader depth within each cell. Z-stacks were compressed into a single image, using the 'max intensity' function in ImageJ, which selects the brightest pixel from each stack for the compressed image. Once this was done, for each cell, the nucleus was removed and total LBPA area was calculated using the method outlined in Cook et al. (2020a).LBPA area was not observed to be increased in HD109, or HTT knockouts, when compared with the $HD22^{ISO\text{-}109}$ controls (Figure 4.5). Interestingly, overnight incubation of the isogenic-corrected NPCs with 2 µg/ml U18666A, to serve as a positive control, failed to display an increase in LBPA area. Regarding HD109, these results do not parallel reports using other cell lines from our lab, and do not strengthen the argument for a shared mechanism between NP-C and HD, however, they do conform to the lack of altered LBPA levels reported in HD109 NPCs as demonstrated by Clark (2017). Regarding HTT knockouts, again, no differences were identified which suggests that HTT is not indispensable to LBPA trafficking or metabolism, and does not evidence an inhibited NPC1 function in HD.

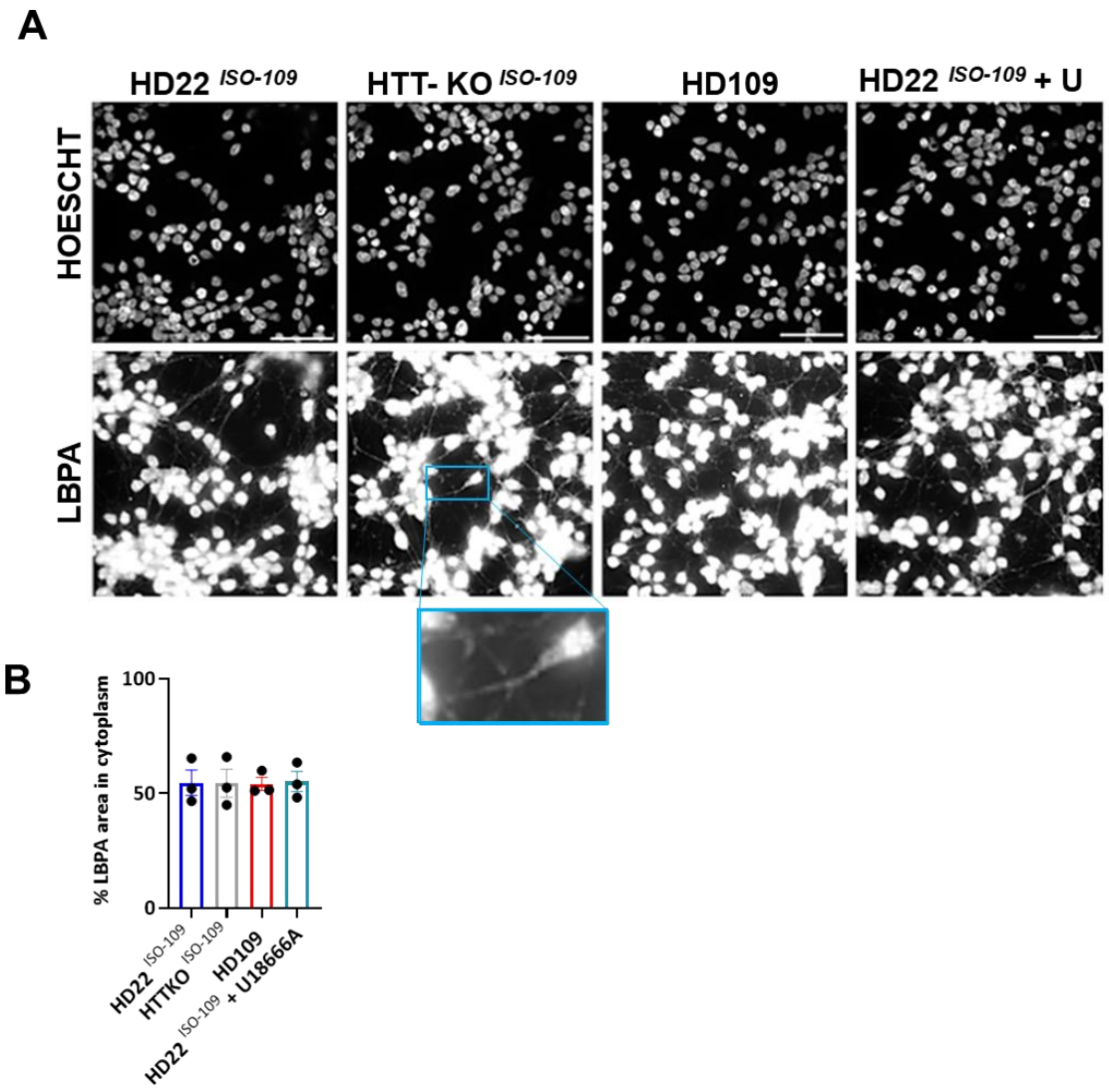

Figure 4.3. Area comparisons of LBPA in HD patient-derived neural progenitors. A) Day 16 NPCs stained with antibodies against LBPA were used to estimate late endosomal area. B) Average cytoplasmic area was measured using ImageJ software. One-way ANOVA with Tukey's multiple comparisons test; Total cells measured per condition: $HD22^{ISO-109}$ = 90, HD109 = 90, HTTKO $^{ISO-109}$, $HD22^{ISO-109}$+ U18666A = 90. N = 3 pools/plates, n = 3 technical replicates (wells), 30 cells measured per pool/plate. Bars represent mean cellular area ± SEM for each cell line and black circles represent the mean cellular area per plate/pool. Scale bar = 50 µm.

4.3.1.3 Perinuclear distribution of NPC1 is not altered with mutant or knockout of HTT in day 16 NPCs or HAP1 cells

Considering that the overall cellular areas of LAMP1, NPC1, NPC2, or LBPA, were not observed to be altered in our mHTT or knockout NPCs, and because NPC1 positioning was previously observed to be altered in both HD and NP-C models, we wanted to ascertain whether this was reproducible in our lines, which would support the suggested link between mHTT, NPC1, and the NP-C phenotypes previously described in HD models. Moreover, we wanted to determine if NPC1 positioning was affected by HTT knockout, which could suggest a relationship between HTT and NPC1 transport and provide evidence for a loss of HTT function in HD.

To accomplish this, the method used to define the perinuclear region outlined in Erie et al. (2015), was applied to our cell lines which were stained with NPC1 and Hoescht. This method was chosen, because it allowed for an automated and consistent extension outward from the edges of the Hoechst-stained nuclei of 0.2 µm, and thus automatically incorporates nuclear shape into the analysis. Once this region was defined, NPC1 area was calculated using the thresholding method outlined in Cook et al. (2020a) . Following this analysis differences due to mHTT or knockout were not detected in the HD cell lines (Figure 4.3). Furthermore, HTT knockout comparisons using KOLF2 NPCs and HAP1 cells also returned non-significant results (Figure 4.4).

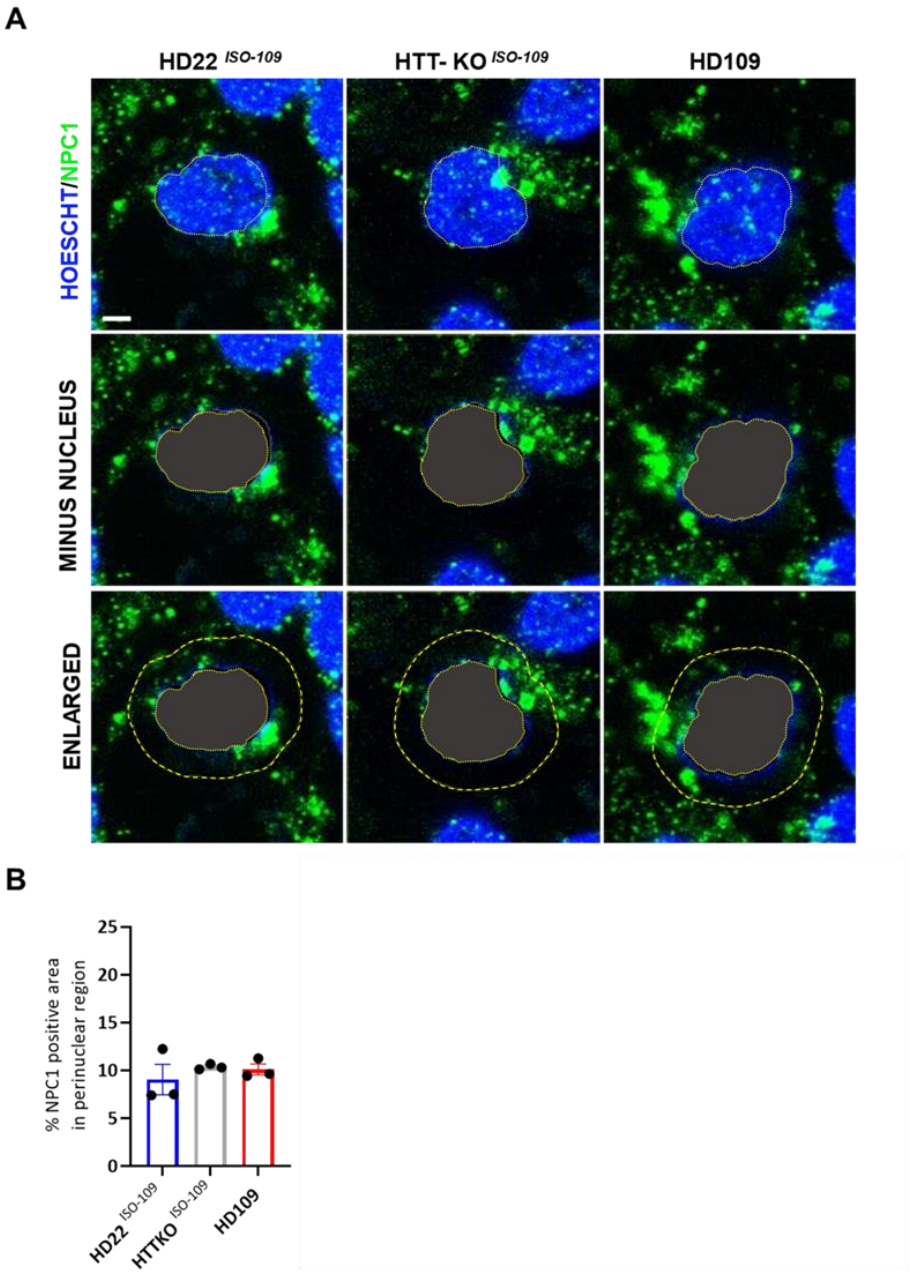

Figure 4.4. NPC1 area in the perinuclear region in day 16 HD patient-derived NPCs does not differ with mHTT or HTT knockout. A) NPC1 positive area was measured in the perinuclear region (the area between the two yellow lines within 2 µm of, and excluding, the nucleus). B) No differences were observed across HD patient-derived day 16 NPCs. One-way ANOVA and Tukey's post-hoc, n = 3 technical replicates (wells), 20-38 cells measured per well. Total cells measured per genotype: HD22 ISO-109 = 91, HTTKO ISO-109 = 91, and HD109 = 90. Bars represent mean cellular area ± SEM for each cell line and black circles represent the mean cellular area per well. Scale bar = 2 µm.

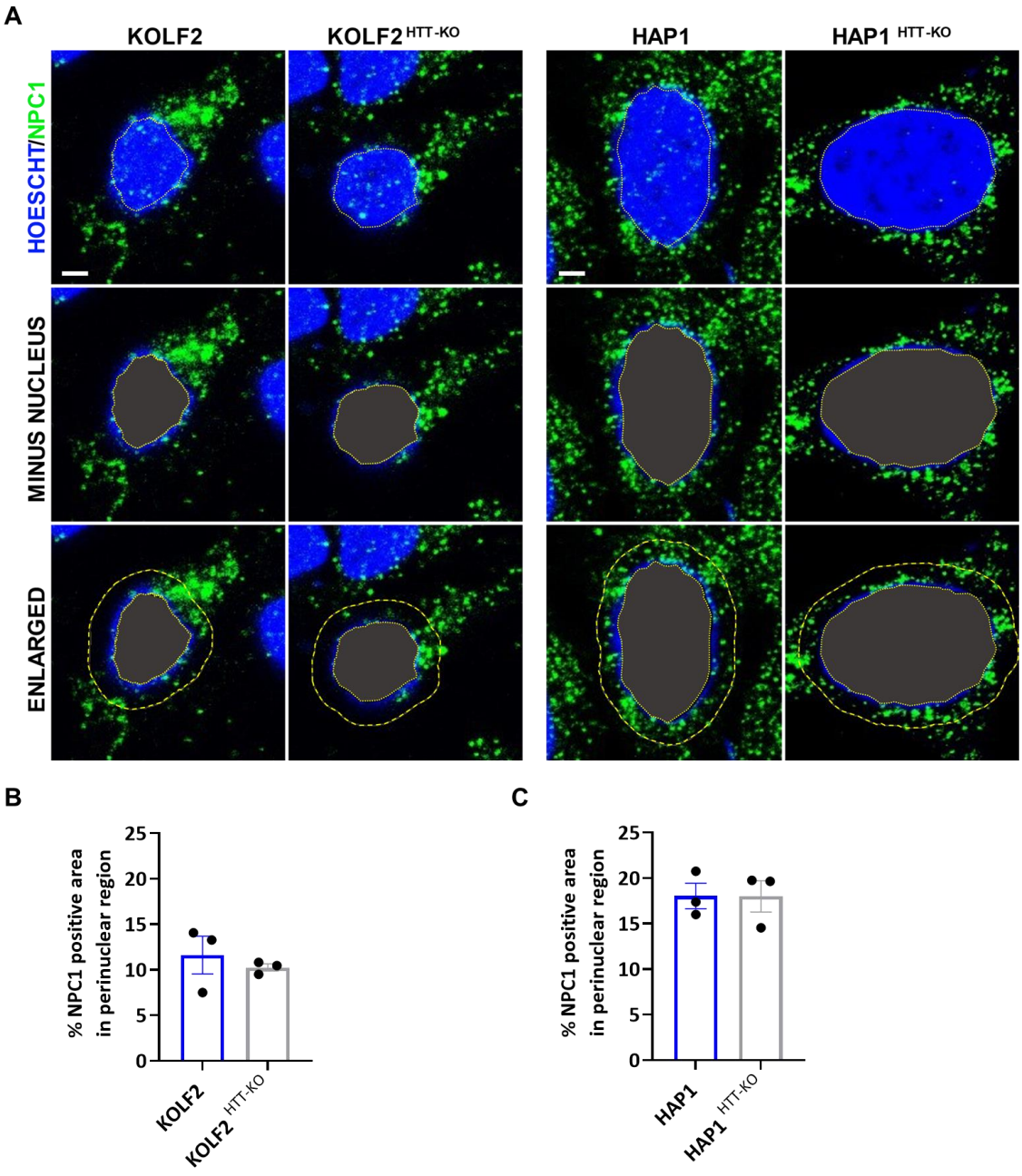

Figure 4.5. NPC1 area in the perinuclear region of day 16 KOLF2 NPCs or HAP1 cells does not differ with HTT knockout. A) NPC1 positive area was measured in the perinuclear region (the area between the two yellow lines within 2 µm of, and excluding, the nucleus). Unpaired t-tests were performed on C) KOLF2 or (D) HAP1 cell lines. Total cells measured per genotype: KOLF2 = 83, KOLF2 HTT-KO = 91, HAP1 = 95, and HAP1 HTT-KO = 92, n = 3 technical replicates (wells), 22 – 31 cells per well. Bars represent mean cellular area ± SEM for each cell line and black circles represent the mean cellular area per well. Scale bar = 2 µm.

4.3.1.4 NPC1 colocalization with LAMP1 or NPC2 is not altered with HTT status in day 16 NPCs or HAP1 cells

Because no differences were identified regarding the area or perinuclear distribution of NPC1-positive vesicles, to test whether NPC1 localization to the LE or lysosome is reduced or abolished by the presence of mutant HTT or by deletion of HTT, HD patient-derived NPCs and HAP1 cells were co-stained with antibodies for NPC1 and LAMP1 (Figure 4.6A). The co-localization of NPC1 to LAMP1 positive pixels as indicated by the M1, Manders' coefficient, was greater than 84.53% in all three conditions, and did not significantly differ, indicating that NPC1 is in large part associated with the lysosomal membrane, regardless of huntingtin status (Figure 4.6B). Manders' M2 coefficient was also determined, and though the percent of LAMP1 pixels that overlapped with NPC1 positive pixels was slightly less than the NPC1 overlap with LAMP1, there were no significant differences associated with mutant or knockout HTT (Figure 4.6C). To verify the results of comparisons between HD22$^{ISO-109}$ and HTTKO $^{ISO-109}$ NPCs, KOLF2 NPCs and HAP1 cells were likewise tested (Figure 4.7A). Results indicated similarly high levels of NPC1 overlap with LAMP1 positive pixels (Figures 4.7B and 4.7D) and vice versa (Figure 4.7C and 4.7E), and no significant differences in colocalization of the two probes were found to be associated with the knockout of HTT. Aggregating the three biological replicates into one analysis, resulted in no significant differences in NPC1 colocalization to LAMP1 positive pixels, based on the presence or absence of HTT, which accounted for 0.5096% of the total variance (Two-way ANOVA; Biological Replicate, $F_{(2, 14)}$ = 2.733, P=0.0996; HTT Status, $F_{(1, 14)}$ = 0.09971, P=0.7568). Similar results were obtained when quantifying LAMP1 colocalization to NPC1 positive pixels, as presence or absence of HTT only accounted for 3.685% of the total variance (Two-way ANOVA; Biological Replicate, $F_{(2, 14)}$ = 17.60, P=0.0002; HTT Status, $F_{(1, 14)}$ = 1.883, P=0.1916).

To summarize, this data is in accordance with previous studies which demonstrated that the NPC1 transmembrane protein is highly associated with LAMP1 positive vesicles, especially when cultured in growth medium containing LDL or sterol derivatives, as was the case here, though some NPC1 positive vesicles are not colocalized with LAMP1 positive vesicles (Neufeld et al. 1999; Garver et al. 2008; Ohgane et al. 2013). Particularly striking was the

similarity of our results to those observed with wildtype NPC1 to LAMP1 colocalization in Ohgane et al. (2013). Thus, these findings reproduce previous basic colocalization studies and further suggests that NPC1 and LAMP1 colocalization is not altered by the presence of mHTT or by HTT knockout.

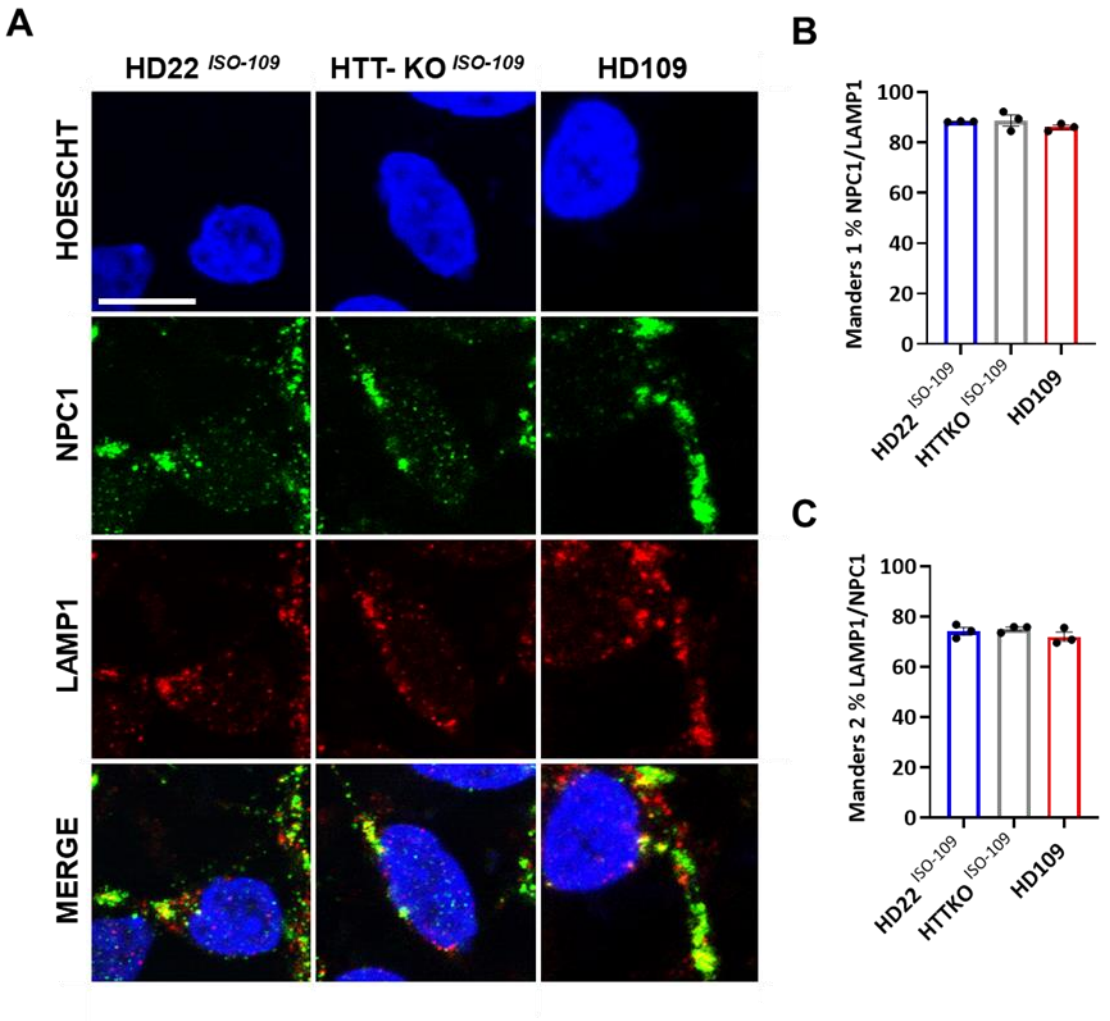

Figure 4.6 NPC1 colocalizes with LAMP1 in day 16 HD109, isogenic, and knockout NPCs. A) Confocal imaging of NPC1 and LAMP1 immunofluorescence reveals similar localization of NPC1 to the lysosome in isogenic wtHTT, mHTT, and HTT knockout day 16 neural progenitor cells. B) Manders' colocalization coefficient indicating the percent of NPC1 positive pixels (green) that localize to LAMP1 positive pixels (red). C) Manders' colocalization coefficient indicating the percent of LAMP1 positive pixels that localize to NPC1 positive pixels. Results indicate no significant differences corresponding to the state of HTT with regards to NPC1 overlap with LAMP1 or vice versa. One-way ANOVA with Tukey's multiple comparisons test; n = 3 technical replicates; technical replicates are defined by the average Manders' coefficients from 10 fields of view analyzed per well; total fields of view analyzed per genotype: HD22ISO-109 = 30, HTTKOISO-109 = 30, and HD109 = 30. Bars represent mean the Manders' coefficient ± SEM for each cell line and black circles represent the mean Manders' coefficient per well. Scale bar = 10 µm.

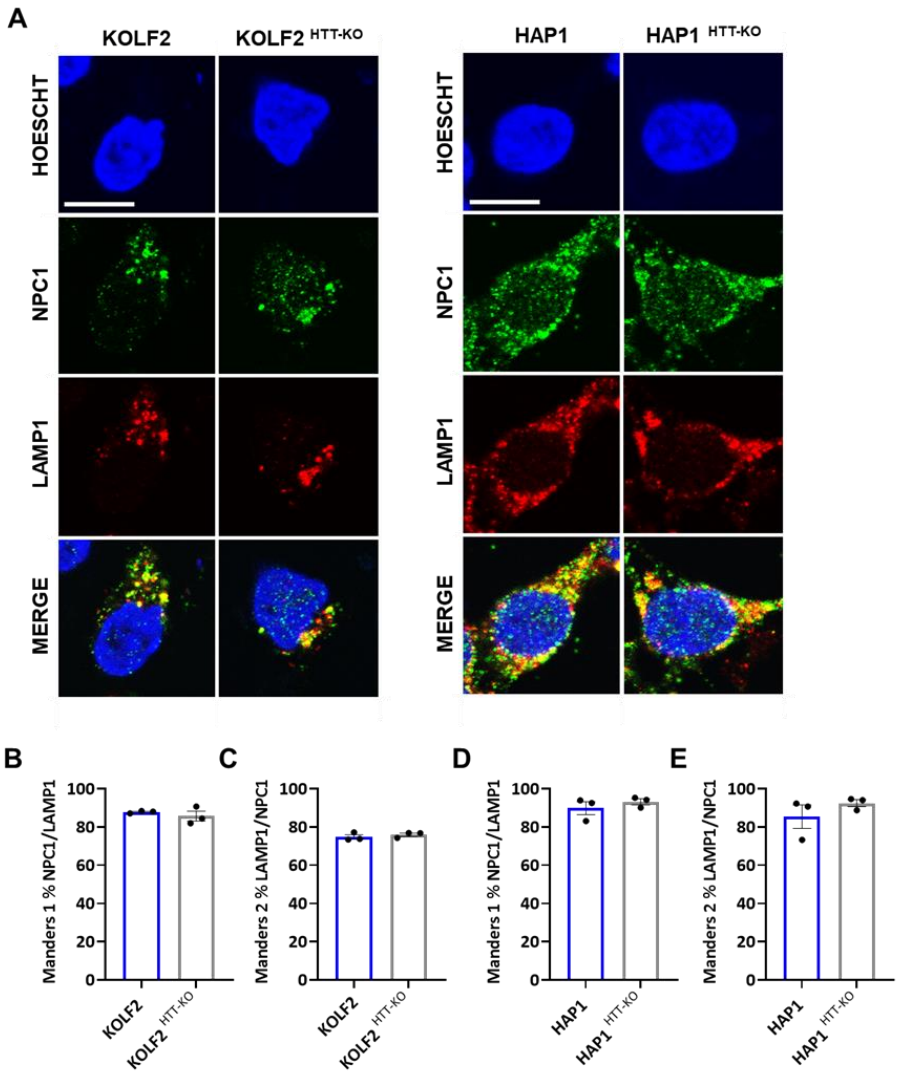

Figure 4.7. NPC1 colocalizes with LAMP1 in wildtype and knockout day 16 KOLF2 NPCS AND HAP1 cells. A) Confocal imaging of NPC1 and LAMP1 immunofluorescence reveals similar localization of NPC1 to the lysosome in KOLF2 neural progenitors and HAP1 cells B) Manders' colocalization coefficient indicating the percent of NPC1 positive pixels (green) that localize to LAMP1 positive pixels (red). C) Manders' colocalization coefficient indicating the percent of LAMP1 positive pixels that localize to NPC1 positive pixels. D) Manders' colocalization coefficient indicating the percent of NPC1 positive pixels that localize to NPC1 positive pixels. E) Manders colocalization coefficient indicating the percent of LAMP1 positive pixels that localize to NPC1 positive pixels. Results indicate no significant differences corresponding to the state of HTT with regards to NPC1 overlap with LAMP1 or vice versa. Unpaired two-tailed t-test; n = 3 technical replicates (technical replicates are defined as the average Manders' coefficients from 9-14 fields of view analyzed per well); total fields of view analyzed per genotype: KOLF2 = 29, KOLF2 HTT-KO = 34, HAP1 = 30, and HAP1 HTT-KO = 28. Bars represent mean the Manders' coefficient ± SEM for each cell line and black circles represent the mean Manders' coefficient per well. Scale bar = 10 µm.

To further investigate the spatial organization of NPC1, the same cells were used to determine NPC1 overlap with NPC2 (Figures 4.6A and 4.7A). In patient-derived NPCs, HD109s and HTT-knockouts displayed similarly high levels of NPC1 colocalization to NPC2 positive locations (86.4 to 94%) with no significant differences from the isogenic wtHTT (Figure 4.6B). In the other direction, NPC2 localization to NPC1 positive positions occurred at lower frequencies than NPC1 to NPC2 (55.4 to 80.6%), which is evidenced by a substantial population of red spots (Figure 4.6A). However, no significant differences were detected in association with mHTT or HTT knockout (Figure 4.6C). The results obtained from the HD patient HTT knockouts were paralleled in the KOLF2 and HAP1 lines (Figures 4.7A). M1, or NPC1 localization to NPC2 positive pixels, was slightly greater than M2, or NPC2 localization to NPC1 positive pixels, though neither M1 nor M2 significantly differed in either KOLF2 or HAP1 cells, in the absence of HTT (Figures 4.7B - 4.7E). Considering the 3 biological replicates collectively, M1 was compared, and the presence or absence of HTT accounted for only 0.3349% of the variance, and this effect was nonsignificant (Two-way ANOVA; Biological Replicate, $F_{(2, 14)} = 7.249$, P=0.0069; HTT Status, $F_{(1, 14)} = 0.09577$, P=0.7615). Similar results were obtained when comparing M2, as presence or absence of HTT only accounted for 0.05619 of the total variance (Two-way ANOVA; Biological Replicate, $F_{(2, 14)} = 12.26$, P=0.0008; HTT Status, $F_{(1, 14)} = 0.02166$, P=0.8851). In sum, these data agree with previous research to show that NPC1 colocalizes with NPC2 (Du et al. 2012), and further suggest that the presence, absence, or mutation of HTT, does not alter the colocalization of NPC1 with NPC2 positive lysosomes.

The comparable levels of colocalization of NPC1 to LAMP1 or NPC2 positive vesicles demonstrated here, suggest at the minimum that HTT is not indispensable to NPC1 trafficking to the LE/lysosomal membrane. At a more fundamental level the images indicate that most NPC1 localizes to LAMP1 or to NPC2 positive vesicles, and that most LAMP1 or NPC2 is localized to NPC1 positive regions.

It should be noted however, that while conducting these experiments, an optical section slightly greater than 1.0 µm was used, and lysosomes are generally smaller than this (roughly 0.1 to 1.2 µm in diameter). As such, it is conceivable that the images would contain sections

that displayed adjacent or overlapping organelles, which might produce a positively colocalized pixel, when in reality it could be two organelles positioned on top of one another, especially in lysosome dense regions. That being said, similar colocalization experiments carried out by Garver et al. (2008), used a single optical section estimated to be 1.0 µm, and observed striking differences in NPC1 and LAMP1 colocalization in fibroblasts, thus establishing that differences can be observed at this level of resolution. However, the optical section is higher than the resolution at Abbe's physical limits of light; at the lowest wavelength used here (488), using a 63x oil immersion lens with a NA of 1.4, and a refraction index of 1.51, this would equal 161.58 nm and at the highest wavelength (647), this would equal 214.23 nm. Thus, in order to increase the precision, it would be advisable to repeat this experiment using either Z-stacks or super resolution confocal microscopy.

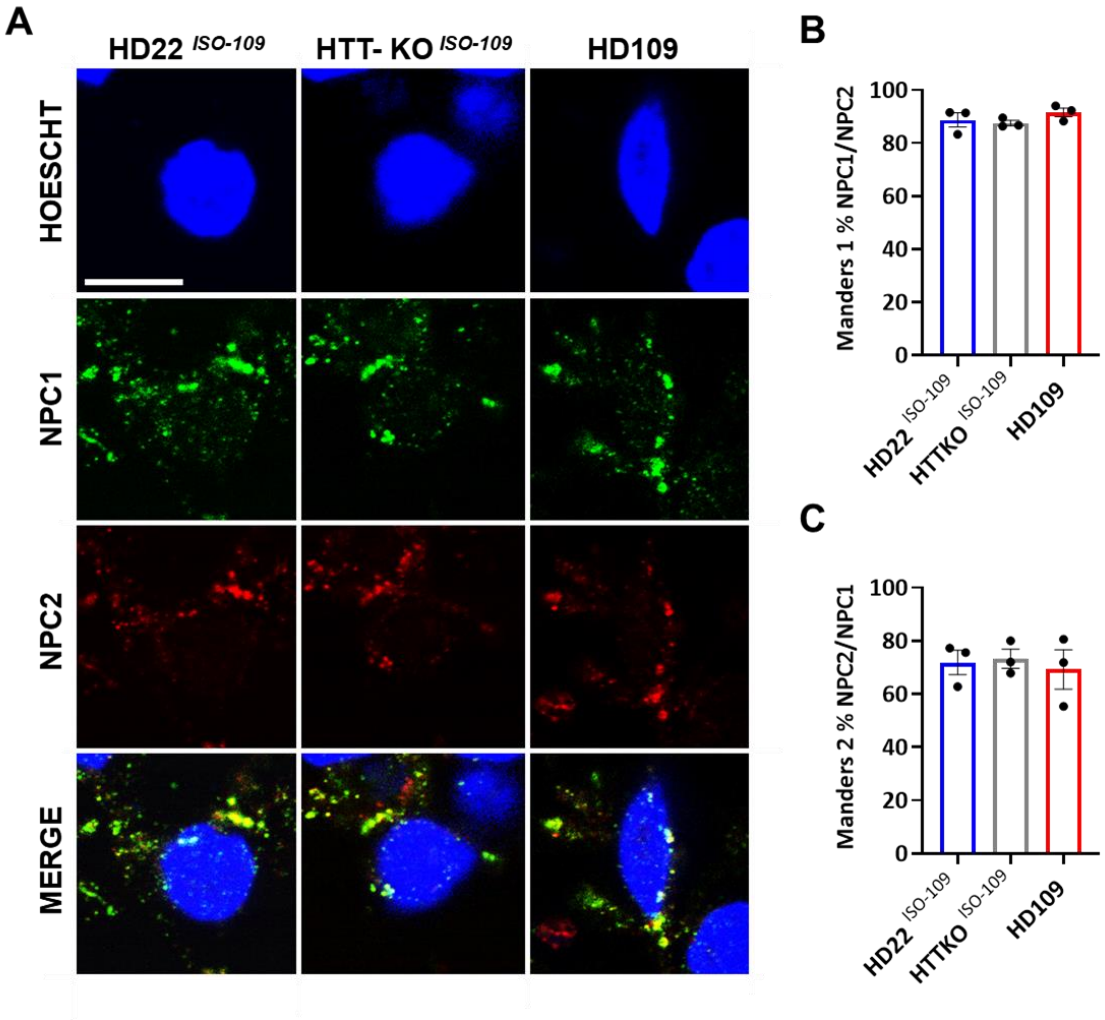

Figure 4.8. NPC1 colocalizes with NPC2 in day 16 HD109, isogenic, and knockout NPCs. A) Confocal imaging of NPC1 and NPC2 immunofluorescence, reveals similar colocalization in isogenic wtHTT, mHTT, and HTT knockout neural progenitor cells. B) Manders' colocalization coefficient indicating the percent of NPC1 positive pixels (green) that localize to NPC2 positive pixels (red). C) Manders' colocalization coefficient indicating the percent of LAMP1 positive pixels that localize to NPC1 positive pixels. Results indicate no significant differences corresponding to the state of HTT with regards to NPC1 overlap with NPC2 or vice versa. One-way ANOVA with Tukey's multiple comparisons test; n = 3 technical replicates (technical replicates are defined as the average Manders' coefficients from 10 fields of view analyzed per well); total fields of view analyzed per genotype: HD22ISO-109 = 30 HTTKOISO-109 = 30, and HD109 = 30. Bars represent mean the Manders' coefficient ± SEM for each cell line and black circles represent the mean Manders' coefficient per well. Scale bar = 10 µm.

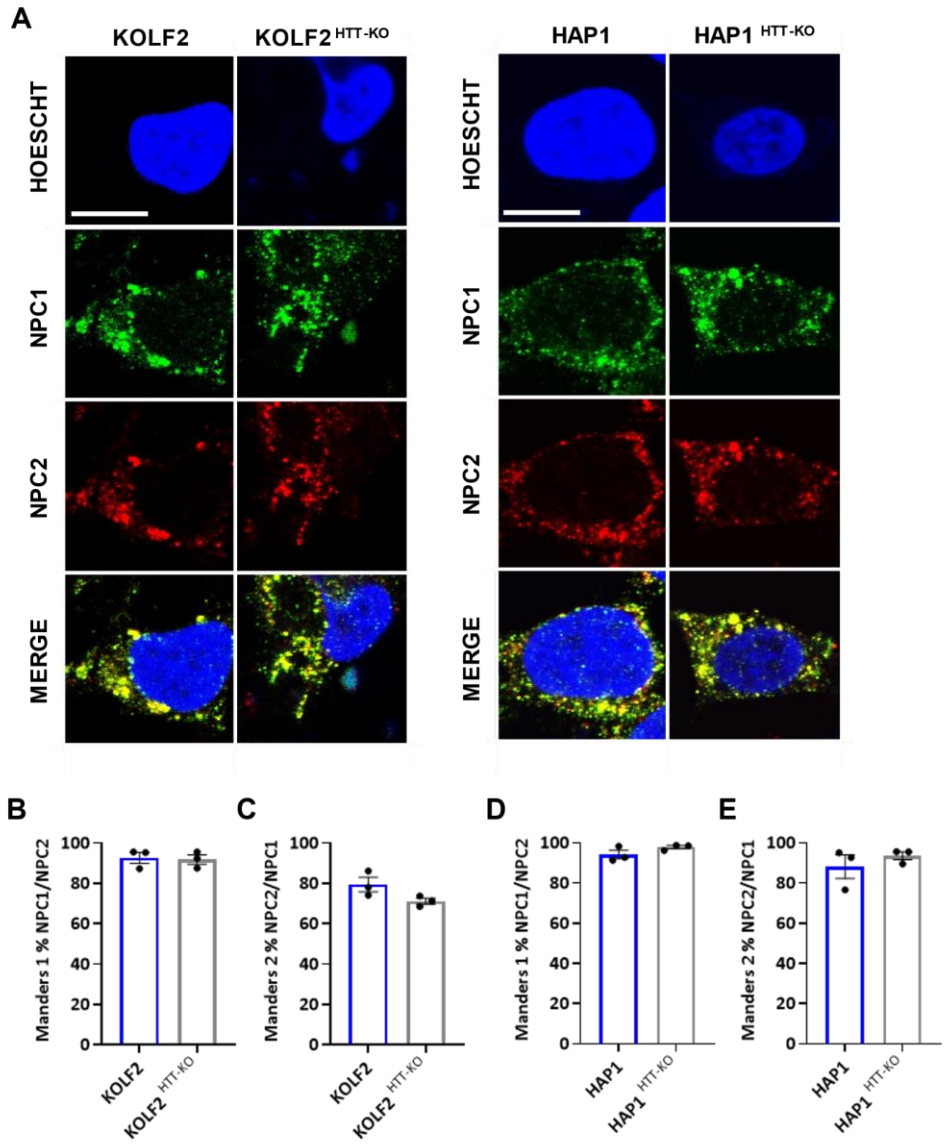

Figure 4.9. NPC1 colocalizes with NPC2 in wildtype and knockout day 16 KOLF2 NPCS AND HAP1 cells. A) Confocal imaging of NPC1 and NPC2 immunofluorescence reveals similar colocalization in KOLF2 neural progenitors and HAP1 cells B) Manders' colocalization coefficient indicating the percent of NPC1 positive pixels (green) that colocalize to NPC2 positive pixels (red). C) Manders' colocalization coefficient indicating the percent of NPC2 positive pixels that colocalize to NPC1 positive pixels. D) Manders' colocalization indicating the percent of NPC1 colocalization to NPC2 positive pixels. E) Manders' colocalization coefficient indicating the percent of NPC2 colocalization to NPC1 positive pixels. F) Manders' colocalization coefficient indicating the percent of NPC2 positive pixels that localize to NPC1 positive pixels. Results indicate that there were no significant differences corresponding to the state of HTT with regards to NPC1 overlap with NPC2 or vice versa. Unpaired two-tailed t-test; n = 3 technical replicates (technical replicates are defined as the average Manders' coefficients from 9-14 fields of view analyzed per well); total fields of view analyzed per genotype: KOLF2 = 27, KOLF2HTT-KO = 33, HAP1 = 29, and HAPHTT-KO = 29. Bars represent mean the Manders' coefficient ± SEM for each cell line and black circles represent the mean Manders' coefficient per well. Scale bar = 10 µm.

4.3.1.5 Autophagy in day 16 NPCs is altered with mHTT and HTT knockout

To assess expansion of the autophagosomal compartment, cells, treated with CYTO-ID and Hoechst, were imaged confocally on the Opera Phenix with a 63x objective, in a Z-stack of six planes spanning 0.0 to 5.0 µm. Maximum projections of stacked images were then imported into image J for organelle area measurement as described in Cook et al. (2020a). Cells were cultured in starvation conditions for 4 hours to induce autophagy, and predominantly macroautophagy, as this is the most prevalent form during the initial 4 to 6 hours of starvation (Mizushima et al. 2008).

At basal levels, while the mean area of autophagy-related vesicles in HD109s was higher than what was observed in the isogenic controls, this was not significant. However, there was a significant increase seen in HTT knockouts relative to the isogenic $HD22^{ISO\text{-}109}$ controls (Figure 4.10A and 4.10B). The trend toward increased levels of basal autophagy seen in HD109 NPCs is in accordance with earlier reports, and might be due to gain of mHTT function, e.g., inhibition of mTOR kinase. However, further increases seen in the HTT knockouts suggest a potential loss of HTT function. In HD, this could arise through loss of wildtype function in the mutant allele, or potentially a dominant-negative effect exerted by mHTT, and which might explain the differences in magnitude observed between these two lines. As the presence of a single functioning wildtype in the HD109s, might have resulted in levels intermediate between the isogenic controls and knockouts. Alternatively, mHTT and HTT knockout-associated increases might have arisen through unrelated mechanisms. As a next step, repeating this experiment using heterozygous huntingtin knockouts, that were identified when generating the double knockouts used in this thesis (though not discussed), could be useful. If increased levels of basal autophagy were associated with a pure loss of wildtype function, then, the presence of a single wildtype allele, might resemble what was observed here in the HD109s, while cells carrying only a single mutant allele, might phenocopy the double HTT knockouts. It would also be valuable to expand on these results by the addition of a lysosomal antibody to clarify the degree of co-labelling with CYTO-ID to assess the levels of fused autolysophagosomes, and in this way the question of loss of HTT function towards

fusion could be approached, as one would expect decreased colocalization in these two probes, if fusion defects were present.

In response to starvation, both the isogenic and HD109 lines showed significant increases in CYTO-ID area when compared to non-starved conditions; this increase was not observed in the HTT knockouts (Figure 4.10A and 4.10B). The increases observed in the isogenic controls and the limited response seen in the knockouts parallels what was reported in *Drosophila* models by Ochaba et al. (2014). The HD109 cells also exhibited significant increases due to starvation, though basal levels were already higher than what was observed in the isogenic controls, which suggests that nonselective autophagy is functional, perhaps because of the presence of wtHTT.

To summarize, the increases in constitutive autophagy correspond with previous research into NP-C and HD, and while overlapping phenotypes were observed, the presence of a common underlying mechanism was not ascertainable within the scope of this experiment. The increased basal autophagy observed in the HTT knockouts could potentially be related to NPC1 mistrafficking, and more direct experiments, for example, costaining with NPC1 and CYTO-ID might be revealing. Moreover, the resulting defects could be due to altered lipid content that arises in both diseases, as altered lipid content inhibits fusion in autophagic vacuoles (Koga et al. 2010), which might increase vacuole counts; altered lipid content is certainly a downstream phenotype associated with NPC1 dysfunction and this is seen in our HD and HD knockout NPCs, which supports the argument for a loss of function associated with mHTT. Finally, it should be mentioned that images for CYTO-ID in the KOLF2 and HAP1 cell lines, are available, though due to time constraints, these images were not quantified in this thesis.

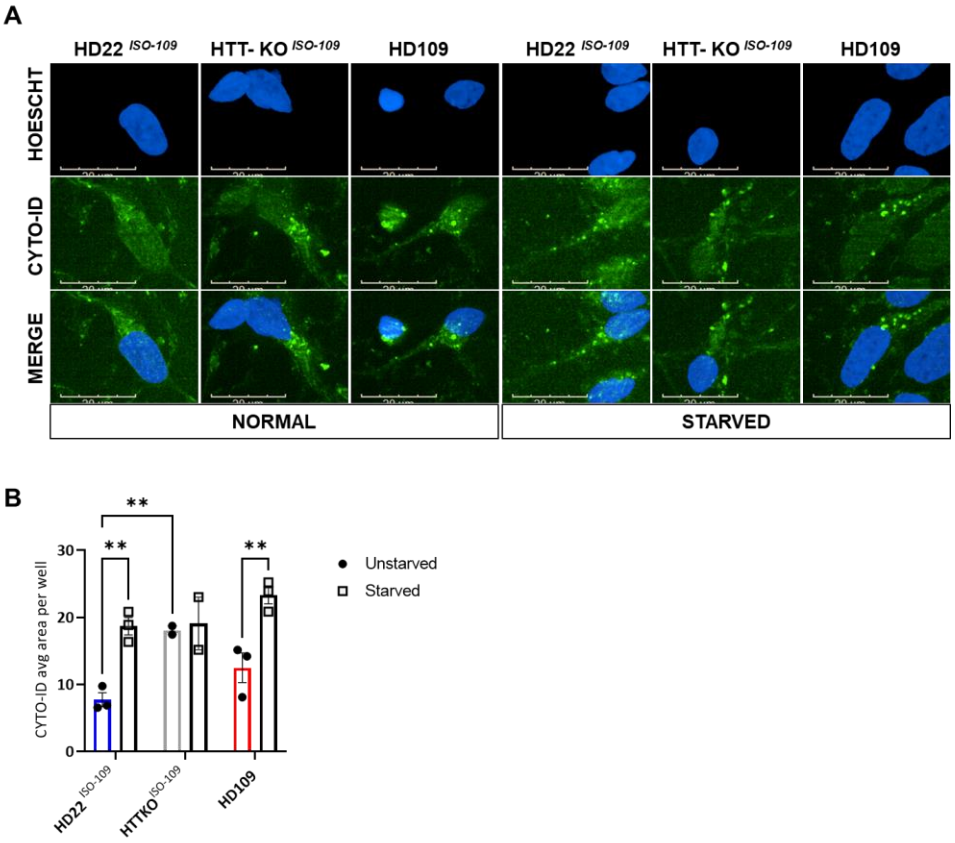

Figure 4.10 Area comparisons of CYTO-ID differ in HD patient-derived neural progenitors. A) Day 16 NPCs stained with CYTO-ID were used to measure the intracellular area of autophagic vacuoles per cell using ImageJ. B) Average cellular area positive for CYTO-ID for isogenic controls, HTT knockouts, and HD109s. Two-way ANOVA with Benjamini, Krieger and Yekutieli post-hoc; Cell line: $F(2,10) = 5.395$, $p = 0.0257$; Starvation: $F(1, 10) = 25.62$, $p = 0.0005$; Interaction: $F(2,10) = 4.205$, $p = 0.0473$. N = 3 differentiations, n = 3 technical replicates (wells), 21 - 37 cells measured per well. Total cells measured: $HD22^{ISO-109} = 543$, $HTTKO^{ISO-109} = 383$, HD109 = 515. Bars represent mean cellular area ± SEM for each cell line and black circles represent the mean cellular area per differentiation. Asterisks indicate significant differences; *p ≤ 0.05, ** p ≤ 0.01, ***p ≤ 0.001, ****p ≤ 0.0001. Scale bar = 20 µm.

4.3.1.6 Mitochondrial length is decreased with mHTT and improved with miglustat in day 18 NPCs

To examine mitochondrial structure in HD and the effects of miglustat, we stained HD109 and HD22$^{ISO-109}$ day 18 NPCs, that had been grown with or without miglustat, with Mitotracker CMTM-ROS, imaged them on the Opera Phenix (Figure 4.11A), and calculated characteristics of mitochondrial morphology using Harmony software (Perkin Elmer). This software includes the PhenoLOGIC machine-learning platform to allow for the automated selection of an optimized cell population for subsequent comparisons, based on a multidimensional regression model composed of multiple linear coefficients that are determined through an interactive, training-based algorithm. Essentially, this allowed for the automated exclusion of dead cells, debris, multinucleated cells, and non-progenitor cells, which could confound the results. This method was chosen as an alternative to manual measurements, because it allows for the comparison of a larger number of cells in a shorter time, in a documented manner that is transparent and reproducible.

We first compared the average area of individual mitochondria in the isogenic controls with the HD109 cells, and as expected this was higher in the isogenic controls (data not shown), which suggests that mitochondrial fragmentation was higher in the HD109s. Next, because area is a function of length and width, length was examined and found to be reduced, though not significantly in HD109s (Figure 4.11), while there was no difference in mitochondrial width (data not shown), which further corroborates previous results to support the increase in mitochondrial fission present in HD models. We then compared the mitochondrial area and length of miglustat-treated HD109s with the isogenic controls, to determine if treatment might ameliorate mHTT-related fragmentation, and correspondingly observed that the differences in both variables were reduced as the mean length of HD109 neurons was increased with miglustat (Figure 4.11).

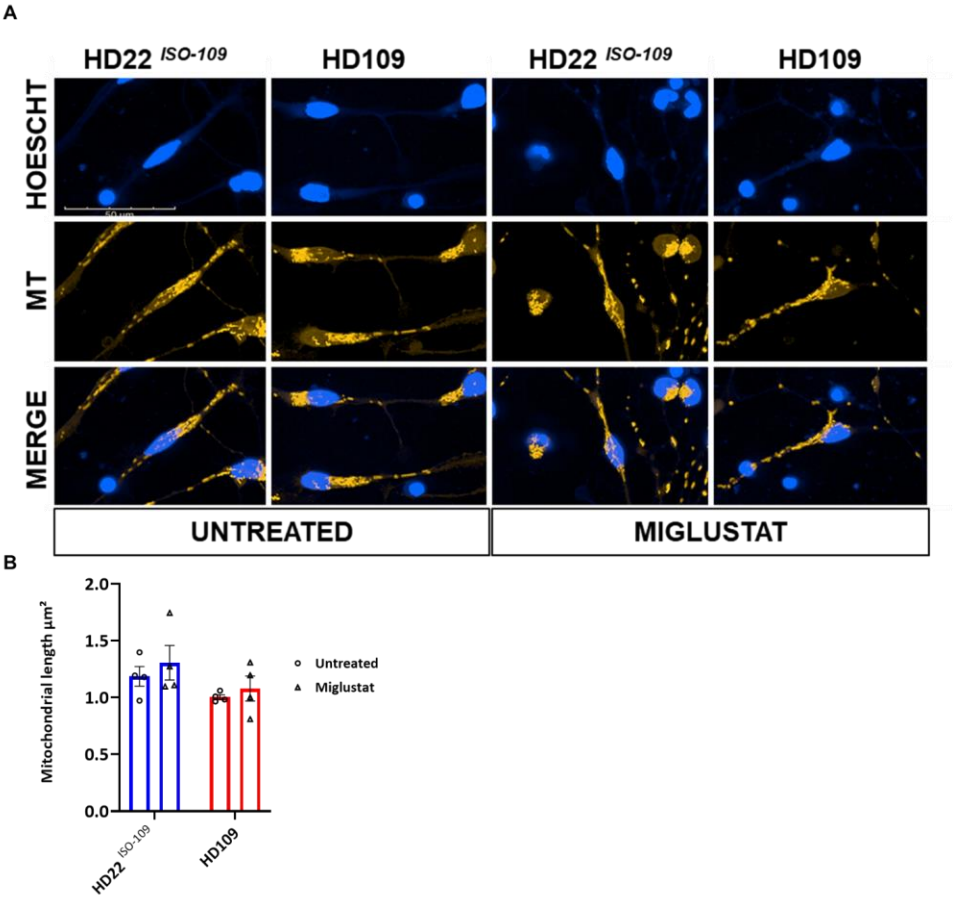

Figure 4.11. Mitochondrial length trends down in HD109 cells. A) Mitotracker CMTM-ROS staining of isogenic and HD109 day 18 NPCs, with and without miglustat treatment were compared using Harmony software. B) Comparisons of mitochondrial length. Mitochondrial length in untreated HD109s trended lower than the isogenic controls; Miglustat treatment increased mitochondrial length but was nonsignificant: Two-way ANOVA; Cell line: F (1, 12) = 3.860, p = 0.0730; Treatment: F (1,12) = 0.8758, p = 0.3678; Interaction: (F,12) 0.0473, p = 0.3678. Total cells measured (B-D) per condition: $HD22^{ISO-109}$ = 3607, HD109 = 1433, HD109 + miglustat = 1208. N = 4 pools/plates, n = 3 technical replicates (wells), 20 fields of view measured per well. Bars represent mean ± SEM for each cell line and black circles represent the mean per well. Asterisks indicate significant differences; *p ≤ 0.05. Scale bar = 50 µm.

4.3.2 Neuronal models of HD

In this section, because of the fundamental differences between dividing cells and post-mitotic neurons (described in Chapter 1.10), structural comparisons were carried out in neurons, to identify possible differences in endolysosomal and autophagic structure. Moreover, because of the putative link between NP-C an HD, and because it remains the only approved therapy for NP-C disease, and rescues several of the LSD phenotypes associated with NPC1 dysfunction, the effects of miglustat-treatment (summarized in Chapter 1.5) on HD neurons were also compared.

4.3.2.1 LAMP1 area in neurons is increased with mHTT and LBPA is unchanged

To assess changes in the LE/lysosomal compartments, day 42 neurons were stained with antibodies against LAMP1 and LBPA, measurements were taken using the method outlined in Cook et al. (2020a), and LAMP1 and LBPA areas, as well as the ratio of LAMP1 to LBPA were compared. The ratio of LAMP1 to LBPA was considered as well, because differences here might signal a shift in the composition of the intracellular vesicle population. Moreover, because no differences were seen in progenitor cells, and because increases in both markers have been reported in multiple models of HD and NP-C, U18666A was added to the isogenic controls, to serve as a positive control by inducing an NP-C phenotype.

LAMP1 area was significantly increased in HD109 cells as well as in the positive controls (Figures 4.12A and 4.12B), which is consistent with previous reports. Moreover, lysosomal expansion occurring in the HD109 neurons was similar to what was seen in the U18666A-treated, positive controls. General increases observed in LBPA area in HD109s, however, were not significant (Figure 4.12C). It is noteworthy, that LBPA area in the positive controls, also yielded nonsignificant increases, which suggests that an increased LBPA area might not have been a strong or detectable phenotype to assay in our cells. Thirdly, the ratio of LAMP1 to LBPA area did not differ in HD109s (Figure 4.12D), though it is notable that in the HD109s there appeared to be less overlap between the two probes, with increased number of LBPA positive structures that do not overlap with LAMP1 positive structures. This was also observed previously in our lab (Clark 2017) and though this has not been quantified it could indicate dysfunctional trafficking, reduced LE/lysosomal fusion, altered maturation in the LE

or lysosomal compartment, and/or the presence of a unique population of organelles in HD. Though this analysis was not carried forward in this thesis, it might be worth revisiting this data to assess colocalization of LAMP1 and LBPA.

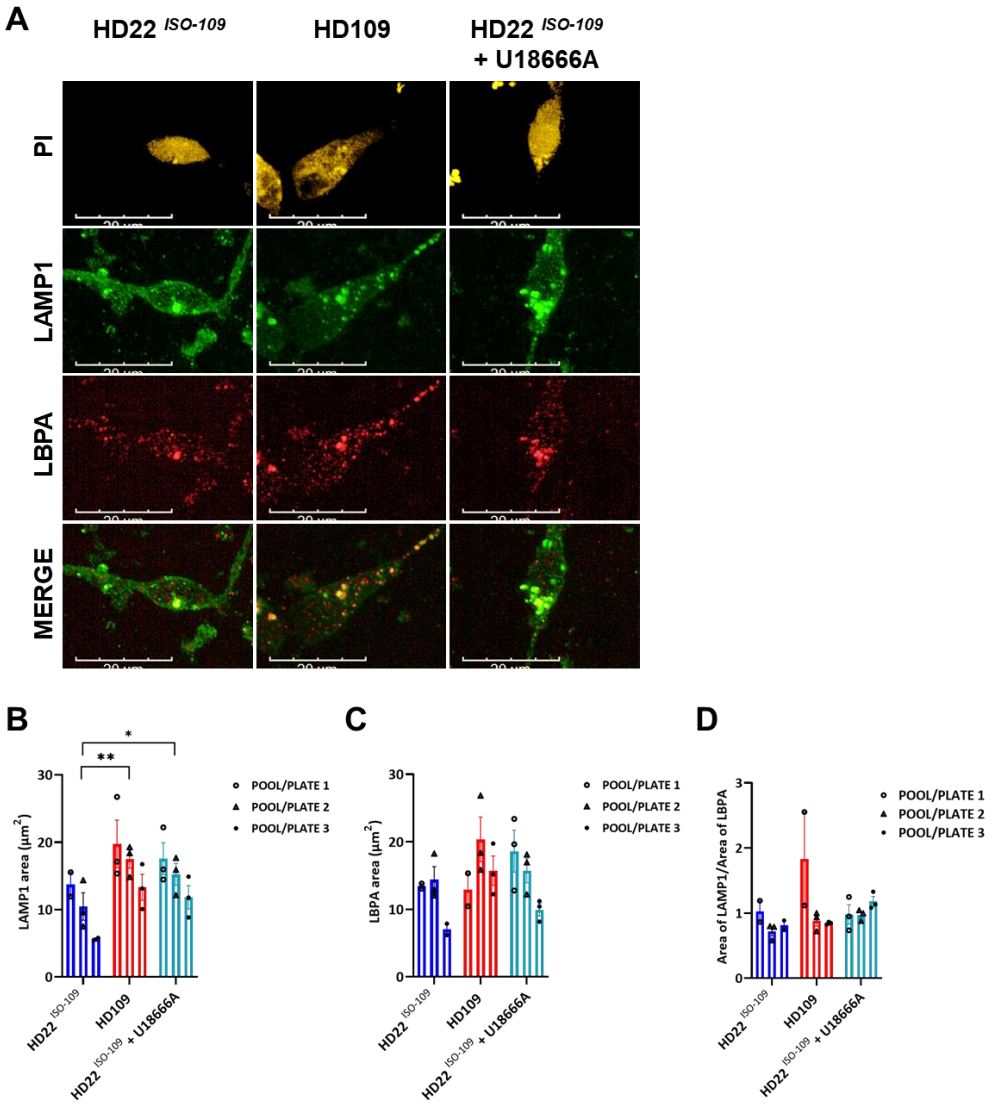

Figure 4.12. Area comparisons of LAMP1 and LBPA in HD patient-derived neurons. A) Day 42 neurons stained with antibodies against LAMP1 and LBPA were used to estimate lysosomal or LE/MVB area, using ImageJ software. B) LAMP1 area was increased in HD109, and wildtypes treated with U18666A. Two-way ANOVA with Tukey's multiple comparisons test; Cell line: $F(2, 20) = 9.083$, $p = 0.0016$; Pool/Plate: $F(2,20) = 8.325$. $p = 0.0023$. C) Area of LBPA staining trended higher, though not significantly, in HD109 cells versus wildtypes. Two-way ANOVA with Tukey's multiple comparisons test; Cell line: $F(2, 19) = 2.976$, $p = 0.0751$; Pool/Plate: $F(2,19) = 4.427$, $p = 0.0264$. D) Ratio of LAMP1 to LBPA across wildtype, HD, and drug-treated wildtype neurons was not significantly different (Two-way ANOVA with Tukey's multiple comparisons test; Cell line: $F(2, 19) = 1.183$, $p = 0.3280$; Pool/Plate: $F(2,19) = 2.301$. $p = 0.1274$). Total cells measured (B-D) per condition: HD22ISO-109 = 109, HD109 = 275, HD22ISO-109+ U18666A = 115. N = 3 pools/plates, n = 3 technical replicates (wells), 5-36 cells measured per well. Bars represent mean cellular area ± SEM for each cell line and black circles represent the mean cellular area per well. Asterisks indicate significant differences *$p \leq 0.05$, **$p \leq 0.01$. Scale bar = 20 µm.

4.3.2.2 Area of autophagic compartments is not altered by mHTT or miglustat in HD neurons

Because of previous reports in NP-C and HD models, as well as in our progenitor models, we hypothesized that an accumulation of autophagic vesicles would be observed in HD109 neurons (day 36) when compared to the corrected isogenic controls, which would result in an increased area. In addition, we wanted to observe the effects of miglustat treatment on these models, because mHTT-associated NPC1 dysfunction might produce a similar result, to what was reported by Hovakimyan et al. (2013). However, because in that study, though the substrate was altered from a predominantly electron dense, to an electron-lucent material, the miglustat-treated neurons still possessed autophagosomes. Therefore, it was unclear whether a phenotype would be observable using CYTO-ID. Though if defective autophagic flux was a secondary event to lysosomal storage due to mHTT or mHTT-associated disruptions to NPC1 in HD, then we might expect that a miglustat-mediated rescue in the lysosome, would promote clearance in the autophagic lysosomal pathway, resulting in a measurable decreased autophagosome area.

To measure this, NPCs were matured for 8 days in SJA and 12 days in SJB medium, with the addition of lipid concentrate and 50 µM miglustat for the final 7 days prior to CYTO-ID treatment. Neurons were then fixed and imaged at 63x on the Opera Phenix with a Z-stack spanning 5 µm at 1 µm intervals, and area was measured using the method outlined in Cook et al. (2020a).

No significant differences in autophagocytic vesicle area were observed between the isogenic controls and the HD109s (Figure 4.13A and 4.13B). Which does not conform to previous reports. However, while other groups evidenced increased autophagic vesicle counts in NP-C and HD neuronal models, area is a different metric, and therefore to clarify whether vesicle numbers might differ while overall area remains static, it would be necessary to revisit this data and perform counts.

Treatment with miglustat, also produced nonsignificant differences (Figures 4.13A and 4.13B). However, both cell lines exhibited an overall trend towards reduced area, as a

response to miglustat treatment. This result indicates that perhaps more investigation would be useful, as it appears that there might be a biological effect occurring. On top of revisiting the images and counting vacuoles, it might also be worthwhile to quantify protein levels of LC3I to examine potential increases associated with autophagy induction and LC3II to assess whether accumulation, which could indicate an obstacle to degradation, is occurring.

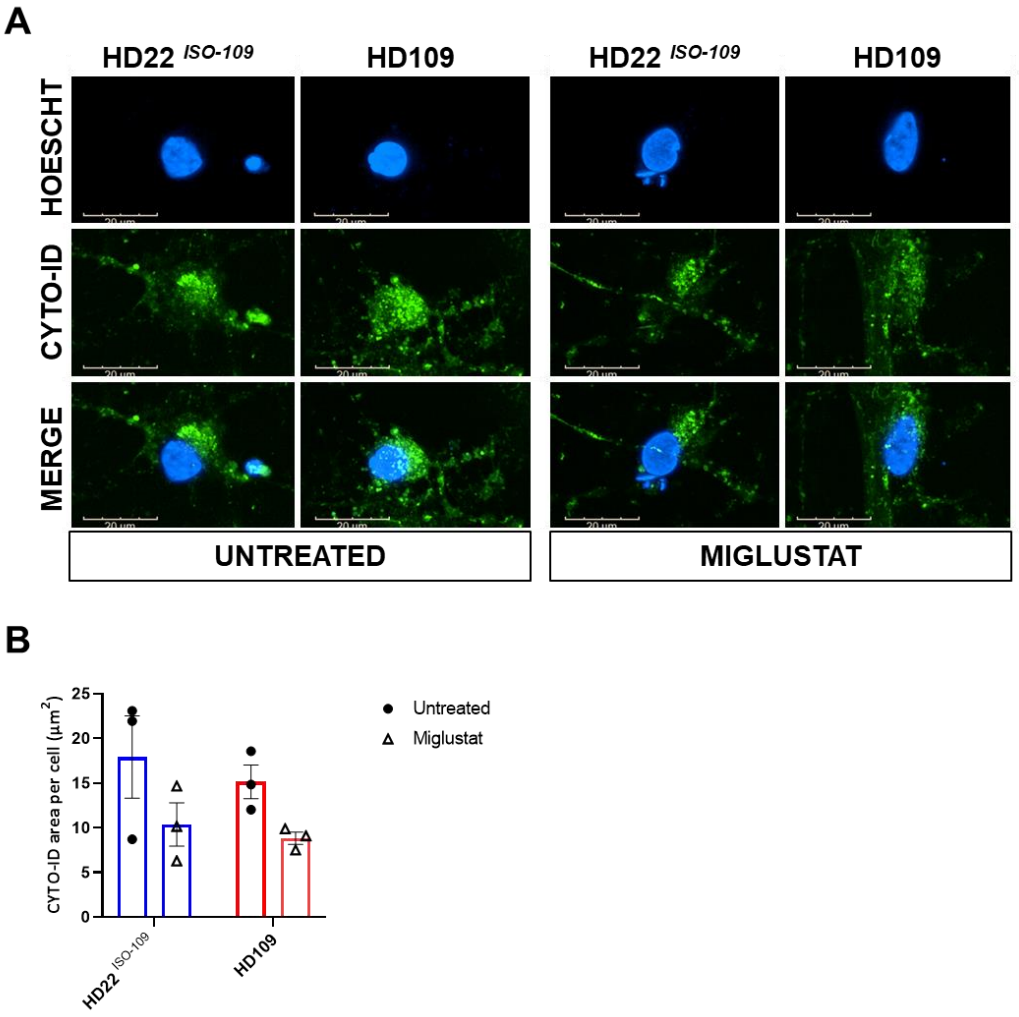

Figure 4.13. CYTO-ID Area in HD109 and isogenic neurons. A) Day 36 neurons stained with CYTO-ID were used to measure the intracellular area of autophagic vacuoles, using ImageJ. B) B) Comparisons of Cyto-ID area in isogenic controls and HD109 neurons both with and without treatment with Miglustat treatment: Two-way ANOVA; Cell line: F (1, 8) = 0.5985, p = 0.4614; Treatment: F (1, 8) = 6.151, p = 0.0381; Interaction: F (1, 8), p = 0.8308. Total cells measured per condition: $HD22^{ISO-109}$ = 159, HD109 = 172, $HD22^{ISO-109}$ + miglustat = 151, HD109 + miglustat = 170. N = 3 pools/plates, n = 3 technical replicates (wells), 8-30 cells measured per well. Bars represent mean cellular area ± SEM for each cell line and black circles represent the mean cellular area per differentiation. Scale bar = 20 µm.

4.3.3 Ultrastructural comparisons and miglustat treatment

Next, we aimed to utilize TEM to examine vesicle storage morphologies. However, because images were comprised mainly of incomplete cells, the comparison of total vesicles per cell was not possible. Moreover, because cells were not immunolabeled, there was no way to ascertain the composition of the accumulated substrate. Therefore, vesicle storage was categorized according to substrate morphology, and the proportion of each vesicle type, relative to the total number of visible vesicles present in each cell, were then averaged across each well, and then compared. This was done to identify possible differences associated with mHTT or HTT knockout, to survey potential convergent phenotypes shared between HD and NP-C, and to examine the effects of miglustat treatment on storage in HD109s and their isogenic counterparts.

First, the most common types of vesicle storage were identified and categorized. We observed four main categories of vesicle storage morphology: fingerprint bodies or curvilinear bodies (Table 4.1; Figures 4.14A and 4.14B) resembling those found in NCL, zebra-like whorls of concentric rings resembling ganglioside storage found in the gangliosidoses (Table 4.1, Figure 4.14C), and empty or low-density storage vacuoles (Table 4.1; Figure 4.14D. and 4.16). As there was no way to verify the species of ganglioside, or whether for example a fingerprint or curvilinear structure was an ATP synthase subunit, or saposin or some other substance entirely, and because fingerprint and curvilinear structures often occur concurrently, we decided to define and categorize our vesicles into two main groups. "NCL-like storage" was comprised of vesicles displaying curvilinear or fingerprint morphologies, while vesicles that contained rounded, concentric, lamellar whorls were placed into the "ganglioside storage" category.

To obtain a general overview, we combined vesicles belonging to both the NCL-like and the ganglioside categories and compared the frequency with which total storage occurred across the treatments (Figure 4.15A) However, while HD109 cells exhibited an increased fraction of total vesicles with storage, this was nonsignificant when compared to the isogenic controls and the HTT knockouts. Additionally, no differences were found in between the KOLF2 wildtype in relation to the KOLF2$^{HTT\text{-}KO}$ versions (data not shown).

We then compared the frequency of vesicles exhibiting an NCL-like storage. Similar to what was observed regarding total storage proportions, though the HD109 cells again displayed a greater average percentage of vesicles with an NCL-like phenotype compared to the isogenic controls or knockouts, this was not significant (Figure 4.15B). This increase, while nonsignificant, corresponds with previous reports from mouse mHTT knock-in striatal cells with autophagic vacuoles possessing fingerprint profiles, suggesting altered lysosomal and autophagic activity (Del Toro et al. 2009). Comparisons between KOLF2 HTT wildtype and HTT knockout neurons also produced no differences (data not shown).

Vesicles containing lipid whorls indicative of ganglioside storage, were also compared and the frequency with which these vesicles were distributed did not differ across the HD patient-derived lines (Figures 4.14C and 4.15C). The same was seen in the KOLF2 neurons (data not shown).

The knockout of huntingtin did not lead to detectable differences in overall, NCL-like, or ganglioside storage when compared with the wildtype (Figure 4.15) and these results do not provide evidence to support our hypothesis that HTT is acting through a loss of function mechanism, especially one that is detrimental to NPC1 function.

We observed a number of structures that resembled MVBs, which was in accordance with what was reported in prior studies, and which was shown to vary with disease progression (Sapp et al. 1997; Aronin et al. 1999; Zhou et al. 2021). However, statistical interpretation was not possible, as there were not enough data points to compare differences across our samples in a meaningful way.

Significant differences were, however, observed in HD109 and isogenic control cells that were treated for 7 days with 50 µM miglustat (Figure 4.15). The proportion of vesicles exhibiting storage, was significantly reduced in treated HD109, and treated isogenic control cells (Figure 4.15A). The frequency of NCL-like storage was also reduced in miglustat-treated HD109s and isogenic controls when compared to their untreated counterparts (Figure 4.15B). In addition to an increased fraction of empty vesicles in the miglustat-treated cells, were vesicles that appeared to contain a less-dense material (Figures 4.14D and 4.16B).

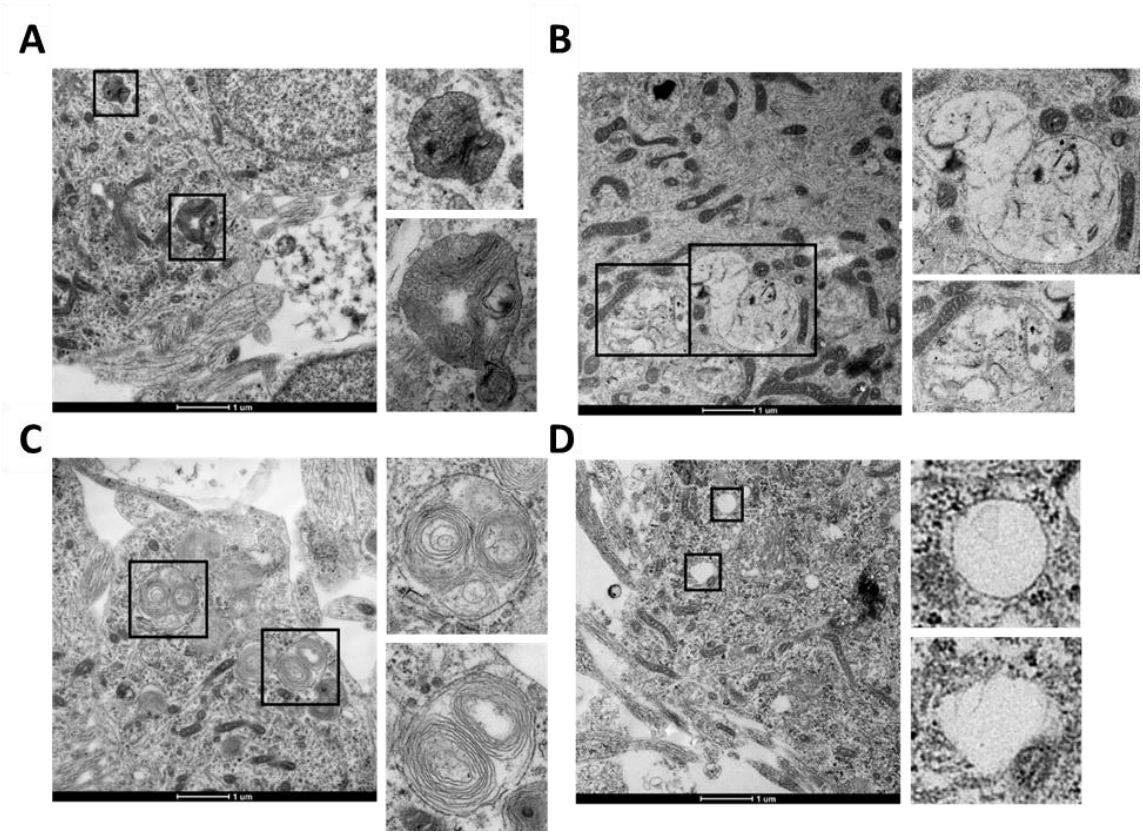

Figure 4.14. Common storage phenotypes in day 32 and day 47 MSN models of HD. A) Fingerprint bodies and B) Curvilinear bodies similar to those found in neuronal ceroid-lipofuscinoses (NCL). C) Ganglioside storage, similar to what is seen in GM1-gangliosidosis and Tay-Sachs disease. D) Empty vacuoles (note vesicle shading is similar to the background) Representative pictures shown. Cells were imaged on a FEI Tecnai 12 BioTwin Spirit TEM.

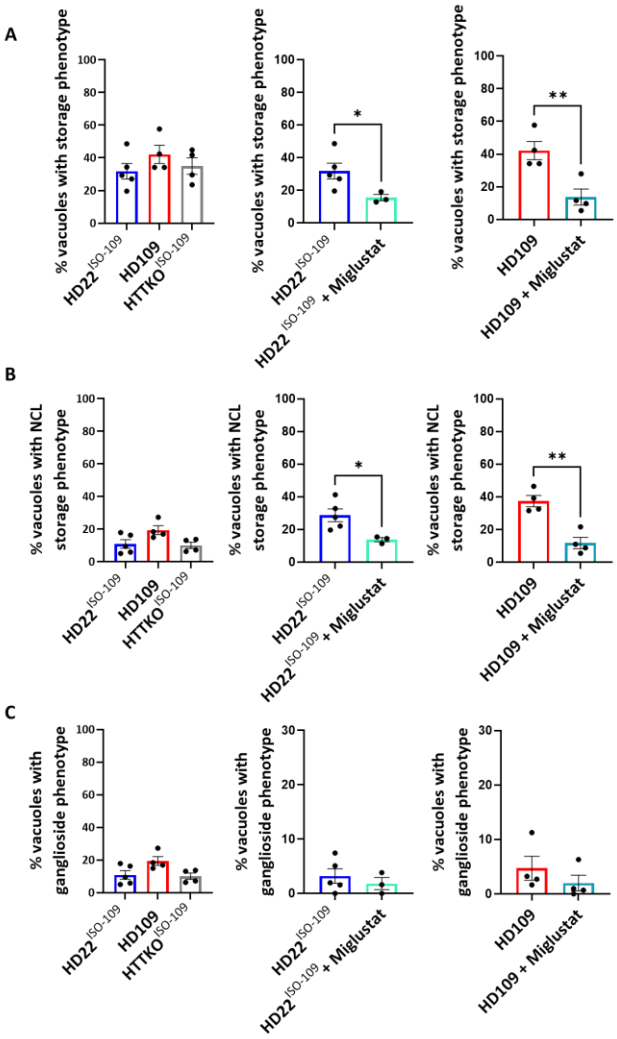

Figure 4.15 Percentages of vacuoles exhibiting storage in day 32 and day 47 neurons is not altered by HTT status but are reduced with the addition of miglustat. A) Total percent of vacuoles containing NCL-like or ganglioside storage did not differ in HD109, isogenics, or knockouts (left); One-way ANOVA with Tukey's multiple comparisons test. Storage in isogenics was decreased with miglustat treatment (middle); unpaired t-test, p = 0.0481. Storage in HD109s was decreased with miglustat treatment (right); unpaired t-test, p = 0.0086. B) Percent of vesicles with NCL-like storage did not differ in HD109, isogenics, or knockouts (left); One-way ANOVA with Tukey's multiple comparisons test. Storage in isogenics was decreased with miglustat treatment (middle); unpaired t-test, p = 0.0020. Storage in HD109s was decreased with miglustat treatment (right), unpaired t-test, p = 0.0086. C) Percent of vesicles with ganglioside storage did not differ in HD109, isogenics, or knockouts (left); One-way ANOVA with Tukey's multiple comparisons test. Ganglioside storage in isogenics was not altered with miglustat (middle); unpaired t-test, p = 0.5061. Ganglioside storage in HD109s was not altered with miglustat (right); unpaired t-test, p = 0.3426. Total cells and vacuoles measured per condition: HD22ISO-109 = 34 cells and 373 vacuoles, HD109 = 28 cells and 519 vacuoles, HD22ISO-109+ miglustat = 34 cells and 391 vacuoles, HD109 + miglustat = 30 cells and 742 vacuoles. N = 3 - 5 individual differentiations per treatment. Bars represent mean percentage of total vesicles ± SEM for each cell line and black circles represent the mean percentage of total vesicles per well. Asterisks indicate significant differences; *p ≤ 0.05, ** p ≤ 0.01.

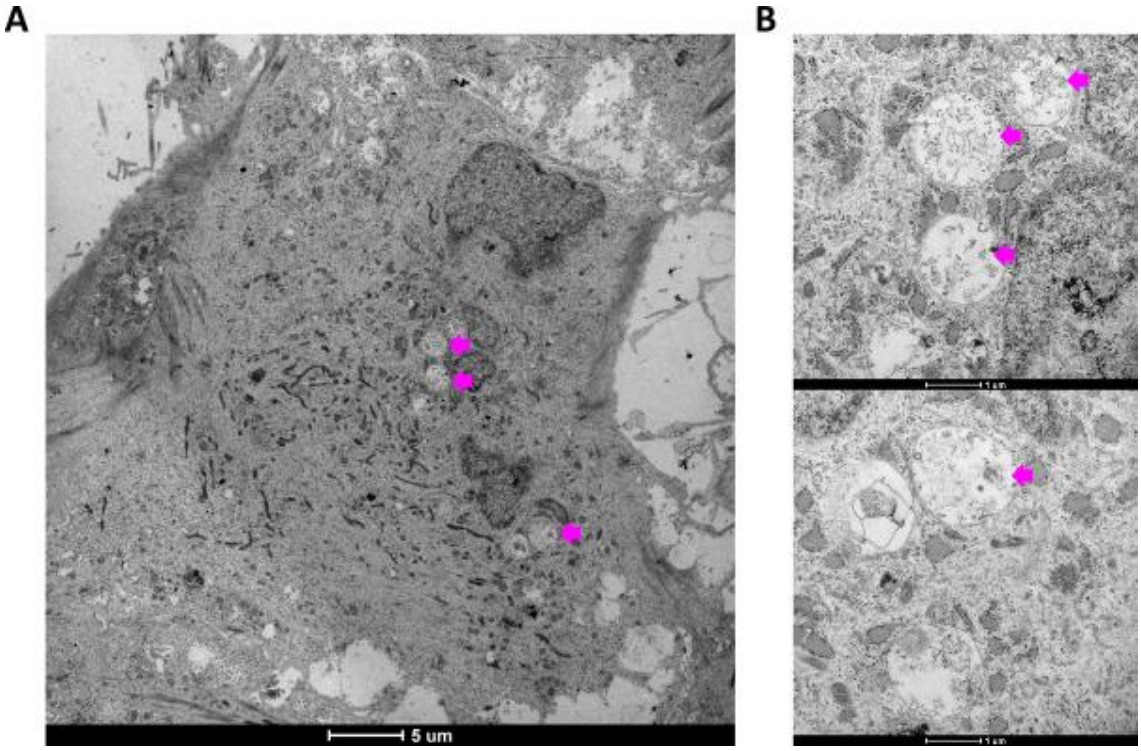

Figure 4.16 Representative images of storage observed in miglustat-treated neurons. A) Overview of the cell and storage vesicles (arrows). B) Under increased magnification diffuse granules can be seen which appear to be in loose aggregation inside vesicles (cyan arrows).

4.4 Discussion

Though a monogenic disease, the precise pathomechanism underlying neurodegeneration in HD remains unresolved. However, there is abundant evidence to suggest defects in the autophagy-endolysosomal system corresponding to altered structure and distribution of lysosomal and late endosomal vesicles (Kegel et al. 2000; Nagata et al. 2004; Camnasio et al. 2012; Castiglioni et al. 2012), an irregular autophagosomal compartment (Nagata et al. 2004; Del Toro et al. 2009; Martinez-Vicente et al. 2010; Martin et al. 2014; Ochaba et al. 2014), and fragmented mitochondria (Costa et al. 2010; Song et al. 2011; Haun et al. 2013; Wong and Holzbaur 2014; Manczak and Reddy 2015). As observed in the majority of lysosomal storage disorders, such defects associated are very often associated with neurodegeneration (Vitner et al. 2010; Cox and Cachon-Gonzalez 2012; Platt et al. 2018; Breiden and Sandhoff 2020). In particular, Schweitzer et al. (2009) and our research group

had previously identified commonalities between NP-C and HD, leading to the investigation of phenotypic similarities between the two diseases and the establishment of a direct link between NPC1 and both mutant and wildtype HTT proteins (Haslett 2015; Clark 2017). To expand on these findings, the HD models developed and discussed in Chapter 3 were examined for LSD phenotypes that are prominent in NP-C. However, a striking limitation of this thesis, and the investigation to commonalities between the two diseases, was the complete reliance on external data or treatment with U18666A, for phenotypes related to NP-C. It would have been worthwhile to generate a NPC1-mutant line from the $HD22^{ISO-109}$ iPSCs to enable direct comparisons.

To summarize the results (Table 4.2), these set of experiments indicate that while neural progenitor and neuronal models were not consistent, several LSD-related structural abnormalities resembling those reported in NP-C disease were present in models of HD. In NPCs, while LE/lysosomal area was not observed to be increased, nor were late endosomes or lysosomes differentially distributed, in HD neurons lysosomal area was increased in a manner similar to that observed in NP-C. Mitochondrial fragmentation was observed in HD progenitors and this phenotype was rescued with miglustat treatment. Autophagy was observed to be disrupted in HD109 and more so HTT knockout NPCs, though in neurons differences were not identified. Vesicle storage ultrastructure, was not observably altered due to the presence of mHTT or huntingtin knockout, though miglustat treatment did result in the increased fraction of vesicles with less-dense, electron-lucent lumens. Additionally, clarification into the proposed mechanistic explanation for the commonalities associated with NP-C and HD, namely that NPC1 trafficking to the LE/lysosomal membrane might be dependent on the proper functioning of wtHTT, was obtained through colocalization experiments indicating that NPC1 is not differentially localized to LAMP1, or NPC2 positive LE/lysosomal vesicles due to mHTT or HTT knockout. The implications of these results are considered in this section.

	NPCs		Neurons	
	HD109	Knockout	HD109	HD + Miglustat
LAMP1 area	≈	≈	↑	n/a
NPC1 area	≈	≈	n/a	n/a
NPC2 area	≈	≈	n/a	n/a
LBPA area	≈	≈	≈	≈
NPC1 and LAMP1 colocalization	≈	≈	n/a	n/a
NPC1 and NPC2 colocalizatation	≈	≈	n/a	n/a
Autophagic compartments	↑	↑↑	≈	≈
Autophagic compartments (starvation)	↑	≈	≈	≈
TEM: total storage	n/a	n/a	≈	↓
TEM: NCL-like storage	n/a	n/a	≈	↓
TEM: ganglioside storage	n/a	n/a	≈	≈
	HD109	HD + Miglustat		
Mitochondrial area	↓	≈	n/a	n/a
Mitochondrial length	↓	≈	n/a	n/a
MItochondrial width	≈	≈	n/a	n/a

Table 4.2. Summarized results of structural comparisons HD109 and HTT knockouts relative to isogenic controls. A highly significant increase is denoted by ↑↑, significant increase is indicated by ↑, no measurable difference is represented with ≈, and n/a indicates that no results were obtained.

4.4.1 HD neurons, but not NPCs, exhibit endolysosomal expansion

Expanded area of endolysosomal vesicles, as measured by LAMP1, NPC1, NPC2, and LBPA was not observed in HD109 or HTTKO$^{ISO-109}$ patient-derived NPCs (Figures 4.1). However, while the late-endosomal lipid, LBPA, was not increased in HD109 neurons, LAMP1 area was (Figure 4.10), and both probes matched what was observed in the U18666A-treated HD22$^{ISO-109}$ neurons, which served as a positive control by phenocopying NP-C disease.

The absence of LAMP1 expansion observed in HD109 NPCs, conforms to a previous report in HD STHdh (Q120) mouse striatal neuronal progenitors (Clark 2017), and suggests that perhaps in less mature, dividing cells, the expansion of LAMP1 positive compartment is not occurring, or if it is, it is not a pronounced phenotype. This result also conforms to

immunoblotting quantifications of LAMP1 in HD (Q111) mouse fibroblasts (with and without serum) and lysosomes isolated from mouse liver (Koga et al. 2011), and STHdh (Q111) cells (Erie et al. 2015), as both groups failed to detect increased levels of LAMP1 protein, though these results would not necessarily prohibit increased (or decreased) LAMP1 area measurements. These results do initially, appear to contrast with lysosomal area increases as detected by Lysotracker staining, in NSCs (Q180) and HD ST14A (Q120) rat striatal NPCs (Haslett 2015), hiPSC-derived NPCs (Camnasio et al. 2012), mouse iPSCs (Castiglioni et al. 2012) and HD patient iPSC-derived NPCs (Q60) and (Q109) (Clark 2017). However, these discrepancies might be explained by fundamental differences in the two probes, as Lysotracker staining is reliant on acidic pH, while LAMP1 is a structural protein, and as such, both have been shown to incompletely colocalize in human hepatocytes and several other mammalian cell lines, to indicate the presence of non-overlapping vesicle populations (Miyagawa et al. 2016; Baba et al. 2020). Lysotracker staining was carried out on our NPC models, though this data has not yet been assessed, and therefore whether an expansion phenotype in the HD109s might have been more pronounced using this probe, is not known. The results of the LAMP1 staining experiment do sharply contrast with the lysosomal expansion seen in NP-C disease, as LAMP1 increases were reported in NP-C patient-derived iNSC models (Sung et al. 2017; Lee et al. 2020). Therefore, if there is a shared pathomechanism in HD and NP-C that causes lysosomal expansion, then the effects of this impairment on neuronal cells seem to be more prominent, earlier in development in NP-C. A limitation of this set of experiments was the lack of a NP-C phenocopy control, which should have been included in order to draw more robust conclusions. Additionally, as mentioned above, these experiments were underpowered, which was not unavoidable, however the experimental design was based on previous studies in which the effect size appeared to be extremely large. In any case, more replication would be required to compensate for the reduced effect size in NPCs before arriving at a conclusion. More robust conclusions, however, were ascertainable when observing the HTT knockouts, because there were three biological replicates available for comparison with matched wildtypes. No differences in LAMP1, NPC1, or NPC2, were observed in any of the three HTT knockout lines, and

correspondingly there is no indication that a HTT loss of function mechanism is involved in the cumulative expansion of the lysosomal compartment.

In HD109 neurons, lysosomal expansion was observed, as evidenced by increased LAMP1 area, and this was also seen in the U18666A-treated isogenic controls, which confirmed that the phenotype was discernible. These results are consistent with lysosomal expansion reported in other neuronal models of HD, as increased size and number of LAMP1-positive puncta (Pircs et al. 2021), increased Lysotracker area (Camnasio et al. 2012; Haslett 2015; Nekrasov et al. 2016), and LAMP2 staining (which included the HD109 neurons, used here)(Haslett 2015). Thus, these findings support the hypothesis that there is an endolysosomal defect occurring in HD neurons, and one that, when considered with the lack of LAMP1 increases observe in NPCs, might become more apparent with maturation.

LBPA the late endosomal marker, which is increased in NP-C brains (Rouser et al. 1968), was not increased in our HD109 NPCs, which contrasts with previous image analysis results in our lab, that showed increased LBPA levels in HD patient iPSC-derived NSCs (Q180), rat ST14A (Q120) cells, mouse STHdh (Q111) cells, and HD (Q60) and (Q180) patient fibroblasts (Haslett 2015; Clark 2017). The differences observed in NPCs here, when compared to animal or human fibroblast models used in these previous studies, might be explained by cell type or differences in model species. Accordingly, similar divergence was seen with contrasting results from TLC experiments in our lab, as increased cellular LBPA content reported in rat ST14A (Q120) cells and rat PC12 (Q145) cells (Haslett 2015), contrasted with a lack of differences observed in human HD patient NPC models (Q60) and (Q109) (Clark 2017). Thus, though TLC was not carried out in this thesis, it would have been useful to compare with these previous results. However, the species or cell type differences do not explain the lack of differences in LBPA fluorescence in the HD109 NPCs observed here, with the particularly striking increases in LBPA reported by Haslett (2015), when assaying (Q180) NSCs. Though this discrepancy, might be explained by the differences in polyQ length between the Q109 and Q180 cells, as perhaps a more severe mutation would result in a more severe phenotype. Finally, as HTT knockouts were not different from the isogenic controls, there was no evidence to suggest a loss of HTT function effect in this capacity.

LBPA area was also unchanged in HD109 neurons, which suggests that this lipid is not accumulating in our HD109 models, though the lack of increased LBPA in the U18666A-treated controls here is curious. Serum supplementation was shown to be important to U18666A-induced LBPA levels, which increased concomitantly with cholesterol in baby hamster kidney (BHK) cells, though only in the presence of serum supplementation with 5% FCS (Chevallier et al. 2008). U18666A-mediated LBPA expansion was seen in mouse STHdh and ST14A cells, both grown in medium supplemented the 10% FBS (Clark 2017). However, the reliability of U18666A towards eliciting this phenotype had previously been shown to be indefinite, as total cellular amounts of LBPA were not increased due to U18666A in HeLa cells cultured with 5% FCS (Lebrand et al. 2002). In any case, our neurons were grown in the presence of a chemically defined lipid concentrate which contains cholesterol and related lipids, and which is used as a serum replacement. However, perhaps this was insufficient to induce increased LBPA levels in our positive controls. During initial experiments, the lipid concentrate was lethal to cells at a 1:100 ratio and therefore it was reduced ten-fold to a 1:1000 ratio, and perhaps a titration between these two concentrations would have been useful to establish a working positive control, however, due to time constraints, this was not carried out here. Thus, though this data fails to provide evidence that the late endosomal compartment altered in HD, it could also indicate that the experimental design was insufficient to elicit the full range of phenotypes. If there is a lack of LBPA expansion, however, then that would suggest that while the LAMP1 positive lysosomal compartment is expanding, the late endosomal compartment is not, which could indicate a defect specific to the lysosome in HD neurons. This would then partially conform to the model outlined in Zhou et al. (2021), and accordingly, it might be interesting to stain for RAB7 (late endosomes) RAB11 (recycling endosomes) RAB7 and CD63 (exosomes) to test for a shift in the vesicle population in HD towards reduced exocytosis and towards autolysosome accumulation.

That lysosomal expansion was observed here, in neurons, while remaining unchanged in NPCs, highlights a potential advantage associated with the use of model cells that are analogous to the disease-affected cells, namely that disease phenotypes might be particular to the cell type that is most affected in the disease itself. To further clarify this assertion, it

would have been ideal to assess LAMP1 expansion in neurons positively labelled with DARPP32 and CTIP2, for subtype specific comparisons. Dividing NPCs and HAP1 cells also confer distinct advantages, though, as noted above, metabolic processes take on a more critical role in non-dividing cells (Malik et al. 2019). In contrast to neurons, NPCs and HAP1 cells require less manipulation and time in culture, which can allow for more consistent comparisons, as small initial differences often produce greater and unpredictable effects with time. Both NPCs and HAP1 cells have larger cell bodies than neurons, which makes it easier to visually inspect, and neither have long extensions or a propensity to form clusters, which can make visual screening of neurons difficult. To follow up these experiments, western blotting to determine total levels of LAMP1 would allow us to determine whether the expansion was due to the upregulation of lysosomal proteins, or whether if LAMP1 levels remained constant, the increased area was primarily a function of increased lysosomal volume. Additionally, an experiment to treat neurons with miglustat to compare rescue effects against lysosomal expansion, in these cell lines, should be pursued.

4.4.2 NPC1 and NPC2 area and distribution

Previous efforts in our lab have provided evidence to support a model whereby pathogenic changes in HD is mechanistically linked to the NPC1 and NPC2 proteins, which are necessary for proper lysosomal and late endosomal functioning and both of which, when dysfunctional, contribute to NP-C disease (Blom et al. 2003; Vanier 2015). NPC1 was shown to accumulate with polyQ length across a allelic series of Q33, Q60, and Q109 HD patient iPSC-derived neurons, though Q60 cells appeared to exhibit higher levels than the Q109s (Haslett 2015). NPC1 accumulation was also observed in HD ST14A (Q120) cells, though reductions were seen in Q180 NSCs, which suggested the potential for increased variability with expanded polyQ length (Haslett 2015). In STHdh cells, while immunocytochemistry and western blotting indicated that NPC1 protein levels remained unchanged, NPC2 levels were increased (Clark 2017). Moreover, both STHdh and ST14A cells displayed increased susceptibility to NPC1 inhibitors, and in sum, support an intrinsic deficit in NPC1 function in HD cells (Clark 2017). However, because many of these conclusions were based on a single replicate, and because of the defects later reported in HD STHdh cells (Singer et al. 2017), this was revisited

here. That the intracellular area of NPC1 remains unchanged in HD109 NPCs, corresponds with what was observed in the STHdh lines, however, this does not correspond to the increases reported in Q60 and Q109 HD neurons nor to the decreases observed in Q180 NSCs, though, as discussed above, these differences might be due to the differences in NPCs and neurons, or model species. NPC1 accumulation may, however, occur in association with increased polyQ length only to a limited extent. Correspondingly, as described above, neurons with a polyQ length of 60 exhibited higher levels of NPC1 than what was seen in the HD109s, and levels below the wildtype were seen in Q180 NSCs (Haslett 2015). Perhaps at a polyQ length of 109, the accumulation begins to reverse, producing no net change in NPC1 levels. It would be necessary to reassess NPC1 levels across several increments of polyQ length in a uniform cellular background, in order to draw a more robust conclusion as to whether NPC1 levels are altered in this way, though that was not carried out in this thesis. The lack of changes observed in NPC2 area in HD109 NPCs, conflicted with previous immunofluorescence and western blotting results (Haslett 2015; Clark 2017), however, this again, may also be due to species differences or the issues with the STHdh lines, and so immunoblotting for NPC1 and NPC2 would have been useful to quantify overall levels. Finally, the lack of differences seen in either protein associated with HTT knockout across three biological replicates, provides no indication of a loss of HTT function in this regard. In summary, though concrete conclusions as to a shared pathomechanism between HD and NP-C cannot be ascertained from these experiments, when taken together with previous results, they do raise the question of a curvilinear relationship between polyQ length and NPC1 levels that could be explored further.

Though conflicting reports of NPC1 accumulation or reductions remain unresolved, previous experiments in our lab provided evidence that NPC1 was abnormally distributed in HD, which would correspond to models of NP-C (Wheeler et al. 2019). In iPSC-derived NSCs (Q180), and ST14A (Q120) cells, NPC1 was found to be distributed largely to the perinuclear region (Haslett 2015). In STHdh cells, NPC1 was observed to be more punctately, and reticularly distributed, and excluded from large regions of the cell, with reduced localization to LBPA positive LE/lysosomes (Clark 2017). To add to these results, the area of NPC1-positive

staining in the perinuclear regions of our HD, isogenic, and knockout lines were measured, though no differences were observed. These results could be interpreted biologically to mean that the distribution of NPC1 positive vesicles is not altered by mHTT, nor by the absence of HTT, as might be expected if mHTT impaired NPC1 function by a gain of toxic function, dominant-negative effect, or by loss of HTT function. Thus, if these results are accurate, they are not consistent with accounts of the increased perinuclear distribution of NPC1, due to the presence of mHTT, as reported by Haslett (2015), nor are they suggestive of an NP-C phenotype in HD. It would have been worthwhile to also examine LAMP1 in the perinuclear region, to determine if the previous mislocalization reported in Erie et al. (2015) were reproducible in our lines; the images are available for this analysis, however, time was a limiting factor and this was not carried out. Moreover, treatment with U18666A, a positive control, which was shown to inhibit outward movements of NPC1 positive vesicles, thereby restricting them to the perinuclear region, to reproduce the NP-C phenotype (Ko et al. 2001), would have also been useful for comparison.

4.4.3 NPC1 colocalization with LAMP1 and NPC2

As mentioned above, co-immunoprecipitation experiments suggested a wtHTT link with NPC1, whether directly or in complex, which suggests a normal functional interaction. In addition, an interaction with mHTT was also observed, and this interaction was hypothesized to interfere with NPC1 localization to the lysosomal membrane, to explain NP-C phenotypes in HD. The results of the colocalization experiments here, add to these results, to suggest that though there might be a relationship between the proteins, that mHTT nor the absence of wtHTT prevent NPC1 from associating with the LAMP1-positive lysosome. These results contradict the hypothesis that through a gain of function, mHTT is sequestering NPC1 away from insertion into the LAMP1-positive lysosomal membrane. Moreover, because loss of wildtype function is also not preventing this, these results fail to provide evidence for an indispensable wildtype huntingtin function regarding NPC1 transport.

In this thesis, NPC1 was shown to be highly colocalized with LAMP1, and by extension LAMP1-positive vesicles, regardless of huntingtin genotype, and in comparable proportions as that described in the literature (Ohgane et al. 2013), especially when cells are grown in the

presence of LDL (Garver et al. 2008). Taken together with previous results in our lab showing that with mHTT, NPC1 localization to LBPA-positive vesicles is reduced, and that LBPA localization to LAMP1 is reduced (Clark 2017). This would then suggest that, in HD, the LBPA vesicle population is abnormally restricted from the LAMP1 and NPC1-positive population, which might indicate a block in trafficking or fusion at the late-endosome/lysosome interface, which is a characteristic of NP-C (Ko et al. 2001; Lloyd-Evans and Platt 2010). Because however, the previous results were obtained using STHdh cell lines which were shown to exhibit abnormalities (Singer et al. 2017), to confirm an altered distribution of LBPA, it would be necessary to, assess the colocalization of LAMP1, NPC1, and LBPA simultaneously, in our HD models.

NPC1 and NPC2 colocalization also was unchanged in response to mHTT or HTT knockout. Thus, these results fail to provide evidence of a role for gain-of-function with mHTT or a loss-of-function, associated with HTT knockout. When considered alongside the lack of NPC2 area increases observed in this thesis, these results do not conform to the suggestion of an NPC2-mediated compensatory mechanism, by upregulation, for NPC1 dysfunction in HD, that was based on increased NPC2 fluorescence observed in ST14A (Q120) cells (Haslett 2015), and by elevated NPC2 protein levels in STHdh cells (Clark 2017). One would expect that if NPC2 compensation and upregulation were occurring in our models, then either total NPC2 area would be increased, or if not, then in HD109 NPCs, NPC1 and NPC2 would colocalize less, to indicate the presence of a separate NPC2-positive vesicle population. Thus, western blotting to compare NPC1 and NPC2 in our NPC models, should carried out in order to further clarify these results, as changes in area might not reflect changes in overall protein content. These cells were grown in the presence of lipid concentrate which contains cholesterol, and in the presence of LDL-cholesterol, it was shown that NPC1 is recruited to RAB7 and RAB9-positive late endosomes, while NPC2 is localized mainly to cathepsin-D positive lysosomes and displays low (though unquantified) levels of colocalization with NPC1 (Zhang et al. 2003a). Thus, the high degree of colocalization between NPC2 and NPC1, observed here, is unexpected, though the differences in results could be cell-type specific, or particular to the lipid concentrate used here. To further clarify the dynamics between NPC1, NPC2, and mHTT,

additional staining and colocalization analyses against mHTT, cathepsin D (lysosomal hydrolase), RAB7 (late endosome), and RAB9 (late endosome), in the presence or absence of cholesterol, might be beneficial, and have been unexplored.

4.4.4 Autophagy

The increased basal autophagy as seen in the HD109 NPCs, is consistently reported in HD (Davies et al. 1997; Sapp et al. 1997; Kegel et al. 2000; Ravikumar et al. 2004; Del Toro et al. 2009; Camnasio et al. 2012; Nekrasov et al. 2016; Malankhanova et al. 2020; Pircs et al. 2021), and in NP-C (Ko et al. 2005; Pacheco et al. 2007; Ordonez et al. 2012; Sarkar et al. 2013), which might indicate the presence of a pathogenic mechanism common to both. Further increases, were also observed in the HTT knockouts, which conflicts with reports obtained using *Drosophila* models of HTT knockout (Ochaba et al. 2014), though these results are consistent with those obtained in human models where silencing both wildtype and mutant huntingtin alleles in HD patient iNs produced even further increases in LC3B (Pircs et al. 2021), thus these discrepancies may be related to the model organism. Because there is no mutant huntingtin in the HTT knockouts, these results suggest the presence of an alternative wildtype function separate to the autophagic upregulation that has been suggested to be a response to mHTT aggregate formation (Ravikumar et al. 2002; Qin et al. 2003; Qi et al. 2012) or due to mHTT-mediated inactivation of mTOR kinase (Kegel et al. 2000; Ravikumar et al. 2004). Because overexpression of full-length wtHTT failed to promote autophagosome synthesis in HD mouse models (Zheng et al. 2010), it is likely that this function is related to clearance.

Reductions in clearance, and accumulation due to HTT knockout might be explained by loss of HTT function as a scaffold for the dynein/dynactin/HAP1 complex, where HTT silencing was shown to interfere with autophagosome transport and autophagosome-lysosome fusion (Ravikumar et al. 2005; Wong and Holzbaur 2014). Loss of function, as was shown with HTT silencing, might also be related to delocalized optineurin/Rab8 which results in perturbations in post-Golgi trafficking to the lysosome, lysosomal dysfunction, and associated impaired autophagy (Del Toro et al. 2009). Basal autophagy in the HD109s was intermediate between the isogenic controls and the knockouts, which again, could suggest a role for wtHTT that is

diminished in HD, and perhaps by a dominant-negative effect associated with the ability of mHTT to sequester wtHTT into insoluble aggregates (Huang et al. 1998; Kazantsev et al. 1999; Narain et al. 1999; Preisinger et al. 1999; Wheeler et al. 2000; Zhang et al. 2009). With regards to the possible pathogenic overlap with NP-C, it would then seem possible that a shared pathomechanism might be related to trafficking or autophagosome-lysosomal fusion as these defects have been reported in NP-C as well (Ko et al. 2005; Pacheco et al. 2007; Sarkar et al. 2013). In summary, though the dynamics between loss of wildtype function and gain of toxic function in HD remain unclarified, in the context of autophagy, these results suggest the possibility of both mechanisms acting towards disruption.

Measurements of CYTO-ID area to determine the cellular capacity for the upregulation of starvation-induced macroautophagy indicated that, similar to the isogenic controls, the HD109 cells were responsive, while the HTT knockouts (though already displaying high levels of basal autophagy) did not exhibit any increase. That the knockouts exhibited a reduced response to starvation stress when compared to the isogenic controls, is in accordance with what was observed by Ochaba et al. (2014), and indicates an inhibited stress response associated with lack of HTT. If this is the case, however, and because this reduced response was not seen in the HD109 NPCs, it might indicate that a dominant-negative effect of mHTT was not sufficient to completely abrogate wildtype function, or that the presence of a single wildtype allele is sufficient to promote a starvation response.

In neurons, the HD109s did not exhibit increased autophagosomal area when compared with the isogenic controls, which conflicts with the general consensus (Camnasio et al. 2012; Malankhanova et al. 2020; Pircs et al. 2021). This was surprising because increased basal autophagy was observed in HD109 NPCs, and it was expected that this phenotype would be compounded in neurons. However, in both the isogenic controls and HD109s, the area of CYTO-ID during constitutive autophagy, was conspicuously elevated, and though neuronal cell bodies are smaller than those of NPCs, the neurons generally exhibited higher areas of CYTO-ID than the progenitors (Figures 4.10 and 4.13). This, therefore, might indicate that basal autophagy in the neurons was artificially elevated, and if so, this might have obscured comparisons. Such increases could have been caused by inhibitors present in the neuronal

medium. For example, CHIR-99021 used in the neuronal maturation medium, is an inhibitor of GSK-3β, which when inhibited, permits TFEB dephosphorylation, nuclear translocation and upregulation of the CLEAR signalling machinery, resulting in lysosome synthesis and increased autophagic flux (Zhang et al. 2022). Efforts to clarify the effects of factors involved in cell fate specification on assay outputs, therefore, might be worthwhile towards discerning between culture-related artifacts and actual disease-related phenotypes.

The effects of miglustat on autophagy in the neurons, were likely also confounded, though miglustat treatment was associated with slight (though not quite significant) reductions in CYTO-ID area in both the isogenic and HD neurons. This might suggest that miglustat acts in a manner to ameliorate autophagosome accumulation in HD, though repeating this experiment would be necessary before arriving at any conclusions. If, however, this were the case, the mechanism by which to explain an effect of miglustat on autophagy in HD is uncertain. Moreover, if autophagy is reduced with miglustat in HD, it is unclear how this would relate to a common pathogenic mechanism, shared between HD and NP-C, as miglustat did not rescue autophagic dysregulation in NP-C patient iPSC-derived progenitor models (Soga et al. 2015). However, cyclodextrin was shown to ameliorate autophagic defects in neuronal and fibroblast models of NP-C, by mobilization of lysosomal cholesterol (Ordonez et al. 2012) and as similar cholesterol reductions were seen with hydroxyl-propyl-β-cyclodextrin treatment in HD patient NCSs (Q180) and ST14A (Q120) cells, and by miglustat treatment in ST14A (Q120) cells (Haslett 2015), this might suggest a similar pathway whereby miglustat-mediated reductions in lysosomal cholesterol may increase autophagosome turnover, though this remains to be determined.

In these experiments, the addition of a repressor of basal autophagy such as chloroquine or hydroxychloroquine would have provided a crucial negative control, and an additional starvation condition, in the neurons, would have been beneficial for comparisons with NPCs, however, due, in part, to technical difficulties this could not be carried out, and correspondingly this experiment should be revisited. Furthermore, as CYTO-ID can detect an accumulation of autophagosomes, changes due to increased synthesis or reduced clearance cannot be determined through CYTO-ID staining, alone, thus this remains to be clarified. A

follow up experiment would be to substantiate these results through western blotting with LC3I and LC3II, to quantify the volumes of autophagosome membranes present in the cells. Moreover staining with anti-p62/SQSTM1 to determine whether selective autophagy is affected would be useful for comparison with results obtained by Ochaba et al. (2014), and perhaps to test whether exogenous expression of wtHTT could rescue the autophagic accumulation observed in the knockouts would provide more information regarding wildtype huntingtin function.

4.4.5 Mitochondrial fragmentation

The reductions in mitochondrial length observed in HD109 NPCs here, is consistent with reports of fragmented mitochondria in HD (Costa et al. 2010; Song et al. 2011; Shirendeb et al. 2012; Haun et al. 2013; Manczak and Reddy 2015), and has been suggested to arise due to dysfunctional mechanisms including imbalanced mitochondrial fission-fusion dynamics (Costa et al. 2010; Song et al. 2011) and diminished mitochondrial degradation due to defects in selective autophagy (Franco-Iborra et al. 2021). Similarly in NP-C, the accumulation of fragmented mitochondria is thought to arise due to mitochondrial defects and impairments in mitophagy (Ordonez et al. 2012).

The restoration of mitochondrial structure with miglustat treatment seen here, might arise from mechanisms similar to rescue effects reported with cyclodextrin administration in NP-C patient fibroblast and neurons, which by mobilization of cholesterol from the lysosomal compartment, potentially increased the available cholesterol pool for autophagosome assembly, or decreased the cholesterol load in the lysosomes to restore lysosomal function in mitophagy (Ordonez et al. 2012). Previous experiments in our lab evidenced reductions of elevated cholesterol levels in HD models by hydroxyl-propyl-β-cyclodextrin, in HD patient NCSs (Q180) and ST14A (Q120) cells, and by miglustat in, ST14A (Q120) cells (Haslett 2015). However, these outcomes were absent in later studies using HD patient NPCs (Q60 and Q109), which found no evidence for miglustat-mediated cholesterol reductions (Clark 2017). Thus, it is unclear whether a similar mechanism might explain the results here. Alternatively,

miglustat-mediated inhibition of glucosylceramide synthase, might be reducing primary lysosomal GSL storage and related secondary-storage lipids, promoting more efficient clearance of mitochondrial fragments during mitophagy, though this has not been studied. Furthermore, sphingolipid accumulation or even slight changes in mitochondrial membrane lipid composition, as was evidenced in PD patient mitochondria, can lead to disruptions in biophysical properties and signalling pathways (Schöndorf et al. 2018), and given the importance of sphingolipids in the regulation of mitochondrial properties (Morales et al. 2003), miglustat-mediated reductions in glycosphingolipid synthesis might be restoring mitochondrial membrane structure. These mechanisms and their connection to the miglustat-mediated reductions in mitochondrial fragmentation seen here, remain unexplored, though mitochondrial function in HD and in response to miglustat treatment is examined in Chapter 5. This experiment should next be repeated in neurons, and with additional cell lines. Importantly, this experiment should be optimized further by the addition of a live cell plasma membrane marker to more precisely define cellular boundaries using the Harmony software, which will aid in delineating long neuronal processes. PM labelling was attempted here using wheat germ agglutinin (WGA), however, this was unsuccessful because WGA also adhered to the Matrigel basement membrane coating, which negated its usefulness.

4.4.6 TEM

That total vesicle and NCL-like storage in the HD109s lacked a clear and significant difference when compared to the corrected versions was unexpected. Previous studies, in our lab as well as others, have recorded changes in the properties associated with endolysosomal vesicles e.g., increased size, increased intensity, punctate arrangement (Del Toro et al. 2009; Camnasio et al. 2012; Castiglioni et al. 2012; Erie et al. 2015; Haslett 2015; Nekrasov et al. 2016; Clark 2017; Pircs et al. 2021). Thus, from these studies it was postulated that a corresponding increase in the proportion of vesicles containing undegraded substrate, would occur. This was not the case, and could be because total vesicle counts per cell did not differ in the HD109 neurons when compared to the isogenic controls, or, if the total number of vesicles per cell had increased, then quantity of vesicles that exhibited substrate

accumulation had not equivalently increased. Therefore, because total vesicle counts per cell were not obtainable in these samples, exactly how this data aligns with previous studies is inconclusive. It should, however, be noted that in the frequency of storage vesicles was higher on average in the HD109s, which could indicate an increase that was undetected, perhaps due to variability and/or small effect size. The next step, now that the effect size can be determined, would be to variability for this by repeating the experiment with increased replicates. Additionally, acquiring images that encompass a complete section through the cell body would also be beneficial.

Though the limitations described above apply throughout this experiment, the lack of differences observed in the frequency of vesicles containing whorled substrate suggestive of ganglioside storage differed from the ganglioside reductions reported in HD caudate samples (Desplats et al. 2007a). They do however correspond to a more recent report, where in human cerebellar samples, overall ganglioside content and distribution were found to be similar in HD and controls, while a singular exception, ganglioside GM1, was increased (Denny et al. 2010). Differences have been reported with regards to subcellular localization of particular ganglioside species and, in hindsight, staining our samples for these would have allowed us to gather information with increased resolution and to better assess phenotypic overlap with NP-C disease.

In the HTT knockout neurons, no differences in overall, NCL-like, or ganglioside storage was observed here that could be associated with loss of HTT function. To our knowledge, though there have been no other studies in which neuronal ultrastructure was interrogated in response to HTT knockout in human models, knockout mouse models point to huntingtin's critical role in early development, though, its necessity later in life remains debatable (Duyao et al. 1995; Nasir et al. 1995b; Zeitlin et al. 1995; Liu and Zeitlin 2017). Beyond the experimental limitations that might explain our lack of results, the consequences of HTT knockout, especially in human culture models, likely differs from that seen during early mouse development. Accordingly, the earliest emergence of TUJ1-positive cells occurs on day (E)8.5 (Easter et al. 1993), and Hdh null mice die between days (E)8.5 and (E)10 (Duyao

et al. 1995; Nasir et al. 1995a; Zeitlin et al. 1995), which could indicate a link, however, Hdh null embryos become significantly underdeveloped, disorganized, with higher levels of apoptotic cells by day E(7.5), indicating that defects associated with HTT knockout occur prior to the presence of neurons. As such, if during the differentiation process cells were lost by a similar mechanism, then this would not have been detectible in this experiment.

Recently, in HD patient-derived iN models, HTT silencing corresponded with an increase in autophagosomal membrane marker LC3 (Pircs et al. 2021), thus it could be predicted that an increased number of autophagic vesicles containing storage material might also be increased. However, though autophagic membrane markers may be elevated, this does not necessarily coincide with increased storage, as HD94 and STHdh (Q111) mice, and human HD lymphoblast cells, displayed increased numbers of empty autophagosomes, thought to arise from defective cargo loading (Martinez-Vicente et al. 2010). If the increases in empty autophagosomes in these models, were associated with a loss of wildtype function then this might explain the lack of vesicle storage seen in both the HD109 and HTT knockouts here. However, this could not be concluded as it was not possible to precisely distinguish nor to determine the quantity of autophagic vacuoles present in our samples.

The presence of MVB-like structures though not statistically comparable, was observed in HD109 and HTT knockout neurons and was also seen in previous studies (Sapp et al. 1997; Aronin et al. 1999; Zhou et al. 2021). Based on these studies, an increase in frequency associated with HD or a difference possibly in the HTT knockouts might be expected. However, though these results remain inconclusive and electron microscopy provided only evidence confirming that MVB-like structures were visible; any statistical analysis would require a much larger sample size for each condition.

Reduction in the fraction of vesicles that contained storage was observed in miglustat-treated HD109 and isogenic control lines alongside an increase in vesicles that contained a less-dense, electron lucent substrate. These results were consistent those described in a previous study using HL-60 cells, in which enlarged secretory vesicles, that were empty or contained low-density contents were upregulated with miglustat treatment (Neises et al.

1997). The appearance of these electron-lucent, 'ghost-like' vesicles were also reported in Purkinje neurons, upon combination therapy with cyclodextrin, allopregnanolone, and miglustat, in NPC1 null mice (Hovakimyan et al. 2013). These results might be explained by miglustat-mediated substrate reduction, increased clearance, increased production of these electron-lucent vesicles, or by some other mechanism. Since miglustat inhibits glycosphingolipid biosynthesis at the first step, it would suggest that a reduction in glycosphingolipid production might be responsible for differences that we observed. However, due to the sharp angles at which the whorls of the fingerprint structures fold back upon themselves, the NCL-like storage, in particular, suggested a protein-based origin (in contrast, lipids form more obtuse and rounded patterns), which would imply that most storage is unrelated to GSL synthesis, and that perhaps the underlying mechanism would be increased clearance, or vesicle synthesis. Thus, a closer inspection of the storage materials in NCL itself, may hint at an explanation.

NCL accumulation consists of mitochondrial ATP synthase subunit C and ceroid lipopigments, which are not directly reliant on glucosylceramide production. Ceroid lipopigments are composed of ceroid and lipofuscin, the latter of which is an amalgamation of cross-linked macromolecules that cannot be degraded or exocytosed, because of its polymeric and highly cross-linked character (Moreno-García et al. 2018). Thus, if the vesicular contents in our models are similar, increased clearance does not seem to be a likely explanation. However, lipofuscin accumulation in *Drosophila*, was proposed to have occurred due imbalances in ceramide and sphingosine during early-stage neurodegeneration, and reduced ceramide biosynthesis was linked to lipofuscin accumulation in mouse Purkinje cells, indicating a potential link (Zhao et al. 2011; Hebbar et al. 2017). Moreover, irregular sphingolipid-protein interactions have been linked to neurodegeneration and while wildtype HTT fragments were shown to associate with phospholipids at the plasma membrane, mHTT aberrantly localized to intracellular regions (Kegel et al. 2005; Piccinini et al. 2010). This gives rise to the possibility, that a variation of this type of accumulation, may be what we observed and what was reduced by miglustat treatment, though it is unclear why these reductions were observed isogenic control cell lines.

Identification of the storage material composition in vesicles in miglustat-treated versus untreated vesicles would be essential to clarifying this and perhaps a follow up lysosomal purification and subsequent proteomics and lipidomics, would be valuable to assess proportional changes in the lumenal contents of the LE/lysosome in HD neurons, similar to what was done with NPC1 knockout HeLa cells in Tharkeshwar et al. (2017).

To briefly summarize, no differences were observed due to the state of huntingtin (mutant, isogenic-corrected, or knockout), however, miglustat did significantly reduce the proportion of vesicles which contained dense storage materials, though whether this was due to an increase in clear vesicles, or a reduction in existing storage remains unresolved. There are a number of possible explanations for the lack differences observed throughout these experiments. One explanation might be the lack of propensity in these particular cell lines, or subclones, or both, to exhibit conspicuous differences. Another could be due to the discrepancy between differentiation periods, as some samples were fixed on day 32 and others on day 47, thereby introducing variability in neuronal maturation status. Perhaps there is a mechanistic explanation e.g., an increase in the proportion of storage vesicles may be countered by compensatory upregulation in vesicle production, or as discussed above defective cargo loading, might result in elevated numbers of empty vesicles. Technical differences arising due to variations in culture techniques may have contributed to increased variance, as replicates were differentiated by both Kim Jones and myself; this is relevant in light of a recent large-cohort RNA-Seq experiment showing that the differentiation process exerts as much or more impact on gene expression than donor genetic background and iPSC culture conditions (Schwartzentruber et al. 2018).

4.4.7 Conclusions

In summary, the comparisons of the endolysosomal structure in HD109 and HTT knockout lines with the corrected isotype versions produced few results. Similar to what is seen in NP-C, mHTT was associated with increased LAMP1 area in neurons, but not NPCs, which suggests that this phenotype might be more pronounced in neurons. Alterations in the autophagic compartment were observed in both HD109 and HTT knockout NPCs, which suggests that at least in part, a loss of wildtype function might be occurring in this regard.

Defects in autophagy, however, were not reproduced in HD109 neurons, though miglustat treatment did appear to slightly reduce an abnormally elevated basal autophagy in both isogenic and HD109 lines. Mitochondrial fragmentation was observed in HD109 NPCs, and this was reduced with miglustat treatment, which when considered in conjunction with the trend towards miglustat-associated trends towards reduced autophagy, suggests a potential rescue that is perhaps related to reductions in lysosomal storage. Furthermore, electron microscopy evidenced no differences in vesicle storage associated with HD or HTT knockout, however miglustat-treatment did result in reduction of the fraction of vesicles containing dense storage material in both HD and isogenic lines, to suggest an effect. Finally, colocalization analyses indicated that HTT was not essential for NPC1 localization to LAMP1 or NPC2 positive vesicles, and similarly that this was not impeded by the presence of mHTT, which suggests that if there is a pathomechanism common to HD and NP-C, then it likely does not result from reduced levels of NPC1 in the lysosomal membrane.

5 INVESTIGATION OF FUNCTIONAL DEFECTS IN HUNTINGTON'S DISEASE

5.1 Introduction

5.1.1 Lipid storage in HD

In the previous chapter, the area of the LAMP1-positive compartment was observed to be expanded in HD109 neurons when compared to isogenic controls. In NPCs, additional structural defects including an expanded autophagic compartment and mitochondrial fragmentation with a trend towards correction with miglustat, were identified. Taken together these structural abnormalities, suggest the possibility of corresponding functional deficits, such as lipid dyshomeostasis and storage, in HD, and further hint at the possibility that miglustat might ameliorate these defects. Thus, in order to determine if there might be overlap functional phenotypes between NP-C and HD and to identify potential storage substrates responsible for structural abnormalities observed in Chapter 4, the distribution of two key lipids, cholesterol and ganglioside GM1 were assessed using the HD and HTT knockout models established in Chapter 3.

5.1.1.1 Cholesterol

The accumulation of cholesterol to the perinuclear region of patient fibroblasts is the primary laboratory diagnostic for NP-C disease. Similar accumulation and distribution have been reported in HD, though inconsistently. In NP-C cholesterol storage is proposed to arise from the reduction of cholesterol efflux from the lysosome, leading to enlarged lysosomes presenting as large puncta in the cell body. Here, we hypothesized that if NP-C and HD share a common pathogenic cause, for example, if NPC1 or NPC2 function in the lysosome, was reduced or abolished by mHTT or by HTT knockout, then we would see an increased percentage of cells displaying cholesterol-positive puncta in these cell lines.

In Chapter 4, the late endosome marker, LBPA, was shown to be elevated, though not significantly, in HD109 neurons. Correspondingly, because LBPA complexes with cholesterol (Chevallier et al. 2008), the possibility of an increase in cholesterol in our cell models was assessed in this chapter, by filipin staining. As discussed in Chapter 1, abnormal cholesterol storage is a primary feature of NP-C disease and dysregulated cholesterol egress from the

lysosome, is argued to be the principle pathomechanism underlying NP-C, though this is contested. Reports of cholesterol accumulation in HD, however, are inconsistent (summarized in Chapter 1.7.7). There is evidence to suggests that cholesterol storage in HD might be associated with a loss of HTT function, as this was reported in mouse ES-derived HTT knockout NSCs (Ritch et al. 2012) and with HTT knockdown in SHSY5Y cells (Badell-Grau, MRes thesis). Therefore, to build on the results of previous experiments carried out in Chapter 4, and because cholesterol accumulation, while prominent in NP-C, has been inconsistently observed in HD, the distribution and accumulation of cholesterol was examined in our models.

5.1.1.2 Ganglioside GM1

Sphingolipids comprise roughly 20% of CNS lipids, where they carry out a wide range of functions (Bouscary et al. 2021). A subcategory of sphingolipids, the gangliosides, constitute 10-12% of CNS lipids and function in cell recognition, adhesion, signal transduction, calcium regulation, CNS development, and axonal growth, amongst other processes (Robert K et al. 2011; Breiden and Sandhoff 2018; Sandhoff and Sandhoff 2018b). Disrupted ganglioside metabolism is frequently observed in neurodegenerative and LSDs, and has been reported in HD and NP-C (Kolter and Sandhoff 2005a; Robert K et al. 2011; Breiden and Sandhoff 2018; Sandhoff and Sandhoff 2018b).

In HD, (as discussed in Chapter 1.7.7.2) altered ganglioside dynamics are thought to contribute to HD pathology, and evidence shows general ganglioside reductions to be associated with HD (Desplats et al. 2007b; Denny et al. 2010). How ganglioside dysregulation is associated with HD pathology, is unresolved (Di Pardo and Maglione 2018), though ganglioside imbalances can promote apoptosis and disruptions in Ca^{2+} signaling, which have both been linked to HD (Ross 2002; Desplats et al. 2007b). In particular, reduced levels of ganglioside GM1, have been reported in several rodent models of HD and HD patient fibroblasts (Denny et al. 2010; Maglione et al. 2010; Di Pardo et al. 2012; Alpaugh et al. 2017), and more recently, reduced GM1 levels were detected, in the caudate nucleus of *post-mortem* HD patient samples (Hunter et al. 2021). However, reports of altered GM1 levels in HD are inconsistent, as increased GM1 was observed in *post-mortem* HD patient

cerebella (Denny et al. 2010), as well as in several other HD patient-derived and animal cell culture models (Del Toro et al. 2010b; Haslett 2015; Clark 2017).

In contrast to biochemical assessments of global changes in gangliosides, immunocytochemical methods, can permit precise measurements of subcellular localization, and accumulation into vesicular structures (Walkley and Vanier 2009). Correspondingly, through immunocytochemistry, GM1 mislocalization in HD models has also been reported, with elevated levels in the plasma membrane of mHTT striatal neurons (Del Toro et al. 2010b), and a punctate perinuclear distribution of GM1 staining has also been seen in several other rodent and human cell culture models (Haslett 2015; Clark 2017). Therefore, as altered GM1 has been observed in previous models of HD, we aimed to quantify this in our cell lines.

Rescue of GM1 mistrafficking has been observed with miglustat treatment in HD models (Haslett 2015), in GM1 gangliosidosis (Tonin et al. 2019), and as discussed previously, inhibition of GSL synthesis by miglustat is used to treat NP-C (Zervas et al. 2001b; Patterson et al. 2007; Pineda et al. 2009). In addition, exogenous GM1 administration resulted in reduced apoptosis, restored motor dysfunction, decreased neurodegeneration, and white matter atrophy in several HD models (Desplats et al. 2007a; Denny et al. 2010; Maglione et al. 2010), evincing a direct link between GM1 and disease progression. Therefore, we also wanted to determine the potential effects of miglustat to restore any HD-related changes in GM1. Finally, because the role of wildtype HTT, relative to GM1 is unknown, and because understanding loss of HTT function has implications towards understanding HD and HD-related treatment, HTT knockout models were examined as well.

5.1.2 Mitochondrial stress

Mitochondrial function is commonly disrupted in neurodegenerative diseases, including PD, AD, and HD (Burté et al. 2015; Stanga et al. 2020). Moreover, the majority of LSDs exhibit profound mitochondrial dysfunction (Plotegher and Duchen 2017), and altered mitochondrial bioenergetics have been widely reported in HD (discussed in Chapter 1.7.6) and NP-C (discussed in Chapter 1.4.4.4). In neuronal models of NP-C, reductions in maximal

and basal respiration, ATP production, and spare respiratory capacity were observed (Prabhu et al. 2021) and similar reductions have been widely reported in HD models (An et al. 2012; Xu et al. 2017; Gardiner et al. 2018; Donaldson 2019a; Ooi et al. 2019b; Franco-Iborra et al. 2021). In Chapter 4, altered mitochondrial structure was observed, with reductions in mitochondrial length, associated with HD109 neurons, and a trend towards restoration with miglustat treatment. Thus, in this section we aimed to assess mitochondrial metabolism in our neuronal models of HD, in order to determine whether, correspondingly, mitochondrial function was altered with mHTT or HTT knockout, as well as to assess the effects of miglustat treatment.

Mitochondria are the principal energy-generating system in the majority of eukaryotic cells, and also function in intermediary metabolism, calcium signaling, and apoptosis. Mitochondria act as the site of oxidative phosphorylation, and enable the cell to efficiently generate ATP from energy-rich molecules. Through a series of redox reactions, electrons are transferred to oxygen, producing H_2O. During this process, protons are pumped from the mitochondrial matrix, across the mitochondrial inner membrane via respiratory complexes, I, III, and IV. ATP is then generated, by complex V (ATP synthase) as protons flow back to the mitochondrial matrix down their electrochemical gradient. Mitochondria are abundant in synapses, presumably to meet the high ATP demand involved in synaptic transmission, and as such, neurons are particularly vulnerable to mitochondrial dysfunction (Chan 2006).

Mitochondrial function can be assessed using the Seahorse XF96 analyzer, which measures oxygen consumption rate (OCR) and extracellular acidification rate (ECAR) in live cells, and provides information regarding mitochondrial respiration by measuring the changes in OCR and ECAR, in response to modulators of respiration, oligomycin, carbonyl cyanide-4 (trifluoromethoxy) phenylhydrazone (FCCP), rotenone, and antimycin. To summarize, after the assay is initiated and prior to oligomycin treatment, basal respiration is measured. Next, the addition oligomycin acts to inhibit ATP synthase, which inhibits electron movement through the electron transport chain (ETC), reducing mitochondrial respiration, and is an indicator of cellular ATP production. Next, FCCP is introduced, which allows unrestricted electron movement through the ETC, and as oxygen consumption through complex IV

reaches its peak, maximal respiration is recorded. Finally, the addition of rotenone and antimycin-A inhibits complexes I and III, respectively, terminating mitochondrial respiration, which permits the measurement of non-mitochondrial respiration (Agilent, 2019). Through these measurements several additional parameters of mitochondrial performance can be calculated.

In previous experiments using isogenic NSC models derived from iPSCs, HD cells displayed reduced levels of maximum respiratory capacity compared with corrected versions (An et al. 2012; Donaldson 2019a), with additional deficits in basal respiration (Xu et al. 2017). Moreover, in an isogenic allelic series, reductions in maximal respiration, basal respiration, and ATP production were shown to correspond with increased polyQ length (Ooi et al. 2019b). In HD patient fibroblasts, maximal respiration and spare respiratory capacity, were reduced commensurate with early disease onset (Gardiner et al. 2018). Reductions to maximal and basal respiration, spare respiratory capacity, and ATP production were also seen in mouse STHdh striatal neurons, along with decreased spare respiratory capacity (Franco-Iborra et al. 2021; Hu et al. 2021). Contrary to the majority of results, HD mESCs exhibited increased maximal respiratory capacity relative to syngeneic wtHTT controls, while in HTT knockouts this was reduced (Ismailoglu et al. 2014). Thus, the literature has very consistently evidenced, though not completely, mitochondrial dysregulation towards a reduced capacity for HD cells to respond to stress and increased energy demands. As such, in this experiment we aimed to not only determine whether mitochondrial function differed in our HD and HTT knockout models and the effects of miglustat, but to also compare the consistency of our results with those obtained in previous studies.

5.1.3 Lysosomal enzyme assays

As discussed in Chapter 1.1, in addition to transporters and activator proteins, the lysosomal lumen contains over 60 acid hydrolases, each of which function toward the degradation of select macromolecules, and which function optimally at an acidic pH (Ballabio and Bonifacino 2020). As discussed in Chapter 1.3, disrupted lysosomal hydrolases are causative for the majority of LSDs. Dysfunctional lysosomal enzymes can result in the accumulation of primary substrates, which can then promote secondary accumulation and contribute to cellular

pathogenesis (Lloyd-Evans and Platt 2010). Not all LSDs arise from decreased enzyme activity, however, and in particular NP-C is unique in that it is caused by defective transport proteins. Correspondingly, though HTT is not a lysosomal hydrolase, several of the phenotypes observed in our HD models, including lysosomal expansion, altered ganglioside and cholesterol levels, overlap with NP-C, and hint at the possibility of lysosomal dysfunction in HD, though whether this dysfunction is related to lysosomal enzyme activity is unknown, and because this has not been investigated thoroughly, we aimed to assess enzyme activity in our models.

5.2 Aims

- To examine functional defects commonly found in LSDs and in NP-C, including lipid storage, altered mitochondrial bioenergetics and lysosomal enzyme activity, using our HD models.
- To investigate functional changes associated with HTT knockout
- To determine if miglustat treatment might rescue any functional abnormalities associated with mHTT.

5.3 Results

5.3.1 Cholesterol distribution is altered in HD NPCs and neurons

HD iPSC-derived, day 16 neural progenitors were stained with filipin, to evaluate cholesterol storage due to mHTT or HTT knockout (Figure 5.1A). Cells were classified by their intracellular distribution of cholesterol storage. The presence of 3 or more large punctae and/or dense perinuclear aggregation indicated a positive storage phenotype, while the presence of 2 or less large punctae, diffuse staining, or no accumulation was considered negative. When compared to isogenic controls, the HD109 NPCs displayed significantly higher frequencies of cells exhibiting positive, perinuclear/punctate storage, as did the U18666A-treated positive controls, which reproduces the NP-C phenotype (Figure 5.1B). HTT knockout NPCs did not differ from the isogenic controls, with fewer cells exhibiting a cholesterol storage phenotype than what was observed in the HD109 and positive controls (Figure 5.1B).

To further explore potential effects of HTT knockout, KOLF2 NPCs and HAP1 cells were also assayed (Figure 5.2) and no differences between wildtype and HTT knockout was observed in either cell line (Figure 5.2A and 5.2B). The three biological replicates were considered together and the presence or absence of HTT accounted for 2.28% of the variance, and this effect was nonsignificant (Two-way ANOVA; Biological Replicate, $F_{(2, 14)} = 5.589$, $p = 0.0142$; HTT Status, $F_{(1, 14)} = 0.6001$, $p = 0.4514$). To summarize, although mHTT is associated with altered cholesterol storage in NPCs, the absence of HTT is not.

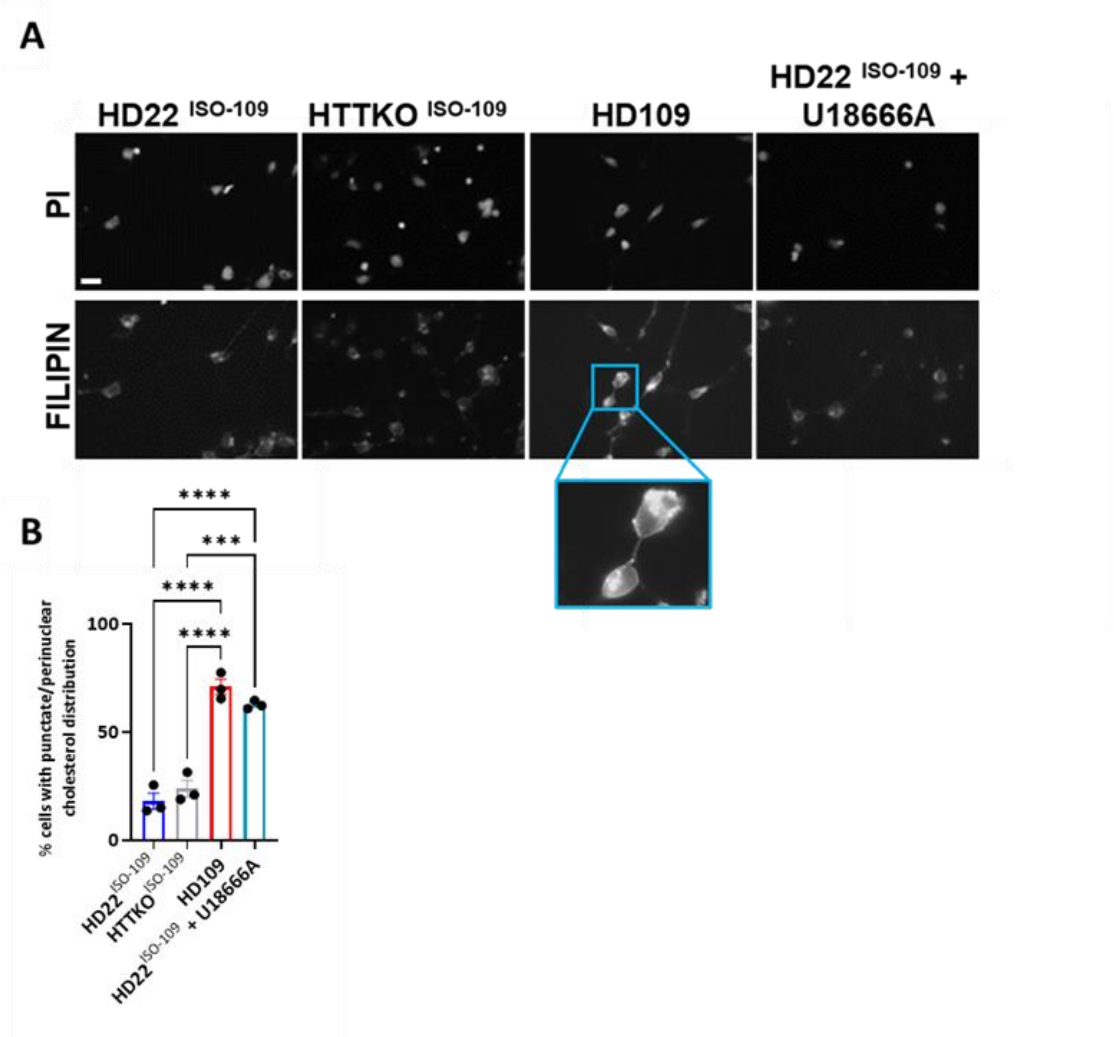

Figure 5.1. Filipin is distributed punctately or in perinuclear aggregates in day 16 HD109 NPCs. A) Day 16 neural progenitors were stained with filipin to assess cholesterol distribution. B) Cells were categorized by intracellular distribution of cholesterol and cells either exhibiting three or more discreet punctae and/or large perinuclear aggregates were considered to be indicative of cholesterol accumulation. One-way ANOVA with Tukey's multiple comparisons test; n = 3 technical replicates (wells), 40-114 cells measured per well. Total cells measured per genotype: HD22ISO-109 = 180, HD109 = 144, HTTKO ISO-109 = 166, HD22ISO-109+ U18666A = 206. Bars represent mean cellular area ± SEM for each cell line and black circles represent the mean cellular area per well. Scale bar = 10 µm.

.

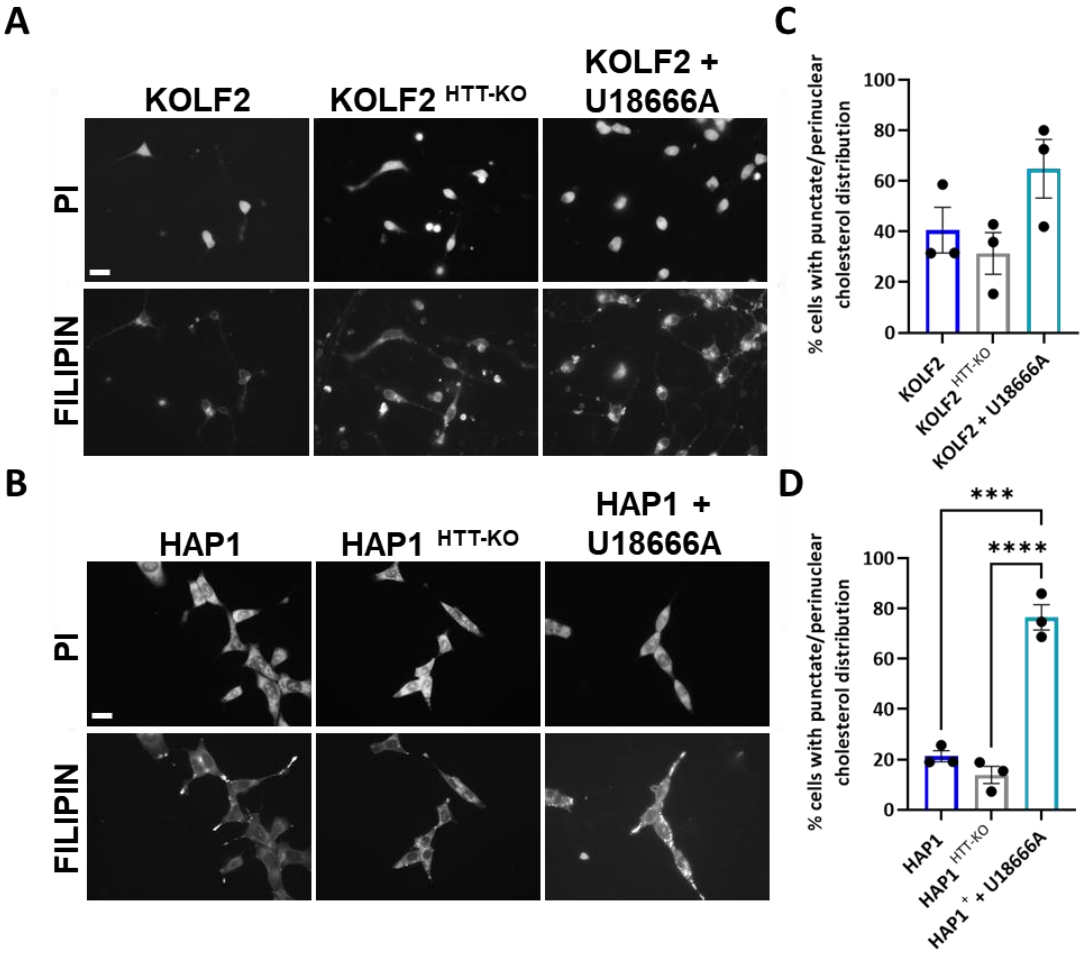

Figure 5.2. Filipin is distribution in Day 16 KOLF2 NPCs and HAP1 cells. A) KOLF2 NPCs, and B) HAP1 cells were stained with filipin to assess cholesterol distribution. Cells were categorized by intracellular distribution of cholesterol and cells either exhibiting three or more discreet punctae and/or large perinuclear aggregates were considered to be indicative of cholesterol accumulation. C) One-way ANOVA with Tukey's multiple comparisons test; n = 3 technical replicates (wells), 14-50 cells measured per well. Total cells measured per genotype: KOLF2 = 83, KOLF2 $^{HTT-KO}$ = 88, KOLF2 + U18666A = 121. D) One-way ANOVA with Tukey's multiple comparisons test; n = 3 technical replicates (wells), 32-103 cells measured per well. Total cells measured per genotype: HAP1 = 124, HAP1 $^{HTT-KO}$ = 181, HAP1 + U18666A = 192. Bars represent mean cellular area ± SEM for each cell line and black circles represent the mean cellular area per well. Scale bar = 10 µm.

Next, the area of filipin in HD iPSC-derived neurons was compared with isogenic controls to determine whether cholesterol accumulation was occurring in a more mature cell context (Figure 5.3). Moreover, HD109 cells were treated with 50 μM miglustat to assess whether treatment might ameliorate cholesterol storage. Images were imported into Image J, the nuclei were outlined and removed, and then cells were outlined and filipin area was calculated using the method outlined in Cook et al. (2020a). HD109 neurons exhibited higher levels of filipin staining when compared to isogenic controls (Figure 5.3B), and though not significant, miglustat treatment reduced filipin levels to an intermediate level between HD and isogenic lines (Figure 5.3B).

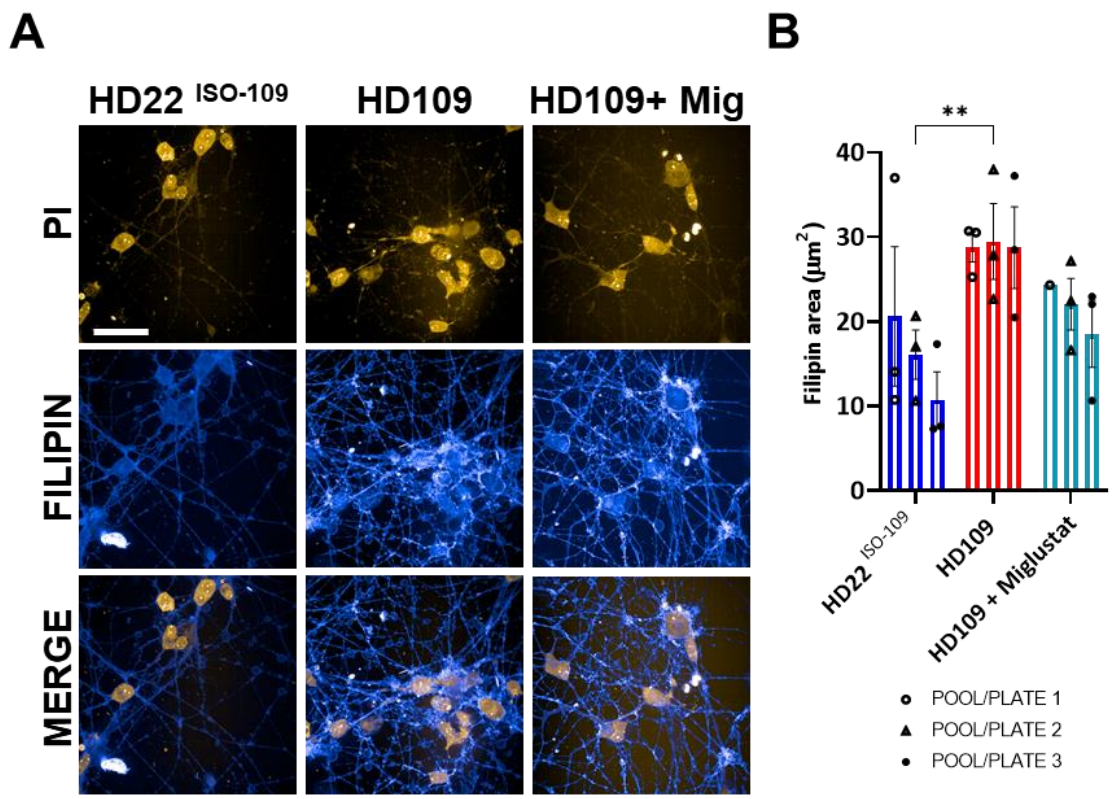

Figure 5.3. Filipin area is elevated and slightly reduced by miglustat in day 54 HD109 neurons. A) Neurons stained with filipin were used to estimate cholesterol area, using Image J software. B) Filipin area was increased in HD109, and isogenic controls treated with U18666A. Two-way ANOVA: Cell line: $F(2, 20) = 7.665$, $p = 0.0034$; Pool/Plate: $F(2,20) = 1.043$. $p = 0.3708$. Tukey's multiple comparisons test: HD22 ISO-109 vs. HD109, $p = 0.0028$; HD22 ISO-109 vs. HD109 + miglustat, $p = 0.4641$; HD109 vs. HD109 + miglustat, $p = 0.1296$. Total cells measured per condition: HD22ISO-109 = 285, HD109 = 232, HD109 + miglustat = 143. N = 3 pools/plates, n = 1-3 technical replicates (wells) per plate, 7-37 cells measured per well. Bars represent mean cellular area ± SEM for each cell line and black circles represent the mean cellular area per well. Asterisks indicate significant differences *$p \leq 0.05$, **$p \leq 0.01$. Scale bar = 50 µm.

5.3.2 Ganglioside GM1 distribution is altered in HD109 NPCs and neurons

To evaluate ganglioside storage in our HD models, associated with mHTT and HTT knockout, and potential similarities to NP-C disease, ganglioside storage in HD109 and HTT knockout NPCs were compared with the isogenic controls, and with a positive, NP-C phenocopy control, U18666A-treated isogenic progenitors. NPCs were stained with FITC-CTxB (Figure 5.4A) and were classified as described above for cholesterol distribution. A positive storage phenotype was defined as the presence of 3 or more large punctae and/or dense perinuclear aggregation, while the presence of 2 or less large punctae, diffuse staining, or no accumulation was considered negative. When compared with the HD22 $^{ISO-109}$ isogenic controls, the HD109 NPCs displayed significantly higher frequencies of cells exhibiting positive, perinuclear/punctate storage, and while HTT knockouts and U18666A-treated positive controls, also trended to higher frequencies of punctate/perinuclear storage, neither were significantly elevated when compared to the HD22 $^{ISO-109}$ isogenic controls (Figure 5.4A).

Additionally, to further assess the effects of HTT knockout on GM1 distribution, KOLF2 NPCs (Figure 5.5A) and HAP1 cells (Figure 5.5B) were also assayed. In KOLF2 cells, the proportion of KOLF2^{HTT-KO} NPCs that exhibited punctate/perinuclear GM1 storage was significantly higher than that of the wildtype controls, as were the U18666A-treated wildtype KOLF2 NPCs (Figure 5.5C). In contrast, in HAP1 cells, HTT knockout cells exhibited a significantly decreased frequency of punctate/perinuclear GM1 distribution, though the U18666A-treated positive controls displayed significant increases when compared to the untreated wildtypes (Figure 5.5D). HTT knockout data from each of the three biological replicates were combined to assess overall effects associated with HTT knockout. The presence or absence of HTT accounted for 0.0033% of the variance, and this effect was nonsignificant (Two-way ANOVA; Biological Replicate, $F_{(2, 14)} = 4.735$, $p = 0.0269$; HTT Status, $F_{(1, 14)} = 0.0007832$, $p = 0.9781$). Thus, though differences were associated with the biological replicates, there was no overall difference associated with HTT knockout.

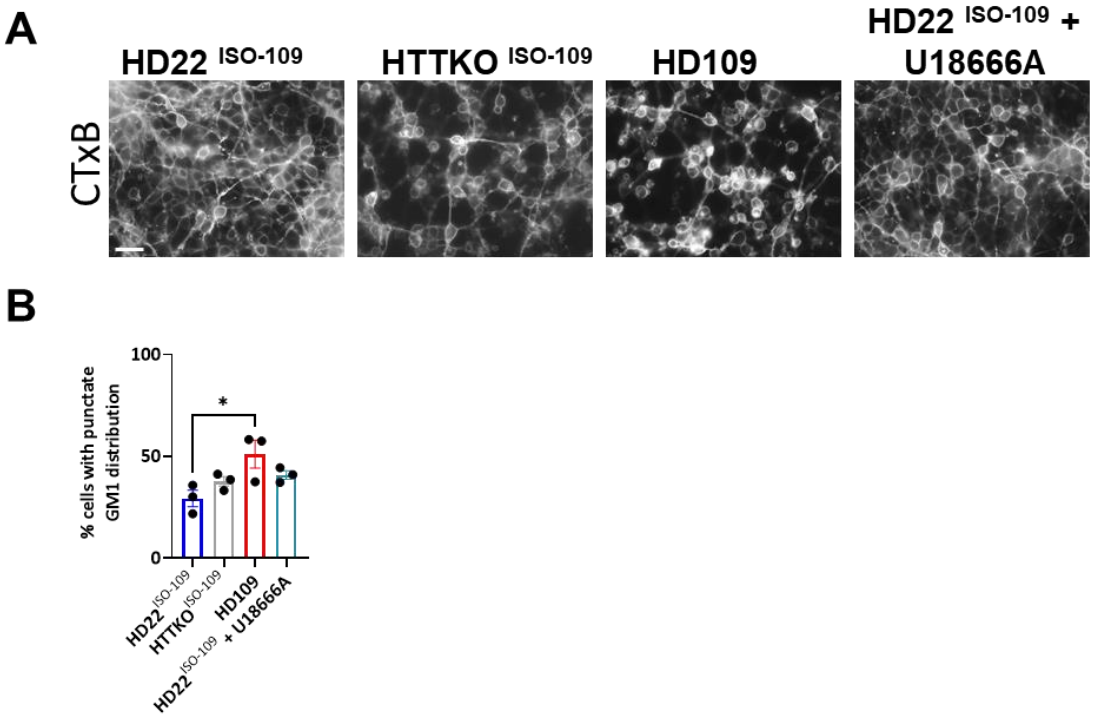

Figure 5.4. Ganglioside GM1 is distributed punctately in day 16 HD109 NPCs. A) Day 16 neural progenitors were stained with cholera toxin subunit B (CTxB), to assess ganglioside GM1 distribution. B) Cells were categorized by intracellular distribution of GM1 and cells either exhibiting three or more discreet punctae and/or large perinuclear aggregates were considered to be indicative of GM1 accumulation. One-way ANOVA with Tukey's multiple comparisons test; n = 3 technical replicates (wells), 27-63 cells measured per well. Total cells measured per genotype: HD22ISO-109 = 155, HD109 = 96, HTTKO ISO-109 = 128, HD22ISO-109+ U18666A = 135. Bars represent mean cellular area ± SEM for each cell line and black circles represent the mean cellular area per well. Scale bar = 10 μm.

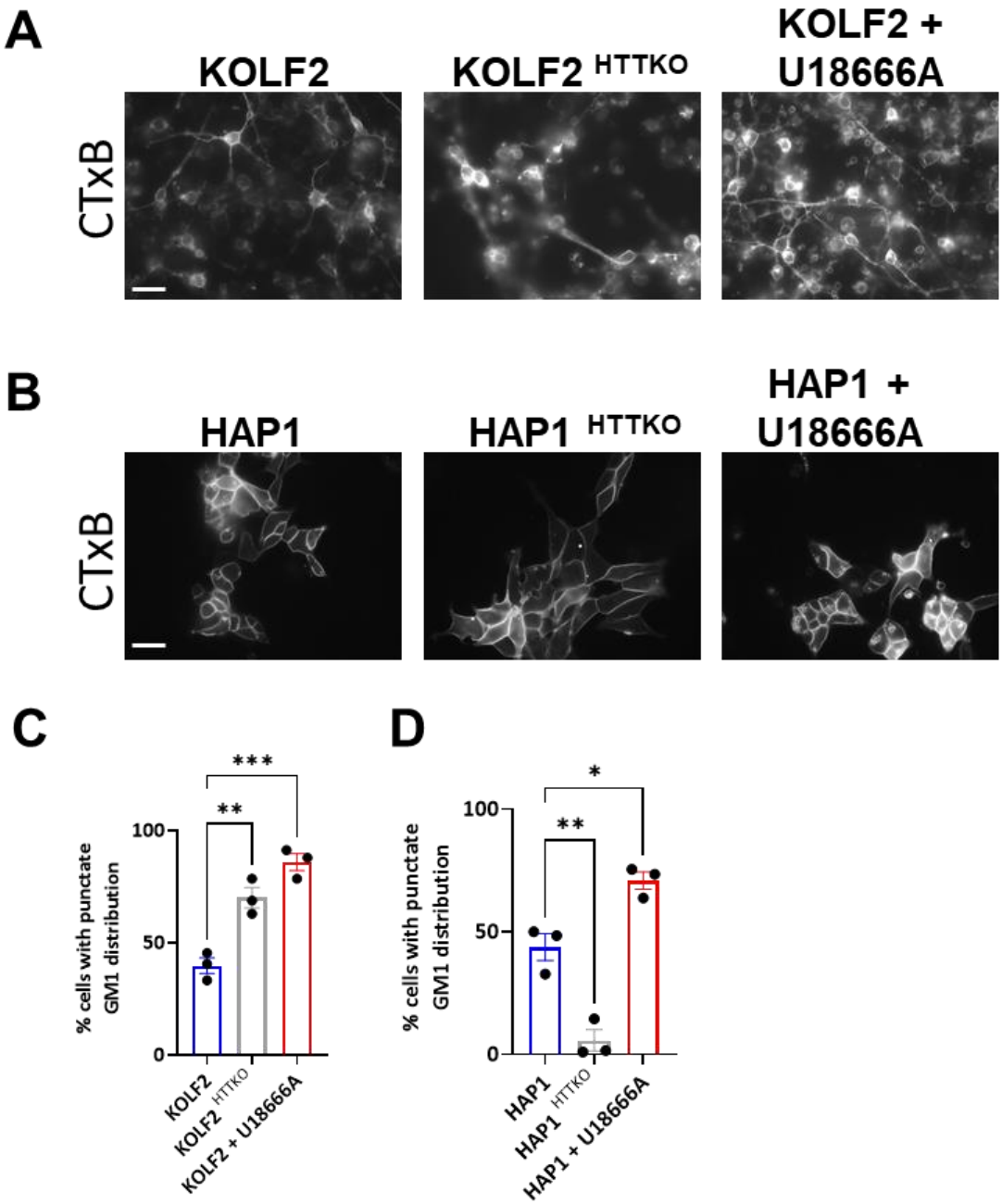

Figure 5.5. Ganglioside GM1 is distributed punctately in day 16 HD109 NPCs and HAP1 cells. Neural progenitors A), and HAP1 cells B) were stained with cholera toxin subunit B (CTxB), to assess ganglioside GM1 distribution. Cells were categorized by intracellular distribution of GM1 and cells either exhibiting three or more discreet punctae and/or large perinuclear aggregates were considered to be indicative of cholesterol accumulation. C) One-way ANOVA with Tukey's multiple comparisons test; n = 3 technical replicates (wells), 31-51 cells measured per well. Total cells measured per genotype: KOLF2 = 108, KOLF2 $^{HTT-KO}$ = 127, KOLF2 + U18666A = 133. D) One-way ANOVA with Tukey's multiple comparisons test; n = 3 technical replicates (wells), 53 -66 cells measured per well. Total cells measured per genotype: HAP1 = 190, HAP1 $^{HTT-KO}$ = 180, HAP1 + U18666A = 174. Bars represent mean cellular area ± SEM for each cell line and black circles represent the mean cellular area per well. Scale bar = 10 µm.

The average percent of GM1 area in the cell bodies, excluding the nucleus, was measured using image J, in HD iPSC-derived neurons was measured as outlined in Cook et al. (2020a). Percent area was calculated instead of total area per cell, due to the high density of neurons and overlapping axons, which prohibited the visual isolation, selection, and measurement of single neurons. HD109 neurons, both with and without the addition of 50 µM miglustat for the final 7 days of differentiation, were compared with isogenic HD22 $^{ISO\text{-}109}$ neurons to ascertain whether GM1 accumulation was occurring (Figure 5.6). The soma of HD109 neurons displayed higher levels of GM1 than what was seen in the isogenic controls (Figure 5.6B) and miglustat-treated HD109 cells exhibited slightly reduced GM1 levels that were not significantly different from the untreated HD109s or the isogenic controls (Figure 5.6B).

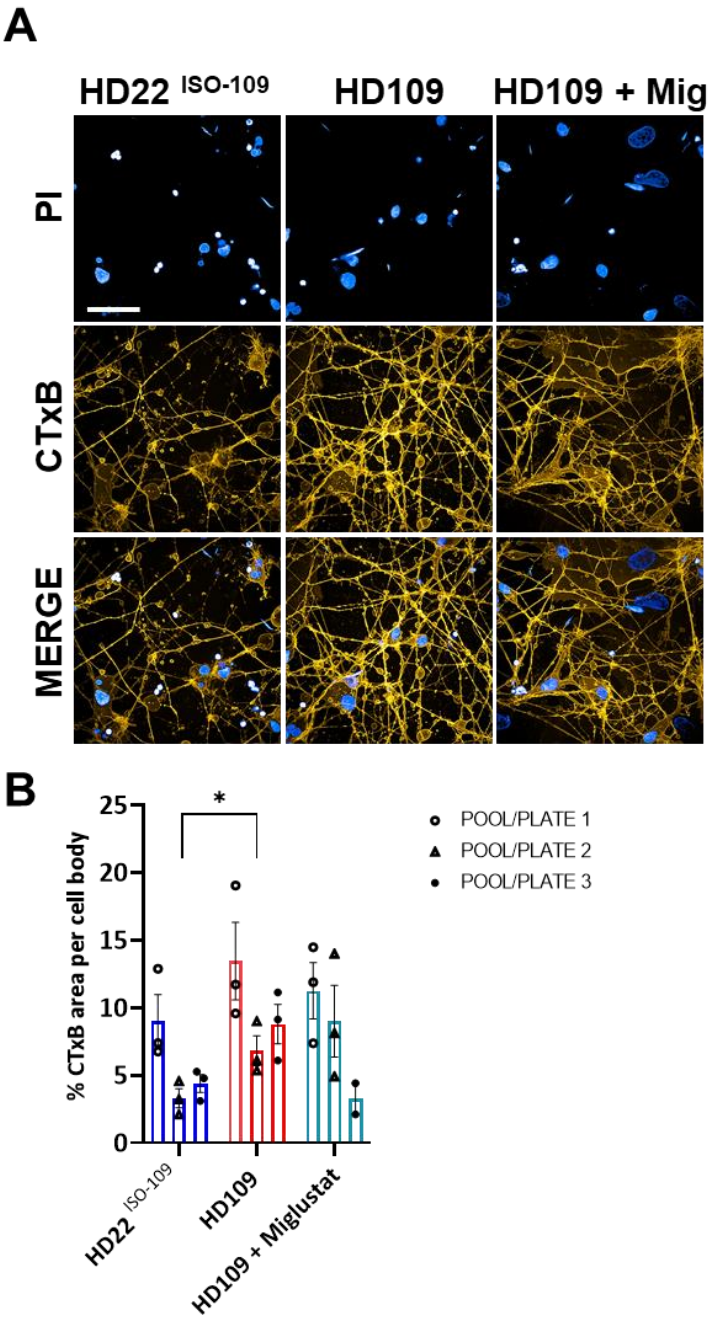

Figure 5.6. Ganglioside GM1 area is elevated and slightly reduced by miglustat in area day 54 HD109 neurons. A) Neurons stained with CTxB were used to estimate ganglioside GM1 area, using Image J software. B) GM1 area was increased in HD109, and isogenic controls treated with U18666A. Two-way ANOVA: Cell line: F (2, 21) = 3.791, p = 0.0393; Pool/Plate: F (2,21) = 7.588. p = 0.0033. Tukey's multiple comparisons test: HD22 ISO-109 vs. HD109, p= 0.0326; HD22 ISO-109 vs. HD109 + miglustat, p = 0.2435; HD109 vs. HD109 + miglustat, p = 0.5992. Total cells measured per condition: HD22ISO-109 = 279, HD109 = 259, HD109 + miglustat = 205. N = 3 pools/plates, n = 2-3 technical replicates (wells) per plate, 11-39 cells measured per well. Bars represent mean cellular area ± SEM for each cell line and black circles represent the mean cellular area per well. Asterisks indicate significant differences *p ≤ 0.05, **p ≤ 0.01. Scale bar = 50 µm.

5.3.3 Mitochondrial stress

Day 16 NPCs were seeded at a density of 2.5 x 10^5 cells per well and differentiated in SJA medium for an additional 8 days, before assaying on day 24 of neuronal differentiation (Figure 5.7A). No differences were seen in basal respiration (Figure 5.7D) which is a measure of OCR levels above non-mitochondrial oxygen consumption (Figure 5.7B), measured prior to the addition of oligomycin (Figure 5.7A). Following oligomycin-mediated ATP synthase inhibition and prior to FCCP injection, ATP production (Figure 5.7F) was calculated by subtracting proton leak (Figure 5.7E) and non-mitochondrial oxygen consumption (Figure 5.7B) from basal respiration measurements (Figure 5.7D), and no differences were observed. Following the addition of FCCP, and preceding the addition of rotenone and antimycin A (Figure 5.7A), maximal respiration (Figure 5.7C) was calculated by subtracting OCR measurements from non-mitochondrial oxygen consumption (Figure 5.7B). Comparisons of maximal respiration though nonsignificant, showed slight reductions in HD109s and increased levels with HTT knockout when compared to the isogenic controls (Figure 5.7A). miglustat treatment, though again nonsignificant, resulted in elevated maximal respiration in the isogenic controls, though reductions were seen in HD109s (Figure 5.7A). Following deactivation of mitochondrial respiration by rotenone and antimycin A injection (Figure 5.7A), spare respiratory capacity was calculated, which measures the difference between maximal respiration (Figure 5.7C) and basal respiration (Figure 5.7D) for each well, and no significant differences were observed, though HD109 both with and without miglustat averaged lower than isogenic controls, while HTT knockouts averaged higher. The percent spare respiratory capacity (Figure 5.7H) was calculated by dividing the maximal respiration (Figure 5.7C) by basal respiration (Figure 5.7D) for each well, thereby reducing inter-well variation. When compared to the isogenic controls, percent spare respiratory capacity was significantly reduced in both miglustat-treated and untreated HD109s. No differences were seen in coupling efficiency, which is calculated by dividing ATP production (Figure 5.7F) by basal respiration (Figure 5.7D), and indicates the amount of oxygen needed to produce ATP.

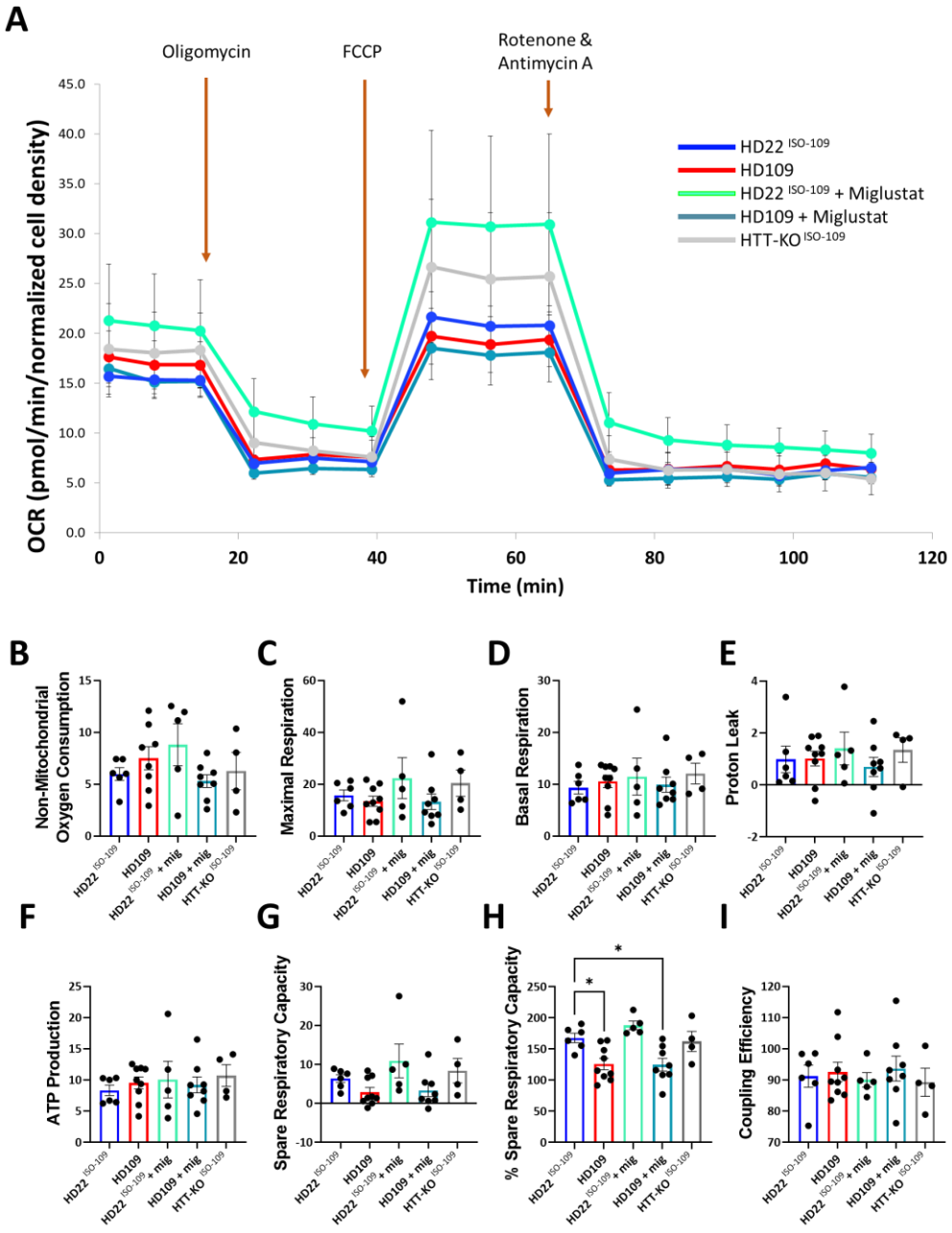

Figure 5.7. Mitochondrial energetics in day 24 neurons. HD109 and isogenic controls with and without miglustat, and HTT knockouts. A) Seahorse Bioanalyzer traces displaying oxygen consumption rates (OCR), in HD immature (Day 24) neuronal models, normalized by direct cell count. Quantitative data and comparisons of B) Non-mitochondrial oxygen consumption, C) maximal respiration, D) basal respiration, E) proton leak, F) ATP production, G) spare respiratory capacity, H) percent spare respiratory capacity, I) coupling efficiency. One-way ANOVA with Tukey's multiple comparisons test; n = 4-9 technical replicates (wells), bars represent mean cellular area ± SEM for each cell line and black circles represent the mean cellular area per well.

5.3.4 Lysosomal enzyme assays

Lysosomal enzyme activity was determined with the aid of Callum Higgins. IPSC lysates were first subjected to a panel of 23 lysosomal enzyme assays as a preliminary screen to select enzymes of interest for further examination in NPCs and neurons (Figure 5.8). HD109 iPS cells showed a wide range of variation when compared to the isogenic controls, as did the miglustat-treated HD109s and the HTT-knockouts (Figure 5.8).

From this initial screen, enzymes were then selected for further assay, based on the magnitude of divergence of the HD109s from the isogenic control cell lines as well as from miglustat-treated HD109s, or the HTT knockouts. Lysosomal acid lipase was selected as it functions in cholesterol metabolism, and was decreased in the HTT knockouts. Acid Phosphate was significantly increased relative to controls. Acid sphingomyelinase activity in HD109s was sharply increased relative to controls, and was reduced with miglustat, and further with HTT knockout. Cathepsin B showed increased activity in HD109s relative to controls, but was decreased in HTT knockouts. Glucocerebrosidase activity was sharply reduced in HD109s, but increased with miglustat, and HTT knockout. Hexosaminidase B activity was moderately increased in HD109s, but sharply reduced in HTT knockouts. NAGLU and NEU activity were both highly increased in HD109 iPSCs. Finally, Beta-Glucuronidase was selected as a control for low variation (Figure 5.8).

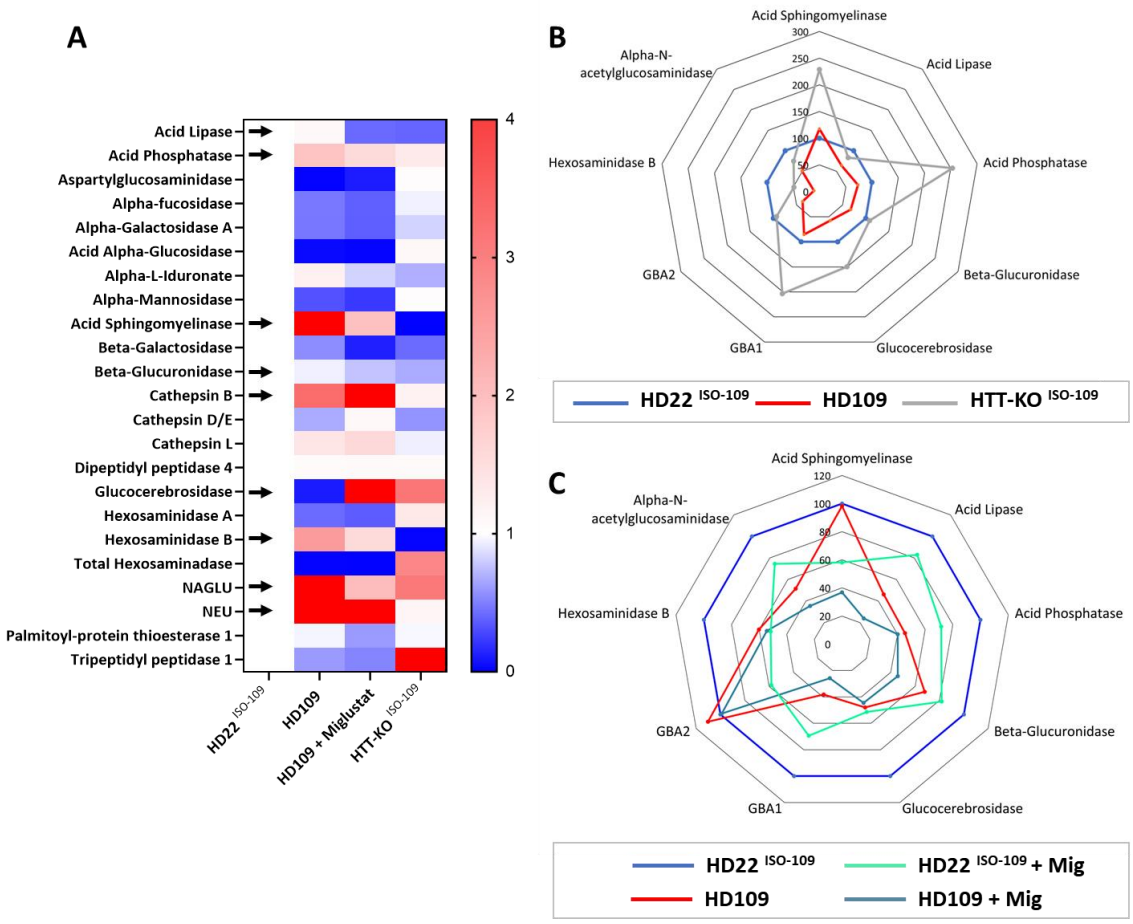

Figure 5.8. Activity of lysosomal enzymes in HD iPSCs, day 16 NPCs, and neurons. A) Heatmap indicating fold-change of enzyme activity in HD iPSC lines relative to the isogenic controls. Black arrows indicate enzymes selected for further experiments. B) Radar plot showing percent activity of selected enzymes in HD109 and HTT-KO $^{ISO-109}$ NPCs relative to HD22 $^{ISO-109}$ controls. C) Radar plot showing percent of enzyme activity in neurons relative to HD22 ISO-109 isogenic controls, including HD109s and both HD22 ISO-109 and HD109 neurons treated with miglustat.

Likely due to high variability in assay results, no significant differences in enzyme activity were observed in HD109 or HTT knockout NPCs (Figure 5.9). However, generally, excepting Acid Sphingomyelinase, overall enzyme activity was reduced in HD109 NPCs relative to the isogenic controls (Figure 5.8B). In the knockouts, the mean enzymatic activity of Acid Sphingomyelinase, GBA1, and Acid Phosphatase, were elevated relative to the isogenic controls, while Hexosaminidase B and Alpha-N-Acetylglucosaminide activity, was reduced (Figure 5.8B). Interestingly, the mean activity of each enzyme was reduced in HD109 NPCs when compared to the HTT knockouts (Figure 5.8B).

The general reductions in enzyme activity seen in HD109 NPCs was also observed in HD109 neurons (Figure 5.8), though again, individually, and likely due to the removal of two replicates due to the presence of trisomy in chromosome 1, these differences were not significant (Figure 5.9). Enzyme activity was further reduced in miglustat-treated HD109s (Figure 5.8), however, only Acid Sphingomyelinase exhibited significant reductions (Figure 5.9). The trend towards reduced enzyme activity associated with miglustat, was also seen in the treated isogenic controls (Figure 5.8).

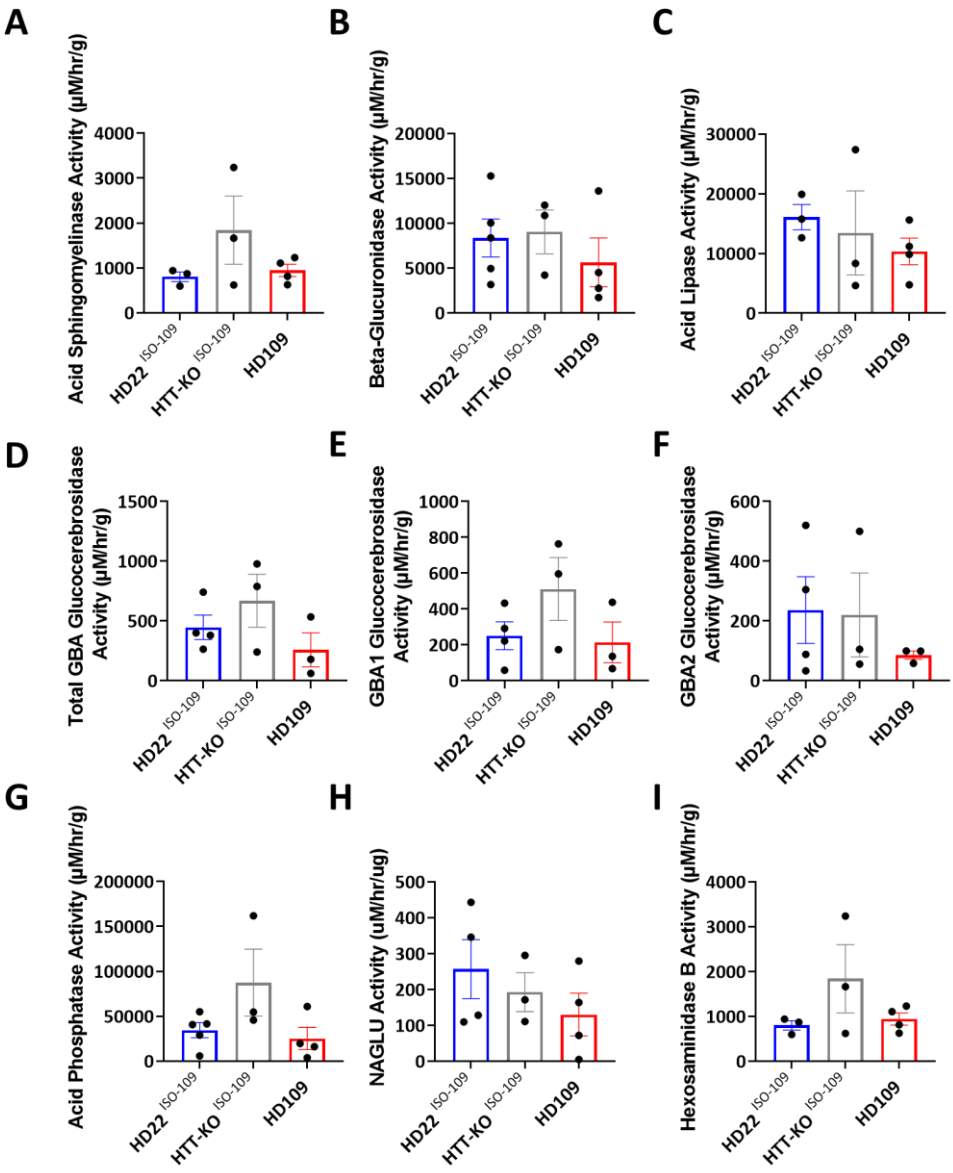

Figure 5.9. Comparison of individual enzyme activity across day 16 HD22 $^{ISO-109}$, HTT-KO $^{ISO-109}$, and HD109 NPCs. One-way ANOVA with Tukey's multiple comparisons test; n = 3 – 5 replicates (subclones). A) Acid Sphingomyelinase; 1-6 wells per subclone. B) Beta-Glucuronidase; 6 wells per subclone. C) Acid Lipase; 2-6 wells per subclone. D) Total GBA; 6 wells per subclone. E) GBA1; 2-6 wells per subclone. F) GBA2; 1-6 wells per subclone. G) Acid Phosphatase; 6 wells per subclone. H) N-Acetyl-Alpha-Glucosaminidase; 6 wells per subclone. I) Hexosaminidase B; 2-6 wells per subclone.

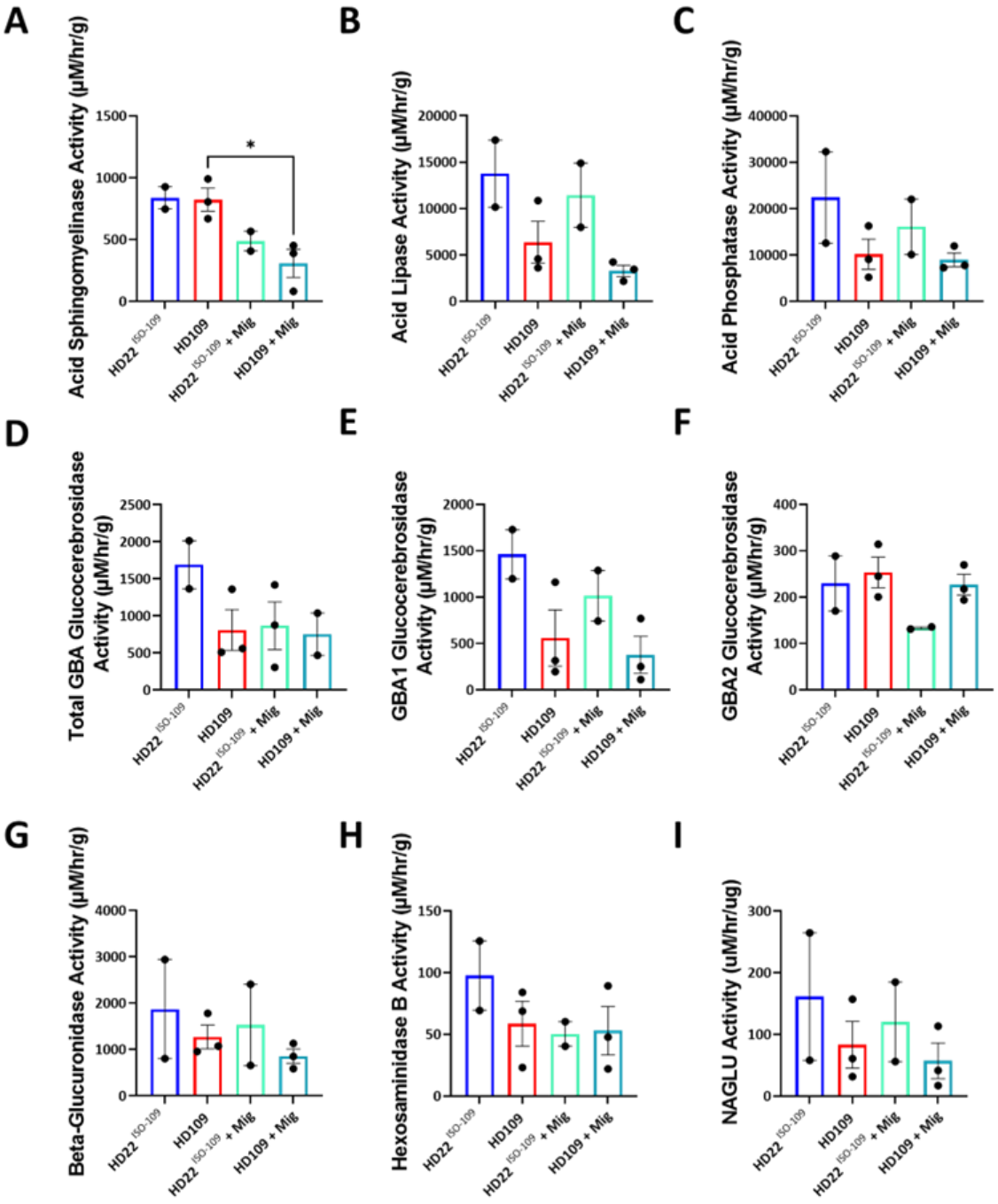

Figure 5.10. Comparison of individual enzyme activity across neuronal models of HD and treatment with miglustat. One-way ANOVA with Tukey's multiple comparisons test; n = 2 to 3 replicates (subclones). A) Acid Sphingomyelinase activity; 2-11 wells per subclone. B) Acid Lipase; 9-12 wells per subclone. C) Acid Phosphatase; 6-12 wells per subclone. D) Total GBA; 9-12 wells per subclone. E) GBA1; 4-10 wells per subclone. F) GBA2; 8-12 wells per subclone. G) Beta-Glucuronidase; 9-12 wells per subclone. H) Hexosaminidase B; 1-12 wells per subclone. I) N-Acetyl-Alpha-Glucosaminidase; 9-12 wells per subclone.

5.4 Discussion

5.4.1 Altered cholesterol in HD

The increased punctate, perinuclear cholesterol storage observed in HD109 neural progenitors, is consistent with previous reports and suggests cholesterol sequestration within the endolysosomal system and mislocalization. The increased presence of filipin-labelled, intracellular deposits was observed in STHdh (Q111) mouse striatal cells (Del Toro et al. 2010b), punctate filipin staining was seen in HD iPSC-derived NSCs (Q180), and punctate/perinuclear cholesterol accumulation was seen in ST14A (Q120) cells (Haslett 2015). Further experiments evidenced punctate filipin staining in STHdh (Q111) and ST14A (Q120) cells both with and without the addition of U18666A, and in preliminary evaluations of HD fibroblast-like cells (Q60 and Q109), though only when cells were cultured in medium supplemented with 10% FBS, and not when NPCs were differentiated in serum-free medium (Clark 2017). Accordingly, lipid supplementation was used in this thesis to compensate for the loss of neuronal ability for *de novo* cholesterol synthesis as they mature and become increasingly reliant on receptor-mediated endocytosis of cholesterol-containing lipoproteins supplied by glial cells (Dietschy 2009; Vitali et al. 2014).

Cholesterol accumulation to endocytic vesicles was not seen in HTT knockouts here, though elevations in total cellular cholesterol were previously described in HTT knockout mESC-derived NSCs (Ritch et al. 2012), and with HTT knockdown in SHSY5Y cells (Badell-Grau, MRes thesis). It was not confirmed whether total cholesterol was altered in these experiments, and unless cholesterol synthesis or uptake, is altered with HTT knockout, this data would suggest that cholesterol excretion or degradation is not impeded, and that abnormal sequestration of cholesterol does not arise due to loss of wildtype function. To eliminate the possibility that the lack of accumulation observed in the knockouts arises from a decrease in cholesterol biosynthesis, measurements of cholesterol precursors or metabolites, both shown to be reduced in HD (Valenza et al. 2007a; Valenza et al. 2007b), and experiments to eliminate the

possibility that these results arise from reductions in cholesterol uptake as described in Siddiqui et al. (2022), could be performed.

In HD109 neurons, the area of positively stained filipin vesicles in the cytoplasm was higher than that in the isogenic controls, indicating cholesterol accumulation due to the presence of mHTT. The results obtained here conform with several reports (Trushina et al. 2006b; del Toro et al. 2010a; Luthi-Carter et al. 2010), as discussed in Chapter 1.7.7.1, of cholesterol accumulation in HD, but are in disagreement with others (Valenza et al. 2005b; Valenza et al. 2007a; Valenza et al. 2010; Marullo et al. 2012; Ritch et al. 2012). Increased filipin levels, especially in the cell bodies, were reported in HD iPSC-derived neurons (Q60 and Q109), which also increased with polyQ length. Total cholesterol levels as measured by thin layer chromatography, indicated elevations in ST14A (Q120) and PC12 (Q145) cells, and similar to what was observed in this thesis, cholesterol levels were reduced with miglustat treatment in ST14A (Q120) cells (Haslett 2015). In contrast, further experiments failed to evidence increases in total cellular cholesterol by TLC in HD iPSC-derived NPCs (Q60 and Q109) (Clark 2017), and a corresponding lack of effect with miglustat, contrasts with the moderate, though inconclusive, reductions associated with miglustat treatment in this thesis. However, as miglustat has been shown to reduce glycosphingolipid accumulation in NP-C, without decreasing cholesterol (te Vruchte et al. 2004; Lloyd-Evans and Platt 2010), the mechanism explaining how miglustat would decrease the filipin levels here, and how this relates to an overlap in phenotypes between the two diseases remains unclear.

When taken together, the results of these experiments add to the evidence to support cholesterol accumulation and mistrafficking associated with HD, comparable to cholesterol dysregulation observed in other LSDs, including NP-C . Whether cholesterol mistrafficking and accumulation exists as an epiphenomenon or whether this contributes to HD pathology is not known. However, as autophagy regulates lipid metabolism (Singh et al. 2009), and as elevated levels of basal autophagy were observed in the HD109 and HTT knockout NPCs (Figure 4.10), the presence of aberrant cholesterol accretion only in HD109s and its absence in the knockouts and isogenic controls, support the idea of a block in catabolism or clearance, related to a gain of function. The results are then in accordance with the model

proposed by Zhou et al. (2021) whereby mHTT aggregates might interfere with lysosomal or autophagic function and with exocytosis. The cellular mechanisms underlying cholesterol egress and transport are unresolved, though these processes are likely carried out through both vesicular and nonvesicular pathways (Hölttä-Vuori and Ikonen 2006). Accordingly, these results could also arise through defective vesicle trafficking, and/or defective fusion with the lysosome to the autophagosome, or late endosome, which might explain increases seen in LAMP1 levels and the lack of increase in LBPA seen in neurons (Chapter 4). The cholesterol mistrafficking associated with mHTT and the lack of a phenotype associated with HTT knockouts, might also correspond to what was observed in the enzyme assays where the trend towards increased activity of lysosomal enzymes in the HTT knockout, with reductions in the HD109s, suggests that lipid degradation is impaired in HD, due to gain of mHTT function. An overall impairment in lipid degradation is also supported by ganglioside GM1 mistrafficking in HD109s, (Figures 5.4. and 5.6).

Finally, because the ability to visually measure cholesterol accumulation in neurons through image analysis was limited due to the lengthy and often intersecting projections, biochemical analysis should be performed to substantiate these results. Additionally, in order to further clarify potential trafficking defects and to determine whether cholesterol was alternately distributed to the lysosome or late endosome, neurons co-stained with filipin, LAMP1, and LBPA, were imaged, however, colocalization analysis has yet to be carried out.

5.4.2 Altered ganglioside GM1 in HD

Gangliosides are fundamental to brain function. In the brain, GM1 is thought to be neurotrophic, with positive effects toward neuronal survival, growth, differentiation, and signaling (Prinetti et al. 2009). As such, disruptions in GM1 metabolism are likely to affect neurophysiological function, and reduced levels of GM1 have been shown to increase susceptibility to apoptosis in HD models (Maglione et al. 2010a). Reports of altered GM1 levels in HD, however, are inconsistent. Reductions have been reported in the brains of HD patients and animal models (Desplats et al. 2007a; Denny et al. 2010; Maglione et al. 2010; Alpaugh et al. 2017; Hunter et al. 2021). Contrastingly, increases were seen in HD patient cerebella (Denny et al. 2010), in HD patient fibroblasts (Clark 2017), in rodent striatal

neurons (Del Toro et al. 2010b; Haslett 2015), and GM1 levels increased with polyQ length across an allelic series (Q21, Q33, Q60, Q109) of HD iPSC-derived neurons. Thus, our findings of increased GM1 levels in HD109 neurons, are in accordance with reports of increased GM1 levels in HD, and contradict reported reductions.

As previously reported, GM1 accumulation in wildtype neurons, was associated with increased time in neuronal differentiation medium (Haslett 2015), which could indicate that culture conditions or the process of neuronal maturation, might have contributed to elevated GM1 content observed in this experiment. However, the increases in the HD109s seen here were compared to an isogenic control, and as both were cultured concurrently, if the process of differentiation promoted GM1 accumulation, then this was exacerbated in HD109s, suggesting accumulation to a greater extent or at an increased rate in HD. When considered with reductions of GM1 synthesis seen in HD patient fibroblasts and animal models (Maglione et al. 2010), and with reduced gene expression levels for GM1 synthesis in patient brains (Desplats et al. 2007a), it would then seem that disrupted GM1 catabolism and/or trafficking, and not a defect in production is underlying GM1 accumulation.

Evidence for catabolic dysregulation or mistrafficking resulting in endolysosomal accumulation of GM1 was seen here by increased punctate perinuclear GM1 staining in HD109 NPCs. These results are in agreement with those obtained in previous experiments, as a perinuclear punctate GM1 distribution was observed in HD patient NSCs and in ST14A cells (Haslett 2015), and punctate GM1 staining was also observed in HD patient fibroblasts, ST14A, and STHdh cells (Clark 2017). Taken together with the increased levels and punctate distribution of cholesterol, discussed above, this further strengthens the idea that altered lipid trafficking and homeostasis might contribute to HD pathogenesis (Trushina et al. 2006a; del Toro et al. 2010a; Trushina et al. 2014).

GM1 distribution as a response to HTT knockout, was variable across cell lines. This variability might be cell type dependent, as increased perinuclear and punctate GM1 staining was observed in both progenitor lines, though only significantly in KOLF2 NPCs. This contrasted sharply with the decreases observed in HAP1 cells, and underscores the

importance of the cell type when modelling disease. However, though HTT knockout produced divergent results in NPCs when compared to HAP1 cells, GM1 distribution was clearly altered in two out of three HTT knockout experiments, and taken together this could indicate a possible loss of function effect of mHTT associated with GM1 mistrafficking, and further experimentation to specify the vesicle population in which GM1 accumulation is occurring, would help towards discerning the cellular processes which might be affected by loss of HTT function. Because an altered distribution with HTT knockout was not observed with cholesterol, this might also suggest a loss of HTT function more particular to GM1, which if true, would parallel glycosphingolipid accumulation in NP-C that occurs prior to cholesterol accumulation (Gondré-Lewis et al. 2003). Therefore, it would be beneficial to assess both the distribution of GM1 and cholesterol, over a time course, to delineate the progression of substrate accumulation.

The altered levels and distribution of GM1 seen here have similarly been observed in LSDs and in NP-C. In CHO models of NP-C, punctate GM1 accumulation was seen in early endosomes (Sugimoto et al. 2001), and increased GM1 has been reported across an array of human animal models of NP-C (Zervas et al. 2001a; Lloyd-Evans et al. 2008; Vite et al. 2015; Cook et al. 2020b). Though similarities are present, whether there is a shared GM1-related mechanism underlying HD that is related to lysosomal storage disease or NP-C pathology is beyond the scope of this experiment. However, the marginal reductions in GM1 associated with miglustat treatment in our neuronal models, are in accordance with rescue of GM1 mistrafficking in ST14A HD models (Haslett 2015) and reductions in elevated GM1 levels seen in HD fibroblasts (Clark 2017), which resemble miglustat-mediated rescue of GSL mistrafficking in NP-C (Lachmann et al. 2004), and in GM1 gangliosidosis (Tonin et al. 2019). The shared miglustat-mediated phenotypic rescue common to HD and NP-C, provides a rationale for potential drug repurposing. However, reducing GM1 levels as a treatment for HD, runs counter to previous findings, whereby GM1 administration has been shown to rescue HD pathologies (Desplats et al. 2007a; Denny et al. 2010; Maglione et al. 2010). Nonetheless, because miglustat treatment across several cell lines, was shown to restore

altered GM1 in HD models towards what is seen in the wildtype controls, further exploration to clarify the impacts of miglustat on HD neurons would be useful.

5.4.3 Mitochondrial stress in HD

Mitochondrial dysfunction, is a common feature of neurodegenerative diseases, lysosomal storage diseases, and is observed in NP-C and in HD. In NPC1-null neuronal models of NP-C, reductions in maximal and basal respiration, ATP production, and spare respiratory capacity were observed (Prabhu et al. 2021), and similar reductions have also been widely reported in HD models (An et al. 2012; Xu et al. 2017; Gardiner et al. 2018; Donaldson 2019a; Ooi et al. 2019b; Franco-Iborra et al. 2021). The parallels between mitochondrial dysfunction in NP-C and HD support the idea of a shared pathomechanism common to both. Thus, in this experiment we aimed to assess mitochondrial function related to mHTT, HTT knockout, and potential rescue effects associated with miglustat. However, comparisons between HD109s and the isogenic lines were, with the exception of reduced percent spare respiratory capacity in both miglustat-treated and untreated HD109s, inconclusive. The inconclusive results might have arisen due to variability between conditions, which when minimized in the calculation of percent spare respiratory capacity, yielded observable differences. However, a recent study evidencing CHIR 99021 as a potent enhancer of mitochondrial function (Hu et al. 2021), described amongst several rescue effects *in vitro* and *in vivo*, a restoration to wildtype levels of basal and maximal respiration, and ATP production in mouse striatal cells, treated for 5 days with 1 µM CHIR 99021. Correspondingly, in this experiment, cells were grown in 3 µM CHIR 99021, a pro-synaptogenic component of the SJA neuronal maturation medium (Kemp et al. 2016), for 8 days, which might explain the lack of differences observed in this experiment. Therefore, it would be advisable to repeat this experiment, both with and without CHIR 99021, as this might have obscured mitochondrial phenotypes related to mHTT and HTT knockout, and confounded results.

Nevertheless, reductions in percent spare respiratory capacity seen here, are consistent with prior studies showing reduced spare respiratory capacity in HD, and further evidence an impaired ability in HD neurons to respond to increased energy demands or stress. Moreover, our findings suggest that miglustat treatment exerts no rescue effect in this regard. However,

it would have been advisable, in addition to counting cells for normalization, to quantify the average number and area of mitochondria per cell, as differences in these might have also contributed to assay results. Thus, repeating the experiment in this way could provide more information specific to mitochondrial function, and allow for interrogation into whether altered mitochondrial bioenergetics in HD arise due to differences in the number and size of mitochondria present within the cell, or whether these differences are actually a result of deficits in mitochondrial function.

5.4.4 Enzyme assays

In addition to the expanded endolysosomal and autophagic compartments described in Chapter 4, the altered distribution and elevated levels of both cholesterol and GM1, seen in this chapter, suggest that storage in the autophagic-endolysosomal system is occurring in our HD models relative to isogenic controls. Because storage in LSDs, often arises from the reduction in the hydrolytic activity of lysosomal enzymes, (Platt and Walkley 2005; Cox and Cachon-Gonzalez 2012), we hypothesized that the function of one or more lysosomal enzymes might be disrupted in our HD models. Moreover, we hypothesized that if wtHTT was critical to lysosomal function, then knockout of HTT might also lead to altered enzyme activity. Therefore, the enzymatic activities of several lysosomal hydrolases were measured in NPCs and neurons to determine whether any might be altered in our HD or HTT knockout models. Additionally, enzyme activity in response to miglustat treatment was assessed to screen for potential restorative effects.

In, both HD109 NPCs and neurons, on an individual basis, there were no substantive changes in enzyme function detected in these experiments. However, when considered as a whole, these results suggest the possibility of an overall decline in the function of lysosomal enzymes in HD, with the exception of acid sphingomyelinase in NPCs and GBA2 in neurons, though clearly more investigation would be required to be convincing. Similarly, the activity of several, though not all, lysosomal enzymes were previously observed to be reduced in HD patient fibroblasts (Alshehri 2019). Though the data obtained here was subject to a high degree of technical variation and low replication, if overall activity of lysosomal enzymes is impaired due to mHTT, then several biological mechanisms might explain this. For example,

increased resistance of mHTT to proteolysis and degradation (Qin et al. 2003; Wellington et al. 2003), altered cholesterol-related gene expression (Sipione et al. 2002), or impaired protein clearance (Ochaba et al. 2014), could result in secondary storage accumulation, an altered intravesicular biochemical composition, and impaired enzyme kinetics. A general reduction in enzyme activity might also arise from a defect in a common processing or trafficking step from the ER through the Golgi/TGN (Walkley and Vanier 2009). Moreover, mitochondrial defects have also been shown to impair lysosomal function and enzymatic activity (Demers-Lamarche et al. 2016).

In NPCs, the effect of HTT knockout was variable, and no individual enzyme displayed significantly altered activity when compared to isogenic controls or HD109 NPCs. However, in the knockouts, Acid Sphingomyelinase, Acid Phosphatase, and GBA1 activity were increased greater than 2-fold when compared to the isogenic controls, and Hexosaminidase B activity was reduced, which might indicate a role of wtHTT towards the function of these enzymes. The overall pattern of enzymatic activity exhibited in the HTT knockouts resembled that seen in HD109s, however, in each case enzyme activity was increased with HTT knockout relative to HD109s. The results of this experiment, coupled with the overall decreased enzyme activity seen in HD109 neurons and NPCs when compared to isogenic controls, then, further supports an inhibitory effect conferred by the presence of mHTT, and not by the loss of wildtype HTT.

Miglustat treatment in HD109 and HD22 isogenic control neurons, produced little effect pertaining to specific enzymes, and only Acid Sphingomyelinase activity was shown to be conclusively reduced with miglustat, which differs from previous work (Lloyd-Evans et al. 2014; Alshehri 2019). However, when interpreted collectively, miglustat treatment was associated with reduced enzyme activity, to varying degrees, in all 9 of the enzymes tested, in both HD109 and the isogenic controls. If the trend towards general reductions in enzyme activity seen with miglustat are accurate, the results of these experiments then suggest that treatment amplifies reductions already present in HD109 neurons. It is unclear how miglustat-treatment could result in such an effect, though miglustat is known to inhibit

glucosylceramide synthase, alpha-glucosidases I and II, GBA1, and GBA2 (Platt et al. 1994; Nietupski et al. 2012; Ridley et al. 2013).

Ideally, more biological and technical replication would have been carried out in these experiments, though this was limited by time and materials. A further limitation of these experiments was the reliance on total cellular protein as a way to standardize and compare lysosomal enzyme activity. This method of standardization assumes that the molecular concentration of each enzyme, as a fraction of total cellular protein, is equal, though direct measurements to confirm this were not carried out. Consequently, in these experiments a change in fluorescence might not only reflect a change in the capacity for a particular enzyme to cleave its substrate, but it could also signify a difference in concentration as a fraction of total cellular protein. Therefore, the scope of what can be inferred from this data set is limited. To resolve this, western blotting across the samples, for each enzyme, might allow for more precise comparisons.

5.5 Conclusion

In this chapter, lipid storage phenotypes were observed in HD109 NPC and neuronal models of Huntington's disease. In particular, cholesterol and ganglioside GM1 levels were observed to accumulate in vesicular structures in NPCs, and both lipids were elevated in neurons. miglustat treatment exhibited potential for therapeutic reductions to lipid accumulation in HD neurons, though further experiments using additional biological replicates should be undertaken to substantiate these results. In HTT knockout NPCs while altered cholesterol was not observed, GM1 accumulation was varied, which might indicate a related wildtype function and potential loss function in HD. Defects in mitochondrial bioenergetics were observed as decreased percent spare respiratory capacity, in the HD109 models, though variation was too high to detect differences in other parameters. This reduction in cellular ability to respond to increased stress and energy demands agrees with the majority of what has been shown previously in HD models, and this deficiency was not restored with miglustat treatment. The results of the lysosomal enzyme assays were variable and largely inconclusive. However, several trends were seen including a general reduction in the enzyme

activity in both NPC and neuronal models of HD. In summary, there are several disease characteristics common to HD, NP-C, and other lysosomal storage diseases, and further exploration into the mechanisms underlying these similarities might provide valuable information for future treatments.

6 RNA SEQUENCING OF ISOGENIC MODELS OF HUNTINGTON'S DISEASE

6.1 Introduction

Transcriptional dysregulation in HD patient cells and mouse models has been repeatedly reported (Bates et al. 2015; Consortium 2017; Malla et al. 2021), with significant dysregulation *in vitro* using both polygenic and isogenic approaches from hESCs and iPSCs (Consortium 2017; Ooi et al. 2019b; Smith-Geater et al. 2020). Relevant to this thesis, dysregulation has been shown to occur in pathways related to the lysosome, autophagy, and mitochondria (Damiano et al. 2010; Martin et al. 2015b; Miller et al. 2016). Because of these differences, and because in previous chapters structural and functional changes associated with mHTT and HTT knockout were identified, we hypothesized that transcriptional profiles related to the endolysosomal, autophagic, or mitochondrial pathways might likewise be altered, in our day 37 model neurons. Thus, in this chapter we compared gene expression across HD109s, HTT knockouts, and isogenic controls. Moreover, the effects of miglustat treatment on HD and isogenic neurons was also investigated and to our knowledge this is the first study to assess transcriptional changes associated with miglustat in human cells.

Initially, using microarrays, and then RNA-sequencing (RNA-Seq), evidence for transcriptomic dysregulation in Huntington's disease as a central and early pathogenic mechanism has been observed in several HD patient, cellular, and animal models; a comprehensive systematic review can be found here by Malla et al. (2021). However, in iPSC based neuronal models the differentially expressed gene (DEG) lists have not been as consistent. In two similar studies, which utilized HD patient-derived iPSCs (including HD109s used in this thesis) differentiated into neural or into MSN-enriched populations, little overlap was observed in DEGs of HD cells relative to controls. In the first, Q60 and Q109 neural cells differentiated for 56 days revealed 1,869 DEGs relative to wildtypes (Consortium 2017), however in the second study only 105 DEGs were identified in juvenile HD cell lines differentiated for 37 days (Q66, Q71 and Q109) with no enrichment for specific GO terms, while 823 DEGs were identified in adult-onset lines (46Q and 53Q) (Smith-Geater et al. 2020). This inconsistency however, might correspond to the length of time in which cells undergo differentiation as a similar study using isogenic hESCs, showed that day 11 NPCs only exhibited 352 DEGs (2.25% of expressed

genes) differentially than hESCs with no associated enrichment, while day 45 neurons differentiated from hESCs displayed 2738 DEGs (15.8% of expressed genes) differentially than control hESCs (Ooi et al. 2019b). Correspondingly, here we observed that the transcriptome of HD109s was relatively unchanged relative to the isogenic controls and moreover, these were not strongly affected by miglustat. Thus, the applicability of subsequent pathway analysis, was then also limited. As such, in order to gain more insight from this data, we then focused on pathways relevant to this thesis, in an exploratory capacity, regardless of significance. Additionally, we reduced the threshold for significance in our DEGS to $p \leq 0.05$, for comparisons to identify common DEGs in our HD109s with those in two other studies (Consortium 2017; Ooi et al. 2019b), in an effort to estimate the extent with which DEGs were shared across the three studies. Our findings indicate that there is little overlap across the three studies.

Next, we identified DEGs associated with HTT knockouts relative to the isogenic controls, which could inform the contribution of wildtype HTT to normal cell function. We also compared DEGs associated with HTT knockout with DEGs found in HD109s relative to isogenic controls, in order to assess the potential for loss of function in HD. Our findings indicated that HTT knockouts exhibited a greater number of DEGs relative to the isogenic controls than what was seen in HD109s, and only 10 DEGs in the HTT knockouts overlapped with those seen in HD109s relative to the isogenic controls. We also compared DEGs identified in this thesis at a more permissive non adjusted $p \leq 0.05$, with those seen in a recent study which used SHSY5Y HTT knockout models (Bensalel et al. 2021), and identified 94 DEGs common to both, with protein-protein interactions focused to NOTCH1, FGFR2, SCRT1, and SOX2 amongst others. Several KEGG pathways were associated with HTT knockout, though significantly enriched pathways, were not directly related to the endolysosomal, autophagic, or mitochondrial focus of this study, with the exception of calcium signalling, and were largely related to development.

6.2 Aims

- To examine differential gene expression in HD109, HTT knockout, and isogenic control neurons using unbiased bulk RNA-sequencing.
- To investigate changes in differential gene expression associated with miglustat treatment in HD109 and isogenic control neurons.
- To examine differential gene expression and pathways which might provide insight into structural or functional abnormalities identified in Chapters 4 and 5 of this thesis, using our neuronal models.

6.3 Results

6.3.1 Experimental design

To assess differences in the transcriptome arising due to mHTT and HTT knockout, and to investigate the impact of miglustat treatment, neuronal RNA was collected and processed for sequencing with Illumina NovaSeq 6000. Five independent treatment groups of neurons were generated, each of which were comprised of 5 subclones which served as technical replicates. Cells were cultured using a modified MSN differentiation protocol (Chapter 2.7.1). HD109 and HD22 $^{ISO\text{-}109}$ were cultured both with and without 50 µM miglustat throughout the entire duration of the final 7 days. Total RNA was collected and delivered to Novogene for sequencing (Chapter 2.7.2). The first set of comparisons were made to assess differences due to the presence of mHTT and HTT knockout (Figure 6.1A). The focus of the second group of comparisons were designed to assess the impacts that miglustat might have on the HD109 transcriptome and to discern whether there might be restoration towards a wildtype, isogenic transcriptomic profile (Figure 6.1B).

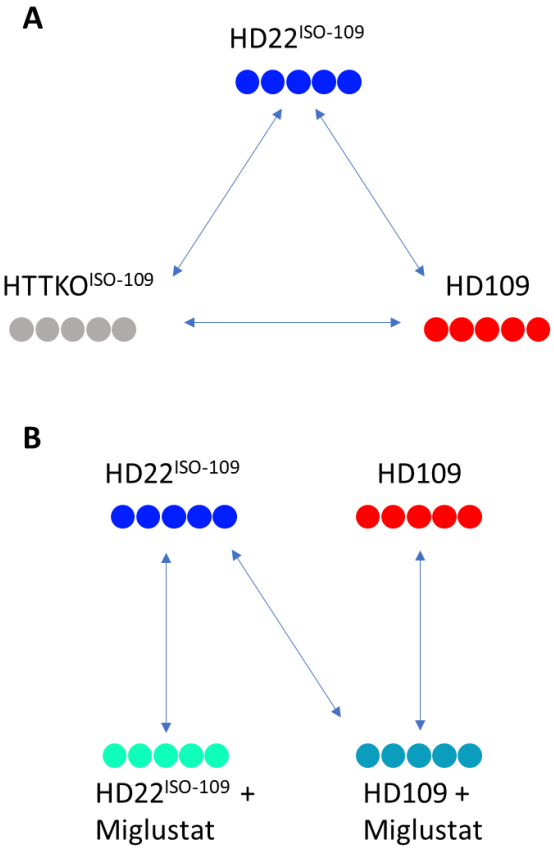

C

CELL LINE	Subclone	Sample Name
HD109	1	H109_3
	2	H109_2h
	3	H109n1
	4	H109_2f
	5	H109_3h
HD22 ISO-109	1	I5h9_1
	2	I5h9_3
	3	I3h2_1
	4	I3h2_2
	5	I3h2_3
HTTKO ISO-109	1	HKO_1
	2	HKO_2
	3	HKO_3
	4	HKO_4
	5	HKO_5
HD109 + Miglustat	1	MH109_3
	2	MH109_2h
	3	MH109n1
	4	MH109_2f
	5	MH109_3h
HD22 ISO-109 + Miglustat	1	MI5h9_w3
	2	MI5h9_1
	3	MI3h2_1
	4	MI3h2_4
	5	MI3H2_5

Figure 6.1. RNA Seq experimental outline. Treatment groups, consisting of 5 subclones, (represented by colored circles). Arrows represent the comparisons made in this chapter. A) The first set of comparisons compare day 37 HD109s and HTT knockout neurons to the isogenics. B) The second set of comparisons examines the effects of miglustat treatment on HD109 and isogenics. C) Key to reference the replicate subclone names.

6.3.2 Quantification

To correct for bias due to gene length and varying total reads, data was normalized by fragment read counts / (gene length x total read counts) or fragments per kilobase per million (FPKM). Gene expression levels were widely and similarly distributed across all treatments, and though the majority of genes were expressed at relatively low levels, a small proportion were highly expressed (Figure 6.2A). Similar distributions were also observed across individual replicates (Figure 6.2B).

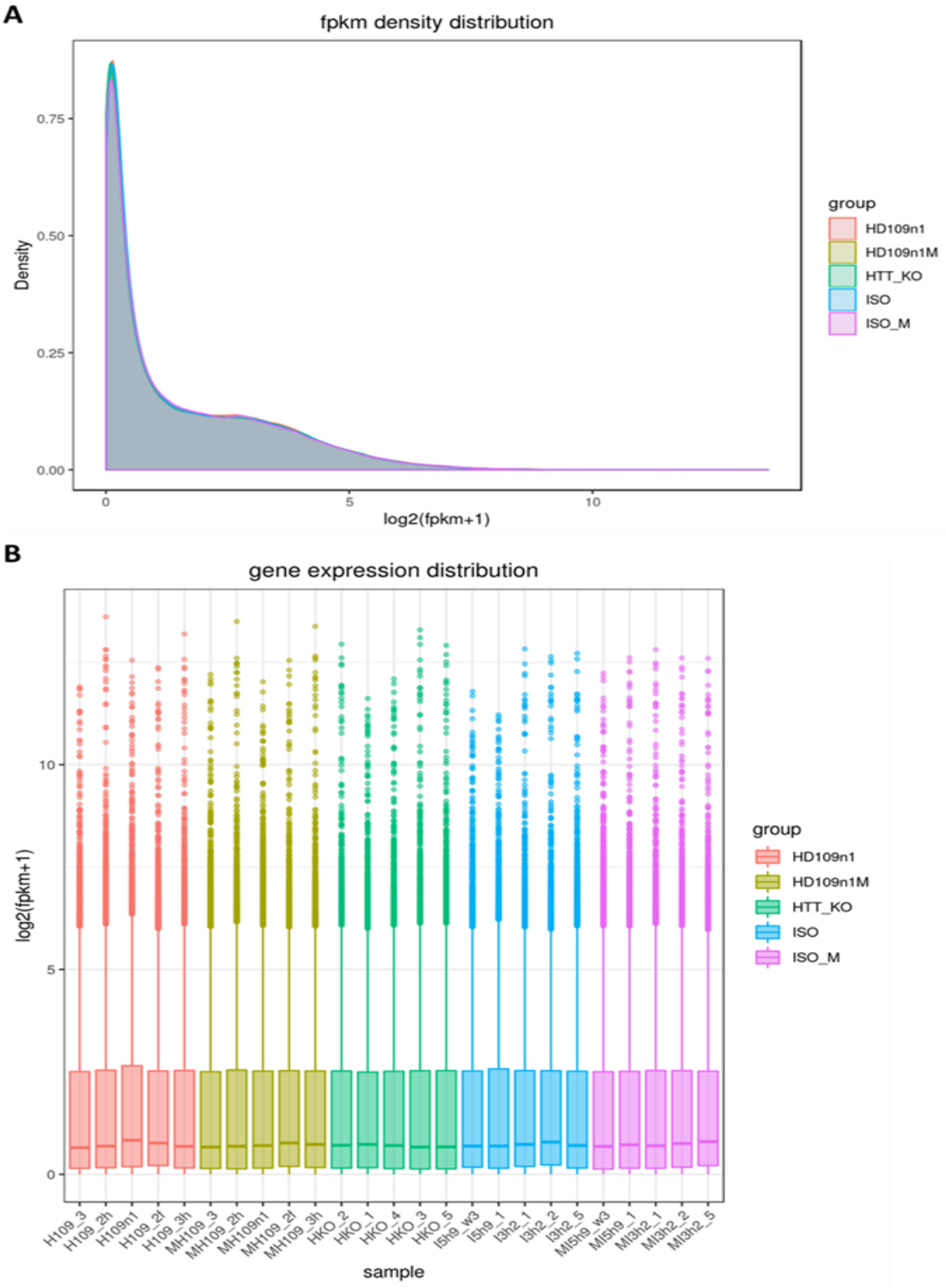

Figure 6.2. Gene expression profiles of day 37 neurons. A) Density curve depicting gene expression levels in HD109s (HD109n1), HD109 + miglustat (HD109n1M), HTT knockouts (HTT_KO), isogenics (ISO), and isogenics treated with miglustat (ISO_M). B) Gene expression distribution of replicate subclones. Colors correspond to the aforementioned individual cell lines and treatments, while replicates (subclones) within groups are labelled on the x-axis.

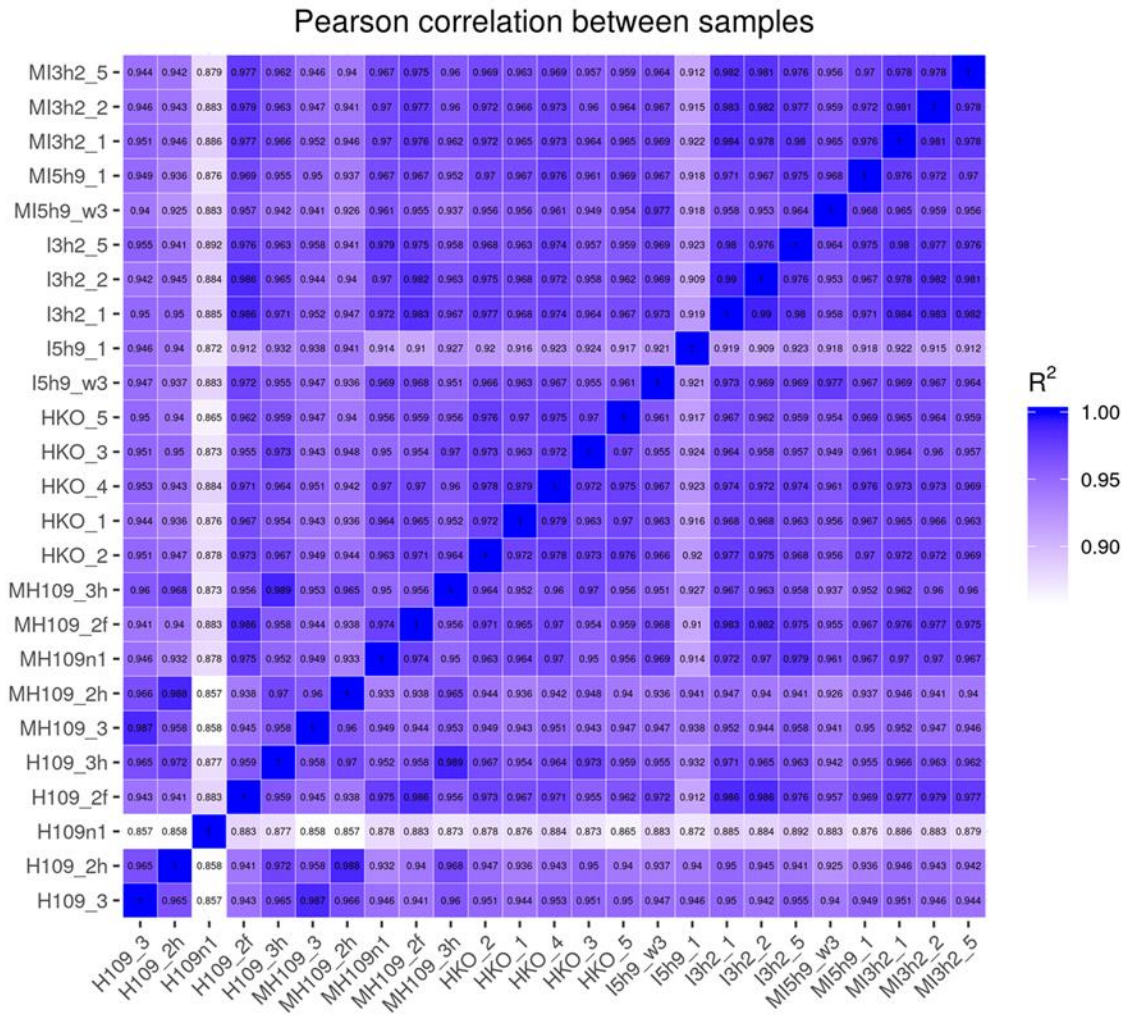

Figure 6.3. Pearson correlation coefficient matrix across subclones. Numbers indicate the R^2 value, as calculated by squaring the Pearson correlation coefficient for pairs of individual replicates (subclones), listed on the x and y axis. Increased darkness corresponds to increased similarity between samples.

After summing the readcounts aligned to each gene using the *featureCounts* software (Liao et al. 2014), the Pearson correlation coefficient was compared across all subclones to assess variability between treatments and replicates (Figure 6.3). The Encyclopedia of DNA Elements (ENCODE) suggests a square of the Pearson correlation coefficient (R^2) greater than 0.92 for replicates (Yu et al. 2022), with an R^2 of 1.0 indicating the highest degree of similarity. All replicates met this standard, with the exception of the H109n1 (the parent line

to the other four HD109 subclones) and I5H9_1, within the HD109 and HD22$^{ISO\text{-}109}$ treatment groups, respectively. The two cell lines were retained in this analysis, however, as removal would have decreased the statistical power. Intra-group similarity did not conspicuously differ from inter-group similarity, which suggests a low degree of difference due to genotype or miglustat treatment.

Additionally, principal component analysis (PCA) was carried out on the normalized data to illustrate the variation in the gene expression profiles of individual subclones that constitute each treatment group (Figure 6.4). PC1 explains 22.39% of the variation between subclones, while PC2 explains 18.45% of the variation. Again, the two subclones H109n1 and I5H9_1, fall outside of their respective clusters, suggesting inconsistency in the model. The isogenic controls largely clustered together, while HD109s were more variable and spread out. The majority of HD109 subclones clustered with their respective miglustat-treated counterparts,

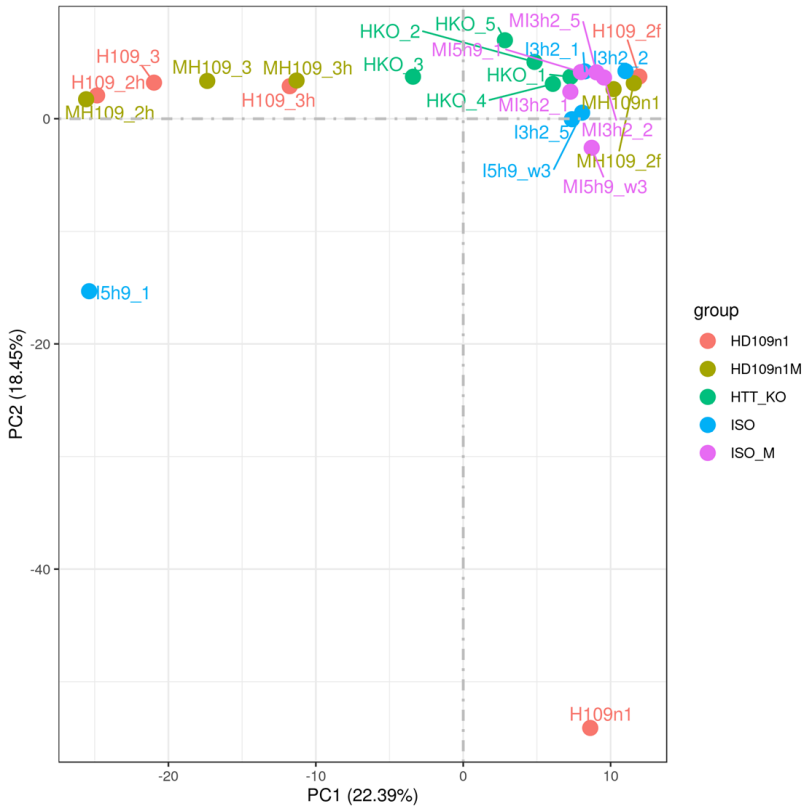

Figure 6.4. Principle component analysis of replicate subclones.

as did the isogenic controls, suggestive of a lack of downstream expression changes due to miglustat treatment. HTT knockouts also clustered with the isogenic controls, suggesting a lack of differences due to presence or absence of HTT. In summary, with the exception two of the subclones, the there was a high degree of intra-group clustering, and only moderate differences between HD lines (with and without miglustat) treatment groups, are visible.

6.3.3 Differential expression

Next, hierarchical cluster analysis on scaled counts at $\log_2$(FPKM+1) was carried out on replicates (Figure 6.5) and on treatment groups (Figure 6.6). Again, H109n1 (HD109 subclone

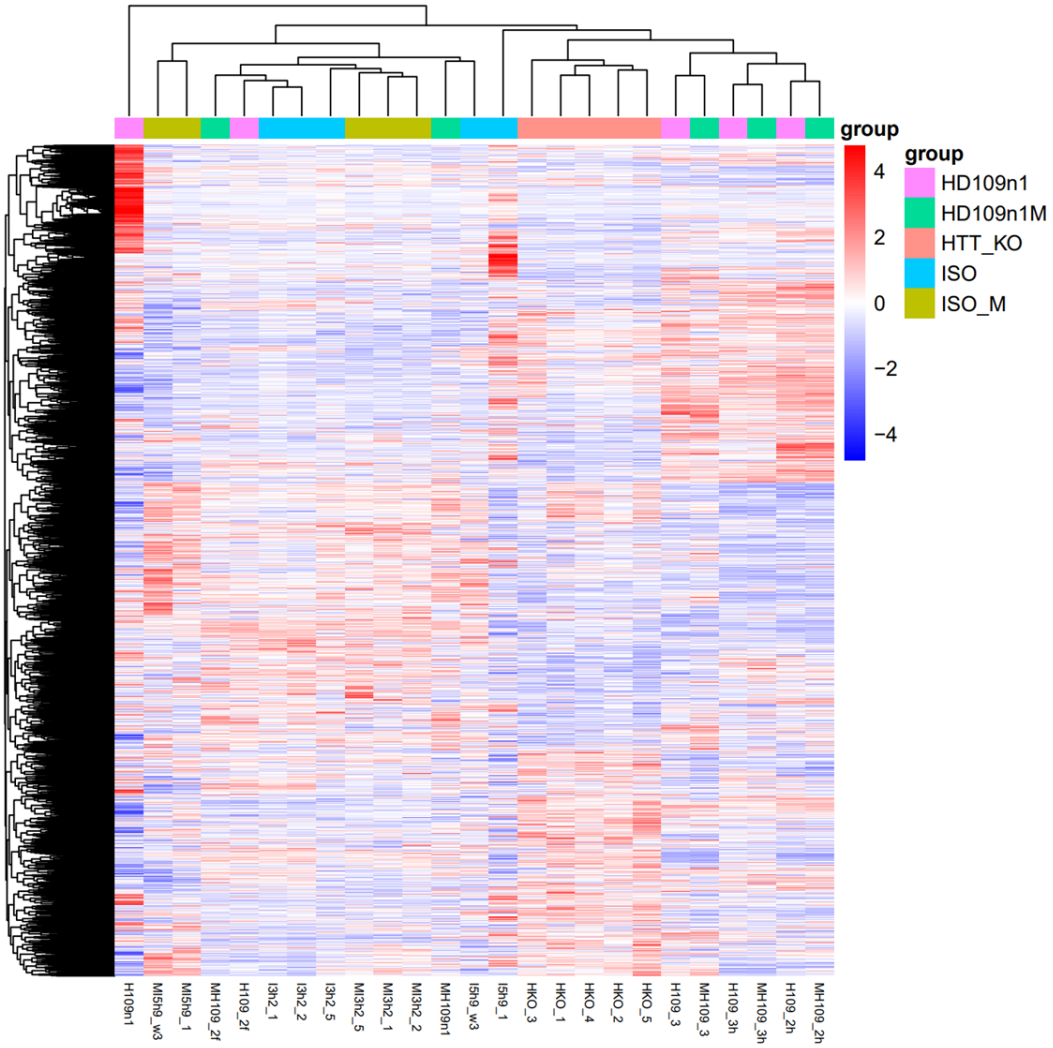

Figure 6.5. Hierarchical clustering heatmap of replicates. Differentially expressed genes in subclones on the bottom x-axis clustered by their scaled logcounts at log2 (FPKM+1) value applied to featureCounts in 'union' mode.

3) and I5H9_1 (isogenic subclone 1) subclones exhibited distinct profiles when compared to their intra-group analogues. HD109 subclones were mainly clustered with their respective miglustat-treated counterparts, though this was not the case with the more varied isogenic controls. HTT knockout lines clustered together in a clear group and exhibited a distinct gene expression profile when compared to the other groups.

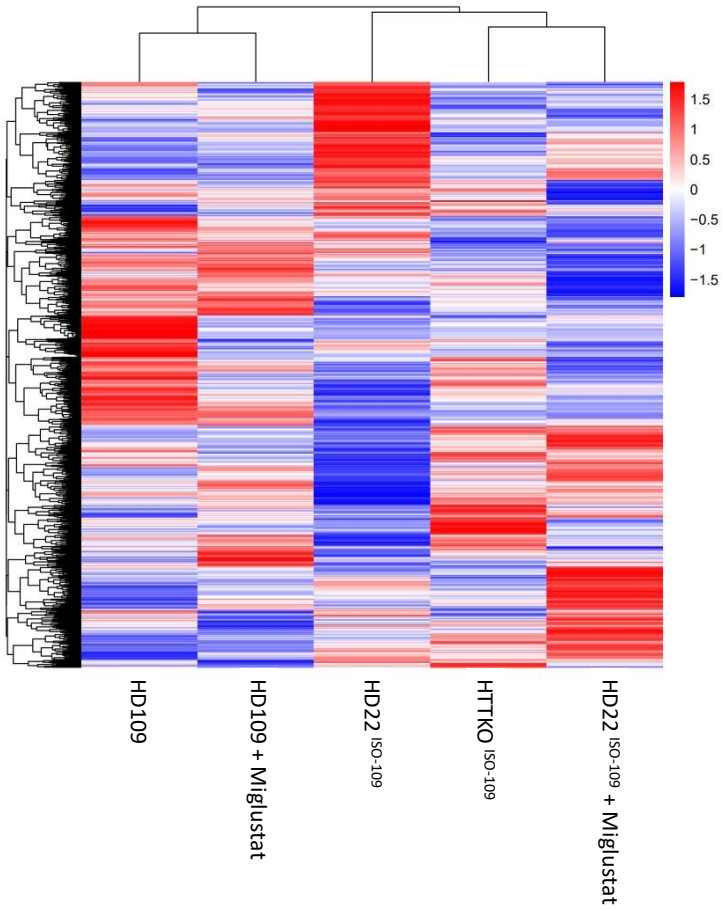

Figure 6.6. Heatmap showing differentially expressed genes across groups. Differentially expressed genes across comparison groups on the bottom x-axis clustered by their scaled logcounts at log2(FPKM+1) value applied to featureCounts in 'union' mode.

Comparisons between groups produced a low number of differentially expressed genes (p-adjusted ≤ 0.05; $\log_2$-fold change ≥ |1|). In HD109s, just 19 genes were significantly upregulated and 4 downregulated, relative to the isogenic controls (Figure 6.7A). Comparisons of HTT knockouts relative to the isogenic controls resulted in a greater number, 475, differentially expressed genes, (Figure 6.7B). Relative to the isogenic controls, HD109s and HTT knockouts shared 10 DEGs (Figure 6.7C), which included *AC136759.1* (unknown function), *AL021395.1* (unknown function), protein tyrosine phosphatase receptor type T (*PTPRT*), and protocadherin gamma subfamily A-10 (*PCDHGA10*) which were downregulated in both (Figure 6.7D), and 6 DEGs that were upregulated in both, including enoyl-CoA hydratase and 3-hydroxyacyl CoA dehydrogenase (*EHHADH*) and adhesion G protein-coupled receptor G5 (*ADGRG5*), mitogen-activated protein kinase kinase kinase 13 (*MAP3K13*), gem nuclear organelle associated protein 8 (*GEMIN8*), eukaryotic translation initiation factor 1A X-linked (*EIF1AX*), gprc5d and hebp1 antisense RNA 1 (*GPRC5D-AS1*).

To examine the effects of miglustat on the HD transcriptome, miglustat-treated HD109s were compared with untreated HD109s, revealing only one significant DEG, Early Growth Response 1 (*EGR1*) (Figure 6.8A). Also, to assess the effects of miglustat on wildtype cells, miglustat-treated and untreated isogenic controls were compared; a single DEG, zinc finger and BTB domain containing 16 (*ZBTB16*), was identified between the two groups (Figure 6.8B). miglustat-treated HD109s exhibited 12 differentially downregulated and 18 differentially upregulated genes relative to the untreated isogenic controls (6.8C and 6.8D).

Differentially expressed genes between miglustat-treated and untreated HD109s, relative to the isogenic controls were compared in order to identify miglustat-associated changes in gene expression (Figure 6.8E). Five of these were exclusive to untreated HD109s, suggestive of a restoration towards wildtype expression levels with miglustat; these included kinesin family members 25 (*KIF25*), *BX322639.1*, chromosome 5 open reading frame 63 (*C5orf63*), *AL512283.1*, and *AC073585.1* (Figure 6.8E). Twelve DEGs were specific to miglustat-treated HD109s (Figure 6.8E), suggestive of miglustat-mediated gene expression changes particular to HD; these included frizzled class receptor 10 antisense divergent transcript (*FZD10-AS1*),

trichohyalin (*TCHH*), homeobox C4 (*HOXC4*), FAM111 trypsin like peptidase B (*FAM111B*), homeobox C4 (*HOXC4*), cellular retinoic acid binding protein 1 (*CRABP1*), ATP/GTP binding protein like 4 (*AGBL4*), *AC079154.1* (unknown function), *AL513318.2* (unknown function), Y-box binding protein 2 pseudogene (*YBX2P1*) aldo-keto reductase family 1 member C3 (*AKR1C3*), and proline-rich 15 like (*PRR15L*). Eighteen DEGs were common to both miglustat-treated and untreated HD109s, relative to the isogenic controls, and thus, were unchanged with miglustat treatment (Figure 6.8E).

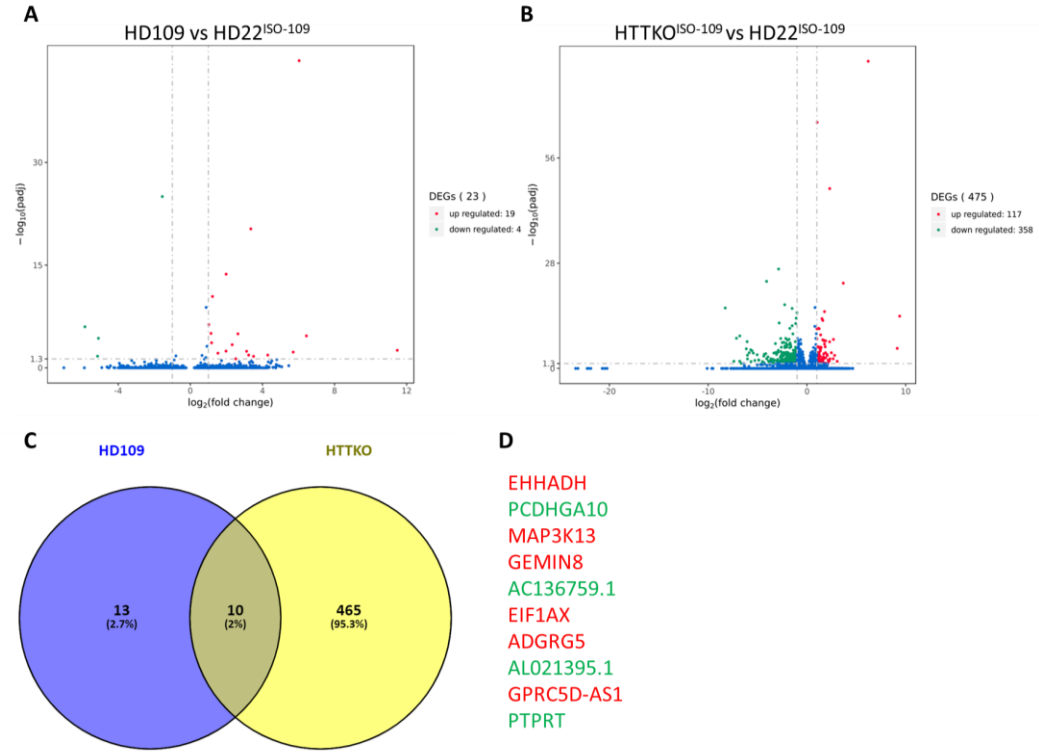

Figure 6.7. Differentially expressed genes in day 37 HD109 and HTT knockout neurons compared to isogenics. Volcano plots of down and upregulated genes. Green and red dots each represent a single gene, where mean expression level for each significant to an adjusted p-value < 0.05 (using the Benjamini and Hochberg's approach for controlling the False Discovery Rate), with log2 fold change expression level differences $\geq|1|$. Blue dots represent single genes that do not meet significance-level or fold change criteria. A) HD109 compared with isogenics or B) in HTT knockouts versus isogenics. C) Venn diagram of DEGs, relative to the isogenics, identified in HD109 versus isogenics, and HTT knockouts. D) List of down regulated (green) and upregulated (red) genes at the intersection in the Venn diagram.

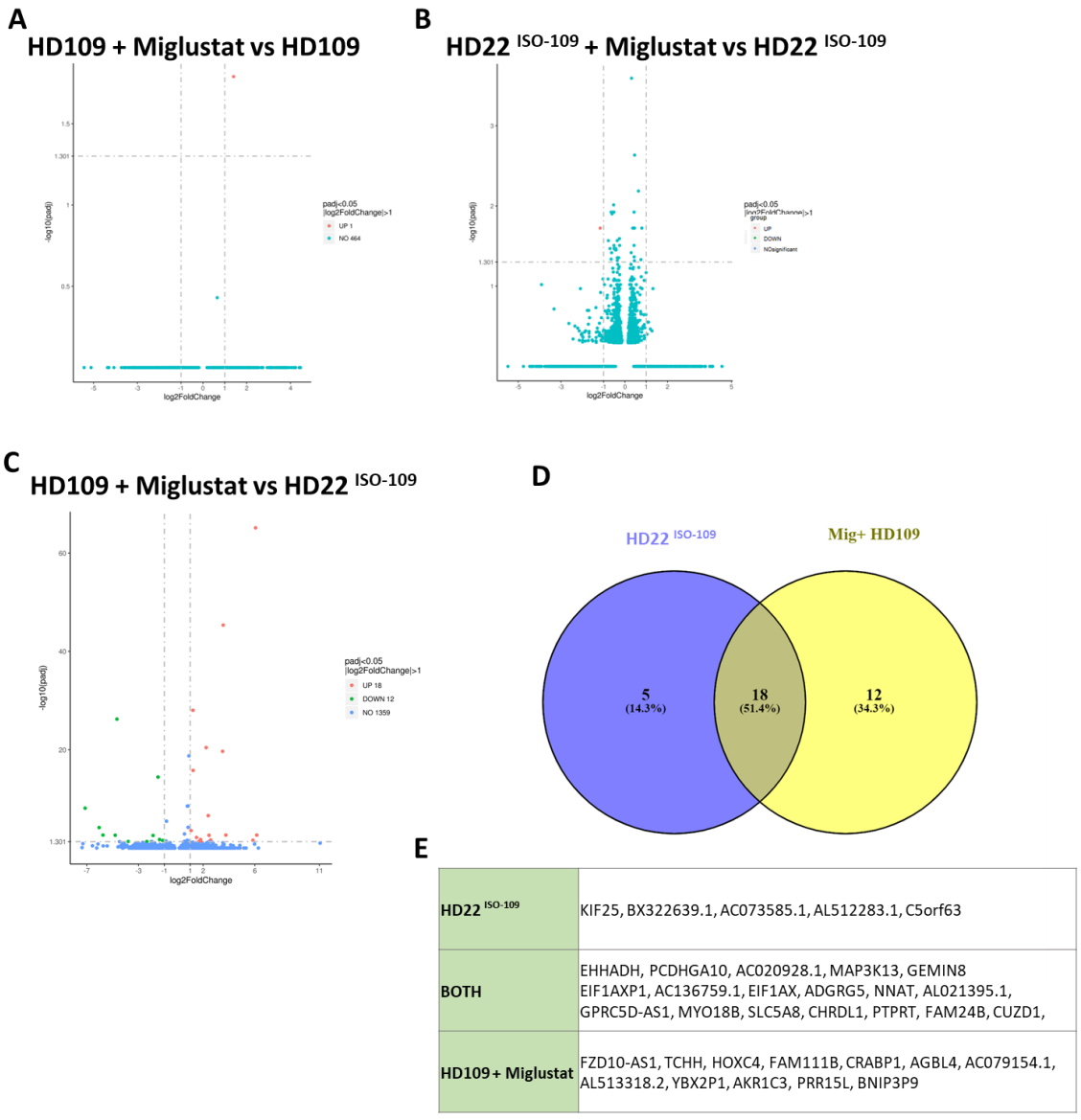

HD22 ISO-109	KIF25, BX322639.1, AC073585.1, AL512283.1, C5orf63
BOTH	EHHADH, PCDHGA10, AC020928.1, MAP3K13, GEMIN8 EIF1AXP1, AC136759.1, EIF1AX, ADGRG5, NNAT, AL021395.1, GPRC5D-AS1, MYO18B, SLC5A8, CHRDL1, PTPRT, FAM24B, CUZD1,
HD109 + Miglustat	FZD10-AS1, TCHH, HOXC4, FAM111B, CRABP1, AGBL4, AC079154.1, AL513318.2, YBX2P1, AKR1C3, PRR15L, BNIP3P9

Figure 6.8. Differentially expressed genes associated with miglustat treatment in day 37 neurons. Volcano plots of down and upregulated genes. Green and red dots each represent a single gene, where mean expression level for each significant to an adjusted p-value < 0.05 (using the Benjamini and Hochberg's approach for controlling the False Discovery Rate), with log2 fold change expression level differences ≥|1|. Blue dots represent single genes that do not meet significance-level or fold change criteria. A) Miglustat-treated HD109s compared to untreated HD109s. B) Miglustat treated isogenics compared with untreated cells. C) Miglustat-treated HD109s versus untreated isogenics. D) Venn diagram and DEGs in HD109 and miglustat-treated HD109s, both relative to the isogenics. E) List of DEGs represented in the Venn diagram (D), exclusive to HD109 and HD109 + miglustat, or shared by both miglustat-treated HD109 neurons compared to the isogenics.

Because there were so few differentially expressed genes in the comparisons between HD109s and isogenic controls, we wanted to compare our gene expression data to that of two similar studies, however, because there were so few DEGs with p adjusted ≤ 0.05 and log fold change ≥ 1 or ≤ -1, the parameters to define DEGs in our study were broadened to include all DEGs with a p ≤ 0.05, regardless of fold change. DEGs from two studies were used for comparison, in the first, Ooi et al. (2019b) used hESCs to generate NPCs and neurons, each of which were assessed relative to isogenic controls using an adjusted p value ≤ 0.05, regardless of fold change. Additionally, in a more related study, DEGs from several neural cell cultures differentiated from HD patient-derived iPSC lines (including HD109 cell line used here), were compared with wildtype controls, at an adjusted p value ≤ 0.05, and a $\log_2$ fold change ≥ $|1.5|$(Consortium 2017). To assess whether the lack of differentially expressed genes in our study might be related to differentiation state, the expanded DEG list in HD109s relative to the isogenic controls were compared with NPCs and neurons from Ooi et al. (2019b). In this study, when compared to wildtype cells, NPCs were observed to display a reduced number of DEGs relative to neurons. Correspondingly, the HD109 neurons generated in this thesis shared a higher percentage of DEGs with neurons (Figure 6.9B), than with the NPCs (Figure 6.9B) assayed in Ooi et al. (2019b). In both comparisons, however, percentages of common DEGs were low. Next, we compared the data obtained from neural cells in the HD iPSC Consortium (2017) study, with that from NPCs and neurons assayed in the Ooi et al. (2019b) study, and though a similar increase in shared DEGs was seen between neural cells and neurons (4.2%) as opposed to neural cells and NPCs (1.4%), the small percentage of overlap between the neural cells and neurons from both studies, indicates a lack of consistency (Figure 6.9B). Finally, neurons from the Ooi et al. (2019b) study, neural cells from the Consortium (2017), and HD109 neurons from this thesis, were compared to assess consistency across all three studies (Figure 6.9C), and identified only 0.1% of DEGs (7 genes) that were commonly and differentially expressed (Figure 6.9D).

Similarly, we compared DEGs identified in our HTT knockout neurons relative to the isogenic controls, to those identified in a recent study by Bensalel et al. (2021), which measured HTT knockouts relative to wildtype SHSY5Y cells (Figure 6.10A). However, because there was an

adequate number of DEGs identified in the HTT knockout neurons in this thesis, the original threshold (adjusted p-value ≤ 0.05, and log2 fold change ≥|1|), was retained for comparison, and only 25, or 3% of differentially expressed genes were shared in HTT knockouts across both studies (Figure 6.10A and 10B). The common DEGs from both studies were entered into STRING: functional protein association networks database (https://string-db.org/), which indicated a significant functional relationship between the genes (Figure 10C). Significantly enriched Gene Ontology (GO) terms for biological processes related to this protein-protein interaction network, determined using the Benjamini–Hochberg procedure with a false discovery rate ≤ 0.05, included a number of terms related to neurodevelopment including, orbitofrontal cortex development, branching morphogenesis of a nerve, neuronal stem cell population maintenance, glial cell fate commitment, and positive regulation of neuroblast proliferation.

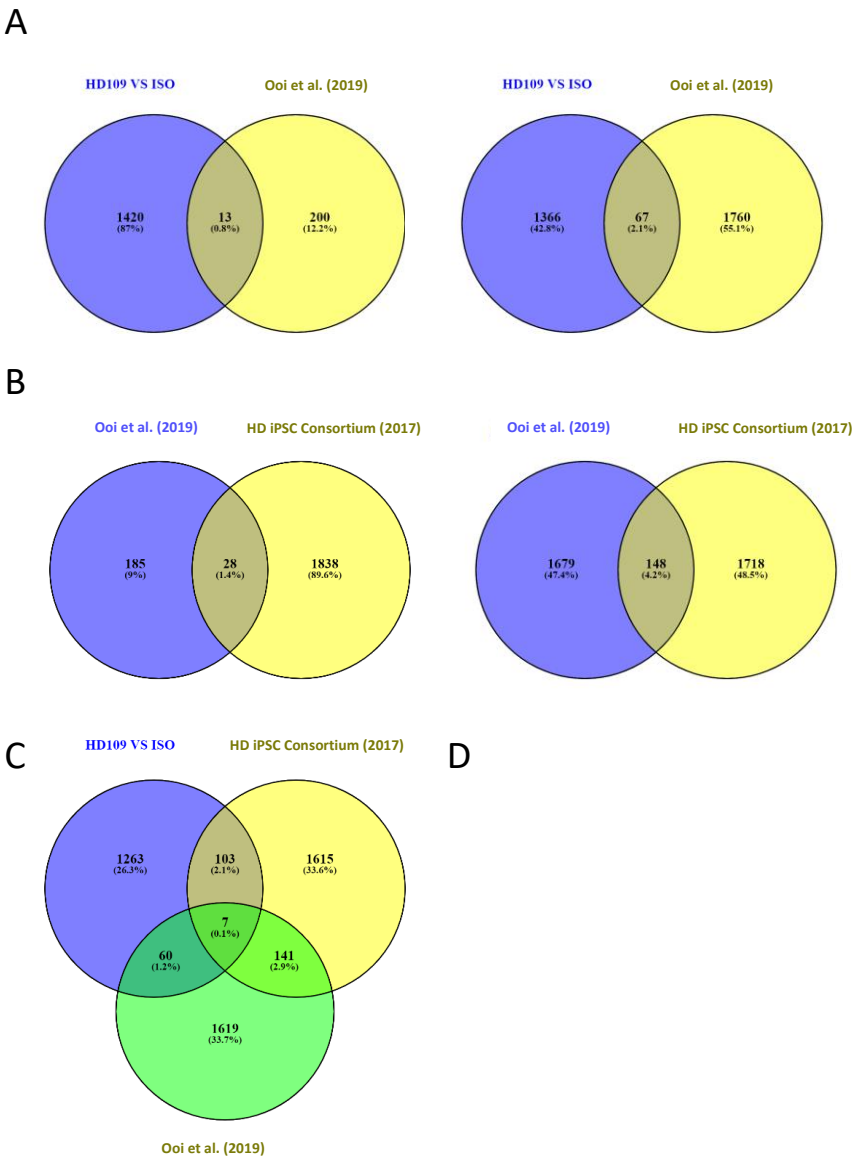

Figure 6.9 Venn diagrams comparing DEGs in day 37 HD109 neurons with other HD models. A) Venn diagrams comparing an expanded set of DEGs in HD109 neurons with ($p \leq 0.05$) relative to the isogenic controls, with NPCs (left) and neurons (right) from Ooi et al. (2019b). B) Venn diagrams comparing DEGs in NPCs (left) and neurons (right) from Ooi et al. (2019b) with neural cells from the HD iPSC Consortium (2017). C) Venn diagram of DEGs in neurons from Ooi et al. (2019b), neural cells from the HD iPSC Consortium (2017), and HD109 neurons from this thesis. D) List of DEGs shared with neurons from Ooi et al. (2019b), neural cells from the HD iPSC Consortium (2017), and HD109 neurons from this thesis.

A

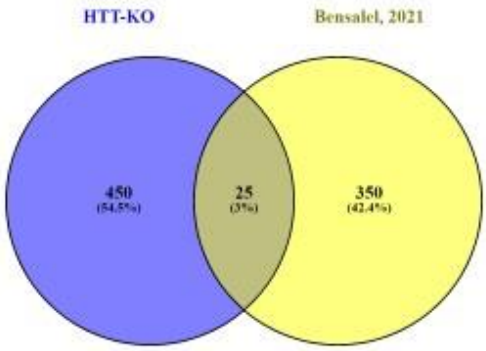

B

DEGS COMMON TO BOTH STUDIES	
NOTCH1	FGFR2
COL5A1	TMEM2
SOX9	ELAVL2
CHRM2	ARHGAP42
CXCL12	TMEM63A
PLPP4	RIPK4
SOX2	STARD8
CALB1	PTPN3
GBP2	ITGA5
ANKRD33B	CD274
INSM1	DRD2
FOXO1	ABCA12
NEDD9	

C

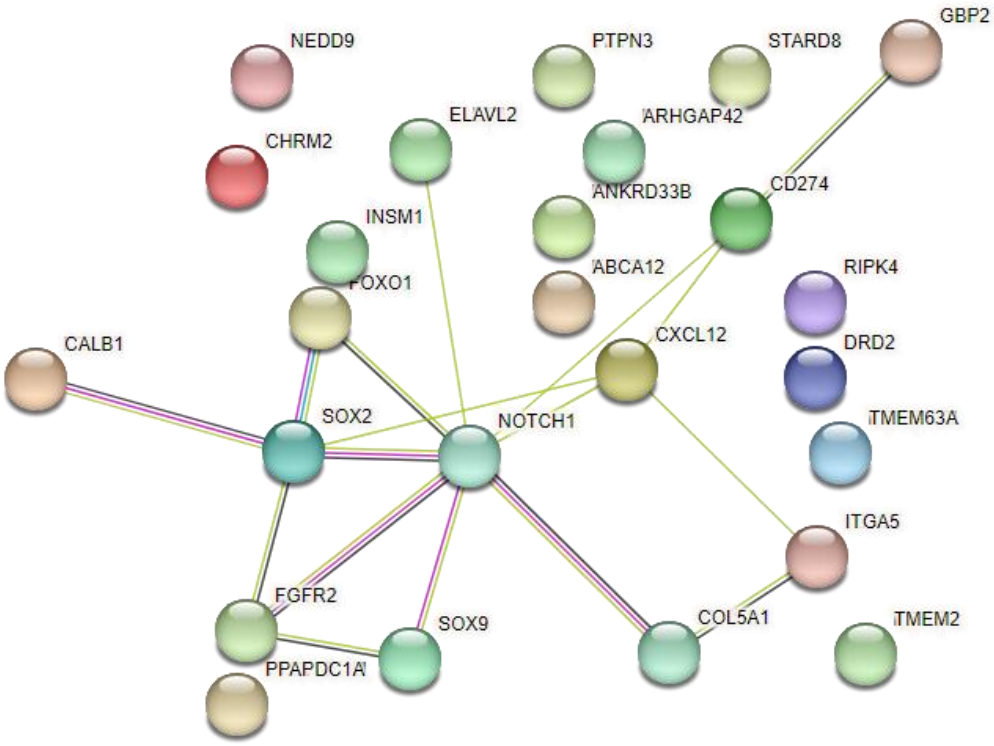

Figure 6.10. Comparisons of HTTKO ISO-109 neurons and HTT knockouts in SHSY5Y cells. A) Venn diagram of DEGs identified in this thesis from HTTKO ISO-109 neurons relative to the isogenic controls ($p_{adj} \leq 0.05$, and log2 fold change $\geq|1|$) with DEGs in HTT knockouts identified in Bensalel et al. (2021). B) List of DEGs shared in HTT knockouts, between the two studies. C) Protein-protein interactions generated using the STRING database; PPI enrichment p = 0.000903, full string network, line thickness represents evidence of interaction, with a minimum required interaction score = 0.4.

6.3.4 Gene Set Enrichment

Next, using defined genes sets within the Kyoto Encyclopedia of Genes and Genomes (KEGG) (http://wwnome.jp/kegg/) database, enrichment analysis across treatment groups was carried out to compare potential differences (or similarities), within higher order physiological pathways. The clusterProfiler (version 3.8.1) R package was used to examine the statistical enrichment of differential expression in KEGG pathways in an unbiased manner (Wu et al. 2021). However, because there were a limited number of significantly enriched gene sets with adjusted p-values ≤ 0.05, and because KEGG analysis is exploratory, we also employed a biased approach to examine pathways relevant to structural or functional differences seen in chapters 4 and 5 structural, with emphasis on the lysosome, autophagy, mitophagy, oxidative phosphorylation, cholesterol metabolism, and sphingolipid metabolism pathways.

6.3.4.1 KEGG Gene Set Enrichment in HD109s relative to isogenic controls

Relative to the isogenic controls, in HD109s the highest ranked downregulated pathways were not pertinent to the endolysosomal system, and the only significantly enriched gene set was neuroactive ligand receptor interaction (Figure 6.11A). Cholesterol and fat digestion and absorption were amongst the most enriched pathways, though again, these did not reach significance (Table 6.2, Figure 6.11B). Common genes in both of these pathways included cluster of differentiation 36 (*CD36*), ATP binding cassette subfamily G member 8 (*ABCG8*), and ATP binding cassette subfamily G member 5 (*ABCG5*). In addition, lipoprotein-A (*LPA*) and lipoprotein-A-like 2 pseudogenes (*LAPL2*) were upregulated in the cholesterol pathway.

Because LAMP1 area was increased in the HD109s relative to the isogenic controls, and because it is central to this thesis, the lysosomal pathway was explored (Figure 6.12). In the lysosomal pathway, deoxyribonuclease 2β (*DNase2B*), a lncRNA associated with cathepsin D (*AC068580.3*), adaptor protein complex-3 mu 2 subunit (*AL354794.2*), and neuraminidase 1 (*NEU1*) are downregulated (Table 6.1), while cathepsin F (*CTSF*), β-glucuronidase pseudogene 5 (*GUSBP5*), arylsulfatase (*GARS*) and adaptor related protein complex 1 subunit mu 2 (*AP1M2*) are upregulated (Table 6.1).

Differences in both autophagy and mitochondrial structure and bioenergetics were seen in Chapters 4 and 5, and relatedly, both autophagy and mitophagy gene sets, showed upregulation particular to AMBRA1 and BNIP3, while autophagy showed downregulation in TRAF6. In the autophagy pathway, HD109 neurons showed an increased expression of BCL2 interacting protein 3 pseudogene 9 (*BNIP3P9*), long intergenic non-protein coding RNA 311 (*LINC00311*), discs large MAGUK scaffold protein 1 (*AC006305.1*), BCL2 interacting protein 3 pseudogene 17 (*BNIP3P17*), BCL2 interacting protein 3 pseudogene 27 (*BNIP3P27*), high mobility group box *1* (*HMGB1*), and intercellular adhesion molecule 2 (*ICAM2*). Upregulation in the mitophagy pathway included most genes that were upregulated in the autophagy pathway including, *BNIP3P9, LINC00311, AC006305.1, BNIP3P17, BNIP3P27 and ICAM2,* with the addition of FUN14 domain containing 1 (*FUNDC1*). Downregulated genes in the autophagy pathway included autophagy related 4A cysteine peptidase (*ATG4A*), TNF receptor associated factor 6 pseudogene 1 (*TRAF6P1*), CD225 family protein FLJ76511 (*AC068580.3*), autophagy related 101 (*ATG101*), BCL2 interacting protein 3 pseudogene 25 (*BNIP3P2*), eukaryotic translation initiation factor 2α kinase 3 (*EIF2AK3*), and BCL2 interacting protein 3 pseudogene 5 (*BNIP3P5*). Genes associated with decreased expression in the mitophagy pathway included Ras homolog family member t1 pseudogene 1 (*RHOT1P1*), Jun proto-oncogene, AP-1 transcription factor subunit (*JUN*), BCL2 interacting protein 3 pseudogene 25 (*BNIP3P25*), Ras homolog family member T1 pseudogene 2 (*RHOT1P2*), *EIF2AK3*, and BCL2 interacting protein 3 pseudogene 5 (*BNIP3P5*).

In chapter 5, percent spare respiratory capacity was shown to be reduced in HD109 neurons relative to isogenic controls, therefore the oxidative phosphorylation pathway was considered. In this pathway, downregulation was present in mitochondrially encoded NADH - ubiquinone oxidoreductase core subunit 3 (*MT-ND3*), mitochondrially encoded cytochrome C oxidase III (*MT-CO3*), and ATP Synthase membrane subunit c locus 1 pseudogene 4 (*ATP5MC1P4*), while upregulation in NADH: ubiquinone oxidoreductase subunit AB1 pseudogene 1 (*NDUFAB1P1*), *AC114491.1* (unknown function), *AC005828.6* (unknown function), cytochrome C oxidase subunit 6C pseudogene 17 (*COX6CP17*), mitochondrially encoded NADH - ubiquinone oxidoreductase core subunit 1 pseudogene (*MTND1P8*), and

mitochondrially encoded cytochrome B pseudogene 43 (*MTCYBP43*), were observed (Table 6.1).

Finally, because GM1 distribution was shown to be altered in HD109 NPCs and neurons, sphingolipid metabolism was assessed, with upregulation seen in sphingosine-1-phosphate phosphatase 2 (*SGPP2*) and alkaline ceramidase 2 (*ACER2*), and downregulation seen in Neuraminidase 1 (*NEU1*) (Table 6.1).

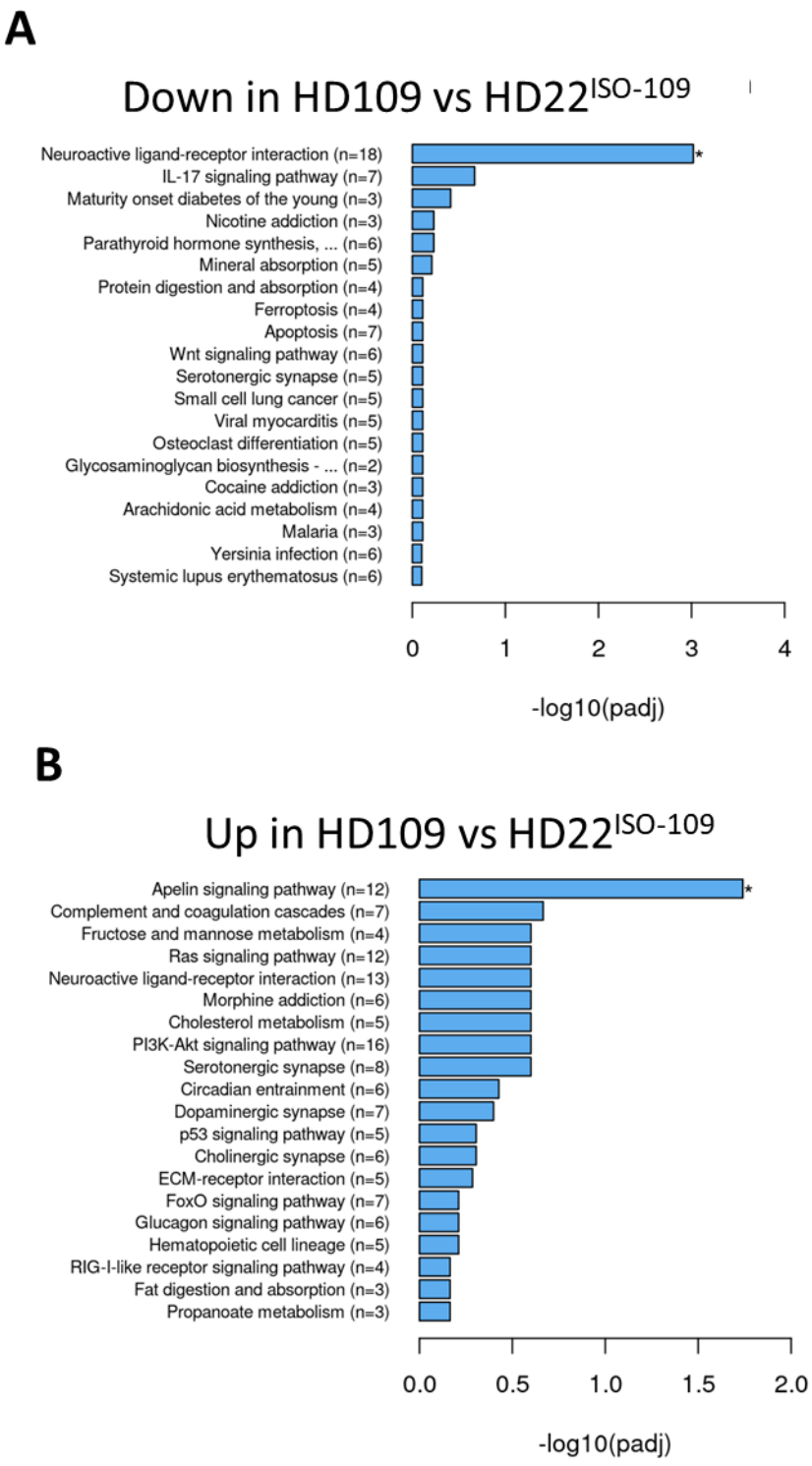

Figure 6.11. Ranked list of top upregulated and downregulated KEGG pathways in day 37 HD109 neurons compared to isogenic controls. A) Negatively enriched gene sets and B) positively enriched gene sets. Asterisks indicate significantly enriched gene sets, hypergeometric test FDR correction method: Benjamini and Hochberg with adjusted p-values ≤ 0.05.

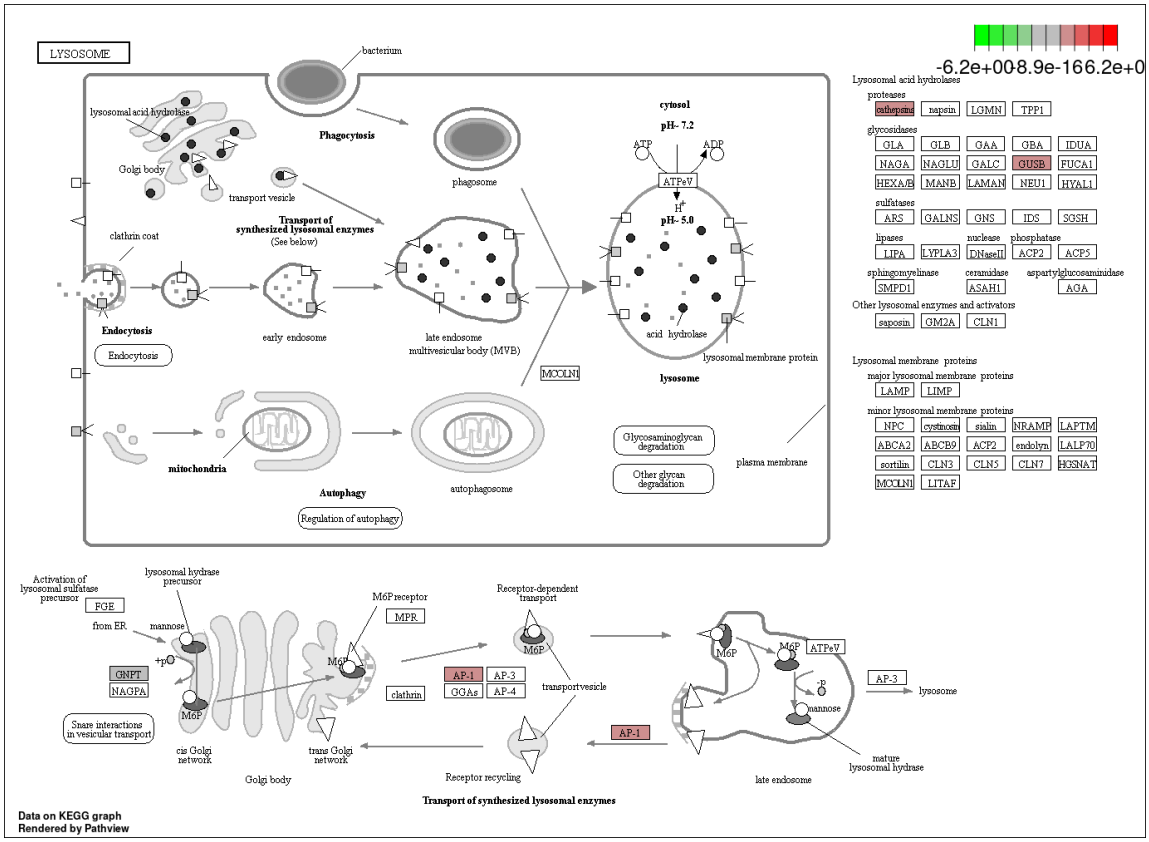

Figure 6.12. Schematic depicting altered components within the KEGG lysosome pathway in HD109 neurons relative to the isogenics.

	PATHWAY OF INTEREST	KEGGID	Description	GeneRatio	BgRatio	pvalue	padj	Gene Names
HD109 UP VS HD22 ISO-109	CHOLESTEROL	hsa04979	Cholesterol metabolism	5|227	67|12447	0.007452	0.251099	CD36/ABCG8/LPA/ABCG5/LPAL2
	LIPID METABOLISM	hsa04975	Fat digestion and absorption	3|227	49|12447	0.059781	0.683426	CD36/ABCG8/ABCG5
	LYSOSOME	hsa04142	Lysosome	4|227	160|12447	0.334071	0.89853622	GUSBP5/CTSF/AP1M2/ARSG
	AUTOPHAGY	hsa04140	Autophagy-animal	7|227	351|12447	0.459335	0.96037177	BNIP3P9/LINC00311/AC006305.1/BNIP3P17/BNIP3P27/HMGB1/ICAM2
	MITOPHAGY	hsa04137	Mitophagy-animal	7|227	260|12447	0.197625	0.80237874	BNIP3P9/FUNDC1/LINC00311/AC006305.1/BNIP3P17/BNIP3P27/ICAM2
	MITO STRESS	hsa00190	Oxidative phosphorylation	3|227	478|12447	0.993322	0.997713	MT-ND3/MT-CO3/ATP5MC1P4
	GANGLIOSIDES	hsa00600	Sphingolipid metabolism	2|227	53|12447	0.251782	0.839083	SGPP2/ACER2
HD109 DOWN VS HD22 ISO-109	CHOLESTEROL	hsa04979	Cholesterol metabolism	1|191	67|12447	0.646145	0.921355	APOE
	LIPID METABOLISM	hsa04975	Fat digestion and absorption	1|191	49|12447	0.531965	0.910549	
	LYSOSOME	hsa04142	Lysosome	4|191	160|12447	0.231216	0.86078929	NEU1/AC068580.3/AL354794.2/DNASE2B
	AUTOPHAGY	hsa04140	Autophagy-animal	7|191	351|12447	0.294	0.87708502	ATG4A/TRAF6P1/AC068580.3/ATG101/BNIP3P25/EIF2AK3/BNIP3P5
	MITOPHAGY	hsa04137	Mitophagy-animal	6|191	260|12447	0.210331	0.86078929	RHOT1P1/JUN/BNIP3P25/RHOT1P2/EIF2AK3/BNIP3P5
	MITO STRESS	hsa00190	Oxidative phosphorylation	6|191	478|12447	0.747358	0.932051	NDUFAB1P1/AC114491.1/AC005828.6/COX6CP17/MTND1P8/MTCYBP43
	GANGLIOSIDES	hsa00600	Sphingolipid metabolism	1|191	53|12447	0.560151	0.911705	NEU1

Table 6.1. KEGG pathways of interest in day 37 HD109 neurons versus isogenic controls. Upregulated genes and down regulated genes associated with each pathway. GeneRatio is defined as the number differentially expressed genes in each pathway divided by all differentially expressed genes within the KEGG database. BgRatio is defined as the ratio of all genes related to this KEGG term to all genes in the KEGG database relevant for this group comparison.

6.3.4.2 KEGG Gene Set Enrichment in HTT knockout cells

In Chapter 4, the area of the autophagic compartment in HTT knockout NPCs was increased relative to both the isogenic controls and the HD109s, and though nonsignificant, the area of the LAMP1 positive lysosomal compartment was on average higher than that measured in the isogenic controls. Therefore, in addition to an unbiased assessment of KEGG pathways that are altered in HTT-null neurons, the lysosome and autophagy pathways were also assessed. This was carried out in an effort to identify into transcriptomic shifts associated with a lack of huntingtin, which might provide insight into to wildtype HTT function and to compare with the HD109s to investigate gain insight into potential loss of function versus gain of function in HD.

In HTT knockouts, both significant downregulation and upregulation were seen within the calcium signalling pathway relative to the isogenic controls (Figure 6.13, Table 6.5). Other top-ranked, though non significantly upregulated pathways in HTT knockouts included the lysosome and fatty acid biosynthesis (Figure 6.13B, Table 6.6).

In the lysosome gene set (Figure 6.14), downregulated components in the knockouts included cathepsins and saposin, V-type proton ATPase (ATPeV), and AP-3. Genes involved in these processes, included *CTSF and AL354794.2* (both of which were affected in the HD109s), cluster of differentiation 164 (*CD164*), prosaposin (*PSAP*), and V-type proton ATPase subunit D2 (*ATP6V0D2*). In the knockouts, upregulated components in the lysosome pathway, involved trafficking including AP-1, AP-3, mannose-6-phosphate receptor (MPR), N-acetylglucosamine-1-phosphodiester alpha-n-acetylglucosaminidase (NAGPA), lysosomal enzymes including cathepsins, phosphomannomutase (MANB), sulfatase (SGSH), sphingomyelinase (SMPD1), and GM2 ganglioside activator (GM2A), as well as lysosomal membrane proteins LAMP and sortilin. Upregulated genes involved in trafficking and transport, included mannose-6-phosphate receptor (*M6PR*), adaptor related protein complex 3 subunit mu 2 (*AP3M2*), (*AP1M2*), adaptor related protein complex 1 subunit beta 1 (*AP1B1*), adaptor related protein complex 3 subunit delta 1 (*AP3D1*), adaptor related protein complex 3 subunit sigma 2 (*AP3S2*), and N-acetylglucosamine-1-phosphodiester alpha-N-acetylglucosaminidase (*NAGPA*). Upregulated genes related to lysosomal enzymes included

cathepsin A (*CTSA*), sphingomyelin phosphodiesterase 1 (*SMPD1*), N-sulfoglucosamine sulfohydrolase (*SGSH*), mannosidase beta (*MANBA*), ganglioside GM2 activator (*GM2A*). Membrane proteins included *LAMP1* and sortilin 1 (*SORT1*).

Upregulated components within the autophagy and mitophagy pathways in the HTT knockout neurons versus the isogenic controls (Table 6.2), included activating molecule in BECN1-regulated autophagy protein 1 (AMBRA1), BCL2/adenovirus E1B 19 kDa protein-interacting protein 3 (BNIP3), both of which were upregulated in HD109s. Enriched genes in both included, *AC012594.1* (unknown function), ribonuclease P/MRP subunit P14 (*RPP14*), *AP000845.1* (unknown function), *AC008443.1* (unknown function), lnc-RNA (*AC092171.2)*, mitogen-activated protein kinase 9 (*MAPK9*); interestingly, none of these coincided with the upregulated AMBRA1- or BNIP3-related genes in the HD109s. In autophagy, several additional components and corresponding transcripts were upregulated, including extracellular signal-regulated kinase (ERK) by mitogen-activated protein kinase 3 (*MAPK3*), PKA by protein kinase CAMP-Activated catalytic subunit alpha (*PRKACA*), c-Jun N-terminal protein kinase 1 (JNK1), BAD by BCL2 associated agonist of cell death *(BAD)*, ATG10 by autophagy related 10 (*ATG10*), WIPI by WD repeat domain, phosphoinositide interacting 1 (*WIPI1*), WD repeat domain 41 (*WDR41*) and LAMP by *LAMP1.* When looking at upregulation in mitophagy, enrichment was seen in FUNDC1 with FUN14 domain containing 1 (FUNDC1), and in CK2 by casein kinase 2 Beta (CSNK2B).

In addition, cholesterol metabolism, glycosphingolipid biosynthesis - ganglio series, and sphingolipid metabolism were also assessed (Table 6.2). In the cholesterol metabolism gene set, neutral cholesterol ester hydrolase 1 (*NCEH1*), VAMP associated protein B and C (*VAPB*), apolipoprotein C1 (*APOC1*), cytochrome P450 family 27 subfamily A member 1 (*CYP27A1*), sortilin 1 (*SORT1*) were upregulated, while ATP binding cassette subfamily A member 1 (*ABCA1*), proprotein convertase subtilisin/kexin type 9 (*PCSK9*), myosin regulatory light chain interacting protein (MYLIP), voltage dependent anion channel 1 pseudogene 3 (*VDAC1P3*), VDAC2 pseudogene 4 (*VDAC2P4*), translocator protein (*TSPO*), and phospholipid transfer protein (*PLTP*) were downregulated. Beta-1,4-N-acetyl-galactosaminyltransferase 1 (*B4GALNT1*) was upregulated in the glycosphingolipid biosynthesis – ganglio series gene set.

Upregulated genes in the sphingolipid metabolism gene set included sphingomyelin phosphodiesterase 1 (*SMPD1*), serine palmitoyltransferase long chain base subunit 2 (*SPTLC2*), and sphingosine kinase 2 (*SPHK2*), while galactose-3-O-sulfotransferase 1 (*GAL3ST1*) and sphingomyelin phosphodiesterase 3 (*SMPD3*) were downregulated.

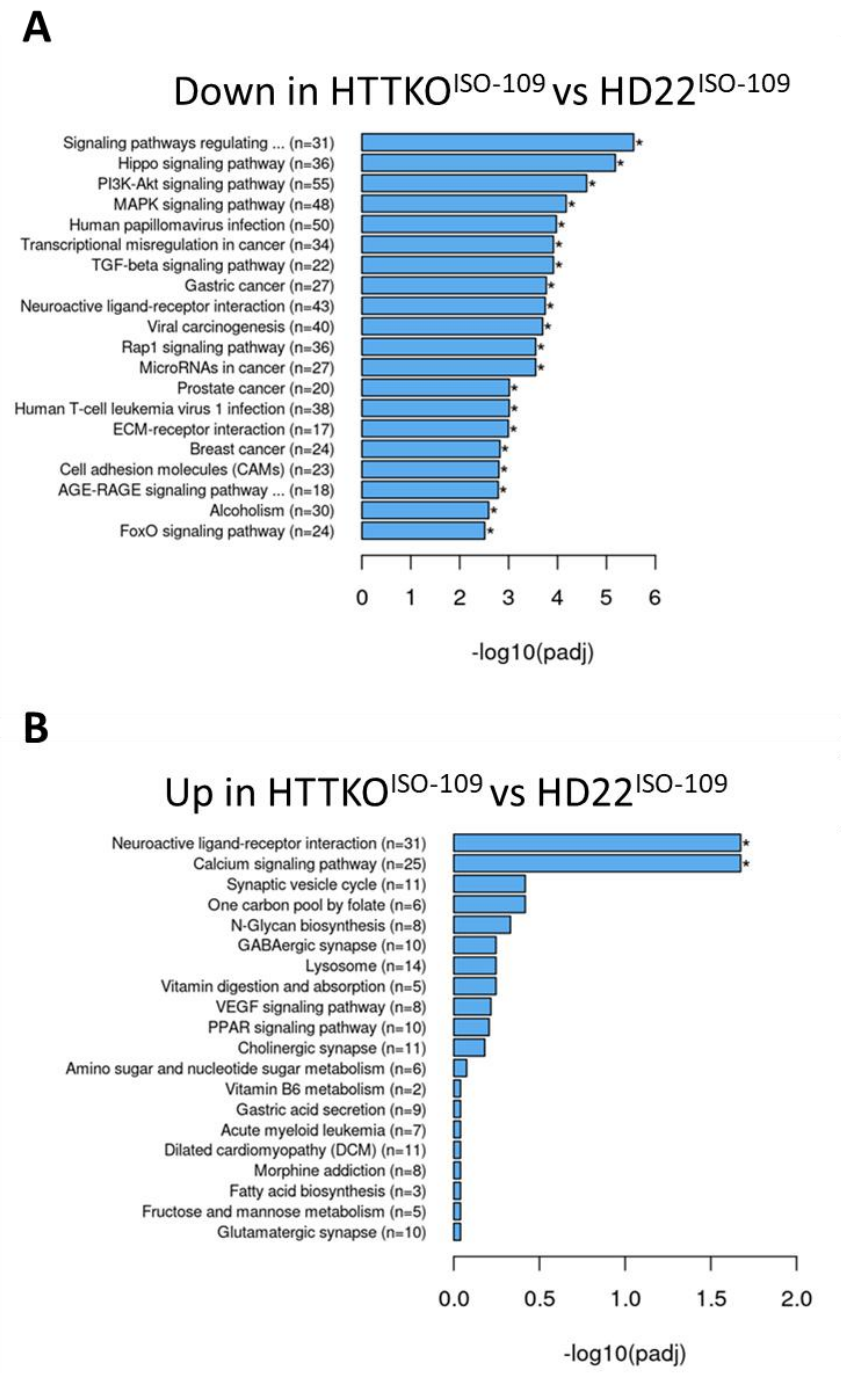

Figure 6.13 Ranked list of top upregulated and downregulated KEGG pathways in day 37 HTT knockout neurons compared to isogenic controls. A) Negatively enriched gene sets and B) positively enriched gene sets. Asterisks indicate significantly enriched gene sets, hypergeometric test FDR correction method: Benjamini and Hochberg with adjusted p-values ≤ 0.05.

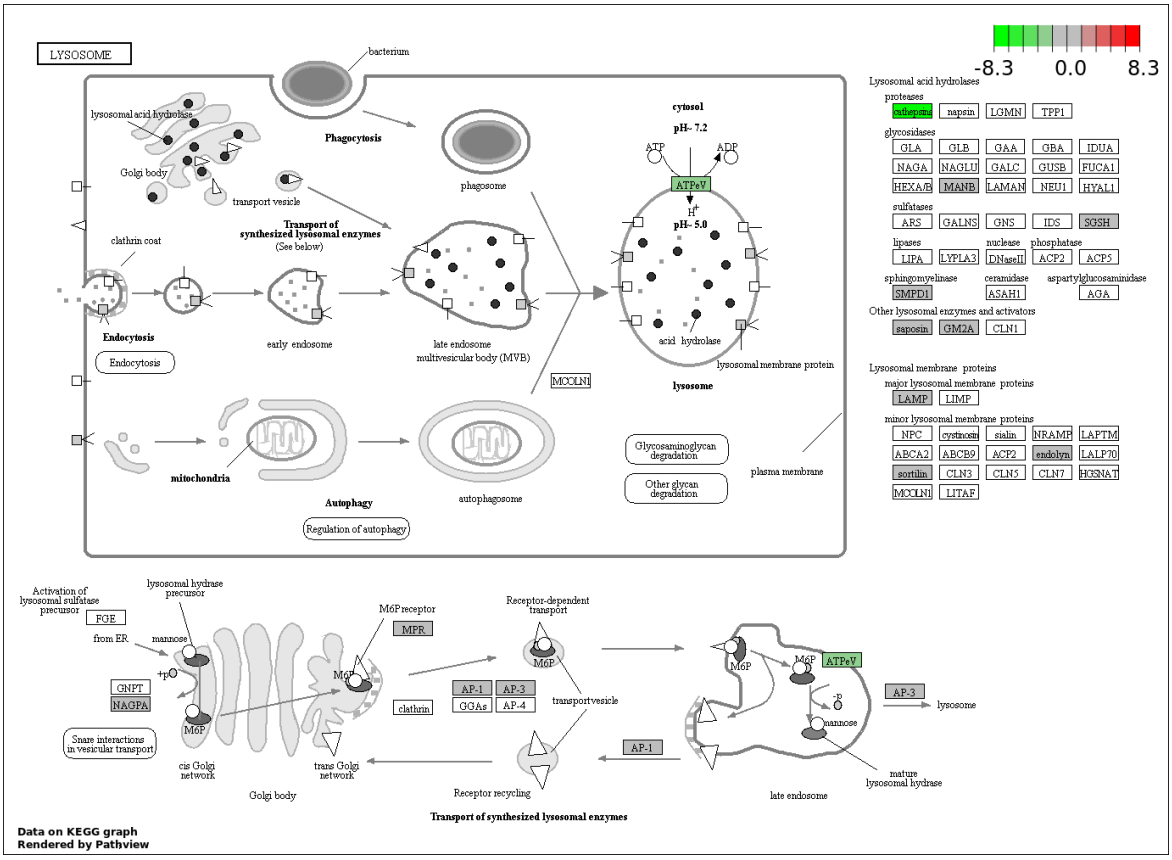

Figure 6.14. Schematic depicting altered components within the KEGG lysosome pathway in day 37 HTT knockout neurons versus isogenic controls.

	PATHWAY OF INTEREST	KEGGID	Description	GeneRatio	BgRatio	pvalue	padj	Gene Names
HTTKO ISO-109 UP VS HD22 ISO-109	LYSOSOME	hsa04142	Lysosome	14|547	159|11981	0.014043	0.56689359	M6PR/CTSA/SMPD1/SGSH/MANBA/GM2A/AP3M2/LAMP1/SORT1/AP1M2/AP1B1/AP3S2/NAGPA/AP3D1
	AUTOPHAGY	hsa04140	Autophagy-animal	13|547	343|11981	0.793357	0.98632296	WIPI1/AC012594.1/RPP14/LAMP1/WDR41/PRKACA/ATG10/AP000845.1/MAPK3/AC008443.1/AC092171.2/BAD/MAPK9
	MITOPHAGY	hsa04137	Mitophagy-animal	8|547	250|11981	0.889736	0.98632296	FUNDC1/AC012594.1/RPP14/AP000845.1/AC008443.1/CSNK2B/AC092171.2/MAPK9
	CHOLESTEROL	hsa04979	Cholesterol metabolism	5|547	65|11981	0.174748	0.918886	NCEH1/VAPB/APOC1/CYP27A1/SORT1
	GANGLIOSIDES	hsa00604	Glycosphingolipid biosynthesis-ganglio series	1|547	11|11981	0.402055	0.945101	B4GALNT1
	GANGLIOSIDES	hsa00600	Sphingolipid metabolism	3|547	53|11981	0.438204	0.945101	SMPD1/SPTLC2/SPHK2
	CALCIUM	hsa04020	Calcium signaling pathway	25|547	239|11981	9.48E-05	0.021191	PTGFR/HTR2C/PRKCB/P2RX5/PLCD3/SLC8A2/DRD1/HRH1/HRH2/CCKBR/TACR2/ADRB1/MYLK3/PRKACA/CHRNA7/PPP3R1/SLC25A4/ORAI2/CHRM3/PHKA1P1/ATP2A2/CACNA1D/CCR12P/SLC25A5/SPHK2
HTTKO ISO-109 DOWN VS HD22 ISO-109	LYSOSOME	hsa04142	Lysosome	5|753	159|11981	0.97484	0.99932085	CTSF/CD164/AL354794.2/PSAP/ATP6V0D2
	AUTOPHAGY	hsa04140	Autophagy-animal	16|753	343|11981	0.919298	0.99932085	AC008467.1/EIF2AK3/C9orf72/HMGB1P41/STK11/AC116535.1/AC090616.6/ATG4A/COMMD10/BNIP3P25/INS/AC068491.4/AC011447.7/LINC00311/AC104134.1/PIK3CA
	MITOPHAGY	hsa04137	Mitophagy-animal	17|753	250|11981	0.404168	0.68433007	CITED2/JUN/AC008467.1/EIF2AK3/SP1/BNIP3L/AC116535.1/AC090616.6/TP53/COMMD10/RPS27AP7/BNIP3P25/AC012170.3/AC068491.4/AC011447.7/LINC00311/AC104134.1
	CHOLESTEROL	hsa04979	Cholesterol metabolism	7|753	65|11981	0.112335	0.278965	ABCA1/PCSK9/MYLIP/VDAC1P3/VDAC2P4/TSPO/PLTP
	GANGLIOSIDES	hsa00600	Sphingolipid metabolism	2|753	53|11981	0.854608	0.999321	GAL3ST1/SMPD3
	CALCIUM	hsa04020	Calcium signaling pathway	27|753	239|11981	0.002202	0.019302	ADCY2/CHRM2/AC136759.1/ERBB4/ADRA1D/HTR7/PTGER3/ITPKA/PHKG1/ITPR2/AVPR1A/VDAC1P3/P2RX2/ADCY4/EDNRB/PTAFR/TBXA2R/TACR1/ATP2B4/RYR3/CASQ1/VDAC2P4/CACNA1H/AGTR1/F2R/PLCG2/MYLK

Table 6.3. Relevant KEGG pathways of interest and associated genes, autophagy and mitophagy, in day 37 HTT knockout neurons versus isogenics. Upregulated genes and down regulated genes associated with each pathway. GeneRatio is defined as the number differentially expressed genes in each pathway divided by all differentially expressed genes within the KEGG database. BgRatio is defined as the ratio of all genes related to this KEGG term to all genes in the KEGG database relevant for this group comparison.

6.3.5 Enrichment and miglustat

6.3.5.1 KEGG gene set enrichment in miglustat-treated HD109s versus untreated HD109s

Because miglustat treatment produced effects towards restoring mitochondrial length in NPCs (Figure 4.11), decreasing the ratio of vesicles exhibiting storage phenotypes in neurons (Figure 4.15), slightly reducing cholesterol and ganglioside storage in HD neurons (Figures 5.3 and 5.6, respectively), we wanted to discern whether miglustat produced related changes to the transcriptomic profile of HD109 neurons relative to untreated HD109 neurons. However, there were no significant changes in KEGG pathways associated with miglustat treatment. Calcium signalling was amongst the top ranked upregulated KEGG pathways, though not significant after adjusting for multiple comparisons (Figure 6.15)

There was no enrichment observed in the lysosomal gene set (Table 6.3). In the autophagy pathway, BCL2 interacting protein 3 pseudogene 22 (*BNIP3P22*), autophagy related 101 (*ATG101*), and *AC007192.1* (unknown function) were upregulated, and long intergenic non-protein coding RNA 327 (*LINC00327*) was downregulated (Table 6.3). In the mitophagy gene set, *BNIP3P22* was upregulated, while *LINC00327* and *AC105402.1* (unknown function), were downregulated (Table 6.3). Cholesterol metabolism showed upregulation in voltage dependent anion channel 1 pseudogene 2 (*VDAC1P2*), and there was no downregulation (Table 6.3). In the sphingolipid signalling pathway, *AC007192.1* (unknown function) was upregulated and there were no results for downward enrichment (Table 6.3). Relevant to a primary functional effect of miglustat, glycosphingolipid biosynthesis - ganglio series showed no upward or downward enrichment (Table 6.3).

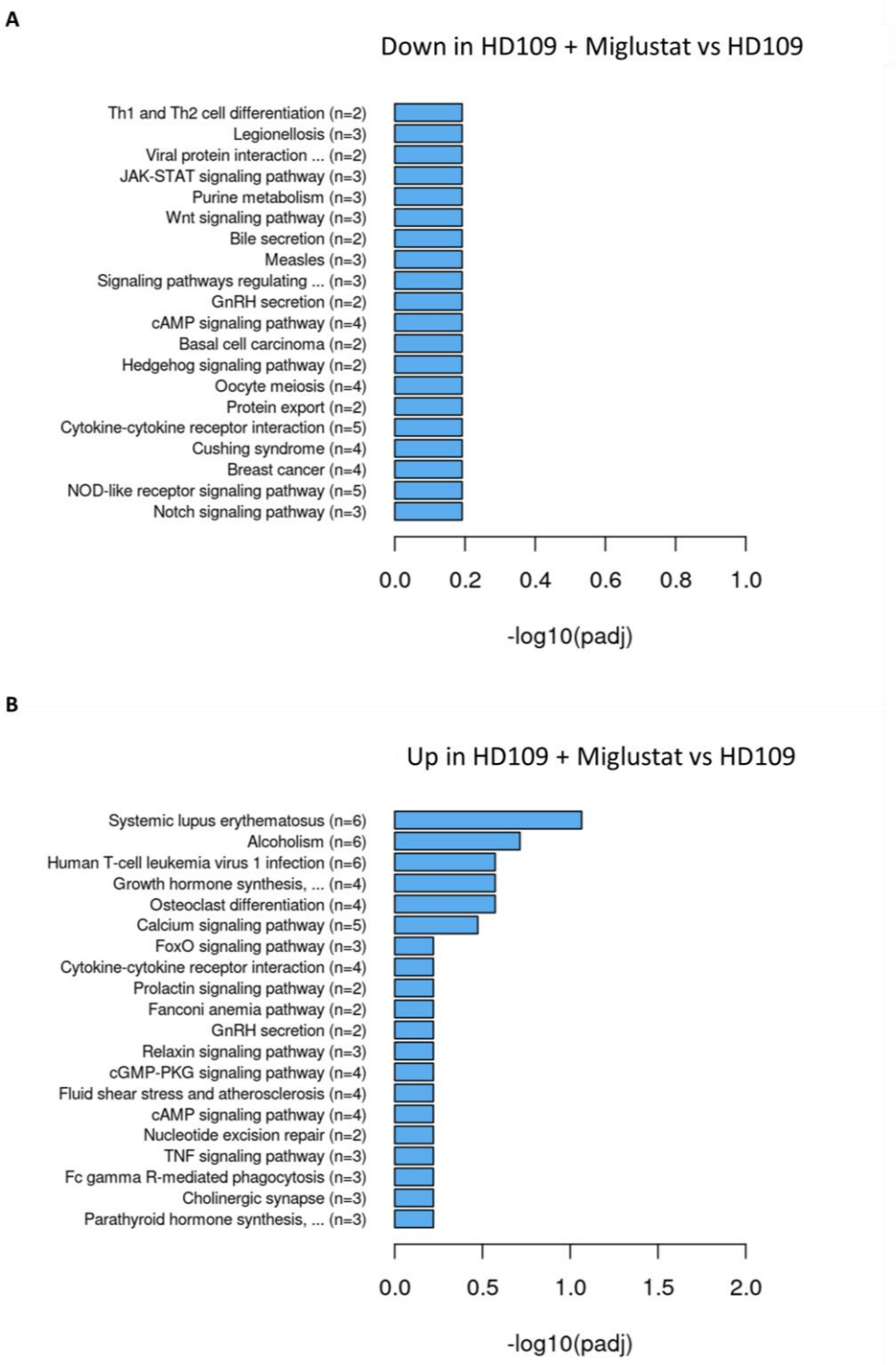

Figure 6.15. KEGG pathways in miglustat-treated day 37 HD109 neurons versus untreated HD109s. A) Top ranked pathways with downregulation in miglustat-treated HD109s versus untreated HD109s. B) Top ranked KEGG pathways with upregulation in miglustat-treated HD109s versus untreated HD109s. Asterisks indicate significantly enriched gene sets, hypergeometric test FDR correction method: Benjamini and Hochberg with adjusted p-values ≤ 0.05.

	PATHWAY OF INTEREST	KEGGID	Description	GeneRatio	BgRatio	pvalue	padj	Gene Names
HD109 + Miglustat UP VS HD109	LYSOSOME	hsa04142	Lysosome	NO RESULTS				
	AUTOPHAGY	hsa04140	Autophagy - animal	3|66	346|12014	0.295979	0.601864	BNIP3P22/ATG101/AC007192.1
	MITOPHAGY	hsa04137	Mitophagy - animal	1|66	251|12014	0.752742	0.791017	BNIP3P22
	CHOLESTEROL	hsa04979	Cholesterol metabolism	1|66	65|12014	0.301645	0.601864	VDAC1P2
	GANGLIOSIDES	hsa04071	Sphingolipid signalling pathway	1|66	138|12014	0.534473	0.645533	AC007192.1
	GANGLIOSIDES	hsa00604	Glycosphingolipid biosynthesis-ganglioseries	NO RESULTS				
	CALCIUM	hsa04020	Calcium signaling pathway	5|66	244|12014	0.010842	0.336095	PHKA1P1/CACNA1S/DRD5/ADRA1B /VDAC1P2
HD109 + Miglustat DOWN VS HD109	LYSOSOME	hsa04142	Lysosome	NO RESULTS				
	AUTOPHAGY	hsa04140	Autophagy - animal	1|76	346|12014	0.892254	0.906645	LINC00327
	MITOPHAGY	hsa04137	Mitophagy - animal	2|76	251|12014	0.473728	0.752632	LINC00327/AC105402.1
	CHOLESTEROL	hsa04979	Cholesterol metabolism	NO RESULTS				
	GANGLIOSIDES	hsa04071	Sphingolipid signalling pathway	NO RESULTS				
	GANGLIOSIDES	hsa00604	Glycosphingolipid biosynthesis-ganglioseries	NO RESULTS				
	CALCIUM	hsa04020	Calcium signaling pathway	NO RESULTS				

Table 6.3. Relevant KEGG pathways of interest and associated genes, in miglustat-treated day 37 HD109 neurons versus untreated HD109 neurons. Upregulated genes and down regulated genes associated with each KEGG pathway. GeneRatio is defined as the number differentially expressed genes in each pathway divided by all differentially expressed genes within the KEGG database. BgRatio is defined as the ratio of all genes related to this KEGG term to all genes in the KEGG database relevant for this group comparison.

6.3.5.2 KEGG gene set enrichment in miglustat-treated versus untreated isogenic controls

Next, because there was little change with miglustat treatment in HD109 neurons, we wanted to assess the effects of miglustat on the isogenic, control neurons to determine whether miglustat alters the transcriptome within a wildtype HTT background. In contrast to the minimal effects seen in HD109 neurons, several gene sets were enriched in the miglustat-treated isogenic controls (Figure 6.16A). None of the downregulated pathways, however, were directly relevant to the endolysosomal or autophagic systems. Significant upregulation was seen in the oxidative phosphorylation gene set (Figure 6.16B), which could correspond with the elevated (though not significantly) OCR levels displayed with miglustat-treated isogenic controls in the previous chapter (Figure 5.7).

The lysosome gene set (Figure 6.17) did not exhibit significant enrichment (Table 6.4). In any case, upregulated genes within this pathway included cathepsin A (*CTSA*), cathepsin D (*CTSD*), adaptor related protein complex 1 subunit mu 2 (*AP1M2*), cystinosin, lysosomal cystine transporter (*CTNS*), ATPase H+ transporting accessory protein 1 (*ATP6AP1*), alpha galactosidase (*GLA*), and *LAMP1*; adaptor related protein complex 3 subunit mu 1 was the single downregulated gene within this pathway.

Other non-significantly enriched pathways and associated upregulated or downregulated genes within these pathways were assessed, including autophagy, mitophagy, cholesterol, glycosphingolipid biosynthesis (ganglio-series), and sphingolipid metabolism (Table 6.4), which might provide insight into the effects of miglustat in a healthy cellular background, though this was not thoroughly examined here.

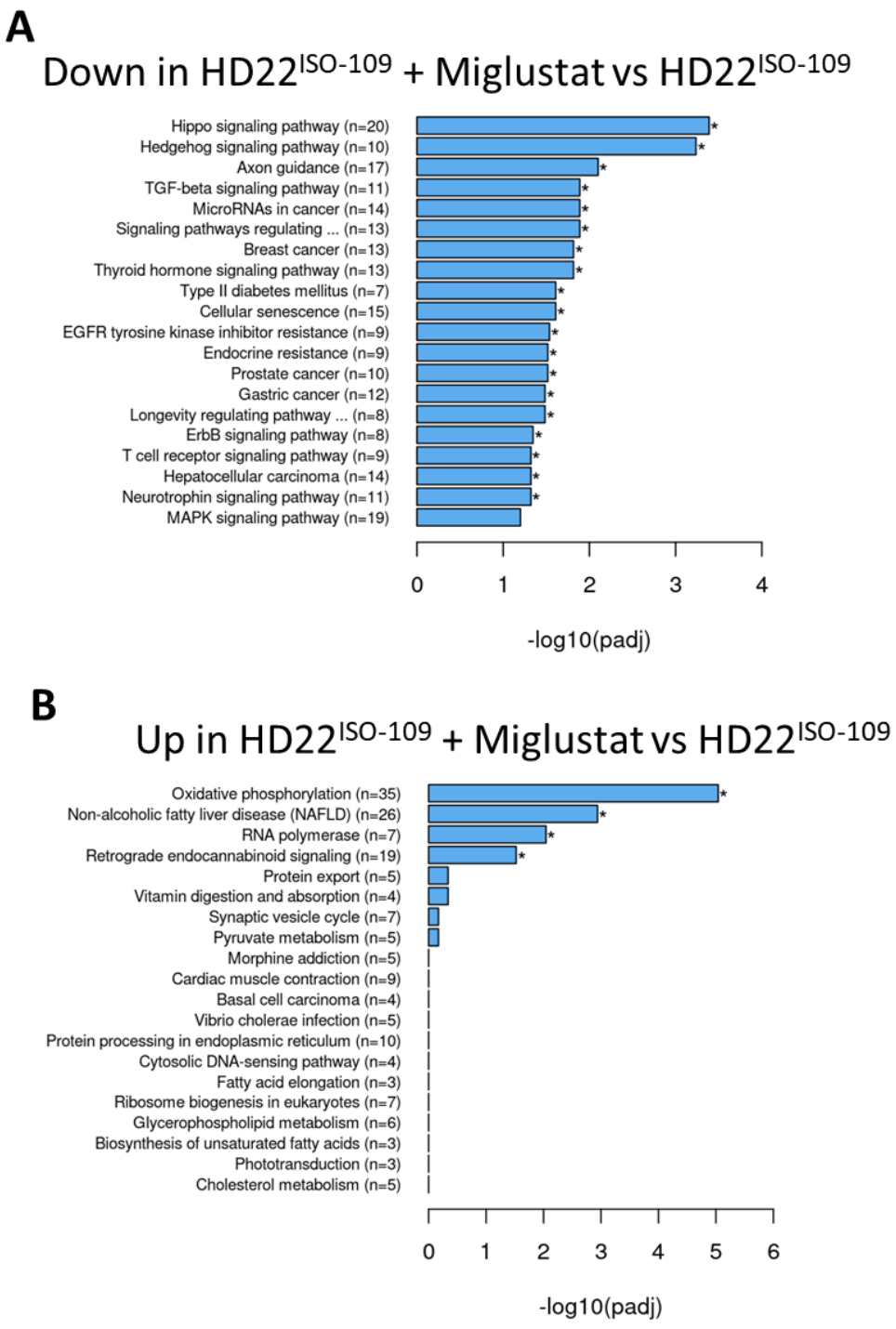

Figure 6.16. KEGG pathways in day 37 miglustat-treated isogenic control neurons versus untreated neurons. A) Top ranked pathways with downregulation in miglustat-treated isogenics versus untreated isogenics B) Top ranked KEGG pathways with upregulation in miglustat-treated isogenics versus untreated isogenics. Asterisks indicate significantly enriched gene sets, hypergeometric test FDR correction method: Benjamini and Hochberg with adjusted p-values ≤ 0.05.

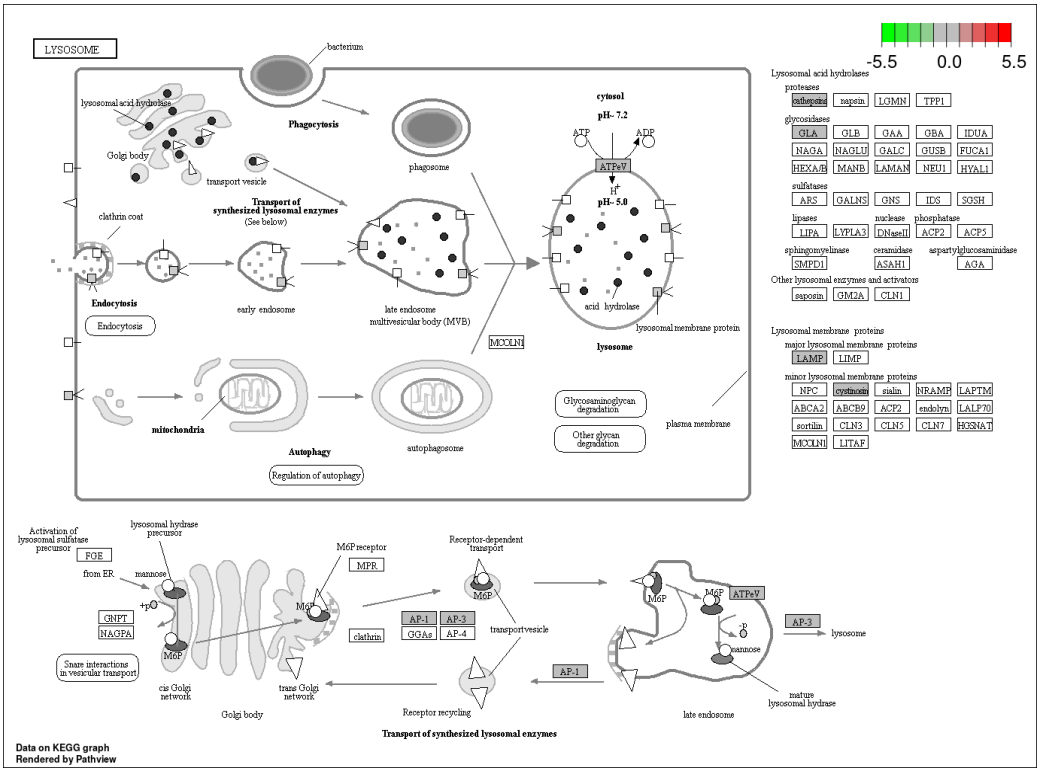

Figure 6.17. Schematic depicting altered components within the KEGG lysosome pathway in day 37 miglustat-treated isogenic control neurons versus untreated isogenics.

	PATHWAY OF INTEREST	KEGGID	Description	GeneRatio	BgRatio	pvalue	padj	Gene Names
HD22 $^{ISO-109}$+ Miglustat UP VS HD22 $^{ISO-109}$	LYSOSOME	hsa04142	Lysosome	7|334	158|11986	0.152544	0.999856	CTSA/CTSD/AP1M2/CTNS/ATP6AP1/LAMP1/GLA
	AUTOPHAGY	hsa04140	Autophagy - animal	4|334	344|11986	0.987845	0.999856	BAD/CTSD/WIPI1/LAMP1
	MITOPHAGY	hsa04137	Mitophagy - animal	2|334	251|11986	0.993572	0.999856	AP000926.1/CSNK2B
	CHOLESTEROL	hsa04979	Cholesterol metabolism	5|334	65|11986	0.034547	0.999856	VDAC1P4/APOC1/VDAC1/APOA1/ABCG5
	GANGLIOSIDES	hsa00604	Glycosphingolipid biosynthesis-ganglioseries	1|334	11|11986	0.267292	0.999856	SLC33A1
	GANGLIOSIDES	hsa00600	Sphingolipid metabolism	2|334	52|11986	0.427442	0.999856	CERS1/GLA
	OX-PHOS	hsa00190	Oxidative phosphorylation	35|334	449|11986	3.46E-08	9.11E-06	ATP5F1D/NDUFB10/ATP5ME/COX5A/ATP6V1F/NDUFA11/NDUFS6/NDUFB2/COX8A/COX7C/NDUFS8/ATP5PF/ATP5MC1/NDUFA12/COX6A1/NDUFB7/ATP5PD/UQCR11/COX6C/ATP5MC3/NDUFB8/LHPP/COX7A2/NDUFA1/NDUFA2/UQCR10/ATP5F1E/NDUFA8/ATP6AP1/NDUFB6/NDUFS4/UQCRQ/NDUFB11/ATP5MF/NDUFC2
HD22 $^{ISO-109}$+ Miglustat DOWN VS HD22 $^{ISO-109}$	LYSOSOME	hsa04142	Lysosome	1|323	158|11986	0.98703	0.998887	AP3M1
	AUTOPHAGY	hsa04140	Autophagy - animal	10|323	344|11986	0.449084	0.752518	TRAF6/PIK3CA/SMCR8/TRAF6P1/PIK3R1/AC012508.1/IRS4/PRKAA2/MTOR/HMGB1P41
	MITOPHAGY	hsa04137	Mitophagy - animal	4|323	251|11986	0.910424	0.995082	FOXO3B/BCL2L13/SP1/AC012508.1
	CHOLESTEROL	hsa04979	Cholesterol metabolism	2|323	65|11986	0.526345	0.786346	LRP6/ABCA1
	GANGLIOSIDES	hsa00604	Glycosphingolipid biosynthesis-ganglioseries	NO RESULTS				
	GANGLIOSIDES	hsa00600	Sphingolipid metabolism	2|323	52|11986	0.410788	0.712416	CERS6/CERS2
	OX-PHOS	hsa00190	Oxidative phosphorylation	NO RESULTS				

Table 6.4. Relevant KEGG pathways of interest and associated genes, in miglustat-treated isogenics versus untreated isogenics. Upregulated genes and down regulated genes associated with each pathway. GeneRatio is defined as the number differentially expressed genes in each pathway divided by all differentially expressed genes within the KEGG database. BgRatio is defined as the ratio of all genes related to this KEGG term to all genes in the KEGG database relevant for this group comparison.

6.3.5.3 KEGG gene set enrichment in miglustat-treated HD109s versus untreated Isogenic controls

Finally, we wanted to determine the differences in HD109s treated with miglustat compared with untreated isogenic controls, as this might provide insight into potential rescue of disease-related phenotypes that were seen in previous chapters, namely, increased mitochondrial length (Figure 4.11), and reduced cholesterol (Figures 5.3) and ganglioside storage (Figure 5.6). miglustat-treated HD109s displayed several significantly altered gene sets compared to untreated isogenic controls, and interestingly several more pathways were altered here (Figure 6.18), when compared to the untreated HD109s versus untreated isogenic controls (Figure 6.9).

Significant downregulation was observed in KEGG signalling pathways not directly linked to the endolysosomal system, including regulating pluripotency of stem cells, Hippo signalling pathway, neuroactive ligand-receptor interaction (Figure 6.18A). Several gene sets were significantly enriched including calcium signalling (Figure 6.18B), though none were relevant within the scope of this thesis.

The lysosomal gene set was not significant though it was assessed (Figure 6.19), and in this pathway, adaptor related protein complex 1 subunit mu (*2AP1M2*), *CTSF*, *CTSA*, N-acetylglucosamine-1-phosphate transferase subunits alpha and beta (*GNPTAB*), and *AC113385.3* (unknown function) were upregulated. There was no downregulation in the lysosomal pathway.

In the autophagy pathway, upregulation was seen in *BNIP3P9*, high-mobility group box 1 pseudogene 44 (*HMGB1P44*), *AC007192.1* (unknown function), 3-phosphoinositide dependent protein kinase 2 pseudogene (*PDPK2P*). Downregulation was seen in TNF receptor associated factor six pseudogene 1 (*TRAF6P1*), insulin like growth factor 1 receptor (*IGF1R*), *AC132872.1* (unknown function), *BNIP3P25*, *ATG4A*, and *AC078846.1* (unknown function). In the mitophagy pathway upregulation was seen in *BNIP3P9* and *FUNDC1* and downregulation in *AC132872.1*, *BNIP3P25*, *AC078846.1*. In the cholesterol pathway,

upregulation was seen in *LPA*, and *CD36*, while downregulation was seen in *VDAC1P3*, *ABCA1*, *PCSK9*, and apolipoprotein E (*APOE*) (Table 6.5).

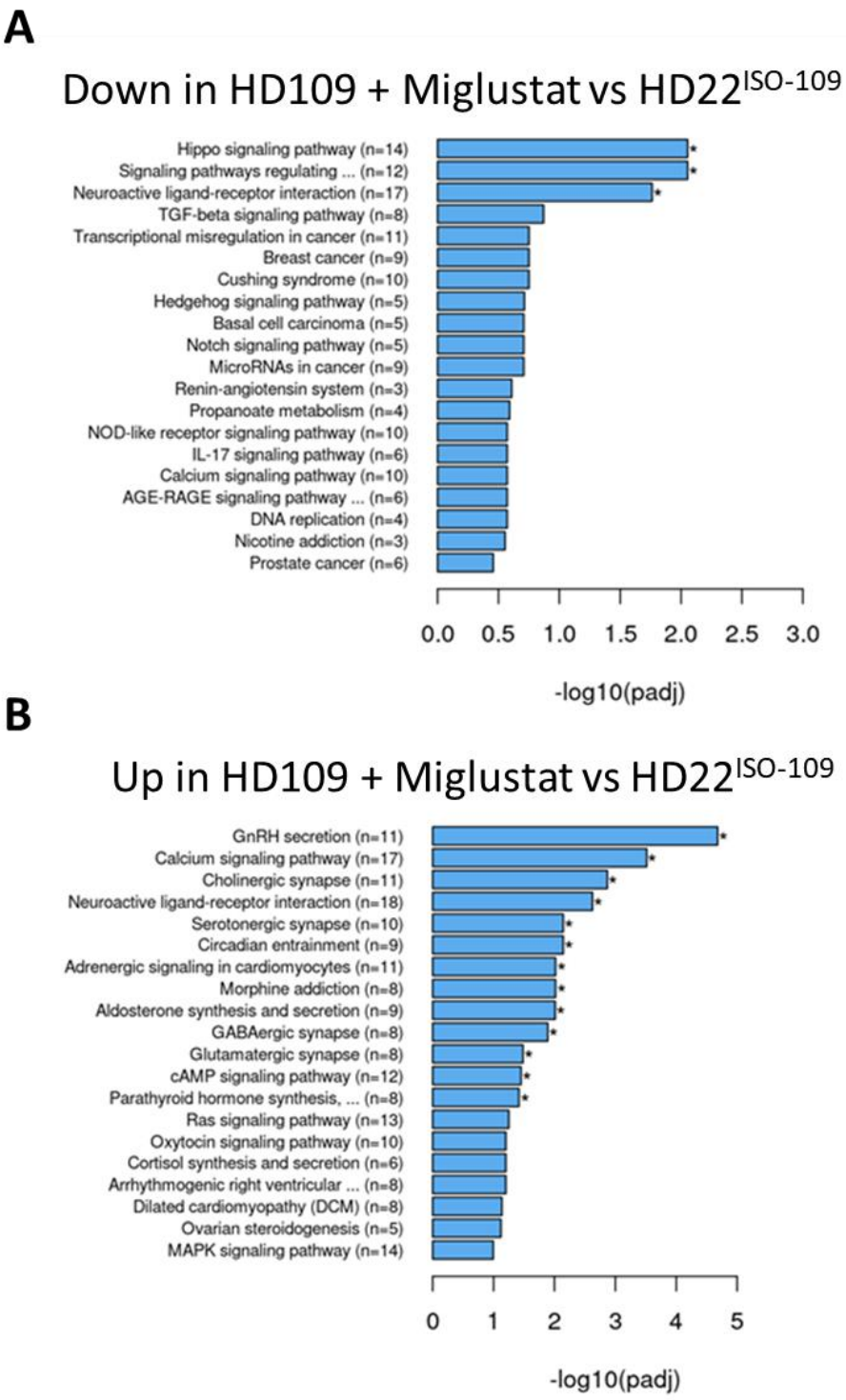

Figure 6.18. KEGG pathways in day 37 miglustat-treated HD109s versus untreated isogenic neurons. A) Top ranked pathways with downregulation in miglustat-treated HD109s versus untreated isogenics. B) Top ranked KEGG pathways with upregulation in miglustat-treated HD109s versus untreated isogenics. Asterisks indicate significantly enriched gene sets, hypergeometric test FDR correction method: Benjamini and Hochberg with adjusted p-values ≤ 0.05.

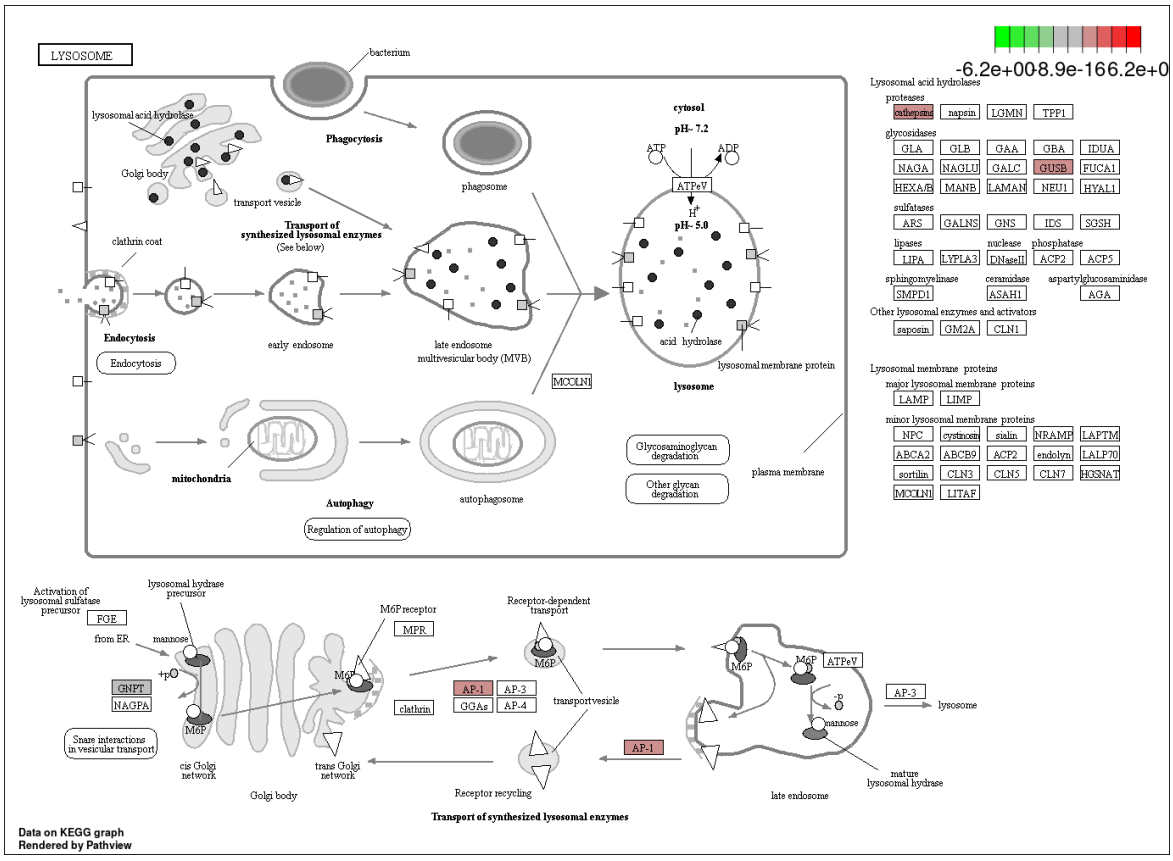

Figure 6.19. Schematic depicting altered components within the KEGG lysosome pathway in day 37 miglustat-treated HD109 neurons versus isogenic controls.

	PATHWAY OF INTEREST	KEGGID	Description	GeneRatio	BgRatio	pvalue	padj	Gene Names
HD109 + Miglustat UP VS HD22 ISO-109	LYSOSOME	hsa04142	Lysosome	5|220	159|12021	0.166973	0.58605	AP1M2/CTSF/GNPTAB/CTSA/AC113385.3
	AUTOPHAGY	hsa04140	Autophagy-animal	4|220	345|12021	0.880615	0.971569	BNIP3P9/HMGB1P44/AC007192.1/PDPK2P
	MITOPHAGY	hsa04137	Mitophagy-animal	2|220	251|12021	0.946658	0.98007	BNIP3P9/FUNDC1
	CHOLESTEROL	hsa04979	Cholesterol metabolism	2|220	65|12021	0.334402	0.757041	LPA/CD36
	GANGLIOSIDES	hsa00600	Sphingolipid metabolism	4|220	52|12021	0.014891	0.151198	SGPP2/SGPP1/SMPD2/NEU3
	GANGLIOSIDES	hsa00604	Glycosphingolipid biosynthesis-ganglioseries					NO RESULTS
	CALCIUM	hsa04020	Calcium signaling pathway	17|220	243|12021	2.31E-06	0.000305	HRH2/TACR3/GNAL/ADCY2/PRKCG/TBXA2R/TACR2/CACNA1I /P2RX5/HTR7P1/CACNA1S/CACNA1D/SLC8A2/CACNA1G/ PTK2B/ATP2B2/AVPR1B
HD109 + Miglustat DOWN VS HD22 ISO-109	LYSOSOME	hsa04142	Lysosome					NO RESULT
	AUTOPHAGY	hsa04140	Autophagy-animal	6|230	345|12021	0.65096	0.948344	TRAF6P1/IGF1R/AC132872.1/BNIP3P25/ATG4A/AC078846.1
	MITOPHAGY	hsa04137	Mitophagy-animal	3|230	251|12021	0.863007	0.948344	AC132872.1/BNIP3P25/AC078846.1
	CHOLESTEROL	hsa04979	Cholesterol metabolism	4|230	65|12021	0.035681	0.392488	VDAC1P3/ABCA1/PCSK9/APOE
	GANGLIOSIDES	hsa00600	Sphingolipid metabolism					NO RESULT
	GANGLIOSIDES	hsa00604	Glycosphingolipid biosynthesis-ganglioseries					NO RESULTS
	CALCIUM	hsa04020	Calcium signaling pathway	10|230	243|12021	0.018574	0.267823	AC136759.1/CD38/PTGER3/CACNA1F/AGTR1/EDNRB/ITPR2/ VDAC1P3/TACR1/NOS3

Table 6.5. Relevant KEGG pathways of interest and associated genes, autophagy and mitophagy, in miglustat-treated day 37 HD109 neurons versus isogenic controls. Upregulated genes and down regulated genes associated with each pathway. GeneRatio is defined as the number differentially expressed genes in each pathway divided by all differentially expressed genes within the KEGG database. BgRatio is defined as the ratio of all genes related to this KEGG term to all genes in the KEGG database relevant for this group comparison.

6.4 Discussion

6.4.1 Overview

In this chapter RNA Sequencing was carried out on HD109, HTT knockout, and corrected isogenic neurons, in an effort to determine whether there might be a transcriptional signature related to the structural and functional differences described in Chapters 4 and 5. Additionally, miglustat-treated HD109s and isogenic controls were evaluated to identify associated changes to the transcriptomic profile, that might occur downstream of structural or functional restoration in treated HD109 neurons and to assess the impacts of miglustat on wildtype neurons. Comparisons of differentially expressed genes and enriched KEGG pathways between HD109s and isogenic controls, revealed surprisingly few differences. Greater numbers of differentially expressed genes and enriched pathways were, however, seen in HTT knockouts relative to controls. miglustat-treatment produced almost no effect on differential expression in HD109s or in the isogenic controls when compared to their untreated analogues. However, though KEGG enrichment in miglustat-treated HD109s showed no change, there were several pathways that were altered in the isogenic controls.

6.4.2 Unbiased RNA sequencing of HD109 Neurons

Transcriptional dysregulation is known to be central to pathogenesis in Huntington's disease (HD-iPSC consortium, Gillian Bates 2015). However, comparisons across previous studies suggest a high degree of variation, and that because differential expression common in HD patient samples, differs from what is seen in cell culture models, that *in vitro* experiments might fail to fully recapitulate the molecular pathology underlying HD (Malla et al. 2021). In this thesis, when compared to the isogenic controls, HD109s displayed only 23 significant DEGs and relative to this thesis, none of these were listed in the human lysosome gene database. Only the neuroactive-ligand receptor interaction and apelin signalling pathway gene sets were enriched, which suggests that at the transcriptional level, there was very little difference, due to the presence of mHTT. This lack of differences could have arisen due to statistical, methodological, or biological reasons.

Statistically, use of isogenic lines should minimize variability, however, the presence of two replicates, the HD109 cell line (H109n1) and isogenic subclone (I5H9_3), both exhibited a relatively low within-group Pearson correlation coefficient and likely added variation which might have resulted in a reduced ability to discern actual biological differences. With regards to the methodology, it is possible that because neurons in this study were only differentiated for 37 days, and to relatively immature biological state, that mechanisms promoting differential gene expression had not yet been able to fully emerge. Correspondingly, the relation between maturity and differential expression was shown in a similar study which used isogenic hESCs for neuronal differentiation, day 11 NPCs displayed a reduced fraction (352 or 2.25%) of DEGs relative to 2738 (15.8%) seen day 45 neurons (Ooi et al. 2019b). Moreover, in another related study, HD patient Q60 and Q109 iPSCs differentiated for 56 days into neural cells, yielded 1,869 DEGs relative to wildtype controls, though these were not isogenic (Consortium 2017). Taken together, these data suggest that a lengthier differentiation and a more mature neuronal population might have produced more differences. Biologically, though iPSCs derived from a juvenile patient, were chosen for this study with the expectation of an increased likelihood for an observable phenotype to develop in our model neurons, which even when subjected to lengthier differentiations, remain biologically similar to neurons at an early embryonic stage, it could be that the juvenile form of HD, which is considered largely developmental, might not undergo high levels of differential expression relative to the adult version of HD. It is also possible that if the juvenile form is largely developmental, altered transcription could be masked by the differentiation process itself, which recapitulates neuronal development through manipulation with small molecules and growth factors. Accordingly, a recent study by Smith-Geater et al. (2020), which used a differentiation protocol similar to that used in this thesis, as well as the HD109 neurons, similarly found reduced levels of differential expression (105 DEGs) in juvenile HD patient-derived day 37 neurons (Q66, Q71 and Q109), while observing increased levels of differential gene expression in neurons derived from adult patients (Q46 and Q53; 823 DEGs). It therefore would be interesting to follow this experiment up by extending the length of differentiation for further comparisons in an isogenic context, or to

compare while utilizing a differentiation protocol that is less reliant on exogenous factors. In addition, defects in alternative mRNA splicing have been shown to be associated with mutant HTT (Tano et al. 2022), and correspondingly, data comparing alternative splicing in HD109s with the isogenic controls, has been generated in this experiment, however, it remains to be analyzed.

6.4.3 Biased Assessment of Enrichment in Endolysosome-related Pathways in HD109s

Because, a nonbiased approach produced little results, pathways relevant to this thesis were considered in a biased and exploratory manner. Though not significantly enriched, transcripts involved with cholesterol metabolism trended upwards in HD109s, and associated upregulation occurred in *CD36, ABCG5, ABCG8, LPA,* and *LPAL2*. Similarly, misregulation and altered distribution of brain cholesterol in HD has been widely reported and has been linked to neurodegeneration (Leoni and Caccia 2015; González-Guevara et al. 2020), with altered ATP binding cassette and low density lipoproteins being commonly disrupted. Interestingly the ABCG5/G8 heterodimer, plays a primary role in neutral sterol transport and cholesterol excretion (Zein et al. 2019), which could indicate a direction for further examination. When looking at the KEGG lysosomal pathway, only 8 genes were differentially expressed with upregulation in *GUSBP5*, *CTSF*, *AP1M2*, and *ARSG*, with downregulation in *NEU1*, DNASE2B. Each of these genes were compared against 3 week hESC neurons (45Q, 65Q, and 81Q), using the interactive, online platform located here (http://isohd.pouladilab.org), and provided by Ooi et al. (2019b). Within this database, all 8 genes were variably expressed with no significance related to fold change, and therefore altered expression was not substantiated. Further examination, into NPC1 expression, which was not significantly altered in this experiment, using the Pouladi lab database, also revealed limited and nonsignificant expression changes related to CAG repeat length. In summary, the results pathway analysis, remain inconclusive, though when considered in an exploratory capacity, might be of interest for future studies.

6.4.4 HTT Knockouts is Associated with an Altered Transcriptome

Normal HTT function is also critical to understand, especially in light of recent ASO-based clinical trials (Tabrizi et al. 2019). To approach an understanding of wildtype function, recent

experiments using HTT knockout models highlighted irregularities in pathways associated with cell communication and signalling, development, neurotransmission, and synaptic signalling (Bensalel et al. 2021). Relative to other comparisons within this experiment, HTT knockouts displayed a greater number, 475 differentially expressed genes, when compared to the isogenic controls, which supports recent work which showed that knocking out huntingtin resulted in widespread transcriptional effects (Bensalel et al. 2021), and could indicate a larger effect of loss of wildtype function in juvenile HD. Comparisons of differentially expressed genes in this thesis, align with earlier studies that showed importance of huntingtin function in mouse embryonic development (Duyao et al. 1995; Nasir et al. 1995a; Zeitlin et al. 1995; Dragatsis et al. 2000)) and proper adult CNS function (Dragatsis et al. 2000). Correspondingly, transcripts that are upregulated in HTT knockouts relative to the isogenic controls, are largely related to MSN development, maturation, and fate specification, while downregulation is related to processes that occur in the earlier stages of neuronal development, and which suggests that maturation is occurring more rapidly in HTT knockouts, relative to wildtype (Appendix Figures 1 and 2). Only 10 differentially expressed genes, in the HTT knockouts, are listed in the human lysosome gene database (*CTSF, PCSK9, LITAF, GPC3, RNASE1, TSPAN1, TMEM63A, ADA, CUBN, HLA-DRB5*), which suggests a marginal relationship between wildtype huntingtin and lysosome-related gene expression. Notably, of all significant differentially expressed genes in the HTT knockouts, cathepsin F exhibited the greatest magnitude of downregulation, and though unfortunately the kinetics of cathepsin F was not examined in Chapter 5, this data suggests that further investigation could be beneficial. When DEGs in this thesis were considered with those found in Bensalel et al. (2021), only 25 genes were shown to be common to both datasets, which suggests a low level of consistency, and which could be a result of the different cell types used in the two studies. Of the 25 genes common to both studies, only transmembrane protein 63A (*TMEM63A*) was also listed in the human lysosome gene database, while the others were mainly related to development.

Upregulated enrichment in the knockouts relative to the isogenic controls was present in the KEGG neuroactive ligand-receptor interaction and calcium signalling pathways. Importantly,

calcium signalling, which was also significantly downwardly enriched, is involved in the CLEAR gene regulatory networks (Medina et al. 2015), which when disrupted can alter lysosomal and autophagosome function. Moreover, altered calcium signalling could indicate a point of potential overlap between HD and NP-C, as calcium dyshomeostasis, has been seen in models of both diseases (Lloyd-Evans et al. 2008; Wheeler et al. 2019, ED Nekrasov, Ross and Tabrizi 2011). The most significantly downregulated enrichment, however, was seen in the KEGG pathway, 'signalling pathways regulating pluripotency of stem cells', which suggests that relative to the isogenic controls, core pluripotency networks are less active, and that HTT knockout cells achieve a more mature stage in neurodevelopment, earlier than wildtypes. Similarly, the downregulation of the Hippo signalling pathway in HTT knockouts further evidences a role for wildtype huntingtin in development. The Hippo signalling pathway is a highly conserved system that regulates organ size and plays a fundamental role in stem cell and progenitor self-renewal and expansion (Yu et al. 2015). Thus, when taken together and considered in light of the embryonic lethality associated with HTT knockout in mouse embryos, downregulated genes in these pathways might provide clues into the neurodevelopmental dysregulation and loss of function that could be occurring in Huntington's disease, and especially the juvenile version of HD.

6.4.5 Biased Assessment of Endolysosome-related Pathways in HTT knockouts

In a biased approach, we then performed an exploratory inspection of pathways relevant to this thesis, though these were non-significantly enriched. Within the KEGG lysosome pathway, downregulated genes included *CTSF, AL354794.2, CD164*, *PSAP*, and *ATP6V0D2*. Several genes were upregulated in the lysosomal pathway, and the unadjusted p-value showed significant enrichment (Table 6.2). Genes related to trafficking and transport, included *M6PR,* and adaptor related proteins *AP3M2*, *AP1M2*, *AP1B1*, *AP3D1*, and *AP3S2*, which could be relevant in a loss of function context, in light of previously described trafficking defects associated with HD (discussed in Chapter 1.8.6). Transcripts for lysosomal enzymes *CTSA*, *SMPD1*, *SGSH*, *MANBA*, *GM2A*, were also downregulated, and could be examined in future assays for enzyme activity. Transcripts encoding lysosomal membrane proteins *LAMP1* and *SORT1* were also downregulated. Several genes were enriched in the

autophagy, mitophagy, cholesterol metabolism, sphingolipid metabolism pathways as well (Table 6.2), and could be candidates for further investigation.

6.4.6 Overlapping Differentially Expressed Genes in HD109s and HTT knockouts

Ten differentially expressed genes (*EHHADH, PCDHGA10, MAP3K13, GEMIN8, AC136759.1, EIF1AX, ADGRG5, AL021395.1, GPRC5D-AS1, PTPRT*) were shared between the HD109s and the HTT knockouts relative to the isogenic controls, potentially indicating transcriptomic dysregulation associated with a loss of wildtype function in HD, and which might be of interest for future studies. Within the DEG list, relative to the isogenic controls, *EHHADH* was the most significantly differentially expressed gene in both HD109 and HTT knockouts. Interestingly, *EHHADH* encodes an enzyme within the peroxisomal beta-oxidation pathway, and which was predicted to be a biomarker for HD and PD (Ni et al. 2015), and which also was identified as highly dysregulated in the study by Smith-Geater et al. (2020). Peroxisomes are small, membrane bound organelles, that contain enzymes involved in energy and lipid metabolism, which generated reactive oxygen species, and imbalances in this vesicle population have been implicated in human disease (Fransen et al. 2012). *PCDHGA10 is* a neural protocadherin gene and is involved in neural adhesion and which has been implicated in benign paroxysmal positional vertigo (Xu et al. 2021). *MAP3K13*, regulates the c-JUN N-terminal kinase pathway, it also regulates NF-kB, is a positive regulator of axonal growth, and inhibition has been shown to protect against neurodegeneration, and *MAP3K13* has been associated with Parkinson's disease (Bensen and Brognard 2021). *GEMIN8* is a subunit of the survival of motor neurons multiprotein complex (SMN) that is involved with pre-mRNA splicing machinery, and is the disease-determining gene of the neurodegenerative disease, spinal muscular atrophy (Gubitz et al. 2004). *PTPRT,* is a type IIB receptor-type protein tyrosine phosphatase, it is only expressed in the nervous system and is thought to be critical towards regulation of synaptic formation and neuronal development (Lee 2015). In summary, this data provides new information relevant to wildtype huntingtin function and potential loss of function in HD pathology.

6.4.7 Miglustat exerts minimal effect on the transcriptomic profile in neuronal models of HD

Gene expression profiles of miglustat treated HD109 neurons were highly similar to untreated HD109s as illustrated by principal component analysis (Figure 6.4) and hierarchical clustering (Figure 6.5), and increased expression was seen in only a single gene, *EGR1,* in the miglustat-treated HD109 neurons, relative to the isogenic controls. *EGR1*, also known as nerve growth factor-induced protein A, is a transcription factor involved with memory formation, neuronal DNA methylation (Sun et al. 2019), VAMP2 expression, and correspondingly, *EGR1* expression was also shown to be increased in mouse osteoblasts treated with miglustat (Mishima et al. 2021). Thus, further investigation into miglustat and *EGR1* expression in HD might be useful, especially in light of potential use in clinical studies, as *EGR1* is linked to neuronal transcription, epigenetics, and exocytosis. We initially, had hypothesized that because of structural and functional rescue effects reported by previous research in our lab, as well as in this thesis, that miglustat treatment of HD109s might shift the transcriptomic profile towards that of the isogenic controls. However, this was not the case as most of the DEGs identified in miglustat-treated or non-treated HD109s relative to isogenic controls, were shared (Figure 6.8D and 6.8E).

Miglustat also exerted minimal effect on the transcriptome of the isogenic controls. The single differentially expressed gene, *ZBTB16*, which was downregulated with miglustat treatment, might also be interesting for further investigation as it is involved with GSKβ, lipid regulation, lipid regulation, metabolic syndrome, and autophagy regulation (Šeda et al. 2017; Ibrahim et al. 2021). Interestingly, both *ZBTB16* and *EGR1* are both involved in the regulation of osteoblast differentiation (Marofi et al. 2019; Mishima et al. 2021), which points to a functional association with miglustat treatment. To our knowledge, this is the first RNA Sequencing experiment investigating the effects of miglustat in human cells, and this data, which indicates minimal transcriptional alterations associated with miglustat, could prove to be useful, as miglustat is currently used in the treatment of Gaucher disease, Pompe disease, and Niemann Pick type C.

6.5 Conclusion

In this chapter, RNA sequencing was carried out on HD109s both with and without miglustat, isogenic controls with and without miglustat, and HTT knockouts. In contrast to the widespread transcriptomic changes, previously reported in HD models, only minor differences were seen here, between HD109s and isogenic controls. miglustat treatment, also minimally altered the transcriptome of HD109, the isogenic controls, and did not shift the transcriptomic profile of HD109 neurons towards that of the isogenic controls. Moderate changes in gene expression were observed in HTT knockouts, which could clarify the role of wildtype huntingtin. Moreover, differentially expressed genes were identified to be common to HD109s and HTT knockouts which could be informative regarding loss of wildtype HTT function.

7 GENERAL DISCUSSION AND CONCLUSIONS

7.1.1 Overview

There are several studies to suggest that disruption to the endolysosomal system is occurring in HD. Expanded lysosomes or endolysosome-like vacuoles have been reported across several models (Sapp et al. 1997; Kegel et al. 2000; Camnasio et al. 2012; Castiglioni et al. 2012; Nekrasov et al. 2016), as well as an altered endolysosomal distribution (Koga and Cuervo 2011; Haslett 2015; Clark 2017). Moreover, structural and functional defects have been reported relating to autophagy (Kegel et al. 2000; Petersén et al. 2001; Martinez-Vicente et al. 2010), mitochondrial function and mitophagy (Kegel et al. 2000; Wong and Holzbaur 2014; Franco-Iborra et al. 2021). Therefore, in this thesis, we used neural progenitors and neurons differentiated from HD patient-derived iPSCs, and from isogenic control iPSCs in which the mutant huntingtin gene had been previously corrected to a wildtype-length CAG repeat, to assess structural, functional, and transcriptional changes that might further clarify endolysosomal, autophagic or mitochondrial dysfunction in HD. In addition, because miglustat is used in the treatment of lysosomal storage diseases e.g., Niemann-Pick Type C, Pompe, and Gaucher disease patients, and because several previous studies indicated an LSD-like component to HD, we assessed the effects of miglustat

treatment in our model neurons. Finally, we generated and used HTT knockouts to investigate LSD-related attributes to discern whether these might arise from a loss-of-wildtype huntingtin function.

7.1.2 Isogenic models to assess wildtype and mutant huntingtin function.

The combination of iPSC technology with efficient genome editing by CRISPR-Cas9, has proven to be a benefit for disease modelling and drug screening, by providing mutable and scalable source material. Isogenic models are particularly useful because comparisons can be made within a shared genetic background, which can enhance the precision with which many questions can be approached, and which circumvent the inherent complexity and confounding effects associated with polygenic models. Moreover, the ability to direct differentiation of iPSCs towards a desired cellular identity for disease-relevant comparisons is critical, because not all cell types are equivalently affected by disease pathomechanisms. The combination of these technologies is particularly advantageous for the study of neurological disorders, due to a prohibitive lack of available primary human tissue and inadequacies associated with animal disease models (Volpato and Webber 2020).

Correspondingly, in this thesis, iPSCs reprogrammed from fibroblasts obtained from a juvenile HD patient, allowed for three-way comparisons in NPCs and neurons, with which we could assess cellular characteristics related to the presence of mutant HTT and HTT knockout, in relation to a corrected wildtype. Thus, though this model system was designed generally, to assess mHTT-mediated, HD-related phenotypes in the context of an individual genetic background, the addition in this thesis of the HTT knockout conferred the ability to consider disease-associated phenotypes in relation to a potential loss of wildtype or gain of mutant function.

7.1.3 Limitations of the model system

Importantly, there are a number of limitations associated with the model system used in this thesis that should be noted. Firstly, the two-dimensional, monoculture, *in vitro* cell culture system inherently lacks the structural complexity and cellular diversity found *in vivo*, and has been shown to be unreliable for predicting drug efficacy and toxicity *in vivo* (Hutchinson and

Kirk 2011; Antoni et al. 2015), and the obscuration of HD-related phenotypes in differentiated models of HD directed from pluripotent cell lines has been suggested to occur due to these systems (Victor et al. 2018; Wiatr et al. 2018). In addition, while isogenic designs minimize the high degree of variation shown to result from genetic differences between donors and are suited to discerning the effects of a specific gene variant (Kilpinen et al. 2017), conclusions drawn from a single genetic background, as was the case in this thesis, are not necessarily appropriate for extrapolation to the general patient population (Brunner et al. 2022). Thus, a major limitation of this thesis was the reliance on a single biological replicate for the neuron- and miglustat-related experiments. Particularly relevant to this thesis, the HD109 patient line, exhibits a CAG trinucleotide repeat length greater than 50 and is associated with the juvenile form of HD that is considered to be largely neurodevelopmental, and distinct from the adult version (Bates et al. 2015; Wiatr et al. 2018). As such, while this cell line was chosen with expectation that more robust phenotypes might be observable in cells that have undergone epigenetic resetting associated with iPSC reprogramming, and subsequent neuronal differentiation that produces neurons approximating to those seen in early embryonic development (Miller et al. 2013), generalizations from the results obtained in this thesis are thus limited with regards to adult onset-HD.

7.1.4 Evidence for a lysosomal storage disease component in HD

Because the pathomechanism responsible for neurodegeneration in HD is unknown, and because previous studies have shown mHTT-related phenotypes to suggest dysregulation in the endolysosomal, autophagic, and mitochondrial systems, the main purpose of this thesis was to survey for evidence to indicate whether this dysfunction was observable within our isogenic NPC and neuronal models of HD. However, evidence to suggest an LSD component within HD were not consistently observed between NPCs and neurons here, which might be expected as each cell type possesses distinct cellular features. For example, in neurons lysosomal area was increased, though this was not seen in NPCs. This difference, could have arisen as consequence of substrate accumulation and lysosomal expansion associated with a lack of mitosis in neurons, as opposed to potential dilution of substrate associated with cell

division in NPCs. Autophagic dysregulation was observed in HD109 and HTT knockout NPCs, though not in neurons, and it is possible that this discrepancy arose due to components present within the neuronal maturation medium. Therefore, in future studies, it might be worthwhile to compare the consistency of phenotypes across a panel of neuronal differentiations, in which selected medium components have been removed.

Reports of expansion within the lysosomal compartment in HD models are inconsistent. The absence of evidence to support the presence of lysosomal expansion in HD109 NPCs, by LAMP1 staining in this thesis, conforms to previous reports (Koga et al. 2011; Erie et al. 2015; Clark 2017), and contrasts with results reported in other studies (Camnasio et al. 2012; Castiglioni et al. 2012; Haslett 2015; Clark 2017), however, the latter relied on the use of Lysotracker for area measurements. Later studies identified the presence of non-overlapping vesicle populations between the two probes (Miyagawa et al. 2016; Baba et al. 2020), which might explain these inconsistencies, and furthermore highlights the importance of technical equivalence when making comparisons, especially when interpretating results in a broader biological context. However, in HD109 neurons, relative to isogenic controls, LAMP1 area was elevated which is in accordance with lysosomal expansion reported in other neuronal models of HD (Camnasio et al. 2012; Haslett 2015; Nekrasov et al. 2016; Pircs et al. 2021). Thus, these findings support the hypothesis that there is a lysosome-related structural defect present in HD and one that is more prominently seen in neurons.

To explain lysosomal expansion seen in HD109 neurons, enzyme assays, assessments of lipid storage, and RNA sequencing were carried out. The results obtained from the lysosomal enzyme assays exhibited a high degree of variance and were inconclusive. A trend towards a general reduction of enzyme activity in both NPC and neuronal models of HD, however, was observed, and which with further replication might provide insight into substrate accumulation as a potential mechanism underlying lysosomal expansion. It is a common feature in LSDs that dysfunctional lysosomal enzyme (or in the case of NP-C, transport proteins), can produce accumulation of the enzyme's target substrate, which can then trigger secondary substrate accumulation, and lysosomal expansion (Figure 1.8). Though dysfunction in a single enzyme was not observed in this thesis, the general reductions in

enzymatic activity associated with HD NPCs and neurons, along with the expansion of vesicle compartments positive for filipin, GM1, LAMP1, and Cyto-ID, suggest the possibility that mutant huntingtin is inhibiting some component of the degradation pathway. Whether this dysregulation might be related to enzyme function, the transport of enzymes to the lysosome, vesicle transport and fusion, mitophagy, or to some unknown mechanism, is difficult to clarify. It is important to note that the number of enzymes assayed in Chapter 5 was minimal, with several enzymes left untested. Thus, the RNA sequencing data which indicated, for example, a downregulation of cathepsin F gene expression, could provide valuable insight for future experiments.

Altered lipid storage was seen in comparisons of cholesterol and ganglioside GM1 in HD109 NPCs and neurons, with the isogenic controls. The more punctate distribution of cholesterol seen in the HD109 NPCs, agreed with previous studies (Del Toro et al. 2010b; Haslett 2015; Clark 2017). The increased area of cholesterol measured in the HD109 neurons, was consistent with several previous reports (Trushina et al. 2006b; del Toro et al. 2010a; Luthi-Carter et al. 2010; Boussicault et al. 2016; Kreilaus et al. 2016; Phillips et al. 2020), though contrasted with others (Valenza et al. 2005a; Valenza et al. 2007a; Valenza et al. 2010; Marullo et al. 2012; Ritch et al. 2012). Similarly, the altered distribution of ganglioside GM1 in HD109 NPCs and the increase in ganglioside GM1 seen in HD109 neurons, is compatible with several previous studies (Del Toro et al. 2010b; Haslett 2015; Clark 2017), while conflicting with others (Desplats et al. 2007a; Denny et al. 2010; Maglione et al. 2010; Alpaugh et al. 2017; Hunter et al. 2021). While RNA sequencing provided little evidence for transcriptional dysregulation related to the lysosome in HD109 neurons, there were slight indications that the cholesterol pathway might be perturbed in HD. In summary, this thesis does provide evidence to support the presence of an altered lysosomal structure within HD that might be associated with lipid accumulation, and which is suggestive of lysosomal storage. However, the underlying mechanism(s) responsible for producing these phenotypes, or whether this contributes to, or is accessory to, HD pathogenesis is unknown.

7.1.5 Evidence for autophagic dysfunction in HD

An increase in basal autophagy was seen in the HD109 NPCs. Similar increases have been widely reported in HD (Davies et al. 1997; Sapp et al. 1997; Kegel et al. 2000; Ravikumar et al. 2004; Del Toro et al. 2009; Camnasio et al. 2012; Nekrasov et al. 2016; Malankhanova et al. 2020; Pircs et al. 2021). In HD109 neurons, however, cumulative autophagosome area was not elevated when compared to the isogenic controls, and disagrees with the majority of previous results in neuronal models (Camnasio et al. 2012; Malankhanova et al. 2020; Pircs et al. 2021). Interestingly, a conspicuously elevated basal level of autophagy was present in the HD109s and the isogenic controls, which might have obscured comparisons and prevented further increases from being detected. As mentioned above, the differences detected in NPCs and the lack of differences seen in neurons, might be a result of the composition of the neuronal maturation medium, as it is changed from SLI and LIA in NPCs, to SJA and SJB in neurons. Literature to support this hypothesis, has shown that CHIR-99021, which is present in the neuronal maturation medium, inhibits GSK-3β, which allows for TFEB dephosphorylation, nuclear translocation and upregulation of the CLEAR signalling machinery, to facilitate lysosome synthesis and increased autophagic flux (Zhang et al. 2022). Thus, future experiments to inspect the effects of medium composition on autophagy-related phenotypes in differentiated neurons, towards discriminating between culture artifacts and genuine disease-related phenotypes, might begin with a comparison of cells cultured in medium both with and without CHIR-99021.

7.1.6 Evidence for mitochondrial dysfunction in HD

The presence of mitochondrial fragmentation has been widely reported in HD (Costa et al. 2010; Song et al. 2011; Shirendeb et al. 2012; Haun et al. 2013; Manczak and Reddy 2015), and similarly, reduced mitochondrial length was seen in HD109 NPCs relative to the isogenic controls. In addition to structural defects, mitochondrial dysfunction was also seen in this thesis, as immature HD109 neurons displayed reductions in percent spare respiratory capacity, paralleling results from other studies that evidenced an impaired ability of mitochondria, to respond to increased energy demands or stress, in HD models (An et al. 2012; Xu et al. 2017; Gardiner et al. 2018; Donaldson 2019a; Ooi et al. 2019b; Franco-Iborra

et al. 2021). However, though mitochondria-related transcriptional dysregulation, has been shown to occur in HD (Damiano et al. 2010), there was little evidence to support this, from the RNA sequencing performed in this thesis. Thus, this thesis provided evidence to support the presence of structural and functional abnormalities in HD, and which could be further clarified in future experiments by directly connecting mitochondrial structure, through quantification of mitochondrial area, shape, counts, and protein levels, to functional assays such as measurements of mitochondrial respiration.

7.1.7 Evidence for NP-C disease phenotypes in HD

More specifically, because a large degree of phenotypic overlap shared between HD and NP-C had been identified (Schweitzer et al. 2009; Haslett 2015; Clark 2017), a secondary objective of this thesis research was to clarify whether phenotypes observed in our models supported a link between the two diseases. However, though there was a degree of overlap between the two, with regard to structure and function, the results were inconsistent, and there were no clear indications of a shared pathomechanism common to both diseases. NP-C disease phenotypes, seen here, included lysosomal expansion in HD109 neurons, increased basal autophagy, fragmented mitochondria in NPCs, elevated and altered distribution of cholesterol and ganglioside GM1, mitochondrial fragmentation and altered bioenergetics were also observed. In contrast, NP-C phenotypes previously reported in HD models, absent here, included a lack of lysosomal expansion in HD109 NPCs and there was no evidence of late endosomal expansion in NPCs or neurons. There was no evidence for HD-related abnormalities with regards to the NPC1 protein, as neither NPC1 or NPC2 were abnormally elevated, NPC1 was not differentially distributed to the perinuclear region, and NPC1 was colocalized to LAMP1 and NPC2 positive vesicles similarly across the isogenic controls, the HD109s, and the HTT knockouts. Thus, whether there is a direct mechanistic link between the two diseases, remains inconclusive. A shortcoming of this thesis was the inconsistent use of U18666A as a positive NP-C phenocopy control. In hindsight, at the minimum, U18666A would have been added to every experiment, and optimally, an NPC1 mutant line would have been generated from the HD22 $^{ISO-109}$ iPSCs, in order to make direct comparisons within an isogenic background.

7.1.8 Effects of miglustat treatment in HD neurons

Miglustat-treatment was associated with several effects, in the HD109s. Differences in mitochondrial length in NPCs between HD109s and isogenic controls were reduced in the presence of miglustat, however, miglustat treatment was not associated with a rescue of mitochondrial stress in immature HD109 neurons. Intracellular cholesterol and ganglioside GM1 storage, both elevated in HD109s relative to the isogenic controls, were reduced to levels intermediate between HD109s and the isogenic controls, with miglustat treatment. A trend towards a slight reduction in autophagosome accumulation was associated with miglustat-treatment in both HD109 and the isogenic control neurons. Ultrastructural analysis indicated that miglustat was associated with a decreased fraction of substrate-filled vesicles in both isogenic control and HD109 neurons, though consistent with previous studies (Neises et al. 1997; Hovakimyan et al. 2013), there also appeared to be an increase in the number of electron-lucent vesicles in both conditions, thus, whether the change in proportion arose due to an increase in clear vesicles, or a reduction in storage, was unclear. As such, using a decreased magnification to allow for absolute vesicle numbers to be counted, and lipidomic profiling of purified lysosomes, might provide additional insight into the proportional distribution and composition of storage material present in each condition. The results of lysosomal enzyme assays indicated a surprising trend towards a general reduction in enzyme activity associated with miglustat, in both HD109 and isogenic control neurons, and one that exacerbated reductions already present in HD109 neurons relative to the isogenic controls. RNA sequencing indicated minimal transcriptional differences associated with miglustat treatment in both HD109 and isogenic controls. In sum, this data suggests that miglustat is associated with structural and functional changes in HD109s, though similar changes were often observed in the isogenic controls, and that these changes occur with minimal effect on gene expression. Thus, though the mechanisms underlying these changes are not known, this thesis provided information which could be used in future experiments for clarification.

7.1.9 Effects of huntingtin knockout

The generation of two HTT knockout iPSC lines, with the addition of the HTT knockout HAP1 cells, allowed for the investigation into the aspects of HD that might be associated with loss

of wildtype huntingtin function or a gain of mutant function, as well as providing insight into the role of wildtype huntingtin. It was hypothesized, based on co-immunoprecipitation experiments, in which NPC1 co-immunoprecipitated with both wildtype and mutant huntingtin (Clark 2017), that wtHTT might be involved in trafficking NPC1 to the lysosomal membrane, and that this process might be disrupted with the mutant protein. Though a role for huntingtin in trafficking NPC1 cannot be ruled out from these experiments, because NPC1 colocalized to LAMP1- and NPC2-positive voxels in HTT knockouts, these results do suggest that wtHTT is not essential for this process. In addition, there was no evidence to indicate a role for wildtype huntingtin in the mobilization of NPC1 to the perinuclear region. The intracellular areas of LAMP1, NPC1, NPC2, and LBPA were also unaffected in HTT knockouts and, as such, failed to provide evidence for a loss of wildtype huntingtin function related to the lysosomal or late endosomal compartments. The distribution of cholesterol was unaffected in HTT knockout lines relative to the isogenic controls, though ganglioside GM1 distribution was widely varied, dependant on which cell line was assayed. Basal autophagy as determined by CYTO-ID staining, was significantly elevated in HTT knockouts, relative to both the isogenic controls and HD109s, which is consistent with similar reports (Pircs et al. 2021), and which could indicate a related loss of wildtype function. Whether loss-of-function related to autophagy might arise due to haploinsufficiency, or due to a dominant-negative effect of the mHTT allele remains unknown, though this could be clarified using hemizygous cell lines obtained while generating the HTT knockout iPSC lines used in this thesis. Interestingly, relative to the isogenic controls, the transcriptional profile of HTT knockouts differed to a far greater extent than did the HD109 neurons. In HTT knockouts, altered gene expression related to the lysosome was limited, however, changes related to neurodevelopment were extensive, and align with early studies that substantiated the importance of huntingtin in development (Duyao et al. 1995; Nasir et al. 1995a; Zeitlin et al. 1995; O'Kusky et al. 1999; Dragatsis et al. 2000). In sum, the experiments involving HTT knockouts, failed to evidence a role for wildtype huntingtin related to the endolysosomal system, though dysregulation in autophagy and development were identified. However, though these experiments were carried out using 3 biological replicates, the reliance on the

haplozygous, HAP1 cell line was not optimal; ideally another HTT knockout isogenic iPSC replicate could be produced, to make comparisons across homogenous cell populations.

7.1.10 Concluding remarks

We have identified several cellular abnormalities associated with mutant huntingtin, by comparing neural progenitors and neurons differentiated from HD patient-derived iPSCs, to those with a corrected version of the huntingtin allele, in which the mutant CAG trinucleotide repeat was exchanged to a non-pathogenic CAG-repeat length. In addition, HTT knockouts generated in this thesis, allowed for investigation into wildtype HTT function and for three-way comparisons to examine disease-associated phenotypes within a loss of function or gain of function framework. Thus, though this work is incomplete, this thesis provided information related to the function of huntingtin and provided novel tools with which further examination can be carried forward.

8 REFERENCES

<Abdullah Alshehri Final submitted thesis Sep 2019 PDF.pdf>.

Adachi, Y. and Nakashima, K. 1999. Population genetic study of Huntington's disease--prevalence and founder's effect in the San-in area, western Japan. *Nihon rinsho. Japanese journal of clinical medicine* 57(4), pp. 900-904.

Albin, R. L. et al. 1992. Preferential loss of striato-external pallidal projection neurons in presymptomatic Huntington's disease. *Annals of Neurology: Official Journal of the American Neurological Association and the Child Neurology Society* 31(4), pp. 425-430.

Aldrich, L. N. et al. 2015. Discovery of a small-molecule probe for V-ATPase function. *Journal of the American chemical society* 137(16), pp. 5563-5568.

Alexander, G. E. 1994. Basal ganglia-thalamocortical circuits: their role in control of movements. *Journal of clinical neurophysiology: official publication of the American Electroencephalographic Society* 11(4), pp. 420-431.

Alpaugh, M. et al. 2017. Disease-modifying effects of ganglioside GM1 in Huntington's disease models. *EMBO molecular medicine* 9(11), pp. 1537-1557.

Alroy, J. and Ucci, A. A. 2006. Skin biopsy: a useful tool in the diagnosis of lysosomal storage diseases. *Ultrastructural pathology* 30(6), pp. 489-503.

Alshehri, A. 2019. *Identifying and characterizing lysosomal storage disease phenotypes for utilization in novel screening and monitoring assays.* Cardiff University.

Ambrose, C. M. et al. 1994. Structure and expression of the Huntington's disease gene: evidence against simple inactivation due to an expanded CAG repeat. *Somatic cell and molecular genetics* 20(1), pp. 27-38.

An, M. C. et al. 2012. Genetic correction of Huntington's disease phenotypes in induced pluripotent stem cells. *Cell stem cell* 11(2), pp. 253-263.

Andersson, B. S., Beran, M., Pathak, S., Goodacre, A., Barlogie, B. and McCredie, K. B. 1987. Ph-positive chronic myeloid leukemia with near-haploid conversion in vivo and establishment of a continuously growing cell line with similar cytogenetic pattern. *Cancer genetics and cytogenetics* 24(2), pp. 335-343.

Andrew, S. et al. 1993. DNA analysis of distinct populations suggests multiple origins for the mutation causing Huntington disease. *Clinical genetics* 43(6), pp. 286-294.

Andrews, N. W., Almeida, P. E. and Corrotte, M. 2014. Damage control: cellular mechanisms of plasma membrane repair. *Trends in cell biology* 24(12), pp. 734-742.

Antoni, D., Burckel, H., Josset, E. and Noel, G. 2015. Three-dimensional cell culture: a breakthrough in vivo. *International journal of molecular sciences* 16(3), pp. 5517-5527.

Arber, C. et al. 2015. Activin A directs striatal projection neuron differentiation of human pluripotent stem cells. *Development* 142(7), pp. 1375-1386.

Arlotta, P., Molyneaux, B. J., Jabaudon, D., Yoshida, Y. and Macklis, J. D. 2008. Ctip2 controls the differentiation of medium spiny neurons and the establishment of the cellular architecture of the striatum. *Journal of Neuroscience* 28(3), pp. 622-632.

Arrasate, M. and Finkbeiner, S. 2005. Automated microscope system for determining factors that predict neuronal fate. *Proceedings of the National Academy of Sciences* 102(10), pp. 3840-3845.

Arthur, J. R., Heinecke, K. A. and Seyfried, T. N. 2011. Filipin recognizes both GM1 and cholesterol in GM1 gangliosidosis mouse brain. *Journal of lipid research* 52(7), pp. 1345-1351.

Ashford, T. P. and Porter, K. R. 1962. Cytoplasmic components in hepatic cell lysosomes. *The Journal of cell biology* 12(1), pp. 198-202.

Atwal, R. S., Xia, J., Pinchev, D., Taylor, J., Epand, R. M. and Truant, R. 2007. Huntingtin has a membrane association signal that can modulate huntingtin aggregation, nuclear entry and toxicity. *Human molecular genetics* 16(21), pp. 2600-2615.

Auerbach, W. et al. 2001. The HD mutation causes progressive lethal neurological disease in mice expressing reduced levels of huntingtin. *Human molecular genetics* 10(22), pp. 2515-2523.

Baba, K. et al. 2020. Different localization of lysosomal-associated membrane protein 1 (LAMP1) in mammalian cultured cell lines. *Histochemistry and cell biology* 153(4), pp. 199-213.

Babalola, J. O., Wendeler, M., Breiden, B., Arenz, C., Schwarzmann, G., Locatelli-Hoops, S. and Sandhoff, K. 2007. Development of an assay for the intermembrane transfer of cholesterol by Niemann-Pick C2 protein.

Bachis, A., Rabin, S. J., Del Fiacco, M. and Mocchetti, I. 2002. Gangliosides prevent excitotoxicity through activation of TrkB receptor. *Neurotoxicity research* 4(3), pp. 225-234.

Baig, S. S. et al. 2016. 22 Years of predictive testing for Huntington's disease: the experience of the UK Huntington's Prediction Consortium. *European Journal of Human Genetics* 24(10), pp. 1396-1402.

Bailus, B. J. et al. 2021. Modulating FKBP5/FKBP51 and autophagy lowers HTT (huntingtin) levels. *Autophagy*, pp. 1-22.

Baine, F. K., Krause, A. and Greenberg, L. J. 2016. The frequency of Huntington disease and Huntington disease-like 2 in the South African population. *Neuroepidemiology* 46(3), pp. 198-202.

Ballabio, A. and Bonifacino, J. S. 2020. Lysosomes as dynamic regulators of cell and organismal homeostasis. *Nature reviews Molecular cell biology* 21(2), pp. 101-118.

Ballabio, A. and Gieselmann, V. 2009. Lysosomal disorders: from storage to cellular damage. *Biochimica et Biophysica Acta (BBA)-Molecular Cell Research* 1793(4), pp. 684-696.

Barrett, A. J. and Kirschke, H. 1981. [41] Cathepsin B, cathepsin H, and cathepsin L. *Methods in enzymology* 80, pp. 535-561.

Bates, G. P. et al. 2015. Huntington disease. *Nature reviews Disease primers* 1(1), pp. 1-21.

Bäuerlein, F. J. B. et al. 2017. In situ architecture and cellular interactions of PolyQ inclusions. *Cell* 171(1), pp. 179-187.

Bayleran, J., Hechtman, P., Kolodny, E. and Kaback, M. 1987. Tay-Sachs disease with hexosaminidase A: characterization of the defective enzyme in two patients. *American journal of human genetics* 41(4), p. 532.

Becher, M. W., Kotzuk, J. A., Sharp, A. H., Davies, S. W., Bates, G. P., Price, D. L. and Ross, C. A. 1998. Intranuclear Neuronal Inclusions in Huntington's Disease and Dentatorubral and Pallidoluysian Atrophy: Correlation between the Density of Inclusions andIT15CAG Triplet Repeat Length. *Neurobiology of disease* 4(6), pp. 387-397.

Beckenkamp, A. et al. 2015. Differential expression and enzymatic activity of DPPIV/CD26 affects migration ability of cervical carcinoma cells. *PLOS one* 10(7), p. e0134305.

Ben Jehuda, R., Shemer, Y. and Binah, O. 2018. Genome editing in induced pluripotent stem cells using CRISPR/Cas9. *Stem Cell Reviews and Reports* 14(3), pp. 323-336.

Benn, C. L. et al. 2005. Contribution of nuclear and extranuclear polyQ to neurological phenotypes in mouse models of Huntington's disease. *Human molecular genetics* 14(20), pp. 3065-3078.

Bensalel, J., Xu, H., Lu, M. L., Capobianco, E. and Wei, J. 2021. RNA-seq analysis reveals significant transcriptome changes in huntingtin-null human neuroblastoma cells. *BMC medical genomics* 14(1), pp. 1-14.

Bensen, R. and Brognard, J. 2021. New therapeutic opportunities for the treatment of squamous cell carcinomas: A focus on novel driver kinases. *International journal of molecular sciences* 22(6), p. 2831.

Bezprozvanny, I. and Hayden, M. R. 2004. Deranged neuronal calcium signaling and Huntington disease. *Biochemical and biophysical research communications* 322(4), pp. 1310-1317.

Björkhem, I. and Meaney, S. 2004. Brain cholesterol: long secret life behind a barrier. *Arteriosclerosis, thrombosis, and vascular biology* 24(5), pp. 806-815.

Bjorkqvist, M. et al. 2008. A novel pathogenic pathway of immune activation detectable before clinical onset in Huntington's disease. *The Journal of experimental medicine* 205(8), pp. 1869-1877.

Blom, T., Li, Z., Bittman, R., Somerharju, P. and Ikonen, E. 2012. Tracking sphingosine metabolism and transport in sphingolipidoses: NPC1 deficiency as a test case. *Traffic* 13(9), pp. 1234-1243.

Blom, T. S. et al. 2003. Defective endocytic trafficking of NPC1 and NPC2 underlying infantile Niemann–Pick type C disease. *Human molecular genetics* 12(3), pp. 257-272.

Bodennec, J., Pelled, D., Riebeling, C., Trajkovic, S. and Futerman, A. H. 2002. Phosphatidylcholine synthesis is elevated in neuronal models of Gaucher disease due to direct activation of CTP: phosphocholine cytidylyltransferase by glucosylceramide. *The FASEB journal* 16(13), pp. 1-29.

Bolam, J. P., Hanley, J. J., Booth, P. A. C. and Bevan, M. D. 2000. Synaptic organisation of the basal ganglia. *The Journal of Anatomy* 196(4), pp. 527-542.

Bossy-Wetzel, E., Barsoum, M. J., Godzik, A., Schwarzenbacher, R. and Lipton, S. A. 2003. Mitochondrial fission in apoptosis, neurodegeneration and aging. *Current opinion in cell biology* 15(6), pp. 706-716.

Bouscary, A. et al. eds. *Sphingolipids metabolism alteration in the central nervous system: amyotrophic lateral sclerosis (ALS) and other neurodegenerative diseases*. 2021. Elsevier.

Bouscary, A. et al. eds. 2021. *Sphingolipids metabolism alteration in the central nervous system: Amyotrophic lateral sclerosis (ALS) and other neurodegenerative diseases*. *Seminars in Cell & Developmental Biology.* Elsevier.

Boussicault, L. et al. 2016. CYP46A1, the rate-limiting enzyme for cholesterol degradation, is neuroprotective in Huntington's disease. *Brain* 139(3), pp. 953-970.

Boustany, R.-M. N., Kaye, E. and Alroy, J. 1990. Ultrastructural findings in skin from patients with Niemann-Pick disease, type C. *Pediatric neurology* 6(3), pp. 177-183.

Bramwell, K. K. C., Ma, Y., Weis, J. H., Chen, X., Zachary, J. F., Teuscher, C. and Weis, J. J. 2014. Lysosomal β-glucuronidase regulates Lyme and rheumatoid arthritis severity. *The Journal of clinical investigation* 124(1), pp. 311-320.

Brattås, P. L., Hersbach, B. A., Madsen, S., Petri, R., Jakobsson, J. and Pircs, K. 2021. Impact of differential and time-dependent autophagy activation on therapeutic efficacy in a model of Huntington disease. *Autophagy* 17(6), pp. 1316-1329.

Braulke, T. and Bonifacino, J. S. 2009. Sorting of lysosomal proteins. *Biochimica et Biophysica Acta (BBA)-Molecular Cell Research* 1793(4), pp. 605-614.

Braun, P. E. and Snell, E. E. 1968. Biosynthesis of sphingolipid bases: II. Keto intermediates in synthesis of sphingosine and dihydrosphingosine by cell-free extracts of Hansenula ciferri. *Journal of Biological Chemistry* 243(14), pp. 3775-3783.

Breiden, B. and Sandhoff, K. 2018. Ganglioside metabolism and its inherited diseases. *Gangliosides*, pp. 97-141.

Breiden, B. and Sandhoff, K. 2020. Mechanism of secondary ganglioside and lipid accumulation in lysosomal disease. *International journal of molecular sciences* 21(7), p. 2566.

Bremova-Ertl, T. et al. 2021. Efficacy and safety of N-acetyl-l-leucine in Niemann–Pick disease type C. *Journal of neurology*, pp. 1-12.

Broadhead, D. M. and Butterworth, J. 1978. Pompe's disease: Diagnosis in kidney and leucocytes using 4-methylumbelliferyl-α-D-glucopyranoside. *Clinical genetics* 13(6), pp. 504-510.

Brunner, J. W. et al. 2022. Power and optimal study design in iPSC-based brain disease modelling. *Molecular Psychiatry*, pp. 1-12.

Bućan, M. et al. 1990. Physical maps of 4p16. 3, the area expected to contain the Huntington disease mutation. *Genomics* 6(1), pp. 1-15.

Buratta, S., Tancini, B., Sagini, K., Delo, F., Chiaradia, E., Urbanelli, L. and Emiliani, C. 2020. Lysosomal exocytosis, exosome release and secretory autophagy: the autophagic-and endo-lysosomal systems go extracellular. *International journal of molecular sciences* 21(7), p. 2576.

Buren, C., Parsons, M. P., Smith-Dijak, A. and Raymond, L. A. 2016. Impaired development of cortico-striatal synaptic connectivity in a cell culture model of Huntington's disease. *Neurobiology of disease* 87, pp. 80-90.

Burté, F., Carelli, V., Chinnery, P. F. and Yu-Wai-Man, P. 2015. Disturbed mitochondrial dynamics and neurodegenerative disorders. *Nature reviews neurology* 11(1), pp. 11-24.

Busch, A., Engemann, S., Lurz, R., Okazawa, H., Lehrach, H. and Wanker, E. E. 2003. Mutant huntingtin promotes the fibrillogenesis of wild-type huntingtin: a potential mechanism for loss of huntingtin function in Huntington's disease. *Journal of Biological Chemistry* 278(42), pp. 41452-41461.

Butler, J. D., Vanier, M. T. and Pentchev, P. G. 1993. Niemann-Pick C disease: cystine and lipids accumulate in the murine model of this lysosomal cholesterol lipidosis. *Biochemical and biophysical research communications* 196(1), pp. 154-159.

Butterworth, J. and Broadhead, D. M. 1977. Diagnosis of Pompe's disease in cultured skin fibroblasts and primary amniotic fluid cells using 4-methylumbelliferyl-α-D-glucopyranoside as substrate. *Clinica Chimica Acta* 78(2), pp. 335-342.

Camargo, F., Erickson, R. P., Garver, W. S., Hossain, G. S., Carbone, P. N., Heidenreich, R. A. and Blanchard, J. 2001. Cyclodextrins in the treatment of a mouse model of Niemann-Pick C disease. *Life sciences* 70(2), pp. 131-142.

Camnasio, S. et al. 2012. The first reported generation of several induced pluripotent stem cell lines from homozygous and heterozygous Huntington's disease patients demonstrates mutation related enhanced lysosomal activity. *Neurobiology of disease* 46(1), pp. 41-51.

Carstea, E. D. et al. 1997. Niemann-Pick C1 disease gene: homology to mediators of cholesterol homeostasis. *Science* 277(5323), pp. 228-231.

Castiglioni, V., Onorati, M., Rochon, C. and Cattaneo, E. 2012. Induced pluripotent stem cell lines from Huntington's disease mice undergo neuronal differentiation while showing alterations in the lysosomal pathway. *Neurobiology of disease* 46(1), pp. 30-40.

Caudron, E., Prognon, P. and Germain, D. P. 2015. Enzymatic diagnosis of Fabry disease using a fluorometric assay on dried blood spots: An alternative methodology. *European journal of medical genetics* 58(12), pp. 681-684.

Caviston, J. P. and Holzbaur, E. L. F. 2009. Huntingtin as an essential integrator of intracellular vesicular trafficking. *Trends in cell biology* 19(4), pp. 147-155.

Caviston, J. P., Ross, J. L., Antony, S. M., Tokito, M. and Holzbaur, E. L. F. 2007. Huntingtin facilitates dynein/dynactin-mediated vesicle transport. *Proceedings of the National Academy of Sciences* 104(24), pp. 10045-10050.

Caviston, J. P., Zajac, A. L., Tokito, M. and Holzbaur, E. L. F. 2011. Huntingtin coordinates the dynein-mediated dynamic positioning of endosomes and lysosomes. *Molecular Biology of the Cell* 22(4), pp. 478-492.

Cha, J.-H. J. 2007. Transcriptional signatures in Huntington's disease. *Progress in neurobiology* 83(4), pp. 228-248.

Chae, J.-I. et al. 2012. Quantitative proteomic analysis of induced pluripotent stem cells derived from a human Huntington's disease patient. *Biochemical Journal* 446(3), pp. 359-371.

Chakraborty, K., Leung, K. and Krishnan, Y. 2017. High lumenal chloride in the lysosome is critical for lysosome function. *Elife* 6, p. e28862.

Chambers, S. M., Fasano, C. A., Papapetrou, E. P., Tomishima, M., Sadelain, M. and Studer, L. 2009. Highly efficient neural conversion of human ES and iPS cells by dual inhibition of SMAD signaling. *Nature biotechnology* 27(3), pp. 275-280.

Chan, D. C. 2006. Mitochondria: dynamic organelles in disease, aging, and development. *Cell* 125(7), pp. 1241-1252.

Chan, D. C. 2007. Mitochondrial dynamics in disease. *New England Journal of Medicine* 356(17), pp. 1707-1709.

Chang, C. M. et al. 1994. Huntington's disease in Hong Kong Chinese: epidemiology and clinical picture. *Clinical and experimental neurology* 31, pp. 43-51.

Chang, D. T. W., Rintoul, G. L., Pandipati, S. and Reynolds, I. J. 2006. Mutant huntingtin aggregates impair mitochondrial movement and trafficking in cortical neurons. *Neurobiology of disease* 22(2), pp. 388-400.

Charbord, J. et al. 2013. High throughput screening for inhibitors of REST in neural derivatives of human embryonic stem cells reveals a chemical compound that promotes expression of neuronal genes. *Stem Cells* 31(9), pp. 1816-1828.

Charman, M., Kennedy, B. E., Osborne, N. and Karten, B. 2010. MLN64 mediates egress of cholesterol from endosomes to mitochondria in the absence of functional Niemann-Pick Type C1 protein. *Journal of lipid research* 51(5), pp. 1023-1034.

Chen, Y.-Y. and Lai, C.-H. 2010. Nationwide population-based epidemiologic study of Huntington's disease in Taiwan. *Neuroepidemiology* 35(4), pp. 250-254.

Chevallier, J. et al. 2008. Lysobisphosphatidic acid controls endosomal cholesterol levels. *Journal of Biological Chemistry* 283(41), pp. 27871-27880.

Chin, D. J. et al. 1984. Nucleotide sequence of 3-hydroxy-3-methyl-glutaryl coenzyme A reductase, a glycoprotein of endoplasmic reticulum. *Nature* 308(5960), pp. 613-617.

Chira, S., Gulei, D., Hajitou, A., Zimta, A.-A., Cordelier, P. and Berindan-Neagoe, I. 2017. CRISPR/Cas9: transcending the reality of genome editing. *Molecular Therapy-Nucleic Acids* 7, pp. 211-222.

Chiu, F.-L. et al. 2015. Elucidating the role of the A2A adenosine receptor in neurodegeneration using neurons derived from Huntington's disease iPSCs. *Human molecular genetics* 24(21), pp. 6066-6079.

Choudhury, A., Sharma, D. K., Marks, D. L. and Pagano, R. E. 2004. Elevated endosomal cholesterol levels in Niemann-Pick cells inhibit rab4 and perturb membrane recycling. *Molecular Biology of the Cell* 15(10), pp. 4500-4511.

Chu, B.-B. et al. 2015. Cholesterol transport through lysosome-peroxisome membrane contacts. *Cell* 161(2), pp. 291-306.

Clark, E. 2017. *Involvement of the lysosomal protein NPC1 in the pathogenesis of Huntington's disease.* Cardiff University.

Colin, E. et al. 2008. Huntingtin phosphorylation acts as a molecular switch for anterograde/retrograde transport in neurons. *The EMBO journal* 27(15), pp. 2124-2134.

Consortium, H. D. i. 2017. Developmental alterations in Huntington's disease neural cells and pharmacological rescue in cells and mice. *Nature neuroscience* 20(5), pp. 648-660.

Consortium, H. D. i. 2020. Bioenergetic deficits in Huntington's disease iPSC-derived neural cells and rescue with glycolytic metabolites. *Human molecular genetics* 29(11), p. 1757.

Cook, S. R. et al. 2020a. Detrimental effect of zwitterionic buffers on lysosomal homeostasis in cell lines and iPSC-derived neurons. *AMRC open research* 2,

Cook, S. R. et al. 2020b. Visualisation of cholesterol and ganglioside GM1 in zebrafish models of Niemann–Pick type C disease and Smith–Lemli–Opitz syndrome using light sheet microscopy. *Histochemistry and cell biology* 154(5), pp. 565-578.

Coppen, E. M. and Roos, R. A. C. 2017. Current pharmacological approaches to reduce chorea in Huntington's disease. *Drugs* 77(1), pp. 29-46.

Cornett, J., Cao, F., Wang, C.-E., Ross, C. A., Bates, G. P., Li, S.-H. and Li, X.-J. 2005. Polyglutamine expansion of huntingtin impairs its nuclear export. *Nature genetics* 37(2), pp. 198-204.

Costa, V. et al. 2010. Mitochondrial fission and cristae disruption increase the response of cell models of Huntington's disease to apoptotic stimuli. *EMBO molecular medicine* 2(12), pp. 490-503.

Costa, V. and Scorrano, L. 2012. Shaping the role of mitochondria in the pathogenesis of Huntington's disease. *The EMBO journal* 31(8), pp. 1853-1864.

Costes, S. V., Daelemans, D., Cho, E. H., Dobbin, Z., Pavlakis, G. and Lockett, S. 2004. Automatic and quantitative measurement of protein-protein colocalization in live cells. *Biophysical journal* 86(6), pp. 3993-4003.

Cowan, C. M. and Raymond, L. A. 2006. Selective neuronal degeneration in Huntington's disease. *Current topics in developmental biology* 75, pp. 25-71.

Cox, T. M. and Cachon-Gonzalez, M. B. 2012. The cellular pathology of lysosomal diseases. *J Pathol* 226(2), pp. 241-254. doi: 10.1002/path.3021

Craufurd, D. and Snowden, J. 2002. Neuropsychological and neuropsychiatric aspects of Huntington's disease. *Oxford Monographs on Medical Genetics* 45, pp. 62-94.

Creasy, B. M., Hartmann, C. B., White, F. K. H. and McCoy, K. L. 2007. New assay using fluorogenic substrates and immunofluorescence staining to measure cysteine cathepsin activity in live cell subpopulations. *Cytometry Part A: the journal of the International Society for Analytical Cytology* 71(2), pp. 114-123.

Croce, K. R. and Yamamoto, A. 2019. A role for autophagy in Huntington's disease. *Neurobiology of disease* 122, pp. 16-22.

Csobonyeiova, M., Polak, S. and Danisovic, L. 2020. Recent overview of the use of iPSCs Huntington's disease modeling and therapy. *International journal of molecular sciences* 21(6), p. 2239.

Cui, L., Jeong, H., Borovecki, F., Parkhurst, C. N., Tanese, N. and Krainc, D. 2006. Transcriptional repression of PGC-1α by mutant huntingtin leads to mitochondrial dysfunction and neurodegeneration. *Cell* 127(1), pp. 59-69.

Culjkovic, B., Stojkovic, O., Vojvodic, N., Svetel, M., Rakic, L., Romac, S. and Kostic, V. 1999. Correlation between triplet repeat expansion and computed tomography measures of caudate nuclei atrophy in Huntington's disease. *Journal of neurology* 246(11), pp. 1090-1093.

Culver, B. P. et al. 2012. Proteomic Analysis of Wild-type and Mutant Huntingtin-associated Proteins in Mouse Brains Identifies Unique Interactions and Involvement in Protein Synthesis. *Journal of Biological Chemistry* 287(26), pp. 21599-21614. doi: 10.1074/jbc.m112.359307

Dabrowska, M., Ciolak, A., Kozlowska, E., Fiszer, A. and Olejniczak, M. 2020. Generation of new isogenic models of Huntington's disease using CRISPR-Cas9 technology. *International journal of molecular sciences* 21(5), p. 1854.

Dacks, J. B. and Field, M. C. 2018. Evolutionary origins and specialisation of membrane transport. *Current opinion in cell biology* 53, pp. 70-76.

Damiano, M., Galvan, L., Déglon, N. and Brouillet, E. 2010. Mitochondria in Huntington's disease. *Biochimica et Biophysica Acta (BBA)-Molecular Basis of Disease* 1802(1), pp. 52-61.

Davidson, C. D. et al. 2009. Chronic cyclodextrin treatment of murine Niemann-Pick C disease ameliorates neuronal cholesterol and glycosphingolipid storage and disease progression. *PLOS one* 4(9), p. e6951.

Davies, J. P., Chen, F. W. and Ioannou, Y. A. 2000. Transmembrane molecular pump activity of Niemann-Pick C1 protein. *Science* 290(5500), pp. 2295-2298.

Davies, S. W. et al. 1997. Formation of neuronal intranuclear inclusions underlies the neurological dysfunction in mice transgenic for the HD mutation. *Cell* 90(3), pp. 537-548.

De Duve, C. and Baudhuin, P. 1966. Peroxisomes (microbodies and related particles). *Physiological reviews* 46(2), pp. 323-357.

De Mario, A. et al. 2016. Calcium handling by endoplasmic reticulum and mitochondria in a cell model of Huntington's disease. *PLoS currents* 8,

De Mezer, M., Wojciechowska, M., Napierala, M., Sobczak, K. and Krzyzosiak, W. J. 2011. Mutant CAG repeats of Huntingtin transcript fold into hairpins, form nuclear foci and are targets for RNA interference. *Nucleic acids research* 39(9), pp. 3852-3863.

Del Toro, D., Alberch, J., Lázaro-Diéguez, F., Martín-Ibáñez, R., Xifro, X., Egea, G. and Canals, J. M. 2009. Mutant huntingtin impairs post-Golgi trafficking to lysosomes by delocalizing optineurin/Rab8 complex from the Golgi apparatus. *Molecular Biology of the Cell* 20(5), pp. 1478-1492.

del Toro, D., Canals, J. M., Ginés, S., Kojima, M., Egea, G. and Alberch, J. 2006. Mutant huntingtin impairs the post-Golgi trafficking of brain-derived neurotrophic factor but not its Val66Met polymorphism. *Journal of Neuroscience* 26(49), pp. 12748-12757.

del Toro, D., Xifro, X., Pol, A., Humbert, S., Saudou, F., Canals, J. M. and Alberch, J. 2010a. Altered cholesterol homeostasis contributes to enhanced excitotoxicity in Huntington's disease. *J Neurochem* 115(1), pp. 153-167. doi: 10.1111/j.1471-4159.2010.06912.x

Del Toro, D., Xifró, X., Pol, A., Humbert, S., Saudou, F., Canals, J. M. and Alberch, J. 2010b. Altered cholesterol homeostasis contributes to enhanced excitotoxicity in Huntington's disease. *Journal of neurochemistry* 115(1), pp. 153-167.

Demais, V., Barthélémy, A., Perraut, M., Ungerer, N., Keime, C., Reibel, S. and Pfrieger, F. W. 2016. Reversal of pathologic lipid accumulation in NPC1-deficient neurons by drug-promoted release of LAMP1-coated lamellar inclusions. *Journal of Neuroscience* 36(30), pp. 8012-8025.

Demers-Lamarche, J. et al. 2016. Loss of mitochondrial function impairs lysosomes. *Journal of Biological Chemistry* 291(19), pp. 10263-10276.

Denny, C. A., Desplats, P. A., Thomas, E. A. and Seyfried, T. N. 2010. Cerebellar lipid differences between R6/1 transgenic mice and humans with Huntington's disease. *Journal of neurochemistry* 115(3), pp. 748-758.

Desplats, P. A. et al. 2007a. Glycolipid and ganglioside metabolism imbalances in Huntington's disease. *Neurobiol Dis* 27(3), pp. 265-277. doi: 10.1016/j.nbd.2007.05.003

Desplats, P. A. et al. 2007b. Glycolipid and ganglioside metabolism imbalances in Huntington's disease. *Neurobiology of disease* 27(3), pp. 265-277.

Devlin, C., Pipalia, N. H., Liao, X., Schuchman, E. H., Maxfield, F. R. and Tabas, I. 2010. Improvement in lipid and protein trafficking in Niemann-Pick C1 cells by correction of a secondary enzyme defect. *Traffic* 11(5), pp. 601-615.

Di Maio, L., Squitieri, F., Napolitano, G., Campanella, G., Trofatter, J. A. and Conneally, P. M. 1993. Suicide risk in Huntington's disease. *Journal of Medical Genetics* 30(4), pp. 293-295.

Di Pardo, A. et al. 2017a. Defective sphingosine-1-phosphate metabolism is a druggable target in Huntington's disease. *Scientific reports* 7(1), pp. 1-14.

Di Pardo, A. et al. 2017b. De novo synthesis of sphingolipids is defective in experimental models of Huntington's disease. *Frontiers in neuroscience* 11, p. 698.

Di Pardo, A. and Maglione, V. 2018. Sphingolipid metabolism: a new therapeutic opportunity for brain degenerative disorders. *Frontiers in neuroscience* 12, p. 249.

Di Pardo, A. et al. 2012. Ganglioside GM1 induces phosphorylation of mutant huntingtin and restores normal motor behavior in Huntington disease mice. *Proceedings of the National Academy of Sciences* 109(9), pp. 3528-3533.

Dietschy, J. M. 2009. Central nervous system: cholesterol turnover, brain development and neurodegeneration.

Dietschy, J. M. and Turley, S. D. 2004. Thematic review series: brain Lipids. Cholesterol metabolism in the central nervous system during early development and in the mature animal. *Journal of lipid research* 45(8), pp. 1375-1397.

DiFiglia, M. et al. 1995. Huntingtin is a cytoplasmic protein associated with vesicles in human and rat brain neurons. *Neuron* 14(5), pp. 1075-1081.

DiFiglia, M., Sapp, E., Chase, K. O., Davies, S. W., Bates, G. P., Vonsattel, J. P. and Aronin, N. 1997. Aggregation of huntingtin in neuronal intranuclear inclusions and dystrophic neurites in brain. *Science* 277(5334), pp. 1990-1993.

Doherty, G. J. and McMahon, H. T. 2009. Mechanisms of endocytosis. *Annual review of biochemistry* 78, pp. 857-902.

Donaldson, J. J. 2019a. *Huntingtin CAG repeat expansions in induced pluripotent stem cell models of Huntington's Disease.* Cardiff University.

Donaldson, J. J. 2019b. Huntingtin CAG repeat expansions in induced pluripotent stem cell models of Huntington's Disease.

Dragatsis, I., Levine, M. S. and Zeitlin, S. 2000. Inactivation of Hdh in the brain and testis results in progressive neurodegeneration and sterility in mice. *Nature genetics* 26(3), pp. 300-306.

Dröge, A. and Wanker, E. E. 2002. Structural biology of Huntingtons disease. *Motulsky, Arno, G. Bobrow, Martin Harper, Peter, S. Scriver, Charles (Hrsg) Huntingtons disease, Bd* 1(3), pp. 332-332.

Drouet, V. et al. 2014. Allele-specific silencing of mutant huntingtin in rodent brain and human stem cells. *PLOS one* 9(6), p. e99341.

Du, X., Kazim, A. S., Brown, A. J. and Yang, H. 2012. An essential role of Hrs/Vps27 in endosomal cholesterol trafficking. *Cell Reports* 1(1), pp. 29-35.

Duff, K. et al. 2010. Mild cognitive impairment in prediagnosed Huntington disease. *Neurology* 75(6), pp. 500-507.

Duyao, M. et al. 1993. Trinucleotide repeat length instability and age of onset in Huntington's disease. *Nature genetics* 4(4), pp. 387-392.

Duyao, M. P. et al. 1995. Inactivation of the mouse Huntington's disease gene homolog Hdh. *Science* 269(5222), pp. 407-410.

Easter, S., Ross, L. S. and Frankfurter, A. 1993. Initial tract formation in the mouse brain. *Journal of Neuroscience* 13(1), pp. 285-299.

Elitt, M. S., Barbar, L. and Tesar, P. J. 2018. Drug screening for human genetic diseases using iPSC models. *Human molecular genetics* 27(R2), pp. R89-R98.

Elrick, M. J., Yu, T., Chung, C. and Lieberman, A. P. 2012. Impaired proteolysis underlies autophagic dysfunction in Niemann–Pick type C disease. *Human molecular genetics* 21(22), pp. 4876-4887.

Engqvist-Goldstein, A. s. E. Y., Warren, R. A., Kessels, M. M., Keen, J. H., Heuser, J. and Drubin, D. G. 2001. The actin-binding protein Hip1R associates with clathrin during early stages of endocytosis and promotes clathrin assembly in vitro. *The Journal of Cell Biology* 154(6), pp. 1209-1224.

Erickson, R. P., Garver, W. S., Camargo, F., Hossian, G. S. and Heidenreich, R. A. 2000. Pharmacological and genetic modifications of somatic cholesterol do not substantially alter the course of CNS disease in Niemann–Pick C mice. *Journal of inherited metabolic disease* 23(1), pp. 54-62.

Erie, C., Sacino, M., Houle, L., Lu, M. L. and Wei, J. 2015. Altered lysosomal positioning affects lysosomal functions in a cellular model of Huntington's disease. *Eur J Neurosci* 42(3), pp. 1941-1951. doi: 10.1111/ejn.12957

Eskelinen, E.-L. 2008. Fine structure of the autophagosome.*Autophagosome and Phagosome*. Springer, pp. 11-28.

Essletzbichler, P. et al. 2014. Megabase-scale deletion using CRISPR/Cas9 to generate a fully haploid human cell line. *Genome research* 24(12), pp. 2059-2065.

Falluel-Morel, A. et al. 2008. Interactions of PACAP and ceramides in the control of granule cell apoptosis during cerebellar development. *Journal of molecular neuroscience* 36(1), pp. 8-15.

Faul, F., Erdfelder, E., Lang, A.-G. and Buchner, A. 2007. G* Power 3: A flexible statistical power analysis program for the social, behavioral, and biomedical sciences. *Behavior research methods* 39(2), pp. 175-191.

Ferrari, G. and Greene, L. A. 1996. Prevention of neuronal apoptotic death by neurotrophic agents and ganglioside GM1: insights and speculations regarding a common mechanism. *Perspectives on developmental neurobiology* 3(2), pp. 93-100.

Fighera, M. R. et al. 2006. GM1 ganglioside prevents seizures, Na+, K+-ATPase activity inhibition and oxidative stress induced by glutaric acid and pentylenetetrazole. *Neurobiology of disease* 22(3), pp. 611-623.

Finkbeiner, S. 2020. The autophagy lysosomal pathway and neurodegeneration. *Cold Spring Harbor perspectives in biology* 12(3), p. a033993.

Fisher, E. R. and Hayden, M. R. 2014. Multisource ascertainment of Huntington disease in Canada: prevalence and population at risk. *Movement Disorders* 29(1), pp. 105-114.

Fraiberg, M. and Elazar, Z. 2020. Genetic defects of autophagy linked to disease. *Progress in Molecular Biology and Translational Science* 172, pp. 293-323.

Fraldi, A. et al. 2010. Lysosomal fusion and SNARE function are impaired by cholesterol accumulation in lysosomal storage disorders. *The EMBO journal* 29(21), pp. 3607-3620.

Franco-Iborra, S., Plaza-Zabala, A., Montpeyo, M., Sebastian, D., Vila, M. and Martinez-Vicente, M. 2021. Mutant HTT (huntingtin) impairs mitophagy in a cellular model of Huntington disease. *Autophagy* 17(3), pp. 672-689.

Fransen, M., Nordgren, M., Wang, B. and Apanasets, O. 2012. Role of peroxisomes in ROS/RNS-metabolism: implications for human disease. *Biochimica et Biophysica Acta (BBA)-Molecular Basis of Disease* 1822(9), pp. 1363-1373.

Friedland, N., Liou, H.-L., Lobel, P. and Stock, A. M. 2003. Structure of a cholesterol-binding protein deficient in Niemann–Pick type C2 disease. *Proceedings of the National Academy of Sciences* 100(5), pp. 2512-2517.

Frolov, A., Srivastava, K., Daphna-Iken, D., Traub, L. M., Schaffer, J. E. and Ory, D. S. 2001. Cholesterol overload promotes morphogenesis of a Niemann-Pick C (NPC)-like compartment independent of inhibition of NPC1 or HE1/NPC2 function. *Journal of Biological Chemistry* 276(49), pp. 46414-46421.

Fu, Y., Sander, J. D., Reyon, D., Cascio, V. M. and Joung, J. K. 2014. Improving CRISPR-Cas nuclease specificity using truncated guide RNAs. *Nature biotechnology* 32(3), pp. 279-284.

Futter, M., Diekmann, H., Schoenmakers, E., Sadiq, O., Chatterjee, K. and Rubinsztein, D. C. 2009. Wild-type but not mutant huntingtin modulates the transcriptional activity of liver X receptors. *Journal of Medical Genetics* 46(7), pp. 438-446.

Gallala, H. D., Breiden, B. and Sandhoff, K. 2011. Regulation of the NPC2 protein-mediated cholesterol trafficking by membrane lipids. *Journal of neurochemistry* 116(5), pp. 702-707.

Galvin, N., Vogler, C., Levy, B., Kovacs, A., Griffey, M. and Sands, M. S. 2008. A murine model of infantile neuronal ceroid lipofuscinosis—ultrastructural evaluation of storage in the central nervous system and viscera. *Pediatric and Developmental Pathology* 11(3), pp. 185-192.

Ganley, I. G. and Pfeffer, S. R. 2006. Cholesterol accumulation sequesters Rab9 and disrupts late endosome function in NPC1-deficient cells. *Journal of Biological Chemistry* 281(26), pp. 17890-17899.

Gardiner, S. L. et al. 2018. Bioenergetics in fibroblasts of patients with Huntington disease are associated with age at onset. *Neurology Genetics* 4(5),

Garg, U. and Smith, L. D. 2017. *Biomarkers in Inborn Errors of Metabolism: Clinical Aspects and Laboratory Determination*. Elsevier.

Garver, W. S., Jelinek, D., Francis, G. A. and Murphy, B. D. 2008. The Niemann-Pick C1 gene is downregulated by feedback inhibition of the SREBP pathway in human fibroblasts. *Journal of lipid research* 49(5), pp. 1090-1102.

Gault, C. R., Obeid, L. M. and Hannun, Y. A. 2010. An overview of sphingolipid metabolism: from synthesis to breakdown. *Sphingolipids as signaling and regulatory molecules*, pp. 1-23.

Gauthier, L. R. et al. 2004. Huntingtin controls neurotrophic support and survival of neurons by enhancing BDNF vesicular transport along microtubules. *Cell* 118(1), pp. 127-138.

Gelman, A., Rawet-Slobodkin, M. and Elazar, Z. 2015. Huntingtin facilitates selective autophagy. *Nature cell biology* 17(3), pp. 214-215.

Gervais, F. G. et al. 2002. Recruitment and activation of caspase-8 by the Huntingtin-interacting protein Hip-1 and a novel partner Hippi. *Nature cell biology* 4(2), pp. 95-105.

Giacomello, M., Oliveros, J., Naranjo, J. and Carafoli, E. 2013. Neuronal Ca2+ dyshomeostasis in Huntington disease. *Prion* 7(1), pp. 76-84.

Gillard, B. K., Clement, R. G. and Marcus, D. M. 1998. Variations among cell lines in the synthesis of sphingolipids in de novo and recycling pathways. *Glycobiology* 8(9), pp. 885-890.

Godin, J. D. et al. 2010. Huntingtin is required for mitotic spindle orientation and mammalian neurogenesis. *Neuron* 67(3), pp. 392-406.

Gondré-Lewis, M. C., McGlynn, R. and Walkley, S. U. 2003. Cholesterol accumulation in NPC1-deficient neurons is ganglioside dependent. *Current Biology* 13(15), pp. 1324-1329.

Gong, X. et al. 2016. Structural insights into the Niemann-Pick C1 (NPC1)-mediated cholesterol transfer and Ebola infection. *Cell* 165(6), pp. 1467-1478.

Gonitel, R., Moffitt, H., Sathasivam, K., Woodman, B., Detloff, P. J., Faull, R. L. M. and Bates, G. P. 2008. DNA instability in postmitotic neurons. *Proceedings of the National Academy of Sciences* 105(9), pp. 3467-3472.

González-Guevara, E., Cárdenas, G., Pérez-Severiano, F. and Martínez-Lazcano, J. C. 2020. Dysregulated brain cholesterol metabolism is linked to neuroinflammation in Huntington's disease. *Movement Disorders* 35(7), pp. 1113-1127.

Gotoda, Y., Wakamatsu, N., Kawai, H., Nishida, Y. and Matsumoto, T. 1998. Missense and nonsense mutations in the lysosomal α-mannosidase gene (MANB) in severe and mild forms of α-mannosidosis. *The American Journal of Human Genetics* 63(4), pp. 1015-1024.

Gould, S. B. 2018. Membranes and evolution. *Current Biology* 28(8), pp. R381-R385.

Gould, S. B., Garg, S. G. and Martin, W. F. 2016. Bacterial vesicle secretion and the evolutionary origin of the eukaryotic endomembrane system. *Trends in microbiology* 24(7), pp. 525-534.

Graham, R. K. et al. 2006. Cleavage at the caspase-6 site is required for neuronal dysfunction and degeneration due to mutant huntingtin. *Cell* 125(6), pp. 1179-1191.

Graham, V., Khudyakov, J., Ellis, P. and Pevny, L. 2003. SOX2 functions to maintain neural progenitor identity. *Neuron* 39(5), pp. 749-765.

Graybiel, A. M. 1998. The basal ganglia and chunking of action repertoires. *Neurobiology of learning and memory* 70(1-2), pp. 119-136.

Groves, P. M. 1983. A theory of the functional organization of the neostriatum and the neostriatal control of voluntary movement. *Brain research reviews* 5(2), pp. 109-132.

Gubitz, A. K., Feng, W. and Dreyfuss, G. 2004. The SMN complex. *Experimental cell research* 296(1), pp. 51-56.

Gunawardena, S. et al. 2003. Disruption of axonal transport by loss of huntingtin or expression of pathogenic polyQ proteins in Drosophila. *Neuron* 40(1), pp. 25-40.

Guo, Q. et al. 2018. The cryo-electron microscopy structure of huntingtin. *Nature* 555(7694), pp. 117-120.

Guo, X., Disatnik, M.-H., Monbureau, M., Shamloo, M., Mochly-Rosen, D. and Qi, X. 2013. Inhibition of mitochondrial fragmentation diminishes Huntington's disease–associated neurodegeneration. *The Journal of clinical investigation* 123(12), pp. 5371-5388.

Gusella, J. F. and MacDonald, M. E. 2000. Molecular genetics: unmasking polyglutamine triggers in neurodegenerative disease. *Nature Reviews Neuroscience* 1(2), pp. 109-115.

Gusella, J. F. and MacDonald, M. E. 2006. Huntington's disease: seeing the pathogenic process through a genetic lens. *Trends in biochemical sciences* 31(9), pp. 533-540.

Gusella, J. F. and MacDonald, M. E. 2009. Huntington's disease: the case for genetic modifiers. *Genome medicine* 1(8), pp. 1-6.

Gusella, J. F. et al. 1983. A polymorphic DNA marker genetically linked to Huntington's disease. *Nature* 306(5940), pp. 234-238.

Gutekunst, C.-A. et al. 1995a. Identification and localization of huntingtin in brain and human lymphoblastoid cell lines with anti-fusion protein antibodies. *Proceedings of the National Academy of Sciences* 92(19), pp. 8710-8714.

Gutekunst, C. A. et al. 1995b. Identification and localization of huntingtin in brain and human lymphoblastoid cell lines with anti-fusion protein antibodies. *Proc Natl Acad Sci U S A* 92(19), pp. 8710-8714. doi: 10.1073/pnas.92.19.8710

Hadzi, T. C. et al. 2012. Assessment of cortical and striatal involvement in 523 Huntington disease brains. *Neurology* 79(16), pp. 1708-1715.

Handley, R. R. et al. 2016. Metabolic disruption identified in the Huntington's disease transgenic sheep model. *Scientific reports* 6(1), pp. 1-11.

Hara, T. et al. 2006. Suppression of basal autophagy in neural cells causes neurodegenerative disease in mice. *Nature* 441(7095), pp. 885-889.

Harper, P. S. 1992. The epidemiology of Huntington's disease. *Human genetics* 89(4), pp. 365-376.

Harzer, K., Massenkeil, G. and Fröhlich, E. 2003. Concurrent increase of cholesterol, sphingomyelin and glucosylceramide in the spleen from non-neurologic Niemann–Pick type C patients but also patients possibly affected with other lipid trafficking disorders. *FEBS letters* 537(1-3), pp. 177-181.

Haslett, L. 2015. *Lysosomal storage disorders and neurodegenerative disease; related mechanisms of pathogenesis and identification of novel therapeutic targets.* Cardiff University.

Haun, F. et al. 2013. S-nitrosylation of dynamin-related protein 1 mediates mutant huntingtin-induced mitochondrial fragmentation and neuronal injury in Huntington's disease. *Antioxidants & redox signaling* 19(11), pp. 1173-1184.

Hayre, J. K., Xu, G., Borgianni, L., Taylor, G. L., Andrew, P. W., Docquier, J.-D. and Oggioni, M. R. 2012. Optimization of a direct spectrophotometric method to investigate the kinetics and inhibition of sialidases. *BMC biochemistry* 13(1), pp. 1-7.

Hd iPsc, C. 2012. Induced pluripotent stem cells from patients with Huntington's disease show CAG-repeat-expansion-associated phenotypes. *Cell stem cell* 11(2), pp. 264-278.

Headlam, H. A., Gracanin, M., Rodgers, K. J. and Davies, M. J. 2006. Inhibition of cathepsins and related proteases by amino acid, peptide, and protein hydroperoxides. *Free Radical Biology and Medicine* 40(9), pp. 1539-1548.

Hebbar, S. et al. 2017. Lipid metabolic perturbation is an early-onset phenotype in adult spinster mutants: a Drosophila model for lysosomal storage disorders. *Molecular biology of the cell* 28(26), pp. 3728-3740.

Heinsen, H. et al. 1999. Nerve cell loss in the thalamic mediodorsal nucleus in Huntington's disease. *Acta neuropathologica* 97(6), pp. 613-622.

Höglinger, D. et al. 2015. Intracellular sphingosine releases calcium from lysosomes. *Elife* 4, p. e10616.

Höglinger, D. et al. 2017. Trifunctional lipid probes for comprehensive studies of single lipid species in living cells. *Proceedings of the National Academy of Sciences* 114(7), pp. 1566-1571.

Hölttä-Vuori, M. and Ikonen, E. 2006. Endosomal cholesterol traffic: vesicular and non-vesicular mechanisms meet. *Biochemical Society Transactions* 34(3), pp. 392-394.

Hölttä-Vuori, M., Tanhuanpää, K., Mobius, W., Somerharju, P. and Ikonen, E. 2002. Modulation of cellular cholesterol transport and homeostasis by Rab11. *Molecular Biology of the Cell* 13(9), pp. 3107-3122.

Hopwood, J. J., Muller, V., Smithson, A. and Baggett, N. 1979. A fluorometric assay using 4-methylumbelliferyl α-L-iduronide for the estimation of α-L-iduronidase activity and the detection of Hurler and Scheie syndromes. *Clinica Chimica Acta* 92(2), pp. 257-265.

Hough, S. H., Ajetunmobi, A., Brody, L., Humphryes-Kirilov, N. and Perello, E. 2016. Desktop genetics. Future Medicine.

Hovakimyan, M. et al. 2013. Combined therapy with cyclodextrin/allopregnanolone and miglustat improves motor but not cognitive functions in Niemann–Pick Type C1 mice. *Neuroscience* 252, pp. 201-211.

Hsu, P. D. et al. 2013. DNA targeting specificity of RNA-guided Cas9 nucleases. *Nature biotechnology* 31(9), pp. 827-832.

Hu, D. et al. 2021. Small-molecule suppression of calpastatin degradation reduces neuropathology in models of Huntington's disease. *Nature communications* 12(1), pp. 1-19.

Hua, X., Nohturfft, A., Goldstein, J. L. and Brown, M. S. 1996. Sterol resistance in CHO cells traced to point mutation in SREBP cleavage–activating protein. *Cell* 87(3), pp. 415-426.

Huang, C. C., Faber, P. W., Persichetti, F., Mittal, V., Vonsattel, J.-P., MacDonald, M. E. and Gusella, J. F. 1998. Amyloid formation by mutant huntingtin: threshold, progressivity and recruitment of normal polyglutamine proteins. *Somatic cell and molecular genetics* 24(4), pp. 217-233.

Hubers, A. A. M., Reedeker, N., Giltay, E. J., Roos, R. A. C., Van Duijn, E. and Van der Mast, R. C. 2012. Suicidality in Huntington's disease. *Journal of affective disorders* 136(3), pp. 550-557.

Hughes, A. C., Mort, M., Elliston, L., Thomas, R. M., Brooks, S. P., Dunnett, S. B. and Jones, L. 2014. Identification of novel alternative splicing events in the huntingtin gene and assessment of the functional consequences using structural protein homology modelling. *Journal of molecular biology* 426(7), pp. 1428-1438.

Hunter, M., Demarais, N. J., Faull, R. L., Grey, A. C. and Curtis, M. A. 2021. An imaging mass spectrometry atlas of lipids in the human neurologically normal and Huntington's disease caudate nucleus. *Journal of neurochemistry* 157(6), pp. 2158-2172.

Hutchinson, L. and Kirk, R. 2011. High drug attrition rates—where are we going wrong? *Nature reviews Clinical oncology* 8(4), pp. 189-190.

Ibata, K. and Yuzaki, M. 2021. Destroy the Old to Build the New: Activity-Dependent Lysosomal Exocytosis in Neurons. *Neuroscience Research*,

Ibrahim, K. S., McLaren, C. J., Abd-Elrahman, K. S. and Ferguson, S. S. 2021. Optineurin deletion disrupts metabotropic glutamate receptor 5-mediated regulation of ERK1/2, GSK3β/ZBTB16, mTOR/ULK1 signaling in autophagy. *Biochemical pharmacology* 185, p. 114427.

Ikonen, E. and Zhou, X. 2021. Cholesterol transport between cellular membranes: A balancing act between interconnected lipid fluxes. *Developmental Cell* 56(10), pp. 1430-1436.

Ioannou, Y. A. 2005. Guilty until proven innocent: the case of NPC1 and cholesterol. *Trends in biochemical sciences* 30(9), pp. 498-505.

Ismael, F. O., Barrett, T. J., Sheipouri, D., Brown, B. E., Davies, M. J. and Hawkins, C. L. 2016. Role of myeloperoxidase oxidants in the modulation of cellular lysosomal enzyme function: a contributing factor to macrophage dysfunction in atherosclerosis? *PLOS one* 11(12), p. e0168844.

Ismailoglu, I., Chen, Q., Popowski, M., Yang, L., Gross, S. S. and Brivanlou, A. H. 2014. Huntingtin protein is essential for mitochondrial metabolism, bioenergetics and structure in murine embryonic stem cells. *Developmental biology* 391(2), pp. 230-240.

Jack, R. M., Gordon, C., Scott, C. R., Kishnani, P. S. and Bali, D. 2006. The use of acarbose inhibition in the measurement of acid alpha-glucosidase activity in blood lymphocytes for the diagnosis of Pompe disease. *Genetics in Medicine* 8(5), pp. 307-312.

Jacobsen, J. C. et al. 2011. HD CAG-correlated gene expression changes support a simple dominant gain of function. *Hum Mol Genet* 20(14), pp. 2846-2860. doi: 10.1093/hmg/ddr195

Jékely, G. 2007. Origin of eukaryotic endomembranes: a critical evaluation of different model scenarios. *Eukaryotic Membranes and Cytoskeleton: Origins and Evolution*, pp. 38-51.

Jenkins, R. W., Canals, D. and Hannun, Y. A. 2009. Roles and regulation of secretory and lysosomal acid sphingomyelinase. *Cellular signalling* 21(6), pp. 836-846.

Jeske, D. J. and Dietschy, J. M. 1980. Regulation of rates of cholesterol synthesis in vivo in the liver and carcass of the rat measured using [3H] water. *Journal of lipid research* 21(3), pp. 364-376.

Jeste, D. V., Barban, L. and Parisi, J. 1984. Reduced Purkinje cell density in Huntington's disease. *Experimental neurology* 85(1), pp. 78-86.

Jimenez-Sanchez, M., Licitra, F., Underwood, B. R. and Rubinsztein, D. C. 2017. Huntington's Disease: Mechanisms of Pathogenesis and Therapeutic Strategies. *Cold Spring Harb Perspect Med* 7(7), p. a024240. doi: 10.1101/cshperspect.a024240

Johnson, R. L. et al. 1996. Human homolog of patched, a candidate gene for the basal cell nevus syndrome. *Science* 272(5268), pp. 1668-1671.

Juopperi, T. A. et al. 2012. Astrocytes generated from patient induced pluripotent stem cells recapitulate features of Huntington's disease patient cells. *Molecular brain* 5(1), pp. 1-14.

Kacher, Y. and Futerman, A. H. 2006. Genetic diseases of sphingolipid metabolism: pathological mechanisms and therapeutic options. *FEBS letters* 580(23), pp. 5510-5517.

Kaltenbach, L. S. et al. 2007. Huntingtin interacting proteins are genetic modifiers of neurodegeneration. *PLoS genetics* 3(5), p. e82.

Kang, B. S. et al. 2007. Heat shock protein 70 alters the endosome-lysosomal localization of huntingtin. *Experimental & molecular medicine* 39(1), pp. 38-46.

Karten, B., Peake, K. B. and Vance, J. E. 2009. Mechanisms and consequences of impaired lipid trafficking in Niemann–Pick type C1-deficient mammalian cells. *Biochimica et Biophysica Acta (BBA)-Molecular and Cell Biology of Lipids* 1791(7), pp. 659-670.

Karten, B., Vance, D. E., Campenot, R. B. and Vance, J. E. 2002. Cholesterol accumulates in cell bodies, but is decreased in distal axons, of Niemann–Pick C1-deficient neurons. *Journal of neurochemistry* 83(5), pp. 1154-1163.

Kay, C. et al. 2018. The molecular epidemiology of Huntington disease is related to intermediate allele frequency and haplotype in the general population. *American Journal of Medical Genetics Part B: Neuropsychiatric Genetics* 177(3), pp. 346-357.

Kaya, E. et al. 2021. Acetyl-leucine slows disease progression in lysosomal storage disorders. *Brain communications* 3(1), p. fcaa148.

Kazantsev, A., Preisinger, E., Dranovsky, A., Goldgaber, D. and Housman, D. 1999. Insoluble detergent-resistant aggregates form between pathological and nonpathological lengths of polyglutamine in mammalian cells. *Proceedings of the National Academy of Sciences* 96(20), pp. 11404-11409.

Kegel, K. B., Kim, M., Sapp, E., McIntyre, C., Castano, J. G., Aronin, N. and DiFiglia, M. 2000. Huntingtin expression stimulates endosomal–lysosomal activity, endosome tubulation, and autophagy. *Journal of Neuroscience* 20(19), pp. 7268-7278.

Kegel, K. B. et al. 2005. Huntingtin associates with acidic phospholipids at the plasma membrane. *Journal of Biological Chemistry* 280(43), pp. 36464-36473.

Kemp, P. J. et al. 2016. Improving and accelerating the differentiation and functional maturation of human stem cell-derived neurons: role of extracellular calcium and GABA. *The Journal of physiology* 594(22), pp. 6583-6594.

Kennedy, B. E., Charman, M. and Karten, B. 2012. Niemann-Pick Type C2 protein contributes to the transport of endosomal cholesterol to mitochondria without interacting with NPC1 [S]. *Journal of lipid research* 53(12), pp. 2632-2642.

Kennedy, B. E., Madreiter, C. T., Vishnu, N., Malli, R., Graier, W. F. and Karten, B. 2014. Adaptations of energy metabolism associated with increased levels of mitochondrial cholesterol in Niemann-Pick type C1-deficient cells. *Journal of Biological Chemistry* 289(23), pp. 16278-16289.

Kent, W. J., Sugnet, C. W., Furey, T. S., Roskin, K. M., Pringle, T. H., Zahler, A. M. and Haussler, D. 2002. The human genome browser at UCSC. *Genome research* 12(6), pp. 996-1006.

Killoran, A. et al. 2013. Characterization of the Huntington intermediate CAG repeat expansion phenotype in PHAROS. *Neurology* 80(22), pp. 2022-2027.

Kilpinen, H. et al. 2017. Common genetic variation drives molecular heterogeneity in human iPSCs. *Nature* 546(7658), pp. 370-375.

Kim, H. S. et al. 2015. Current status of Huntington's disease in Korea: a nationwide survey and national registry analysis. *Journal of movement disorders* 8(1), p. 14.

Kingma, S. D. K. et al. 2013. An algorithm to predict phenotypic severity in mucopolysaccharidosis type I in the first month of life. *Orphanet journal of rare diseases* 8(1), pp. 1-11.

Kitatani, K., Idkowiak-Baldys, J. and Hannun, Y. A. 2008. The sphingolipid salvage pathway in ceramide metabolism and signaling. *Cellular signalling* 20(6), pp. 1010-1018.

Klein, A. et al. 2011. Oxidative stress activates the c-Abl/p73 proapoptotic pathway in Niemann-Pick type C neurons. *Neurobiology of disease* 41(1), pp. 209-218.

Klumperman, J. and Raposo, G. 2014. The complex ultrastructure of the endolysosomal system. *Cold Spring Harbor perspectives in biology* 6(10), p. a016857.

Knoll, M. and Ruska, E. 1932. Das elektronenmikroskop. *Zeitschrift für physik* 78(5), pp. 318-339.

Ko, D. C., Gordon, M. D., Jin, J. Y. and Scott, M. P. 2001. Dynamic movements of organelles containing Niemann-Pick C1 protein: NPC1 involvement in late endocytic events. *Molecular Biology of the Cell* 12(3), pp. 601-614.

Ko, D. C., Milenkovic, L., Beier, S. M., Manuel, H., Buchanan, J. and Scott, M. P. 2005. Cell-autonomous death of cerebellar purkinje neurons with autophagy in Niemann-Pick type C disease. *PLoS genetics* 1(1), p. e7.

Kobayashi, T. et al. 2002. Separation and characterization of late endosomal membrane domains. *Journal of Biological Chemistry* 277(35), pp. 32157-32164.

Kobayashi, T., Stang, E., Fang, K. S., de Moerloose, P., Parton, R. G. and Gruenberg, J. 1998. A lipid associated with the antiphospholipid syndrome regulates endosome structure and function. *Nature* 392(6672), pp. 193-197.

Kobayashi, T., Startchev, K., Whitney, A. J. and Gruenberg, J. 2001. Localization of lysobisphosphatidic acid-rich membrane domains in late endosomes. Walter de Gruyter.

Koga, H. and Cuervo, A. M. 2011. Chaperone-mediated autophagy dysfunction in the pathogenesis of neurodegeneration. *Neurobiology of disease* 43(1), pp. 29-37.

Koga, H., Kaushik, S. and Cuervo, A. M. 2010. Altered lipid content inhibits autophagic vesicular fusion. *The FASEB journal* 24(8), pp. 3052-3065.

Koga, H., Martinez-Vicente, M., Arias, E., Kaushik, S., Sulzer, D. and Cuervo, A. M. 2011. Constitutive upregulation of chaperone-mediated autophagy in Huntington's disease. *Journal of Neuroscience* 31(50), pp. 18492-18505.

Koh, C. H. V. et al. 2006. Chronic exposure to U18666A is associated with oxidative stress in cultured murine cortical neurons. *Journal of neurochemistry* 98(4), pp. 1278-1289.

Kolter, T. and Sandhoff, K. 2005a. Lysosomal glycosphingolipid storage diseases. *Neuroglycobiology (Molecular and Cellular Neurobiology). Oxford University Press, Oxford, United Kingdom*, pp. 199-223.

Kolter, T. and Sandhoff, K. 2005b. Principles of lysosomal membrane digestion: stimulation of sphingolipid degradation by sphingolipid activator proteins and anionic lysosomal lipids. *Annu. Rev. Cell Dev. Biol.* 21, pp. 81-103.

Komatsu, M. et al. 2006. Loss of autophagy in the central nervous system causes neurodegeneration in mice. *Nature* 441(7095), pp. 880-884.

Korolchuk, V. I. et al. 2011. Lysosomal positioning coordinates cellular nutrient responses. *Nature cell biology* 13(4), pp. 453-460.

Kosugi, S., Ohashi, Y., Nakajima, K. and Arai, Y. 1990. An improved assay for β-glucuronidase in transformed cells: methanol almost completely suppresses a putative endogenous β-glucuronidase activity. *Plant Science* 70(1), pp. 133-140.

Kreilaus, F., Spiro, A. S., McLean, C. A., Garner, B. and Jenner, A. M. 2016. Evidence for altered cholesterol metabolism in H untington's disease post mortem brain tissue. *Neuropathology and applied neurobiology* 42(6), pp. 535-546.

Kremer, H. P. 1992. The hypothalamic lateral tuberal nucleus: normal anatomy and changes in neurological diseases. *Progress in brain research* 93, pp. 249-261.

Kremer, H. P. H., Roos, R. A. C., Dingjan, G. M., Bots, G. T. A. M., Bruyn, G. W. and Hofman, M. A. 1991. The hypothalamic lateral tuberal nucleus and the characteristics of neuronal loss in Huntington's disease. *Neuroscience letters* 132(1), pp. 101-104.

Kwon, H. J., Abi-Mosleh, L., Wang, M. L., Deisenhofer, J., Goldstein, J. L., Brown, M. S. and Infante, R. E. 2009. Structure of N-terminal domain of NPC1 reveals distinct subdomains for binding and transfer of cholesterol. *Cell* 137(7), pp. 1213-1224. doi: 10.1016/j.cell.2009.03.049

Labbadia, J. and Morimoto, R. I. 2013. Huntington's disease: underlying molecular mechanisms and emerging concepts. *Trends in biochemical sciences* 38(8), pp. 378-385.

Lachmann, R. H. et al. 2004. Treatment with miglustat reverses the lipid-trafficking defect in Niemann–Pick disease type C. *Neurobiology of disease* 16(3), pp. 654-658.

Leake, D. S., Heald, B. and Peters, T. J. 1982. Properties and subcellular localization of acid phosphatase activity in cultured arterial smooth muscle cells. *European journal of biochemistry* 128(2-3), pp. 557-563.

Leavitt, B. R. et al. 2006. Wild-type huntingtin protects neurons from excitotoxicity. *Journal of neurochemistry* 96(4), pp. 1121-1129.

Lebrand, C. et al. 2002. Late endosome motility depends on lipids via the small GTPase Rab7. *The EMBO journal* 21(6), pp. 1289-1300.

Lee, H. et al. 2014. Inhibition of GM3 synthase attenuates neuropathology of Niemann-Pick disease Type C by affecting sphingolipid metabolism. *Molecules and cells* 37(2), p. 161.

Lee, J.-M. et al. 2019. CAG repeat not polyglutamine length determines timing of Huntington's disease onset. *Cell* 178(4), pp. 887-900.

Lee, J.-M. et al. 2015. Identification of genetic factors that modify clinical onset of Huntington's disease. *Cell* 162(3), pp. 516-526.

Lee, J.-R. 2015. Protein tyrosine phosphatase PTPRT as a regulator of synaptic formation and neuronal development. *BMB reports* 48(5), p. 249.

Lee, S.-E., Shin, N., Kook, M. G., Kong, D., Kim, N. G., Choi, S. W. and Kang, K.-S. 2020. Human iNSC-derived brain organoid model of lysosomal storage disorder in Niemann–Pick disease type C. *Cell death & disease* 11(12), pp. 1-13.

Legendre-Guillemin, V. et al. 2002. HIP1 and HIP12 display differential binding to F-actin, AP2, and clathrin: Identification of a novel interaction with clathrin light chain. *Journal of Biological Chemistry* 277(22), pp. 19897-19904.

Lendahl, U., Zimmerman, L. B. and McKay, R. D. 1990. CNS stem cells express a new class of intermediate filament protein. *Cell* 60(4), pp. 585-595.

Leoni, V. and Caccia, C. 2015. The impairment of cholesterol metabolism in Huntington disease. *Biochimica et Biophysica Acta (BBA)-Molecular and Cell Biology of Lipids* 1851(8), pp. 1095-1105.

Leoni, V. et al. 2008. Plasma 24S-hydroxycholesterol and caudate MRI in pre-manifest and early Huntington's disease. *Brain* 131(11), pp. 2851-2859.

Li, H., Li, S.-H., Cheng, A. L., Mangiarini, L., Bates, G. P. and Li, X.-J. 1999. Ultrastructural localization and progressive formation of neuropil aggregates in Huntington's disease transgenic mice. *Human molecular genetics* 8(7), pp. 1227-1236.

Li, H., Li, S.-H., Yu, Z.-X., Shelbourne, P. and Li, X.-J. 2001. Huntingtin aggregate-associated axonal degeneration is an early pathological event in Huntington's disease mice. *Journal of Neuroscience* 21(21), pp. 8473-8481.

Li, J.-Y. and Conforti, L. 2013. Axonopathy in Huntington's disease. *Experimental neurology* 246, pp. 62-71.

Li, Z., Gu, Y., Wen, R., Shen, F., Tian, H.-L., Yang, G.-Y. and Zhang, Z. 2019. Lysosome exocytosis is involved in astrocyte ATP release after oxidative stress induced by H2O2. *Neuroscience letters* 705, pp. 251-258.

Liao, Y., Smyth, G. K. and Shi, W. 2014. featureCounts: an efficient general purpose program for assigning sequence reads to genomic features. *Bioinformatics* 30(7), pp. 923-930.

Lieberman, A. P., Puertollano, R., Raben, N., Slaugenhaupt, S., Walkley, S. U. and Ballabio, A. 2012. Autophagy in lysosomal storage disorders. *Autophagy* 8(5), pp. 719-730.

Lim, D., Fedrizzi, L., Tartari, M., Zuccato, C., Cattaneo, E., Brini, M. and Carafoli, E. 2008. Calcium homeostasis and mitochondrial dysfunction in striatal neurons of Huntington disease. *Journal of Biological Chemistry* 283(9), pp. 5780-5789.

Lin, B. et al. 1993. Differential 3’ polyadenylation of the Huntington disease gene results in two mRNA species with variable tissue expression. *Human molecular genetics* 2(10), pp. 1541-1545.

Liot, G., Zala, D., Pla, P., Mottet, G., Piel, M. and Saudou, F. 2013. Mutant Huntingtin alters retrograde transport of TrkB receptors in striatal dendrites. *Journal of Neuroscience* 33(15), pp. 6298-6309.

Liscum, L. 2000. Niemann–Pick type C mutations cause lipid traffic jam. *Traffic* 1(3), pp. 218-225.

Liscum, L. and Faust, J. R. 1987. Low density lipoprotein (LDL)-mediated suppression of cholesterol synthesis and LDL uptake is defective in Niemann-Pick type C fibroblasts. *Journal of Biological Chemistry* 262(35), pp. 17002-17008.

Liscum, L., Ruggiero, R. M. and Faust, J. R. 1989. The intracellular transport of low density lipoprotein-derived cholesterol is defective in Niemann-Pick type C fibroblasts. *The Journal of Cell Biology* 108(5), pp. 1625-1636.

Liscum, L. and Sturley, S. L. 2004. Intracellular trafficking of Niemann–Pick C proteins 1 and 2: obligate components of subcellular lipid transport. *Biochimica et Biophysica Acta (BBA)-Molecular and Cell Biology of Lipids* 1685(1-3), pp. 22-27.

Liu, B. 2012. Therapeutic potential of cyclodextrins in the treatment of Niemann–Pick type C disease. *Clinical lipidology* 7(3), pp. 289-301.

Liu, B., Turley, S. D., Burns, D. K., Miller, A. M., Repa, J. J. and Dietschy, J. M. 2009. Reversal of defective lysosomal transport in NPC disease ameliorates liver dysfunction and neurodegeneration in the npc1−/− mouse. *Proceedings of the National Academy of Sciences* 106(7), pp. 2377-2382.

Liu, J.-P. and Zeitlin, S. O. 2017. Is huntingtin dispensable in the adult brain? *Journal of Huntington's disease* 6(1), pp. 1-17.

Liu, Q. et al. 2020. Loss of Hap1 selectively promotes striatal degeneration in Huntington disease mice. *Proceedings of the National Academy of Sciences* 117(33), pp. 20265-20273.

Liu, Y., Qiao, F., Leiferman, P. C., Ross, A., Schlenker, E. H. and Wang, H. 2017. FOXOs modulate proteasome activity in human-induced pluripotent stem cells of Huntington's disease and their derived neural cells. *Human molecular genetics* 26(22), pp. 4416-4428.

Liu, Y. et al. 2000. Alleviation of neuronal ganglioside storage does not improve the clinical course of the Niemann–Pick C disease mouse. *Human molecular genetics* 9(7), pp. 1087-1092.

Lloyd-Evans, E., Haslett, L. J. and Clark, E. 2014. Uncovering the mechanism by which miglustat mediates benefit in NPC disease; role of acid sphingomyelinase in NPC disease pathogenesis. *Molecular genetics and metabolism* 2(111), pp. S69-S70.

Lloyd-Evans, E. et al. 2008. Niemann-Pick disease type C1 is a sphingosine storage disease that causes deregulation of lysosomal calcium. *Nature medicine* 14(11), pp. 1247-1255.

Lloyd-Evans, E. and Platt, F. M. 2011. Lysosomal Ca2+ homeostasis: role in pathogenesis of lysosomal storage diseases. *Cell calcium* 50(2), pp. 200-205.

Lloyd-Evans, E. and Platt, F. M. 2010. Lipids on trial: the search for the offending metabolite in Niemann-Pick type C disease. *Traffic* 11(4), pp. 419-428.

Lo Sardo, V. et al. 2012. An evolutionary recent neuroepithelial cell adhesion function of huntingtin implicates ADAM10-Ncadherin. *Nature neuroscience* 15(5), pp. 713-721.

Lombardi, G. and Moroni, F. 1992. GM1 ganglioside reduces ischemia-induced excitatory amino acid output: a microdialysis study in the gerbil hippocampus. *Neuroscience letters* 134(2), pp. 171-174.

Lombardi, G., Zanoni, R. and Moroni, F. 1989. Systemic treatments with GM1 ganglioside reduce quinolinic acid-induced striatal lesions in the rat. *European journal of pharmacology* 174(1), pp. 123-125.

Lopes, C. et al. 2020. Mitochondrial and redox modifications in huntington disease induced pluripotent stem cells rescued by CRISPR/Cas9 CAGs targeting. *Frontiers in cell and developmental biology*, p. 967.

Lumsden, A. L., Henshall, T. L., Dayan, S., Lardelli, M. T. and Richards, R. I. 2007. Huntingtin-deficient zebrafish exhibit defects in iron utilization and development. *Human molecular genetics* 16(16), pp. 1905-1920.

Luo, J., Jiang, L., Yang, H. and Song, B. L. 2017. Routes and mechanisms of post-endosomal cholesterol trafficking: A story that never ends. *Traffic* 18(4), pp. 209-217.

Luthi-Carter, R. et al. 2010. SIRT2 inhibition achieves neuroprotection by decreasing sterol biosynthesis. *Proceedings of the National Academy of Sciences* 107(17), pp. 7927-7932.

Luzio, J. P., Hackmann, Y., Dieckmann, N. M. G. and Griffiths, G. M. 2014. The biogenesis of lysosomes and lysosome-related organelles. *Cold Spring Harbor perspectives in biology* 6(9), p. a016840.

Luzio, J. P., Pryor, P. R. and Bright, N. A. 2007. Lysosomes: fusion and function. *Nature reviews Molecular cell biology* 8(8), pp. 622-632.

MacDonald, M. E. et al. 1993. A novel gene containing a trinucleotide repeat that is expanded and unstable on Huntington's disease chromosomes. *Cell* 72(6), pp. 971-983.

Macdonald, V. and Halliday, G. 2002. Pyramidal cell loss in motor cortices in Huntington's disease. *Neurobiology of disease* 10(3), pp. 378-386.

Macdonald, V., Halliday, G. M., Trent, R. J. and McCusker, E. A. 1997. Significant loss of pyramidal neurons in the angular gyrus of patients with Huntington's disease. *Neuropathology and applied neurobiology* 23(6), pp. 492-495.

Maglione, V., Marchi, P., Di Pardo, A., Lingrell, S., Horkey, M., Tidmarsh, E. and Sipione, S. 2010. Impaired ganglioside metabolism in Huntington's disease and neuroprotective role of GM1. *J Neurosci* 30(11), pp. 4072-4080. doi: 10.1523/JNEUROSCI.6348-09.2010

Mahadik, S. P., Hungund, B. L., Gokhale, V. S., Ortiz, A., Makar, T. K. and Karpiak, S. E. 1993. Monosialoganglioside (GM1) restores membrane fatty acid levels in ischemic tissue after cortical focal ischemia in rat. *Neurochemistry international* 23(2), pp. 163-172.

Mahadik, S. P., Vilim, F., Korenovsky, A. and Karpiak, S. E. 1988. GM1 ganglioside protects nucleus basalis from excitotoxin damage: reduced cortical cholinergic losses and animal mortality. *Journal of neuroscience research* 20(4), pp. 479-483.

Malankhanova, T. et al. 2020. A human induced pluripotent stem cell-derived isogenic model of Huntington's disease based on neuronal cells has several relevant phenotypic abnormalities. *Journal of personalized medicine* 10(4), p. 215.

Malik, B. R., Maddison, D. C., Smith, G. A. and Peters, O. M. 2019. Autophagic and endo-lysosomal dysfunction in neurodegenerative disease. *Molecular brain* 12(1), pp. 1-21.

Malik, V., Rodino-Klapac, L. R., Viollet, L. and Mendell, J. R. 2010. Aminoglycoside-induced mutation suppression (stop codon readthrough) as a therapeutic strategy for Duchenne muscular dystrophy. *Therapeutic advances in neurological disorders* 3(6), pp. 379-389.

Malla, B., Guo, X., Senger, G., Chasapopoulou, Z. and Yildirim, F. 2021. A Systematic Review of Transcriptional Dysregulation in Huntington's Disease Studied by RNA Sequencing. *Frontiers in genetics*, p. 1898.

Mamelak, M. 2017. Energy and the Alzheimer brain. *Neuroscience & Biobehavioral Reviews* 75, pp. 297-313.

Manczak, M. and Reddy, P. H. 2015. Mitochondrial division inhibitor 1 protects against mutant huntingtin-induced abnormal mitochondrial dynamics and neuronal damage in Huntington's disease. *Human molecular genetics* 24(25), pp. 7308-7325.

Manders, E. M. M., Verbeek, F. J. and Aten, J. A. 1993. Measurement of co-localization of objects in dual-colour confocal images. *Journal of microscopy* 169(3), pp. 375-382.

Marcora, E., Gowan, K. and Lee, J. E. 2003. Stimulation of NeuroD activity by huntingtin and huntingtin-associated proteins HAP1 and MLK2. *Proceedings of the National Academy of Sciences* 100(16), pp. 9578-9583.

Marofi, F., Vahedi, G., Solali, S., Alivand, M., Salarinasab, S., Zadi Heydarabad, M. and Farshdousti Hagh, M. 2019. Gene expression of TWIST1 and ZBTB16 is regulated by methylation modifications during the osteoblastic differentiation of mesenchymal stem cells. *Journal of cellular physiology* 234(5), pp. 6230-6243.

Marques, A. R. A. et al. 2015. Reducing GBA2 activity ameliorates neuropathology in Niemann-Pick type C mice. *PLOS one* 10(8), p. e0135889.

Martín-Flores, N. et al. 2016. RTP801 is involved in mutant huntingtin-induced cell death. *Molecular Neurobiology* 53(5), pp. 2857-2868.

Martin, D. D., Heit, R. J., Yap, M. C., Davidson, M. W., Hayden, M. R. and Berthiaume, L. G. 2014. Identification of a post-translationally myristoylated autophagy-inducing domain released by caspase cleavage of huntingtin. *Human molecular genetics* 23(12), pp. 3166-3179.

Martin, D. D., Ladha, S., Ehrnhoefer, D. E. and Hayden, M. R. 2015a. Autophagy in Huntington disease and huntingtin in autophagy. *Trends Neurosci* 38(1), pp. 26-35. doi: 10.1016/j.tins.2014.09.003

Martin, D. D. O., Ladha, S., Ehrnhoefer, D. E. and Hayden, M. R. 2015b. Autophagy in Huntington disease and huntingtin in autophagy. *Trends in neurosciences* 38(1), pp. 26-35.

Martin, W. F., Garg, S. and Zimorski, V. 2015c. Endosymbiotic theories for eukaryote origin. *Philosophical Transactions of the Royal Society B: Biological Sciences* 370(1678), p. 20140330.

Martina, J. A., Raben, N. and Puertollano, R. 2020. SnapShot: lysosomal storage diseases. *Cell* 180(3), pp. 602-602.

Martinez-Vicente, M. et al. 2010. Cargo recognition failure is responsible for inefficient autophagy in Huntington's disease. *Nature neuroscience* 13(5), pp. 567-576.

Marullo, M. et al. 2012. Pitfalls in the detection of cholesterol in Huntington's disease models. *PLoS Curr* 4, p. e505886e505889a501968. doi: 10.1371/505886e9a1968

Mason, R. P. et al. 2013. Glutathione peroxidase activity is neuroprotective in models of Huntington's disease. *Nature genetics* 45(10), pp. 1249-1254.

Matos, C. R. R., Lopes, R. S. C. and Lopes, C. C. 1999. Synthesis of 1-deoxynojirimycin and N-butyl-1-deoxynojirimycin. *Synthesis* 1999(04), pp. 571-573.

Mauri, V., Lotfi, P., Segatori, L. and Sardiello, M. 2013. A rapid and sensitive method for measuring N-acetylglucosaminidase activity in cultured cells. *PLOS one* 8(6), p. e68060.

Mayes, J. S., Scheerer, J. B., Sifers, R. N. and Donaldson, M. L. 1981. Differential assay for lysosomal alpha-galactosidases in human tissues and its application to Fabry's disease. *Clinica Chimica Acta* 112(2), pp. 247-251.

Mayran, N., Parton, R. G. and Gruenberg, J. 2003. Annexin II regulates multivesicular endosome biogenesis in the degradation pathway of animal cells. *The EMBO journal* 22(13), pp. 3242-3253.

Medina, D. L. et al. 2015. Lysosomal calcium signalling regulates autophagy through calcineurin and TFEB. *Nature cell biology* 17(3), pp. 288-299.

Mengel, E. et al. 2021. Efficacy and safety of arimoclomol in Niemann-Pick disease type C: Results from a double-blind, randomised, placebo-controlled, multinational phase 2/3 trial of a novel treatment. *Journal of inherited metabolic disease* 44(6), pp. 1463-1480.

Merrill Jr, A. H. and Sandhoff, K. 2002. Sphingolipids: Metabolism and cell signaling.*New comprehensive biochemistry*. Vol. 36. Elsevier, pp. 373-407.

Merscher, S. and Fornoni, A. 2014. Podocyte pathology and nephropathy–sphingolipids in glomerular diseases. *Frontiers in endocrinology* 5, p. 127.

Miller, B. R., Walker, A. G., Shah, A. S., Barton, S. J. and Rebec, G. V. 2008. Dysregulated information processing by medium spiny neurons in striatum of freely behaving mouse models of Huntington's disease. *Journal of neurophysiology* 100(4), pp. 2205-2216.

Miller, J. D. et al. 2013. Human iPSC-based modeling of late-onset disease via progerin-induced aging. *Cell stem cell* 13(6), pp. 691-705.

Miller, J. R. et al. 2016. RNA-Seq of Huntington’s disease patient myeloid cells reveals innate transcriptional dysregulation associated with proinflammatory pathway activation. *Human molecular genetics* 25(14), pp. 2893-2904.

Mills, I. G., Gaughan, L., Robson, C., Ross, T., McCracken, S., Kelly, J. and Neal, D. E. 2005. Huntingtin interacting protein 1 modulates the transcriptional activity of nuclear hormone receptors. *The Journal of Cell Biology* 170(2), pp. 191-200.

Mishima, Y. et al. 2021. Contribution of Glucosylceramide Synthase to the Proliferation of Mouse Osteoblasts. *in vivo* 35(6), pp. 3111-3123.

Mitsche, M. A., McDonald, J. G., Hobbs, H. H. and Cohen, J. C. 2015. Flux analysis of cholesterol biosynthesis in vivo reveals multiple tissue and cell-type specific pathways. *Elife* 4, p. e07999.

Miyagawa, K., Oe, S., Honma, Y., Izumi, H., Baba, R. and Harada, M. 2016. Lipid-induced endoplasmic reticulum stress impairs selective autophagy at the step of autophagosome-lysosome fusion in hepatocytes. *The American journal of pathology* 186(7), pp. 1861-1873.

Mizushima, N., Levine, B., Cuervo, A. M. and Klionsky, D. J. 2008. Autophagy fights disease through cellular self-digestion. *Nature* 451(7182), pp. 1069-1075.

Moheimani, F., Kim, C. H. J., Rahmanto, A. S., van Reyk, D. M. and Davies, M. J. 2012. Inhibition of lysosomal function in macrophages incubated with elevated glucose concentrations: a potential contributory factor in diabetes-associated atherosclerosis. *Atherosclerosis* 223(1), pp. 144-151.

Mollica, P. A. et al. 2018. Epigenetic alterations mediate iPSC-induced normalization of DNA repair gene expression and TNR stability in Huntington's disease cells. *Journal of cell science* 131(13), p. jcs215343.

Monk, R. and Connor, B. 2021. Cell Reprogramming to Model Huntington's Disease: A Comprehensive Review. *Cells* 10(7), p. 1565.

Morales, A., Colell, A., Mari, M., Garcia-Ruiz, C. and Fernandez-Checa, J. C. 2003. Glycosphingolipids and mitochondria: role in apoptosis and disease. *Glycoconjugate journal* 20(9), pp. 579-588.

Moreno-García, A., Kun, A., Calero, O., Medina, M. and Calero, M. 2018. An overview of the role of lipofuscin in age-related neurodegeneration. *Frontiers in neuroscience* 12, p. 464.

Morfini, G. A. et al. 2009. Pathogenic huntingtin inhibits fast axonal transport by activating JNK3 and phosphorylating kinesin. *Nature neuroscience* 12(7), pp. 864-871.

Morozko, E. L. et al. 2021. PIAS1 modulates striatal transcription, DNA damage repair, and SUMOylation with relevance to Huntington's disease. *Proceedings of the National Academy of Sciences* 118(4),

Morozova, K. N., Suldina, L. A., Malankhanova, T. B., Grigor'eva, E. V., Zakian, S. M., Kiseleva, E. and Malakhova, A. A. 2018. Introducing an expanded CAG tract into the huntingtin gene causes a wide spectrum of ultrastructural defects in cultured human cells. *PLOS one* 13(10), p. e0204735.

Mutka, A.-L., Lusa, S., Linder, M. D., Jokitalo, E., Kopra, O., Jauhiainen, M. and Ikonen, E. 2004. Secretion of sterols and the NPC2 protein from primary astrocytes. *Journal of Biological Chemistry* 279(47), pp. 48654-48662.

Myers, R. H. 2004. Huntington's disease genetics. *NeuroRx* 1(2), pp. 255-262.

Nagata, E., Sawa, A., Ross, C. A. and Snyder, S. H. 2004. Autophagosome-like vacuole formation in Huntington's disease lymphoblasts. *Neuroreport* 15(8), pp. 1325-1328.

Narain, Y., Wyttenbach, A., Rankin, J., Furlong, R. A. and Rubinsztein, D. C. 1999. A molecular investigation of true dominance in Huntington's disease. *Journal of Medical Genetics* 36(10), pp. 739-746.

Narita, K. et al. 2005. Protein transduction of Rab9 in Niemann-Pick C cells reduces cholesterol storage. *The FASEB journal* 19(11), pp. 1558-1560.

Nasir, J. et al. 1995a. Targeted disruption of the Huntington's disease gene results in embryonic lethality and behavioral and morphological changes in heterozygotes. *Cell* 81(5), pp. 811-823. doi: 10.1016/0092-8674(95)90542-1

Nasir, J. et al. 1995b. Targeted disruption of the Huntington's disease gene results in embryonic lethality and behavioral and morphological changes in heterozygotes. *Cell* 81(5), pp. 811-823.

Naureckiene, S. et al. 2000. Identification of HE1 as the second gene of Niemann-Pick C disease. *Science* 290(5500), pp. 2298-2301.

Neises, G. R., Woodman, P. G., Butters, T. D., Ornberg, R. L. and Platt, F. M. 1997. Ultrastructural changes in the Golgi apparatus and secretory granules of HL-60 cells treated with the imino sugar N-butyldeoxynojirimycin. *Biology of the Cell* 89(2), pp. 123-131.

Nekrasov, E. D. and Kiselev, S. L. 2018. Mitochondrial distribution violation and nuclear indentations in neurons differentiated from iPSCs of Huntington's disease patients. *Journal of Stem Cells & Regenerative Medicine* 14(2), p. 80.

Nekrasov, E. D. et al. 2016. Manifestation of Huntington's disease pathology in human induced pluripotent stem cell-derived neurons. *Molecular neurodegeneration* 11(1), pp. 1-15.

Neueder, A. et al. 2017. The pathogenic exon 1 HTT protein is produced by incomplete splicing in Huntington's disease patients. *Scientific reports* 7(1), pp. 1-10.

Neufeld, E. B. et al. 1999. The Niemann-Pick C1 protein resides in a vesicular compartment linked to retrograde transport of multiple lysosomal cargo. *Journal of Biological Chemistry* 274(14), pp. 9627-9635.

Ng, C. W. et al. 2013. Extensive changes in DNA methylation are associated with expression of mutant huntingtin. *Proceedings of the National Academy of Sciences* 110(6), pp. 2354-2359.

Ni, Q., Su, X., Chen, J. and Tian, W. 2015. Prediction of metabolic gene biomarkers for neurodegenerative disease by an integrated network-based approach. *BioMed research international* 2015,

Nietupski, J. B. et al. 2012. Iminosugar-based inhibitors of glucosylceramide synthase prolong survival but paradoxically increase brain glucosylceramide levels in Niemann–Pick C mice. *Molecular genetics and metabolism* 105(4), pp. 621-628.

Nixon, R. A. and Yang, D.-S. 2012. Autophagy and neuronal cell death in neurological disorders. *Cold Spring Harbor perspectives in biology* 4(10), p. a008839.

Novikoff, A. B., Beaufay, H. and de Duve, C. 1956. Electron microscopy of lysosome-rich fractions from rat liver. *The Journal of Cell Biology* 2(4), pp. 179-184.

Nowakowski, R. W., Thompson, J. N. and Baker, H. J. 1988. Diagnosis of feline GM1 gangliosidosis by enzyme assay of cultured conjunctival cells. *Investigative ophthalmology & visual science* 29(3), pp. 487-490.

Nowroozi, N., Kawata, T., Liu, P., Rice, D. and Zernik, J. H. 2001. High β-galactosidase and ganglioside GM1 levels in the human parotid gland. *Archives of Otolaryngology–Head & Neck Surgery* 127(11), pp. 1381-1384.

O'Kusky, J. R., Nasir, J., Cicchetti, F., Parent, A. and Hayden, M. R. 1999. Neuronal degeneration in the basal ganglia and loss of pallido-subthalamic synapses in mice with targeted disruption of the Huntington's disease gene. *Brain research* 818(2), pp. 468-479.

Ochaba, J. et al. 2014. Potential function for the Huntingtin protein as a scaffold for selective autophagy. *Proceedings of the National Academy of Sciences* 111(47), pp. 16889-16894.

Ohgane, K., Karaki, F., Dodo, K. and Hashimoto, Y. 2013. Discovery of oxysterol-derived pharmacological chaperones for NPC1: implication for the existence of second sterol-binding site. *Chemistry & biology* 20(3), pp. 391-402.

Okamura, N. et al. 1999. A porcine homolog of the major secretory protein of human epididymis, HE1, specifically binds cholesterol. *Biochimica et Biophysica Acta (BBA)-Molecular and Cell Biology of Lipids* 1438(3), pp. 377-387.

Olivova, P. et al. 2009. Effect of sample collection on α-galactosidase A enzyme activity measurements in dried blood spots on filter paper. *Clinica Chimica Acta* 403(1-2), pp. 159-162.

Ooi, J. et al. 2019a. Unbiased profiling of isogenic Huntington disease hPSC-derived CNS and peripheral cells reveals strong cell-type specificity of CAG length effects. *Cell reports* 26(9), pp. 2494-2508.

Ooi, J. et al. 2019b. Unbiased profiling of isogenic Huntington disease hPSC-derived CNS and peripheral cells reveals strong cell-type specificity of CAG length effects. *Cell Reports* 26(9), pp. 2494-2508. e2497.

Ordonez, M. P., Roberts, E. A., Kidwell, C. U., Yuan, S. H., Plaisted, W. C. and Goldstein, L. S. B. 2012. Disruption and therapeutic rescue of autophagy in a human neuronal model of Niemann Pick type C1. *Human molecular genetics* 21(12), pp. 2651-2662.

Ory, D. S. et al. 2017. Intrathecal 2-hydroxypropyl-β-cyclodextrin decreases neurological disease progression in Niemann-Pick disease, type C1: a non-randomised, open-label, phase 1–2 trial. *The Lancet* 390(10104), pp. 1758-1768.

Pacheco, C. D., Kunkel, R. and Lieberman, A. P. 2007. Autophagy in Niemann–Pick C disease is dependent upon Beclin-1 and responsive to lipid trafficking defects. *Human molecular genetics* 16(12), pp. 1495-1503.

Pacheco, C. D. and Lieberman, A. P. 2008. The pathogenesis of Niemann–Pick type C disease: a role for autophagy? *Expert reviews in molecular medicine* 10,

Pagano, R. E. 2003. Endocytic trafficking of glycosphingolipids in sphingolipid storage diseases. *Philosophical Transactions of the Royal Society of London. Series B: Biological Sciences* 358(1433), pp. 885-891.

Pal, A., Severin, F., Lommer, B., Shevchenko, A. and Zerial, M. 2006. Huntingtin–HAP40 complex is a novel Rab5 effector that regulates early endosome motility and is up-regulated in Huntington's disease. *Journal of Cell Biology* 172(4), pp. 605-618.

Palidwor, G. A. et al. 2009. Detection of alpha-rod protein repeats using a neural network and application to huntingtin. *PLoS computational biology* 5(3), p. e1000304.

Panov, A. V., Gutekunst, C.-A., Leavitt, B. R., Hayden, M. R., Burke, J. R., Strittmatter, W. J. and Greenamyre, J. T. 2002. Early mitochondrial calcium defects in Huntington's disease are a direct effect of polyglutamines. *Nature neuroscience* 5(8), pp. 731-736.

Pantiya, P., Thonusin, C., Chattipakorn, N. and Chattipakorn, S. C. 2020. Mitochondrial abnormalities in neurodegenerative models and possible interventions: Focus on Alzheimer’s disease, Parkinson’s disease, Huntington’s disease. *Mitochondrion* 55, pp. 14-47.

Parenti, G., Medina, D. L. and Ballabio, A. 2021. The rapidly evolving view of lysosomal storage diseases. *EMBO molecular medicine* 13(2), p. e12836.

Parker, J. A., Connolly, J. B., Wellington, C., Hayden, M., Dausset, J. and Neri, C. 2001. Expanded polyglutamines in Caenorhabditis elegans cause axonal abnormalities and severe dysfunction of PLM mechanosensory neurons without cell death. *Proceedings of the National Academy of Sciences* 98(23), pp. 13318-13323.

Paşca, A. M. et al. 2015. Functional cortical neurons and astrocytes from human pluripotent stem cells in 3D culture. *Nature methods* 12(7), pp. 671-678.

Patterson, M. C. 2001. Niemann-Pick disease type C: a lipid trafficking disorder. *The metabolic and molecular bases of inherited disease*, pp. 3611-3634.

Patterson, M. C. et al. 2020a. Long-term survival outcomes of patients with Niemann-Pick disease type C receiving miglustat treatment: A large retrospective observational study. *Journal of inherited metabolic disease* 43(5), pp. 1060-1069.

Patterson, M. C., Mengel, E., Vanier, M. T., Moneuse, P., Rosenberg, D. and Pineda, M. 2020b. Treatment outcomes following continuous miglustat therapy in patients with Niemann-Pick disease Type C: a final report of the NPC Registry. *Orphanet journal of rare diseases* 15(1), pp. 1-10.

Patterson, M. C., Vecchio, D., Prady, H., Abel, L. and Wraith, J. E. 2007. Miglustat for treatment of Niemann-Pick C disease: a randomised controlled study. *The Lancet Neurology* 6(9), pp. 765-772.

Penney Jr, J. B., Vonsattel, J. P., Macdonald, M. E., Gusella, J. F. and Myers, R. H. 1997. CAG repeat number governs the development rate of pathology in Huntington's disease. *Annals of Neurology: Official Journal of the American Neurological Association and the Child Neurology Society* 41(5), pp. 689-692.

Pentchev, P. G., Blanchette-Mackie, E. J. and Dawidowicz, E. A. 1994. The NP-C gene: a key to pathways of intracellular cholesterol transport. *Trends in cell biology* 4(10), pp. 365-369.

Pentchev, P. G., Comly, M. E., Kruth, H. S., Vanier, M. T., Wenger, D. A., Patel, S. and Brady, R. O. 1985. A defect in cholesterol esterification in Niemann-Pick disease (type C) patients. *Proc Natl Acad Sci U S A* 82(23), pp. 8247-8251. doi: 10.1073/pnas.82.23.8247

Perera, R. M. and Zoncu, R. 2016. The lysosome as a regulatory hub. *Annual review of cell and developmental biology* 32, pp. 223-253.

Petrov, A. M., Kasimov, M. R. and Zefirov, A. L. 2016. Brain cholesterol metabolism and its defects: linkage to neurodegenerative diseases and synaptic dysfunction. *Acta Naturae (англоязычная версия)* 8(1 (28)),

Phillips, G. R., Hancock, S. E., Brown, S. H. J., Jenner, A. M., Kreilaus, F., Newell, K. A. and Mitchell, T. W. 2020. Cholesteryl ester levels are elevated in the caudate and putamen of Huntington's disease patients. *Scientific reports* 10(1), pp. 1-11.

Phillips, G. R. et al. 2021. The long and the short of Huntington's disease: how the sphingolipid profile is shiftevad in the caudate of advanced clinical cases. *Brain communications*,

Piccinini, M. et al. 2010. Deregulated sphingolipid metabolism and membrane organization in neurodegenerative disorders. *Molecular Neurobiology* 41(2), pp. 314-340.

Pineda, M. et al. 2009. Miglustat in patients with Niemann-Pick disease Type C (NP-C): a multicenter observational retrospective cohort study. *Molecular genetics and metabolism* 98(3), pp. 243-249.

Pipalia, N. H., Hao, M., Mukherjee, S. and Maxfield, F. R. 2007. Sterol, protein and lipid trafficking in Chinese hamster ovary cells with Niemann-Pick type C1 defect. *Traffic* 8(2), pp. 130-141.

Pircs, K. et al. 2021. Distinct subcellular autophagy impairments in induced neurons from Huntington's disease patients. *Brain*,

Platt, F. M., Boland, B. and van der Spoel, A. C. 2012. Lysosomal storage disorders: The cellular impact of lysosomal dysfunction. *Journal of Cell Biology* 199(5), pp. 723-734.

Platt, F. M., d'Azzo, A., Davidson, B. L., Neufeld, E. F. and Tifft, C. J. 2018. Lysosomal storage diseases. *Nature reviews Disease primers* 4(1), pp. 1-25.

Platt, F. M. et al. 2001. Inhibition of substrate synthesis as a strategy for glycolipid lysosomal storage disease therapy. *Journal of inherited metabolic disease* 24(2), pp. 275-290.

Platt, F. M., Neises, G. R., Dwek, R. A. and Butters, T. D. 1994. N-butyldeoxynojirimycin is a novel inhibitor of glycolipid biosynthesis. *Journal of Biological Chemistry* 269(11), pp. 8362-8365.

Platt, F. M. and Walkley, S. U. 2005. Lysosomal disorders of the brain.

Platt, F. M., Wassif, C., Colaco, A., Dardis, A., Lloyd-Evans, E., Bembi, B. and Porter, F. D. 2014. Disorders of cholesterol metabolism and their unanticipated convergent mechanisms of disease. *Annual review of genomics and human genetics* 15, pp. 173-194.

Plotegher, N. and Duchen, M. R. 2017. Mitochondrial dysfunction and neurodegeneration in lysosomal storage disorders. *Trends in molecular medicine* 23(2), pp. 116-134.

Podvin, S., Reardon, H. T., Yin, K., Mosier, C. and Hook, V. 2019. Multiple clinical features of Huntington's disease correlate with mutant HTT gene CAG repeat lengths and neurodegeneration. *Journal of neurology* 266(3), pp. 551-564.

Poirier, S., Mayer, G., Murphy, S. R., Garver, W. S., Chang, T. Y., Schu, P. and Seidah, N. G. 2013. The cytosolic adaptor AP-1A is essential for the trafficking and function of Niemann-Pick type C proteins. *Traffic* 14(4), pp. 458-469.

Prabhu, A. V. et al. 2021. A human iPSC-derived inducible neuronal model of Niemann-Pick disease, type C1. *BMC biology* 19(1), pp. 1-12.

Preisinger, E., Jordan, B. M., Kazantsev, A. and Housman, D. 1999. Evidence for a recruitment and sequestration mechanism in Huntington'sdisease. *Philosophical Transactions of the Royal Society of London. Series B: Biological Sciences* 354(1386), pp. 1029-1034.

Prence, E. M. and Natowicz, M. R. 1992. Diagnosis of α-mannosidosis by measuring α-mannosidase in plasma. *Clinical chemistry* 38(4), pp. 501-503.

Prinetti, A., Loberto, N., Chigorno, V. and Sonnino, S. 2009. Glycosphingolipid behaviour in complex membranes. *Biochimica et Biophysica Acta (BBA)-Biomembranes* 1788(1), pp. 184-193.

Pringsheim, T., Wiltshire, K., Day, L., Dykeman, J., Steeves, T. and Jette, N. 2012. The incidence and prevalence of Huntington's disease: a systematic review and meta-analysis. *Mov Disord* 27(9), pp. 1083-1091. doi: 10.1002/mds.25075

Qi, L., Zhang, X.-D., Wu, J.-C., Lin, F., Wang, J., DiFiglia, M. and Qin, Z.-H. 2012. The role of chaperone-mediated autophagy in huntingtin degradation.

Qian, X. et al. 2020. Sliced human cortical organoids for modeling distinct cortical layer formation. *Cell stem cell* 26(5), pp. 766-781.

Qin, Z.-H. et al. 2003. Autophagy regulates the processing of amino terminal huntingtin fragments. *Human molecular genetics* 12(24), pp. 3231-3244.

Rangone, H., Humbert, S. and Saudou, F. 2004. Huntington's disease: how does huntingtin, an anti-apoptotic protein, become toxic? *Pathologie Biologie* 52(6), pp. 338-342.

Ravikumar, B. et al. 2005. Dynein mutations impair autophagic clearance of aggregate-prone proteins. *Nature genetics* 37(7), pp. 771-776.

Ravikumar, B., Duden, R. and Rubinsztein, D. C. 2002. Aggregate-prone proteins with polyglutamine and polyalanine expansions are degraded by autophagy. *Human molecular genetics* 11(9), pp. 1107-1117.

Ravikumar, B. et al. 2004. Inhibition of mTOR induces autophagy and reduces toxicity of polyglutamine expansions in fly and mouse models of Huntington disease. *Nat Genet* 36(6), pp. 585-595. doi: 10.1038/ng1362

Rawlins, M. D., Wexler, N. S., Wexler, A. R., Tabrizi, S. J., Douglas, I., Evans, S. J. W. and Smeeth, L. 2016. The prevalence of Huntington's disease. *Neuroepidemiology* 46(2), pp. 144-153.

Reagan, J. W., Hubbert, M. L. and Shelness, G. S. 2000. Posttranslational regulation of acid sphingomyelinase in niemann-pick type C1 fibroblasts and free cholesterol-enriched chinese hamster ovary cells. *Journal of Biological Chemistry* 275(48), pp. 38104-38110.

Reddy, A., Caler, E. V. and Andrews, N. W. 2001. Plasma membrane repair is mediated by Ca2+-regulated exocytosis of lysosomes. *Cell* 106(2), pp. 157-169.

Reddy, P. H. and Shirendeb, U. P. 2012. Mutant huntingtin, abnormal mitochondrial dynamics, defective axonal transport of mitochondria, and selective synaptic degeneration in Huntington's disease. *Biochimica et Biophysica Acta (BBA)-Molecular Basis of Disease* 1822(2), pp. 101-110.

Reiner, A., Albin, R. L., Anderson, K. D., D'Amato, C. J., Penney, J. B. and Young, A. B. 1988. Differential loss of striatal projection neurons in Huntington disease. *Proceedings of the National Academy of Sciences* 85(15), pp. 5733-5737.

Ridley, C. M. et al. 2013. β-Glucosidase 2 (GBA2) activity and imino sugar pharmacology. *Journal of Biological Chemistry* 288(36), pp. 26052-26066.

Rigamonti, D. et al. 2000. Wild-type huntingtin protects from apoptosis upstream of caspase-3. *Journal of Neuroscience* 20(10), pp. 3705-3713.

Ring, K. L. et al. 2015. Genomic analysis reveals disruption of striatal neuronal development and therapeutic targets in human Huntington's disease neural stem cells. *Stem cell reports* 5(6), pp. 1023-1038.

Ritch, J. J. et al. 2012. Multiple phenotypes in Huntington disease mouse neural stem cells. *Molecular and Cellular Neuroscience* 50(1), pp. 70-81.

Robert K, Y., Tsai, Y.-T., Ariga, T. and Yanagisawa, M. 2011. Structures, biosynthesis, and functions of gangliosides-an overview. *Journal of oleo science* 60(10), pp. 537-544.

Rockabrand, E. et al. 2007. The first 17 amino acids of Huntingtin modulate its sub-cellular localization, aggregation and effects on calcium homeostasis. *Human molecular genetics* 16(1), pp. 61-77.

Rodriguez-Lafrasse, C., Rousson, R., Pentchev, P. G., Louisot, P. and Vanier, M. T. 1994. Free sphingoid bases in tissues from patients with type C Niemann-Pick disease and other lysosomal storage disorders. *Biochimica et Biophysica Acta (BBA)-Molecular Basis of Disease* 1226(2), pp. 138-144.

Roff, C. F. et al. 1991. Type C Niemann-Pick disease: use of hydrophobic amines to study defective cholesterol transport. *Developmental neuroscience* 13(4-5), pp. 315-319.

Roney, J. C. et al. 2021. Lipid-mediated impairment of axonal lysosome transport contributing to autophagic stress. *Autophagy* (just-accepted), pp. 1-3. doi: 10.1080/15548627.2021.1938916

Roos, R. A. C. 2010. Huntington's disease: a clinical review. *Orphanet journal of rare diseases* 5(1), pp. 1-8.

Ross, C. A. 2002. Polyglutamine pathogenesis: emergence of unifying mechanisms for Huntington's disease and related disorders. *Neuron* 35(5), pp. 819-822.

Ross, C. A. and Tabrizi, S. J. 2011. Huntington's disease: from molecular pathogenesis to clinical treatment. *The Lancet Neurology* 10(1), pp. 83-98.

Rouser, G., Kritchevsky, G., Knudson, A. G. and Simon, G. 1968. Accumulation of a glycerolphospholipid in classical Niemann-Pick disease. *Lipids* 3(3), pp. 287-290.

Rubinstein, D. C. 2003. Molecular biology of Huntingtons Disease (HD) and HD-like disorders. Pulst S, ed. *Genetics of movement disorders. Academic Press*, pp. 365-377.

Rubinsztein, D. C. 2006. The roles of intracellular protein-degradation pathways in neurodegeneration. *Nature* 443(7113), pp. 780-786.

Rubinsztein, D. C. et al. 1996. Phenotypic characterization of individuals with 30–40 CAG repeats in the Huntington disease (HD) gene reveals HD cases with 36 repeats and apparently normal elderly individuals with 36–39 repeats. *American journal of human genetics* 59(1), p. 16.

Rui, Y.-N. et al. 2015a. Huntingtin functions as a scaffold for selective macroautophagy. *Nature cell biology* 17(3), pp. 262-275.

Rui, Y.-N., Xu, Z., Patel, B., Cuervo, A. M. and Zhang, S. 2015b. HTT/Huntingtin in selective autophagy and Huntington disease: A foe or a friend within? *Autophagy* 11(5), pp. 858-860.

Ruzo, A. et al. 2018. Chromosomal instability during neurogenesis in Huntington's disease. *Development* 145(2), p. dev156844.

Saftig, P. and Klumperman, J. 2009. Lysosome biogenesis and lysosomal membrane proteins: trafficking meets function. *Nature reviews Molecular cell biology* 10(9), pp. 623-635.

Samara, A., Galbiati, M., Luciani, P., Deledda, C., Messi, E., Peri, A. and Maggi, R. 2014. Altered expression of 3-betahydroxysterol delta-24-reductase/selective Alzheimer's disease indicator-1 gene in Huntington's disease models. *Journal of endocrinological investigation* 37(8), pp. 729-737.

Sambri, I. et al. 2017. Lysosomal dysfunction disrupts presynaptic maintenance and restoration of presynaptic function prevents neurodegeneration in lysosomal storage diseases. *EMBO molecular medicine* 9(1), pp. 112-132.

Sameni, S., Malacrida, L., Tan, Z. and Digman, M. A. 2018. Alteration in fluidity of cell plasma membrane in huntington disease revealed by spectral phasor analysis. *Scientific reports* 8(1), pp. 1-10.

Sanchez, I., Mahlke, C. and Yuan, J. 2003. Pivotal role of oligomerization in expanded polyglutamine neurodegenerative disorders. *Nature* 421(6921), pp. 373-379. doi: 10.1038/nature01301

Sandhoff, R. and Sandhoff, K. 2018a. Emerging concepts of ganglioside metabolism. *FEBS letters* 592(23), pp. 3835-3864.

Sandhoff, R. and Sandhoff, K. 2018b. Emerging concepts of ganglioside metabolism. *FEBS Lett* 592(23), pp. 3835-3864. doi: 10.1002/1873-3468.13114

Sapp, E. et al. 2001. Early and progressive accumulation of reactive microglia in the Huntington disease brain. *Journal of Neuropathology & Experimental Neurology* 60(2), pp. 161-172.

Sapp, E. et al. 1997. Huntingtin localization in brains of normal and Huntington's disease patients. *Annals of Neurology: Official Journal of the American Neurological Association and the Child Neurology Society* 42(4), pp. 604-612.

Sarkar, S. et al. 2013. Impaired autophagy in the lipid-storage disorder Niemann-Pick type C1 disease. *Cell Reports* 5(5), pp. 1302-1315.

Sarkar, S. and Rubinsztein, D. C. 2008. Huntington's disease: degradation of mutant huntingtin by autophagy. *The FEBS journal* 275(17), pp. 4263-4270.

Sathasivam, K. et al. 2013a. Aberrant splicing of HTT generates the pathogenic exon 1 protein in Huntington disease. *Proc Natl Acad Sci U S A* 110(6), pp. 2366-2370. doi: 10.1073/pnas.1221891110

Sathasivam, K. et al. 2013b. Aberrant splicing of HTT generates the pathogenic exon 1 protein in Huntington disease. *Proceedings of the National Academy of Sciences* 110(6), pp. 2366-2370.

Saudou, F., Finkbeiner, S., Devys, D. and Greenberg, M. E. 1998. Huntingtin acts in the nucleus to induce apoptosis but death does not correlate with the formation of intranuclear inclusions. *Cell* 95(1), pp. 55-66.

Saudou, F. and Humbert, S. 2016. The Biology of Huntingtin. *Neuron* 89(5), pp. 910-926. doi: 10.1016/j.neuron.2016.02.003

Sawkar, A. R., Cheng, W.-C., Beutler, E., Wong, C.-H., Balch, W. E. and Kelly, J. W. 2002. Chemical chaperones increase the cellular activity of N370S β-glucosidase: a therapeutic strategy for Gaucher disease. *Proceedings of the National Academy of Sciences* 99(24), pp. 15428-15433.

Schneider, J. S. 2014. Gangliosides and glycolipids in neurodegenerative disorders.*Glycobiology of the Nervous System*. Springer, pp. 449-461.

Schöndorf, D. C. et al. 2018. The NAD+ precursor nicotinamide riboside rescues mitochondrial defects and neuronal loss in iPSC and fly models of Parkinson's disease. *Cell Reports* 23(10), pp. 2976-2988.

Schroeder, R., London, E. and Brown, D. 1994. Interactions between saturated acyl chains confer detergent resistance on lipids and glycosylphosphatidylinositol (GPI)-anchored proteins: GPI-anchored proteins in liposomes and cells show similar behavior. *Proceedings of the National Academy of Sciences* 91(25), pp. 12130-12134.

Schubert, M., Turk, R., Jacobi, A., Speicher, N., Barr, J. and Behlke, M. 2017. Fluorescently labeled tracrRNA provides efficient genome editing while allowing cellular microscopy and FACS analysis. *Genome Editing*, pp. 1-3.

Schultz, M. L. et al. 2018. Coordinate regulation of mutant NPC1 degradation by selective ER autophagy and MARCH6-dependent ERAD. *Nature communications* 9(1), pp. 1-13.

Schulze, H. and Sandhoff, K. 2011. Lysosomal lipid storage diseases. *Cold Spring Harbor perspectives in biology* 3(6), p. a004804.

Schwake, M., Schröder, B. and Saftig, P. 2013. Lysosomal membrane proteins and their central role in physiology. *Traffic* 14(7), pp. 739-748.

Schwartzentruber, J. et al. 2018. Molecular and functional variation in iPSC-derived sensory neurons. *Nature Genetics* 50(1), pp. 54-61. doi: 10.1038/s41588-017-0005-8

Schwarz, A. and Futerman, A. H. 1997. Distinct roles for ceramide and glucosylceramide at different stages of neuronal growth. *Journal of Neuroscience* 17(9), pp. 2929-2938.

Schwarz, A. and Futerman, A. H. 1998. Inhibition of sphingolipid synthesis, but not degradation, alters the rate of dendrite growth in cultured hippocampal neurons. *Developmental brain research* 108(1-2), pp. 125-130.

Schwarz, A., Rapaport, E., Hirschberg, K. and Futerman, A. H. 1995. A regulatory role for sphingolipids in neuronal growth: inhibition of sphingolipid synthesis and degradation have opposite effects on axonal branching. *Journal of Biological Chemistry* 270(18), pp. 10990-10998.

Schweitzer, J. K., Krivda, J. P. and D'Souza-Schorey, C. 2009. Neurodegeneration in Niemann-Pick Type C disease and Huntington's disease: impact of defects in membrane trafficking. *Current drug targets* 10(7), pp. 653-665.

Šeda, O., Šedová, L., Včelák, J., Vaňková, M., Liška, F. and Bendlová, B. 2017. ZBTB16 and metabolic syndrome: a network perspective. *Physiological research* 66, pp. S357-S365.

Seong, I. S. et al. 2005. HD CAG repeat implicates a dominant property of huntingtin in mitochondrial energy metabolism. *Human molecular genetics* 14(19), pp. 2871-2880.

Settembre, C. et al. 2013. TFEB controls cellular lipid metabolism through a starvation-induced autoregulatory loop. *Nature cell biology* 15(6), pp. 647-658.

Settembre, C. et al. 2011a. TFEB links autophagy to lysosomal biogenesis. *Science* 332(6036), pp. 1429-1433.

Settembre, C. et al. 2011b. TFEB links autophagy to lysosomal biogenesis. *Science* 332(6036), pp. 1429-1433. doi: 10.1126/science.1204592

Shacham, T., Sharma, N. and Lederkremer, G. Z. 2019. Protein misfolding and ER stress in Huntington's disease. *Frontiers in molecular biosciences* 6, p. 20.

Shammas, H., Kuech, E.-M., Rizk, S., Das, A. M. and Naim, H. Y. 2019. Different Niemann-Pick C1 genotypes generate protein phenotypes that vary in their intracellular processing, trafficking and localization. *Scientific reports* 9(1), pp. 1-12.

Sharp, A. H. et al. 1995. Widespread expression of Huntington's disease gene (IT15) protein product. *Neuron* 14(5), pp. 1065-1074.

Shenkman, M., Eiger, H. and Lederkremer, G. Z. 2015. Genesis of ER Stress in Huntington's Disease. *Cell Pathology* 2(1), pp. 94-106.

Shirasaki, D. I. et al. 2012. Network organization of the huntingtin proteomic interactome in mammalian brain. *Neuron* 75(1), pp. 41-57.

Shirendeb, U. P. et al. 2012. Mutant huntingtin's interaction with mitochondrial protein Drp1 impairs mitochondrial biogenesis and causes defective axonal transport and synaptic degeneration in Huntington's disease. *Human molecular genetics* 21(2), pp. 406-420.

Siddiqui, H., Yevstigneyev, N., Madani, G. and McCormick, S. 2022. Approaches to Visualising Endocytosis of LDL-Related Lipoproteins. *Biomolecules* 12(2), p. 158.

Simons, K. and Ikonen, E. 1997. Functional rafts in cell membranes. *Nature* 387(6633), pp. 569-572.

Sinadinos, C., Burbidge-King, T., Soh, D., Thompson, L. M., Marsh, J. L., Wyttenbach, A. and Mudher, A. K. 2009. Live axonal transport disruption by mutant huntingtin fragments in Drosophila motor neuron axons. *Neurobiology of disease* 34(2), pp. 389-395.

Singer, E. et al. 2017. Reduced cell size, chromosomal aberration and altered proliferation rates are characteristics and confounding factors in the STHdh cell model of Huntington disease. *Scientific reports* 7(1), pp. 1-13.

Singh, R. et al. 2009. Autophagy regulates lipid metabolism. *Nature* 458(7242), pp. 1131-1135.

Sipione, S. et al. 2002. Early transcriptional profiles in huntingtin-inducible striatal cells by microarray analyses. *Human molecular genetics* 11(17), pp. 1953-1965.

Sitaula, S. and Burris, T. P. 2016. Cholesterol and Other Steroids.

Skaper, S. D., Leon, A. and Facci, L. 1991. Death of cultured hippocampal pyramidal neurons induced by pathological activation of N-methyl-D-aspartate receptors is reduced by monosialogangliosides. *Journal of Pharmacology and Experimental Therapeutics* 259(1), pp. 452-457.

Sleat, D. E. et al. 2004. Genetic evidence for nonredundant functional cooperativity between NPC1 and NPC2 in lipid transport. *Proceedings of the National Academy of Sciences* 101(16), pp. 5886-5891.

Slow, E. J. et al. 2005. Absence of behavioral abnormalities and neurodegeneration in vivo despite widespread neuronal huntingtin inclusions. *Proceedings of the National Academy of Sciences* 102(32), pp. 11402-11407.

Smith-Geater, C. et al. 2020. Aberrant development corrected in adult-onset Huntington's disease iPSC-derived neuronal cultures via WNT signaling modulation. *Stem cell reports* 14(3), pp. 406-419.

Smits, A. H. et al. 2019. Biological plasticity rescues target activity in CRISPR knock outs. *Nature methods* 16(11), pp. 1087-1093.

Soga, M. et al. 2015. HPGCD outperforms HPBCD as a potential treatment for Niemann-Pick disease type C during disease modeling with iPS cells. *Stem Cells* 33(4), pp. 1075-1088.

Solsona-Vilarrasa, E. et al. 2019. Cholesterol enrichment in liver mitochondria impairs oxidative phosphorylation and disrupts the assembly of respiratory supercomplexes. *Redox biology* 24, p. 101214.

Son, J. H., Shim, J. H., Kim, K.-H., Ha, J.-Y. and Han, J. Y. 2012. Neuronal autophagy and neurodegenerative diseases. *Experimental & molecular medicine* 44(2), pp. 89-98.

Song, W. et al. 2011. Mutant huntingtin binds the mitochondrial fission GTPase dynamin-related protein-1 and increases its enzymatic activity. *Nature medicine* 17(3), pp. 377-382.

Spargo, E., Everall, I. P. and Lantos, P. L. 1993. Neuronal loss in the hippocampus in Huntington's disease: a comparison with HIV infection. *Journal of Neurology, Neurosurgery & Psychiatry* 56(5), pp. 487-491.

Stanga, S., Caretto, A., Boido, M. and Vercelli, A. 2020. Mitochondrial dysfunctions: a red thread across neurodegenerative diseases. *International journal of molecular sciences* 21(10), p. 3719.

Steffan, J. S. et al. 2000. The Huntington's disease protein interacts with p53 and CREB-binding protein and represses transcription. *Proceedings of the National Academy of Sciences* 97(12), pp. 6763-6768.

Stein, J. L. et al. 2014. A quantitative framework to evaluate modeling of cortical development by neural stem cells. *Neuron* 83(1), pp. 69-86.

Stoffel, W., Lekim, D. A. C. and Sticht, G. 1968. Metabolism of Sphingosine Bases, VIII. Distribution, Isolation and Properties of D-3-Oxosphinganine Reductase. Stereospecificity of the NADPH-dependent Reduction Reaction of 3-Oxodihydrosphingosine (2-Amino-1-hydroxyoctadecane-3-one).

Stout, J. C. et al. 2011. Neurocognitive signs in prodromal Huntington disease. *Neuropsychology* 25(1), p. 1.

Streeter, I., Harrison, P. W., Faulconbridge, A., HipSci, C., Flicek, P., Parkinson, H. and Clarke, L. 2017. The human-induced pluripotent stem cell initiative—data resources for cellular genetics. *Nucleic acids research* 45(D1), pp. D691-D697.

Strehlow, A. N. T., Li, J. Z. and Myers, R. M. 2007. Wild-type huntingtin participates in protein trafficking between the Golgi and the extracellular space. *Human molecular genetics* 16(4), pp. 391-409.

Sugimoto, Y., Ninomiya, H., Ohsaki, Y., Higaki, K., Davies, J. P., Ioannou, Y. A. and Ohno, K. 2001. Accumulation of cholera toxin and GM1 ganglioside in the early endosome of Niemann–Pick C1-deficient cells. *Proceedings of the National Academy of Sciences* 98(22), pp. 12391-12396.

Sun, A. 2018. Lysosomal storage disease overview. *Annals of translational medicine* 6(24),

Sun, Z. et al. 2019. EGR1 recruits TET1 to shape the brain methylome during development and upon neuronal activity. *Nature communications* 10(1), pp. 1-12.

Sung, E.-A. et al. 2017. Generation of patient specific human neural stem cells from Niemann-Pick disease type C patient-derived fibroblasts. *Oncotarget* 8(49), p. 85428.

Sunwoo, J.-S., Lee, S.-T. and Kim, M. 2010. A case of juvenile huntington disease in a 6-year-old boy. *Journal of movement disorders* 3(2), p. 45.

Suzuki, K. 1987. [61] Enzymatic diagnosis of sphingolipidoses.*Methods in enzymology*. Vol. 138. Elsevier, pp. 727-762.

Suzuki, K. et al. 2014. Targeted gene correction minimally impacts whole-genome mutational load in human-disease-specific induced pluripotent stem cell clones. *Cell stem cell* 15(1), pp. 31-36.

Swami, M., Hendricks, A. E., Gillis, T., Massood, T., Mysore, J., Myers, R. H. and Wheeler, V. C. 2009. Somatic expansion of the Huntington's disease CAG repeat in the brain is associated with an earlier age of disease onset. *Human molecular genetics* 18(16), pp. 3039-3047.

Świtońska, K. et al. 2019. Identification of altered developmental pathways in human juvenile HD iPSC with 71Q and 109Q using transcriptome profiling. *Frontiers in cellular neuroscience* 12, p. 528.

Szebenyi, G. et al. 2003. Neuropathogenic forms of huntingtin and androgen receptor inhibit fast axonal transport. *Neuron* 40(1), pp. 41-52.

Szlachcic, W. J., Switonski, P. M., Krzyzosiak, W. J., Figlerowicz, M. and Figiel, M. 2015. Huntington disease iPSCs show early molecular changes in intracellular signaling, the expression of oxidative stress proteins and the p53 pathway. *Disease models & mechanisms* 8(9), pp. 1047-1057.

Tabrizi, S. J. et al. 2019. Targeting huntingtin expression in patients with Huntington's disease. *New England Journal of Medicine* 380(24), pp. 2307-2316.

Takano, H. and Gusella, J. F. 2002. The predominantly HEAT-like motif structure of huntingtin and its association and coincident nuclear entry with dorsal, an NF-kB/Rel/dorsal family transcription factor. *BMC neuroscience* 3(1), pp. 1-13.

Tamiji, J. and Crawford, D. A. 2010. The neurobiology of lipid metabolism in autism spectrum disorders. *Neurosignals* 18(2), pp. 98-112.

Tamura, H., Takahashi, T., Ban, N., Torisu, H., Ninomiya, H., Takada, G. and Inagaki, N. 2006. Niemann–Pick type C disease: novel NPC1 mutations and characterization of the concomitant acid sphingomyelinase deficiency. *Molecular genetics and metabolism* 87(2), pp. 113-121.

Tan-Chen, S., Guitton, J., Bourron, O., Le Stunff, H. and Hajduch, E. 2020. Sphingolipid Metabolism and Signaling in Skeletal Muscle: from physiology to physiopathology. *Frontiers in endocrinology* 11,

Tano, V., Utami, K. H., Yusof, N. A. B. M., Pouladi, M. A. and Langley, S. R. 2022. Widespread dysregulation of mRNA splicing implicates RNA processing in the development and progression of Huntington's disease. *bioRxiv*,

te Vruchte, D. et al. 2004. Accumulation of glycosphingolipids in Niemann-Pick C disease disrupts endosomal transport. *Journal of Biological Chemistry* 279(25), pp. 26167-26175.

Te Vruchte, D. et al. 2014. Relative acidic compartment volume as a lysosomal storage disorder–associated biomarker. *The Journal of clinical investigation* 124(3), pp. 1320-1328.

Telezhkin, V. et al. 2016. Forced cell cycle exit and modulation of GABAA, CREB, and GSK3β signaling promote functional maturation of induced pluripotent stem cell-derived neurons. *American Journal of Physiology-Cell Physiology* 310(7), pp. C520-C541.

Tepper, J. M., Koós, T., Ibanez-Sandoval, O., Tecuapetla, F., Faust, T. W. and Assous, M. 2018. Heterogeneity and diversity of striatal GABAergic interneurons: update 2018. *Frontiers in neuroanatomy* 12, p. 91.

Tharkeshwar, A. K. et al. 2017. A novel approach to analyze lysosomal dysfunctions through subcellular proteomics and lipidomics: the case of NPC1 deficiency. *Scientific reports* 7(1), pp. 1-20.

Tonin, R. et al. 2019. Pre-diagnosing and managing patients with GM1 gangliosidosis and related disorders by the evaluation of GM1 ganglioside content. *Scientific reports* 9(1), pp. 1-10.

Torres, S. et al. 2017. Mitochondrial GSH replenishment as a potential therapeutic approach for Niemann Pick type C disease. *Redox biology* 11, pp. 60-72.

Trottier, Y. et al. 1995. Cellular localization of the Huntington's disease protein and discrimination of the normal and mutated form. *Nat Genet* 10(1), pp. 104-110. doi: 10.1038/ng0595-104

Trushina, E., Canaria, C. A., Lee, D.-Y. and McMurray, C. T. 2014. Loss of caveolin-1 expression in knock-in mouse model of Huntington's disease suppresses pathophysiology in vivo. *Human molecular genetics* 23(1), pp. 129-144.

Trushina, E. et al. 2004. Mutant huntingtin impairs axonal trafficking in mammalian neurons in vivo and in vitro. *Molecular and cellular biology* 24(18), pp. 8195-8209.

Trushina, E. et al. 2006a. Mutant huntingtin inhibits clathrin-independent endocytosis and causes accumulation of cholesterol in vitro and in vivo. *Hum Mol Genet* 15(24), pp. 3578-3591. doi: 10.1093/hmg/ddl434

Trushina, E. et al. 2006b. Mutant huntingtin inhibits clathrin-independent endocytosis and causes accumulation of cholesterol in vitro and in vivo. *Human molecular genetics* 15(24), pp. 3578-3591.

Tsvetkov, A. S., Miller, J., Arrasate, M., Wong, J. S., Pleiss, M. A. and Finkbeiner, S. 2010. A small-molecule scaffold induces autophagy in primary neurons and protects against toxicity in a Huntington disease model. *Proceedings of the National Academy of Sciences* 107(39), pp. 16982-16987.

Vakulskas, C. A. et al. 2018. A high-fidelity Cas9 mutant delivered as a ribonucleoprotein complex enables efficient gene editing in human hematopoietic stem and progenitor cells. *Nature medicine* 24(8), pp. 1216-1224.

Valenza, M. et al. 2007a. Cholesterol biosynthesis pathway is disturbed in YAC128 mice and is modulated by huntingtin mutation. *Human molecular genetics* 16(18), pp. 2187-2198.

Valenza, M. and Cattaneo, E. 2011. Emerging roles for cholesterol in Huntington's disease. *Trends in neurosciences* 34(9), pp. 474-486.

Valenza, M. et al. 2010. Cholesterol defect is marked across multiple rodent models of Huntington's disease and is manifest in astrocytes. *Journal of Neuroscience* 30(32), pp. 10844-10850.

Valenza, M., Leoni, V., Tarditi, A., Mariotti, C., Björkhem, I., Di Donato, S. and Cattaneo, E. 2007b. Progressive dysfunction of the cholesterol biosynthesis pathway in the R6/2 mouse model of Huntington's disease. *Neurobiology of disease* 28(1), pp. 133-142.

Valenza, M. et al. 2005a. Dysfunction of the cholesterol biosynthetic pathway in Huntington's disease. *Journal of Neuroscience* 25(43), pp. 9932-9939.

Valenza, M. et al. 2005b. Dysfunction of the cholesterol biosynthetic pathway in Huntington's disease. *J Neurosci* 25(43), pp. 9932-9939. doi: 10.1523/JNEUROSCI.3355-05.2005

Van Diggelen, O. P., Keulemans, J. L. M., Winchester, B., Hofman, I. L., Vanhanen, S.-L., Santavuori, P. and Voznyi, Y. V. 1999. A rapid fluorogenic palmitoyl-protein thioesterase assay: pre-and postnatal diagnosis of INCL. *Molecular genetics and metabolism* 66(4), pp. 240-244.

Van Diggelen, O. P. et al. 2005. A new fluorimetric enzyme assay for the diagnosis of Niemann–Pick A/B, with specificity of natural sphingomyelinase substrate. *Journal of inherited metabolic disease* 28(5), pp. 733-741.

van Duijn, E., Fernandes, A. R., Abreu, D., Ware, J. J., Neacy, E. and Sampaio, C. 2021. Incidence of completed suicide and suicide attempts in a global prospective study of Huntington's disease. *BJPsych open* 7(5),

Van Meel, E. and Klumperman, J. 2008. Imaging and imagination: understanding the endo-lysosomal system. *Histochemistry and cell biology* 129(3), pp. 253-266.

Vanier, M., Duthel, S., Rodriguez-Lafrasse, C., Pentchev, P. and Carstea, E. 1996. Genetic heterogeneity in Niemann-Pick C disease: a study using somatic cell hybridization and linkage analysis. *American journal of human genetics* 58(1), p. 118.

Vanier, M. T. 1983. Biochemical studies in Niemann-Pick disease I. Major sphingolipids of liver and spleen. *Biochimica Et Biophysica Acta (BBA)-Lipids and Lipid Metabolism* 750(1), pp. 178-184.

Vanier, M. T. 1999. Lipid changes in Niemann-Pick disease type C brain: personal experience and review of the literature. *Neurochemical research* 24(4), pp. 481-489.

Vanier, M. T. 2010. Niemann-Pick disease type C. *Orphanet journal of rare diseases* 5(1), pp. 1-18.

Vanier, M. T. 2015. Complex lipid trafficking in Niemann-Pick disease type C. *Journal of inherited metabolic disease* 38(1), pp. 187-199.

Vanier, M. T. and Latour, P. 2015. Laboratory diagnosis of Niemann–Pick disease type C: the filipin staining test.*Methods in cell biology*. Vol. 126. Elsevier, pp. 357-375.

Vanier, M. T. and Millat, G. 2004. Structure and function of the NPC2 protein. *Biochimica et Biophysica Acta (BBA)-Molecular and Cell Biology of Lipids* 1685(1-3), pp. 14-21.

Victor, M. B. et al. 2018. Striatal neurons directly converted from Huntington's disease patient fibroblasts recapitulate age-associated disease phenotypes. *Nature neuroscience* 21(3), pp. 341-352.

Vigont, V. et al. 2018. Patient-specific iPSC-based models of Huntington's disease as a tool to study store-operated calcium entry drug targeting. *Frontiers in Pharmacology* 9, p. 696.

Visentin, S., De Nuccio, C., Bernardo, A., Pepponi, R., Ferrante, A., Minghetti, L. and Popoli, P. 2013. The stimulation of adenosine A2A receptors ameliorates the pathological phenotype of fibroblasts from Niemann-Pick type C patients. *Journal of Neuroscience* 33(39), pp. 15388-15393.

Viswanathan, K., Hoover, D. J., Hwang, J., Wisniewski, M. L., Ikonne, U. S., Bahr, B. A. and Wright, D. L. 2012. Nonpeptidic lysosomal modulators derived from Z-Phe-Ala-diazomethylketone for treating protein accumulation diseases. *ACS medicinal chemistry letters* 3(11), pp. 920-924.

Vitali, C., Wellington, C. L. and Calabresi, L. 2014. HDL and cholesterol handling in the brain. *Cardiovascular research* 103(3), pp. 405-413.

Vite, C. H. et al. 2015. Intracisternal cyclodextrin prevents cerebellar dysfunction and Purkinje cell death in feline Niemann-Pick type C1 disease. *Science translational medicine* 7(276), pp. 276ra226-276ra226.

Vitner, E. B., Platt, F. M. and Futerman, A. H. 2010. Common and uncommon pathogenic cascades in lysosomal storage diseases. *Journal of Biological Chemistry* 285(27), pp. 20423-20427.

Volpato, V. and Webber, C. 2020. Addressing variability in iPSC-derived models of human disease: guidelines to promote reproducibility. *Disease models & mechanisms* 13(1), p. dmm042317.

Vonsattel, J.-P., Myers, R. H., Stevens, T. J., Ferrante, R. J., Bird, E. D. and Richardson, E. P. 1985. Neuropathological classification of Huntington's disease. *Journal of Neuropathology & Experimental Neurology* 44(6), pp. 559-577.

Vonsattel, J. P. G. and DiFiglia, M. 1998. Huntington disease. *Journal of neuropathology and experimental neurology* 57(5), p. 369.

Vonsattel, J. P. G., Keller, C. and del Pilar Amaya, M. 2008. Neuropathology of Huntington's disease. *Handbook of clinical neurology* 89, pp. 599-618.

Vozyi, Y. V., Keulemans, J. L. M., Lleijer, W. J., Aula, P., Gray, G. R. and Van Diggelen, O. P. 1993. Applications of a new fluorimetric enzyme assay for the diagnosis of aspartylglucosaminuria. *Journal of inherited metabolic disease* 16(6), pp. 929-934.

Waelter, S. et al. 2001. The huntingtin interacting protein HIP1 is a clathrin and α-adaptin-binding protein involved in receptor-mediated endocytosis. *Human molecular genetics* 10(17), pp. 1807-1817.

Walker, F. O. 2007. Huntington's disease. *The Lancet* 369(9557), pp. 218-228.

Walkley, S. U., Suzuki, K. and Suzuki, K. 2018. Lysosomal diseases.*Greenfield's Neuropathology-Two Volume Set*. CRC Press, pp. 463-546.

Walkley, S. U. and Vanier, M. T. 2009. Secondary lipid accumulation in lysosomal disease. *Biochimica et Biophysica Acta (BBA)-Molecular Cell Research* 1793(4), pp. 726-736.

Walter, M., Chen, F. W., Tamari, F., Wang, R. and Ioannou, Y. A. 2009. Endosomal lipid accumulation in NPC1 leads to inhibition of PKC, hypophosphorylation of vimentin and Rab9 entrapment. *Biology of the Cell* 101(3), pp. 141-153.

Wang, X., Perez, E., Liu, R., Yan, L. J., Mallet, R. T. and Yang, S. H. 2007. Pyruvate protects mitochondria from oxidative stress in human neuroblastoma SK-N-SH cells. *Brain Res* 1132(1), pp. 1-9. doi: 10.1016/j.brainres.2006.11.032

Wang, Y.-H., Twu, Y.-C., Wang, C.-K., Lin, F.-Z., Lee, C.-Y. and Liao, Y.-J. 2018. Niemann-Pick type C2 protein regulates free cholesterol accumulation and influences hepatic stellate cell proliferation and mitochondrial respiration function. *International journal of molecular sciences* 19(6), p. 1678.

Warby, S. C. et al. 2009. CAG expansion in the Huntington disease gene is associated with a specific and targetable predisposing haplogroup. *The American Journal of Human Genetics* 84(3), pp. 351-366.

Wastney, M. E., Pentchev, P. G. and Neufeld, E. B. 2003. Fitting a mathematical model to biological data: Intracellular trafficking in niemann-pick C disease.*Mathematical Modeling in Nutrition and the Health Sciences*. Springer, pp. 63-75.

Wellington, C. L., Ellerby, L. M., Leavitt, B. R., Roy, S., Nicholson, D. W. and Hayden, M. R. 2003. Huntingtin proteolysis in Huntington disease. *Clinical neuroscience research* 3(3), pp. 129-139.

Wheeler, S., Schmid, R. and Sillence, D. J. 2019. Lipid–protein interactions in Niemann–Pick type C disease: insights from molecular modeling. *International journal of molecular sciences* 20(3), p. 717.

Wheeler, S. and Sillence, D. J. 2020. Niemann–Pick type C disease: cellular pathology and pharmacotherapy. *Journal of neurochemistry* 153(6), pp. 674-692.

Wheeler, V. C. et al. 2000. Long glutamine tracts cause nuclear localization of a novel form of huntingtin in medium spiny striatal neurons in Hdh Q92 and Hdh Q111 knock-in mice. *Human molecular genetics* 9(4), pp. 503-513.

White, J. K., Auerbach, W., Duyao, M. P., Vonsattel, J.-P., Gusella, J. F., Joyner, A. L. and MacDonald, M. E. 1997. Huntingtin is required for neurogenesis and is not impaired by the Huntington's disease CAG expansion. *Nature genetics* 17(4), pp. 404-410.

Wiatr, K., Szlachcic, W. J., Trzeciak, M., Figlerowicz, M. and Figiel, M. 2018. Huntington disease as a neurodevelopmental disorder and early signs of the disease in stem cells. *Molecular Neurobiology* 55(4), pp. 3351-3371.

Wigger, D., Gulbins, E., Kleuser, B. and Schumacher, F. 2019. Monitoring the sphingolipid de novo synthesis by stable-isotope labeling and liquid chromatography-mass spectrometry. *Frontiers in cell and developmental biology* 7, p. 210.

Wijdeven, R. H., Janssen, H., Nahidiazar, L., Janssen, L., Jalink, K., Berlin, I. and Neefjes, J. 2016. Cholesterol and ORP1L-mediated ER contact sites control autophagosome transport and fusion with the endocytic pathway. *Nature communications* 7(1), pp. 1-14.

Winchester, B., Barker, C., Baines, S., Jacob, G. S., Namgoong, S. K. and Fleet, G. 1990. Inhibition of α-L-fucosidase by derivatives of deoxyfuconojirimycin and deoxymannojirimycin. *Biochemical Journal* 265(1), pp. 277-282.

Winter, R., Swallow, D., Baraitser, M. and Purkiss, P. 1980. Sialidosis type 2 (acid neuraminidase deficiency): clinical and biochemical features of a further case. *Clinical genetics* 18(3), pp. 203-210.

Wiprich, M. T. and Bonan, C. D. 2021. Purinergic Signaling in the Pathophysiology and Treatment of Huntington's Disease. *Frontiers in neuroscience* 15, p. 787.

Wong, Y. C. and Holzbaur, E. L. F. 2014. The regulation of autophagosome dynamics by huntingtin and HAP1 is disrupted by expression of mutant huntingtin, leading to defective cargo degradation. *Journal of Neuroscience* 34(4), pp. 1293-1305.

Wu, T. et al. 2021. clusterProfiler 4.0: A universal enrichment tool for interpreting omics data. *The Innovation* 2(3), p. 100141.

Wu, Z. et al. 1999. Mechanisms controlling mitochondrial biogenesis and respiration through the thermogenic coactivator PGC-1. *Cell* 98(1), pp. 115-124.

Xu, H. and Ren, D. 2015. Lysosomal physiology. *Annual review of physiology* 77, pp. 57-80.

Xu, S., Benoff, B., Liou, H.-L., Lobel, P. and Stock, A. M. 2007. Structural basis of sterol binding by NPC2, a lysosomal protein deficient in Niemann-Pick type C2 disease. *Journal of Biological Chemistry* 282(32), pp. 23525-23531.

Xu, X. et al. 2017. Reversal of phenotypic abnormalities by CRISPR/Cas9-mediated gene correction in Huntington disease patient-derived induced pluripotent stem cells. *Stem cell reports* 8(3), pp. 619-633.

Xu, Y. et al. 2021. Identification of a genetic variant underlying familial cases of recurrent benign paroxysmal positional vertigo. *PLOS one* 16(5), p. e0251386.

Yamada, T., Tsuji, S., Ariga, T. and Miyatake, T. 1983. Lysosomal sialidase deficiency in sialidosis with partial β-galactosidase deficiency. *Biochimica et Biophysica Acta (BBA)-General Subjects* 755(1), pp. 106-111.

Yambire, K. F., Fernandez-Mosquera, L., Steinfeld, R., Mühle, C., Ikonen, E., Milosevic, I. and Raimundo, N. 2019. Mitochondrial biogenesis is transcriptionally repressed in lysosomal lipid storage diseases. *Elife* 8, p. e39598.

Yañez, M. J., Marín, T., Balboa, E., Klein, A. D., Alvarez, A. R. and Zanlungo, S. 2020. Finding pathogenic commonalities between Niemann-Pick type C and other lysosomal storage disorders: Opportunities for shared therapeutic interventions. *Biochimica et Biophysica Acta (BBA)-Molecular Basis of Disease* 1866(10), p. 165875.

Yano, H. et al. 2014. Inhibition of mitochondrial protein import by mutant huntingtin. *Nature neuroscience* 17(6), pp. 822-831.

Yim, W. W.-Y. and Mizushima, N. 2020. Lysosome biology in autophagy. *Cell discovery* 6(1), pp. 1-12.

Yin, F., Sancheti, H., Patil, I. and Cadenas, E. 2016. Energy metabolism and inflammation in brain aging and Alzheimer's disease. *Free Radical Biology and Medicine* 100, pp. 108-122.

Young, S. A., Mina, J. G., Denny, P. W. and Smith, T. K. 2012. Sphingolipid and ceramide homeostasis: potential therapeutic targets. *Biochemistry Research International* 2012,

Yu, A., Shibata, Y., Shah, B., Calamini, B., Lo, D. C. and Morimoto, R. I. 2014. Protein aggregation can inhibit clathrin-mediated endocytosis by chaperone competition. *Proceedings of the National Academy of Sciences* 111(15), pp. E1481-E1490.

Yu, F.-X., Zhao, B. and Guan, K.-L. 2015. Hippo pathway in organ size control, tissue homeostasis, and cancer. *Cell* 163(4), pp. 811-828.

Yu, N., Liang, Y., Wang, Q., Peng, X., He, Z. and Hou, X. 2022. Transcriptomic analysis of OsRUS1 overexpression rice lines with rapid and dynamic leaf rolling morphology. *Scientific reports* 12(1), pp. 1-16.

Yu, W., Gong, J.-S., Ko, M., Garver, W. S., Yanagisawa, K. and Michikawa, M. 2005. Altered cholesterol metabolism in Niemann-Pick type C1 mouse brains affects mitochondrial function. *Journal of Biological Chemistry* 280(12), pp. 11731-11739.

Zala, D., Hinckelmann, M.-V. and Saudou, F. 2013. Huntingtin's function in axonal transport is conserved in Drosophila melanogaster. *PLOS one* 8(3), p. e60162.

Zein, A. A., Kaur, R., Hussein, T. O., Graf, G. A. and Lee, J.-Y. 2019. ABCG5/G8: a structural view to pathophysiology of the hepatobiliary cholesterol secretion. *Biochemical Society Transactions* 47(5), pp. 1259-1268.

Zeitlin, S., Liu, J.-P., Chapman, D. L., Papaioannou, V. E. and Efstratiadis, A. 1995. Increased apoptosis and early embryonic lethality in mice nullizygous for the Huntington's disease gene homologue. *Nature genetics* 11(2), pp. 155-163.

Zervas, M., Dobrenis, K. and Walkley, S. U. 2001a. Neurons in Niemann-Pick disease type C accumulate gangliosides as well as unesterified cholesterol and undergo dendritic and axonal alterations. *Journal of Neuropathology & Experimental Neurology* 60(1), pp. 49-64.

Zervas, M., Somers, K. L., Thrall, M. A. and Walkley, S. U. 2001b. Critical role for glycosphingolipids in Niemann-Pick disease type C. *Current Biology* 11(16), pp. 1283-1287.

Zhang, M. et al. 2001. Cessation of rapid late endosomal tubulovesicular trafficking in Niemann–Pick type C1 disease. *Proceedings of the National Academy of Sciences* 98(8), pp. 4466-4471.

Zhang, M. et al. 2003a. Differential trafficking of the Niemann-Pick C1 and 2 proteins highlights distinct roles in late endocytic lipid trafficking. *Acta paediatrica* 92, pp. 63-73.

Zhang, N., An, M. C., Montoro, D. and Ellerby, L. M. 2010. Characterization of Human Huntington's Disease Cell Model from Induced Pluripotent Stem Cells. *PLoS Curr* 2, p. RRN1193. doi: 10.1371/currents.RRN1193

Zhang, S. and Cui, W. 2014. Sox2, a key factor in the regulation of pluripotency and neural differentiation. *World journal of stem cells* 6(3), p. 305.

Zhang, S., Feany, M. B., Saraswati, S., Littleton, J. T. and Perrimon, N. 2009. Inactivation of Drosophila Huntingtin affects long-term adult functioning and the pathogenesis of a Huntington's disease model. *Disease models & mechanisms* 2(5-6), pp. 247-266.

Zhang, X. et al. 2016. MCOLN1 is a ROS sensor in lysosomes that regulates autophagy. *Nature communications* 7(1), pp. 1-12.

Zhang, Y. et al. 2003b. Depletion of wild-type huntingtin in mouse models of neurologic diseases. *Journal of neurochemistry* 87(1), pp. 101-106.

Zhang, Y. et al. 2022. GSK-3β inhibition elicits a neuroprotection by restoring lysosomal dysfunction in neurons via facilitation of TFEB nuclear translocation after ischemic stroke. *Brain research* 1778, p. 147768.

Zhang, Z. et al. 2007. Regulated ATP release from astrocytes through lysosome exocytosis. *Nature cell biology* 9(8), pp. 945-953.

Zhao, L. et al. 2011. A deficiency of ceramide biosynthesis causes cerebellar purkinje cell neurodegeneration and lipofuscin accumulation. *PLoS Genetics* 7(5), p. e1002063.

Zheng, J., Winderickx, J., Franssens, V. and Liu, B. 2018. A mitochondria-associated oxidative stress perspective on Huntington's disease. *Frontiers in molecular neuroscience* 11, p. 329.

Zheng, S., Clabough, E. B. D., Sarkar, S., Futter, M., Rubinsztein, D. C. and Zeitlin, S. O. 2010. Deletion of the huntingtin polyglutamine stretch enhances neuronal autophagy and longevity in mice. *PLoS genetics* 6(2), p. e1000838.

Zhou, Y. et al. 2021. Correlative light and electron microscopy suggests that mutant huntingtin dysregulates the endolysosomal pathway in presymptomatic Huntington's disease. *Acta neuropathologica communications* 9(1), pp. 1-21.

Zuccato, C. et al. 2001. Loss of huntingtin-mediated BDNF gene transcription in Huntington's disease. *Science* 293(5529), pp. 493-498.

Zuccato, C. et al. 2005. Progressive loss of BDNF in a mouse model of Huntington's disease and rescue by BDNF delivery. *Pharmacological research* 52(2), pp. 133-139.

Zuccato, C. et al. 2003a. Huntingtin interacts with REST/NRSF to modulate the transcription of NRSE-controlled neuronal genes. *Nature genetics* 35(1), pp. 76-83.

Zuccato, C. et al. 2003b. Huntingtin interacts with REST/NRSF to modulate the transcription of NRSE-controlled neuronal genes. *Nat Genet* 35(1), pp. 76-83. doi: 10.1038/ng1219

Zuccato, C., Valenza, M. and Cattaneo, E. 2010. Molecular mechanisms and potential therapeutical targets in Huntington's disease. *Physiological reviews* 90(3), pp. 905-981.

9 APPENDIX

Gene Symbol	Adjusted p-value	Log_2 Fold Change
HD109 vs HD22 $^{ISO-109}$		
EHHADH	1.35323E-45	6.036703525
PCDHGA10	9.63518E-26	-1.554863722
AC020928.1	5.04925E-21	3.355632243
MAP3K13	2.06133E-14	1.987201148
GEMIN8	3.77799E-11	1.230884259
EIF1AXP1	4.76233E-07	1.021558341
AC136759.1	1.00558E-06	-5.847370401
EIF1AX	9.25007E-06	1.147025779
ADGRG5	1.07611E-05	2.641588251
NNAT	2.14283E-05	6.440339876
AL021395.1	4.83842E-05	-5.097746748
KIF25	0.000219844	1.179689397
GPRC5D-AS1	0.000421875	2.321684415
BX322639.1	0.002745671	11.48285493
MYO18B	0.003632942	1.981563128
AC073585.1	0.003837377	3.122660073
SLC5A8	0.005033426	5.709381074
CHRDL1	0.007283036	1.532642122
AL512283.1	0.013654101	3.236940779
C5orf63	0.013654101	4.29683395
PTPRT	0.020146229	-5.146220314
FAM24B	0.021103836	3.506768195
CUZD1	0.048694482	2.522068509
HTTKO $^{ISO-109}$ vs HD22$^{ISO-109}$		
EHHADH	1.73687E-82	6.20786201
EIF1AX	3.23122E-66	1.041091778
MAP3K13	1.3576E-48	2.305856503
KLF4	3.41869E-27	-2.871625452
TUBBP5	6.66112E-24	-4.084905418
ADGRG5	1.98939E-23	3.680412304
CPXM1	1.119E-17	-2.252383213
CTSF	8.21125E-17	-8.270627725
PCDHGA10	1.07915E-16	-1.49935082
IRX6	7.58771E-16	1.780863583
QKI	1.42826E-15	-1.008326368

CRYZ	1.23176E-14	9.388477136
SDHAF4	4.26304E-14	-1.086655226
PPP1R1B	5.61897E-14	1.52200823
GOLT1A	1.67828E-13	1.60807431
ZBTB16	7.81677E-13	-2.810960145
FLRT2	1.13563E-12	-1.140040391
CNTN3	4.34827E-12	-1.492544921
ADCY2	2.14614E-11	-1.731776747
KISS1R	2.14614E-11	1.168383131
DDN	2.72348E-11	1.242477592
FUNDC1	2.88016E-11	1.017167135
POU5F1	6.32842E-10	-1.425028597
PRMT8	1.21484E-09	1.391715727
AC073389.2	2.27252E-09	-6.797303341
LINC00865	9.21175E-09	-7.133959844
TMEM132D	1.00839E-08	-2.145803265
TUSC1	1.09331E-08	-2.652901742
C12orf75	1.37632E-08	1.008109272
LTBP1	1.71947E-08	-1.812208096
PIK3AP1	1.88155E-08	2.688732612
ABCA12	2.4874E-08	1.596773197
CHRM2	2.93517E-08	-1.973078132
EGFL6	3.60632E-08	1.770075228
PLA2G4A	4.6039E-08	1.891472664
SLC10A4	5.14778E-08	1.746120459
PTPRT	7.55929E-08	-6.053912367
PCDH11X	7.55929E-08	-1.177301053
PTGFR	8.28853E-08	2.29589513
NR4A2	1.1462E-07	-2.349198413
CDH20	1.39175E-07	-2.49747744
UNC5C	1.61239E-07	-1.709793369
PMAIP1	2.15619E-07	-2.107997539
ZNF439	2.49012E-07	-3.188704798
HTR2C	3.35279E-07	1.783931968
GPR50	3.88304E-07	-1.768286627
EGR1	5.16228E-07	-1.657444436
FILIP1L	6.28275E-07	-1.999287009
DLK1	1.15758E-06	-2.234924987
CSGALNACT1	1.64117E-06	1.119384836

PAQR5	1.77405E-06	1.854217544
GPC6	1.79745E-06	-1.619905108
SCN5A	2.10295E-06	1.378796934
MIR4435-2HG	2.15711E-06	-1.152994568
LRRTM4	2.20133E-06	1.168182874
TOX3	2.27483E-06	-2.051911525
IRX2	2.31536E-06	-2.58966722
BCL6	2.84001E-06	-2.236832451
ZNF503	2.84001E-06	1.443620685
BTBD11	2.89557E-06	1.229561216
KC877982.1	3.0797E-06	-1.743889186
TYW3	4.68071E-06	9.142265343
AL021395.1	5.97609E-06	-6.138301546
NXNL2	1.02902E-05	1.364710994
SAMD5	1.12732E-05	-1.21513195
AC239800.2	1.15197E-05	-5.688164631
ZC3HAV1	1.37935E-05	-1.376929217
IL1RAPL2	1.56874E-05	-2.898824269
EPS8L1	1.59676E-05	-1.102257384
HIST2H2BB	1.9421E-05	-5.56234365
CPNE5	2.55593E-05	1.341999512
NR2F1-AS1	3.00592E-05	-1.298179726
CITED2	3.05554E-05	-1.183328687
SOX9	3.34333E-05	-2.630607768
FST	5.33473E-05	-3.122203128
CRYGD	5.33473E-05	-2.916340136
EGR2	5.33473E-05	-2.106722502
BCL2L11	5.33473E-05	-1.998456149
PRKAG2-AS1	5.64538E-05	1.074569206
GEMIN8	5.99817E-05	1.064726629
PNLIP	6.02875E-05	-2.344042485
SOCS2-AS1	6.02875E-05	1.110287286
NR2F1	6.14459E-05	-1.918835635
OPN3	6.14459E-05	-1.267629543
ADGRL4	6.64472E-05	-3.187750873
AC010931.3	6.66662E-05	1.882316722
MAT1A	6.66662E-05	2.475246777
FOXF1	6.70082E-05	-5.843764064
C17orf107	6.70082E-05	-2.498268239

GNG7	6.8589E-05	1.212586156
HLA-DRB5	6.8627E-05	1.002243723
SCGN	8.11799E-05	-3.351589032
AC136759.1	8.257E-05	-5.429227604
GABRQ	8.257E-05	-2.225799336
PCDH9	8.257E-05	-2.066496502
TEX14	8.257E-05	-1.06490355
CHRNE	8.98068E-05	-1.84921366
MYOZ1	9.35538E-05	-2.515898093
PIWIL2	9.45311E-05	-1.055254812
AEBP1	9.94599E-05	-1.250678125
PTPN3	0.000105358	-1.190917921
TMEM2	0.000106072	-1.408535954
ETS1	0.000112733	1.21225427
LINC02381	0.000121655	-4.169388813
ERBB4	0.000129651	-1.57217404
EPHA7	0.00013732	-1.146315019
STRIP2	0.00013732	1.696445579
ADRA1D	0.000139911	-1.206363171
FZD7	0.00014758	-1.841493603
MKRN3	0.000150735	-1.05613289
CNTNAP4	0.000151909	-1.045234384
PTPRU	0.000160264	-1.265430543
SLC44A5	0.000160793	-1.428392917
C5orf38	0.000173382	-4.317061018
HAS3	0.000178524	1.055119478
AC104129.1	0.00018488	-1.580704496
IRX1	0.000188199	-2.192310751
IGFBP5	0.000194301	-3.078564741
GABRD	0.000194301	1.1756619
SAMSN1	0.000194301	2.039061668
LITAF	0.000202071	-2.510222366
AL035252.2	0.000226649	-5.039961537
HOXC9	0.000226649	-1.797041038
HTR7	0.00024673	-1.61150446
IL31RA	0.000257041	-2.538188947
BOC	0.000269927	-2.068419764
FBLN5	0.000284742	1.260299002
HOXB3	0.000299389	-6.019912446

CYTOR	0.0003233	-1.318408926
VSTM4	0.000327251	1.070387591
PPP1R3A	0.000333447	2.804841995
NMRK2	0.000353873	2.062054697
NR2E1	0.000358639	-1.778311264
GPC3	0.000363189	-2.427826892
NEFH	0.00036752	1.144392721
SOX2	0.000371601	-1.744709554
TGFB2	0.00040025	-1.335878447
DDR2	0.000413741	-1.037287297
AC239798.2	0.000434752	-2.636562166
PBXIP1	0.000434752	-1.58162484
CDH18	0.000463743	-1.244125159
FBXL7	0.00047897	-2.378914918
NEDD9	0.000528471	-1.447826189
LRRTM2	0.000540297	-1.35863829
CCDC80	0.000557469	-4.364917929
TMEM144	0.000558402	1.284374086
AASS	0.000564117	-1.773811352
MET	0.000607422	-1.836090979
LMO3	0.000610711	1.070244849
NRARP	0.000628854	-1.347520277
AC117489.1	0.000637443	1.367697311
YPEL4	0.000677432	-1.718542191
AP000688.2	0.000805038	-2.595712174
ZNF503-AS2	0.000853813	1.218233648
AP002840.1	0.000855869	1.662919006
AC020951.1	0.000865598	-3.939934421
KISS1	0.000930514	1.27608528
MOXD1	0.000959797	-1.244893631
FYB1	0.001024758	-2.69430724
ADAMTS9	0.001024758	1.100802359
C1QL2	0.001038137	-2.021252828
EYA4	0.001103168	-1.771179066
NR2F2	0.001118531	-1.175840085
ISLR2	0.001139976	1.083171176
PTGER3	0.001140987	-1.8726164
SEL1L3	0.001140987	-1.777861465
TSPAN1	0.001140987	-1.431719075

ITPRIPL1	0.001140987	-1.399690917
CRIM1	0.001140987	-1.180474285
FAM46A	0.001142316	-1.166726158
KRT75	0.00116125	-1.533785934
FOXO1	0.001213864	-1.472040731
AL445623.2	0.001213864	-1.364690011
GEM	0.00121501	-1.660196073
NPR3	0.001229003	-1.36578351
NPC1L1	0.001233577	-1.203461187
S100A10	0.001273589	1.088820988
LINC00654	0.001318899	-1.736934166
WEE1	0.001320807	-1.601867759
NPTX1	0.001340945	-2.687762232
CUBN	0.001381674	-1.060729163
ULK4P1	0.001422646	1.897167883
ZADH2	0.001601791	-1.011441402
AC009264.1	0.001651566	-2.117649641
ELAVL2	0.001820889	-1.328881768
TNNI3	0.001882055	-1.891049736
NXPH1	0.002122219	-1.936956538
TSPAN11	0.002136223	-1.401649851
UCP2	0.002444151	-2.159776007
ITPKA	0.002518671	-1.142843552
RN7SL471P	0.002591076	-4.080733132
DCBLD1	0.002591076	1.209808274
BMP2	0.002592574	-1.548594613
PCDH11Y	0.002592574	-1.322203035
C1orf127	0.002628813	1.23001065
HMGB3P10	0.002649559	1.540082535
SERPINI2	0.00268642	2.659407982
AOAH	0.002695131	1.713297815
MRC2	0.002744448	-3.645331231
AL049775.1	0.002744448	-1.129214863
FOS	0.002798899	-1.817883365
TMEM63A	0.002835684	-1.231252112
MEI4	0.002835684	2.334484364
PRICKLE1	0.002852454	1.00359004
NCKAP5	0.002978805	-1.630050931
HOXB2	0.003041897	-6.019568982

KMO	0.003174764	-2.185789055
RIPK4	0.00318081	-1.222599688
PHLDB2	0.003246821	-2.544614566
ANKFN1	0.003343603	-2.420872508
CBLN2	0.003380308	-1.604070106
GLI2	0.003478157	-1.778027506
SALL3	0.003738331	-3.42175316
PID1	0.003802952	1.035129348
FBN2	0.003860535	-1.605206726
FANCD2	0.003860535	-1.056626629
MMRN2	0.003884432	-1.571118845
CPA2	0.0039423	1.498783754
AC008467.1	0.004021011	-2.507294532
LINC01320	0.004114652	-2.972840587
PAPPA	0.004251181	-1.350779042
AC010997.4	0.004352752	1.050063674
AC092681.1	0.004663397	1.586018732
CACNA2D1	0.004804173	-2.484329007
SYDE1	0.004804173	1.088260329
SLC30A3	0.00488953	-1.635575251
CDKN1C	0.004900232	-1.47470307
IQUB	0.004919537	-1.007400041
INSM1	0.005117667	-1.524408306
TSHZ1	0.005220981	-1.252913115
AC007490.1	0.005237306	-2.431632835
PHKG1	0.005237528	-1.716433995
HOXC4	0.005464707	-4.892780111
EDIL3	0.005464707	-2.007736817
LRIG1	0.005464707	-1.940160897
RBM20	0.005779833	1.308025949
AC138409.2	0.00579863	-1.021392248
ADAM12	0.005859096	-2.232415951
C2orf83	0.005994572	2.146057729
RHBG	0.006026863	-1.604482558
ABCA1	0.006120114	-1.572842432
PCP4L1	0.006133673	1.003629212
PTN	0.006317693	-2.535789499
PRKCH	0.006459056	1.522387305
BARHL2	0.006487184	-4.864920223

DRD2	0.006506538	1.511386291
SLC17A6	0.006695532	-3.254421991
MMP10	0.006736881	-1.762606623
AL392083.1	0.006736881	-1.404450541
RNASE10	0.006901981	-2.973965413
HIST1H3H	0.006901981	-1.318176284
SNTG2	0.007005822	-1.383976392
COLEC12	0.007085425	-1.871398737
STARD8	0.007085425	-1.212049369
BDNF	0.007114829	-1.127168419
APOC1	0.007114829	1.56811783
SERPING1	0.007191786	-1.027988206
PDE4DIPP1	0.007191786	1.308402123
MATN2	0.007218351	-1.755661552
Z82186.1	0.007310817	-2.052933474
FAM50B	0.007472392	1.071967185
SFRP2	0.007580631	-5.280812359
CAPN6	0.00761542	1.520266783
LLGL2	0.007645449	-1.428859183
FZD10-AS1	0.008106919	-3.666596253
MEGF10	0.008223179	-1.986911534
MYO1G	0.008340332	-1.201688877
MYBL2	0.00858138	-2.743547159
C1orf61	0.009099442	-1.29755049
MAB21L1	0.009179185	-3.653439571
PENK	0.009351807	1.114326312
ARID5A	0.009577178	-1.237407472
LINC01896	0.009617587	-3.906136867
FAM237A	0.009687916	1.514345613
CALB1	0.009821188	-1.731154338
COL9A3	0.010142245	-1.198880832
FGFR1	0.010296887	-1.459424909
AC104009.1	0.01036998	-2.768249672
PLPP4	0.010370848	-1.829681654
TNFAIP8	0.010370848	-1.532842681
IKBKGP1	0.010797195	-1.534355361
LRRC55	0.010840871	-1.114285602
A2M-AS1	0.011186693	1.604643618
RPA4	0.011200645	1.444070618

IRX4	0.011271713	-2.31159822
FEZF1-AS1	0.011271713	-1.709529382
FZD2	0.011321196	-1.794974623
SEMA6A	0.011355562	-1.304148228
CLEC4GP1	0.011608865	1.480500661
NUGGC	0.011608865	2.257485436
DRD1	0.011662513	1.401682902
GLP1R	0.011667625	-1.31149312
NPTX2	0.011732054	-1.257694392
LINC01239	0.012010895	-2.909767231
AC006453.2	0.012047678	-1.739948146
MYOT	0.012082674	1.216900544
FZD10	0.012275397	-6.803103502
AC026356.1	0.01254314	-1.252338828
SALL1	0.012694082	-1.638353755
HOXB4	0.012754058	-7.398108823
EXPH5	0.012817468	-1.325314658
UNCX	0.012861738	-3.01073111
TECRL	0.012941093	3.069684668
DOCK6	0.012973078	-1.665479173
AC092614.1	0.013018842	-1.538242276
FGFR2	0.013496437	-1.435008289
PRND	0.013750904	-2.897815835
AC008591.1	0.013750904	1.05680891
GCNA	0.013758316	-1.343731536
NOG	0.014072482	-1.654926021
TGFB2-AS1	0.014577841	-1.556085597
UNC5B-AS1	0.014818752	-1.626769348
PGGHG	0.014818752	-1.381978486
LINC00504	0.014924776	1.324755978
NOTCH1	0.014975654	-4.495595263
GBP2	0.015081395	-1.646078284
LINC02003	0.015241659	-2.289045211
SOX21	0.015341834	-5.66391197
ADAMTS18	0.015341834	-2.054412967
SEMA5A	0.01563259	-1.280385726
IRX3	0.015905249	-2.896084251
HIST1H4E	0.016138886	-1.400339259
FRMD6	0.016279447	-1.573002926

TBX15	0.016299413	-1.993463492
CREB5	0.016336246	-1.064806353
ITGA5	0.016999897	-1.161120323
FOXE1	0.017597407	-1.604220796
FAM129A	0.017737245	1.327346431
PCSK9	0.017865432	-2.799059816
UGT3A2	0.018196978	1.500293539
IAPP	0.018318833	-1.829305771
SATB1	0.018631644	-1.437427536
RFX4	0.018884245	-3.418444887
COL1A1	0.018884245	-1.109601944
SPAG6	0.018983317	-1.98740337
LINC00645	0.018983317	-1.625097021
ACTC1	0.019050327	-1.613975864
NID1	0.019083326	-1.709859217
PAUPAR	0.019582923	-1.718495824
ITPR2	0.019701785	-1.16419113
PTCHD1-AS	0.019701785	1.248822249
CD274	0.019777586	1.04301794
EMILIN2	0.019896857	-1.495571042
DPY19L1	0.019987887	-1.224925737
MIR1-1HG-AS1	0.019990858	1.223678869
KCNG3	0.020488833	1.126261421
PPP1R17	0.0207956	-2.241140845
TMEM123	0.021117598	-1.50271949
LINC01605	0.021432622	-2.015591985
LUZP2	0.021620733	-1.058504511
TGIF1	0.023007926	-2.432802244
ZFPM2-AS1	0.023302526	-1.791857122
TMIE	0.023454685	-1.078373963
KIAA1211L	0.023566002	-2.541367546
FBXO40	0.023999177	1.097318413
HLA-G	0.024648792	-1.439690615
TOP2A	0.024701634	-3.748510248
MEG8	0.024867763	-1.346583479
ARHGEF26	0.025227573	-2.123491214
SASH1	0.025398279	-1.137563903
NECTIN4	0.025542925	-1.741976343
EPAS1	0.025822037	-1.497839245

GIPC3	0.025824269	-1.72694072
PRTG	0.026171027	-3.826257426
AC092666.2	0.026200913	1.121023592
CHRD	0.026275614	-1.165407453
IL11	0.026491012	-1.054916347
EFS	0.026603461	-1.421462745
LY6G6C	0.026967966	-1.132100549
LPAR1	0.027102085	-1.447541182
UHRF1	0.027264547	-1.336206125
PAX3	0.027317945	-3.576329746
ADA	0.027320586	-1.179891129
PROKR1	0.027418541	-3.385782576
GAS1	0.027673865	-1.640097849
ARHGAP42	0.027673865	-1.322786133
PDGFD	0.027912585	-1.234813643
FOXI3	0.028053894	-1.86798354
NPFFR2	0.028053894	-1.312725544
SLC19A3	0.028053894	1.210306693
PBK	0.028194465	-3.713080037
AP000894.4	0.028295979	-1.130049132
IGF1	0.028885397	-2.202876334
AC004947.1	0.028885397	-1.852377448
ANXA1	0.029286099	-2.111655445
VWC2L	0.02955797	-2.081148954
PKD1L2	0.029879365	-1.75170394
AC105118.1	0.030158158	-1.258400623
TRIM55	0.030220249	-3.029997465
FAM19A1	0.030592159	-4.339220021
E2F7	0.030656595	-1.993227221
MT-TR	0.030799709	1.283578691
CTDSP1	0.030846427	-1.244469827
CKAP2L	0.031425354	-1.958290244
CLDN5	0.031934873	-2.111809863
CTGF	0.031934873	-1.080339168
AC012507.2	0.031934873	1.016110121
AL672207.1	0.03197429	1.18751326
NFATC1	0.033498525	-1.90790383
AL118522.1	0.033614214	-2.272432139
AC009166.2	0.033660008	-2.869475109

UBE2C	0.034188339	-1.932109574
RASGRP3	0.034198749	1.094112377
IQGAP2	0.034200991	-1.085154528
CADPS2	0.034626072	-2.219164856
KLRD1	0.034626072	-1.621597596
LINC01068	0.034626072	-1.447240681
ABCB1	0.034626072	-1.369745919
LIMS2	0.034626072	1.15277745
LINC00629	0.034702391	-2.037936477
RNASE1	0.034702391	-1.962705787
AC009812.3	0.035172554	-1.277091387
CNTN4	0.03532828	-1.28773671
CNGA3	0.035527882	-2.315692253
ANKRD33B	0.035758506	-1.585721867
TEAD2	0.03587916	-4.509414014
LIN28A	0.03587916	-3.005780061
CXCL12	0.03587916	-1.915795276
EPHB4	0.03587916	-1.720765976
ITGAL	0.03587916	-1.592831383
TCIM	0.036095046	-1.771605515
TGFBR3	0.037366032	-3.715816606
MEGF11	0.037366032	-2.208675801
MAGEA6	0.037992145	-2.842370683
LINC01508	0.038056583	1.102493277
PLAT	0.038347601	-2.158948345
AC106881.1	0.038573051	-1.583187411
ATAD3C	0.038573051	-1.375251507
SOCS1	0.038647697	-1.178317755
FSTL1	0.038808267	-2.663805842
GPRC5D-AS1	0.038946709	1.790545165
LINC01694	0.039589583	1.397730405
FOXM1	0.04023887	-1.345872156
DHX58	0.04023887	-1.111852481
GPR88	0.04023887	1.212654174
RPLP0P2	0.040287682	-1.44514692
PNPO	0.041142205	1.042994252
CDH17	0.041337285	-2.037768669
AC012594.1	0.042124918	2.110069742
KLF5	0.042176508	-1.041321474

TRIM29	0.042176508	1.991686074
ALDH1A3	0.043112245	-1.023201183
AC078923.1	0.043112245	1.160597677
FAM111A	0.043272424	-2.351797058
CYP4F26P	0.043475746	1.723268872
HS3ST4	0.043645708	1.335227584
LHX1	0.043936147	-2.472490351
PROX1	0.044289625	-1.401983105
ASPM	0.044344178	-1.319658897
TTC34	0.044409516	1.138118219
TRPC6	0.044449914	-2.176478448
AC009318.4	0.044726601	1.174854715
RTL1	0.04477688	-1.815576273
SPON1	0.04477688	-1.201918015
AVPR1A	0.04480433	-1.232763088
TKTL1	0.044882609	-1.667331431
AC233702.4	0.045136834	-6.65325406
CENPF	0.04525219	-2.976722486
CRABP1	0.046061232	-1.416778126
LINC01317	0.046221785	-1.789407652
AKAP2	0.046221785	1.23063093
C1orf226	0.046542646	-1.563789969
COL5A1	0.046770013	-2.658730036
MAPK15	0.046770013	-1.260200876
SATB2-AS1	0.047627728	-1.93661645
MYH2	0.047866403	-1.80533571
GTSE1	0.047866403	-1.714931687
RMST	0.047866403	-1.016511346
ZAR1	0.047866403	1.484223431
AC104964.3	0.047901465	-1.600786039
CNTNAP3B	0.04815433	-1.63386118
CDH12	0.048167262	-2.208271703
DOCK8	0.048540489	-2.167071622
LINC01201	0.048896224	1.114822909
KCP	0.049912841	-1.33022141
HD109 + Miglustat vs HD109		
EGR1	0.016215556	1.399371257
HD22 $^{ISO-109}$ + Miglustat vs HD22 $^{ISO-109}$		
ZBTB16	0.018850124	-1.158756718

HD109 + Miglustat vs HD22 ISO-109		
PTPRT	7.74737E-09	-7.129068431
AL021395.1	6.8441E-05	-6.046906654
FZD10-AS1	0.00231956	-5.747770943
AC136759.1	0.002486891	-4.80108947
TCHH	5.90517E-27	-4.667751453
HOXC4	0.046887758	-3.787650782
FAM111B	0.046960707	-2.355998755
CRABP1	0.048281505	-1.992260557
AGBL4	0.002781476	-1.873518374
PCDHGA10	3.64447E-15	-1.486046694
AC079154.1	0.018691322	-1.372021621
AL513318.2	0.029420036	-1.133664168
GEMIN8	0.000283298	1.066069006
EIF1AX	9.4688E-29	1.211429318
EIF1AXP1	1.63005E-16	1.223086335
CHRDL1	0.007081259	1.488649282
YBX2P1	0.048281505	1.661485269
AKR1C3	0.018691322	1.802554619
PRR15L	0.048281505	1.837293239
MAP3K13	3.68702E-21	2.23397789
MYO18B	2.58379E-07	2.392826363
CUZD1	0.048281505	2.456955134
GPRC5D-AS1	0.002541927	2.457593146
BNIP3P9	0.023399929	2.58576173
ADGRG5	2.13036E-20	3.512702077
AC020928.1	4.45654E-46	3.555403512
FAM24B	0.00231956	3.760072945
SLC5A8	0.02664236	5.852773858
EHHADH	7.20381E-66	6.058517085
NNAT	0.00231956	6.150417305

Appendix Table 1. Comparison list of differentially expressed genes

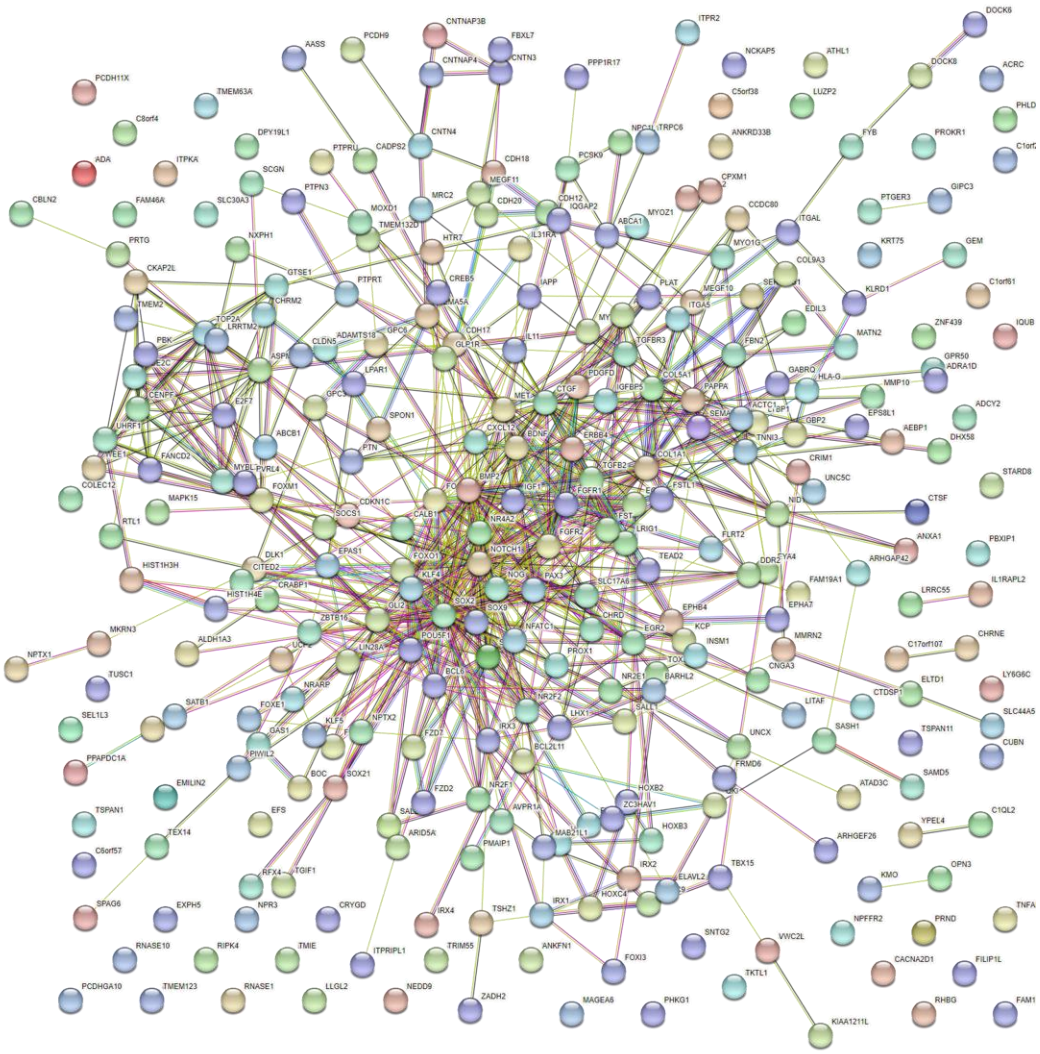

Appendix Figure 1. Protein-protein interactions of significantly down-regulated DEGs associated with HTT knockouts relative to isogenic controls. Interaction network generated using the STRING database; PPI enrichment p < 1.0e-16, full string network, line thickness represents evidence of interaction, with a minimum required interaction score of 0.4.

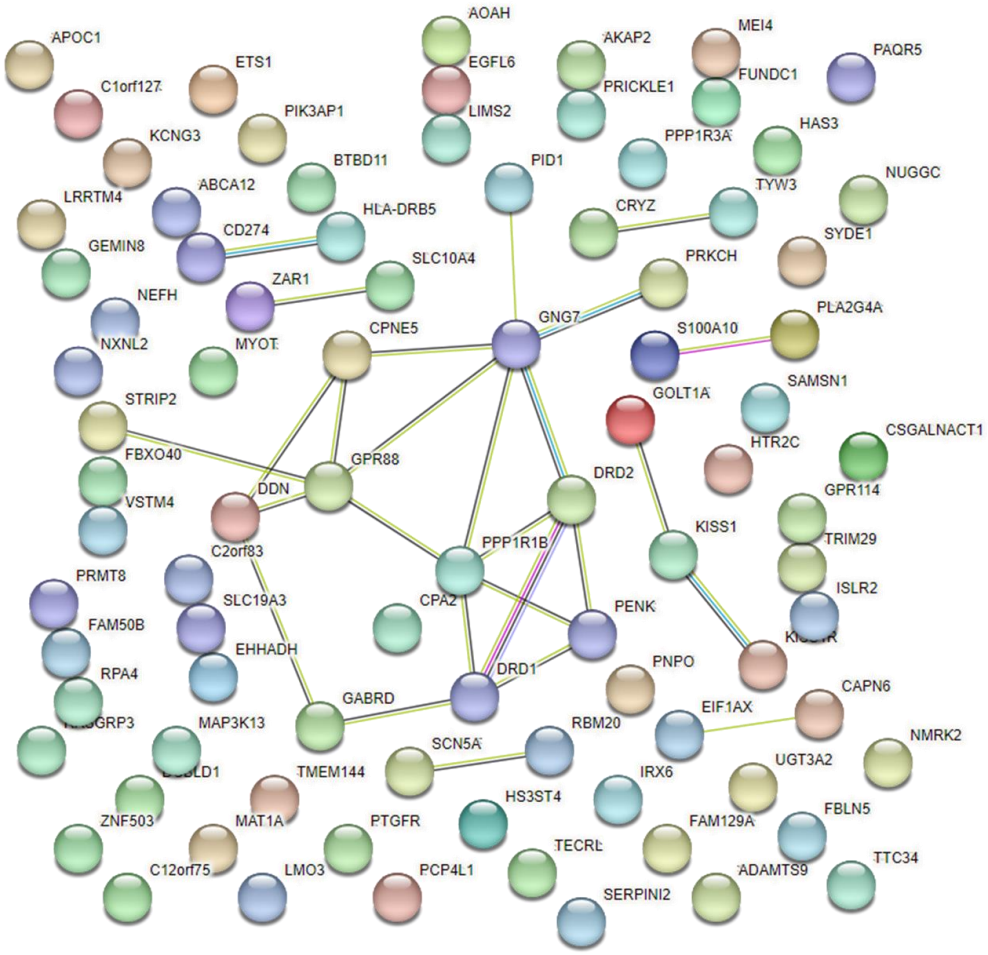

Appendix Figure 2. Protein-protein interactions of significantly up-regulated DEGs associated with HTT knockout relative to isogenic controls. Interaction network generated using the STRING database; PPI enrichment p < 1.0e-16, full string network, line thickness represents evidence of interaction, with a minimum required interaction score of 0.4.